A. I. Ch. E. JOURNAL

MICAL ENGINEERING RESEARCH AND DEVELOPMENT / MARCH, 1960

THE UNIVERSITY OF MICHIGAN

MAR 28 1960

ENGINEERING LIBRARY

CONTENTS

Maximum Stable Droplets in Dispersoids	R. A. Mugele
Evaporation from Drops Containing Dissolved Solids	D. H. Charlesworth and W. R. Marshall, Jr.
The Application of Boundary-Layer Theory to Power-Law Pseudoplastic Fluids: Similar Solutions	W. R. Schowalter
Heat and Mass Transfer in Spray Drying	Jan Dlouhy and W. H. Gauvin
The Effect of Dynamic Surface Tension on Nucleate Boiling Coefficients	P. D. Jontz and J. E. Myers
Thermodynamic Behavior of Hydrogen-Hydrocarbon Mixtures	R. L. Motard and E. I. Organick
The Constant-Volume Heat Capacities of Gaseous Perfluorocyclobutane and Propylene	Noel De Nevers and Joseph J. Martin
The Critical Constants of the Elements	David S. Gates and George Thodos
Effect of a Cylindrical Boundary on a Fixed Rigid Sphere in a Moving Viscous Fluid	A. M. Fayon and John Happel
Centrifugal Filtration Through Beds of Small Spheres	J. B. Bingeman and Jesse Coates
Thermal Conductivity of Packed Beds	William Schotte
Calculation of Equilibrium Flash Vaporization Curves by an Integration Method	C. O. Bennett, C. J. Brasket, and J. W. Tierney
Heat Transfer Characteristics of Porous Rocks	Daizo Kunii and J. M. Smith
Hypothetical Standard States and the Thermodynamics of High-Pressure Phase Equilibria	J. M. Prausnitz
The Effects of Superheat and Surface Roughness on Boiling Coefficients	H. M. Kurihara and J. E. Myers
Detonation Characteristics of Hydrogen-Oxygen Mixtures	Morton P. Moyle, Richard B. Morrison, and Stuart W. Churchill
Studies on Heat Transfer Near Wall Surface in Packed Beds	Sakae Yagi and Daizo Kunii
Thermodynamic Consistency of Binary Liquid-Vapor Equilibrium Data When One Component Is Above Its Critical Temperature	S. B. Adler, Leo Friend, R. L. Pigford, and G. M. Rosselli
Flow Patterns in Agitated Vessels	A. B. Metzner and J. S. Taylor
Density Fluctuations in Fluidized Beds	P. K. Baumgarten and R. L. Pigford
Mechanics of Particle Bounce	W. E. Ranz, G. R. Talandis, and Bernard Gutterman
Compressibility and Vapor Pressure of Methyl Borate	Richard G. Griskey, Walter E. Gorgas, and Lawrence N. Canjar
The Motion of Two Spheres Following Each Other in a Viscous Fluid	John Happel and Robert Pfeffer
Photographic Study of Solid-Gas Fluidization	Leopoldo Massimilla and J. W. Westwater
Mass Transfer in Liquid-Lithium Systems	William N. Gill, Richard P. Vanek, Robert V. Jelinek, and C. S. Grove, Jr.
Mass Transfer Inside Drops	A. I. Johnson and A. E. Hamielec
Compression of Liquids	
I. Apparatus and Method of Measurement	Arthur K. Doolittle, Ivan Simon, and Raymond M. Cornish
II. Critical Evaluation of New *n*-Alkane Data: *n*-Heptane to *n*-Tetracontane	Arthur K. Doolittle and Dortha B. Doolittle
mperature and Molecular Weight Dependence of the Hudleston Parameters for the *n*-Alkanes	Arthur K. Doolittle and Dortha B. Doolittle
Temperature Measurements in a Spherical Field	
Transfer Coefficients and Corrections for Thermocouples in Boundary Flows	W. W. Short and B. H. Sage
On the Separation of Gas Mixtures in a Jet	Earl E. Gose

From Vulcan-Cincinnati

a new evaporator for the concentration of heat-sensitive materials

The Stora-Vulcan Evaporator—an important new concept in the design of evaporation equipment for heat-sensitive materials—offers you improved product quality, low maintenance costs, minimum utilities consumption, and minimum capital investment. Here's why:

- Unusually low retention time minimizes thermal degradation of heat-sensitive materials.
- Highly turbulent action—with resulting high heat transfer coefficients—is achieved without the use of agitation equipment requiring close mechanical tolerances.
- Channeling of process liquids, and non-uniform wetting of heat transfer surfaces, are prevented by centrifugal re-distribution at frequent intervals.
- Efficient contact between liquid and vapor (or gas) assures high mass transfer rates in stripping operations, and when the evaporation process is augmented by the use of an inert carrier.

These are just a few of the reasons why the Stora-Vulcan Evaporator is ideal for the efficient evaporation or concentration of urea melt, tall oil and fatty acids, ammonium nitrate melt, plasticizers, monomers and polymers, as well as other heat-senstive liquids.

If you'd like to know more about the Stora-Vulcan Evaporator—and how it can help solve your processing problems—write Vulcan today.

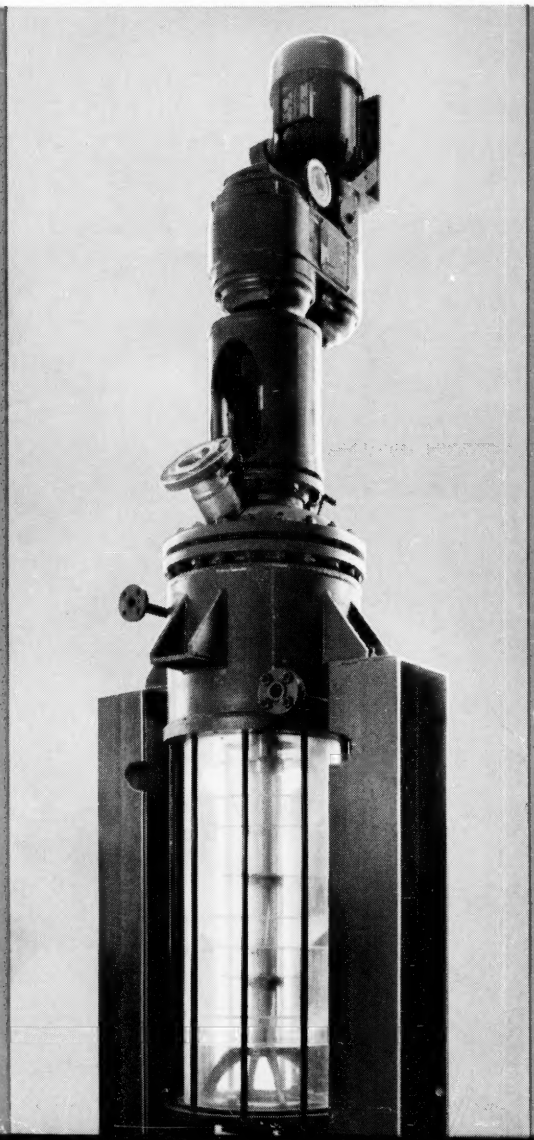

Experimental hydraulic studies are conducted in this test model Stora-Vulcan Evaporator.

VULCAN-Cincinnati, Inc.
ENGINEERS AND CONSTRUCTORS • 120 Sycamore St., Cincinnati 2, Ohio

A.I.Ch.E. JOURNAL

MARCH, 1960 • VOL. 6, NO. 1

The A.I.Ch.E. Journal, an official publication of the American Institute of Chemical Engineers, is devoted in the main to theoretical developments and research in chemical engineering and allied branches of engineering and science. Manuscripts should be submitted to the New York office.

PUBLISHER
F. J. Van Antwerpen

EDITOR
Harding Bliss

ASSISTANT PUBLISHER
L. T. Dupree

MANAGING EDITOR
Sylvia Fourdrinier

ADVERTISING MANAGER
P. A. Jolcuvar

ADVISORY BOARD

C. M. Cooper	R. H. Newton
O. E. Dwyer	R. L. Pigford
W. C. Edmister	E. L. Piret
E. R. Gilliland	J. M. Smith
A. N. Hixson	Theodore Vermeulen
H. F. Johnstone	R. R. White
W. R. Marshall, Jr.	R. H. Wilhelm

Publication Office, 215 Canal Street, Manchester, New Hampshire. Published quarterly in March, June, September, and December by the American Institute of Chemical Engineers, 25 West 45 Street, New York 36, New York. Manuscripts and other communications should be sent to the New York office. Correspondence with the editor may be addressed to him at Yale University, 225 Prospect Street, New Haven 11, Connecticut. Statements and opinions in the *A.I.Ch.E. Journal* are those of the contributors, and the American Institute of Chemical Engineers assumes no responsibility for them. Subscriptions: one year, member $6.00; nonmember $12.00; industrial libraries $25.00; additional yearly postage, Canada 50 cents, Pan American Union $1.50, other foreign $2.00 (foreign subscriptions payable in advance). Single copies: $4.00. Second-class mail. Postage paid at Manchester, New Hampshire.

Copyright 1960 by the American Institute of Chemical Engineers.

National headquarters of A.I.Ch.E. is concerned about nondelivery of copies of the *A.I.Ch.E. Journal* and urgently requests subscribers to give prompt notification of any change of address. Sixty days must be allowed for changes to be made in the records.

Conservation and Engineering: III. Food Problems 1
Maximum Stable Droplets in Dispersoids ..... *R. A. Mugele* 3
Evaporation from Drops Containing Dissolved Solids
D. H. Charlesworth and W. R. Marshall, Jr. 9
The Application of Boundary-Layer Theory to Power-Law Pseudoplastic Fluids: Similar Solutions ..... *W. R. Schowalter* 24
Heat and Mass Transfer in Spray Drying ..... *Jan Dlouhy and W. H. Gauvin* 29
The Effect of Dynamic Surface Tension on Nucleate Boiling Coefficients
P. D. Jontz and J. E. Myers 34
Thermodynamic Behavior of Hydrogen-Hydrocarbon Mixtures
R. L. Motard and E. I. Organick 39
The Constant-Volume Heat Capacities of Gaseous Perfluorocyclobutane and Propylene ..... *Noel De Nevers and Joseph J. Martin* 43
The Critical Constants of the Elements .... *David S. Gates and George Thodos* 50
Effect of a Cylindrical Boundary on a Fixed Rigid Sphere in a Moving Viscous Fluid ..... *A. M. Fayon and John Happel* 55
Centrifugal Filtration Through Beds of Small Spheres
J. B. Bingeman and Jesse Coates 58
Thermal Conductivity of Packed Beds ..... *William Schotte* 63
Calculation of Equilibrium Flash Vaporization Curves by an Integration Method ..... *C. O. Bennett, C. J. Brasket, and J. W. Tierney* 67
Heat Transfer Characteristics of Porous Rocks .... *Daizo Kunii and J. M. Smith* 71
Hypothetical Standard States and the Thermodynamics of High-Pressure Phase Equilibria ..... *J. M. Prausnitz* 78
The Effects of Superheat and Surface Roughness on Boiling Coefficients
H. M. Kurihara and J. E. Myers 83
Detonation Characteristics of Hydrogen-Oxygen Mixtures
Morton P. Moyle, Richard B. Morrison, and Stuart W. Churchill 92
Studies on Heat Transfer Near Wall Surface in Packed Beds
Sakae Yagi and Daizo Kunii 97
Thermodynamic Consistency of Binary Liquid-Vapor Equilibrium Data When One Component Is Above Its Critical Temperature
S. B. Adler, Leo Friend, R. L. Pigford, and G. M. Rosselli 104
Flow Patterns in Agitated Vessels ..... *A. B. Metzner and J. S. Taylor* 109
Density Fluctuations in Fluidized Beds .... *P. K. Baumgarten and R. L. Pigford* 115
Mechanics of Particle Bounce
W. E. Ranz, G. R. Talandis, and Bernard Gutterman 124
Compressibility and Vapor Pressure of Methyl Borate
Richard G. Griskey, Walter E. Gorgas, and Lawrence N. Canjar 128
The Motion of Two Spheres Following Each Other in a Viscous Fluid
John Happel and Robert Pfeffer 129
Photographic Study of Solid-Gas Fluidization
Leopoldo Massimilla and J. W. Westwater 134
Mass Transfer in Liquid-Lithium Systems
William N. Gill, Richard P. Vanek, Robert V. Jelinek, and C. S. Grove, Jr. 139
Mass Transfer Inside Drops ..... *A. I. Johnson and A. E. Hamielec* 145
Compression of Liquids
I. Apparatus and Method of Measurement ..... *Arthur K. Doolittle, Ivan Simon, and Raymond M. Cornish* 150
II. Critical Evaluation of New *n*-Alkane Data: *n*-Heptane to *n*-Tetracontane
Arthur K. Doolittle and Dortha B. Doolittle 153
III. Temperature and Molecular Weight Dependence of the Hudleston Parameters for the *n*-Alkanes
Arthur K. Doolittle and Dortha B. Doolittle 157
Temperature Measurements in a Spherical Field: Transfer Coefficients and Corrections for Thermocouples in Boundary Flows
W. W. Short and B. H. Sage 163
On the Separation of Gas Mixtures in a Jet ..... *Earl E. Gose* 168
Communications to the Editor
Japanese Translations ..... *Robert S. Schechter and Eugene H. Wissler* 170
Pseudocritical Constants for Gas Mixtures ..... *L. C. Case and H. C. Weber* 171
A Distribution Function for Oil Mixtures and Polymers ..... *Otto Redlich* 173
Liquid-side Mass Transfer Coefficients in Packed Towers
H. L. Shulman, Stanley Press, and W. G. Whitehouse 174
Abstracts 176
Symposium Series 3M
Computer Interchange Program .....

new... **HEVI-DUTY**

CIRC-O-THERM OVEN

Temperatures to 250° C. (480° F.)

Improved Temperature Uniformity. With Hevi-Duty's "circle-of heat" design, there are *no cold corners.*

Fast Heat-Up. To 200° C. in less than one hour.

Low-Cost Operation on either 115 or 230 volts. Selector switch permits high or low input to enclosed heating elements.

Durable Double-Wall Construction. Steel outer shell is prime coated on both sides to prevent corrosion.

Accurate Temperature Control by sensitive bulb-type thermostat permits little lag or overshoot.

For complete information, write for Bulletin 458.

Model	Price	Chamber Size		Watts	Volts	Overall Dimensions			Shipping Weight
		Diameter	Depth			Width	Depth	Height	
HK	$169.	15	13	600	115/230	20	18	23	80
HL	$265.	20	18	1000	115	25	23	28	100

FOR GENERAL AND SPECIALIZED LABORATORY APPLICATIONS

HEVI-DUTY "Multiple Unit" TUBE TYPE COMBUSTION FURNACES

in Two Temperature Ranges, 1850° F. or 2200° F.

Hevi-Duty Combustion Tube Furnaces are available in either the split* (illustrated) or solid type and can be used horizontally or modified for vertical operation. Long-life "Multiple Unit" brand heating units offer fast heat-up because the heat is radiated directly into the heating chamber. The heated length may be divided for zone temperature control which gives greater temperature uniformity over a specified length. A few of the standard furnaces are shown below. Many sizes are in stock. Special sizes with diameters up to 16 inches can be built to your specifications.

*5-in. and smaller diameters are hinged.

HINGED-TYPE TUBE FURNACE FOR 1850° F.					
TYPE	CHAMBER		RATING WATTS	SHIPPING WEIGHT	PRICE
	DIA.	LENGTH			
70	1¼"	12"	750	35	$ 75.00
M-2012	2⅜"	12"	1400	90	$ 165.00
M-3024	3"	24"	3400	135	$ 250.00
M-5036	5"	36"	7500	325	$ 650.00
M-8040	8"	40"	14500	520	$1180.00

HEVI-DUTY

Write for Bulletin 552 for complete details.

A DIVISION OF BPC BASIC PRODUCTS CORPORATION

HEVI-DUTY ELECTRIC COMPANY, MILWAUKEE 1, WISCONSIN

Industrial Furnaces and Ovens, Electric and Fuel • Laboratory Furnaces • Dry Type Transformers • Constant Current Regulators

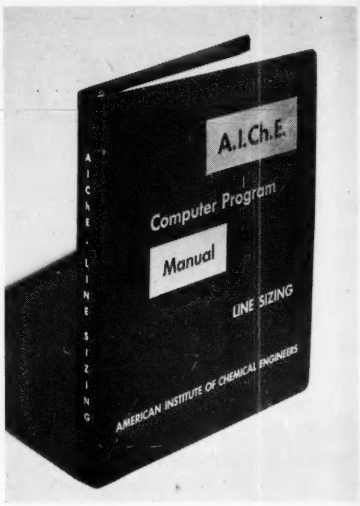

The first of the COMPUTER PROGRAM MANUALS

developed from the programs abstracted monthly in *Chemical Engineering Progress.*

LINE SIZING

Performs necessary calculations to convert the units of flow and density; to size liquid, vapor, or water lines on the basis of a specified maximum pressure drop; and to determine the pressure drop for a given diameter and length of pipe.

$30

AMERICAN INSTITUTE OF CHEMICAL ENGINEERS
25 West 45 Street
New York 36, New York

Please send _____ copies of the Line Sizing Manual. Our check for $_____ is enclosed. (Please add 3% sales tax for delivery in New York City)

PRINT Name _____

Company _____

Street _____

City _____ Zone _____ State _____

☐ Member ☐ Nonmember

☐ Check enclosed (add 3% sales tax for delivery in New York City)

☐ Bill me

J-3-60

Conservation and Engineering

III. Food Problems

It may seem absurd to write of food shortages when we read so much about the enormous farm surpluses and the staggering costs of maintaining and enlarging them. However, in the perspective of the population growth predicted for the next fifty years and beyond, these surpluses vanish. They are a drop in the bucket compared to world needs now; they are little more than our own present annual needs.

Supplying food for the burgeoning populations expected is a serious problem, and the prospect of its solution through science and technology is not very promising. Diversions of land may be made, as discussed in a previous editorial, but the increased acreage is small relative to our needs. Improvements may be made through cooperation among soil scientists, ecologists, and technologists in the development of better fertilizers and machinery, but such alleviation is minor.

The land available for food production in this country is plainly limited and is probably insufficient for the population to be expected unless we can increase the productivity of that land. Our production of food per acre is about half that of Western Europe and about one-fifth that of Japan. Obviously, then, we can increase our productivity but probably only in the way the West Europeans and Japanese have done. They have largely avoided the principal waste in which we indulge—the grazing of animals, particularly beef cattle. An ox consumes in a lifetime as many calories as do six and one-half men, but on butchering it yields only enough calories to keep one man going for 8 months. It is unhappily true that the best contribution we as engineers can make to this problem is the same as that to be made by housewives, lawyers, and politicians—all of us will have to learn to eat less meat.

There are, of course, some revolutionary proposals for the growth of foodstuff on our rooftops, in special factories, and in the ocean, and some real "advances" have been made here. Algae can be grown with high productivity per acre, and it is quite rich in protein. This observer must confess, however, a certain lack of zeal for this prospect. Rare, medium, or well-done, with or without A-1 sauce, even in the convivial company of one's best friends, "algae" steak is peculiarly uninviting. To paraphrase an old poem,

> Algy met a bear;
> The bear was bulgy.
> The bulge was not algae.

Wholly synthetic foods are, of course, possible, and it would seem essential that some scientific effort should be directed toward developing them. This, at least, has the potentiality (as in the case of fibers) of yielding vastly more "food" per acre than conventional methods or than algae culture. According to a perhaps apocryphal tale, the Germans during the last war found that although synthetic fats could be stored in the body, they were incapable of release, and so fattened animals could starve to death. If science could find out how synthetic "foods" could be made digestible, then such would appear to be a more promising approach than algae culture because of the highly effective productivity of factories and because such "food" could hardly be less attractive than algae.

These unhappy prospects are real, and they must be faced in time. Perhaps a little population control would be preferable. H. B.

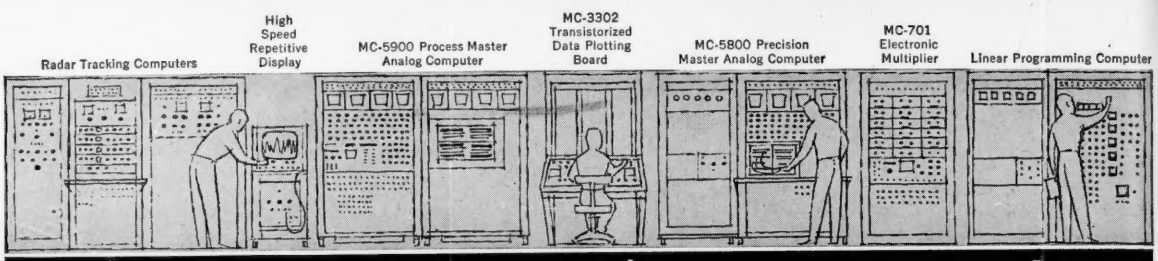
Radar Tracking Computers
High Speed Repetitive Display
MC-5900 Process Master Analog Computer
MC-3302 Transistorized Data Plotting Board
MC-5800 Precision Master Analog Computer
MC-701 Electronic Multiplier
Linear Programming Computer

DYSTAC

A NEW COMPUTER TECHNOLOGY

solving problems hitherto unsolvable

DYSTAC (Dynamic Storage Analog Computer) synthesizes the advantages of both analog and digital computers. DYSTAC combines the analog's speed, lower cost, ease of programming, and improved output data presentation with the digital computer's unique capacity for data storage and time sharing of computer elements. With DYSTAC you can now solve the most complex problems, ranging from distillation column design to multi-dimensional heat transfer... from boundary value problems to transport lags.

In distillation column design, for example, DYSTAC employs only 44 amplifiers on a four-component problem; the number of amplifiers required is independent of the number of plates. With any other analog computer each plate must be reproduced in the circuitry—for a 30-plate column, over 1200 amplifiers are needed unless manual reprogramming is employed. What's more, only DYSTAC yields a plate-by-plate display of all column conditions.

In heat transfer studies, DYSTAC will speedily and accurately solve hitherto unsolvable partial differential equations. It also makes practical for the first time instantaneous solutions to such trial-and-error problems as automatic optimization, automatic correlations, data fitting, probability distribution, Fourier analysis, convolution and superposition integrals and eigenvalue.

When you buy a CSI computer with DYSTAC you are buying more than the finest general purpose analog computer. You buy additional capacity as well as capability. For when DYSTAC elements are not in use as memory devices they are available to the computer as operational amplifiers. Planning to interconnect digital and analog computers? DYSTAC is the answer.

See DYSTAC in operation at our plant. If you can't attend a demonstration write, phone or wire for full information.

COMPUTER SYSTEMS, INC., 611 Broadway, New York 12, New York, SPring 7-4016

A Schlumberger Subsidiary • formerly Mid-Century Instrumatic Corp.

Maximum Stable Droplets in Dispersoids

R. A. MUGELE

Shell Development Company, Emeryville, California

Maximum stable droplet size in nonuniform dispersoids may be ignored or treated as a statistical-limiting parameter or as a physically significant quantity. In this paper the author shows that treatment as a physically significant quantity is always permissible and in most cases advantageous. It is found that maximum stable droplet size as well as mean droplet size can be calculated in some cases from theory and in other cases from correlated experimental data; this is illustrated with examples involving sprays and emulsions.

The importance of knowing something about particle sizes in dispersoids has often been noted (*4, 5, 15, 20*). But the importance of recognizing a maximum particle size is frequently overlooked; therefore, some evidence is presented that the acceptance of a maximum particle size is always permissible and in most cases advantageous. On the other hand the author indicates how the acceptance of a negligible fraction of infinitely large particles may be misleading, giving wrong answers in certain theoretical calculations and process evaluations. In this paper particles are considered which are liquid droplets. In this case the maximum stable size (*MSD*) is such that it may not be exceeded by any droplet which is in equilibrium with the environment. Methods are proposed for calculating the maximum stable diameter, in some cases from theory, and in other cases from correlated experimental data.

BASIC CONCEPTS: SIZE DISTRIBUTION, STABILITY, MAXIMUM STABLE DROPLET

The distribution of particle sizes in dispersoids has been treated in various ways by various authors. We are only indirectly concerned here with the relative merits of these treatments. It has been found that a Gaussian distribution of a certain parameter y adequately represents size distributions of many dispersoids (*17*). This distribution is assumed to prevail whenever no other is specified.

The parameter y nas the form ln $a(x^s - x_o^s)/(x_m^s - x^s)$. Here a is a dimensionless skewness parameter ($a=1$ for symmetric distributions.) The exponent s is related to the manner of dispersion but is not especially critical in fitting the distribution to data. For the examples treated in this paper, $s=1$. The variable x is a linear measure of particle size (usually diameter, although any dimension proportional to diameter will do). The particular values x_o and x_m apply to the smallest and largest stable particle size that may exist in the dispersoid.

In some situations one is concerned with the minimum particle size, x_o. However these situations are rare, and for practical purposes x_o can usually be taken as zero (an approximation for a molecular diameter when compared with droplet sizes in ordinary aerosols, sprays, and emulsions).

However no such simple approximation is available for the maximum particle size. By analogy to the approximation $x_o = 0$, one might say $x_m = \infty$, but this can be quite misleading. More rationally one can think of a dispersoid in its proper environment and calculate (either from correlation or theory) a maximum stable size, using this as an approximation for x_m. As an example of such a calculation an idealized situation wherein a droplet is acted on only by the drag of a continuous medium is considered. When this drag overcomes the molecular force field at the interface, the droplet becomes unstable and bursts. Thus its maximum stable size is governed by the force balance

$$C_D \cdot \frac{1}{2}\rho_c V^2 \cdot \frac{\pi}{4} x_m^2 = \pi x_m \cdot \sigma \quad (1)$$

Hence

$$x_m = 8\sigma/C_D\rho_c V^2 \quad (2)$$

This relation may also be expressed by the definition of a critical Weber number:

$$We_m = x_m\rho_c V^2/\sigma = 8/C_D \quad (3)$$

In the following sections the processes of mechanical atomization and mechanical emulsification are examined. Correlations for size of the mean droplet in a spray and also for the maximum stable droplet are developed. For completeness in representing the size distribution, values of the sharpness parameter are also deduced for some types of atomizers.

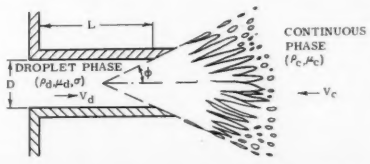

Fig. 1. Atomization variables (schematic).

THE PROCESS OF ATOMIZATION

The term *atomization* is used in its usual sense of breakup of bulk liquid into droplets. Mechanical atomization is achieved in many different ways. Among the devices commonly employed are pressure nozzles, Venturi or gas-atomizing nozzles, rotating cups or disks, and bubble caps or grids or perforated plates.

Although details of the drop forming process vary widely among the different types of apparatus, certain events normally occur in all of these processes:

1. The applied force, whether due to pressure or rotation, separates protuberances, filaments, or sheets of liquid from the bulk liquid.
2. These protuberances, filaments, or sheets are broken up (owing to their inherent instability and to interaction with a mass of gas or liquid) into small particles.
3. These particles assume spherical shape if they are small enough. Or, if large enough to be unstable, they break

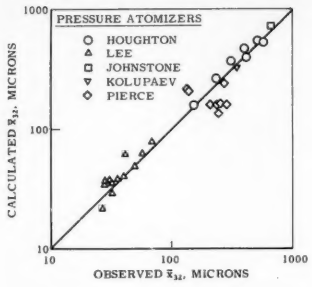

Fig. 2. Comparison of experimental and calculated values of $\bar{x}_{32}$ (pressure nozzles).

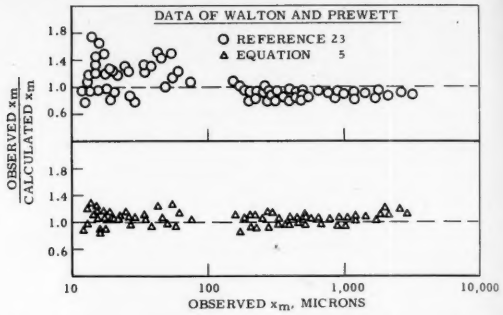

Fig. 4. Comparison of experimental and calculated values of x_m (spinning disks).

into smaller masses which then become spherical.

A detailed treatment of the motions of droplets is not part of the present subject but may be found in references *10* and *1*.

FUNDAMENTAL VARIABLES IN ATOMIZATION

The average size of droplets in a spray, as well as the distribution of droplet sizes, will depend on certain physical properties of the fluids involved, on design of the atomizer, and on operating conditions. The relevant physical properties include ρ_d *and* ρ_c, μ_d and μ_c, and σ.

The relevant design variables are not easily stated in general terms because of the wide variety of spray generators to be considered. For the majority of atomizers D, L, and ϕ will suffice.

The relevant operating conditions again will depend on the particular type of atomizer used. For example the important variables may appear as pressures (for a pressure nozzle), volume flow rates (for a Venturi nozzle), or angular velocity (for a rotating cup). But generally by the use of mechanical and hydrodynamic relations these may be reduced to V_d and V_c, or V, and β. Fundamental variables are illustrated schematically in Figure 1.

GENERAL CORRELATING EQUATION FOR ATOMIZATION

Having considered the fundamental variables which determine the droplet-size distribution in atomization one proceeds to investigate their relation to the representative droplet size in the resulting spray.

Dimensional analysis indicates that the following dimensionless groups are sufficient to describe this relation: the size ratios $\bar{x}/D$ and $\bar{x}/L$ and the design angle ϕ, the Froude number $V^2/D\beta$, the Reynolds numbers $D\rho_c V_c/\mu_c$ and $D\rho_d V_c/\mu_d$, the interfacial-tension groups $\mu_c V_c/\sigma$ *and* $\mu_d V_d/\sigma$, and the density ratio ρ_c/ρ_d.

A simple form in which the most general relation between these groups may be written is

$$f\left(\frac{\bar{x}}{D}, \frac{V_d^2}{D\beta}, \frac{L}{D}, \phi, \frac{D\rho_d V_d}{\mu_d}, \frac{\mu_d V_d}{\sigma}, \frac{\rho_c}{\rho_d}, \frac{\mu_c}{\mu_d}, \frac{V_c}{V_d}\right) = 0 \qquad (4)$$

In this equation the representative size may be one of the mean diameters (*17*), the median diameter, or the maximum diameter. The form of the function will vary according to which of these diameters one chooses. In general at least three independent diameters are needed to define the distribution completely (for example $\bar{x}_{32}$, x_m, and x_{50}). But if one has an independent method for determining one of the distribution parameters, two of the diameters may suffice. In this paper $\bar{x}_{32}$ and x_m are individually correlated, and the distribution parameter δ [Equation (8) and reference *17*] is tabulated for certain types of atomizers. Concerning the distribution parameters, one notes that even more than three might sometimes be needed, because of the complex nature of the dispersion mechanism, not merely because of the form of the distribution equation.

CORRELATION OF MAXIMUM AND MEAN DROPLET SIZES FOR ATOMIZATION IN PRESENCE OF GASES

Equation (*4*) shows the dimensionless groups found to affect x_m or $\bar{x}_{32}$. Most atomization data have been obtained by dispersing liquid into gases not greatly different from atmospheric air. Thus the effect of continuous-phase properties (that is, the groups ρ_c/ρ_d and μ_c/μ_d) on drop size is less clearly defined than is the effect of other dimensionless groups involving only dispersed-phase properties. For this reason the correlations of x_m and $\bar{x}_{32}$ discussed

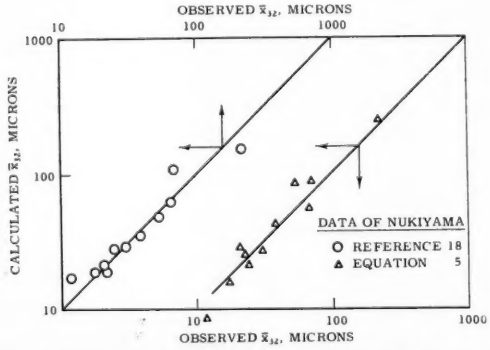

Fig. 3. Comparison of experimental and calculated values of $\bar{x}_{32}$ (Venturi atomizers).

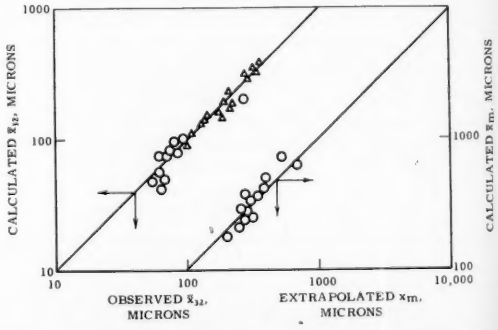

Fig. 5. Comparison of experimental and calculated values of $\bar{x}_{32}$ and x_m (effective diameter method).

TABLE 1. SUMMARY OF CONSTANTS TO BE USED IN ESTIMATING DROP SIZE DISTRIBUTION

Type of atomizer	Calculation of $\bar{x}_{32}$* A	B	C	Standard deviation, %	Calculation of x_m* A_m	B_m	C_m	Standard deviation, %
Straight pressure or** tangential nozzle	5.0	−0.35	−0.20	22	57	−0.48	−0.18	34
Venturi atomizer††	1140	−0.82	−0.45	30				
Modified pressure nozzles** (pintle, lip, impinging jet, etc.)†	5.0	−0.35	−0.20	30	57	−0.48	−0.18	22
Spinning disks or cups	—	—	—	—	1.73	−0.50	−0.45	15
Whirl chambers	5.0	−0.35	−0.20	26	57	−0.48	−0.18	42

* Constants A, B, and C for use in the equation $\frac{\bar{x}}{D} = A\left[\frac{D\rho_d V}{\mu_d}\right]^B \left[\frac{\mu_d V}{\sigma}\right]^C$.

** V_d calculated from Equation (6); D calculated from Equation (7).

† For pictures of these and other atomizers see references 5 and 9.

†† Values apply for Venturi atomizers only when volumetric ratio of liquid to vapor rate $Q_d/Q_c \leq 0.0001$.

in this paper are recommended only for atomization into gases having about the same viscosity and density as atmospheric air.

The few experimental data available indicate that the groups L/D and ϕ have little effect on drop sizes. These groups have been neglected in the present correlations. In addition, no detectable effect of Froude number was found in correlation of the data. After elimination of the above groups the following equation has been devised for the calculation of $\bar{x}_{32}$ or x_m for atomization into air:

$$\frac{\bar{x}}{D} = A\left[\frac{D\rho_d V}{\mu_d}\right]^B \left[\frac{\mu_c V}{\sigma}\right]^C \qquad (5)$$

It is interesting to note that the correlations or theories of Hinze (6), Milborn (8), and Walton and Prewett (23) also lead to these same dimensionless groups when continuous phase properties are neglected.

Constants for Equation (5) have been evaluated from experimental data for a number of different atomizer types and are shown in Table 1. Values of x_m used in obtaining the above correlation were calculated from distribution data by the use of the upper-limit method of Mugele and Evans (17). Fewer data are available for x_m than for $\bar{x}_{32}$, since some authors reported only $\bar{x}_{32}$ without giving the distribution data necessary to calculate x_m. For this reason correlation of x_m is considered less reliable than correlation of $\bar{x}_{32}$.

The relative velocity between phases, V rather than V_d, has been required for use in Equation (5) to correlate the experimental data. Relative velocity has also been used for correlation purposes by Merrington and Richardson (16) and Nukiyama and Tanasawa (18). For spinning atomizers the peripheral velocity $D\omega/2$ should be used for dispersed-phase velocity. For atomizer types other than those shown in Table 1, V_d can be calculated from

$$V_d = C_o\sqrt{2\Delta p/\rho_d} \qquad (6)$$

In this equation Δp is meant to be the pressure drop corresponding to energy which is directed toward breakup of the bulk liquid. If certain turns, constrictions, baffles, etc., produce friction before the liquid reaches the atomizing zone, the pressure losses so produced should be estimated and subtracted from the over-all pressure drop to determine Δp. On the other hand, if a whirl chamber or rotor contributes to turbulence in the bulk liquid and hence to instability which persists until breakup, then a corresponding pressure loss is properly part of Δp. Pressure losses across nozzles, as reported in the literature, are ordinarily close enough to Δp to be used without modification. There is some question about the use of the orifice velocity as in Equation (6), when actually the vena-contracta velocity may be more appropriate to conditions in jet breakup. Since this question has not been resolved with the available data, the best suggestion for the present is that V_d of Equation (6) be regarded as an effective velocity which merely interprets the effect of Δp.

If the effective discharge coefficient is unknown, a value of 0.7 is recommended. In cases where continuous-phase velocity is important, it must be estimated from flow or pressure-drop considerations. It should be noted that no continuous-phase velocity should be used when this velocity is created by flow of the dispersed phase, that is, by surface drag.

For spinning atomizers the representative diameter D to be used in Equation (5) is the outer diameter of the spinning part. For pressure or Venturi atomizers it is the orifice diameter (or hydraulic diameter) of the liquid disperser. If the geometry of the spray generator is complicated by interior grooves, vanes, multiple inlets, or pintles (or for the swirl type of atomizers which have an air cone), D cannot be calculated as readily. However it has been found that the effective diameters for use in Equation (5) can be calculated from Equation (7) if the volumetric flow and pressure drop are known:

$$D = \sqrt{4Q_d/\pi V_d} \qquad (7)$$

where V_d is calculated from Equation (6).

THE UNIFORMITY PARAMETER

The parameter δ is a measure of uniformity of the spray, a larger value of δ indicating a more uniform spray. Various attempts to correlate δ have failed to produce a general correlation with atomizer dimensions. Table 2 shows the range of values of δ found in various atomizer types together with recommended values. For further discussion of the parameter the reader should consult reference 17. The defining equation for δ is

$$\frac{dv}{dy} = \frac{\delta}{\sqrt{\pi}} e^{-\delta^2 y^2} \qquad (8)$$

For atomizers not classified in Table 2 and for which specific data are not

TABLE 2

Atomizer type	Source of data	Range of δ	Recommended δ
Straight pressure nozzle	(11) (9)	0.618-0.670	0.64
Modified pressure nozzle (pintle, lip, impinging jet, etc.)	(21) (13)	0.861-1.108	0.98
Tangential nozzle (Spraco-T)	(9)	0.600-0.750	0.68
Rotating-cup atomizer	(8)	0.71 -1.11	1.00
Whirl-chamber atomizer	(12) (19)	1.134-1.145	1.14
Venturi atomizer (gas injection)	(14) (3)	1.03 -1.52	1.28

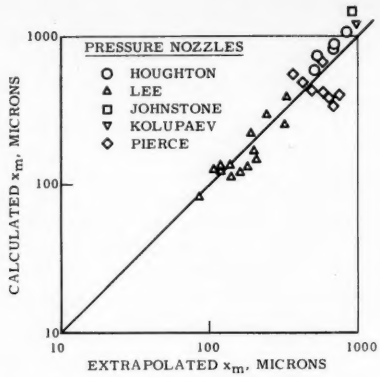

Fig. 6. Comparison of extrapolated and calculated values of x_m (pressure nozzles).

available the value $\delta = 1.00$ is suggested.

COMPARISON WITH EXPERIMENTAL DATA

Values of x_m and $\overline{x}_{32}$ calculated from Equation (5) by the use of values of constants shown in Table 1 are compared with experimental data in Figures 2 to 6. Some of these figures also show comparisons with other correlations. Standard deviations of data from correlation are included in Table 1. No general advantage is claimed for this correlation method over others. The author is aware of many recent and excellent presentations of spray data and correlations of various kinds, including those of references *15* and *20*. The calculations that have been presented here were made before the spray data became plentiful and will be revised to do justice to the recent data. However the foregoing calculations have been presented to illustrate the efficacy of separately correlating a mean droplet size and a maximum stable droplet size.

APPLICATION OF THE CORRELATIONS

Values of x_m, $\overline{x}_{32}$, and δ estimated from the correlations in this paper may be used to calculate the complete drop-size distribution resulting from various atomization conditions when continuous-phase viscosity and density do not differ appreciably from the values for atmospheric air. Sample calculations showing the application of the upper-limit method for calculating the complete distribution are shown later.

In many instances the complete drop-size distribution is not required, and the correlations may merely be used to estimate the trend of $\overline{x}_{32}$ or x_m with physical properties, apparatus design, or flow conditions. Thus even though absolute magnitude of predicted drop size may be in error, it is still possible to evaluate the effect of condition changes on drop size. This information is frequently useful in relating pilot-plant studies to large-scale performance.

Although the correlations have been derived for relatively simple atomizer types, it is believed that they will prove useful in estimating magnitude or trends of drop size in more complex apparatus. As was pointed out in a previous paper on this subject, such estimates are necessary for fundamental analysis of heat or mass transfer or of the separation of phases in a dispersed system. As an example of such an application the author has analyzed a photograph of the spray over a 3- by 3-ft. experimental grid tray having ¾-in. full round bars with ¼-in. spacing. The water rate was 5 gal./min. and the air rate 2,500 cu. ft./min. This photograph was taken at a 2-mm. depth of focus about 1in. inside the glass wall of the column. Drop sizes for this spray were counted by projecting the negative by a photographic enlarger onto a white blotter at magnification of 10. The only images suitable for measurement were those in sharp focus, that is, spherical images showing high lights. The following table shows a comparison of experimentally determined x_m and $\overline{x}_{32}$ with those calculated from Equation (5), the hydraulic diameter ($2w_s$) being substituted for D and constants shown in Table 1 for straight pressure nozzles used.

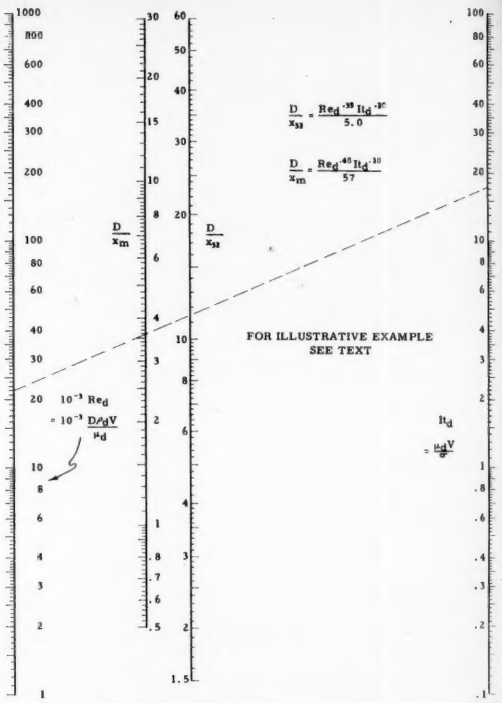

Fig. 7. Nomograph for droplet sizes, atomization via pressure nozzles into gases similar to atmospheric air.

	Calculated	Experimental
x_m, cm.	0.27	0.22 (largest drop measured)
$\overline{x}_{32}$, cm.	0.12	0.12

The agreement between experimental and calculated values is considerably better than could be expected in view of the uncertainties in interpreting the photograph. However it indicates that the correlation methods yield the correct order of magnitude.

The reader should be cautioned not to regard the conditions above as typical of grid-tray operations. The liquid rate was intentionally kept low to reduce the spray density.

ESTIMATION OF DROPLET-SIZE DISTRIBUTIONS WITH THE MAXIMUM STABLE DROPLET SIZE

Figure 7 shows a nomograph which can be used for rapid estimates of x_m or $\overline{x}_{32}$ as functions of the interfacial tension and Reynolds number groups for straight or modified pressure nozzles and whirl chambers. This nomograph applies only to atomization into gases similar to atmospheric air. Similar nomographs could be constructed for other atomizers by the use of the constants given in Table 1. One should note that $\overline{x}_m$ as well as $\overline{x}_{32}$ can be readily evaluated by using this nomograph. This application is illustrated in the following example.

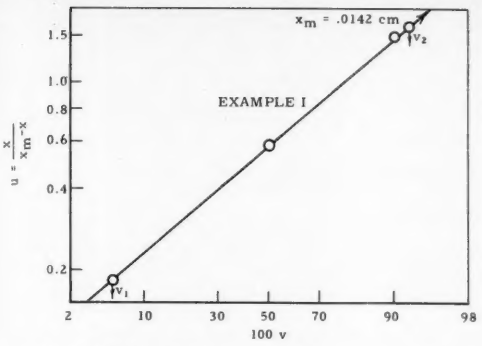

Fig. 8. Example of estimated droplet-size distribution.

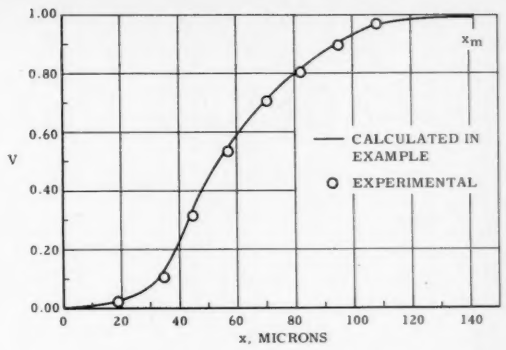

Fig. 9. Comparison of estimated distribution with data (example).

Example

Consider an oil of density $\rho_d = 0.86$ g./cc., viscosity $\mu_d = 0.0311$ poise, surface tension $\sigma = 28$ dynes/cm. Let it be injected into slightly compressed air (density 0.0015 g./cc.) via a modified pressure nozzle with diameter $D = 0.0508$ cm., with a pressure drop $\Delta p = 286 \times 10^6$ dynes/sq. cm. across the nozzle and a discharge coefficient of 0.6. One wishes to estimate the mean droplet size $\bar{x}_{32}$ in the resulting spray, also the volume percentage of spray which appears in droplets of diameter less than $\bar{x}_{32}/2$ and in droplets greater than $2\,\bar{x}_{32}$.

First one evaluates V.

$$V \cong 0.60\sqrt{2\Delta p/\rho_d}$$

$$= 0.60\sqrt{2 \times 286 \times 10^6/0.86}$$

$$= 15{,}500 \text{ cm./sec.} \quad (9)$$

Hence

$$\frac{D\rho_d V}{\mu_d} = 21{,}800; \quad \frac{\mu_d V}{\sigma} = 17.2 \quad (10)$$

From the nomograph (Figure 7)

$$\frac{D}{\bar{x}_{32}} = 11.5 \quad (11)$$

Therefore

$$\bar{x}_{32} = 0.00442 \text{ cm.}$$

Also

$$\frac{D}{x_m} = 3.58 \quad (12)$$

Therefore

$$x_m = 0.0142 \text{ cm.} \quad (13)$$

To complete the distribution picture, one assumes $\delta = 0.98$ (Table 2). From Equation (10.1) of reference *17*

$$r_{32} = \frac{x_m}{\bar{x}_{32}} = 1 + a\,e^{1/4\delta^2} \quad (14)$$

Therefore

$$a = \left(\frac{0.0142}{0.00442} - 1\right) \Big/ e^{1/4(0.98)^2}$$

$$= \frac{2.21}{1.297} = 1.704 \quad (15)$$

$$\frac{x_{50}}{x_m - x_{50}} = u_{50} = \frac{1}{a} = 0.587 \quad (16)$$

From Equation (9.6) of reference *17*

$$\log \frac{u_{90}}{u_{50}} = \frac{0.394}{\delta} \quad (17)$$

Therefore

$$\frac{u_{90}}{u_{50}} = 2.53; \; u_{90} = 1.49 \quad (18)$$

From the values of u_{90} and u_{50} one can plot the distribution line (Figure 8).

For the last part of the problem, the droplet sizes in question are

$$\left.\begin{aligned} x_1 &= \bar{x}_{32}/2 = 0.00221 \text{ cm.} \\ \text{and} \\ x_2 &= 2\,\bar{x}_{32} = 0.00884 \text{ cm.} \end{aligned}\right\} \quad (19)$$

The corresponding u values are

$$u_1 = 0.184 \text{ and } u_2 = 1.65 \quad (20)$$

Reference to Figure 8 gives the corresponding values of v:

$$v_1 = 0.052 \text{ and } v_2 = 0.923 \quad (21)$$

Thus this estimate gives 5.2% of the spray volume in droplets of diameter less than $\bar{x}_{32}/2$ and 7.7% in droplets of diameter greater than $2\,\bar{x}_{32}$.

Since the data used in this example correspond to those of a particular experiment [Lee (*13*)], it is possible to compare estimated results with experimental ones (Figure 9). The value of $\bar{x}_{32}$ given by these data is 0.00452 cm. and the value of x_m 0.0140 cm.

ERRORS ARISING FROM EXTRAPOLATION BEYOND THE MAXIMUM STABLE DROPLET SIZE

Some attempts to extrapolate distribution data to infinite particle size lead to untenable results. For example, extrapolation based on the Nukiyama-Tanasawa equation sometimes leads to a calculated value of $\bar{x}_{32}$ larger than any experimentally observed droplet diameter. In this connection one observes a weakness of distribution equations of form

$$\frac{dn}{dx} = A_1 x^{A_2} \exp\,(-A_3 x^{A_4}) \quad (22)$$

The mean diameter is found to be

$$\bar{x}_{pq} = A_3^{-1/A_4}\left[\Gamma\left(\frac{A_2 + 1 + p}{A_4}\right)/\Gamma\left(\frac{A_2 + 1 + q}{A_4}\right)\right]^{1/(p-q)} \quad (23)$$

Thus, considering the properties of the gamma function, one finds that p and q can be chosen to produce arbitrarily large values of $\bar{x}_{pq}$, even with p and q in a reasonable range. For example, with $A_2 = -5$, $A_3 = \bar{x}_{32}$, and $A_4 = -1$ one finds that x_{p3} increases without bound as p approaches 4.

When they are anticipated, errors of this kind can be avoided by various devices. But a more subtle kind of error can arise in process calculations when the effect of extrapolation is less spectacular. For example if one is concerned with Langmuir evaporation of spray droplets, then (as shown in reference *17*) the evaporation rate is proportional to the mean diameter $\bar{x}_{10}$. If one assumes an unlimited log-normal distribution with parameter $\delta = 1$, the calculated mean is

$$\bar{x}_{10} = x_{50} \exp\,(-5/4\,\delta^2)$$

$$= x_{50}/3.48 \quad (24)$$

But if one uses an upper-limit distribution with $\delta = 1$ and $a = 1$ (symmetrical), the result is

$$\bar{x}_{10} = 2x_{50}\,\frac{1 + 2a\exp\,(1/4\,\delta^2) + a^2\exp\,(1/\delta^2)}{1 + 3a\exp\,(1/4\,\delta^2) + 3a^2\exp\,(1/\delta^2) + a^3\exp\,(9/4\,\delta^2)} \quad (25)$$

$$= x_{50}/1.79$$

Thus the assumption of unlimited droplet size may cause a significant underestimation of the evaporation rate.

Similar calculations can be made to illustrate the effects on other processes involving dispersoids. In each case one should use the mean diameter appropriate to the process. The following table illustrates some further comparisons of the kind calculated above:

Ratio	Calculated by Log normal	Upper limit
$\bar{x}_{32}/x_{50}$	0.780	0.875
$\bar{x}_{31}/x_{50}$	0.606	0.798
$\bar{x}_{30}/x_{50}$	0.472	0.707
$\bar{x}_{10}/x_{50}$	0.287	0.559
$\bar{x}_{32}/x_{10}$	2.72	1.57

As previously indicated in reference *17*, the maximum stable droplet size is of some importance in understanding and correlating the generation of liquid-liquid dispersions, that is unstable emulsions. This fact has been noted (*2, 7, 22*), and some theories have been advanced as to the maximum stable droplet size in such systems (*7, 22*).

A theoretical treatment which proves useful in correlating many of the liquid-liquid dispersion data is that of Hinze (*7*). According to this the maximum stable droplet size in an unstable emulsion may be calculated from

$$k_m = x_m\,(\rho_c/\sigma)^{3/5}\,\epsilon^{2/5} \qquad (26)$$

Examples similar to those exhibited for sprays can be constructed to show the essential role played by the maximum stable droplet sizes in calculating the behavior of dispersoids of this kind (continuous-phase liquid).

SUMMARY

As proposed at the start, reasons have been stated for giving careful consideration to the maximum stable droplet size in describing dispersoids. Evidence has been given to show that the maximum stable droplet diameter can be separately correlated for many dispersoids and then used in process calculations and that the omission of this parameter may be misleading.

ACKNOWLEDGMENT

The author wishes to thank the Shell Development Company for permission to publish this material, and also his numerous colleagues whose contributions to the field are inextricably woven into the material of this paper. Special thanks are due to Mott Souders and Harry Evans, who supervised the research summarized here.

NOTATION

a = parameter in distribution equation
A, B, C = correlation constants, Table 1
C_D = drag coefficient
C_o = effective discharge coefficient
D = representative dimension perpendicular to flow
e = natural constant (2.718. . .)
f = function
It = interfacial tension group, $\mu V/\sigma$
k = size parameters, miscellaneous
k_m = constant, Equation (26)
L = representative dimension parallel to flow
n = numerical fraction of spray in droplets of diameter less than x
p = liquid pressure
Δp = pressure drop effective in producing atomization
Q_c = volume flow rate of continuous phase
Q_d = volume flow rate of droplet phase
r_{32} = ratio of x_m to $\bar{x}_{32}$
Re = Reynolds number, $\rho VD/\mu$
s = dispersion parameter (See definition for y)
u = function of droplet size, $= x/(x_m - x)$
u_{50} = value of u at $v = 0.50$
u_{90} = value of u at $v = 0.90$
v = volume fraction of spray in droplets of diameter less than x
V = velocity of droplet phase relative to continuous phase
V_c = velocity of continuous phase relative to atomizer
V_d = velocity of droplet phase relative to atomizer
w_s = slot width in grid tray
We_m = critical Weber number, $x_m\rho_c V^2/\sigma$
x = droplet diameter
x_m = maximum stable droplet diameter
$\bar{x}$ = representative or average droplet size
$\bar{x}_{pq}$ = generalized mean diameter
$\bar{x}_{32}$ = surface-volume (Sauter) mean diameter
x_{50} = volume median diameter
y = a function of droplet diameter; $y = \ln a(x^s - x_o^s)/(x_m^s - x^s)$; y has the Gaussian distribution indicated in Equation (8)

Greek Letters

β = acceleration imparted to liquid by body forces
Γ = gamma function (generalized factorial)
δ = uniformity parameter in distribution equation
ϵ = rate of energy dissipation in turbulent flow (per unit mass)
μ_c = viscosity of continuous phase
μ_d = viscosity of droplet phase
π = natural constant (3.14. . .)
ρ_c = density of continuous phase
ρ_d = density of droplet phase
σ = interfacial tension
ϕ = representative angle for diverging outlet
ω = angular velocity (rotating cup or disk), radians/sec.

LITERATURE CITED

1. Baron, T., *Eng. Exp. Sta. Tech. Rept. No. 4*, Univ. Illinois, Urbana (1947).
2. Clay, P. H., *Proc. Neder. Akad., Wetensch. (Holl.)*, **42**, 852, 979 (1940).
3. Conroy, E. H., Jr., and H. F. Johnstone, *Ind. Eng. Chem.*, **41**, 2741 (1949).
4. "Bibliography on Sprays," 2 ed., Texas Co., New York (December, 1953).
5. Doble, S. M., *Engineering*, **159**, 21, 61, 103 (1945).
6. Hinze, J. O., *J. Appl. Sci. Res.*, A1, 273 (1949).
7. ———, *A.I.Ch.E. Journal*, **1**, 289 (1955).
8. ———, and H. Milborn, *J. Appl. Mech.*, **17**, 145 (1950).
9. Houghton, H. G., in "Chemical Engineers' Handbook," ed. by J. H. Perry, 3 ed., p. 1170, McGraw-Hill, New York (1950).
10. Hughes, R. R., and E. R. Gilliland, *Chem. Eng. Progr.*, **48**, 497 (1952).
11. Johnstone, H. F., and R. V. Kleinschmidt, *Trans. Am. Inst. Chem. Engrs.*, **34**, 181 (1938).
12. Kolupaev, P. G., thesis, Mass. Inst. Technol., Cambridge (1941).
13. Lee, D. W., *Natl. Advisory Comm. Aeronaut-Tech. Rep. 425* (1932).
14. Lewis, H. C., D. G. Edwards, M. J. Goglia, R. I. Rice, and L. W. Smith, *Ind. Eng. Chem.*, **40**, 67 (1948).
15. Marshall, W. R., Jr., *Chem. Eng. Progr. Monograph Ser. No. 2*, **50** (1954).
16. Merrington, A. C., and E. G. Richardson, *Proc. Phys. Soc.*, **59** (1947).
17. Mugele, R. A., and H. D. Evans, *Ind. Eng. Chem.*, **43**, 1317 (June, 1951).
18. Nukiyama, S., and Y. Tanasawa, *Trans. Soc. Mech. Engrs. (Japan)*, **4**, 14, 86 (1938); **5**, 18, 62, 68 (1939); **6**, 22, p. II-7, II-15 (1939); **23**, p. II-18 (1940).
19. Pierce, N. C., M. S. thesis, Univ. Illinois, Urbana (1947).
20. Ranz, William E., *Bull. No. 65*, The Penn. State Univ., State College (1956).
21. Rupe, J. H., "A Technique for the Investigation of Spray Characteristics of Constant Flow Nozzles," Third Symposium on Combustion, Flame, and Explosion Phenomena, Univ. Wisconsin, Madison (1948).
22. Vermeulen, Theodore, G. M. Williams, and G. E. Langlois, *Chem. Eng. Progr.*, **51**, 85-F (1955).
23. Walton, W. H., and W. C. Prewett, *Proc. Phys. Soc. (London)*, **62B**, 341 (1949).

Manuscript received February 17, 1959; revision received June 15, 1959; paper accepted June 18, 1959. Paper presented at A.I.Ch.E. Cincinnati meeting.

EVAPORATION FROM DROPS CONTAINING DISSOLVED SOLIDS

D. H. CHARLESWORTH and W. R. MARSHALL, JR., University of Wisconsin, Madison, Wisconsin

A study was made of the evaporation from single drops containing solids. By means of a specially designed sensitive balance, drops were suspended over a hot-air stream and their drying behavior was observed. Weight changes were measured during evaporation. Experimental data are presented on the time of appearance of the first solid phase and the formation of a solid crust for a wide range of drying conditions and materials. A theory is advanced for predicting the formation of a solid phase in drying a droplet containing a dissolved solid. This theory shows reasonable agreement with the experimental results. A tentative proposal for the application of the results to spray-dryer performance is suggested.

PART I

The aim of the investigation reported here was to develop a method of predicting the drying rates of drops containing dissolved solids for application to design calculations for spray dryers and to obtain fundamental information on the phenomena occurring during the drying process. Considerable attention was given to the problem of predicting the formation of a solid phase in drying a droplet of an inorganic salt solution. The need for such information has become more pressing as spray-drying techniques have become widely applied to the production of dried foodstuffs, pharmaceuticals, and tonnage chemicals.

As in most drying operations, the spray-drying process can be subdivided into periods. The first period is characterized by evaporation from a free liquid surface, the second by evaporation from or through a solid structure which forms at an intermediate point in the process. Accordingly this study was divided into the following sections: (1) evaporation rates and droplet conditions during the first period of drying, (2) formation of the solid phase about the droplet, and, (3) evaporation rates during the second period of drying.

REVIEW OF PREVIOUS WORK

Studies of the evaporation of pure-liquid droplets can be related directly to the first period of spray drying. The theory of evaporation into still air has been treated by Fuchs (*6*) and Luchak and Langstroth (*9*). Experimental verification of the relationships for a number of pure liquids was carried out by Ranz and Marshall (*10*) and by Langstroth *et al.* (*8*). Studies of the evaporation of pure-liquid drops having a finite velocity relative to the surrounding air were made by Frössling (*5*) and by Ranz and Marshall (*10*).

Information on the evaporation from droplets containing solids and on the formation of a solid phase is sparse. Ranz and Marshall (*10*) in addition to their work with pure liquids presented some observations of evaporation from droplets of solutions and suspensions and concluded that if the presence of the solid affects the vapor pressure, drying proceeds during the first period as if the entire droplet were saturated. The investigation also included measurements of the temperature history of droplets containing suspended or dissolved solids evaporating in still air.

The mechanism of the drying of small particles such as are encountered in spray drying has received little attention with the exception of the manner in which hollow particles are formed, a number of investigators (*2, 4, 7, 10*) having hypothesized reasons for the occurrence of internal voids.

THEORETICAL CONSIDERATIONS

The complexity of the process of evaporation from a droplet having a velocity relative to the surrounding air is greatly increased by the presence of nonvolatile dissolved solids in the droplet. Whereas, in the consideration of heat and mass transfer from a droplet of pure liquid, conditions within the droplet may justifiably be assumed uniform, they cannot be if there is a nonvolatile material present.

In general the concentration of solute is initially uniform in the droplet; however as soon as some evaporation has taken place from the droplet surface, concentration gradients are set up and there is diffusion of solvent toward the surface and solute toward the center. In addition, since the drop is necessarily decreasing in size, the solute in the surface layer is swept inward by the retreating interface, which is impermeable to the solute.

If the evaporation rate were constant over the entire surface, as would be the case for zero relative velocity between the droplet and the surroundings, the concentration gradients within the droplet should have spherical symmetry. However if the relative velocity is not zero, boundary-layer theory predicts, and Frössling (*5*) has demonstrated experimentally, that the evaporation rate varies from a maximum at the point of impingement at the front of the drop, through a minimum at some latitude beyond the equator, to a second but lower maximum at the rear. As a result, diffusion has a tangential component toward the rear of the drops in addition to the radial one. The concentration profiles are consequently not simple.

Superimposed on the flow, owing to diffusion, may be internal circulation from density gradients caused by temperature and concentration and from the viscous drag of the passing air. Droplet rotation as a whole may also be present. The latter, if sufficiently rapid and random, would tend to restore the spherical symmetry. If, however, the droplet initially has no rotational motion and its relative velocity is in the direction of gravity, the maximum evaporation rate at the front of the droplet results in a high concentration of solute in that area. This ordinarily implies a greater than average density at the front of the drop, a situation which could add to the stability against rotation.

It is postulated that the surface solute concentration does not remain uniform but rather rises smoothly from its initial value. Since the rate of evaporation is almost constant (depending on the vapor pressure-concentration relation and any changes in the Reynolds number of the flow) and the surface concentration is increasing, the rate of accumulation at the surface increases. When the surface concentration reaches the saturation value, it can no longer continue to increase and solute must be deposited as a solid phase. Consequently, if the surface concentration of solute could be expressed as a function of time and drying conditions, the time of formation of the solid phase could be predicted. If rigorous, such a function would be complicated by the lack of spherical symmetry and by internal circulation.

Using this concept of the process as a basis and assuming internal transfer by diffusion only, one can express the

D. H. Charlesworth is with Atomic Energy of Canada, Limited, Chalk River, Ontario, Canada.

surface concentration of solute as a function of time and drying conditions and estimate the time of formation of the solid phase. Such a function should also take into account the lack of spherical symmetry in and around the droplet, as well as internal circulation. Their inclusion, however, renders the problem so complex as to be insoluble. The solution of the simplified problem cannot be expected to predict values accurately, but the form of the solution should be useful in the correlation of experimental data.

A formulation of the problem is best accomplished by considering a synthetic model which most closely approximates the drying droplet and yet is sufficiently simple to be expressed in a usable mathematical form. If transfer in the droplet by diffusion only is assumed, together with spherical symmetry, then the radial diffusion equation in spherical coordinates may be used as the basic differential equation. One of the boundary conditions results from the practical situation that the droplet is initially of uniform concentration. The second boundary condition must express the accumulation of solute in the surface layer of the droplet resulting from water evaporation and droplet shrinkage. Since a moving boundary presents serious mathematical difficulties, the model droplet is considered to be of constant diameter and to be receiving solute through the surface in an amount per unit time equal to the solute in a surface layer of volume equivalent to the actual drop volume decrease per unit time.

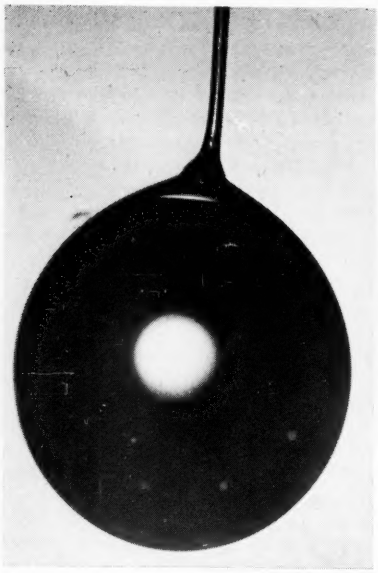

Fig. 1. Suspended drop.

Mathematically this boundary-value problem becomes

$$\frac{\partial c}{\partial \theta} = D\left(\frac{\partial^2 c}{\partial r^2} + \frac{2}{r}\frac{\partial c}{\partial r}\right) \quad (1)$$

The boundary conditions may be written

$$c(r,\theta) = c_o \quad 0 < r < x_o/2 \quad (2)$$

$$D\left(\frac{\partial c}{\partial r}\right)_{r=x/2} = \frac{-\frac{dm}{d\theta}\cdot\bar{v}\,c}{\pi x^2} \quad (3)$$

A practical approximation in most cases is that the evaporation rate $dm/d\theta$ from a droplet of solution is equal to that from a pure-water droplet of the same size.

For an evaporating droplet of pure liquid

$$-\frac{d(x^2)}{d\theta} = -\frac{dm}{d\theta}\cdot\frac{4\bar{v}}{\pi x} \quad (4)$$

At low Reynolds numbers and for small ranges of x, $[d(x^2)]/d\theta$ may be considered constant. An evaporation constant K is therefore defined by

$$-\frac{d(x^2)}{d\theta} = 8K \quad (5)$$

or

$$-\frac{dm}{d\theta} = \frac{2\pi x K}{\bar{v}} \quad (6)$$

Substituting Equation (6) into Equation (3) yields

$$\left(\frac{\partial c}{\partial r}\right)_{r=x/2} = \frac{2\beta c}{x} \quad (7)$$

Solution of Equations (1), (2), and (7) leads to

$$c(r,\theta) = 2c_o\beta\left[\frac{\cosh\phi\,\sinh\left(\frac{2\phi r}{x}\right)\exp\left(\frac{-4\phi^2 D\theta}{x^2}\right)}{\phi\,(\sinh^2\phi - \beta)} - \sum_{n=1}^{\infty}\frac{\cos\alpha_n\,\sin\left(\frac{2\alpha_n r}{x}\right)\exp\left(\frac{-4\alpha_n^2 D\theta}{x^2}\right)}{\alpha_n(\sin^2\alpha_n + \beta)}\right] \quad (8)$$

where

ϕ is the positive real root of

$$\tanh y = \frac{y}{\beta+1} \quad (8a)$$

and

α_n $(n = 1, 2, 3, \ldots)$ are the positive real roots of $\tan z = \frac{z}{\beta+1}$ (8b)

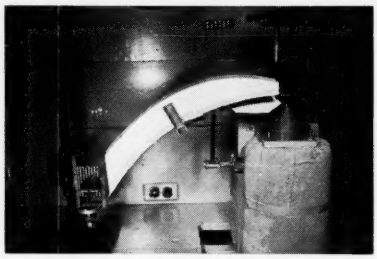

Fig. 2. Drop balance.

Fig. 3. Drop-suspension and thermoelement combination.

Compensation for changing drop size is made by inserting the relation

$$x^2 = x_o^2 - 8K\theta \quad (9)$$

Since it is postulated that a solid phase appears as soon as the surface becomes saturated, the time of the formation of a solid phase about the droplet will be that at which

$$c(x/2,\theta_c) = c_s \quad (10)$$

Equation (10) is much too complicated to be satisfactorily solved for θ_c. Fortunately several compensatory approximations can be made to render a solution possible. Calculation omitting the terms under the summation sign yields a somewhat high value of $c(x/2,\theta)$. This discrepancy is counteracted to a large extent by replacement of $(2\beta\cosh\phi\,\sinh\phi)/[\phi(\sinh^2\phi - \beta)]$ by unity. The simplified expression is then

$$c(x/2,\theta) = c_o\exp\left[\frac{(4\phi^2 D\theta)}{x_o^2 - 8K\theta}\right] \quad (11)$$

It can be seen that the two approximations are exactly compensating

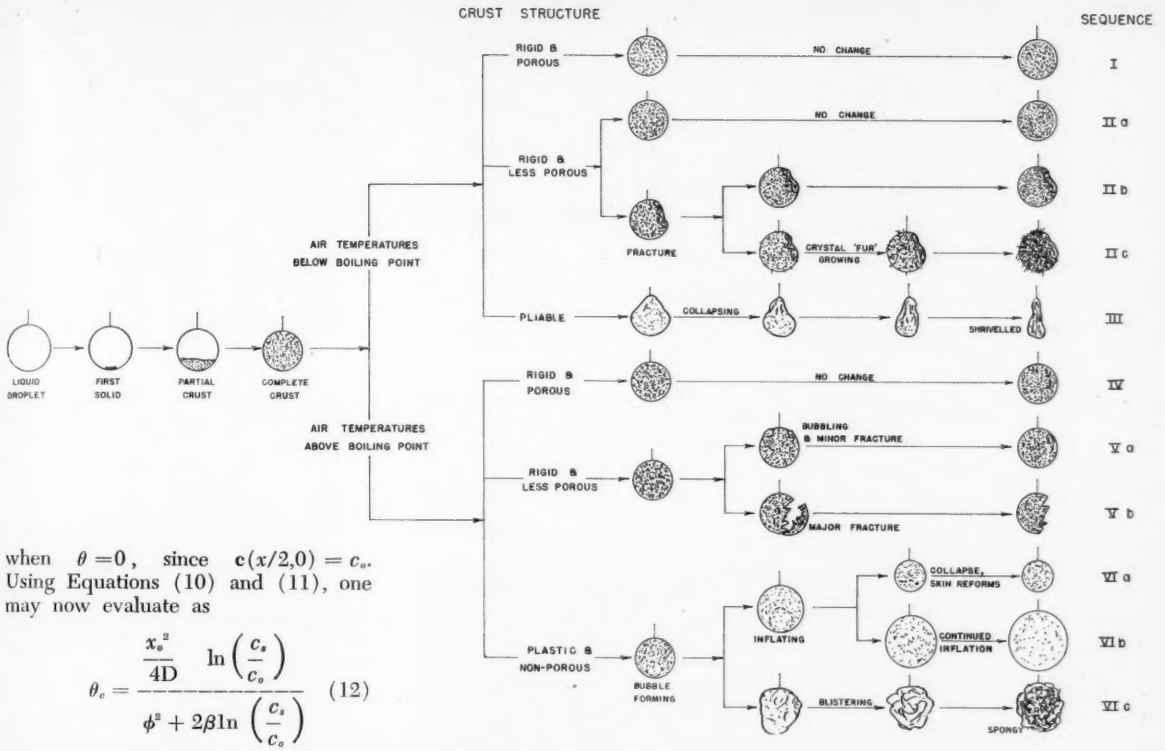

Fig. 4. Appearance changes in drying droplets.

when $\theta = 0$, since $c(x/2,0) = c_o$. Using Equations (10) and (11), one may now evaluate as

$$\theta_c = \frac{\dfrac{x_o^2}{4D} \ln\left(\dfrac{c_s}{c_o}\right)}{\phi^2 + 2\beta \ln\left(\dfrac{c_s}{c_o}\right)} \qquad (12)$$

A convenient substitution for calculation is $c_s/c_o = (\rho_s C_s)/(\rho_o C_o)$.

Equation (12) will be used as a correlating equation for experimental data concerning the formation of a solid phase about a droplet.

EXPERIMENTAL EQUIPMENT AND PROCEDURES

For study of the drying of droplets of aqueous solutions, a technique was developed wherein an individual droplet was suspended in a controlled air stream, and its weight or temperature was measured as the drying progressed. Visual observations of the appearance and size of the particle were recorded.

Control and Measurement of Air Stream Conditions

The metering and control of the test air stream were accomplished with essentially the same equipment used by Ranz and Marshall (*10*) with the exception that the 140-mesh screen on the convergent nozzle over which the drop was suspended was omitted, since it was easily clogged by stray droplets of solution.

Droplet Formation and Suspension

The droplets to be dried were formed from a microburette, the tip of which was fitted with a glass capillary tube of approximately 275-μ diameter thoroughly coated inside and out with Dri-film to facilitate the transfer of the droplet to the suspension filament. The transfer was accomplished by picking the droplet from the tip of the burette with a horizontally held glass filament, touching it to the end of the suspension filament, then drawing the transferring filament out through it. This allowed the droplet to slide off one filament and be left clinging to the other.

The suspension adopted was a vertical glass filament, the tip of which was drawn to small diameter and then touched to a flame to give a small knob on the end. Typical diameters were 340μ for the main filament, 70μ for the necked-in portion, and 200μ for the knob. The upper portion of the knob and the adjoining filament were coated with Dri-film to prevent the droplets from climbing the filament, but sufficient wettable area was left to support the droplet. The vertical positioning of the filament with the air stream blowing up from below minimized flow disturbances and eliminated transverse convection currents in the jet.

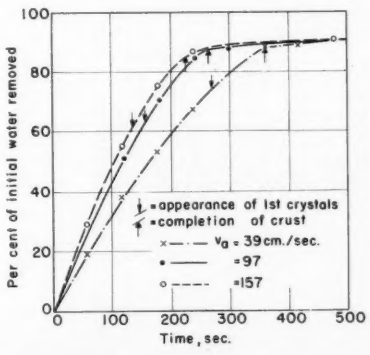

Fig. 5. Effect of air velocity on drying aqueous sodium-sulfate drops $t_a = 94°F.$, $x_o = 0.1565$ cm., $C_o = 0.082$ g./g. solution.

The surface of a drop suspended from the filament intersected the knob approximately at its equator as shown in Figure 1. The immersed portion of the knob, therefore, added only about 0.1% to the volume of a 2- by 10^{-5}-ml. droplet, the size most frequently used in the investigation. The cross-sectional area of the knob amounted to just 0.5% of the droplet area. It was estimated that the heat conducted to the droplet along the filament did not exceed 1% of the total heat input to the droplet.

Measurement of Droplet Weight

The visual technique of measuring evaporation rates from pure-liquid drops (*10*) is not admissible to the study of drops around which a solid structure has formed. For this study the balance shown in Figure 2 was developed, whereby the weight of a suspended droplet could be measured at intervals throughout the course of the drying. The main element of the balance was a glass filament 43 cm. in length tapered from a diameter of 425μ at its fixed end to 210μ at its free end. The large end was fixed to the vertically travelling micrometer stage of a cathetometer. Welded at right angles to the free end was a 3.2-cm. suspension filament of the type described above. As mounted, the

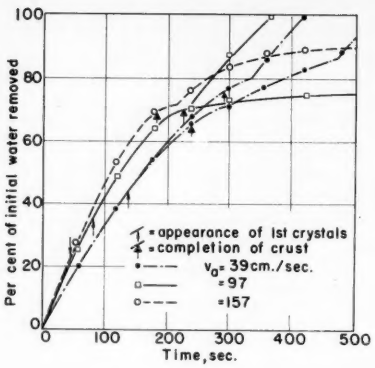

Fig. 6. Effect of air velocity on drying aqueous sodium-sulfate drops $t_a = 94°F.$, $x_o = 0.1565$ cm., $C_o = 0.164$ g./g. solution.

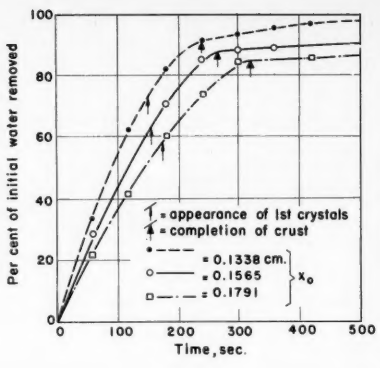

Fig. 7. Drying of aqueous sodium sulfate drops of different initial diameters $t_a = 94°F.$, $v_o =$ 97 cm./sec., $C_o = 0.082$ g./g. solution.

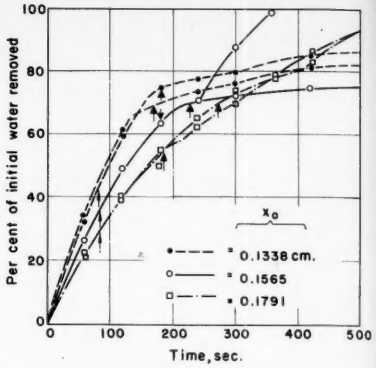

Fig. 8. Drying of aqueous sodium sulfate drops of different initial diameters $t_a = 94°F.$, $v_a =$ 97 cm./sec., $C_o = 0.165$ g./g. solution.

fixed end of the weighing filament was inclined at 45 deg., whereas the free end came to rest under its own weight in an almost horizontal position. Under the weight of a droplet suspended on it the free end of the filament deflected a distance which was a unique function of the drop weight. The amount of deflection could be determined by measuring the vertical distance through which it was necessary to raise the fixed end of the filament so that the free end was restored to its zero position. The drop weight could then be determined from a calibration curve relating weight to deflection. The calibration curve was almost linear and showed that the filament deflected an average of 12.8 mm./mg. and had a capacity of 4.0 mg., approximately the weight of a 1,970-μ drop. It was estimated that changes in drop weight could be measured within ± 0.01 mg.

To permit weighing of a droplet evaporating in flowing air from the nozzle, a deflecting shield was swung over the nozzle opening at the time a weight reading was made.

Measurement of Droplet Temperature

Figure 3 shows the suspension and thermoelement combination used for runs in which the temperature history of the droplet was recorded. It consisted of a fork of glass tubing, to hold the thermocouple, and a suspension filament. The thermoelement was formed from ½-ml. manganin and constantan wires and was connected to a quick-response recording potentiometer.

Visual Observation System

During all runs the evaporating droplets were observed under magnification from two perpendicular directions, in silhouette on the ground glass of a microscope camera and by reflected light in a microscope fitted with a micrometer eyepiece.

Experimental Procedures

It was impractical to measure the droplet temperature and its weight loss during the same experiment. Parallel runs under identical conditions therefore measured mass transfer in one and drop temperature in the other.

Mass transfer data in the form of a weight history of a droplet were obtained. Under most conditions the particle was weighed at 1-min. intervals. The time during which the air flow was cut off from the particle to permit one weighing was about 10 sec. and was not included in the recorded drying time. A change in the number or spacing of weighings did not noticeably affect the results.

The recorded temperature histories of the droplets were continuous, since there was no necessity for interrupting the air flow to obtain readings.

The drying particle was kept under almost continuous observation during that portion of the drying in which significant changes in appearance could be detected. Special notice was made of the times at which the solid phase first appeared and at which it completely encased the particle.

Materials and Range of Conditions Studied

Weight loss, temperature history, and time necessary for solid formation were measured for droplets of a number of aqueous solutions and suspensions. Parallel sets of runs under similar conditions in which weight loss and temperature history were measured were made with aqueous solutions of the following materials with initial solute concentrations as indicated; sodium sulfate (8.2 and 16.4 wt. %), potassium sulfate (5.3 and 10.7 wt. %), copper sulfate (10.7 wt. %), ammonium nitrate (12.5, 25.0 and 50.0 wt. %), calcium chloride (10.0, 19.4, 30.0, and 41.0 wt. %), sodium acetate (12.4 and 25.0 wt. %), and coffee extract (26.0 wt. % solids).

A variety of aqueous solutions and suspensions were dried as individual droplets under close observation with regard to solid-phase formation and general appearance during drying. No droplet weights or temperatures were recorded, only drying conditions. Included in this group were ammonium sulfate, ammonium chloride,

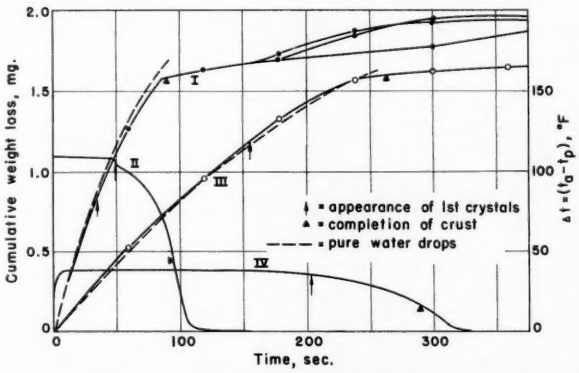

Fig. 9. Effect of temperature on the drying of drops of sodium sulfate solution; $x_o = 0.1565$ cm., $C_o = 0.082$ g./gm. solution.
I. Cumulative weight loss, $t_a = 197°F.$, $v_a = 117$ cm./sec.
II. Temperature difference, $t_a = 191°F.$, $v_a = 114$ cm./sec.
III. Cumulative weight loss, $t_a = 94°F.$, $v_a = 97$ cm./sec.
IV. Temperature difference, $t_a = 93°F.$, $v_a = 97$ cm./sec.

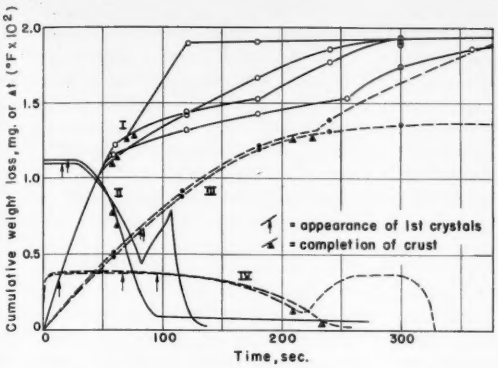

Fig. 10. Effect of temperature on the drying of drops of sodium sulfate solution; $x_o = 0.1565$ cm., $C_o = 0.164$ g./g. solution.

I. Cumulative weight loss, $t_a = 197°F.$, $v_a = 117$ cm./sec.
II. Temperature difference, $t_a = 193°F.$, $v_a = 114$ cm./sec.
III. Cumulative weight loss, $t_a = 94°F.$, $v_a = 97$ cm./sec.
IV. Temperature difference, $t_a = 94°F.$, $v_a = 97$ cm./sec.

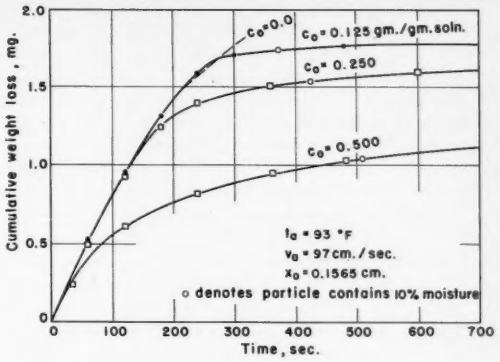

Fig. 11. Effect of initial concentration on the drying of drops of ammonium nitrate solution.

sodium chloride, potassium nitrate, lithium hypochlorite, sucrose, a dispersible blue dye, whole fresh milk, and a dispersion of polyvinyl acetate resin in water.

The experimental techniques required the use of drying conditions which produced relatively slow rates of evaporation. The majority of the work was done at moderate air temperatures and velocities and with large droplets. Unfortunately, these are not the conditions usually encountered in practical spray drying. Where possible, practical conditions were approached. Tests were carried out over as wide a range of the variables as the techniques and apparatus would permit in order to aid the extrapolation of the experimental data to commercial conditions.

The ranges of variables under which droplets were dried were

Air temperature	88° to 318°F
Air velocity	39 to 157 cm./sec. (1.2 to 5.2 ft./sec.)
Droplet volume	125 x 10^{-5} to 300 x 10^{-5} ml.
Droplet diameter	1.3 to 1.8 mm.
Initial solute concentration	5.3 to 50 wt. %
Ratio of initial concentrate to saturation concentration	0.18 to 0.89

EXPERIMENTAL RESULTS AND THEIR CORRELATION

General Appearance of Droplet During Drying

A generalized description of the appearance of a suspended droplet of an aqueous solution of an inorganic salt drying under conditions similar to those used in this investigation will be useful in understanding the experimental data obtained (Figure 4). Up to a point the sequences of events which were observed were similar for all droplets no matter what the solute or the drying conditions. During the first portion of the drying the droplet decreased in size with no appearance of a solid phase. The presence of a solid phase was first evidenced by the formation of crystals at the bottom of the drop. As drying progressed, more crystals appeared, forming a surface crust which grew steadily up the sides of the droplet. If the droplet did not rotate, the advancing front of the crust remained symmetrical about the vertical axis and continued to rise until the droplet was completely encased in a layer of solid material. The rate of advance of the solid front was initially relatively fast. It slowed markedly as it approached the droplet equator; then, once past it, it speeded up, completing the upper half of the crust in appreciably less time than was required for the formation of the lower portion. If the drop (or its surface) rotated, swinging the solid up the side of the drop, there was a strong tendency for the crust to re-form in its previous position. That portion of the crust which bodily advanced past the latitude of the old solid front rapidly redissolved. Also the crust quickly grew over any liquid surface which was exposed below the normal front latitude. The redissolution process was in general more rapid than the reformation process.

The results of further drying after the completion of the crust about the droplet differed depending on the nature of the solute and the surrounding air temperature.

If the air temperature was below

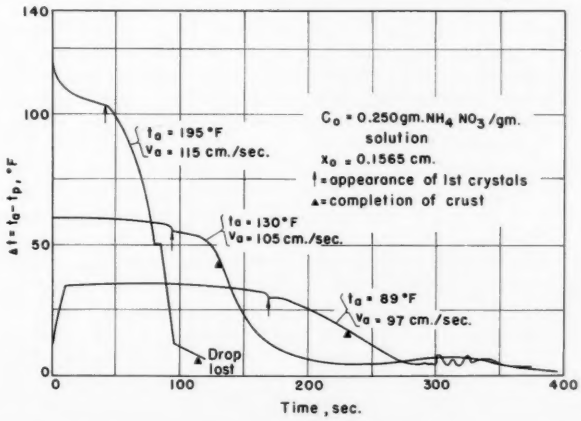
Δt = ta - tp, °F
Time, sec.
Co = 0.250 gm. NH4 NO3 /gm. solution
xo = 0.1565 cm.
= appearance of 1st crystals
= completion of crust
ta = 195 °F
va = 115 cm./sec.
ta = 130°F
va = 105 cm./sec.
ta = 89 °F
va = 97 cm./sec.
Drop lost

Fig. 12. Effect of temperature on the drying of drops of ammonium nitrate solution.

the boiling point of the solution, several different phenomena were possible. If the crust was rigid and quite porous (sequence I, Figure 4), its appearance did not change appreciably with further drying. The liquid-vapor interfaces retreated into the pores between the crystals. This retreat could be detected by a twinkling within the crust. Examples of such behavior were observed in the drying of potassium sulfate, ammonium chloride, and sodium chloride solutions. If the crust was rigid but not too porous (sequence II), stresses set up by the further crystal growth or by the surface tension of the liquid phase often

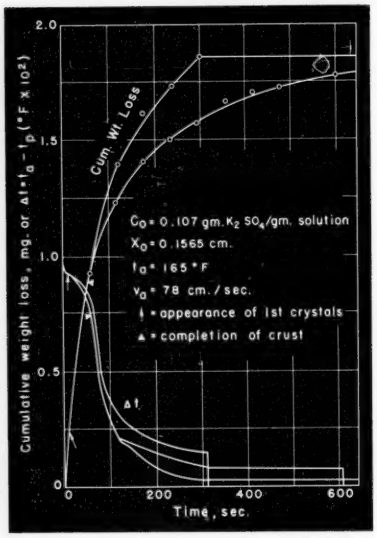
Cumulative weight loss, mg. or Δt=t_a−t_p (°F x 10²)
Cum. Wt. Loss
C_o = 0.107 gm. K_2 SO_4/gm. solution
X_o = 0.1565 cm.
t_a = 165 °F
V_a = 78 cm./sec.
= appearance of 1st crystals
▲ = completion of crust
Δt
Time, sec.

Fig. 13. Drying of several drops of potassium sulfate solution.

fractured the crust. This allowed air to enter the particle, and the liquid-vapor interface returned to the crust surface under the influence of capillary forces. Further formation of solid occurred as a crystal "fur" growing either out from the particle surface (sequence II*b*) or within the crust structure (sequence II*a*) or both. During this formation the break in the solid shell was sometimes closed, disrupting the supply of air to the particle center. If such was the case, the liquid interface once more retreated into the crust interstices, approximating the condition existing before the crust fracture occurred. If no additional breakdown of the shell occurred, the solid which formed as a result of the continued drying was deposited within the crust or on its inside surface. As the amount of liquid diminished, successively smaller pores were emptied. Once a pore pathway between the outer and inner shell surfaces was emptied of liquid, air could enter the core of the particle forming an air bubble at its center. If the crust was transparent or translucent, the bubble could be observed to grow. Solutions of ammonium sulfate, sodium sulfate, copper sulfate, and ammonium nitrate exhibited the characteristics of sequence II.

If the solid which encased the drop formed a pliable and relatively impervious skin (sequence III), the decrease in particle volume which resulted from drying after completion of the skin caused it to dimple or wrinkle. This behavior was observed in the drying of coffee extract and in the early stages of the drying of ammonium nitrate, sodium acetate, and ammonium chloride solutions. Rupture by implosion could eventually

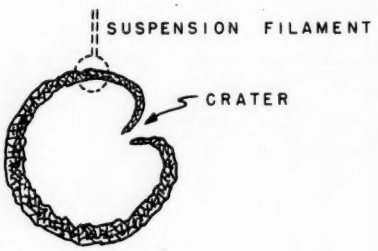

Fig. 14. Cross section of potassium sulfate particle.

occur as the skin thickened and stiffened.

Somewhat different results were observed after the closure of the crust about the droplet, if the surrounding air temperature was appreciably above the boiling point of the solution. The slowing of the mass transfer rate as a result of the additional mass-transfer resistance offered by the crust allowed the particle temperature to approach that of the surrounding air. When the boiling point of the solution was reached, vapor formed and a positive pressure was created within the particle. What effect this pressure had depended on the nature of the solid shell. If the structure was very open (sequence IV), the liquid was merely forced through the pores to the surface, where it quickly evaporated. If the crust was not sufficiently permeable to allow easy passage of the liquid, pressure built up within the particle. Under this internal stress rigid crusts (sequences V) usually fractured and plastic ones (sequence VI) inflated. In the latter case the stretching sometimes increased the skin permeability to a sufficient degree to allow the needed transmission (sequence VI*b*). If not, the skin ruptured, then collapsed (sequences VI*a* and VI*c*). Observed examples of these classifications were sodium chloride, copper sulfate (V*a*), ammonium sulfate (V*b*), lithium hypochlorite, sucrose, ammonium sulfate (VI*a*), potassium nitrate, whole fresh milk, dispersion of polyvinyl acetate (VI*b*), and coffee extract (VI*c*).

In virtually all cases the final particle consisted of a hollow, thin, nearly spherical crust. The outer surface was usually quite smooth, whereas the inner surface was rough and uneven.

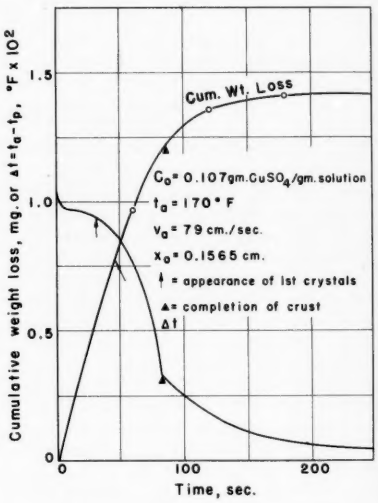
Cumulative weight loss, mg. or Δt=t_a−t_p, °F x 10²
Cum. Wt. Loss
C_o = 0.107gm.CuSO_4/gm. solution
t_a = 170 °F
V_a = 79 cm./sec.
X_o = 0.1565 cm.
= appearance of 1st crystals
▲ = completion of crust
Δt
Time, sec.

Fig. 15. Drying of droplets of copper sulfate solution.

Occasionally the inner core contained an open network of large crystals.

General Forms of the Weight-Loss and Temperature vs. Time Curves

When a droplet of pure solvent was evaporated, the cumulative weight-loss vs. time relation that was obtained was a smooth curve, concave downward and of increasing curvature. The temperature-time curve was a horizontal straight line until the droplet became extremely small, when the external effects of the suspension filament and the thermocouple became appreciable.

Early in the drying of a droplet of an aqueous solution of an inorganic salt which had little effect on the vapor pressure, the cumulative weight-loss-vs.-time curve, closely followed the curve for a pure-water droplet of the same initial volume. Generally the coincidence of the weight-loss curves for droplets of water and of

solutions persisted past the first formation of the solid phase and almost to the completion of the crust.

At the start of drying, the temperature of a droplet of solution was only slightly above that of a water droplet evaporating under the same conditions. The extent of the difference was dependent on the relative lowering of the vapor pressure by the dissolved salt. As evaporation continued and the surface layer of solution became more concentrated, the drop temperature rose slowly. The rate of rise increased somewhat with the first appearance of the solid phase and increased rapidly as the crust neared completion.

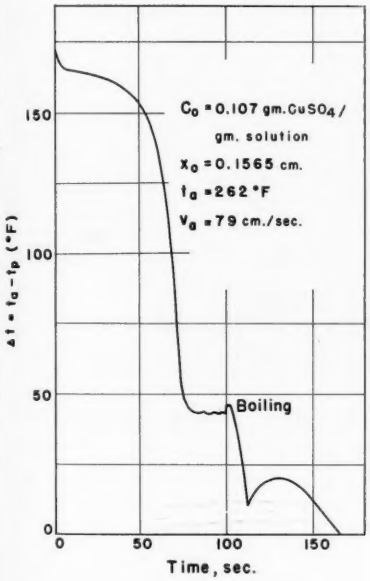

Fig. 16. Drying of droplet of copper sulfate solution in 262°F. air.

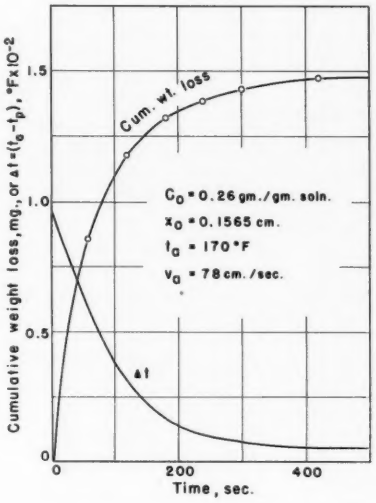

Fig. 17. Drying of droplets of coffee extract.

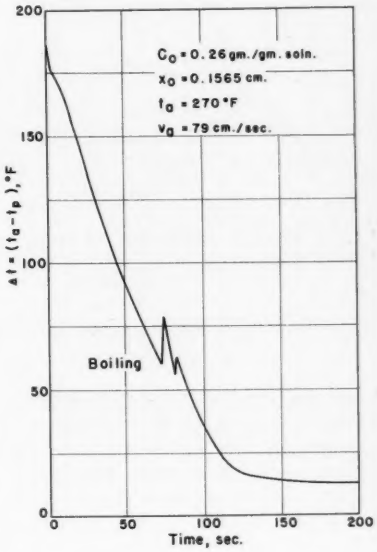

Fig. 18. Drying of droplet of coffee extract in 270°F. air.

Curves of Weight Loss and Temperature vs. Time

Figures 5 to 13 and 15 to 19 are specific examples of the weight-loss and temperature curves obtained in this study. Additional examples are given in the thesis (*1*) on which this paper is based. The weight-loss curves were experimentally measured weight-time relations, while the Δt curves were derived from the continuous chart records, smoothed to remove the effect of the rapid oscillations of air temperature. A reproduction of an actual temperature is given in Figure 20.

The data obtained for the drying of drops of sodium sulfate solutions under various conditions are shown in Figures 5 to 10. In a majority of the droplets dried there was some inward collapse of the solid shell after it had formed, sometimes revealing a liquid surface or the hollow interior of the particle. These fractures were reflected in the weight and temperature curves by the sharp breaks in the second-period portion of the curves as shown in Figures 6, 8, 9, and 10. Greater initial solute concentrations increased the tendency of the crust to fracture. If the final particle were crushed and observed under the microscope, it was found to be a thin-walled hollow sphere with a crust thickness about one twentieth of the particle diameter. The outside of the shell was quite smooth, excluding any furry growth, whereas the inner surface was rough and jagged.

Figure 11 shows the data for the drying of ammonium nitrate solutions of three different initial concentrations expressed as cumulative weight loss against the elapsed drying time. Not only was more water removed in a given time from the droplet of lower initial concentration, but also the particle so formed approached dryness more quickly. It was also noted that at the moment the crust was completed the average concentration of the particle was approximately the same no matter what the initial concentration or the drying conditions.

The temperature behavior of droplets of ammonium nitrate solution evaporating under various conditions is shown in Figure 12. Immediately after the first crystals had formed, the Δt between air stream and particle dropped off quite rapidly. At least part of this effect can be ascribed to the large heat of crystallization of ammonium nitrate.

The weight-loss curves obtained from the drying of droplets of potassium sulfate solution in a 165°F. air stream (Figure 13) were exceptional in that the completion of the crust about the drop did not cause the evaporation rate to drop off too sharply. In fact, relatively fast rates of evaporation persisted until the particle was completely dry, as shown by the cumulative weight-loss curves running into their maximum values and Δt dropping suddenly to zero. Apparently the crust was quite open in structure and easily drew the liquid from the interior to the outer surface. So rapid was this flow that the crust did not have time to completely cover the droplet. As the crust neared completion, the liquid was drawn away from the open area, leaving a sizable crater in the crust. When fractured and viewed under the microscope, the dried particle proved to be a very thin shell composed of large crystals. A cross section of the shell through the crater is shown in Figure 14.

The crust formed upon the drying of droplets of copper sulfate solution was of low permeability, as is evidenced by the flattening of the cumulative weight-loss curve (Figure 15) soon after the completion of the solid shell. During the drying of one particle the crust fractured, and immediately the drying rate jumped to an appreciably higher value and maintained it until the particle reached a composition equivalent

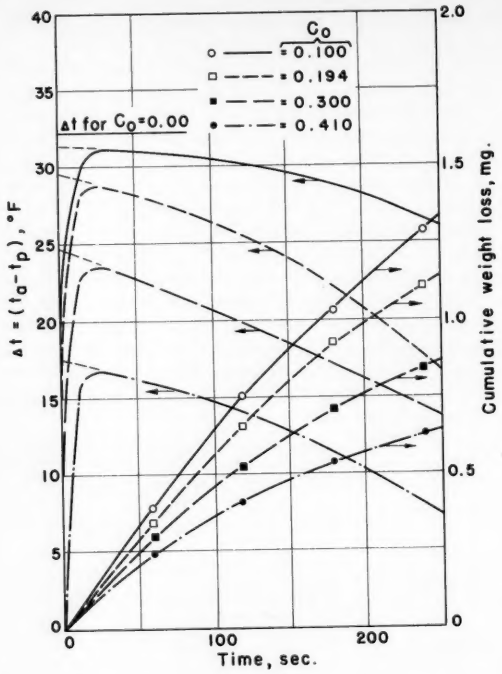

Fig. 19. Effect of concentration on drying aqueous calcium chloride drops x_o = 0.1565 cm., t_a = 81°F., v_a = 95 cm./sec.

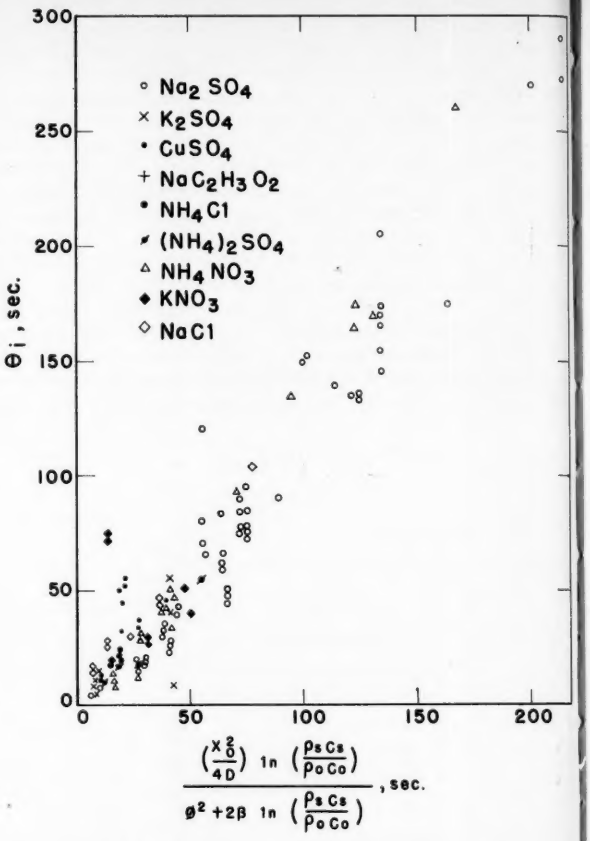

Fig. 21. Correlation of first appearance of crystals by Equation (12).

to the pentahydrate. This indicated that before the fracture of the crust the evaporation rate was controlled by the diffusion of vapor from the liquid-vapor interface through the crust to the particle surface. In a 262°F. air stream a solid crust quickly formed about the drop. The particle temperature reached the boiling point, and the particle bubbled vigorously, fracturing the crust at several points. The final particle was white, shiny, and quite smooth. The Δt time curve is shown in Figure 16.

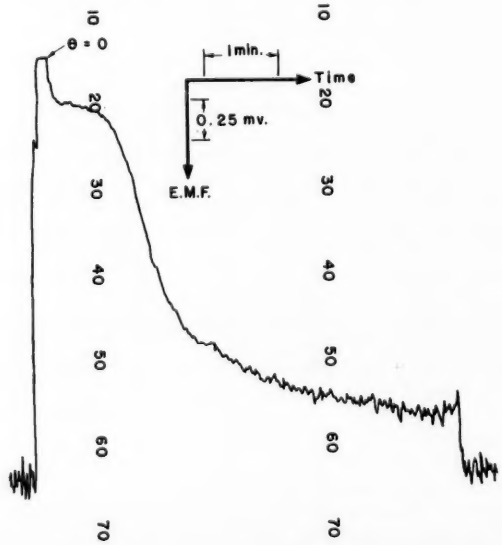

Fig. 20. Sample temperature-vs.-time data from recorder-strip chart.

When dried below the boiling point, a droplet of coffee extract first skinned over and then shriveled. The skin acted as a pliable sack suspended from the filament. As more and more of the liquid was evaporated, the upper portions of the skin wrinkled and the particle became longer than it was wide. Weight-loss and Δt curves are given in Figure 17.

If the air temperature was above the boiling point of the extract, the final dried particle took on a completely different appearance. It first shriveled in a manner similar to that described above. When the droplet reached the boiling point, internal vaporization inflated the surface skin until rupture occurred. The skin then repeatedly inflated and collapsed, forming a spongy structure. Each small bubble in the

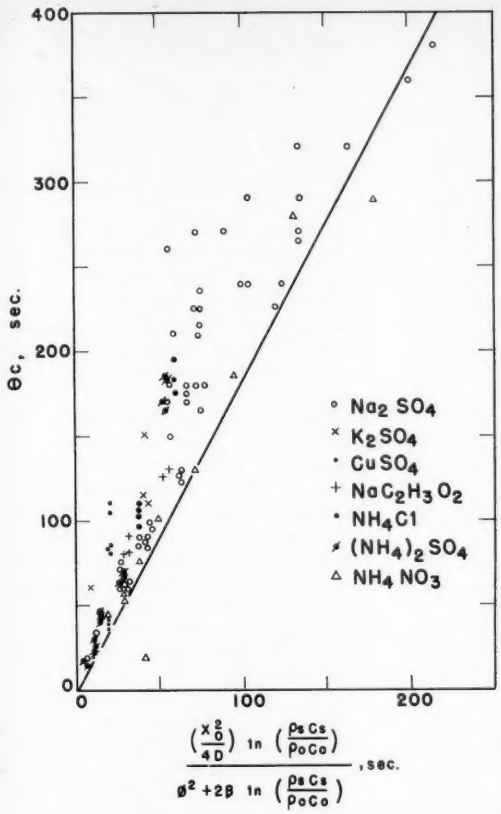

Fig. 22. Correlation of time of crust completion by Equation (12).

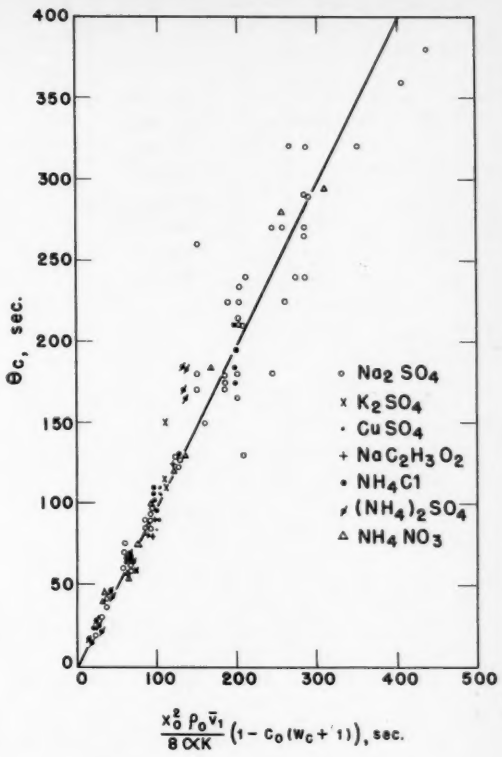

Fig. 23. Correlation of time of crust completion by Equation (14).

final dried particle appeared to be the result of one cycle of inflation and collapse. The temperature history of a droplet dried in air at 270°F. is given in Figure 18.

Surface Concentrations

Ranz and Marshall (*10*) suggested that droplets of solutions evaporated at all times as if they were saturated, even though the average solute concentration in the droplet was well below the saturation value. To test this hypothesis, a number of measurements of droplet weight loss and temperature were made with calcium chloride solutions of four different initial concentrations. The results are plotted in Figure 19. Pronounced differences in droplet temperatures and evaporation rates were noted between the droplets of different initial concentration. It is thus apparent that droplets of all aqueous solutions of any concentration do not necessarily evaporate as if saturated.

Formation of a Solid Phase in Drying a Droplet of Solution

The time of the formation of a solid phase around a drying droplet is important since it limits the period of relatively rapid drying. It also has an important bearing on the size and properties of the final dry product.

In all but a few of the runs in which droplets of salt solutions were dried, the times of appearance of the first crystals and of the completion of a

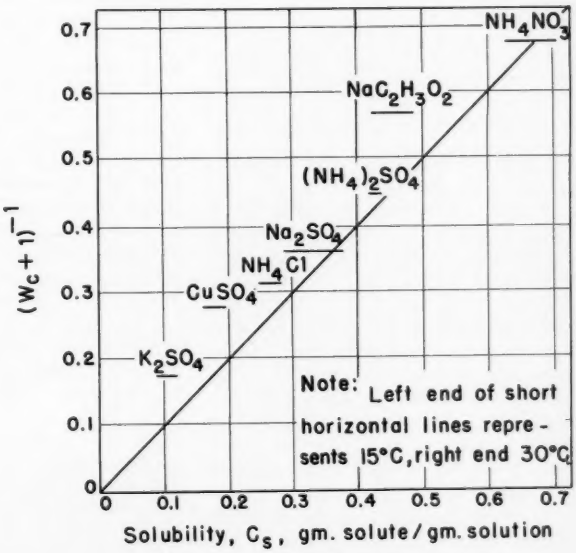

Fig. 24. Variation of the parameter W_c with solute solubility.

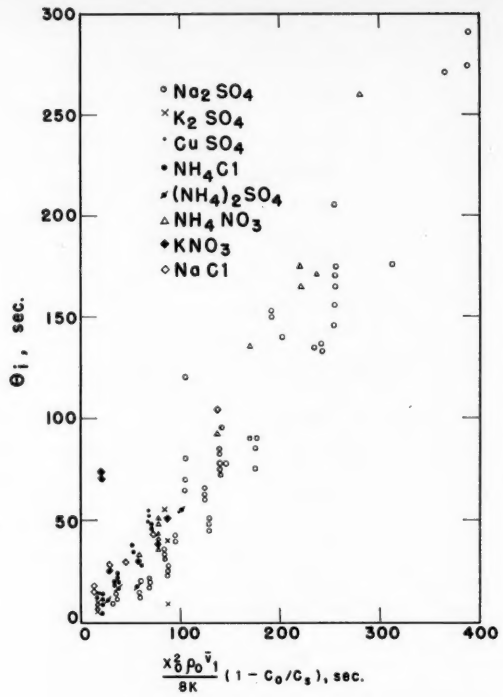

Fig. 25. Correlation of first appearance of crystals by Equation (16).

solid crust about the droplet were noted. These results were correlated by means of Equation (12). Figures 21 and 22 show the observed time of formation of the first crystals and of the completed crust, respectively, plotted against the value calculated from Equation (12). In Figure 22 a straight line having the equation

$$\theta_c = \frac{1.84x_o^2 \ln\left(\frac{\rho_s C_s}{\rho_o C_o}\right)}{4D\left[\phi^2 + 2\beta\ln\left(\frac{\rho_s C_s}{\rho_o C_o}\right)\right]} \quad (13)$$

has been drawn along the minimum bound of the data.

In the calculation of values of θ_c from Equation (12) the following practical assumptions were made: (1) the droplet was at the wet bulb temperature, (2) the initial evaporation rate was equal to the rate of evaporation of a pure-water droplet of the same size as calculated from the mass transfer correlation of Ranz and Marshall (*10*), (3) K was evaluated at initial conditions, and, (4) the partial specific volume of water in the solution was assumed to be 1.0 cc./g.

A severe limitation on the accuracy of the calculations is imposed by the lack of reliable data for the diffusivities of salts in aqueous solution. Most data in the literature are reported as average values for concentration ranges from fixed values of infinite dilution. The values used in the calculations were based on those reported in the International Critical Tables adjusted as well as possible to the experimental conditions of concentration and temperature.

From the results of the runs in which the weight loss from the drops was measured, it was noted that for any one solute the average moisture content of the particle at the time of crust completion had approximately the same value for all droplets dried and was apparently independent of initial droplet diameter, initial solute concentration, and drying conditions. If this is assumed always to be true, the following expression for θ_c can be derived:

Table 1. Values of the Parameter W_c for Various Solutes

Solute	W_c, lb./lb. dry solid
Sodium sulfate	1.75
Potassium sulfate	4.32
Ammonium nitrate	0.45
Copper sulfate	2.47
Sodium acetate	0.70
Ammonium sulfate	1.22
Ammonium chloride	2.20

$$\theta_c = \frac{x_o^2\rho_o\bar{v}}{12\alpha K}[1-C_o(W_c+1)] \quad (14)$$

For the solutes studied, an average value of α was found to be 0.67. Table 1 lists values of W_c chosen so that values of θ_c calculated from Equation (14) would best fit the experimental data.

In Figure 23 the observed values of θ_c are plotted against those calculated from Equation (14) with the parameters of Table 1. Agreement is quite good between observed and calculated values. However the correlation seems more coincidental than logical. It is quite evident that it will not yield satisfactory results at conditions greatly removed from those under which the experiments were carried out; for instance, it would be expected that, if the initial solute concentration were equivalent to the saturation value at the evaporating temperature, the solid crust would form immediately. To predict this the term $[1-C_o(W_c+1)]$ in Equation (14) must equal zero if C_o is the saturation value. Consequently, since solubility varies with temperature, W_c must also if the correlation is to hold for all temperatures. Such a dependency could not be detected in the experimental results. From solute to solute, however, W_c does seem to be related to solubility as is indicated in Figure 24. If the relation represented by the 45-deg. line in Figure 24 is used for the approximation of W_c values, Equation (14) may be used without the need of experimentally determining parameter values. Also, a zero value of θ_c is then indicated for droplets initially saturated. The equation of the 45-deg. line of Figure 25 is

$$(W_c + 1) = \frac{1}{C_s} \quad (15)$$

Inserting Equation (15) into Equation (14) gives

$$\theta_c = \frac{x_o^2\rho_o\bar{v}}{8K}[1-(C_o/C_s)] \quad (16)$$

Figures 25 and 26 show the observed time of the formation of the first crystals and of the completed crust, respectively, plotted against values calculated from Equation (16).

Final Particle Diameters

The final dried particle was not always spherical, and consequently its final volume was difficult to estimate. Within the experimental error the decrease in the volume of particles from initial droplet to dried particle, when drying was carried out at temperatures below the boiling point, was equal to the volume of the water evaporated before the completion of the solid crust. For drying at temperatures above the boiling point insufficient data were

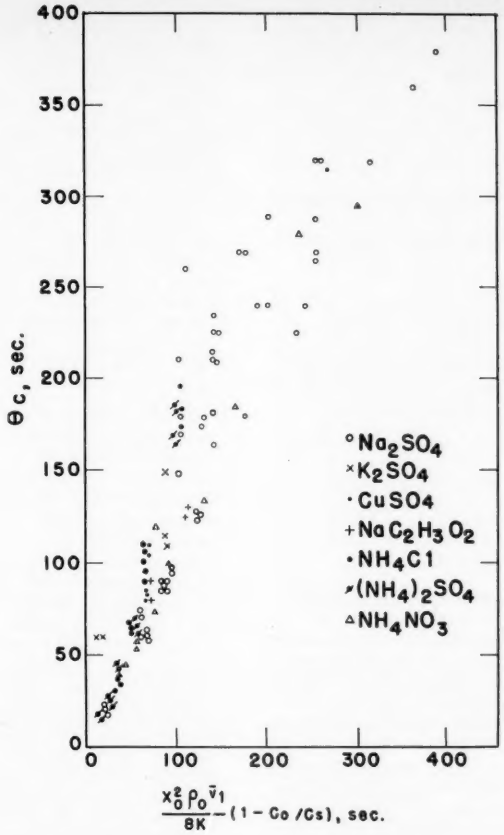

Fig. 26. Correlation of time of crust completion by Equation (16).

obtained to justify any conclusions. In many cases the final particle was larger than the original droplet because of inflation of the crust by internal pressure. The amount of inflation varied from particle to particle, even though drying conditions were constant. Some materials, such as sodium sulfate, showed little expansion under any circumstance.

Circulation Within Drying Droplets

Evidence of liquid movement was noted during the drying of a number of the droplets. However since with few exceptions the circulation appeared to be either on the surface or parallel to it, the movement may be attributed to either circulation within the droplet or rotation of the droplet as a whole. The majority of the observations seemed to indicate the latter. The particles of solid phase which formed during the drying frequently moved about on the droplet surface but were never observed to move into the interior. This does not negate a radial movement of the liquid but may only be an indication of the effect of surface tension and concentration gradients. However on the few occasions when dust particles were observed within the droplet, their motion always appeared to be parallel to the surface.

NOTATION

B = constant in falling-rate equation $= R'_o/W_c$
C = solute weight fraction, g. solute/g. solution
c = concentration, g. solute/cc. solution
D = diffusivity, sq. cm./sec.
F = fraction of initial water removed
H = humidity, lb. water/lb. dry air
h = heat transfer coefficient, cal./(sec.) (sq. cm.) (°C.)
K = evaporation constant, sq. cm./sec.
k = thermal conductivity, cal./(sec.) (sq. cm.) (°C./cm.)
L = vertical distance along spray-dryer axis
m = weight of droplet, g.
N_{Nu} = Nusselt number for heat transfer $= hx/k$
R'_o = rate of evaporation in constant-rate period
r = distance from center of drop
s = weight of total solute in droplet, g.
t = temperature, °C.
v = velocity, cm./sec.
$\bar{v}$ = partial specific volume, cc./g.
W = moisture content, lb. water/lb. dry solid
w = weight of water in droplet, g.
W_c = constant for any particular solute, moisture content
x = diameter of droplet, cm.

Greek Letters

α = constant for any particular solute
$\alpha_n (n=1,2,3\ldots)$ = positive real roots of tan $z = z/(\beta+1)$
β = dimensionless ratio $= K/D$
θ = time variable, sec.
θ_c = time for completion of solid crust
λ = latent heat of vaporization, cal./g.
ρ = density, g./cc.
ϕ = positive real root of tanh $y = y/(\beta+1)$

Subscripts

a = air stream
c = value at instant of crust completion
d = value for dried particle
i = value at instant of appearance of first crystal
m = mean value
o = initial condition
s = value at saturation
t = value at terminal velocity

PART II

The practical value of the observations and correlations reported in Part I of this paper is their applicability to design calculations. In the following numerical example illustrating their use it has been necessary, since much information is not yet available concerning many phases of the spray-drying process, to make reasonable estimates and simplifying assumptions in order to give continuity to the calculations.

A spray dryer operates under the following conditions:

Inlet	Air temperature,	500°F.
	Humidity,	0.010 lb. water/lb. dry air
Outlet	Wet-bulb temperature,	126.5°F.
	Air temperature,	280°F.
	Humidity,	0.060 lb. water/lb. dry air
	Wet-bulb temperature:	126.5°F.

(Negligible heat losses assumed)

Feed	Solute, sodium sulfate Initial solute concentration, 20.0% by weight
Drop size	Distribution, log-probability, by volume Volume median drop size, 100μ Minimum drop size (at 1% level), 40μ Maximum drop size (at 1% level), 250μ

If Equation (15, Part I) is assumed to hold, the moisture content of a particle at time of crust completion equals 2.16 lb. of water/lb. of sodium sulfate. Then the fraction of water removed by the time of crust completion equals

$$\frac{4.0 - 2.16}{4.0} = 0.46$$

If the spray has a homogeneous drop size, then the humidity at crust completion time is $H_c = 0.010 + 0.46(0.060 - 0.010) = 0.033$ lb. of water/lb. of dry air. This corresponds to an air temperature, t_{ac}, of 390°F. For calculation of the time of crust completion, the air conditions may be taken as an average of the initial values and those at crust completion. Hence

$$t_{am} = \frac{500 + 390}{2} = 445°\text{F.}$$

Wet-bulb temperature = 126.5°F.
Humidity (corresponding to above temperatures)
= 0.0223 lb. of water/lb. of dry air

The drops are assumed to have a velocity relative to the air equal to their terminal velocity; then K may be evaluated.

From Equation (13) the crust completion time may be calculated for particular drop sizes; hence

x_o, μ	40	100	250
θ_c, sec.	0.027	0.14	0.53

On the basis of these figures, the spray tower should be designed so that the airflow pattern keeps the spray droplets away from the walls for at least 0.6 sec. after atomization to prevent solid buildup on the walls. Likewise, if there are eddies present around the nozzle which will entrain the fines, there is likely to be buildup if airborne time is less than 0.03 sec.

If it is assumed that the final particle size is the same as the droplet size at the time of crust completion, as appears to be the case with salts as sodium sulfate, then the final particle density and diameter may be calculated.

The amount of evaporation taking place before crust completion can be calculated from the correlations for the drying rate and the completion of the solid crust. The fraction of the initial water removed by crust completion time can be calculated as

$$F_c = \frac{-\left(\frac{dm}{d\theta}\right)_m \cdot \theta_c}{\text{initial water in droplet}} = \frac{0.67\left(\frac{dm}{d\theta}\right)_o \cdot \theta_c}{\frac{\pi}{6} x_o^3 \rho_o (1 - C_o)}$$

The final particle diameter and particle density are then

$$x_d = x_o \left\{ \frac{\rho_o}{\rho_c} [1 - F_c (1 - C_o)] \right\}^{1/3}$$

$$\rho_d = \frac{C_o \rho_c}{1 - F_c (1 - C_o)}$$

For this example numerical results are

x_o, μ	ρ_d, g./cc.	x_d, μ
50	0.350	43.5
100	0.346	87.5
250	0.327	223

Although information on solid-phase formation and product properties is very important for design considerations, a major need is a method of predicting drying times and tower height required for a product of the desired moisture content.

Two drying periods, somewhat analogous to those in tray drying, must be considered in the drying of a spray droplet. The first period is characterized by evaporation from a free liquid surface, and the second by evaporation from or through a solid structure.

The amount of drying taking place in the first period has already been discussed. No extensive data were taken on evaporation rates during the second period. However a linear relationship between evaporation rate and moisture content is common in tray drying, and it is reasonable to assume that such a relationship may be employed to give a first approximation as to rates during the second period of spray drying, provided the proper proportionality constant is used and the particle size does not change appreciably once the solid crust is completed.

As the second period of drying begins in high-temperature drying, the particle temperature is usually near the boiling point of the solution. On the basis of this fact, the calculated particle size, and the heat transfer correlation for spheres (*10*), it is possible to calculate the drying rate at the start of the second period. This enables the estimation of the proper proportionality constant between the drying rate and the moisture content.

For the second period

$$-\frac{dm}{d\theta} = BW$$

where

$$B \frac{R'_o}{W_c}$$

and

$$W_c = (1 - F)\, W_o$$

$$R'_o = \frac{hA\Delta t}{\lambda} = \frac{kN_{Nu}}{x_c} \pi x_c^2 \frac{\Delta t}{\lambda} = \frac{\pi k}{\lambda} \cdot x_c N_{Nu} \cdot \left(\frac{t_a - 212}{1.8} \right)$$

The Nusselt number is evaluated at the terminal velocity of the particle at the instant of crust completion.

Expressed in terms of moisture content, $-(s/B)(dW/W) = d\theta$, where $s = (\pi/6)\rho_o x_o^3 C_o$; hence $\theta = \theta_o + (s/B)\ln(W_c/W)$. This equation gives a relationship between moisture content and drying time. From this can be obtained a relationship between moisture content and distance fallen, if plug flow of air in the tower is assumed.

For any particular particle size

$$L = \int_o^\theta (v_t + v_a)\, d\theta$$

The terminal velocity v_t may be evaluated at an average temperature, since the mean film temperature varies to a much lesser degree than either the particle or air temperatures. For this example v_a, the net downward air velocity in the tower, is taken as 1.5 ft./sec.

The equations may then be applied to the heterogeneous spray, with the approximate temperature profile assumed. This yields a more exact profile. The procedure may then be repeated if necessary.

To apply this method to the numerical example, the original spray was divided into five size classes, equal in volume, the behavior of each class being taken as that of its own median-diameter droplet. The moisture contents as functions of time and of position were determined for the five size classes and for the minimum and maximum droplet sizes. These are plotted in Figures 27 and 28, the resulting temperature profile is plotted in Figure 29.

To carry out this procedure for a heterogeneous spray, it is first necessary to determine an approximate temperature profile in the tower, preferably by carrying out the procedure on the assumption of a homogeneous spray of droplets with diameter equal to the median droplet diameter in the real distribution, that is 100μ for the numerical example treated here.

Assuming that there is no mixing in the tower and that plug flow of air exists one can obtain from the temperature profile an indication of the highest temperatures to which the solid is exposed. This is based on the observation that soon after the solid phase covers the droplet the particle temperature rises sharply toward the air temperature. From Figure 29 it can be seen that the fines might reach 477°F. and that the majority of the particles will be exposed to 350°F.

In these calculations the values used for the crust completion times were the minimum values to be expected. Experiment has shown that the first drying period may persist considerably longer than these values would indicate, but use of the minimum values is preferable, as they represent the worst picture of the process from the drying point of view. A longer duration of the first drying period for a portion of the particles than that assumed would result, in practice, in a lower temperature exposure and a

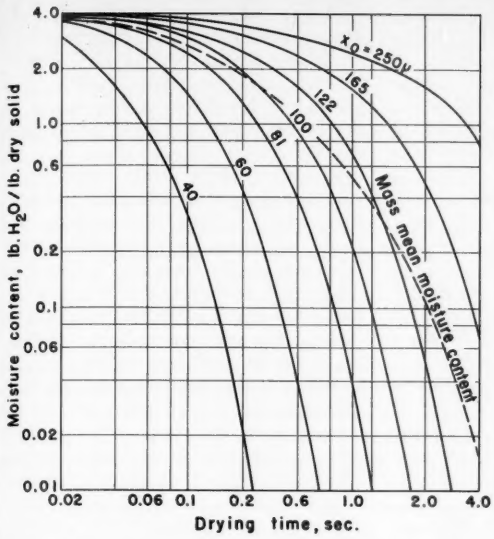

Fig. 27. Variation of moisture content for droplet of sodium sulfate solution with time in a spray dryer.

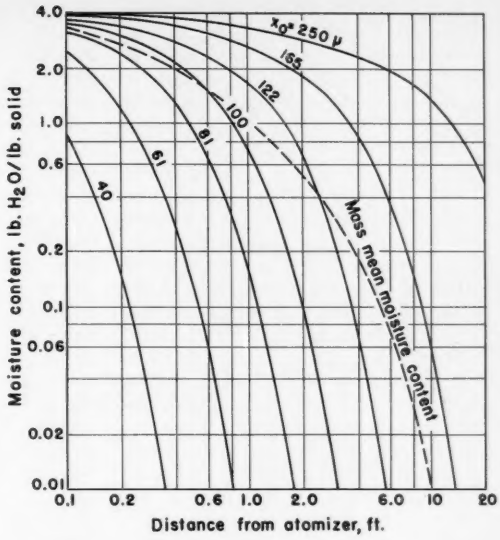

Fig. 28. Particle moisture-content profiles in a spray dryer.

drier product. The only design factor in which a maximum length of the first period might be considered is the air-borne time necessary to prevent buildup on the dryer walls. In the numerical example considered here it would be preferable if dryer size and air-flow pattern were adjusted so that no particle reached the walls in less than 1 sec.

DISCUSSION OF RESULTS

The First Period of Drying

The first period of drying is characterized by evaporation from a free liquid surface. It is natural therefore to compare the evaporation during this period with that taking place from a pure-water droplet. It is doubtful that, as discussed earlier, the assumption of Ranz and Marshall (*10*) that a drop of solution evaporates at all times as if it were saturated, regardless of the average solute concentration in the droplet, is realized in practice. The results of the drying of droplets of calcium chloride solutions seem to confirm this (Figure 19). Apparently the surface concentration rises from its initial value toward the saturation value in a manner similar to that predicted by Equation (8). Consequently the evaporation rate during the first period of drying is less affected by the change in vapor pressure caused by the presence of the solute than would be predicted by the use of the Ranz and Marshall assumption. Also since the majority of salts have only a small effect on vapor pressure, even when present at saturation concentrations, from the standpoint of practical usage rather than theory the increased difficulties to calculation introduced by taking into account a vapor pressure changing with time would not be justified. Except in the drying of solutions of materials, such as calcium chloride, which have a very marked effect on the vapor pressure, it is preferable to assume that the evaporation rate for a solution is the same as that for a pure-water droplet. Greater errors are usually introduced in assumptions concerning the relative velocity of the droplet with respect to the air, especially immediately after atomization, and the air temperature and humidity.

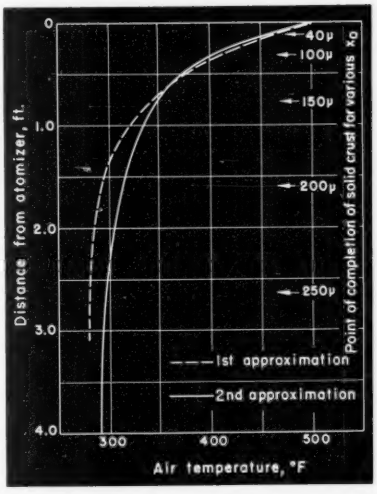

Fig. 29 Calculated temperature profiles in a spray dryer.

A similar argument can be advanced for the use of the wet-bulb temperature as that of the evaporating droplet.

Examination of Figures 9 and 11 shows the approach to equivalence of evaporation rates from droplets of solutions and water initially of the same size. It will be noted that the rate from a droplet of solution remains close to that from a water droplet even after the solid phase has appeared and almost until the droplet is covered with solid. The solid crust is evidently sufficiently porous so that its surface remains wetted and continues to expose a liquid surface to the air stream. From the combination of weight-loss and temperature data it can be shown that during this period the heat transfer coefficient does not show any changes not attributable to the changes in the droplet diameter and temperature. This is further evidence that the liquid interface remains close to the particle surface until the crust completely covers the dropiet.

The Formation of the Solid Phase

The solid-phase formation data as plotted in Figures 22, 23, and 26 show considerable scatter. It is reduced to some extent in Figure 23, since the correlating Equation (14) contains an empirically adjusted parameter. No form of correlating equation, however, could remove all the scatter, since the observed times for crust completion for consecutive runs under identical conditions varied as much as ± 15% from the mean. The usual variation was about ± 7%. A good deal of the scatter of the data can be attributed to natural randomness inherent in the crystalliza-

tion of the crust, the circulation in the drop, and the movement of the partially formed crust about the surface of the drop. Consequently it obscures in small samples the average behavior of a droplet. The fact that such a spread does occur must be considered in analyzing the behavior of a spray. Even though for computing temperature profiles, for example, the large number of droplets could be considered as having an average behavior, the extreme variations from the mean would have to be considered if it were essential that all particles reach a certain level or dryness.

A droplet suspended and drying under the conditions used in this investigation is stabilized to a large extent by the density gradients which accompany the concentration gradients. The solid phase is formed first at the bottom of the droplet and moves progressively up its sides until the entire surface is covered. In a commercial dryer, however, spherical symmetry is approached in the droplets because of rotation induced by atomization and turbulent air. In addition, for free-falling droplets less than 100μ in diameter the terminal velocity is too small to have a significant effect on evaporation rates (*10*). Since the experimental data were taken in a situation in which spherical symmetry was definitely not present and must be applied to one in which it is, direct equivalence cannot be assumed. However it is possible to estimate qualitively the effects of the different conditions and to arrive at a conclusion which is probably as accurate as other uncertainties warrant.

The evaporation rates around a droplet with an air stream impinging on it from one direction are not uniform but vary from a maximum at the point of impingement through a minimum to a second, but smaller, maximum at the opposite pole. A solid phase is formed first in the region of highest evaporation rate and appears sooner than if the mean rate prevailed over the entire surface. Similarly in the areas in which the evaporation rate is lower than the mean, the solid will form later than it would under uniform conditions. Experimentally two periods of time were recorded for each drying droplet, that at which the first solid appeared and that at which the crust completely covered the drop. Theoretically for a droplet having perfect spherical symmetry these two times would coincide. That value would lie between the two experimental values, other factors being equal; the other factors would include circulation within the drop and supersaturation of the surface, as well as the more obvious and easily measured ones of temperature, drop size, initial concentration, etc. It seems more than coincidental that the experimental values of θ_c, as plotted in Figure 22, exhibit a minimum bound equal to 1.84 times the value of θ_c calculated from Equation (12). This bound lies between the values of the times for the appearance of the first crystals and those for the completion of the crust. It is suggested, therefore, that its use would give a good estimate of the time of completion of a solid crust about a free-falling droplet. In the light of some results of Ranz and Marshall this choice seems sound. They dried a droplet of ammonium nitrate solution suspended in still air. Since there was no imposed air velocity, the evaporation rates about the droplet should have been almost uniform. They observed a crust completion time of 600 sec.; the value calculated from Equation (13) is 606 sec.

The final decision as to the soundness of the choice of Equation (13) and of its accuracy must be left until a technique is developed whereby observations, similar to those made in this investigation, can be made for free-falling droplets.

The Second Period of Drying

Drying rates in the second period showed so much variation from particle to particle, even though they were dried consecutively under identical conditions, that a quantitative analysis of the results is impossible. For example, the results of the drying of three droplets of potassium sulfate solution, given in Figure 13, indicate a severalfold variation in total drying time. However the data serve to point out some of the factors involved in the drying process in the second period and give an insight into the physical phenomena which occur.

In the spray drying of a solution, unlike the tray drying of granular and slab materials, the properties of the structure through which the moisture must move are not predetermined. They are dependent not only on the nature of the material being dried but also on the conditions under which the solid is deposited from solution. The previous history of a particle plays a large role in determining its subsequent drying. A factor such as the air velocity past the particle, which ordinarily would be expected to have only a minor effect on drying occurring within a porous structure, may have a large indirect effect as a factor determining the dimensions and nature of that structure.

Some information with regard to moisture movement in the drying particle can be deduced from the experimental observations. The data for the drying of droplets at temperatures less than the boiling point show that the heat transfer coefficient drops markedly at the end of the first period of drying. This indicates an added resistance to transfer of heat from the air stream to the liquid-vapor interface, a result of the retreat of the interface into the interstices of the solid crust. Visual evidence of this retreat was a twinkling, frequently seen in the crust as the liquid withdrew. The retreat of the interface results from the inability of the particle to supply liquid to the surface at a rate equal to the evaporation rate from a continuous liquid surface. The crust is rigid and cannot contract as liquid is removed from the particle. Therefore the liquid will move to the surface from the core of the particle only if the core is supplied with air from without or internal vaporization occurs under an internal pressure reduced by the capillary forces. At subboiling-point temperatures the latter is difficult to realize. If a continuous pathway through the crust, empty of liquid, is not available to permit the passage of air into the particle core, then the volume decrease resulting from evaporation must be compensated for by a retreat of the vapor-liquid interface into the crust. If the withdrawal is sufficient, the necessary pathway may be opened for air to enter the core. This will allow the capillary forces once more to draw the liquid to the particle surface, the result of which will be a rise in evaporation rate to a value comparable to that existing at the end of the first drying period. A fracture of the crust by surface tension or other forces will have the same result as the emptying of a pathway. Once a pore is emptied or the crust fractures, admitting air to the particle core, the moisture is susceptible to movement through the crust under the influence of capillary forces. The situation is complicated by the continual deposition of solid in the crust structure. It is thus possible that the entrance for the air can be sealed off and the cycle repeated.

Further experimental evidence of the occurrence of the events postulated above appears in Figure 10. Similar observations of the return of drying rates to high values were reported by Ernst *et al.* (3) in connection with tray-drying studies. They found that shortly after the falling-rate period of drying had begun, the breaking of the seal at the bottom of the trays by the admittance of air caused drying rates to rise sharply.

Since the moment when a pore will open or the crust will fracture to admit air to the particle depends, in part, on the structure of the crust, which itself is quite random, drying rates in the second period are very unpredictable.

As a result few general conclusions can be drawn. In addition the weakening effect on the crust because of the presence of the suspension filament cannot be discounted.

The situation is little improved at air temperatures above the boiling point. If the particle reaches the boiling point, internal vaporization occurs, and it is no longer necessary for air to be admitted to the core. However the internal pressure frequently fractures the crust, and the further history of the drying becomes dependent on the nature of the fracture. In addition experimental measurement becomes more difficult and, as a result, less accurate. Each of the factors of crust structure, crust strength, and rigidity, crystal form, etc., which are unique properties of the material dried, become of major importance in determining the drying rate and final particle characteristics. Further work is necessary to establish their effect on the drying process.

A few indications of the results to be expected may be found from the data of this investigation. In Figure 11 the weight-loss curves for droplets of three concentrations of ammonium nitrate solutions show that not only was more water removed in a given time from the droplet of lowest initial concentration but also the particle so formed approached dryness more quickly. It has been noted that at the moment the crust is completed the average concentration in the particle is approximately the same no matter what the initial concentration or the drying conditions. This means that if two droplets of the same size are dried, one having twice the original solute concentration of the other, then the more concentrated one will have a particle volume at shell completion approximately twice that of the less concentrated one. The ratio of the surface areas will be about 1.6. Since the more concentrated one contains twice the amount of solid, its shell will be thicker for the same degree of dryness and will offer more resistance to transfer of water through it. When one assumes that the porosity of the crust is equal in both cases and that the evaporation rate per unit area will vary inversely as the thickness of the crust, the gross rate of evaporation from the particle which was originally more concentrated will be 1.26 times that from the originally less concentrated one. However for the same average moisture content the former will contain twice as much water. It would thus be expected that the time required, after the crust completion, to reach a certain average moisture content in the particle would be 2/1.26, or 1.51, times as long if the initial concentration were doubled. Experimentally this has been

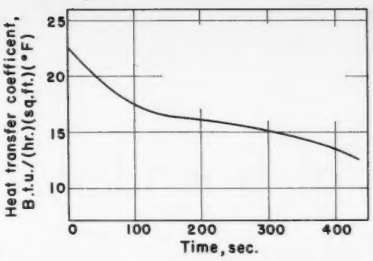

Fig. 30. Variation of heat transfer coefficient during the drying of a droplet of coffee extract.

shown to be of the right order of magnitude. It is not to be presumed, however, that the actual situation is that simple. For example, the original concentration and drying conditions probably have a significant effect on the shell porosity. It should be noted also that the total drying time, which is the final measure of the speed of the drying, depends as well on the time necessary for crust completion.

The Drying of Materials Other Than Inorganic Salts

The correlation methods which have been derived for crust formation are not applicable to suspensions and complex mixtures for which the properties of solubility and diffusivity do not exist in their normal sense. In fact, with materials such as coffee extract, it is difficult to define the transition from a liquid to a solid surface about the drop. However the process of the drying of a droplet containing inorganic salts from its initial formation to the final dried particle cannot be correlated as a whole, since the two drying periods involve different mechanisms. The periods must be treated separately as two interrelated but distinct parts of the same process. There is evidence that the drying of other materials should be treated period by period also.

Ranz and Marshall (*10*) dried droplets of whole milk and of a suspension

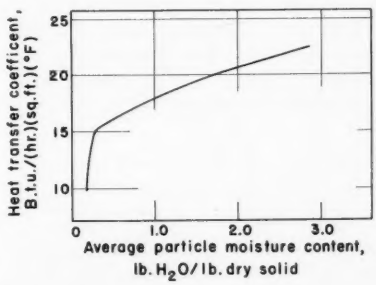

Fig. 31. Change of heat transfer coefficient with the moisture content during the drying of a droplet of coffe extract.

of dye in still air and found that they exhibited a first period during which evaporation occurred at rates which were close to the rate from a water droplet. A second period followed in which lower rates were observed.

When coffee extract was dried in this investigation, the first period of drying seemed to be absent. There was no period during which the particle temperature remained approximately constant; rather it rose steadily from the outset. Both the temperature and weight-loss curves (Figure 17) for drying at temperatures below the boiling point were smooth with no break points and would indicate that all the drying could be considered as having taken place in one period. If, however, the data are analyzed further, evidence of a change in mechanism develops.

The over-all heat transfer coefficient can be estimated from the weight-loss and temperature curves if it is assumed that the area of the particle changes as a result of the weight loss in the same manner as would a sphere. Figures 30 and 31 present the calculated values of h plotted against drying time and average particle moisture content, respectively. From Figure 31 it can be concluded that at a moisture content of 0.4 either there was a sharp retreat of the liquid-vapor interface into the particle or the remainder of the water in the particle was bound and had a higher heat of vaporization. Either explanation is plausible.

ACKNOWLEDGMENT

The authors wish to acknowledge the financial assistance of the Wisconsin Alumni Research Foundation and the Proctor and Gamble Company.

LITERATURE CITED

1. Charlesworth, D. H., doctoral thesis, Univ. of Wis., Madison (1954).
2. Duffie, J. A., and W. R. Marshall, Jr., *Chem. Eng. Progr.*, **49**, 417 and 480 (1953).
3. Ernst, R. C., *et al.*, *Ind. Eng. Chem.*, **30**, 1119 (1938).
4. Fogler, B. B., and R. B. Kleinschmidt, *ibid.*, 1372 (1938).
5. Frössling, N., *Gerlands Beitr. zur Geophysik*, **52**, 170 (1938).
6. Fuchs, V. M., *Phys. Z. Sowjet.*, **6**, 224 (1934).
7. Kirschbaum, E., *Chem. Eng. Tech.*, **24**, 3 (1952).
8. Langstroth, G. O., C. H. H. Diehl, and E. J. Winhold, *Can J. Research*, **28A**, 580 (1950).
9. Luchak, G., and G. O. Langstroth, *ibid.*, **28A**, 574 (1950).
10. Ranz, W. E., and W. R. Marshall, Jr., *Chem. Eng. Progr.*, **48**, 141 and 173 (1952)

Manuscript received August 13, 1957; revision received July 20, 1959; paper accepted August 4, 1959. Paper presented at A.I.Ch.E. Baltimore meeting.

The Application of Boundary-Layer Theory to Power-Law Pseudoplastic Fluids: Similar Solutions

W. R. SCHOWALTER

Princeton University, Princeton, New Jersey

Two- and three-dimensional boundary-layer equations have been developed for pseudoplastic non-Newtonian fluids which can be characterized by a power-law relationship between shear stress and velocity gradient. The types of potential flows necessary for similar solutions to the boundary-layer equations have been determined. For two-dimensional flow the results are similar to those obtained for Newtonian fluids. For three-dimensional flow, however, the possibility of similar solutions depends on the nature of the expression which describes effective viscosity of the fluid. At most, similar solutions are possible only for the case of flow past a flat plate where the potential velocity vector is not perpendicular to the leading edge of the plate; this is a much more restrictive condition than is obtained for Newtonian fluids.

Most problems in fluid mechanics require a solution of the equation of motion

$$\vec{f} - \rho \frac{D\vec{V}}{Dt} = \nabla \cdot (\vec{\tau} + I p) \qquad (1)$$

The solution of this equation is beset with two difficulties: evaluation of $\vec{\tau}$ in terms of known variables and solution of the resulting differential equation. The first difficulty is readily overcome in the case of incompressible Newtonian fluids:

$$\vec{\tau} = -\mu \vec{\Delta} \qquad (2)$$

where

$$\vec{\Delta} = \nabla \vec{V} + (\nabla \vec{V})^{+}$$

and

$$\Delta_{ij} = \frac{\partial v_i}{\partial x_j} + \frac{\partial v_j}{\partial x_i}$$

The formulation of $\vec{\tau}$ for non-Newtonian fluids is a difficult problem which has not progressed very far from a theoretical standpoint; consequently, several empirical descriptions have been used with varying degrees of success. A number of non-Newtonian fluids can be characterized by a so-called "power-law" description.

$$\frac{1}{\rho} \tau_{xy} = -K \left| \frac{\partial u}{\partial y} \right|^{n-1} \frac{\partial u}{\partial y} \qquad (3)$$

When $n > 1$, the fluid is dilatant; $n < 1$ denotes a pseudoplastic fluid. As Reiner (8) points out, this is not a law at all but merely an empirical description which in most cases is not entirely adequate. Nevertheless, for want of a more fundamental understanding, Equation (3) has become a well-established device for the description of certain fluids.

Exact solution of Equation (1) has been possible for only a few restricted types of flow geometries. In an attempt to give a wider application to Equation (1), Prandtl in 1904 introduced the concept of the boundary layer. This concept is based upon the approximation that $\vec{\tau}$ is important only in a thin layer near the flow boundaries. The boundary-layer approximations for Newtonian fluids require that

$$\frac{L U_\infty}{\nu} >> 1$$

Boundary-layer theory has been of great value in determining velocity profiles, drag coefficients, and heat transfer coefficients for systems involving the flow of Newtonian fluids past various shapes of solid surfaces (9). The purpose of this paper is to discuss the applicability of boundary-layer theory to the two- and three-dimensional flow of pseudoplastic power-law fluids. Special emphasis is given to the formulation of boundary-layer equations which provide similar solutions.

It should be noted that a solution of the non-Newtonian boundary-layer equation has recently been obtained for the case of two-dimensional flow past a flat plate at zero incidence to the free-stream velocity (1).

BOUNDARY-LAYER APPROXIMATIONS

The usual application of Equation (3) is to symmetrical flow geometries where $v = w = 0$ and $\partial/(\partial x) = 0$, x being taken in the direction of flow. However, general boundary-layer flow is more complicated, since one is faced with the problem of expressing all the components of the tensor $\vec{\tau}$. It is at this point that the empirical nature of Equation (3) must be remembered. The empirical constants K and n are usually evaluated with one of the standard types of viscometers (5), but there is no *a priori* reason that the indices so evaluated will be the appropriate K and n to use for all the components of $\vec{\tau}$ when the fluid is undergoing a general three-dimensional flow. There is a need for experimental study of this problem. In the present analysis it will be assumed that the fluid is isotropic.

Whatever form is chosen for a pseudoplastic power-law description of $\vec{\tau}$, it is necessary for $\vec{\tau}$ to obey the laws of tensor transformation and for τ_{xy} to have the form given by Equation (3)

for simple rectilinear flow. The tensor character of $\vec{\vec{\tau}}$ has been discussed by Oldroyd (7), who suggests that if

$$-\frac{\vec{\vec{\tau}}}{\rho} = \nu_{eff}\,\vec{\vec{\Delta}} \qquad (4)$$

then ν_{eff} can be expressed in terms of the three invariants of $\vec{\vec{\Delta}}$, namely

$$I_1 = 2\,\nabla\cdot\vec{V}$$

$$I_2 = \frac{1}{2}(\vec{\vec{\Delta}}:\vec{\vec{\Delta}}) = \sum_{j=1}^{j=3}\sum_{i=1}^{i=3}\left\{\frac{\partial v_i}{\partial x_j}\,\frac{\partial v_j}{\partial x_i} + \left(\frac{\partial v_j}{\partial x_i}\right)^2\right\}$$

$$I_3 = |\Delta_{ij}|$$

where $|\Delta_{ij}|$ refers to the determinant of $\vec{\vec{\Delta}}$. Since the continuity equation for incompressible fluids

$$\nabla\cdot\vec{V} = 0$$

ensures that I_1 is zero, ν_{eff} will be a function of I_2 and I_3. Hence a possible expression for ν_{eff} in the general case is

$$\nu_{eff} = K\left[(I_2)^{\frac{n-1}{2}} + f_1(n, I_2, I_3)\right] \qquad (5)$$

where f_1 is some function which must be zero for $n = 1$ and/or $I_3 = 0$. These restrictions ensure that $\vec{\vec{\tau}}$ reduces to (2) for a Newtonian fluid and to (3) for simple rectilinear flow, since I_3 is zero for two-dimensional flow. The exact nature of f_1 is not known, and it is of course possible that f_1 is zero for all values of I_3. Substitution of Equation (5) into (4) results in an expression for $\vec{\vec{\tau}}$ which obeys the laws of tensor transformation. When the external force term is neglected, the $\vec{i}$ component of the equation of motion for steady flow becomes

$$u\frac{\partial u}{\partial x} + v\frac{\partial u}{\partial y} + w\frac{\partial u}{\partial z} = -\frac{1}{\rho}\frac{\partial p}{\partial x} + \vec{i}\cdot\left(\nabla\cdot\frac{\vec{\vec{\tau}}}{\rho}\right) \qquad (6)$$

The other components are similar. Equation (6) may be rewritten in dimensionless form by referring all lengths to a characteristic length and all velocities to a characteristic velocity U_∞. Thus if $u^\circ = u/U_\infty$, $v^\circ = v/U_\infty$, $x^\circ = x/L$, $p^\circ = p/\rho U_\infty^2$, etc., and the coordinates are chosen as shown in Figure 1

$$u^\circ\frac{\partial u^\circ}{\partial x^\circ} + v^\circ\frac{\partial u^\circ}{\partial y^\circ} + w^\circ\frac{\partial u^\circ}{\partial z^\circ} = -\frac{\partial p^\circ}{\partial x^\circ} + \frac{KU_\infty^{n-2}}{L^n}\,\vec{i}\cdot\{\nabla^\circ\cdot[[(I^\circ_2)^{\frac{n-2}{2}} + f^\circ_1(n, I_2, I_3)]\vec{\vec{\Delta}}^\circ]\} \qquad (7)$$

Following Schlichting (9), one can determine the relative magnitudes of the terms in Equation (7), if the usual boundary-layer approximation is made; namely that the dimensionless ratio of the boundary-layer thickness to the characteristic length is small. Hence $\delta << 1$. The characteristic velocity is of the order of magnitude of the velocity outside the boundary layer, and so u° is of order one. Also L is selected so that $(\partial u^\circ)/(\partial x^\circ) \gtrless 1$, and it is assumed that w° and $(\partial w^\circ)/(\partial z^\circ)$ are of an order of magnitude $\gtrless 1$. Then if one defines a Reynolds number $R = L^n/(KU_\infty^{n-2})$ and assigns to it a magnitude R_m, the magnitudes of the terms in Equation (7) are as follow:

Term 1: $u^\circ\dfrac{\partial u^\circ}{\partial x^\circ} \sim 1$

Term 2: $v^\circ\dfrac{\partial u^\circ}{\partial y^\circ} \sim \delta\cdot\dfrac{1}{\delta}$

The quantity v° is of the order δ, since the continuity equation requires $\dfrac{\partial v^\circ}{\partial y^\circ} \sim 1$.

Term 3: $w^\circ\dfrac{\partial u^\circ}{\partial z^\circ} \sim 1$

Term 4: $\dfrac{\partial p^\circ}{\partial x^\circ}$ unknown

Term 5: $\dfrac{1}{R}\dfrac{\partial}{\partial y^\circ}\{[(\dfrac{\partial u^\circ}{\partial y^\circ})^2 + (\dfrac{\partial w^\circ}{\partial y^\circ})^2]^{\frac{n-1}{2}}(\dfrac{\partial u^\circ}{\partial y^\circ})\} + \dfrac{1}{R}f^\circ_{zz} \sim \dfrac{1}{R_m}\dfrac{1}{\delta^{n+1}}$

Only the largest terms have been retained in Term 5 for $n>0$. The quantity f°_{zz}, which denotes the significant terms of the operation $\vec{i}\cdot\nabla^\circ\cdot[f^\circ_1\vec{\vec{\Delta}}^\circ]$, is assumed to be of no greater order of magnitude than the largest terms which result from $i\cdot\nabla^\circ\cdot[(I^\circ_2)^{\frac{n-2}{2}}\vec{\vec{\Delta}}]$. To give indentical orders of magnitude to the inertial and friction terms of Equation (7), R_m must be of order $1/\delta^{n+1}$.

From the dimensionless equation of motion in the $\vec{j}$ direction one finds that $(\partial p^\circ)/(\partial y^\circ)$ can be of no greater magnitude than δ. This means that $(\partial p^\circ)/(\partial x^\circ)$ must be of the same order of magnitude within the boundary layer as it is in the potential-flow region outside the boundary layer. Hence the boundary-layer approximation for the $\vec{i}$ component of the equation of motion becomes

$$u\frac{\partial u}{\partial x} + v\frac{\partial u}{\partial y} + w\frac{\partial u}{\partial z} = U\frac{\partial U}{\partial x} + W\frac{\partial U}{\partial z} + K\frac{\partial}{\partial y}\left\{\left[\left(\frac{\partial u}{\partial y}\right)^2 + \left(\frac{\partial w}{\partial y}\right)^2\right]^{\frac{n-1}{2}}\frac{\partial u}{\partial y}\right\} + Kf_{zz} \qquad (8)$$

where $U=U(x,z)$ and $W=W(x,z)$. A similar analysis for the $\vec{k}$ component of the equation of motion results in

$$u\frac{\partial w}{\partial x}+v\frac{\partial w}{\partial y}+w\frac{\partial w}{\partial z}=U\frac{\partial W}{\partial x}+W\frac{\partial W}{\partial z}+K\frac{\partial}{\partial y}\left\{\left[\left(\frac{\partial u}{\partial y}\right)^2+\left(\frac{\partial w}{\partial y}\right)^2\right]^{\frac{n-1}{2}}\frac{\partial w}{\partial y}\right\}+Kf_{zz} \qquad (9)$$

It is important to recognize that the applicability of Equations (8) and (9) is determined in part by the extent to which the inequality

$$R \cong \frac{1}{\delta^{n+1}} >> 1$$

is true and that R does not depend on the effective viscosity in the same way that it does on the viscosity of a Newtonian fluid. Thus while it is sometimes stated that boundary-layer theory applies to liquids of low viscosity and therefore not to non-Newtonian fluids, which are characterized by a "high" viscosity, it is the magnitude of the Reynolds number which is ultimately the criterion for applicability. For example, for a 33% lime suspension in water flowing under such conditions that $L = 1$ ft. and $U_\infty = 5$ ft./sec., using the rheological properties tabulated by Metzner (5) one finds that $R \cong 310$ or $\delta \cong 7 \times 10^{-3}$, thus fulfilling the condition $\delta << 1$.

SIMILAR SOLUTIONS

One of the important considerations of boundary-layer theory is a determination of the types of potential flows for which the boundary-layer equations will possess similar solutions. Solutions which provide expressions for u/U or w/W as functions of a single parameter η, where $\eta = \eta(x, y, z)$, are similar. A study of similar solutions has been made by Hansen and Herzig (3) for incompressible Newtonian fluids in three-dimensional flow and by Schlichting and others (2, 4, 9) for two-dimen-

sional flow. The remainder of this paper is concerned with similar solutions for pseudoplastic non-Newtonian fluids which can be characterized by a power-law relationship such as that of Equation (5). Only similarity with respect to rectangular Cartesian coordinates is considered in the present analysis. It is possible that more general results can be obtained by the use of an approach analogous to that outlined by Morgan (6).

As before, the potential velocity is given by

$$U = U(x, z)$$
$$W = W(x, z)$$

Two functions $F(\eta)$ and $G(\eta)$ are defined so that

$$u = UF'(\eta) \qquad (10)$$
$$w = WG'(\eta) \qquad (11)$$

The prime denotes differentiation with respect to η, where

$$\eta = \frac{y R^N}{Lg(x, z)} \qquad (12)$$

The form of η is analogous to that of the similarity parameter commonly used with Newtonian fluids. It is possible that other similarity parameters could be used (*cf.* reference 3), but they do not appear to have any advantage over Equation (12).

The boundary conditions require that

$$u = v = w = 0 \text{ at } y = 0$$

and

$$\lim_{\eta \to \infty} F' = \lim_{\eta \to \infty} G' = 1$$

Following Hansen and Herzig (3), one can show from the continuity equation that

$$v\left(\frac{R^N}{L}\right) = -g\left(F\frac{\partial U}{\partial x} + G\frac{\partial W}{\partial z}\right) + \frac{\partial g}{\partial x}U(\eta F' - F) + W\frac{\partial g}{\partial z}(\eta G' - G) \qquad (13)$$

where $F(0) = G(0) = 0$.

Application of Equations (10) through (13) to Equation (8) and subsequent conversion to dimensionless quantities result in

$$\frac{g^{n+1}}{(U^\circ)^{n-1}}\frac{\partial U^\circ}{\partial x^\circ}[(F')^2 - FF'' - 1] + \frac{g^{n+1}W^\circ}{U^\circ}\frac{\partial U^\circ}{\partial z^\circ}[F'G' - 1] - \frac{g^{n+1}}{(U^\circ)^{n-1}}GF''\frac{\partial W^\circ}{\partial z^\circ} - \frac{g^n}{(U^\circ)^{n-2}}\frac{\partial g}{\partial x^\circ}FF'' - \frac{g^n W^\circ}{(U^\circ)^{n-1}}F''G\frac{\partial g}{\partial z^\circ} = R^{N(n+1)-1}\frac{\partial}{\partial \eta}\left\{[(F'')^2 + (\frac{W}{U}G'')^2]^{\frac{n-1}{2}}F''\right\} + \frac{KLg^{n+1}}{U_\infty^2(U^\circ)^n}f_{2z} \qquad (14)$$

The explicit Reynolds number dependence is removed by setting $N = 1/(n+1)$. Rearranging terms yields

$$\frac{1}{(U^\circ)^{n-1}}\frac{\partial U^\circ}{\partial x^\circ}[(F')^2 - FF'' - 1] + W^\circ\frac{\partial \ln U^\circ}{\partial z^\circ}[F'G' - 1] - \frac{1}{(U^\circ)^{n-1}}\frac{\partial W^\circ}{\partial z^\circ}GF'' - \frac{1}{(U^\circ)^{n-2}}\frac{\partial \ln g}{\partial x^\circ}FF'' - \frac{W^\circ}{(U^\circ)^{n-1}}\frac{\partial \ln g}{\partial z^\circ}F''G = \frac{1}{g^{n+1}}\frac{\partial}{\partial \eta}\left\{\left[(F'')^2 + \left(\frac{W}{U}G''\right)^2\right]^{\frac{n-1}{2}}F''\right\} + \frac{KL}{U_\infty^2(U^\circ)^n}f_{2z} \qquad (15)$$

A similar result is obtained from Equation (9):

$$\frac{1}{(W^\circ)^{n-1}}\frac{\partial W^\circ}{\partial z^\circ}[(G')^2 - GG'' - 1] + U^\circ\frac{\partial \ln W^\circ}{\partial x^\circ}[F'G' - 1] - \frac{1}{(W^\circ)^{n-1}}\frac{\partial U^\circ}{\partial x^\circ}FG'' - \frac{1}{(W^\circ)^{n-2}}\frac{\partial \ln g}{\partial z^\circ}GG'' - \frac{U^\circ}{(W^\circ)^{n-1}}\frac{\partial \ln g}{\partial x^\circ}FG'' = \frac{1}{g^{n+1}}\frac{\partial}{\partial \eta}\left\{\left[\left(\frac{U}{W}F''\right)^2 + (G'')^2\right]^{\frac{n-1}{2}}G''\right\} + \frac{KL}{U_\infty^2(W^\circ)^n}f_{2z} \qquad (16)$$

If Equations (15) and (16) can be expressed in terms of functions of η alone, the equations will be ordinary differential equations and solutions will provide the form of F' and G' to be used in Equations (10) and (11). Such solutions for u/U or w/W are similar. The author wishes to establish the types of three-dimensional potential flows which will permit elimination of all quantities from Equations (15) and (16) which are not expressible as functions of η alone. An immediate problem is posed by the presence of W/U and U/W in the right sides of Equations (15) and (16) respectively. If the equations are to reduce to ordinary differential equations, it is apparent that one must have W/U = const. unless F'' and G'' are zero. However the latter condition does not permit fulfillment of the boundary conditions for Equations (10) and (11).

If W/U = const. and it is presumed for the moment that f_1 is zero, Equations (15) and (16) can be expressed as ordinary differential equations in η for the case where $n<1$ if

$$(U^\circ)^{1-n}\frac{\partial U^\circ}{\partial x^\circ} = a_1 W^\circ\frac{\partial \ln U^\circ}{\partial z^\circ} = a_2(U^\circ)^{1-n}\frac{\partial W^\circ}{\partial z^\circ} = a_3(U^\circ)^{2-n}\frac{\partial \ln g}{\partial x^\circ} = a_4(U^\circ)^{1-n}W^\circ\frac{\partial \ln g}{\partial z^\circ} = \frac{a_5}{g^{n+1}} = a_6(W^\circ)^{1-n}\frac{\partial W^\circ}{\partial z^\circ} = a_7 U^\circ\frac{\partial \ln W^\circ}{\partial x^\circ} = a_8(W^\circ)^{1-n}\frac{\partial U^\circ}{\partial x^\circ} = a_9(W^\circ)^{2-n}\frac{\partial \ln g}{\partial z^\circ} = a_{10}(W^\circ)^{1-n}U^\circ\frac{\partial \ln g}{\partial x^\circ} \qquad (17)$$

where the a_i represent proportionality coefficients not equal to zero, and it has been assumed that all the terms in Equations (15) and (16) other than those arising from f_1 have nonzero values. The requirement of proportionality between U and W is also stated in Equation (17):

$$(U^\circ)^{1-n} = a_8(W^\circ)^{1-n}$$

Therefore

$$(U^\circ)^{1-n}\frac{\partial U^\circ}{\partial x^\circ} = a_7 U^\circ\frac{\partial \ln\left(U^\circ a_8^{\frac{1}{n-1}}\right)}{\partial x^\circ} = a_7\frac{\partial U^\circ}{\partial x^\circ} \qquad (18)$$

Equation (18) can be satisfied only if $\partial U^\circ/\partial x^\circ = 0$, a condition which is incompatible with the statement that

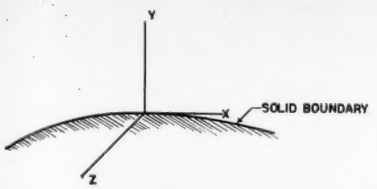

Fig. 1. Orientation of coordinate system with respect to solid surface.

no terms of Equation (17) are zero. A similar result is obtained for $\partial W^\circ/\partial z^\circ$ from the requirement that $a_2(U^\circ)^{1-n}(\partial W^\circ)/(\partial z^\circ) = a_9(W^\circ)^{1-n}(\partial W^\circ)/(\partial z^\circ)$. Hence for similar solutions

$$\frac{\partial U^\circ}{\partial x^\circ} = \frac{\partial W^\circ}{\partial z^\circ} = 0$$

$$\frac{W^\circ}{U^\circ} = \text{const.}$$

or

$$U^\circ = \text{const.}$$

$$W^\circ = \text{const.}$$

If U° and W° are constant, the similarity condition reduces to

$$a_3(U^\circ)^{2-n}\frac{\partial \ln g}{\partial x^\circ} = a_4(U^\circ)^{1-n}W^\circ\frac{\partial \ln g}{\partial z^\circ} = \frac{a_3}{g^{n+1}} = a_9(W^\circ)^{2-n}\frac{\partial \ln g}{\partial x^\circ} = a_{10}(W^\circ)^{1-n}U^\circ\frac{\partial \ln g}{\partial x^\circ} \quad (19)$$

Equation (19) leads to the result

$$g^{n+1} = a_3(n+1)\left[\frac{1}{a_3}(U^\circ)^{n-2}x^\circ + \frac{1}{a_9}(W^\circ)^{n-2}z^\circ\right] \quad (20)$$

The above analysis shows that similar solutions to the three-dimensional boundary-layer equations can be obtained only for the case of flow past a flat plate, where the potential velocity vector is not parallel to one of the coordinate axes. On the other hand, similar solutions for Newtonian fluids exist for several types of potential flows (3). If the potential velocity vector is perpendicular to the leading edge of the plate, the flow is really two dimensional, but the coordinate axes have been chosen in such a way that $W \neq 0$. For such a flow I_3, and therefore f_1, are zero. However, U° = const. and W° = const. may also describe flow past a flat plate whose leading edge is not perpendicular to the potential velocity vector. In this case f_1 may be nonzero, and additional proportionality conditions may preclude similarity. Thus at most one can expect similar solutions to the three-dimensional boundary-layer equations only for the case of flow past a flat plate where the potential velocity vector is not perpendicular to the leading edge of the plate.

It should be noted that the terms of Equations (15) and (16) could have been collected differently; however, the results would not be affected.

Next the case of two-dimensional flow is considered, where $W^\circ = 0$, $U^\circ = U^\circ(x)$, and $g = g(x)$. Equation (15) reduces to

$$\frac{g^{n+1}}{(U^\circ)^{n-1}}\frac{dU^\circ}{dx^\circ}[1-(F')^2] + \frac{g^n}{(U^\circ)^{n-1}}\frac{d(U^\circ g)}{dx^\circ}FF'' + \frac{d}{d\eta}\left\{[(F'')^2]^{\frac{n-1}{2}}F''\right\} = 0 \quad (21)$$

When one sets

$$\alpha = \frac{g^n}{(U^\circ)^{n-1}}\frac{d(U^\circ g)}{dx^\circ}$$

and

$$\beta = \frac{g^{n+1}}{(U^\circ)^{n-1}}\frac{dU^\circ}{dx^\circ}$$

Equation (21) becomes

$$\beta[1-(F')^2] + \alpha FF'' + \frac{d}{d\eta}\left\{[(F'')^2]^{\frac{n-1}{2}}F''\right\} = 0 \quad (22)$$

and has a form identical to that given by Schlichting (9).

If Equation (22) is to possess similar solutions, it is a necessary condition that α and β be constants. Furthermore from the definitions of α and β

$$\frac{d}{dx^\circ}[g^{n+1}(U^\circ)^{2-n}] = \alpha(n+1) + \beta(1-2n) \quad (23)$$

If one stipulates that $\alpha(n+1) + \beta(1-2n) \neq 0$ and that $g^{n+1}(U^\circ)^{2-n} = 0$ at $x = 0$, Equation (23) can be integrated to give

$$g = \{(U^\circ)^{n-2}x^\circ[\alpha(n+1) + \beta(1-2n)]\}^{\frac{1}{n+1}} \quad (24)$$

It is also true that

$$(\alpha-\beta)\frac{d\ln U^\circ}{dx^\circ} = \beta\frac{d\ln g}{dx^\circ} \quad (25)$$

so that

$$(U^\circ)^{\alpha-\beta} = Ag^\beta \quad (26)$$

Combining Equations (24) and (26) leads to the result

$$U^\circ = [A^{n+1}\{x^\circ[\alpha(n+1) + \beta(1-2n)]\}^\beta]^{\frac{1}{\alpha(n+1)+\beta(1-2n)}} \quad (27)$$

Equations (24) and (27) can be simplified by choosing g in such a way that $\alpha = 1$ (when one assumes $\alpha \neq 0$). Such an operation will alter g only by a constant factor and therefore will not interfere with the analysis. If one then defines

$$\gamma = \frac{\beta}{n+1+\beta(1-2n)}$$

$$\beta = \frac{\gamma(n+1)}{1-\gamma(1-2n)} \quad (28)$$

Equations (24) and (27) become

$$g = \left[(U^\circ)^{n-2}\frac{(n+1)x^\circ}{1+\gamma(2n-1)}\right]^{\frac{1}{n+1}} \quad (29)$$

$$U^\circ = A^{1+\gamma(2n-1)}\left[\frac{(n+1)x^\circ}{1+\gamma(2n-1)}\right]^\gamma \quad (30)$$

These two equations show that for the case of $\alpha \neq 0$ and $\alpha(n+1) + \beta(1-2n) \neq 0$ similar solutions are possible whenever the potential velocity is proportional to x° raised to some power. This is exactly the same conclusion which is obtained for Newtonian fluids (9).

If for example a potential flow can be described by

$$U^\circ = a(x^\circ)^c \quad (31)$$

the boundary-layer equation can be transformed by setting

$$g = \left[a^{n-2}(x^\circ)^{c(n-2)+1}\frac{n+1}{1+c(2n-1)}\right]^{\frac{1}{n+1}}$$

Then from Equation (12)

$$\eta = y\left[\frac{1+c(2n-1)}{(n+1)KU_\infty^{n-2}La^{n-2}(x^\circ)^{c(n-2)+1}}\right]^{\frac{1}{n+1}}$$

For the special case where $\alpha = 0$, Equations (24) and (27) reduce to

$$g = [(U^\circ)^{n-2}x^\circ\beta(1-2n)]^{\frac{1}{n+1}} \quad (32)$$

$$U^\circ = [A^{\frac{n+1}{\beta}}x^\circ\beta(1-2n)]^{\frac{1}{1-2n}} \quad (33)$$

In the event that $\alpha \neq 0$ but $\alpha(n+1) + \beta(1-2n) = 0$, one obtains from

Equation (23)

$$g^{n+1}(U^\circ)^{2-n} = B \qquad (34)$$

Using the definition of β along with the special constraint which relates α and β, one gets

$$\alpha - \beta = \frac{n-2}{n+1} B \frac{d\ln U^\circ}{dx^\circ} \qquad (35)$$

or

$$U^\circ = C\, e^{mx^\circ} \qquad (36)$$

where

$$m = \left(\frac{n+1}{n-2}\right)\frac{\alpha-\beta}{B}$$

Equation (36) is identical in form to the result obtained for Newtonian fluids when $2\alpha - \beta = 0$.

From the definitions of α and β

$$\alpha - \beta = g^n (U^\circ)^{2-n} \frac{dg}{dx^\circ} \qquad (37)$$

When one substitutes Equation (36) into (37) and integrates,

$$g^{n+1} = \frac{(\alpha-\beta)(n+1)}{C^{2-n}m(n-2)} e^{mx^\circ(n-2)} \qquad (38)$$

In this case $g(0)$ has been chosen so that

$$[g(0)]^{n+1} = \frac{(\alpha-\beta)(n+1)}{C^{2-n}m(n-2)}$$

The function g can again be chosen in such a way that $\alpha = 1$; then

$$\beta = \frac{n+1}{2n-1}$$

and

$$g^{n+1} = \frac{(n+1)\, C^{n-2} e^{m(n-2)x^\circ}}{m(2n-1)} \qquad (39)$$

Equation (39) gives g in terms of quantities known from the potential velocity and from the physical properties of the fluid.

SUMMARY

The foregoing analysis shows that similar solutions to the boundary-layer equations for pseudoplastic power-law fluids are mathematically possible for certain types of potential-velocity relationships. In two-dimensional flow the potential flows which permit similar solutions are analogous to those which allow similar solutions in the case of Newtonian fluids. In three-dimensional flow the possibility for similar solutions depends on the form of f_1. At most, similar solutions will be possible only for the case of flow past a flat plate where the potential-velocity vector is not perpendicular to the leading edge of the plate. This is a much more restrictive result than is obtained for Newtonian fluids in three-dimensional flow.

ACKNOWLEDGMENT

The author is grateful to R. B. Bird for helpful comments concerning the invariance of ν_{eff} and to Arthur G. Hansen for his careful review of the manuscript.

NOTATION

A = constant of integration in Equation (26)

a = constant in Equation (31)

a_i = proportionality constants in Equation (17)

B = constant of integration in Equation (34)

C = constant of integration in Equation (36)

c = constant in Equation (31)

F = function of η

f = external force

f_1 = function defined by Equation (5)

f_{2x} = largest terms which result from the operation $\vec{i}\cdot\nabla^\circ\cdot[f_1^\circ\vec{\Delta}^\circ]$

f_{2z} = largest terms which result from the operation $\vec{k}\cdot\nabla^\circ\cdot[f_1^\circ\vec{\Delta}^\circ]$

G = function of η

g = function of x and z

$\vec{\vec{I}}$ = unit tensor

I_1, I_2, I_3 = the three invariants associated with $\vec{\vec{\Delta}}$

$\vec{i}, \vec{j}, \vec{k}$ = unit vectors in the directions shown in Figure 1

K = kinematic fluid consistency index

L = characteristic length

m = $\left(\frac{n+1}{n-2}\right)\frac{\alpha-\beta}{B}$

N = $\frac{1}{n+1}$

n = flow-behavior index

p = pressure

R = $\frac{L^n}{KU_x^{n-2}}$

R_m = order of magnitude of R

U, V, W = potential velocity components in the $\vec{i}$, $\vec{j}$, and $\vec{k}$ directions, respectively

u, v, w = velocity components in the $\vec{i}$, $\vec{j}$, and $\vec{k}$ directions, respectively

v_i = the i^{th} component of $\vec{V}$

U_x = characteristic velocity which is of the order of magnitude of the potential velocity

$\vec{V}$ = velocity vector

x, y, z = distance components in the $\vec{i}$, $\vec{j}$, and $\vec{k}$ directions, respectively

x_i = x, y, or z for $i = 1$, 2, or 3, respectively

Greek Letters

α = $g^n(U^\circ)^{1-n}\frac{d(U^\circ g)}{dx^\circ}$

β = $g^{n+1}(U^\circ)^{1-n}\frac{dU^\circ}{dx^\circ}$

γ = $\frac{\beta}{n+1+\beta(1-2n)}$

$\vec{\vec{\Delta}}$ = $\nabla\vec{V} + (\nabla\vec{V})^+$

Δ_{ij} = $\frac{\partial v_i}{\partial x_j} + \frac{\partial v_j}{\partial x_i}$

δ = dimensionless boundary-layer thickness

η = $\frac{yR^x}{Lg(x,z)}$

μ = viscosity

ν = kinematic viscosity

ν_{eff} = effective kinematic viscosity defined by Equation (4)

$\vec{\vec{\pi}}$ = pressure tensor

ρ = density

$\vec{\vec{\tau}}$ = $\vec{\vec{\pi}} - \vec{\vec{I}}p$

τ_{xy} = component of the pressure tensor on the $\vec{j}$ face of an element of fluid and acting in the $\vec{i}$ direction

Superscripts

$^\circ$ denotes dimensionless quantity

$'$ denotes differentiation with respect to η

$(\nabla\vec{V})^+$ = transpose of $\nabla\vec{V}$

LITERATURE CITED

1. Acrivos, Andreas, *et al.*, Paper presented at Christmas Symposium of Industrial and Engineering Chemistry Division of American Chemical Society (December, 1958).
2. Falkner, V. M., and S. W. Skan, *Phil. Mag.*, **7**, 865 (1931).
3. Hansen, Arthur G., and Howard Z. Herzig, *Natl. Advisory Comm. Aeronaut. Tech. Note 3768* (October, 1956).
4. Hartree, D. R., *Proc. Camb. Phil. Soc.*, **33**, 223 (1937).
5. Metzner, A. B., in "Advances in Chemical Engineering," Vol. 1, Academic Press, New York (1956).
6. Morgan, A. J. A., *Trans. Am. Soc. Mech. Engrs.*, **80**, 1559 (1958)
7. Oldroyd, J. G., in "Rheology," Vol. 1, Academic Press, New York (1956).
8. Reiner, M., "Deformation and Flow," Lewis, London, England (1949).
9. Schlichting, Hermann, "Boundary Layer Theory," Pergamon Press, New York, (1955).

Manuscript received December 18, 1958; revision received June 4, 1959; paper accepted June 8, 1959.

Heat and Mass Transfer in Spray Drying

JAN DLOUHY and W. H. GAUVIN

McGill University, Montreal, Quebec, Canada

Studies of the evaporation and drying rates in an experimental concurrent spray dryer, 8 in. in diameter and 14 ft. high, are reported for various operating air temperatures. It was found that the total evaporation and drying time could be accurately predicted by employing a step-by-step method of calculation. Owing to the probable absence of internal diffusional resistance in the small particles, less than 30 μ, produced in the dryer, no significant falling-rate period was observed. This was in marked contrast with tray-drying experiments carried out on the same substance, under similar drying conditions. The results also confirmed that a Nusselt number of 2 can safely be used in spray-drying heat transfer calculations.

The evaporation and subsequent drying of the atomized droplets in a spray dryer involve simultaneous considerations of heat, mass, and momentum transfer. Similar considerations also form the basis of related operations of chemical engineering such as spray cooling, flash drying, spray crystallization, and cyclone evaporation. In spite of the growing industrial importance of these various operations there are still certain aspects of the mechanism of evaporation and drying of atomized sprays which have not been sufficiently investigated to permit the formulation of sound design criteria. In particular the rate of evaporation of small droplets suspended in a turbulent gas stream has never been properly ascertained, nor has the rate of drying of such droplets been experimentally determined under conditions likely to be encountered in spray dryers.

Most of the research pertaining to heat and mass transfer in spray drying has been carried out on single, relatively large, stationary drops of pure solvent. The more important contributions are due to Froessling (*1*) who made an experimental as well as a theoretical analysis of the problem, and to Ranz and Marshall (*2*) who in 1952 presented the following equations for heat and mass transfer to a drop under forced or natural convection:

$$N_{Nu} = 2+0.60\ (N_{Re})^{1/2}(N_{Pr})^{1/3} \quad (1)$$

$$N_{Nu'} = 2+0.60\ (N_{Re})^{1/2}(N_{Sc})^{1/3} \quad (2)$$

$$N_{Nu} = 2+0.60\ (N_{Gr})^{1/4}(N_{Pr})^{1/3} \quad (3)$$

$$N_{Nu'} = 2+0.60\ (N_{Gr})^{1/4}(N_{Sc})^{1/3} \quad (4)$$

The Nusselt number as given in these equations is termed the "apparent" Nusselt number and applies only at low evaporation rates. At higher rates the diffusing vapor leaving the drop surface changes the temperature gradient in the gas film surrounding the drop, and use of a correction has been recommended by several workers (*3, 4, 5, 6*).

The reliability of Equations (1) to (4) has been amply demonstrated, but to permit the calculation of the evaporation rate, the temperature of the droplet must of course be known. With pure solvents there is no problem, since the drops will be at or at least very close to the wet-bulb temperature of the air, provided that dynamic equilibrium is attained and that the surroundings are not at too high a temperature (*2, 4*). In the presence of a solute however the vapor pressure of the solvent will be depressed, and the droplet temperature will rise. From a rather limited study Ranz and Marshall (*2*) suggested that a saturated film is established very rapidly at the drop surface and that the rate of evaporation will correspond to saturated conditions, independent of the bulk concentration. Their work was done on single drops of ammonium nitrate solutions (about 1 mm. in diameter) suspended from a capillary, through which solvent was added continuously to maintain the diameter constant throughout the test, and the Reynolds number was 66.6. Although it is apparent that under these conditions a saturated film does form, later work at the University of Wisconsin indicated that this mechanism did not apply to certain soluble salts (*7*), and in any case it is doubtful whether it will prevail under actual spray-drying conditions.

The same general theoretical considerations apply for heat transfer to clouds of particles as do to single drops, but again certain complicating factors must be taken into account, such as the turbulence of the conveying gas stream, the particle-size distribution, and the effect of the lowered vapor pressure due to the presence of a solute (*8*).

Kessler (*9*) studied experimentally the diffusion of atomized sprays in turbulent air streams and concluded from his results that the eddy diffusivities of the particles and of the gas stream were essentially equal. Using alcohol drops he also found that the Nusselt number had a numerical value of approximately 2, although his study of the evaporation rate was only of a secondary nature. This would indicate then that the relative velocity between the particles and the gas stream is negligible despite the turbulent eddies. Soo (*10*) made a theoretical analysis of this problem, and the equation he presented tends to confirm this conclusion, at least for small particle diameters.

Further evidence has also been presented by the authors (*11*) in a study of the heat and mass transfer coefficients to clouds of water droplets in turbulent air streams. For mean Sauter diameters ranging from 11.5 to 38.5 μ, the Nusselt number was found to have the value 2.07 $\pm$ 0.06 under various conditions of air velocity and temperature, which is in good agreement with Kessler's conclusions.

Marshall (*12*) also used a Nusselt number of 2 in proposing a step-by-step method for the calculation of the rate of evaporation of a cloud of water droplets of a given size distribution.

The question of a falling-rate period* in spray drying has received little attention, principally because of the difficulties associated with the experimental measurements. The calculation of particle temperature and the estimation of diffusional resistance in the final stages of drying still remain largely a matter of trial and error (*8*). Some qualitative information can be obtained from the examination of the physical state of the spray-dried product (*13*), but such observations are inadequate for quantitative calculations.

EXPERIMENTAL

In most conventional spray dryers the particle trajectories and gas-flow patterns are of such complexity that it is difficult to follow the progressive evaporation and drying of the particles. A special vertical concurrent spray dryer was therefore built in which all the pertinent variables could be measured along the drying path. The rate of evaporation and drying of Lignosol (trade name of dried calcium spent sulphite liquors, consisting essentially of calcium lignosulphonate) was determined in this chamber under various operating conditions, and the experimental results were compared with theoretical calculations. No attempt was made in this study to take measurements close to the nozzle, as this was the object of a separate investigation (*14*).

Jan Dlouhy is with Cyanamid of Canada, Ltd., Niagara Falls, Ontario, Canada.

* Although the rate of evaporation from a solution steadily falls as the solute concentration increases, the term "falling-rate period" as used here is restricted to its conventional meaning and applies only to the drying of the solid formed near the end of the operation.

TABLE 1. OPERATING DATA AND EXPERIMENTAL RESULTS
RUN NO. 20

Feed rate — 5.68 lb./hr. Feed concentration — 18.2% Feed temp. — 86°F.

Atom. air pressure — 20 lb./sq. in. gauge Drying air rate — 891 lb. dry air/hr.

x, ft.	t, °F.	H, lb. water / lb. dry air	D_{vs}, μ	X, lb. water /lb. Lignosol	X_{hb},	X_{mb},
0	147.0	0.0031	—	4.49	4.49	4.49
1.46	134.0	—	—	—	2.00	
1.79	—	0.0064	28.9	1.86	—	1.65
1.96	129.9	—	—	—	1.22	
2.86	126.5	—	—	—	0.45	
3.19	—	0.0079	21.1	0.42	—	0.36
4.86	125.3	—	—	—	0.19	
5.19	—	0.0082	16.1	0.02	—	0.10
6.86	125.2	—	—	—	0.10	
7.19	—	0.0083	16.9	0.02	—	0.01
8.86	125.1	—	—	—	0.10	
9.19	—	0.0084	15.8	0.01	—	0.00
11.19	—	—	15.0	0.01		

Equipment

The experimental spray dryer, a detailed description of which has been given previously (*11*), consisted of the same basic components as an industrial installation.

The well-insulated drying chamber was 14 ft. high and 8 in. in diameter. Sampling ports were provided throughout the length of the unit, and electric heaters with automatic control were used to heat the air to the desired temperature. The pressure in the chamber was maintained at nearly atmospheric value by means of a push-pull blower arrangement.

An internal-mixing pneumatic nozzle, was used for atomization of the Lignosol solution, and a pressurized feed tank provided a steady flow to the nozzle.

Methods of Measurement

To follow the progressive evaporation and drying of the droplets special sampling techniques had to be used which would permit conditions along the entire length of the drying chamber to be determined. In addition methods for the measurement of air temperature, humidity, particle size, and solid concentration were developed.

Air temperature. The presence of liquid droplets in the air stream necessitated the use of shielding. Thermocouple probes were found to be unsatisfactory. A semicircular shield, 0.4 in. in diameter and 1.5 in. long, installed on the bulb of a precision mercury thermometer (0.2-in. diameter) was found to give the best results, particularly when the stem of the thermometer was protected with glass tubing to minimize heat losses. Calibration checks (*11*) have shown that drop impingement on the bulb was insignificant and that the true gas temperature was determined.

Air humidity. The more common methods of humidity determination were rejected either because they lacked sufficient accuracy or because they required too large an air sample. A special volumetric method of measurement was therefore developed.

In essence the technique consisted of absorbing the water vapor from a known volume of air by contact with magnesium perchlorate and of noting the resulting change in volume. A precision 100-ml. mine-air gas burette was used, calibrated in 0.05-ml. subdivisions in the upper range. Calibration tests carried out with air of known humidity showed that under rigidly constant conditions of temperature and pressure results with an error of less than 1% could be obtained (*11*).

Air samples were drawn from the drying chamber countercurrently to the main stream, through an inverted aluminum cup, 0.75-in. I.D., which was inserted into the chamber at a predetermined sampling port. The air was sucked into an evacuated sampling bottle at such a rate that the air velocity in the cup was well below the average terminal velocity of the droplets, thus achieving the desired gas-liquid separation.

Particle size. The method developed by J. H. Rupe (*15*) was used to determine the droplet size and size distribution along the chamber. It consisted of collecting a sample of the spray in a small immersion cell, 0.22-in. O.D. and 0.18-in. I.D., the bottom of which was made of optical glass and filled with Varsol. The glass was coated so that the droplet remained spherical. The sample was obtained by quickly traversing the spray with the cell held in a special holder. Because of the very low surface tension between Varsol and water no tendency for the drops to coalesce was observed. The target efficiency was excellent, as shown by the number of very small droplets which were collected. The droplets were photographed immediately upon sampling, and from 150 to 300 particles were measured in each sample. To test the accuracy of the method, determinations were carried out on several samples collected under identical operating conditions, and the agreement was found to be excellent. A log-normal distribution was found to be approximated by the drop-size data, and at an atomizing air pressure of 20 lb./sq. in. gauge the maximum droplet size was found to be around 100 μ.

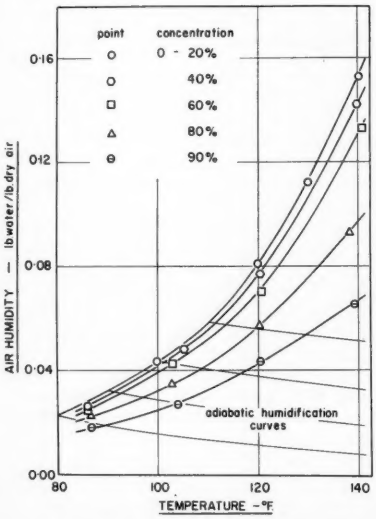

Fig. 1. Saturation humidities of Lignosol solutions.

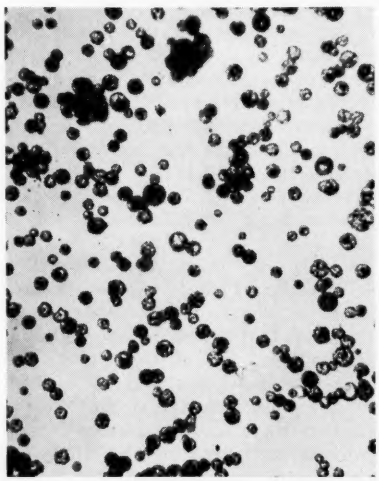

Fig. 2. Photomicrograph of Lignosol particles, run number 20 (220 X).

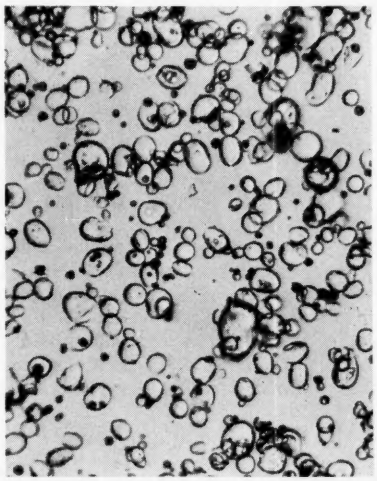

Fig. 3. Photomicrograph of Lignosol particles, run number 23 (220 X).

TABLE 2. OPERATING DATA AND EXPERIMENTAL RESULTS
RUN NO. 23

Feed rate — 5.70 lb./hr. Feed concentration — 18.2% Feed temp. — 86°F.

Atom. air pressure — 20 lb./sq. in. gauge Drying air rate — 530 lb. dry air/hr.

x, ft.	t, °F.	H, lb. water / lb. dry air	X_{hb} lb. water/lb. Lignosol	X_{mb} lb. water/lb. Lignosol
0	419.0	0.0261	4.50	4.50
0.79	406.0	—	3.10	
1.12	385.5	—	0.85	
1.46	379.5	—	0.19	
1.79	—	0.0347	—	0.00
1.96	377.8	—	0.00	
2.86	377.8	—	0.00	
3.19	—	0.0348	—	0.00

Lignosol concentration. The concentration of Lignosol in the particles at various distances from the nozzle was determined on small samples of the spray by means of a colorimetric method.

The major problem was in collecting the sample, since it was essential that evaporation be stopped as soon as the droplets entered the sampler, while at the same time it was necessary to know the total mass of sample collected. A small immersion cell was therefore used, filled with a silicone fluid, immiscible with both water and Lignosol solutions. Since the vapor pressure of the former is only about 0.5 mm. Hg at 70° to 100°C., no measurable evaporation could occur and the net increase in mass of the tared cell corresponded to the mass of sample collected, which ranged from 25 to 150 mg.

Lignosol is brown in color when in the presence of water, and concentrations around 0.1% can readily be measured in a colorimeter with a 425 μ filter. The instrument was calibrated by means of standard solutions carefully prepared from Lignosol of almost zero moisture content. Following dilution of the samples from the cell the total Lignosol content, and hence the solids concentration of the spray, could easily be determined by this method.

Physical Properties of Lignosol

To analyze the operation of the spray dryer certain pertinent physical properties of Lignosol solutions were required. The density and specific heat capacity were readily determined by the use of standard laboratory methods, and the following approximate equations were obtained in the temperature range from 70° to 120°F.:

$$\rho_s = 62 + 25/(1 + X) \qquad (5)$$

$$C_{ps} = 1 - 0.61/(1 + X) \qquad (6)$$

The heat of solution was found to be negligible, but the vapor pressure of Lignosol solutions of various concentrations had to be determined over a range of temperatures. A dew-point apparatus immersed in a constant-temperature bath (*16*) was used for this purpose, and the results obtained are shown in the form of a humidity chart in Figure 1. It can be seen that up to a concentration of about 20% Lignosol solutions exhibit typical colloidal properties, while above that concentration a decrease in vapor pressure takes place.

Procedure and Results

A rigidly standardized procedure was used to make runs on the experimental spray dryer (*11*). The major precautions were concerned with the determination of heat losses to permit proper heat balances and the establishment of equilibrium conditions prior to the taking of any readings.

Four runs were made with Lignosol solutions used as feed under approximately the same conditions of air velocity, feed rate, feed concentration, and atomizing pressure, but with inlet drying-air temperatures ranging from 106° to 419°F. The operating conditions used and experimental results obtained for two temperatures are shown in Tables 1 and 2. In the first table (run 20, inlet air temperature 147°F.) X denotes the solid concentration as determined experimentally. No such data could be obtained in run 23, shown in Table 2 (inlet air temperature 419°F.), because the fluid decomposed at the temperature used, and no samples could be collected for the determination of solid concentration. Samples were still taken for particle-size measurement however.

The values of X_{hb} *and* X_{mb} shown in the tables were calculated from heat and material balances respectively; they provided a valuable check on the accuracy of the data. Figure 2 shows a typical photomicrograph of the product obtained in run 20, while Figure 3 shows the hollow particles produced in run 23. Photomicrographs of samples taken at increasing distances from the nozzle showed clearly that the droplets were still liquid at an average concentration of at least 84% and that expansion of the particles in run 23 did not occur until the very last stages of drying.

To permit a comparison between spray drying and tray drying an experimental run was made in a standard laboratory tray dryer, by means of a transite tray with a dummy front and a 5- by 5- by ⅜-in. depression in the center, in which the Lignosol solution was placed. The air temperature, air humidity, and initial concentration of the solution for the tray-drying test were practically identical with the conditions used in run 20, and the drying curve obtained is shown in Figure 4. The drying rate was constant up to 65 min., at which time a thin crust started to form on the surface. The crust was completed after about 140 min. and assumed a hard consistency after 190 min., at which point all drying practically stopped in spite of the fact that the bulk-moisture content was only about 50%.

Discussion of Results

The good agreement between the observed and the calculated values of the particle moisture content (X, X_{hb}, and X_{mb}), as shown in Figure 5, reflects the accuracy of the results. It should be noted that because the Lignosol concentrations were experimentally measured as a function of the distance from the nozzle, they there-

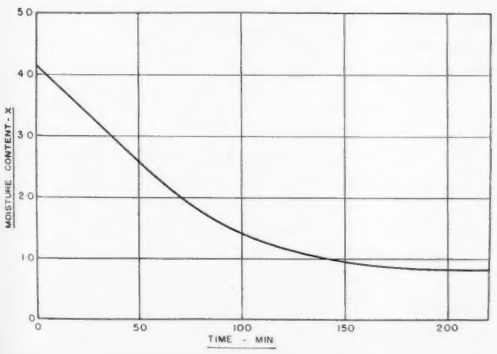

Fig. 4. Drying curve, tray-drying experiment.

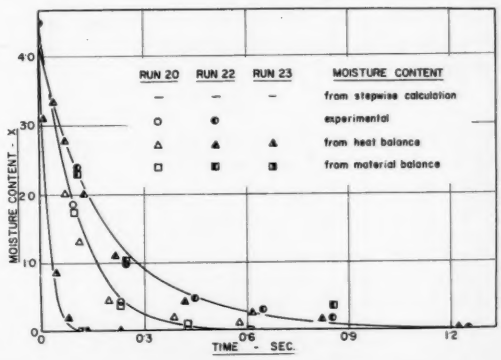

Fig. 5. Drying curve, spray-drying experiments.

fore had to be expressed on the basis of time elapsed before comparison with theoretical calculations could be established. The conversion could readily be made for the so-called "fall zone" of the drying chamber, in which the particle velocity is the same as that of the drying air, since their terminal velocity is negligibly small. In the nozzle zone however the particle velocity is not known and extrapolation is necessary. When distance vs. concentration was plotted, a curve with an inflection at a distance of about 10-in. from the nozzle was obtained for all four runs. The lower portion of this curve, which applies to the fall zone, was therefore extrapolated, and the intercept between this curve and the feed concentration was taken as the zero distance from the nozzle for the purpose of time calculations.

Good agreement was also found between the experimental and calculated values of the air humidities, as shown in Figure 6 (run no. 22, inlet air temperature 106°F.) on which the observed variations in air temperature down the chamber are also indicated. The same type of extrapolation as explained above was again carried out, as indicated by the dotted lines.

Further evidence of the accuracy of the experimental data was obtained from the particle-size measurements. The mean volume diameter of the spray must be a function of concentration and density only, if the particles are not hollow and no agglomeration occurs, as shown by

$$(n\pi D_v^3)/(6) = (Z)/(c) \qquad (7)$$

Since the value of n was not known accurately, the experimental value of D_v at a distance of 1.79 ft. from the nozzle was taken as a basis, and the value of D_v was calculated from Equation (7) at various points (and hence various concentrations) down the chamber. Table 3 shows that excellent agreement with the experimentally observed values was obtained. This, incidentally, confirms the validity of the particle-size determinations, since in contrast to the estimation of D_{vs} the small particles are no longer unimportant in the measurement of D_v.

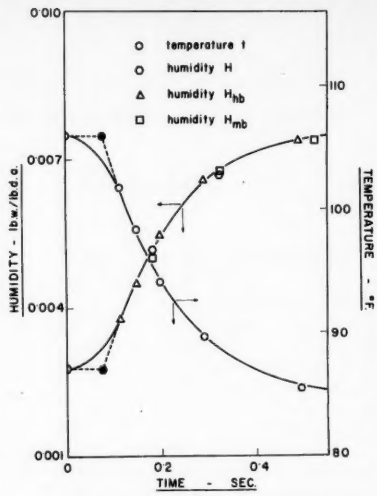

Fig. 6. Temperature and humidity distribution, run number 22.

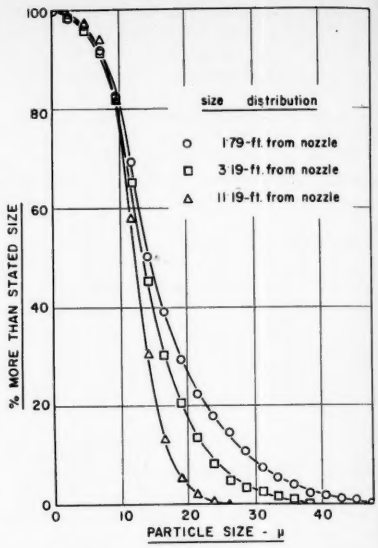

Fig. 7. Particle size distribution, run number 20.

Calculation of Evaporation and Drying Times

The experimental runs were carried out primarily to determine the observed evaporation and drying rates of Lignosol sprays under known conditions and to compare them with values calculated from theoretical considerations.

The theoretical approaches developed by Probert (*17*), Daskin (*18*), Miesse (*19*), and Shapiro and Erickson (*20*), among others, can be used for the estimation of the evaporation time only. When solid particles are formed, a step-by-step method of calculation must be resorted to, as advocated by Marshall (*12*), since it is no longer permissible to use average values for the physical properties of the particles. This is clearly indicated by Figure 7, which gives the size distribution (on a number basis) at various distances from the nozzle for run 20; it is obvious that the smaller particles are completely dried at a point where the larger ones are still almost at the feed concentration.

The calculations were therefore carried out by division of the particles into several groups, each of a given size range. For each group the rate of heat transfer (when one neglects the sensible heat effects due to the increase in wet-bulb temperature) can be expressed as

$$(dQ/d\theta) = n_i h \pi D_i^2 (t - t_w) = \lambda_w (dm/d\theta) \qquad (8)$$

It has been pointed out that the Nusselt number in Equations (1) and (3), and hence the heat transfer coefficient which it includes, is the apparent one. Godsave (*6*) has proposed the following equation for the calculation of the actual Nusselt number at the drop surface:

$$(N_{Nu})_{\text{actual}} = (N_{Nu})_{E=0} \, [E(1/R_1 - 1/R_2)]/[e^{E(1/R_1 - 1/R_2)} - 1] \qquad (9)$$

In a discussion of this equation Marshall (*3*) points out that the actual value of the Nusselt number can be significantly lower than the apparent one at high evaporation rates, that is when E is large, and that the convective heat transfer coefficient for high air temperatures should be calculated from the equation

$$h_{act} = (h_{app})(a)/(e^a - 1) \qquad (10)$$

where $a = E(1/R_1 - 1/R_2)$. At low Reynolds numbers a is also equal to $\ln(1 + \Delta t c_p/\lambda_w)$. Under the experimental conditions used in this study the correction indicated by Equation (10) was found to be negligibly small, and h_{app} was used in the calculations.

When one combines Equations (8), (10), and (7), the following expression is derived for each group:

$$dm = \frac{6 h_{app} Z_i \, (t - t_w)}{D_i \rho_{si} c_i \lambda_w} \, d\theta \qquad (11)$$

TABLE 3. MEAN VOLUME DIAMETERS

x, ft.	Run 20		Run 21		Run 22	
	Exp.	Calc.	Exp.	Calc.	Exp.	Calc.
1.79	21.6	21.6	20.3	20.3	22.2	22.2
3.19	17.7	16.9	16.6	15.7	—	
5.19	14.9	15.1	15.2	14.7	15.8	16.0
7.19	14.4	14.6	14.3	14.2	—	
9.19	14.3	14.5	—	—	—	
11.19	13.9	14.5	13.7	13.9	—	
13.19	—	—	—	—	13.9	13.9

Table 4. Calculated Drying Time for Lignosol Solutions (Particle Concentration Percentage)

Run 20

Diameter, μ	Z_i, lb. dry Lignosol/hr.
2.4	0.0002
7.2	0.0282
11.9	0.3458
16.7	0.4690
21.4	0.1530
26.2	0.0387

θ, sec.	Dry particle diameter, μ 2.4	7.2	11.9	16.7	21.4	26.2	X_{avg}, lb. water / lb. Lignosol	t, °F.
0	18.2	18.2	18.2	18.2	18.2	18.2	4.49	147.0
0.10	100	100	56.9	30.9	24.9	22.3	1.85	134.4
0.20	100	100	100	60.4	34.5	27.3	0.68	128.5
0.30	100	100	100	100	49.7	33.7	0.22	126.2
0.40	100	100	100	100	76.7	42.5	0.09	125.6
0.55	100	100	100	100	100	63.1	0.02	125.3

In this equation the particle concentration, density, diameter, and temperature for each group will be functions of dm, as will h_{app} [which can be obtained from $(N_{Nu})_{app} = 2$].

To carry out the calculations a knowledge of Z_i in each group is required. This is the only information which must be obtained experimentally, since it depends on the size distribution peculiar to the atomizing nozzle. In the present study it was obtained as follows: the spectrum of dry particles of Lignosol collected at the bottom of the chamber was divided into six groups of average diameters 2.4, 7.2, 11.9, 16.7, 21.4, and 26.2 μ, respectively. From the size-distribution curve the number of particles in each group, and Z_i for the group, could be calculated, if one remembered that $\Sigma Z_i =$ the rate of solids fed in the Lignosol solution per hour. Equation (11) was then used to calculate the change in concentration for each group in incremental intervals. More specifically the calculations were based on the following procedure:

1. For each size group the initial diameter of the droplet was back calculated from Equation (7) and its temperature obtained from Figure 1 with the bulk concentration of the feed used to determine the saturation vapor pressure.

2. The amount of water evaporated in the time increment was calculated from Equation (11) with the inlet conditions used for all the values in the equation and $(N_{Nu})_{app} = 2$ assumed.

3. The new conditions of air properties (temperature and humidity) and particle properties following evaporation occurring during the incremental period were calculated from the change in concentration that was obtained in step 2.

4. The calculations in step 2 were repeated, but this time the prevailing conditions as obtained in step 3 were used.

5. The values of Δm obtained in steps 2 and 4 were averaged to give a more accurate change in concentration for each size group in the time interval.

6. The step-by-step calculations given in 1 to 5 were repeated for new time intervals, until the average concentration of the product was almost 100%. Corrections for the residual, equilibrium, moisture content of each fraction of particles were attempted but found to have negligible effect on the results.

The results of these step-by-step calculations for run 20 are summarized in Table 4, which shows the average values of the moisture content and the calculated values of the corresponding air temperature at 0.05-sec. intervals. Similar calculations were also made for runs 22 and 23, and the calculated moisture contents are represented by the continuous curves shown in Figure 5. The good agreement with the experimental points is obvious.

It should be pointed out that the particle-size distribution could not be determined experimentally from the dried product obtained in run 23, since the latter consisted of hollow particles which expanded during the last stages of the driving process. However since identical atomizing conditions and feed concentration were used in run 20, the distribution data obtained in the latter case were used instead.

CONCLUSIONS

The results of this study indicate that the drying time for a spray can be calculated with good accuracy, at least for highly soluble materials such as Lignosol. A Nusselt number of 2 can be safely assumed, and the estimation of particle temperature should be based on the bulk concentration of the droplets. To carry out the calculations knowledge of the droplet-size distribution for the atomizing nozzle employed must be available. This may be obtained from a spray sample taken in the nozzle range if unheated air near saturation is admitted to the chamber to minimize evaporation, which is otherwise appreciable in that region (*14*), or it may be obtained from a size-distribution determination on the dry product, as was done in the present study. Care must be taken in the latter case that the particles are completely solid. Marshall pointed out that it is not a simple matter to produce solid particles by spray drying (*12*). Table 2 clearly shows however that solid particles of Lignosol were produced at low air temperatures. At higher temperatures (run 23) hollow particles were obtained in accordance with the general behavior (*12, 13*).

It is interesting to note that no significant falling-rate period (as defined earlier) could be detected, which is in marked contrast with the tray-drying experiment (Figure 4). In the latter the start of a very definite falling-rate period was detected at a moisture content of about 2.35 lb. water/lb. Lignosol, and drying almost stopped at a value of 0.83 lb. water/lb. Lignosol. In contrast Figure 5 and Table 4 indicate that the rate of moisture removal in the spray dryer is governed by the rate of evaporation under free liquid condition up to very high solid concentrations.

The difference lies in the concentration at which crust formation takes place. In the tray-drying experiment the depth of the sample was relatively large, and a heavy crust formed at a low bulk concentration. The diffusional resistance through this crust effectively reduced the evaporation rate. In the spray-drying experiments, on the other hand, the droplets were very small, and a crust did not form until the very last stages of drying; visual observations showed no evidence of crust formation below a solid content of 0.85.

Most authors argue from indirect evidence that the formation of a solid phase at the droplet surface introduces a diffusional resistance which slows down the rate of evaporation. The fact that residual moisture is almost always found in spray-dried products has been attributed to this cause (*21*) (in addition, of course, to equilibrium moisture considerations), although Table 4 shows that it may also be due to the comparatively long time required by

the larger particles to dry under free liquid condition. With solutions other than Lignosol it is possible that the falling-rate period will become significant, but this will have to be determined experimentally for each individual case.

ACKNOWLEDGMENT

Financial assistance from the National Research Council of Canada in the form of a research grant and of the award of a fellowship to Jan Dlouhy is gratefully acknowledged.

NOTATION

a = $E(1/R_1 - 1/R_2)$;
c = solution concentration, lb. solids/lb. solution
c_i = solution concentration in ith group, lb. solids/lb. solution
C_{ps} = heat capacity of particles, B.t.u./(lb.)(°F.)
C_p = heat capacity of water vapor, B.t.u./(lb.)(°F.)
D = particle diameter, ft.
D_i = average particle diameter in ith group, ft.
D_v = mean volume diameter, ft.
D_{vs} = mean Sauter diameter, μ
E = $(dm/d\theta)(C_p/4\pi k_f)$
h = heat transfer coefficient, B.t.u./(hr.)(sq.ft.)(°F.)
H = air humidity, lb. water/lb. dry air
H_{hb} = air humidity calculated from heat balance, lb. water/lb. dry air
H_{mb} = air humidity calculated from material balance, lb. water/lb. dry air
k_f = thermal conductivity of gas film surrounding the drop, B.t.u./(hr.)(ft.)(°F.)
m = evaporation, lb.
n = rate of particles, No./hr.
Q = heat transferred to droplets, B.t.u.
R_1 = radius of particle, ft.
R_2 = radius of outer limit of gas film surrounding the drop, ft.
t = temperature of air, °F.
t_w = temperature of particles, °F.
X = moisture content, lb. water/lb. dry Lignosol
X_{hb} = moisture content calculated from heat balance, lb. water/lb. dry Lignosol
X_{mb} = moisture content calculated from material balance, lb. water/lb. dry Lignosol
x = distance from nozzle, ft.
Z = total rate of dry Lignosol, lb./hr.
Z_i = rate of dry Lignosol in particles in ith group, lb./hr.
Δm = amount of water evaporated
$\Delta\theta$ = time increment
θ = time, hr.
λ_w = latent heat of evaporation at the particle temperature, B.t.u./lb.
ρ_s = density of particles, lb./cu.ft.
ρ_{si} = average density of particles in ith group, lb./cu.ft.
N_{Gr} = Grashof number
N_{Nu} = Nusselt number
N_{Nu}' = modified Nusselt number
N_{Pr} = Prandtl number
N_{Re} = Reynolds number
N_{Sc} = Schmidt number

LITERATURE CITED

1. Froessling, N., *Gerlands Beitr. Geophys.*, **52**, 170 (1938).
2. Ranz, W. E., and W. R. Marshall, Jr., *Chem. Eng. Progr.*, **48**, 141, 173 (1952).
3. Marshall, W. R., Jr., *Chem. in Can.*, **7**, 37 (1955).
4. Ranz, W. E., *Trans. Am. Soc. Mech. Engrs.*, **78**, 909 (1956).
5. Sleicker, C. A., Jr., and S. W. Churchill, *Ind. Eng. Chem.*, **48**, 1819 (1956).
6. Godsave, G. A. E., *Collected Papers of the 4th Int. Symp. on Combustion*, Cambridge, Massachusetts (September 1952).
7. Charlesworth, D. H., Ph.D. thesis, Univ. Wisconsin, Madison (1954).
8. Marshall, W. R., Jr., *Chem. Eng. Progr. Symposium Ser. No. 2*, **50** (1954).
9. Kesler, G. H., Thesis, Mass. Inst. Technol., Cambridge (1952).
10. Soo, S. L., *Chem. Eng. Sci.*, **5**, 57 (1956).
11. Dlouhy, Jan, and W. H. Gauvin, *Can. J. Chem. Eng.*, in press.
12. Marshall, W. R., Jr., *Trans. Am. Soc. Mech. Engrs.*, **77**, 1377 (1955).
13. Duffie, J. A., and W. R. Marshall, Jr., *Chem. Eng. Progr.*, **49**, 417 (1953).
14. Manning, W. P., Ph.D. thesis, McGill University, Montreal, Quebec, Canada (1958).
15. Rupe, J. H., "Third Symposium on Combustion, Flame and Explosion Phenomena," The Williams and Wilkins Co., Baltimore, Maryland (1949).
16. Glasstone, Samuel, "Textbook of Physical Chemistry," 2 ed., p. 632, Van Nostrand, New York (1946).
17. Probert, R. P., *Phil. Mag.*, **37**, 94 (1946).
18. Daskin, W., *Proc. Fourth Midwestern Conf. on Fluid Mechanics*, Purdue Univ., Lafayette, Indiana (Sept. 8-9, 1955).
19. Miesse, C. C., *J. Franklin Inst.*, **264**, No. 5, 391 (1957).
20. Shapiro, A. H., and A. J. Erickson, *Trans. Am. Soc. Mech. Engrs.*, **79**, 775 (1957).
21. Kirschbaum, E., *Chem.-Ing.-Tech.*, **24**, 3 (1952).

Manuscript received January 14, 1959; revision received June 1, 1959; paper accepted June 8, 1959. Paper presented at A.I.Ch.E. Cincinnati meeting.

The Effect of Dynamic Surface Tension on Nucleate Boiling Coefficients

P. D. JONTZ and J. E. MYERS

Purdue University, West Lafayette, Indiana

A study was made of the effects the surface tension of aqueous solutions of surface-active agents had on the bubble-formation characteristics of these solutions. Bubbles were formed by two processes: by passing air through a horizontal orifice submerged in the solution and by nucleate boiling at an electrically heated surface. The experimental measurements taken with the air-bubble system were used to determine the nature of the surface-tension effect on air-bubble formation. This knowledge was then applied to the interpretation of boiling measurements made with the same solutions. The boiling coefficients of the Tergitol-water solution were found to vary inversely with dynamic surface tension. Boiling coefficients for Aerosol-water solutions, however, varied in a manner which could not be related to surface-tension effects.

Numerous investigators have studied the role of surface tension in boiling and have reported widely contradictory results. Westwater (*10*) summarizes the results in terms of the value assigned to the exponent n in an assumed exponential relationship, $h \alpha 1/\sigma^n$; the range of values he reports is 2.5 to −1.275. As Westwater points out, there

P. D. Jontz is with Union Oil Company of California, San Francisco, California.

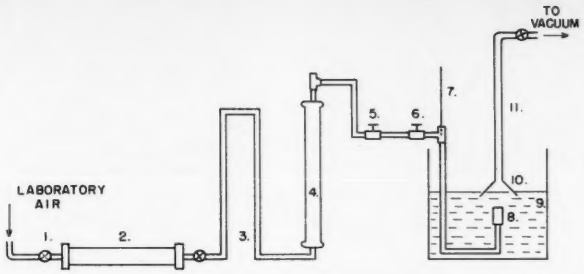

1. PRESSURE REDUCER
2. SURGE TANK
3. BACKFLOW CHECK
4. HUMIDIFIER
5. COARSE CONTROL VALVE
6. FINE CONTROL VALVE
7. GAS THERMOMETER
8. ORIFICE
9. LIQUID BATH AND TANK
10. FUNNEL
11. BURETTE

Fig. 1. Diagram of bubble apparatus.

are theoretical grounds for considering surface tension to be an important variable in boiling, and these have led numerous investigators to attempt quantitative measurements of the relationship. Experimental evidence gathered to date, however, has not proved the existence of such an effect.

The commonest experimental approach has been to add a surface-active agent to a boiling solution and from the results to establish an exponential relationship between the measured boiling coefficients and the static surface tension of the solution. It is known that the surface tension of a solution of a surface-active agent is dependent on the history of the system. For example, DuNouy (3) reports equilibrium values for aqueous sodium oleate solutions which are only 40% of the measured dynamic values. The time necessary to achieve equilibrium was between 2 and 10 min., depending on concentration. Tests with rabbit serum required up to 2 hr. for equilibrium to be established. Weiser (9) shows large differences between static and dynamic surface tensions for solutions of sodium oleate, saponin, heptylic acid, and lauryl sulfonic acid; dynamic determinations were made by the capillary-wave method and static surface tensions by the capillary-tube method.

Because the formation of bubbles in a boiling system is an extremely rapid process, sometimes requiring only a few milliseconds, it would seem that if surface tension has any effect on boiling solutions it would be the dynamic surface tension which would apply and not the static surface tension. Several methods have been reported for the measurement of dynamic surface tension (8). These involve measurements of such diverse quantities as the oscillation rate of a falling drop, the distance between nodes in a vibrating liquid jet issuing from an elliptic orifice, and the cone angle produced by two impinging jets. However the total lack of geometric similarity between these systems and a boiling system makes it unlikely that they would be of use in predicting the dynamic surface tension of a boiling system.

In the present investigation (4) an attempt was made to measure the surface tension of aqueous solutions of surface-active agents under nonboiling conditions which nevertheless approximated the boiling process. These results were used to interpret the effect of surface tension on boiling coefficients under actual boiling conditions.

The nonboiling studies were based on the work of Benzing and Myers (2), who, studying factors affecting gas-bubble formation at horizontal circular orifices, found that for a number of gas-liquid systems the bubble volumes could be predicted with considerable accuracy by

$$\frac{D}{d} = 1.82 \left(\frac{\sigma}{\rho_L g d^2} \right)^{0.25} \quad (1)$$

This was based on an equation derived by writing a force balance on a bubble which was just at the point of breaking off. The theoretical expression however contains an exponent of 0.33 on the right-hand side instead of 0.25. The data obtained under a variety of conditions fitted this expression, including results obtained with an aqueous solution containing 1.0 wt. % of the commercial preparation Drene. The surface tension employed in Equation (1) for this solution was a static value. Conversely, results obtained with a 0.1 wt. % solution of Drene in water deviated considerably from the correlation. The conclusion drawn from these experiments was that at a concentration of 1.0 wt. % there was sufficient surface-active agent present in the water to achieve orientation in the vapor-liquid interface in the time available during bubble formation. Thus the measured static surface tension of the solution was approximately the same as the dynamic surface tension, but the 0.1 wt. % solution was apparently so dilute that a longer orientation time was required than was available. The static surface tension in this case, therefore, was not equivalent to the dynamic surface tension, and the use of the static value in the correlation resulted in substantial deviations. The measured values of the static surface tension were 30.6 and 26.0 dynes/cm. for the 0.1 and 1.0 wt. % solutions respectively.

Further evidence supporting this interpretation was obtained by studying the effect of bubble-formation rate on bubble volume. The volume of air bubbles in water was approximately twice the volume of air bubbles in 1.0 wt. % Drene solution in water, which was in accordance with the predicted effects of surface tension in Equation (1). The results obtained with a 0.1 wt. % solution of Drene in water were intermediate. At high rates of bubble formation, when very little time was available for surface concentration, the bubble volumes approached those measured for pure water. However at low bubble-formation rates the surface had more time to approach equilibrium, and the bubble volumes approached those measured for the 1.0 wt. % Drene solution.

From these experiments it was concluded that there may be concentrations of surface-active agent for which, under certain circumstances, the dynamic surface tension is equal to the static surface tension. It appears that this condition is approached by increasing the concentration of the agent or by decreasing the bubble-formation rate.

The information described above was used in the present study by performing a series of air-bubble experiments at various air rates and solution concentrations to determine the values of the dynamic surface tension. Boiling experiments were then conducted under conditions as nearly like the air-bubble studies as possible. The measured boiling coefficients from the heat transfer experiments were then correlated with the dynamic surface-tension measurements from the air-bubble experiments.

EXPERIMENTAL

Air-bubble and boiling investigations were performed with aqueous solutions of detergents known as Tergitol and Aerosol. Tergitol is a water-soluble yellow liquid containing 25% sodium tetradecyl sulfate in water; Aerosol-22 is an anionic agent containing *n*-octadecyl tetrasodium 1,2 dicarboxyethyl sulfosuccinamate and is soluble in both hot and cold water.

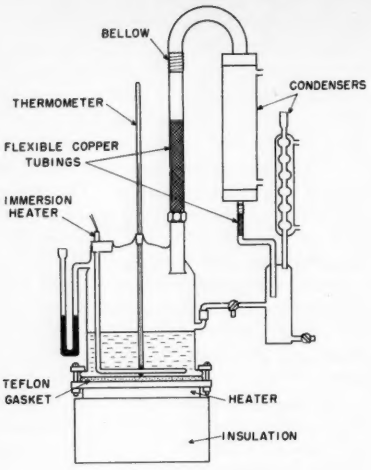

Fig. 2. Boiling apparatus.

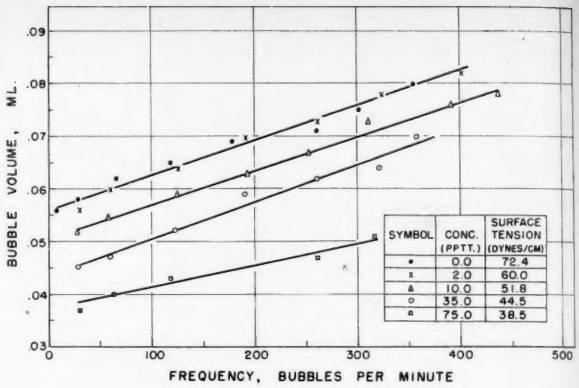

Fig. 4. Volume-frequency-concentration plot for Tergitol solution at 72° to 76°F.

Air-Bubble Experiments

The investigation of air-bubble volumes was done on an apparatus essentially the same as that described by Benzing and Myers (2) (Figure 1). Air passed through a pressure-reducing valve, discharging at approximately 5 lb./sq. in. gauge into a surge tank constructed from a 14-in. section of 2-in. pipe. This was followed by passage through a humidifier, constructed of 12 in. of 2-in. pipe. The flow rate was controlled by two needle valves in series. The orifice employed was made from brass bar stock and had a throat ½ in. long with an I.D. of 0.357 cm. The orifice was immersed 3 in. beneath the surface of the liquid, which was contained in a cylindrical glass jar 1 ft. in diameter and 1 ft. high. The bubble-collection system consisted of an inverted funnel connected by rubber tubing to a 50-ml. burette, which was connected through a valve to an aspirator.

All data in this phase of the project were taken at room temperature, which ranged from 72° to 76°F. A platinum ring tensiometer was used to measure the static surface tension of the solution. Solutions were prepared on a volumetric basis and concentrations recorded as volumetric parts of surface-active agent per ten thousand parts of water.

Boiling Experiments

The boiling data were taken with an apparatus (Figure 2) built by Kurihara (5) and described by Kurihara and Myers (6). The heater was cut from a cylinder of copper to a diameter of 3 in. Seven fins on the bottom of the block were heated by nichrome ribbon wound on a mica core and inserted between the fins. A stainless steel skirt (5-in. O.D.) was silver-soldered to the top of the block, and the copper and stainless steel were turned down till the skirt had a thickness of 1/16 in. No boiling was observed from the stainless steel skirt. Thermocouples of No. 30 copper-constantan, located as shown in Figure 3, were used to measure temperatures in the heater block and on the skirt. Liquid temperatures were measured with a mercury thermometer whose bulb was 1/2 in. above the center point of the heater surface. All thermocouples and the thermometer were checked against an N.B.S. calibrated thermometer and were considered to be accurate within ± 0.1°F.

The liquid was confined in an 8-in.–diameter inverted glass bell jar, 11 in. high, which was bolted to the heater skirt and sealed by a Teflon gasket. An auxiliary heater inserted in a 6-mm. glass tube encircled the periphery of the heater to compensate for minor heat losses in the upper part of the apparatus. The external heater circuit included a 7-kv.-amp. variac rated at 20 amp. and 270 v.; two wattmeters, a high-range meter with 4,000 w. minimum and a low-range meter with 500 w. maximum; a 300-v. voltmeter; and a 25-amp. ammeter. Table 1 shows a sample of the experimental boiling data and results. All boiling data were taken at an approximately constant heat input of 400 B.t.u./hr. with heat flux from the heater surface varying from 7,460 to 8,040 B.t.u./(hr.)(sq. ft.), depending on heat loss. Estimated bubble-formation rates were between 800 and 1,000 bubbles/min. for pure water. Upon the addition of the detergents these rates increased to values which could not be estimated visually.

In the Tergitol-water runs there were approximately twenty active nuclei on the heater surface when pure water was boiled and approximately seventy nuclei when the concentration of Tergitol was 75 p.p.t.t.; for the Aerosol-water runs there were thirty bubble columns with pure water and about 200 when the concentration was 7.5 p.p.t.t.

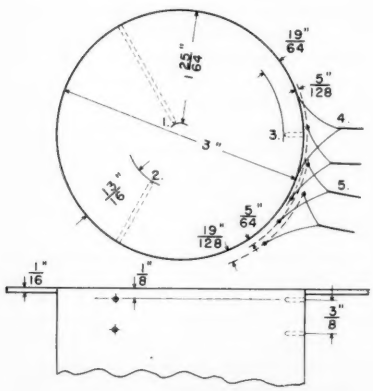

Fig. 3. Locations of thermocouples.

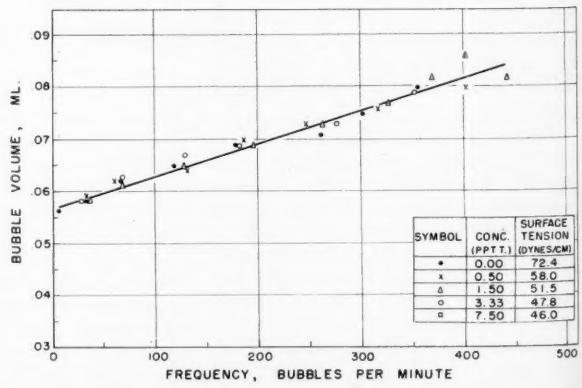

Fig. 5. Volume-frequency-concentration plot for Aerosol solution at 72° to 76°F.

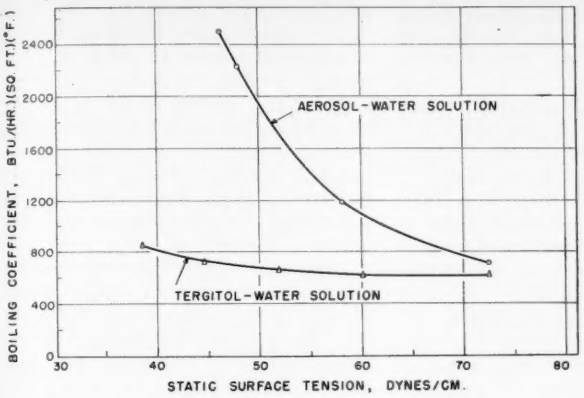

Fig. 6. Boiling coefficient vs. static surface tension.

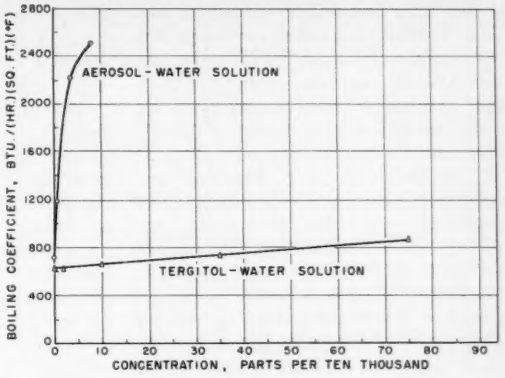

Fig. 7. Boiling coefficient vs. concentration.

The heat flux was determined by subtracting the skirt loss from the power input. A description of the details of the experimental measurements, including the method of determining average surface temperature, is given by Kurihara and Myers (*6*).

The boiling surface was prepared before each set of runs by systematic polishing with No. 2 emery paper. The differences in the boiling coefficient for pure water (716 for the Aerosol runs to 627 for the Tergitol runs) may be attributed to slight differences in the surface roughness (25.0 μin. root mean square for the Aerosol runs and 22.6 μin. root mean square for the Tergitol runs). The roughness was measured in the manner described by Kurihara and Myers (*6*).

The boiling surface was examined for fouling after each run. No visible deposits were left on the surface; however a slight increase of root mean square microroughness was observed (25.0 to 26.9 μin. in one set of Aerosal runs and 25.0 to 26.4 in another set). This commonly occurs when pure water is boiled on a copper surface and is to be expected with aqueous solutions. It seems probable however that most of this change occurred during the 2 hr. of boiling which always preceded the taking of data.

Air-Bubble Results

The results of air-bubble measurements made in solutions of Tergitol are shown in Figure 4. It is apparent that over the entire range of bubble frequencies employed there is a significant effect of detergent concentration, and thus of surface tension, on the measured bubble volumes. Measurements could not be taken at rates greater than 500 bubbles/min. in pure water because the bubbles were no longer uniform in volume or shape beyond this point. The limiting rate was even lower in solutions of detergent. There does not appear to be any major effect of bubble rate on the relative behavior of solutions of different concentrations, contrary to the observations of Benzing and Myers (*2*). With the exception of the most concentrated solution, the lines representing the various solutions appear to have nearly the same slope.

The results of air-bubble studies with solutions of Aerosol in water are shown in Figure 5. It may be seen that none of the solutions appeared to be affected by the presence of the detergent, as the bubble volumes were in all cases the same as for pure water. Thus the dynamic surface tension in this case is the same as the surface tension of pure water and, as far as surface tension can affect boiling, it would seem that the boiling coefficients of these solutions should be the same as for water.

Boiling Results

The results of the boiling experiments are shown in Figures 6 and 7. As was expected from the air-bubble experiments with Tergitol solutions, there was a noticeable effect produced on the boiling coefficients. Addition of Tergitol up to 75 p. p. t. t. increased the boiling coefficient by about 50%. Although the air-bubble rates were below 500 bubbles/min. and the boiling rates generally above 1,000 bubbles/min., an estimate was made of the effect of surface tension on the boiling coefficients.

The first step in the calculation was to determine the values of the effective or dynamic surface tension from measurements of bubble volume by the use of Equation (1). The results of these calculations, based on bubble volumes taken from the straight lines of Figure 4, are given in Table 2 which also contains static readings for the same solutions.

If the heat transfer coefficient is assumed to follow a relation of the form $h\alpha(1/\sigma^n)$, then the exponent can be evaluated from a proportionality consisting of the ratios of heat transfer coefficients and dynamic surface tensions. This was done by using the data of Figure 6 and Table 2 with pure water as the reference state and produced the values shown in Table 3.

The heat flux for these runs was held between 7,400 and 7,710 B.t.u./(hr.) (sq. ft.). Temperature-difference driving force ranged from 9.0 to 12.1°F. The values of the exponent n ranged from 0.65 to 1.04, not a large range in view of the assumptions made. Although widely scattered values of the exponent have been reported by other authors, Bankoff (*1*) in a recent paper predicts a value of $n = 2/3$.

The results presented in Tables 1,

Table 1. Sample Experimental Boiling Data and Results

System: Tergitol-water Surface roughness: 22.6μin.

Concentration, p.p.t.t. (by volume)	Static surface tension at 72° to 76°F., dynes/cm	Average surface temperature, °F.	Liquid temperature, °F.	Power input, B.t.u./hr.	Skirt loss, B.t.u./hr.	Heat flux q/A, B.t.u./(hr.)(sq. ft.)	Film temperature drop, °F.	Boiling coefficient, B.t.u./(hr.)(sq. ft.)(°F.)
0	72.4	223.5	211.6	399	33	7,640	11.9	627
2.0	60.0	223.2	211.1	399	31	7,510	12.1	621
10.0	51.8	222.4	211.1	399	32	7,490	11.3	663
35.0	44.5	221.2	211.1	392	29	7,400	10.1	732
75.0	38.5	220.1	211.1	403	25	7,710	9.0	856

2, and 3 are based on the dynamic surface tensions measured by air-bubble experiments at 72° to 76°F. When one uses this information to evaluate boiling performance at temperatures of 212° to 220°F., however, only the ratios of the surface-tension values at 72° to 76°F. are used. For this procedure to be valid, therefore, it is necessary only that the ratios not change with temperature. This point was investigated in the initial stages of the research by a series of measurements of the static surface tension of Tergitol solutions at temperatures up to 210°F. These values decreased by about 15% over the range of 70° to 210°F. However, the ratio of the static surface tension of a Tergitol solution to the static surface tension of water changed by amounts ranging only from 3 to 6%. Ratios of dynamic surface tension were assumed to have the same response to temperature change.

Preliminary experiments were made in which the air-bubble system was operated at 210°F. However, convection effects made it impossible to reproduce the results even when insulation was applied to the system.

The boiling results obtained with the Aerosol solutions were in direct contrast to what was expected. In Figure 5 it can be seen that the addition of the surface-active agent Aerosol had no effect on the volume of air bubbles. Thus it might be expected that it would have no effect on the boiling coefficients. An examination of Figures 6 and 7 shows, however, that the addition of 7.5 parts of Aerosol/10,000 parts of solution increases the boiling coefficient from 716 to 2,500 B.t.u./(hr.) (sq. ft.) (°F.). In these runs the heat transfer rate varied from 7,740 to 8,040 B.t.u./(hr.) (sq. ft.) and the temperature-difference driving force from 10.8° to 3.2°F.

The presence of an effect in boiling but not in the air-bubble measurements clearly indicates that the effect of the detergent in this case is not related to the break-off dimensions of the bubbles in boiling. In fact, it would seem to have nothing to do with surface tension, since the dynamic surface tension of the solution is apparently unaffected by the presence of the detergent.

Lowery and Westwater (7) have suggested that large organic molecules in a solution may serve as nuclei for the formation of bubbles at smaller degrees of superheat than would be necessary at a liquid-solid interface. This explanation is attractive in view of the fact that the highest boiling coefficient [h = 2,500 B.t.u./(hr.) (sq. ft.) (°F.)] occurred with a temperature-difference driving force of 3.2°F. At this superheat stable nucleate boiling is seldom attained, and the usual mechanism is one of natural convection.

CONCLUSIONS

It appears that the addition of surface-active agents to liquids may affect nucleate boiling coefficients in two quite different ways. First there may be a decrease in the dynamic surface tension with a consequent increase in the boiling coefficient. A method of studying this effect quantitatively has been proposed and tried with solutions of Tergitol in water. Results indicate that the exponent n in the relation $h\alpha(1/\sigma^n)$ varies between 0.65 and 1.04.

The second effect, which is much stronger, was found to occur in solutions of Aerosol and water. The presence of this detergent was found to have no effect on the dynamic surface tension. However a fourfold increase resulted in the boiling coefficient, which is, perhaps, due to the effect of the detergent on the number of active nuclei in the solution.

The authors suggest that a pluralistic explanation of the effects of detergents on the boiling behavior of solutions may be necessary to explain the extreme divergence of results obtained by previous workers in this field.

Table 2. Static and Dynamic Surface Tensions
Tergitol-water solutions

Concentration by volume, p.p.t.t.	Liquid temperature, °F.	Static surface tension, dynes/cm.	Dynamic surface tension, dynes/cm. Air-bubble rates, bubbles/min. 30	100	200	300
0	72	72.4	72.4	72.4	72.4	72.4
2	73	60.0	72.4	72.4	72.4	72.4
10	75	51.8	65.5	65.7	66.0	66.6
35	75	44.5	56.3	58.0	60.2	61.9
75	73	38.5	48.6	47.6	47.4	47.2

Table 3. Values of Exponent n for Tergitol-Water System

[Equation $h\alpha(1/\sigma^n)$]

Solution concentration, p.p.t.t.	Air-bubble rates, bubbles/min. 30	100	200	300
10	0.65	0.68	0.70	0.78
35	0.66	0.74	0.89	1.04
75	0.79	0.76	0.76	0.75

ACKNOWLEDGMENT

The authors acknowledge the generosity of the Carbide and Carbon Chemical Company and the American Cyanamid Company, which donated the Tergitol and Aerosol, respectively.

NOTATION

d = orifice diameter, cm.
D = bubble diameter, cm.
g = acceleration due to gravity, 980 cm./sec.^{2}
h = boiling heat transfer coefficient, B.t.u./(hr.) (sq. ft.) (°F.)
n = constant in exponential relation $h\alpha(1/\sigma^n)$
q/A = heat flux, B.t.u./(hr.) (sq.ft.)
ΔT = average surface temperature of heater minus bulk temperature of boiling liquid, °F.
ρ_L = liquid density, g./cc.
σ = surface tension, dynes/cm.

LITERATURE CITED

1. Bankoff, S. G., *Chem. Eng. Progr. Symposium Ser. No. 29*, **55** (1959).
2. Benzing, R. J., and J. E. Myers, *Ind. Eng. Chem.*, **47**, 2087 (1955).
3. Du Nouy, P. L., "Surface Equilibria of Colloids," p. 35, Chemical Catalog Co., New York (1926).
4. Jontz, P. D., M.S. thesis, Purdue Univ., Lafayette, Indiana (1956).
5. Kurihara, H. M., Ph.D. thesis, Purdue Univ., Lafayette, Indiana (1956).
6. ———, and J. E. Myers, *A.I.Ch.E. Journal*, **6**, 1 (1960).
7. Lowery, A J., and J. W. Westwater, *Ind. Eng. Chem.*, **49**, 1445 (1957).
8. Schwartz, A. M., and J. W. Perry, "Surface Active Agents," Vol. I, 271, Interscience Publishers, New York (1949).
9. Weiser, H. B., "Colloid Chemistry," p. 21, John Wiley, New York (1949).
10. Westwater, J. W., "Advances in Chemical Engineering," Vol. I, Chap. 1, Academic Press, New York (1956).

Manuscript received January 12, 1959; revision received September 30, 1959; paper accepted October 5, 1959.

Thermodynamic Behavior of Hydrogen-Hydrocarbon Mixtures

R. L. MOTARD and E. I. ORGANICK

University of Houston, Houston, Texas

By use of the Benedict-Webb-Rubin (BWR) equation of state an attempt has been made to correlate experimental vapor-liquid equilibrium data on hydrogen-methane-propane mixtures in the temperature range from 0° to —250°F. and pressure range from 500 to 1,500 lb./sq. in. abs. Considerable improvement in hydrogen *K* values has been obtained by adjusting the coefficient γ in the BWR equation for hydrogen. In the final adjustment it was necessary to specify a new value of γ for hydrogen at each temperature. The root-mean-square deviation of calculated from observed *K* values for hydrogen is 6.6%

As a further check the recommended BWR coefficients for hydrogen have been used to calculate the low-temperature hydrogen *K* values in mixtures with ethane and ethylene with good results.

The predicted *K* values for propane at temperatures below —150°F. have not been altered and are still in error by as much as 2 orders of magnitude.

The expanding use of digital computing equipment in the simulation of processes has developed a strong incentive for the compact quantitative expression of physical phenomena. In the area of hydrocarbon vapor-liquid equilibrium ratios some attempts have been made to fit the experimental relationships to a curve, but an equally promising approach, for light hydrocarbons at least, is the use of an equation of state, the Benedict-Webb-Rubin (BWR) equation (*1, 2*). This equation has been used to predict from single-phase pressure-volume-temperature (*PVT*) data of pure hydrocarbons both the singular two-phase behavior and the phase behavior in multicomponent mixtures of these hydrocarbons. While considerable success has been obtained in the use of the BWR equation for mixtures of paraffins and olefins, several deficiencies in the equation have been noted in areas of its application critical to its utility. For instance, prior to this investigation it had been established that the equation would not predict satisfactorily the subatmospheric vapor pressures of pure compounds (*2*) and would not adequately represent the phase behavior of mixtures of hydrocarbons with light gases such as hydrogen (*9*), nitrogen (*5*), and carbon dioxide (*15*).

In an effort to expand the utility of the equation Benedict (*2*) suggested first that the prediction of pure-component vapor pressures at low temperatures could be improved by adjusting C_o at every temperature in such a manner as to satisfy the two criteria:

$$P(d_L) = P(d_g) = P_{obs.}$$
$$f(d_L) = f(d_g)$$

The phase behavior of mixtures is predicted from the equation-of-state coefficients for pure compounds based on combining rules inferred from statistical mechanics. In cases of poor agreement with data on the phase behavior of mixtures it has been assumed that an improvement or revision of the interaction coefficients is necessary to correct the assumed combining rule. Thus Benedict and Stotler (*5*) modified the combining rule for A_o in correlating *V-L* data on the nitrogen-methane system.

The prediction of the phase behavior of hydrogen-hydrocarbon mixtures is of immediate technical interest and represents one area where the BWR equation has not been too successful (*9*). It is well known that the vapor-liquid equilibrium ratios for hydrogen do not apparently follow the conventional behavior observed for mixtures of light hydrocarbons. For all temperatures above —250°F. *K* values for hydrogen decrease with increasing temperature in contrast with normal expectations, where the *K* values should increase with increasing temperature. One might suppose that such radical behavior could not possibly lend itself to prediction by the conventional equation-of-state approach; however Katz (*14*) has pointed out that this behavior of hydrogen is really only a manifestation to a larger degree of a phenomenon observed in all hydrocarbon mixtures involving very light and very heavy components.

In the light of these observations and because of the burden of calculations involved, a series of studies was undertaken with an IBM 650 to adapt the BWR equation-of-state approach to vapor-liquid equilibrium in hydrogen-hydrocarbon mixtures at low temperatures. A computer program (*20*) was available to calculate vapor-liquid equilibria from the BWR equation of state. The data employed in the study were those of Benham and Katz (*3*) for hydrogen-methane-propane mixtures. To extend the range of the hydrogen-

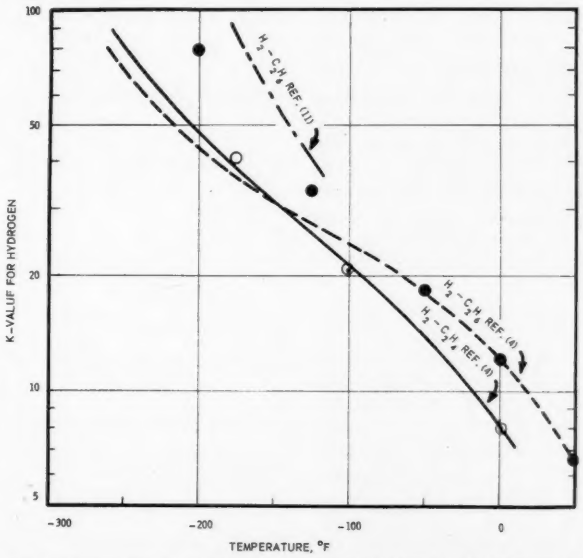

Fig. 1. Comparison of calculated *K* values with observed for hydrogen in hydrogen-ethylene and hydrogen-ethane mixtures at 1,000 lb./sq. in. abs. ● = calculated K_{H_2} in hydrogen-ethane mixture, ○ = calculated K_{H_2} in hydrogen-ethylene mixture.

propane binary data, two runs were selected from the Williams and Katz data (4).

Previous studies had indicated that the best available set of BWR coefficients (7) for hydrogen did not satisfactorily correlate hydrogen phase behavior. A new set of hydrogen coefficients was obtained from *PVT* data (8) over the range of interest, namely −250° to 100°F. and 0 to 2,000 lb./sq. in. abs. by means of a digital computer program (20).

To improve the prediction of pure-component vapor pressures, a general-purpose computer program for adjusting C_o was developed.

The BWR equation of state approach was checked at this point in the study by evaluating the new coefficients for hydrogen and the adjusted C_o values for methane and propane in the calculation of phase equilibria. Since further refinements were necessary to fit the hydrogen *K* values, the work proceeded with the objective of finding improved binary interaction coefficients from *V-L* data on binary mixtures of hydrogen methane and hydrogen propane and of using these coefficients in the calculation of the phase equilibria of ternary mixtures. It was found that improved binary interaction coefficients for hydrogen in hydrocarbon mixtures were not necessary. The behavior of hydrogen could be adequately represented by modifying γ at each temperature.

The BWR coefficients used in the calculations for all substances other than hydrogen are those recommended by Benedict (2), with the exception that C_o has been adjusted where necessary to fit the observed vapor pressure.

RESULTS

Fitting Hydrogen PVT

The method employed in fitting hydrogen *PVT* data is that of Brough, Schlinger, and Sage (6), where the coefficients are obtained by a least-squares fit of the *PVT* data for assumed values of γ. Several guesses are made of γ, and the value which yields the minimum standard deviation of the fit is selected as best.

A set of hydrogen coefficients had been obtained by Eubanks (7), shown in Table 1, but preliminary calculations conducted at the university laboratory indicated poor agreement between computed hydrogen *K* values with observed ones. The root-mean-square (RMS) error was 137%. Eubanks fitted hydrogen *PVT* data at temperatures below −172°F. only; therefore a new set of hydrogen coefficients was obtained with a different range of hydrogen *PVT*. The data were obtained from the same source (8) but were restricted to the range of interest, namely temperatures from 100° to −250°F. and pressures to 2,000 lb./sq. in. abs. The results of the fit of hydrogen *PVT* over the range of interest are shown in Table 1. As a by-product of the curve-fitting work, it was found that the fit of the hydrogen *PVT* over the range of interest described above was insensitive to the value of γ over the range from 0.4 to 1.0.

One aspect of the curve-fitting results needs clarification. As was found by Eubanks, the best values of a and α for hydrogen are negative. Such a result need not influence the ability of the BWR equation to fit the *PVT* data, but it leads to an incongruity in defining the fugacity of hydrogen in the pure state and in a mixture. Thus the coefficient for the fifth power of the density, the product $a\alpha$, is positive in the equation for the fugacity of pure hydrogen, but the corresponding term $[\alpha(a^2a_i)^{1/3} + a(a^2\alpha_i)^{1/3}]$ is negative for hydrogen in a mixture. To resolve the difficulty, Eubanks suggested that the signs of a and α be changed and that b be modified to correct the third virial coefficient, $(bRT\text{-}a)$. The modified b is defined by

$$b' = b + \frac{2\,|a|}{RT}$$

The results obtained in calculating *K* values with the new set of BWR coefficients for hydrogen, set 1, Table 1, were somewhat better, as indicated by a root-mean-square error of 36%.

Adjustment of C_o for Pure Substances

All calculations of *K* values described in this paper included the use of C_o values which satisfactorily fit the BWR equation to the observed vapor pressures of pure substances at the temperature in question.

Improvement in Combining Rules

The combining rules employed in deriving the BWR coefficients for a mixture are as follows:

$$B_{om} = \Sigma x_i B_{oi}$$
$$A_{om} = [\Sigma x_i A_{oi}^{1/2}]^2$$
$$C_{om} = [\Sigma x_i C_{oi}^{1/2}]^2$$
$$b_m = [\Sigma x_i b_i^{1/3}]^3$$
$$a_m = [\Sigma x_i a_i^{1/3}]^3$$
$$c_m = [\Sigma x_i c_i^{1/3}]^3$$
$$\alpha_m = [\Sigma x_i \alpha_i^{1/3}]^3$$
$$\gamma_m = [\Sigma x_i \gamma_i^{1/2}]^2$$

Stotler and Benedict (5) empirically adjusted the interaction term A_{om} to fit vapor-liquid equilibrium data in the system nitrogen-methane.

According to the recommended combining rule for A_o, the interaction term in a binary mixture should be $2x_1x_2A_{o_1}^{1/2}A_{o_2}^{1/2}$. If the coefficient of x_1x_2 is to be determined formally and empirically from vapor-liquid equilibrium measurements, an iterative procedure can be devised on the basis of the Newton-Raphson method. In the present study it is reasoned that the vapor-phase fugacities of hydrogen are fairly accurate, since hydrogen vapor behaves almost ideally. It was decided therefore to adjust the interaction term in the combining rule for C_o, for the liquid-phase hydrogen fugacity only, by a much shorter procedure. Thus in the adjustment of the combining rule for C_o in the liquid phase only of a binary mixture, a direct solution for the interaction term can be obtained if one ignores the small change in d_L accompanying the

Table 1. Benedict-Webb-Rubin Equation of State Coefficients for Hydrogen
Units: lb./sq. in. abs., lb. moles/cu. ft., °R.

	Eubanks (7)	Coefficients for this paper			
		Set 1*	Set 2	Set 3	Set 4
A_o	791.5	585.127	→	→	→
B_o	0.3782	0.333937	→	→	→
C_o	0.625×10^6	4.8282×10^6	2.25×10^6	4.41×10^6	4.41×10^6
a	30.375	98.597	→	→	→
b'	$0.131143 + \frac{60.75}{RT}$	$0.08682 + \frac{197.194}{RT}$	→	→	→
c	0.55029×10^6	1.42317×10^6	→	→	→
α	0.868577	0.479116	→	→	→
γ	0.9	0.9	0.9	0.74909	†

* From least-squares fit of Woolley *et al.*(8) hydrogen *PVT*. Mean absolute relative deviation = 0.0013%.

† γ is a function of temperature as follows:

t°, F.	γ	$\gamma^{1/2}$
0	0.82810	0.9100
−100	0.77440	0.8800
−150	0.74909	0.8655
−200	0.70057	0.8370
−250	0.70057	0.8370

change in Q. The combining rule for C_o becomes

$$C_{om} = x_1^2 C_{o1} + x_2^2 C_{o2} + Q x_1 x_2$$

where Q is originally $2C_{o1}^{1/3} C_{o2}^{1/3}$. If $\ln f^L_1$ is to equal $\ln f^G_1$ at the observed composition, then

$$Q = \frac{RT^2}{d_L x_2} \ln f^L_1 / f^G_1 + 2C_{o1}^{1/3} C_{o2}^{1/3}$$

The results of adjusting the C_o combining rule by the short procedure for binary mixtures indicated that a large part of the error in predicting hydrogen K values could be eliminated by merely adjusting C_o for pure hydrogen. Thus in the idealized combining rule for C_o suggested by Benedict $Q = 2C_{o1}^{1/3} C_{o2}^{1/3}$, and a calculated new value of C_o for hydrogen could be obtained from the above relationship. The new C_o for hydrogen calculated from the values of Q, that is from binary V-L data, is shown in Table 1 as set 2. The results of the K values calculated with the modified hydrogen C_o indicated an improvement in the fit (by the reduction of the RMS error to 25%) but mainly in the predicted K values for hydrogen in the binary mixtures. In order to improve the prediction of hydrogen K in ternary mixtures, the coefficient γ for hydrogen was adjusted; a degree of freedom was available here, namely that the least-squares fit of hydrogen PVT had been found to be independent of γ. However every adjustment of γ to improve K_{H_2} in ternary mixtures resulted in a poorer fit of the agreement in K values in binary mixtures. An iterative trial-and-error procedure was developed whereby γ and C_o for hydrogen were adjusted alternately to arrive at the optimum combination to fit hydrogen K in both binary and ternary mixtures.

Adjusting γ for Hydrogen

The best set of C_o and γ for hydrogen developed by the trial-and-error procedure described in the last section is

$$C_o = 4.41 \times 10^6$$
$$C_o^{1/2} = 2.1 \times 10^3$$
$$\gamma = 0.74909$$
$$\gamma^{1/3} = 0.8655$$

These coefficients are shown as set 3 in Table 1, and the RMS error in computed K values is 14%. The final value of C_o does not differ greatly from the original value obtained from a least-squares fit of the hydrogen PVT.

Further improvements in hydrogen K values were obtained by making γ a function of temperature as shown in Table 1. The final results are listed in Table 2, and the recommended BWR coefficients for hydrogen are listed as set 4 in Table 1. The root-mean-square deviation in hydrogen K values for twenty-eight runs with the recommended hydrogen coefficients is 6.6%, excluding one error of 56.2%.

Table 2. Comparison of Observed K Values with Those Calculated from BWR Equation for Two and Three Component Mixtures in the System Hydrogen Methane Propane. Data: (3)

Benham and Katz run number	Liquid-phase composition parameter, $z_{C_1}/(z_{C_1}+z_{C_3})$	Observed K_H	Observed K_{C_1}	Observed K_{C_3}	Calculated* K_H	Calculated* K_{C_1}	Calculated* K_{C_3}
					0°F., 500 lb./sq. in. abs.		
46	0	39.4	—	0.095	40.6	—	0.094
30	0.119	34.9	3.70	0.125	34.5	3.58	0.119
28	0.163	30.8	3.76	0.137	31.8	3.54	0.131
26	0.238	25.3	3.40	0.150	27.6	3.42	0.146
					0°F., 1,000 lb./sq. in. abs.		
46	0	19.8	—	0.062	20.4	—	0.057
35	0.185	19.1	1.93	0.082	16.4	1.99	0.082
33	0.265	17.0	1.86	0.094	14.4	1.97	0.095
1	0.53	—	1.70	0.206	—	1.72	0.204
					−100°F., 500 lb./sq. in. abs.		
46	0	63.9	—	0.0099	65.4	—	0.0077
18	0.216	56.3	1.42	0.0106	50.6	1.63	0.0107
22	0.437	36.0	1.75	0.0214	34.6	1.69	0.0181
20	0.498	31.8	1.69	0.0242	29.4	1.66	0.0211
1	0.62	—	1.59	0.034	—	1.59	0.0289
					−100°F., 1,000 lb./sq. in. abs.		
46	0	32.8	—	0.0071	33.3	—	0.0050
38	0.354	18.9	1.07	0.022	20.4	1.01	0.012
40	0.606	11.8	0.909	0.099	12.0	1.034	0.024
					−150°F., 500 lb./sq. in. abs.		
†	0	82.0	—	0.00198	82.7	—	0.00114
3	1.0	9.31	0.856	—	9.11	0.852	—
					−150°F., 1,000 lb./sq. in. abs.		
†	0	43.6	—	0.00133	42.5	—	0.00082
4	1.0	4.63	0.651	—	4.45	0.650	
					−200°F., 500 lb./sq. in. abs.		
46	0.086	121	0.441	0.0053	112	0.189	0.00009
44	0.445	46.6	0.365	0.0125	72.8	0.186	0.00012
2A	1.0	18.6	0.374	—	18.8	0.340	
					−200°F., 1,000 lb./sq. in. abs.		
45	0.1032	55.4	0.0365	0.00716	57.2	0.122	0.00008
43	0.577	29.2	0.215	0.00633	31.2	0.207	0.00012
42	0.595	29.6	0.208	0.00664	30.4	0.208	0.00012
41	0.616	27.8	0.221	0.00715	29.4	0.212	0.00013
47	0.863	13.4	0.241	0.0242	15.1	0.234	0.0002
5	1.000	9.74	0.259	—	9.24	0.246	
					−250°F., 490 lb./sq. in. abs.		
12	1.0	29.1	0.0745	—	29.6	0.0732	
					−250°F., 1,490 lb./sq. in. abs.		
13	1.0	9.98	0.059	—	9.68	0.061	

* Set 4—BWR coefficients for hydrogen; K values computed at observed composition.
† Data of Williams and Katz (4).

K Values for Components Other Than Hydrogen

The calculated K values for methane in the final comparison of Table 2 are in reasonable agreement with observed values except for three runs. Since no trend is detectable in the deviations for methane, these discrepancies could be partly attributed to experimental error.

The agreement in propane K values is a different story. The present BWR equation of state approach is still inadequate to represent propane K values below −100°F. This result is not related primarily to the presence of hydrogen in the system but has been observed for all hydrocarbons heavier than methane at low temperatures, specifically for ethane and propane in the methane-ethane-propane system (9) and n-butane in the methane–n-butane system (10). The Lorentz combining rule for B_{om} was explored to

Table 3. Comparison of Observed K Values with Those Calculated from BWR Equation for Binary Mixtures of Hydrogen Ethylene and Hydrogen Ethane

Temperature, °F.	Pressure, lb./sq. in. abs.	Reference	K observed H_2	K observed C_2	K calculated H_2	K calculated C_2
		System hydrogen ethylene				
0	500	(4)	17.1	0.863	13.7	0.871
0	2,000	(4)	3.94	0.496	3.29	0.513
−100	250	(4)	84.2	0.320	83.3	0.301
−100	2,000	(4)	10.8	0.0924	10.2	0.0827
−175	250	(4)	147	0.0408	162	0.0350
−175	2,000	(4)	20.2	0.0179	21.8	0.0128
		System hydrogen ethane				
+50	500	(4)	12.1	0.922	11.6	0.936
+50	2,000	(4)	3.21	0.567	3.00	0.568
0	250	(4)	48.8	0.896	42.9	0.912
0	2,000	(4)	6.12	0.264	5.79	0.261
−50	250	(4)	75.4	0.424	72.5	0.424
−50	2,000	(4)	9.05	0.113	9.07	0.108
−125	250	(4)	112	0.077	131	0.075
−125	2,000	(4)	14.	0.0246	17.1	0.022
−200	250	(4)	160.	0.00462	292.	0.00431
−200	2,000	(4)	23.6	0.00272	43.1	0.00228
−121	302.7	(11)	91.2	0.088	105.4	0.0709
−121	1171.	(11)	29.8	0.0465	27.8	0.0284
−175	204.3	(11)	378	0.0551	260	0.0157
−175	1,137.5	(11)	76.1	0.0111	49.7	0.0111

Table 4. Comparison of Observed K Values with Those Calculated from BWR Equation for Ternary Mixtures of Hydrogen Methane Ethylene and Hydrogen Methane Ethane

Temperature, °F.	Pressure, lb./sq. in. abs.	Reference	K observed H_2	K observed C_1	K observed C_2	K calculated H_2	K calculated C_1	K calculated C_2
		System hydrogen methane ethylene						
−121	441	(13)	44.3	1.50	0.115	42.5	1.39	0.133
−121	1,176	(13)	9.77	0.674	0.0978	8.89	0.700	0.118
−175	441	(13)	25.2	0.631	0.0306	30.5	0.591	0.378
−175	1,176	(13)	25.9	0.438	0.0311	26.4	0.295	0.0158
		System hydrogen methane ethane						
−121	441	(12)	162	1.36	0.0890	40.4	1.40	0.0750
−121	1,176	(12)	11.8	0.921	0.0966	10.5	0.706	0.0648
−175	441	(12)	24.2	0.638	0.0443	39.6	0.597	0.0150
−175	1,176	(12)	12.4	0.352	0.125	12.3	0.334	0.0137
−100	500	(19)	34.8	1.56	0.114	33.8	1.63	0.107
−100	1,000	(19)	12.2	0.98	0.120	11.0	0.98	0.110
−200	500	(19)	21.2	0.34	0.011	21.5	0.33	0.0072
−200	1,000	(19)	28.8	0.24	0.0041	33.2	0.21	0.0032

assess the improvement in predicted K values of propane which might result, but the effect, while large by the usual standards, did not warrant further investigation. K values for propane were increased by a factor of 3 at −200°F. with the Lorentz combination for B_o used, whereas a factor of several hundred is needed to match the observed values.

COMPARISON OF PREDICTED HYDROGEN K VALUES WITH INDEPENDENT DATA

The values of the BWR coefficients for hydrogen given in Table 1 have been employed to predict the phase behavior of hydrogen in hydrogen-ethane (4,11) and hydrogen-ethylene (4) binary mixtures and hydrogen-methane-ethane (12, 19) and hydrogen-methane-ethylene ternary mixtures. These results are shown in Tables 3 and 4 and have been plotted in Figure 1 for the binary system hydrogen-ethylene and hydrogen-ethane at a pressure of 1,000 lb./sq.in.abs.

Generally the calculated K values for hydrogen agree very well with those of Williams and Katz (4) except at very low temperatures, below −175°F., in the hydrogen-ethane system. It should be noted that there are marked differences in the experimental data of Williams and Katz and those of Levitskaya (11) on the hydrogen-ethane system at these conditions. Further, curves for the Williams and Katz experimental data on hydrogen-ethylene and hydrogen-ethane cross at −150°F., which seems to be contrary to experience, to the trends shown in the calculated K values, and to the qualitative relationship demonstrated by the Levitskaya data.

While the calculated hydrogen K values show serious disagreement with some of the Russian experiments, these differences are within the ±0.5 mole% accuracy claimed by Levitskaya *et al.* for their component analyses. The agreement between calculated K values and the data of Cosway (19) is good.

CONCLUSIONS

An empirical approach to improving the prediction of hydrogen K values in mixtures with methane and propane at low temperatures has resulted in a redefinition of the Benedict-Webb-Rubin equation of state coefficient γ as a function of temperature for hydrogen and in a small adjustment to C_o for pure hydrogen.

The predicted behavior of hydrogen in binary mixtures can be markedly improved by refitting only C_o in the BWR equation for hydrogen to binary V-L data, but in ternary mixtures such a correction to C_o obtained from single-phase PVT is inadequate.

The predicted K values for propane in mixtures with hydrogen and methane at very low temperatures ($<-$150°F.) are still too low by 2 orders of magnitude.

NOTATION

A_o, a = BWR equation of state coefficients

B_o, b, b' = BWR equation of state coefficients

C_o, c = BWR equation of state coefficients

C_1, C_2, C_3 = methane propane, ethane propane, or ethylene propane

d_g = vapor-phase density, lb.-moles/cu. ft.

d_L = liquid-phase density, lb.-moles/cu. ft.

f = fugacity

f^v = vapor-phase fugacity, lb./sq. in.

f^L = liquid-phase fugacity, lb./sq. in.

K = vapor-liquid equilibrium

P = pressure, lb./sq. in.

Q = interaction term in combining rule for equation of state coefficients

R = universal gas content, (lb.) cu. ft./(sq. in.) (lb.-mole) (°R.)
T = temperature, °R.
x = mole fraction
α = BWR equation of state coefficients
γ = BWR equation of state coefficients

Subscripts

i = component i
m = mixture property
1, 2 = components 1 and 2

LITERATURE CITED

1. Benedict, Manson, G. B. Webb, and L. C. Rubin, *J. Chem. Phys.*, **8**, 334 (1940).
2. ———, and Leo Friend, *Chem. Eng. Progr.*, **47**, 419 (1950).
3. Benham, A. L., and D. L. Katz, *A.I.Ch.E. Journal*, **3**, 33 (1957).
4. Williams, R. B., and D. L. Katz, *Ind. Eng. Chem.*, **46**, 2512 (1954).
5. Stotler, H. H., and Manson Benedict, *Chem. Eng. Progr. Symposium Ser. No. 6*, **49**, 25 (1953).
6. Brough, H. W., W. G. Schilinger, and B. H. Sage, *Ind. Eng. Chem.*, **43**, 2442 (1951).
7. Eubanks, L. S., Ph.D. Thesis, Rice Institute, Houston, Texas (May, 1957).
8. Woolley, H. W., R. B. Scott, and F. G. Brickwedde, *J. Research Nat. Bur. Standards*, **41**, 379 (1948).
9. Price, A. R., T. W. Leland, and Riki Kobayashi, *Chem. Eng. Progr. Symposium Ser. No. 21*, **55**, 13 (1959).
10. Kobayashi, Riki, unpublished results.
11. Levitskaya, E., and K. Priannikov, *J. Tech. Phys.* (*U.S.S.R.*), **9**, No. 20, 1849 (1939).
12. Levitskaya, E., *ibid.*, **11**, No. 3, 197 (1941).
13. Lichter, A. I., and N. P. Tikhonowitch, *ibid.*, **10**, No. 14, 1201, (1940).
14. Benham, A. L., D. L. Katz, and R. B. Williams, *A.I.Ch.E. Journal*, **3**, 236 (1957).
15. Cullen, E. J., and K. A. Kobe, *ibid.*, **1**, 452 (1955).
16. Keyes, F. G., R. S. Taylor, and L. B. Smith, *J. Math. and Phys.*, **1**, 211 (1922).
17. Dana, L. I., A. C. Jenkins, J. N. Burdick, and R. C. Timm, *Refrig. Eng.*, **12**, 387 (1926).
18. Rossini, F. D., *et al.*, "Selected Values of Physical and Thermodynamic Properties of Hydrocarbons and Related Compounds," Carnegie Press, Pittsburgh, Pennsylvania (1953).
19. Cosway, H. F., and D. L. Katz, *A.I.Ch.E. Journal*, **5**, 46 (1959).
20. International Business Machines Corporation, Reference Manual B-20-4012.

Manuscript received February 19, 1959; revision received June 2, 1959; paper accepted June 8, 1959.

The Constant-Volume Heat Capacities of Gaseous Perfluorocyclobutane and Propylene

NOEL DE NEVERS and JOSEPH J. MARTIN

University of Michigan, Ann Arbor, Michigan

The constant-volume heat capacities of gaseous perfluorocyclobutane and propylene have been measured over a considerable range of temperatures and densities with a new type of adiabatic calorimeter. This calorimeter differs from previous constant-volume gas calorimeters in having very thin walls and being equipped with an internal motor stirrer to provide temperature uniformity. The experimental results have been compared with the predictions of the Benedict-Webb-Rubin and Martin-Hou equations, by use of published values of the zero-pressure-constant-volume heat capacity. The over-all agreement is satisfactory, with a maximum difference between the experimental and calculated heat capacities of 6.7%; however the comparison reveals several interesting systematic differences between the experimental and calculated values of the derivatives of the constant-volume heat capacity with respect to temperature and density.

Although the constant-volume heat capacity has been less intensively investigated than the constant-pressure heat capacity, it is just as useful in thermodynamic calculations as C_p. At zero pressure the two are related by the equation $C_v^\circ = C_p^\circ - R$. At finite pressures C_v and C_p may be computed from the corresponding zero-pressure values and PVT data as represented by an equation of state by use of the relations

$$C_v - C_v^\circ = -\int_v^\infty T \left(\frac{d^2P}{dT^2}\right)_v dV_r \qquad (1)$$

$$C_p - C_p^\circ = -\int_0^P T \left(\frac{d^2V}{dT^2}\right)_P dP_r \qquad (2)$$

(Although in principle the necessary second derivatives can be computed directly from PVT data, in practice such data are rarely available in such quantity and precision that the second derivatives can be calculated without recourse to a numerical equation of state or a graphical one, for example a compressibility plot.)

Comparison of the experimental values of $C_v - C_v^\circ$ or $C_p - C_p^\circ$ with those calculated by Equations (1) and (2) is a very sensitive test of the accuracy of an equation of state. Inspection of Equations (1) and (2) reveals that $C_v - C_v^\circ$ is readily calculated by means of a pressure-explicit equation of state, $P = f(V, T)$, and that $C_p - C_p^\circ$ is readily calculated by means of a volume-explicit equation $V = f(P, T)$. Computation of $C_v - C_v^\circ$ from a volume-explicit equation or of $C_p - C_p^\circ$ from a pressure-explicit equation is possible but awkward. Most currently used equations are pressure-explicit, for example the Beattie-Bridgeman (*1*), Benedict-Webb-Rubin (*2*), and Martin-Hou (*14*) equations; the accuracy of these equations can be tested and possible improvements suggested by $C_v - C_v^\circ$ data, but such tests cannot be conveniently made with $C_p - C_p^\circ$ data. Furthermore C_p increases without limit near the critical state, whereas C_v does not; so C_v may be used to check state data near the critical point but C_p may not.

The major experimental problems of C_p calorimetry have long been solved (*17*); C_v calorimetry presents a different set of experimental problems, which have not yet been completely overcome. Measurements of C_p are performed in a flow calorimeter at steady state. As the temperature of the apparatus does not change with respect to time, the heat capacity of the calorimeter does not enter the calculations of C_p. Measurements of C_v, however, are performed in an unsteady state by heating a known mass of gas plus its container through a measured temperature interval. The heat capacity of the container must be subtracted from the measured heat capacity to compute the

Noel De Nevers is with California Research Corporation, Richmond, California.

heat capacity of the contents. In previous C_v calorimetry (*3, 4, 5, 7, 10, 11, 19, 21*) the heat capacity of the calorimeter has been up to twenty times that of its contents; under these circumstances a small error in the measured heat capacity corresponds to a large error in the heat capacity of the contents. Michels and Strijland (*19*) using a differential calorimeter measured the C_v of carbon dioxide with fair precision. Theirs has been the only work to date which shows C_v over a wide range of temperature and density for any compound.

In this research a new type of calorimeter was used. In principle the calorimeter was the simple adiabatic type; the experimental substance was contained in the calorimeter, which was placed in an evacuated space and surrounded by a shield whose temperature was maintained as close as possible to that of the calorimeter. Measured amounts of heat were added to the calorimeter and its contents, and from the measured temperature rise the heat capacity of the aggregate was computed. The calibrated heat capacity of the calorimeter was subtracted from the heat capacity of the aggregate to find the heat capacity of the contents. This calorimeter was novel in two respects. First, it was very thin-walled. Being designed to operate in the pressure range of 200 to 900 lb./sq. in. and to burst at a pressure of 1,000 lb./sq. in., it had a heat capacity much lower than that of a comparable calorimeter designed with a normal safety factor; naturally it was necessary to provide shielding to limit the destructive effects of rupture of the calorimeter. Second, this calorimeter had an internal, electric motor stirrer to provide temperature uniformity. The several constant-volume calorimeters of Sage *et al.* (*4*) have used internal stirring, dependent on external motors; all other previous C_v calorimeters have depended on natural convection and conduction of heat through their thick metal walls to provide temperature uniformity. The internal motor stirrer was chosen in preference to an external one because it was simple (no shaft seals or magnetic coupling), because it made calculation of the stirring energy input simple (all the electrical energy used by the motor entered the gas as motor heat loss or as stirring energy), and because it eliminated the problem of heat conduction along the stirrer shaft or magnetic coupling shaft.

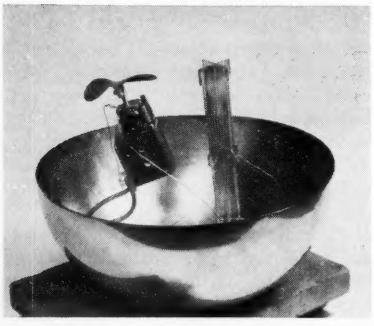

Fig. 1. View of lower half of the unassembled calorimeter.

EXPERIMENTAL APPARATUS AND MATERIALS

The calorimeter proper was a sphere of type-304 extra-low-carbon stainless steel, 8.015 in. I.D. and with a wall thickness of 0.031 in. Inside it were a platinum coil, which served both as a heater and as a platinum-resistance thermometer, and a 12-volt D.C. motor which drove a 2½-in. propeller. The electrical leads to these instruments left the calorimeter through kovar-glass lead seals, silver-soldered into the wall of the calorimeter. A small needle valve, also silver-soldered into the wall of the calorimeter was used for loading and unloading the calorimeter. Figure 1 shows the lower half of the calorimeter before assembly; on it the thermometer heater and motor are visible. The two cold-drawn halves of the calorimeter were joined by Heliarc fusion welding, and the outside of the calorimeter was copper-plated to reduce its emissivity for radiant heat transfer. Figure 2 is a cross section of the calorimeter assembly, showing the calorimeter, adiabatic shield, and vacuum container.

The calorimeter was supported in place by three Fiberglas strings. Surrounding it was an adiabatic shield in the form of a cubical box made of six copper plates, each 10 in. square and ¼ in. thick. The inside surfaces of the shield were coated with aluminum foil to reduce radiant heat transfer. Electric heaters attached to the outside of the shield were used to control its temperature. Three differential thermocouples measured the differences in temperature between the top, side, and bottom of the calorimeter and corresponding points on the adiabatic shield.

The shield was supported within a steel vacuum container, which was designed to contain the experimental substance and any fragments in case of a rupture of the calorimeter. It was constructed of ¼-in.-thick mild steel and had a removable top, retained by 8½-in. bolts, with a silicone-rubber gasket making a vacuum seal at the top. A vacuum pump was used to evacuate the container and to provide the necessary vacuum for loading and unloading the calorimeter. The container was covered with Fiberglas insulation to reduce heat leakage to the surroundings. The electrical leads to the calorimeter and to the differential thermocouples left the vacuum system through a vacuum junction box placed several feet from the vacuum container in order to prevent thermal electromotive forces from forming in the soldered junctions.

During heating periods the current input to the calorimeter passed through the motor and thermometer heater in series. About three quarters of the power was dissipated by the thermometer heater and the remainder by the motor. The current through the thermometer heater and motor was determined by measuring the voltage across a standard resistor in series with them; the voltage across the thermometer heater and motor was determined by measuring the voltage across a standard resistor in a circuit parallel to them. A balancing resistor (*9*) in series with the

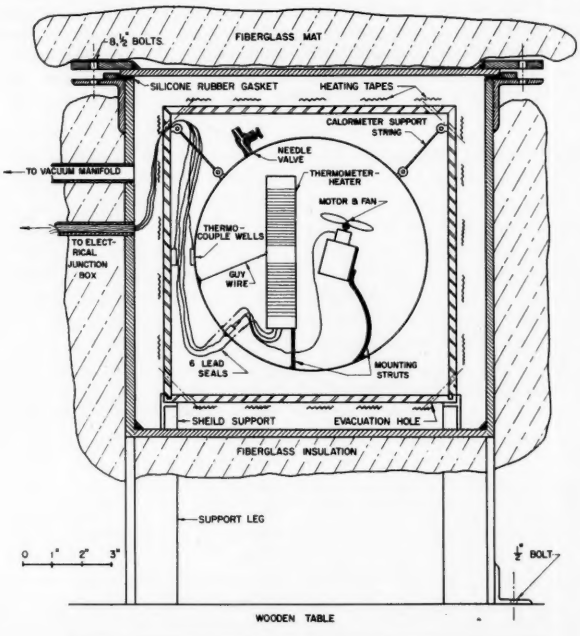

Fig. 2. Cross section of the calorimeter assembly.

TABLE 1. THE CONSTANT-VOLUME HEAT CAPACITY OF PERFLUOROCYCLOBUTANE

Density, g./cc.	T_{mean}, °C.	Heat capacity, cal./(g.)(°C.)
0.1569	101.58	0.2117
	103.45	0.2164
	114.99	0.2190
	126.33	0.2212
	137.41	0.2243
	146.61	0.2250
0.1927	109.18	0.2204
	119.24	0.2237
	131.73	0.2257
	144.05	0.2277
0.2394	110.50	0.2272
	118.11	0.2269
	127.20	0.2279
	136.20	0.2287
	145.10	0.2301
0.3201	117.32	0.2357
	126.40	0.2339
	135.43	0.2356
	144.40	0.2341
0.3902	114.67	0.2482
	118.37	0.2436
	124.01	0.2393
	131.58	0.2377
	139.12	0.2373
	146.69	0.2374
0.4465	119.27	0.2492
	123.01	0.2445
	127.74	0.2416
	134.37	0.2398
	141.97	0.2388
	147.66	0.2390
0.5366	119.04	0.2594
	123.56	0.2498
	129.42	0.2445
	136.16	0.2417
	142.95	0.2400

heater and motor minimized the changes in heater power that occurred with changes in thermometer-heater and motor resistance. The temperature of the calorimeter was determined from the resistance of the thermometer heater. (This measurement was never made while current was flowing through the thermometer heater and motor.) Elapsed time of a heating period was measured with a synchronous timer, whose clutch was actuated by the switch which controlled the power to the calorimeter.

The perfluorocyclobutane was stated to be 99.78 weight % pure; the propylene was C.P. grade, specified to be 99.0 mole % pure. Neither of these materials was subjected to any additional purification.

EXPERIMENTAL PROCEDURE

The material to be investigated was placed in a light-weight stainless steel transfer container, which was weighed, and then an amount of substance was transferred to the calorimeter by vacuum transfer methods. The transfer container was reweighed and the calorimeter loading thus determined. For this operation and for unloading, the top of the vacuum container and the top member of the adiabatic shield were removed and the calorimeter was suspended from a crane above the vacuum container. When loading was complete, the calorimeter was lowered into place, the adiabatic shield and vacuum container were reassembled, and the system was evacuated (normally to about 0.050 mm. Hg).

When the calorimeter had been heated

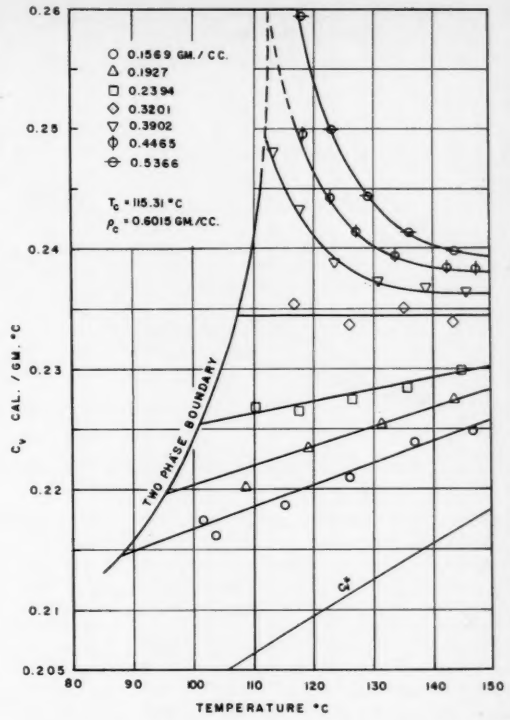

Fig. 3. Constant-volume heat capacity of perfluorocyclobutane.

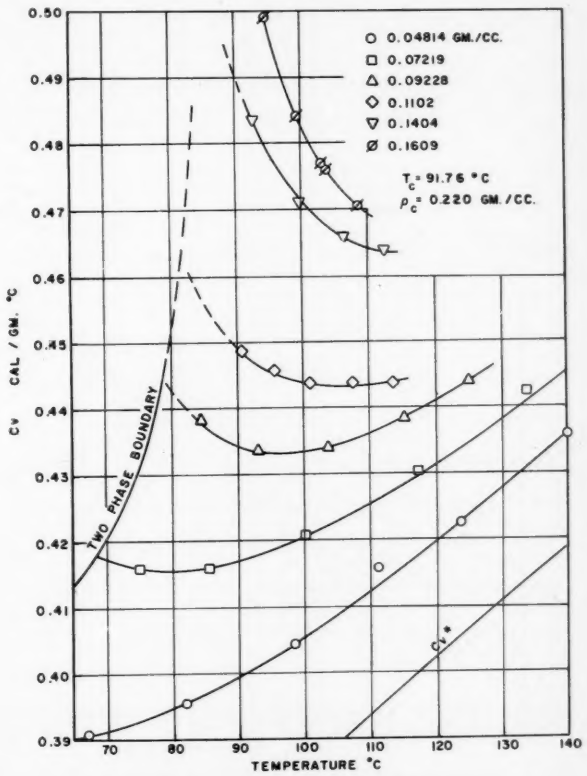

Fig. 4. Constant-volume heat capacity of propylene.

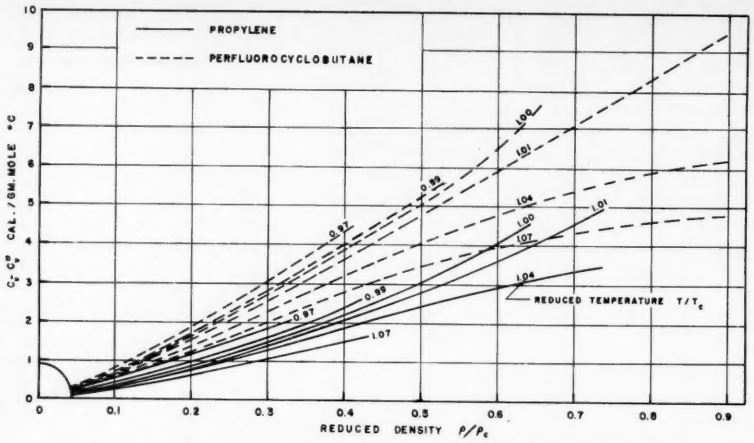

Fig. 5. C_v-C_v* as a function of reduced temperature and reduced density.

to the desired starting temperature, the shield was controlled to maintain zero average temperature differences between the control points on the surfaces of the calorimeter and the shield. The temperature was measured at 5 min. intervals until its rate of change with respect to time or "drift" had been determined. (This drift was normally about 0.002°C./min.) Then the power was switched to the thermometer heater and motor. At times corresponding to one quarter, one half, and three quarters of the heating period the power input to the thermometer heater and motor was measured, and the average of these three power readings was used in subsequent calculations. Heating periods were of 15-, 20-, 25-, 30- and 40-min. duration, depending on the desired temperature change. At the end of the heating period the power was switched away from the calorimeter. The temperature was again measured at 5-min. intervals until the drift had been determined. This drift was used to extrapolate the temperature-time curve to the time of power shut-off. If only one measurement was planned, operations ceased after this drift had been found; if several measurements were planned, a new heating period was begun as soon as this drift had been determined. When the heat capacity had been measured over the planned temperature range, the calorimeter was cooled and unloaded by methods similar to the loading procedure. The difference between the measured load and the quantity of material recovered seldom exceeded 0.1% of the load.

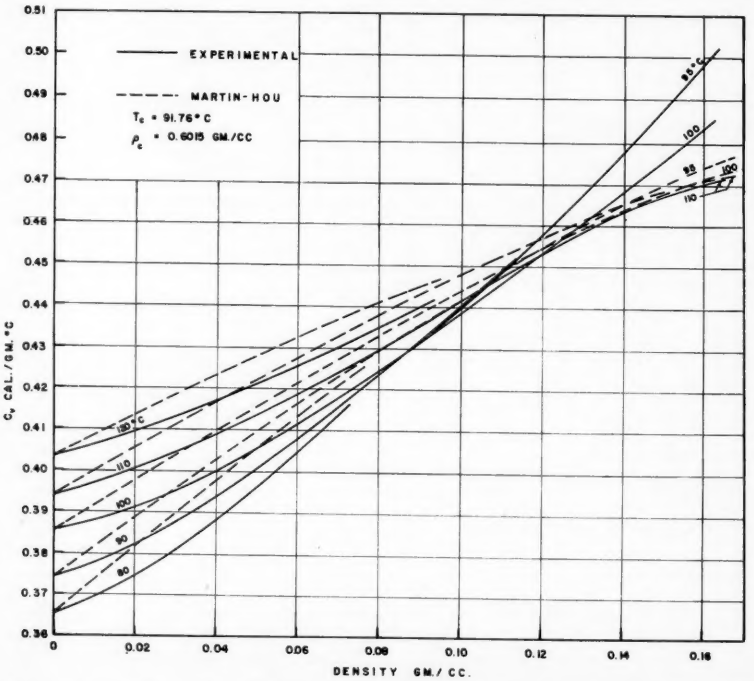

Fig. 6. Comparison of the experimental C_v of propylene with the C_v predicted by the Martin-Hou equation.

Table 2. The Constant-Volume Heat Capacity of Propylene

Density, g./cc.	T_{mean}, °C.	Heat capacity, cal./(g.)(°C.)
0.04814	67.15	0.3903
	82.14	0.3952
	98.45	0.4047
	111.62	0.4159
	123.90	0.4226
	140.21	0.4357
0.07219	75.09	0.4160
	85.21	0.4163
	99.93	0.4208
	117.06	0.4305
	133.72	0.4412
	145.92	0.4485
0.09228	84.64	0.4380
	92.91	0.4337
	103.71	0.4341
	115.35	0.4385
	125.32	0.4439
0.1102	90.71	0.4486
	95.75	0.4460
	101.28	0.4438
	107.59	0.4439
	113.37	0.4438
0.1404	93.17	0.4842
	99.58	0.4710
	106.68	0.4659
	112.47	0.4638
0.1609	94.92	0.4991
	99.51	0.4840
	104.51	0.4761
	103.74	0.4768
	108.41	0.4704

All the data reported in this paper were collected at calculated pressures less than 800 lb./sq. in. An attempt was made to make a final measurement on propylene in the pressure range of 800 to 900 lb./sq. in.; however during this measurement the calorimeter ruptured at a pressure estimated to be about 860 lb./sq. in. The vacuum container had been designed to contain the propylene in case the thin-walled sphere leaked, but the sphere split in half along the weld almost instantly, blowing the top off the vacuum container. The propylene rushed out, mixed with the air, and exploded. A new container—cylindrical instead of cubical—is being constructed with better safety features.

CALCULATIONS

The gross heat capacity C_g of the calorimeter plus contents was determined at the mean temperature of a given experiment by the equation

$$C_g = q_{mean}\,\Delta\theta/(\Delta T - \Delta T_{corr}) \quad (3)$$

ΔT_{corr} was that change in temperature which would have occurred in time $\Delta\theta$ if no energy had been added electrically. It was computed from the drift before the heating period, $drift_1$, and the one after, $drift_2$, by

$$\Delta T_{corr} = \Delta\theta\,(drift_1 + drift_2)/2 \quad (4)$$

Equation (3) assumes that the gross heat capacity varies linearly with respect to temperature and that the

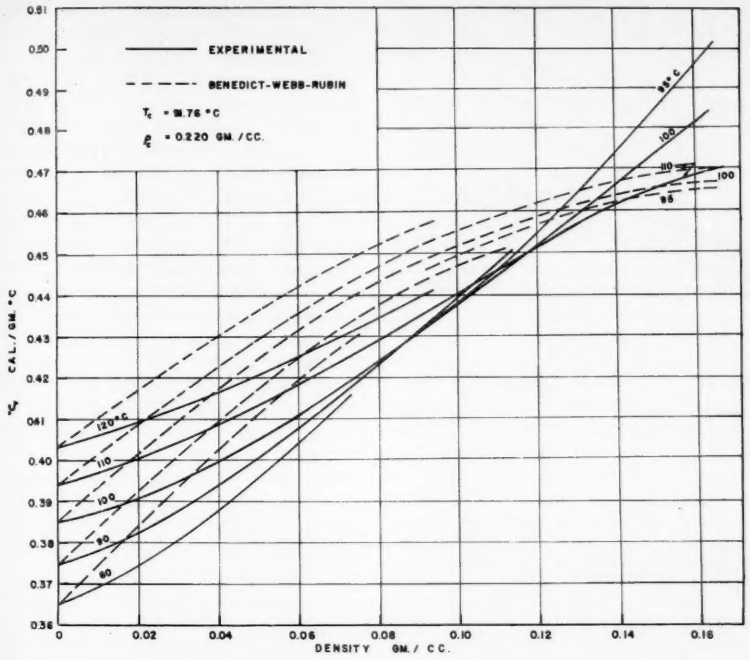

Fig. 7. Comparison of the experimental C_v of propylene with the C_v predicted by the Benedict-Webb-Rubin equation.

mean power varies linearly with time. The error introduced by these assumptions is negligible.

The estimated maximum uncertainty in C_v due to the uncertainties in the various measurements is q_{mean}, 0.3%; $\Delta\theta$, negligible; ΔT, 0.3% and ΔT_{corr}, 0.2%. Thus the maximum uncertainty in C_v if these uncertainties had had the same sign would have been 0.8%. If an error of 0.8% had been made in one direction in the calibration and in the other direction in the heat-capacity measurements, this would have led to an error in C_v of 1.1% at the highest density used and of 3.2% at the lowest. The internal consistency of the data (maximum scatter of 0.7%, average scatter of less than 0.3%) indicates that the uncertainties were random in direction and thus that the accuracy of the data is much better than the above maxima. The maximum error in density was estimated to be 0.3%.

CALIBRATION

The heat capacity of the calorimeter as a function of temperature was determined by filling the calorimeter with materials of known heat capacities, measuring C_v, and subtracting the heat capacities of the contents according to

$$\text{calibration} = C_v - MC_v^\circ - M(C_v - C_v^\circ) \qquad (5)$$

Two calibration substances were used, propylene and dichlorodifluoromethane (Freon 12). The values of C_v° used for propylene were those given by Kilpatrick and Pitzer (*12*); for dichlorodifluoromethane those of Masi (*18*) were used. The values of $C_v - C_v^\circ$ used were calculated by the Martin-Hou equation, from constants presented in (13) and (14). For none of the calibration values did the value of MC_v° exceed 7% of the value of C_v, nor did the value of $M(C_v - C_v^\circ)$ exceed 0.1% of C_v. The maximum scatter of the calibration points from the curve drawn through them was 0.8%, and the average was 0.4%.

THE CONSTANT-VOLUME HEAT CAPACITY OF PERFLUOROCYCLOBUTANE

The constant-volume-heat-capacity results for perfluorocyclobutane are shown in Table 1. Seven densities were used ranging from 0.1569 (26.2% of the critical density) to 0.5366 g./cc. (89.6% of the critical density). The temperature range for each density was from the saturation temperature to 150°C. The measured heat capacity over this temperature and density range varies from 0.2164 to 0.2594 cal./(g.) (°C.). These data are shown in Figure 3 on a C_v-vs.-temperature plane; a smooth curve has been drawn through the individual points for each density. Also shown on Figure 3 are the boundary of the two-phase region calculated from the *PVT* data, the values of C_v°, and the critical temperature and density reported by Martin *et al.* (*15*).

THE CONSTANT-VOLUME HEAT CAPACITY OF PROPYLENE

Table 2 shows the constant-volume-heat-capacity results for propylene. Six densities were used, ranging from 0.04814 (21.8% of the critical density) to 0.1609 g./cc (72.6% of the critical density). There is some question about the value of the critical density of propylene; throughout this paper

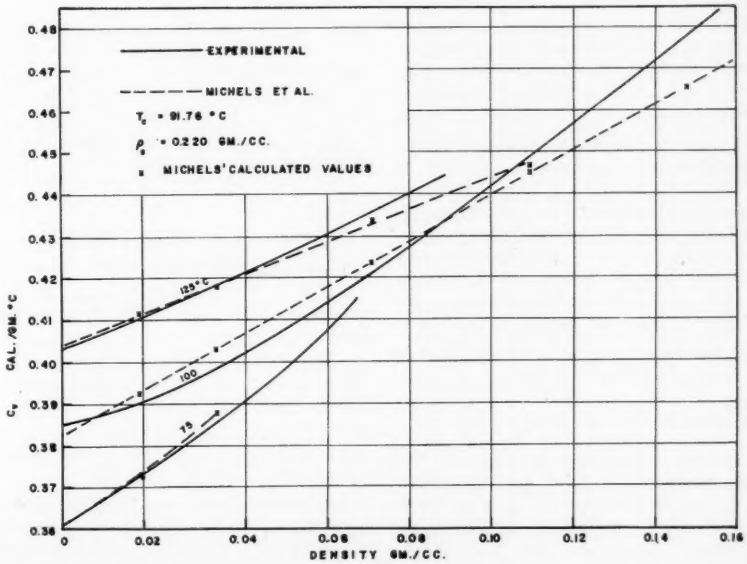

Fig. 8. Comparison of the experimental C_v of propylene with the calculated C_v according to Michels *et al.*

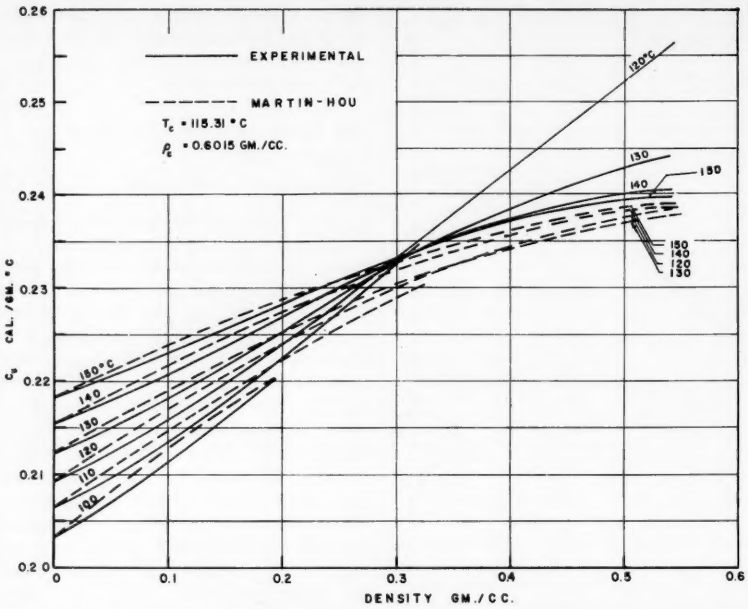

Fig. 9. Comparison of the experimental C_v of perfluorocyclobutane with the C_v predicted by the Martin-Hou equation.

the value of 0.220 g./cc. reported by Marchman, Prengle, and Motard (*16*) has been used. Farrington and Sage (*8*) report a value of 0.230 g./cc., which seems more reasonable in comparison with other compounds. The temperature range for the two lowest densities was from the saturation temperature to 150°C.; for the two intermediate densities, from the saturation temperature to that temperature at which the calculated pressure was 700 lb./sq. in.; for the two highest densities, from the saturation temperature to that temperature at which the calculated pressure was 800 lb./sq. in. Over this range of temperatures and densities the measured C_v varies from 0.3903 to 0.4991 cal./(g.)(°C). These data are shown in Figure 4 on a C_v-vs.-temperature plane. Also shown on this figure are the values of the critical temperature and the critical density, the boundary of the two-phase region calculated from the *PVT* data of Marchman *et al.* (*16*), and the values of C_v^* reported by Kilpatrick and Pitzer (*12*).

DISCUSSION

Several interesting features of the data are revealed by Figure 5, which is a modified cross plot of Figures 3 and 4. On it, for equal reduced temperatures, isotherms for both compounds have been constructed on a molar $C_v - C_v^*$-vs.-reduced-density plane. According to the law of corresponding states (*6*), which says that the compressibility factor ($Z=PV/RT$) is the same function of reduced temperature and reduced density for all gases, the molar value of $C_v - C_v^*$ must be the same for all gases at the same reduced temperature and reduced density:

$$C_v - C_v^* = -RT_R \int_0^{\rho_R} \left[\frac{T_R}{\rho_R} \left(\frac{d^2Z}{dT_R^2} \right)_{\rho_R} + \frac{2}{\rho_R} \left(\frac{dZ}{dT_R} \right)_{\rho_R} \right] d\rho_{RT} \qquad (6)$$

As is seen from Figure 5, the values of $C_v - C_v^*$ for perfluorocyclobutane are 1.6 to 2 times those for propylene at the same reduced temperatures and reduced densities. Thus it is clear that although the law of corresponding states is sufficiently accurate to make approximate generalizations of *PVT* data, it is not sufficiently accurate to generalize $C_v - C_v^*$ data. The reason for this is apparent from Equation (6); an error of several per cent in Z is made by assuming that perfluorocyclobutane and propylene have the same $Z = f(T_R, \rho_R)$, and the two differentiations and one integration in Equation (6) greatly magnify this error.

As noted above, comparison of C_v data over a range of temperatures and densities with C_v calculated from C_v^* and an equation of state is a very sensitive test of a pressure-explicit equation of state. The measured C_v values of perfluorocyclobutane have been compared with the C_v predicted by the Martin-Hou equation, by use of the constants and values of C_v^* presented by Martin *et al.* (*15*). The measured C_v values of propylene have been compared with the predictions of the Martin-Hou equation by use of the constants presented by Martin and Hou (*14*) and the C_v^* values of Kilpatrick and Pitzer (*12*). They have also been compared with the predictions of the Benedict-Webb-Rubin equation through the constants presented by Marchman *et al.* (*16*) and the above C_v^* values; finally they have been compared with the C_v values calculated from *PVT* data by Michels *et al.* (*20*). [Michels *et al.* used the C_v^* values of Stull and Mayfield (*22*), which differ slightly from those mentioned above.] The comparisons for propylene are shown in Figures 6, 7, and 8, and the the comparison for perfluorocyclobutane is shown in Figure 9.

In general the agreement is good; the maximum difference between the experimental and calculated values in any of the above comparisons is 6.7% of C_v. This maximum occurred between the experimental and calculated values of C_v for perfluorocyclobutane at 89.6% of the critical density and 4.67°C. above the critical temperature. Further from the critical state the agreement is much better. However the comparison reveals the following systematic differences between the experimental data and the predictions of the equations of state.

1. The experimental isotherms on a C_v-vs.-density plane (or a $C_v - C_v^*$-vs.-density plane) curve upward at low densities. (If the lowest density C_v values were extrapolated linearly to zero density, errors of 1 to 4% in C_v^* would result.) Mathematically this means that

$$\left(\frac{d^2C_v}{d\rho^2} \right) = \frac{d}{d\rho_T} \left[\frac{-T}{\rho^2} \left(\frac{d^2P}{dT^2} \right)_\rho \right] = T \left[\frac{2}{\rho^3} \left(\frac{d^2P}{dT^2} \right)_\circ - \frac{1}{\rho^2} \left(\frac{d^3P}{dT^2 d\rho_T} \right) \right] \qquad (7)$$

is positive at low densities. This upward curvature decreases with increasing temperature. The Beattie-Bridgeman equation predicts that Equation (7) is positive at low densities, while the Martin-Hou and Benedict-Webb-Rubin equations predict that it is negative.* For this reason both the latter

* An improved form in the Martin-Hou equation has been developed and will be published soon. In the improved form the C_4 constant, which was previously zero, has a finite positive value, and the C_3 constant, which was previously positive, is negative. The values of A_3, B_3, A_4, A_5, B_5, and C_5 are changed slightly, but their signs are not changed. This improved version makes $[(d^2C_v)/(d\rho^2)]_T$ positive at low densities.

equations predict C_v values which are too high in the density range from zero to about one-quarter the critical density as seen in Figures 6, 7, and 9. Michels *et al.* (*20*) do not present formulas for the calculation of C_v but only tabulated values of the 75°, 100°, and 125°C isotherms. These tabulated values show that the 75°C isotherm curves upward slightly more than the experimental isotherm, while the 100° and 125°C. isotherms are almost exactly straight, as is shown in Figure 8.

2. The experimental isotherms are straight or nearly straight in the density range of one-quarter to one-half the critical density; that is, Equation (7) is zero or very small in this region. The Beattie-Bridgeman equation has a zero value of Equation (7) at one point in this region, and the Benedict-Webb-Rubin and Martin-Hou equations predict that it is negative throughout the region. According to the isotherms of Michels *et al.*, Equation (7) is zero throughout this region.

3. The experimental data show that for densities greater than one-half of the critical density the isotherms for temperatures near the critical temperature are straight or curve upward, but those at higher temperatures curve downward; that is, Equation (7) is zero or positive for low temperatures and negative for higher temperatures. All three of the above equations represent $C_v - C_v^\circ$ as the product of a function of temperature and a function of density:

$$C_v - C_v^\circ = f(T) \cdot f(\rho) \qquad (8)$$

Thus these equations predict that the isotherms on a $C_v - C_v^\circ$-vs.-density plane will be similar; that is, given one isotherm it will be possible to construct any other isotherm by multiplying the ordinates of the first isotherm by a constant multiplier. In particular these equations predict that Equation (7) must have the same sign for all temperatures at a given density, since $f(T)$ is always positive in these equations. Thus the above equations cannot accurately represent both the high- and low-temperature isotherms over the density range of the data. In order to represent accurately all the C_v data, an equation which predicts a more complicated $C_v - C_v^\circ$ function will be necessary.

4. At densities greater than one-half of the critical density C_v decreases with increasing temperature; that is, $(dC_v/dT)_\rho$ is negative, as shown in Figures 3, 4, 6, and 7. From Figures 6 and 7 it is seen that for propylene the Martin-Hou equation predicts this behavior qualitatively but does not predict $(dC_v/dT)_\rho$ accurately and that the Benedict-Webb-Rubin equation predicts that $(dC_v/dT)_\rho$ is positive over the entire range of the data. For perfluorocyclobutane the Martin-Hou equation predicts that $(dC_v/dT)_\rho$ is negative for temperatures below 130°C. and positive for higher temperatures. Because the Beattie-Bridgeman equation uses the same $f(T)$ in Equation (8) as the Benedict-Webb-Rubin equation, their predictions of $(dC_v/dT)_\rho$ at these densities should be similar.

5. The measured C_v increases very rapidly with decreasing temperatures at high densities and temperatures close to the saturation temperature. Michels and Strijland (*19*) observed similar behavior in their measurements on carbon dioxide, as did Pall, Broughton, and Maass (*21*) in their measurements on ethylene. None of the above equations predict this rapid increase, an indication that the true value of $(d^2P/dT^2)_v$ in this region must be much larger than that predicted by the above equations; there is a little precise *PVT* data available in this region to verify or refute this conclusion. The work of Pall *et al.* (*21*) suggests an alternate explanation, namely that the currently accepted model of phase behavior in this region may be too simple and that one-phase thermodynamic relations, for example Equations (1) and (2), may not apply.

ACKNOWLEDGMENT

The authors wish to thank Yu-Tang Hwang, who assisted in the construction and operation of the equipment. They are also grateful for the financial assistance of the Faculty Research and Equipment Fund of the University of Michigan and the National Science Foundation Fellowship Program.

NOTATION

C_g = gross heat capacity of the calorimeter and contents
C_p = heat capacity at constant pressure
C_p° = heat capacity at constant and zero pressure
C_v = heat capacity at constant volume
C_v° = heat capacity at constant volume and zero pressure
d = differential operator
f = function
M = mass
P = absolute pressure
q = power input
q_{mean} = average power input
R = universal gas constant
T = absolute temperature
V = specific volume
Z = compressibility factor
$^\circ$ = zero pressure or ideal gas state
Δ = finite-change operator
θ = time
ρ = density
$\Delta\theta$ = time interval of power input
ΔT = change in temperature
ΔT_{corr} = correction for the heat leakages from the calorimeter

Constants

The following constants have been used throughout this research:
1 cal. = 1 thermochemical cal. = 4.1840 absolute j.
Temperature °K. = temperature °C. plus 273.16
1 atm. = 14.70 lb./sq. in.

LITERATURE CITED

1. Beattie, J. A., and O. C. Bridgeman, *Proc. Am. Acad. Arts Sci.*, **63**, 229 (1924).
2. Benedict, Manson, G. B. Webb, and L. C. Rubin, *J. Chem. Phys*, **8**, 334 (1940); **10**, 747 (1942).
3. Bennetwitz, K., and E. Splittgerber, *Z. Phys. Chem.*, **124**, 49 (1940).
4. Connolly, T. J., B. H. Sage, and W. N. Lacey, *Ind. Eng. Chem.*, **43**, 946 (1951).
5. Dieterici, C., *Ann. der Physik*, **12**, 144 (1903).
6. Dodge, B. F., "Chemical Engineering Thermodynamics," p. 159, McGraw-Hill, New York (1944).
7. Eucken, A., and F. Hauck, *Z. Phys. Chem.*, **134**, 161 (1928).
8. Farrington, P. S., and B. H. Sage, *Ind. Eng. Chem.*, **41**, 1734 (1949).
9. Hoge, H. J., *Rev. Sci. Instru.*, **20**, 59 (1949).
10. ———, *J. Research Natl. Bur. Standards*, **44**, 312 (1950).
11. Joly, J., *Proc. Roy. Soc.*, **55**, 390 (1894).
12. Kilpatrick, J. E., and K. E. Pitzer, *J. Research Natl. Bur. Standards*, **37**, 163 (1946).
13. McHarness, R. C., B. J. Eiseman, Jr., and J. J. Martin, *Refrig. Eng.*, **63**, 31 (1955).
14. Martin, J. J., and Y. C. Hou, *A.I.Ch.E. Journal*, **1**, 142 (1955)
15. Martin, J. J., R. M. Kapoor, B. G. Bray, R. B. Reimus, M. L. Salive, and R. K. Bhada, "Data and Equations for the Thermodynamic Properties of 'Freon C-318' Perfluorocyclobutane," Engineering Research Institute of the University of Michigan (1956).
16. Marchman, H., H. W. Prengle, Jr., and R. L. Motard, *Ind. Eng. Chem.*, **41**, 2658 (1949).
17. Masi, J. F., *Trans. Am. Soc. Mech. Engrs.*, **76**, 1067 (1954).
18. ———, *J. Am. Chem. Soc.*, **74**, 4338 (1952).
19. Michels, A., and J. Strijland, *Physica*, **18**, 613 (1952).
20. Michels, A., T. Wassenaar, P. Lowerse, R. J. Lunbeck, and G. J. Wolkers, *Physica*, **19**, 287 (1953).
21. Pall, D. B., J. W. Broughton, and O. Maass, *Can. J. Research*, **A16**, 230 (1938).
22. Stull, D. R., and F. D. Mayfield, *Ind. Eng. Chem.*, **35**, 639 (1943).

Manuscript received March 12, 1959; revision received July 13, 1959; paper accepted July, 23, 1959.

The Critical Constants of the Elements

DAVID S. GATES and GEORGE THODOS

The Technological Institute, Northwestern University, Evanston, Illinois

The critical temperatures available in the literature for seventeen elements constitute the basis of this study for predicting critical temperatures from normal boiling points. When not available, the normal boiling point can be estimated from vapor-pressure data. The extension of the vapor-pressure data beyond the normal boiling point establishes the critical pressure from the estimated critical temperature.

In accordance with this procedure, critical temperatures and pressures have been predicted for thirty-six elements included in the periodic table from lithium to uranium. These critical constants constitute the core of this study and have been used to calculate both van der Waals' constants. These constants, when plotted against their atomic numbers, produce correlations that may permit the further prediction of van der Waals' constants for other elements.

A simple relationship between the critical volume and the volume van der Waals' constant is found to exist and is presented as a basis for predicting the critical volume of elements.

Considerable attention has been directed in the literature to the prediction of critical constants for organic compounds. In this respect Riedel (*49, 50, 51*) and Lydersen (*27*) present methods of calculating the critical temperatures, pressures, and volumes from group contributions, the normal boiling points, and the molecular weights of these substances. Another approach has been demonstrated (*67, 68*) for the calculation of van der Waals' constants which are used to predict the critical constants of aliphatic hydrocarbons from molecular structural considerations.

Because modern technology requires information on the state of materials at elevated temperatures and pressures, it is necessary to learn about hitherto unexplored areas, such as the high-temperature and pressure regions. In order to fill in some of the existing voids, the study of the critical state of the elements was undertaken without restrictions of temperature and pressure. In this study procedures were adopted that permitted the extension of meager vapor-pressure information obtained at moderate conditions into the critical region.

David S. Gates is with E. I. du Pont de Nemours and Company, Wilmington, Delaware.

CRITICAL TEMPERATURE

Experimental critical temperatures are limited primarily to those reported by Kobe and Lynn (*31*). In addition, values reported by Hoge and Lassiter (*26*) for hydrogen deuteride and deuterium, by Cady and Hildebrand (*9*) for fluorine, and by Marckwald and Helmholtz (*37*) for phosphorus constitute present knowledge of the critical temperatures of the elements. These critical temperatures are presented in Table 1 along with their corresponding normal boiling points. The following relationship between the normal boiling point and the critical temperature was proposed by Guldberg in 1890 for simple molecules containing one and two atoms (*21*):

$$\frac{T_b}{T_c} = 0.567 \qquad (1)$$

In 1942 Meissner and Redding (*42*) presented the following relationship for all the elements:

$$T_c = 1.70T_b - 2.0 \qquad (2)$$

The available critical temperatures and corresponding normal boiling points of the elements presented in Table 1 have been correlated on logarithmic scales to produce the relationship of Figure 1. With the exception of helium, the sixteen elements correlate linearly to define the critical temperature as

$$T_c = 1.4732T_b^{1.0313} \qquad (3)$$

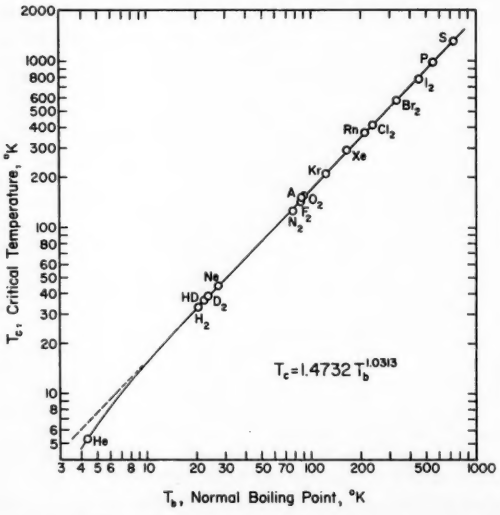

Fig. 1. Relationship of critical temperatures and normal boiling points for the elements.

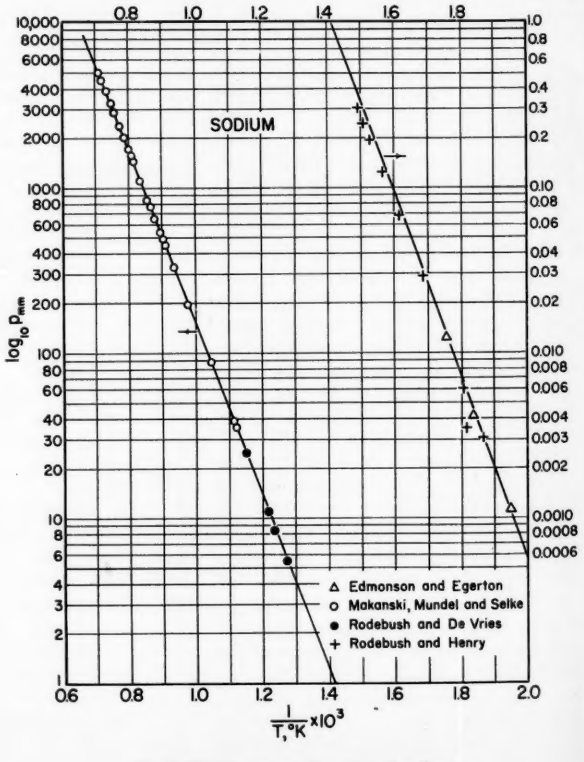

Fig. 2. Vapor-pressure function of sodium.

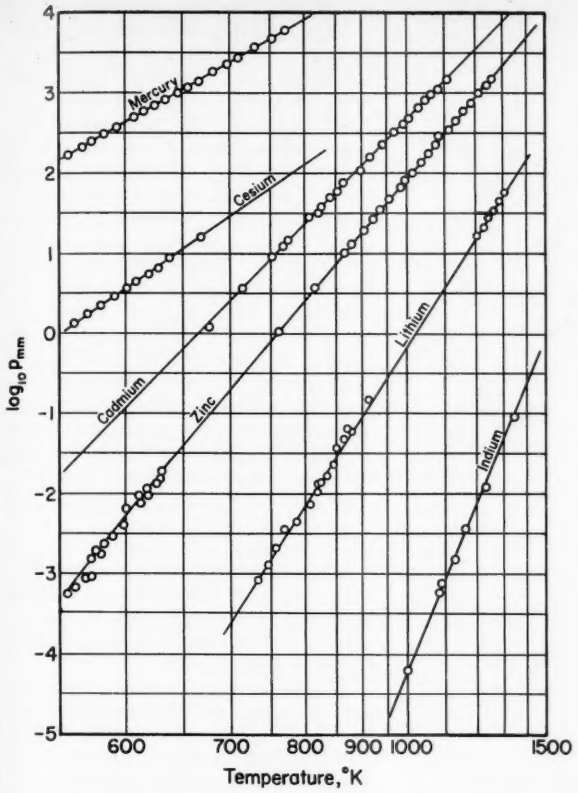

Fig. 3. Vapor-pressure relationships for low-boiling metals.

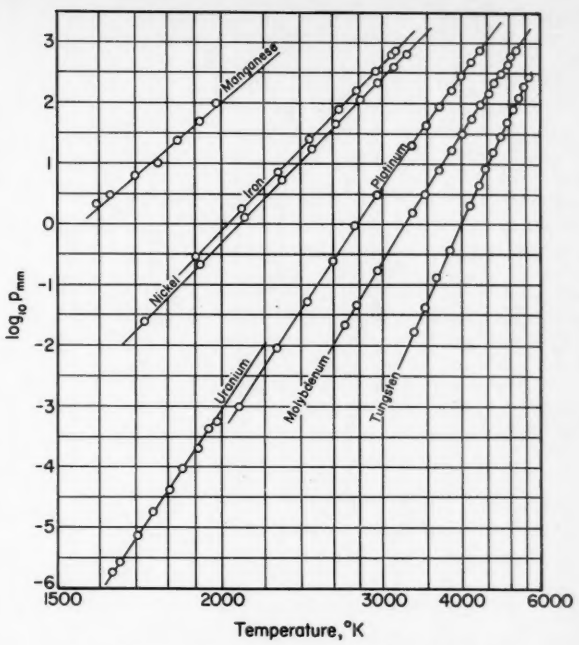

Fig. 4. Vapor-pressure relationships for high-boiling metals.

Values calculated with Equation (3) are found to have a mean deviation of 1.38% from the experimental values reported in Table 1 for elements ranging from hydrogen to phosphorus and sulfur. In view of this close agreement, Equation (3) appears to be reliable and has been assumed applicable to the elements.

With Equation (3) the prediction of the critical temperature is readily made for those elements for which normal boiling points are available. For several elements this value is either not reported or agreed upon by different sources. This condition necessitated a critical review of vapor-pressure data available in the literature to establish not only dependable normal boiling points but also information that would enable the extension of the vapor-pressure function above its normal boiling point.

INTERPRETATION OF VAPOR-PRESSURE DATA

Vapor-pressure data reported in the literature for high-boiling elements are limited to the low-pressure range. The correlation of these data on a logarithmic pressure scale vs. reciprocal absolute temperature does not necessarily produce a straight-line relationship, and consequently the extension of this function up to and past the normal boiling point becomes unreliable. Therefore the direct use of vapor-pressure data alone cannot be relied upon to extend a knowledge of normal boiling points and critical pressures. In view of these limitations, the use of a vapor-pressure reference-state correlation has been adopted. This method of plotting was introduced by Cox (*12*) and later more fully discussed by Othmer (*45*).

The elements for which extensive information is lacking can be roughly classified as those of intermediate and low volatility. In order to correlate the vapor-pressure data of these elements properly, two reference-state plots have been utilized, with the vapor-pressure data of sodium used to construct the plot for elements of intermediate volatility and those of copper used to establish the low-volatility plot.

SODIUM

The current interest in sodium as a heat transfer medium for nuclear reactors has accelerated the determination of properties for this element. As a result vapor-pressure data have been determined for temperatures as high as 1400°K. and pressures up to 6.4 atm. (*36*). The vapor-pressure data for sodium available in the literature (*14, 36, 52, 56*) are presented in Figure 2 and indicate a curvature in the low-pressure region. The vapor-pressure function for pressures above 10 mm. of mercury is linear, and the straight-line portion has been assumed to extend up to the critical point. For this portion of the curve the vapor-pressure of sodium can be defined as

$$\log p = 7.41417 - \frac{5{,}242}{T} \qquad (4)$$

A reference-state plot based on sodium has been constructed by considering the coexisting vapor pressures of the substance and of sodium at the same temperature. In accordance with this approach, the vapor-pressure behavior for a number of elements has been translated to a Cox-Othmer type of chart as presented in Figure 3. In this figure the abscissa has been translated directly to temperatures corresponding to the vapor pressures of sodium. Only vapor-pressure curves of representative elements have been included in this plot. The complete listing of references selected for this study is presented in Table 2.

COPPER

In an approach similar to that used for sodium, the data of Edwards, Johnston, and Ditmars (*15*), Harteck (*23*), Hersch (*25*), and Marshall, Dornte, and Norton (*38*) have been utilized in conjunction with the normal boiling

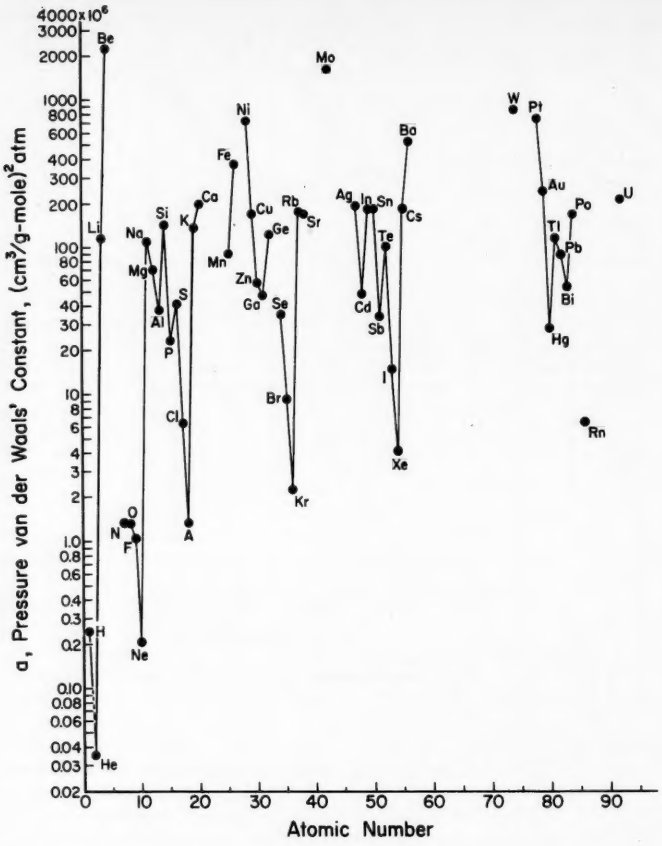

Fig. 5. Relationship of pressure van der Waals' constant and atomic number of the elements.

point reported by Brewer (*47*). On the basis of this information the vapor-pressure relationship for copper below its normal boiling point becomes

$$\log p = 8.464 - \frac{16{,}352}{T} + 0.036 \log T \qquad (5)$$

For the selection of vapor-pressure data those of Jones, Langmuir, and Mackay (*30*) have not been used to produce Equation (5). Their data for copper on a log p vs. $1/T$ plot produce a curve that is essentially parallel to that obtained with Equation (5). This equation produces a vapor-pressure function having a slight curvature which becomes insignificant in the vicinity of the normal boiling point. This vapor-pressure function from the normal boiling point, 2,868°K., to the critical point has been assumed to be linear and to have the slope calculated from Equation (5) at 2,868°K. This straight-line portion of the vapor-pressure function for copper has been found to be

$$\log p = 8.600 - \frac{16{,}402}{T} \qquad (6)$$

Equations (5) and (6) permit the calculation of exacting vapor pressures for the construction of a plot similar to Figure 3 in which the available vapor pressures of the elements having low volatilities have been correlated.

Vapor-pressure data for certain high-boiling metals are reported by Jones, Langmuir, and Mackay (*30*). This group indirectly establishes vapor pressures by heating the substance in vacuum and accounting for the rate of evaporation (*33*). Using this method, Jones, Langmuir, and Mackay established the vapor pressures for copper, iron, nickel, platinum, molybdenum, and tungsten. A slight discrepancy has been found between the values reported by the Langmuir group and those calculated from Equation (5) for copper. In view of this disagreement with copper, it is reasonable to assume that this difference also exists in the vapor-pressure data reported for iron, nickel, platinum, molybdenum, and tungsten. Consequently the vapor-pressure data of Jones, Langmuir, and Mackay have been translated to make them consistent with Equation (5). As a result of this correction, normal boiling points have been obtained that are in closer agreement with those reported in the current literature (*47*) for these elements.

The information resulting from the data of Langmuir and associates has been utilized to produce the vapor-pressure relationships presented in Figure 4. The abscissa of this figure has been generated from the vapor pressures of copper resulting from Equations (5) and (6). In addition to the data for iron, nickel, platinum, molybdenum, and tungsten, relationships are also presented in Figure 4 for manganese and uranium.

CRITICAL PRESSURE

The reference plots of Figures 3 and 4 include curves that are essentially

Table 1. Comparison of Experimental and Calculated Critical Values

	Critical constants (experimental)				Van der Waals' constants		Calculated values	
	T_b, °K.	T_c, °K.	P_c, atm.	v_c, cc./g. mole	$a\times10^{-6}$, (cc./g.-mole)² atm.	b, cc./g.-mole	T_c, °K.	v_c, cc./g. mole
Hydrogen	20.5	33.3	12.80	65.0	0.246	26.68	33.2	62.2
Hydrogen deuteride	22.1	35.91	14.64	62.8	0.250	25.16	35.94	58.7
Deuterium	23.6	38.26	16.28	60.3	0.255	24.10	38.45	56.2
Helium	4.3	5.3	2.26	57.8	0.0353	24.05		56.1
Nitrogen	77.4	126.2	33.5	90.1	1.350	38.64	130.6	90.2
Oxygen	90.0	154.8	50.1	74.4	1.359	31.69	152.6	73.9
Fluorine	86.2	144	55		1.071	26.85	146	62.6
Neon	27.3	44.5	26.9	41.7	2.091	16.97	44.6	39.6
Phosphorus	553	993.8	120.8		23.22	84.38	987.2	196.9
Sulfur	718	1,313	116		42.21	116.10	1,299	270.9
Chlorine	238.6	417	76.1	124	6.491	56.20	417	131.1
Argon	87.6	151	48.0	75.2	1.349	32.27	148	75.3
Bromine	331.9	584	102	144	9.498	58.73	586	137.0
Krypton	121.4	209.4	54.3	92.2	2.294	39.56	207.8	92.3
Iodine	457.5	785	116		15.09	69.41	816	162.0
Xenon	164.1	289.75	58.0	118.8	4.116	51.24	283.59	119.6
Radon	211	377.16	62.0		6.517	62.40	367.53	145.6

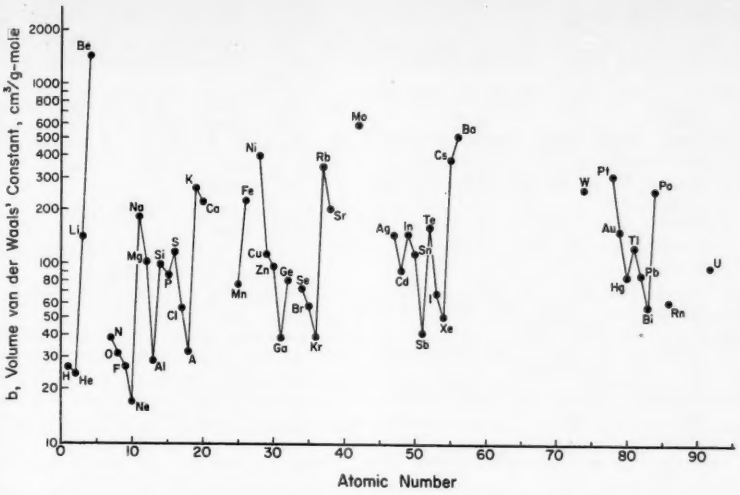

Fig. 6. Relationship of volume van der Waals' constant and atomic number of the elements.

TABLE 2. SUMMARY OF CALCULATED CRITICAL CONSTANTS FOR SOME ELEMENTS

	Calculated critical constants				
	T_b, °K.	T_c, °K.	P_c, atm.	v_c, cc./g.-mole	References used
Sodium reference plot					
Lithium	1,598	2,966	215	329.7	*24, 39*
Sodium	1,156	2,124	116	437.6	*14, 36, 52, 56*
Potassium	1,026	1,878	72.6	618.2	*19, 32, 35*
Rubidium	982	1,795	52.4	818.7	*22, 62*
Cesium	964	1,760	46.7	900.7	*2, 22, 32, 66*
Beryllium	3,243	6,153	47.2	3,115	*3*
Magnesium	1,373	2,535	254	238.5	*11, 24, 34, 58, 61*
Calcium	1,755	3,267	151	517.1	*24*
Strontium	1,647	3,059	155	471.7	*24*
Barium	1,961	3,663	72.3	1,211	*24*
Aluminum	2,520	4,744	1,695	67.0	*3, 6*
Gallium	2,418	4,546	1,208	89.9	*23*
Indium	2,331	4,377	301	347.5	*1*
Thallium	1,730	3,219	263	292.5	*11, 20, 34*
Silicon	2,739	5,159	530	232.6	*3, 59*
Germanium	2,982	5,642	715	188.6	*63, 65*
Tin	3,067	5,809	524	264.9	*64*
Lead	1,878	3,584	416	205.9	*17, 28, 70*
Antimony	1,610	2,989	740	96.7	*57*
Bismuth	1,764	3,284	574	136.7	*10, 57, 71*
Selenium	962	1,757	249	168.6	*7, 44, 46*
Tellurium	1,264	2,329	148	376.1	*7*
Polonium	1,239	2,281	90	605.7	*8*
Gold	2,938	5,557	371	358.0	*57, 60*
Zinc	1,180	2,169	229	226.4	*3, 4, 11, 29, 41, 53, 69*
Cadmium	1,039	1,903	209	217.6	*4, 16, 18, 29, 34, 55*
Mercury	630	1,135	134	202.4	*13, 43, 54*
Copper reference plot					
Molybdenum	5,165	9,880	169	1,399	*30*
Tungsten	5,950	11,500	445	618	*30*
Manganese	2,305	4,327	561	184	*3*
Iron	3,147	5,966	271	526	*30*
Nickel	3,315	6,294	158	952	*30*
Platinum	4,323	8,280	267	741	*30*
Copper	2,868	5,421	493	263	*15, 23, 25, 38, 47*
Silver	2,532	4,767	336	339	*23*
Uranium	3,946	7,533	778	231	*48*

linear; hence their extension to atmospheric pressure establishes the normal boiling point. The prediction of the critical temperature is then made with Equation (3) and the estimated normal boiling point. The further extension of the vapor-pressure functions in Figures 3 and 4 beyond the normal boiling point and up to the predicted critical temperature locates the critical pressure. This approach was utilized for the prediction of critical pressures of thirty-six additional elements for which a limited number of vapor-pressure data were available. These predicted critical temperatures and pressures are presented in Table 2.

The critical temperatures and pressures reported in the literature for the elements are summarized in Table 1, those predicted from this study, in Table 2. These critical values have been used to calculate both van der Waals' constants a and b from the relationships

$$a = \frac{27R^2T_c^2}{64P_c} \tag{7}$$

and

$$b = \frac{RT_c}{8P_c} \tag{8}$$

The resulting van der Waals' constants, when correlated with their atomic numbers, produce the relationships of Figures 5 and 6. These van der Waals' constant correlations exhibit a typical periodic variation similar to those already available for molecular volume and normal boiling point.

CRITICAL VOLUME

The critical volume defined in terms of the volume van der Waals' constant has been theoretically derived to be

$$v_c = 3b \tag{9}$$

For the critical volumes of hydrocarbons (*67, 68*), the ratio of v_c/b was not found to be equal to 3 but varied with the nature and size of the hydrocarbon molecule.

The volume van der Waals' constant for the elements of Table 1, when divided into the experimental critical volume, produced essentially constant ratios. For the elements for which complete information was available, the ratio v_c/b was found to be as follows:

	v_c/b
Hydrogen	2.43
Hydrogen deuteride	2.50
Deuterium	2.50
Helium	2.40
Nitrogen	2.33
Oxygen	2.35
Neon	2.36
Chlorine	2.20
Argon	2.33

Bromine	2.46
Krypton	2.33
Xenon	2.32

Since helium, hydrogen, and to some extent neon possess quantum effects, their ratios have been excluded to produce an average value of $v_c/b = 2.335$ for the remaining seven elements. This ratio suggests that the critical volume for the elements may be predicted with the expression

$$v_c = \frac{7}{3}b \qquad (10)$$

Values calculated with Equation (10) have been compared with the available experimental values presented in Table 1 and produce an average deviation of 1.75%.

Figures 5 and 6 can be used to predict the critical constants of the elements. Volume van der Waals' constants, obtained from Figure 6, when substituted in Equation (10) enable the calculation of the critical volumes of the elements. It is noteworthy that for this development the state of association of the elements in the critical region has not been utilized. A review points to some interesting speculations about the state of aggregation for elements such as sodium and copper. For these elements critical volumes are calculated to be 438 and 263 cc./g.-mole respectively, as compared with 75.3 and 90.2 cc./g.-mole for argon and nitrogen.

As a result of these studies Equations (3) and (10) are presented for the prediction of the critical temperature and volume of the elements. In addition to the experimental critical temperatures and pressures for seventeen elements, the critical temperatures and pressures for thirty-six other elements have been estimated through the use of vapor-pressure data and Equation (3).

Attention should be directed to the fact that the proposed critical constants for elements for which no experimental data exist must be considered tentative until these values are verified experimentally.

NOTATION

- a = pressure van der Waals' constant, (cc./g.-mole)^2 atm.
- b = volume van der Waals' constant, cc./g.-mole
- p = vapor pressure, mm. of mercury
- P_c = critical pressure, atm.
- R = gas constant, 82.055 (cc.) (atm.)/(g.-mole) (°K.)
- T = absolute temperature, °K.
- T_b = normal boiling point, °K.
- T_c = critical temperature, °K.
- v_c = critical volume, cc./g.-mole

LITERATURE CITED

1. Anderson, J. S., *J. Chem Soc.*, **141** (1943).
2. Bartels, H., *Ann. Physik (4)*, **65**, 143 (1921).
3. Baur, Emil, and Roland Brunner, *Helv. chim. Acta*, **17**, 958 (1934).
4. Braune, H., *Z. anorg. Chem.*, **11**, 109 (1920).
5. Brewer, Leo, and R. F. Porter, *J. Chem. Phys.*, **21**, 2012 (1953).
6. Brewer, Leo, and A. W. Searcy, *J. Am. Chem. Soc.*, **73**, 5308 (1951).
7. Brooks, L. S., *ibid.*, **74**, 227 (1952).
8. *Ibid.*, **77**, 3211 (1955).
9. Cady, G. H., and J. H. Hildebrand, *ibid.*, **52**, 3839 (1930).
10. Chuanko, Chang, *J. Franklin Inst.*, **217**, 173 (1934).
11. Coleman, F. F., and A. Egerton, *Trans. Roy. Soc. (London)*, **A243**, 177 (1935).
12. Cox, E. R., *Ind. Eng. Chem.*, **15**, 592 (1923).
13. Douglas, T. B., A. F. Ball, and D. C. Ginnings, *J. Research Natl. Bur. Standards*, **46**, 334 (1951).
14. Edmondson, W., and A. Egerton, *Proc. Roy. Soc. (London)*, **A113**, 520 (1927).
15. Edwards, J. W., H. L. Johnston, and W. E. Ditmars, *J. Am. Chem. Soc.*, **75**, 2467 (1953).
16. Egerton, A. C., *Phil. Mag.*, **33**, 33 (1917).
17. ———, *Proc. Roy. Soc. (London)*, **A103**, 469 (1923).
18. ———, and F. V. Raleigh, *J. Chem. Soc. (London)*, **123**, 3024 (1923).
19. Fiock, E. F., and W. H. Rodebush, *J. Am. Chem. Soc.*, **48**, 2525 (1926).
20. Fischer, Joseph, *Chem. Zentr.*, **1**, 4208 (1937).
21. Guldberg, C. M., *Z. physik. Chem.*, **5**, 374 (1890).
22. Hackspill, M. L., *Compt. rend.*, **154**, 877 (1912).
23. Harteck, P., *Z. physik. Chem.*, **134**, 1 (1928).
24. Hartmann, H., and R. Schneider, *Z. anorg. Chem.*, **180**, 275 (1929).
25. Hersh, H. N., *J. Am. Chem. Soc.*, **75**, 1529 (1953).
26. Hoge, H. J., and J. W. Lassiter, *J. Research Natl. Bur. Standards*, **47**, 75 (1951).
27. Hougen, O. A., K. M. Watson, and R. A. Ragatz, "Chemical Process Principles," pp. 87-95, John Wiley, New York (1954).
28. Ingold, C. K., *J. Chem. Soc. (London)*, **121**, 2419 (1922).
29. Jenkins, C. H. M., *Proc. Roy. Soc. (London)*, **A110**, 456 (1926).
30. Jones, H. A., Irving Langmuir, and G. M. J. Mackay, *Phys. Rev.*, **30**, 201 (1927).
31. Kobe, K. A., and R. E. Lynn, Jr., *Chem. Rev.*, **52**, 117 (1953).
32. Kröner, A., *Ann. Physik*, **40**, 438 (1913).
33. Langmuir, Irving, *Phys. Rev.*, **2**, 329 (1913).
34. Leitgebel, W., *Z. anorg. Chem.*, **202**, 305 (1931).
35. Makanski, M. M., M. Madsen, W. A. Selke, and C. F. Bonilla, *J. Phys. Chem.*, **60**, 128 (1956).
36. Makanski, M. M., C. H. Mundel, and W. A. Selke, *J. Phys. Chem.*, **59**, 40 (1955).
37. Marckwald, W., and K. Helmholtz, *Z. anorg. Chem.*, **124**, 81 (1922).
38. Marshall, A. L., R. W. Dornte, and F. J. Norton, *J. Am. Chem. Soc.*, **59**, 1161 (1937).
39. Maucherat, M., *J. phys. radium (7)*, **10**, 441 (1939).
40. McCabe, C. L., and C. E. Birchenall, *J. Metals*, **5**, 707 (1953).
41. McKinley, J. D., and J. E. Vance, *J. Chem. Phys.*, **22**, 1120 (1954).
42. Meissner, H. P., and E. M. Redding, *Ind. Eng. Chem.*, **34**, 521 (1942).
43. Menzies, A. W. C., *Z. physik. Chem.*, **130**, 90 (1927).
44. Neumann, Kurt, and Ernst Lichtenberg, *ibid.*, **A184**, 89 (1939).
45. Othmer, D. F., *Ind. Eng. Chem.*, **32**, 841 (1940).
46. Preuner, G., and I. Brockmöller, *Z. physik. Chem.*, **81**, 129 (1913).
47. Quill, L. L., "The Chemistry and Metallurgy of Miscellaneous Materials," p. 30, McGraw-Hill, New York (1950).
48. Rauh, E. G., and R. J. Thorn, *J. Chem. Phys.*, **22**, 1414 (1954).
49. Riedel, L., *Z. Elektrochem.*, **53**, 222 (1949).
50. ———, *Chem. Ing. Tech.*, **24**, 353 (1952).
51. *Ibid.*, **26**, 259 (1954).
52. Rodebush, W. H., and Thomas De Vries, *J. Am. Chem. Soc.*, **47**, 2489 (1925).
53. Rodebush, W. H., and A. L. Dixon, *ibid.*, 1036 (1925).
54. ———, *Phys. Rev.*, **26**, 851 (1925).
55. Rodebush, W. H., and M. F. Fogler, *J. Am. Chem. Soc.*, **45**, 2080 (1923).
56. Rodebush, W. H., and W. F. Henry, *ibid.*, **52**, 3159 (1930).
57. Ruff, Otto, and Bernhard Bergdahl, *Z. anorg. Chem.*, **106**, 76 (1919).
58. Ruff, Otto, and Hellmuth Hartmann, *ibid.*, **133**, 29 (1924).
59. Ruff, Otto, and Martin Konschak, *Z. Elektrochem.*, **32**, 515 (1926).
60. *Ibid.*, **41**, 346 (1935).
61. Schneider, Armin, and Udo Esch, *ibid.*, **45**, 888 (1939).
62. Scott, D. H., *Phil. Mag. (6)*, **47**, 32 (1924).
63. Searcy, A. W., *J. Am. Chem. Soc.*, **74**, 4789 (1952).
64. ———, and R. D. Freeman, *ibid.*, **76**, 5229 (1954).
65. ———, *J. Chem. Phys.*, **23**, 88 (1955).
66. Taylor, J. B., and Irving Langmuir, *Phys. Rev.*, **51**, 753 (1937).
67. Thodos, George, *A.I.Ch.E. Journal*, **1**, 165 (1955).
68. *Ibid.*, 168.
69. Vance, J. E., and C. I. Whitman, *J. Chem. Phys.*, **19**, 744 (1951).
70. von Wartenberg, H., *Z. Elektrochem.*, **19**, 482 (1913).
71. Weber, A. H., and S. C. Kirsch, *Phys. Rev.*, **57**, 1042 (1940).

Manuscript received July 17, 1958; revision received June 4, 1959; paper accepted June 10, 1959.

Effect of a Cylindrical Boundary on a Fixed Rigid Sphere in a Moving Viscous Fluid

A. M. FAYON and JOHN HAPPEL

New York University, New York, New York

In this investigation of the effect of a cylindrical boundary on a spherical particle suspended in a moving viscous fluid the pressure drop due to the motion of fluid past a stationary sphere and the drag on the sphere are independently measured, and the sphere- to-cylinder-diameter ratios varying from 0.1250 to 0.3125 are studied at different positions of eccentricity. The investigation shows that in the range of Reynolds numbers from 0.1 to 40.0, based on the approach velocity to the sphere and the diameter of the sphere, the pressure drop due to the presence of a sphere and the drag on it can be represented by a semiempirical relationship containing two terms. One term, owing to the effect of the cylindrical boundary, is derived theoretically from the creeping-motion equations which neglect inertial effects. The second term, owing to the inertial effects, is established from data on the drag coefficient of a sphere in an unbounded medium.

The effect of the boundary on the resistance to flow through an assemblage of particles in a moving fluid is important in problems involving such phenomena as fluidization, sedimentation, and flow through fixed beds. To obtain an insight into the fundamental hydrodynamics involved in problems of this type, the motion of a sphere in a cylinder was selected as a mathematical model.

When motion occurs at low Reynolds numbers, a suitable theoretical treatment is possible by omitting the inertial terms from the Navier-Stokes equations of motion to obtain the so-called "creeping-motion" equations. On the basis of these equations theoretical studies (*4, 7*) indicate that for the case where a sphere settles axially in a vertical cylinder containing a viscous fluid which is stationary, the drag is

$$\frac{W}{6\pi\mu u\, a} = \frac{1}{1-2.105\left(\frac{a}{R}\right)+2.087\left(\frac{a}{R}\right)^3} \quad (1)$$

An extension of this treatment (*6, 11*) gives the following expression for the drag on a stationary sphere at the axis of a cylindrical tube through which fluid is moving:

$$\frac{W}{6\pi\mu u_o\, a} = \frac{1-\frac{2}{3}\left(\frac{a}{R}\right)^3}{1-2.105\left(\frac{a}{R}\right)+2.087\left(\frac{a}{R}\right)^3} \quad (2)$$

The case for sedimentation has been checked experimentally, but that for the drag on a stationary sphere has not. Haberman (*5*) has developed more exact equations for the above two cases, especially applicable to high sphere-to-cylinder-diameter ratios.

Faxen (*4*) on the basis of Oseen's (*9*) equation, which partially takes inertial terms in the Navier-Stokes equations into consideration, derived the following expression for a sphere settling axially:

$$\frac{W}{6\pi\mu ua} = \frac{1}{1-\frac{3}{16}N_{Re_o}-\frac{d}{D}\left[f\left(N_{Re_o}\frac{D}{d}\right)\right]+2.09\left(\frac{d}{D}\right)^3} \quad (3)$$

Faxen calculated $f(N_{Re_o}D/d)$ as equal to 2.105 for N_{Re_o} equal to zero. He obtained values for $f(N_{Re_o}D/d)$ which decreased rapidly as N_{Re_o} increased.

McNown *et al.* (*8*) conducted an extensive experimental study for the case of a sphere sedimenting along the axis of a cylinder. Reynolds numbers up to 70 and d/D from 0.2 to 0.8 were included.

Brenner and Happel (*1*) developed solutions of the creeping-motion equations for the case of a sphere located eccentrically in a cylinder; they gave the following theoretical equation for a stationary sphere in a moving fluid:

$$\frac{W}{6\pi\mu u_o a} = (1-\beta^2)\left[1-F(\beta)\frac{a}{R}+\left\{F^2(\beta)-\frac{2}{3(1-\beta^2)}\right\}\left(\frac{a}{R}\right)^2\cdots\right] \quad (4)$$

where $-F(\beta) = 2.105 - 0.6977\,\beta^2$

and $\beta = \frac{b}{R}$

Equation (4) may be written as follows to preserve analogy with Equations (1) and (2):

$$\frac{W}{6\pi\mu u_o a(1-\beta^2)} = \frac{1-\frac{2}{3(1-\beta^2)}\left(\frac{a}{R}\right)^2}{1-F(\beta)\frac{a}{R}} \quad (4a)$$

or for the case of a sedimenting sphere

$$\frac{W}{6\pi\mu ua} = \frac{1}{1-F(\beta)\left(\frac{a}{R}\right)} \quad (4b)$$

For the case of sedimentation of an eccentric sphere the experimental data of Craig (*2*) show that for values of $\beta \leqq 0.5$, $-F(\beta)$ will be close to 2.105, as indicated by the expression above. It was also not possible in this work to establish the validity of the constant 0.6977, which has only a small effect on $F(\beta)$ in the range where it is applicable (that is near the axis of the cylinder).

The purpose of the present investigation was to study the effect of higher Reynolds numbers on the drag of a stationary sphere at various eccentricities. This technique is superior to sedimentation, because it is possible to support the sphere in a fixed position. Otherwise it would tend, in either case, to move toward the center of the tube, owing to inertial effects.

DESCRIPTION OF APPARATUS

The apparatus for measuring the pressure drop and drag on a single sphere in a moving fluid consisted of a glass tube 4 in. in diameter and 1 ft. long, flanged with gaskets at both ends to sections of 4-in. standard brass pipe. The upper section was 1½ ft. long and the lower section 4½ ft. long, the total length of the column being 7 ft. The circulating system was started with a 50 gal./min. capacity gear pump, which was provided with a bypass and driven by a 5-hp. motor.

The circulating fluid, which consisted of a 98% glycerol solution in water, entered the column through one of two rotameters, having a capacity of 0.3 to 3 and 3 to 38 gal./min. respectively. From the rota-

meter the liquid was introduced to the bottom of the column, upward through the column, and from the top back to a recirculating drum, which was provided with cooling coils. All flow lines in and out of the column, leading to the various pieces of the experimental setup, were 1.5-in. standard brass pipe.

Pressure taps were mounted 18.2 in. apart on the upper and lower side of the 4-in. brass pipe, near the flanges which held the 4-in. glass tube. The pressure taps were connected to a differential hook gauge which consisted of two glass tubes 4 in. long and 2.5 in. in diameter, flanged on both ends through suitable gaskets to prevent leakage and connected to each other from the upper flanges by copper tubing. Each glass tube had an opening at the bottom flange to connect to the leads from the pressure taps and contained two immiscible liquids at different densities; the heavier liquid was glycerol, the circulating liquid, and the lighter was dye-colored benzene. A micrometer was mounted at the bottom of each container, with the spindle extending vertically upward into the liquid. The end of the spindle was sharpened to a point which could then be raised and lowered to locate the position of the interface in both glass tubes with an accuracy of $\pm$ 0.002 in. The gauge was provided with a suitable venting device.

Thermometers were inserted at the inlet and exit side of the column, at the exit of the rotameters, and adjacent to the hook gauge.

In measuring the pressure drop due to a sphere, the sphere in question was mounted on the end of a 0.0625-in. wire connected to a rod having a diameter of 0.22 in. A 0.25-in. thick brass sliding plate was held in position at the upper end of the column by a brass ring having six uniformly spaced thumb screws. This sliding plate was provided with a vent valve and a packing gland, through which the 0.22-in. rod was inserted. This rod could be raised and lowered to introduce the sphere and part of the 0.0625-in. wire into the pressure-tap zone. The position of the sphere was at equal distances from either pressure tap. The wire and sphere could also be removed from the pressure-tap zone. The sliding plate could be moved horizontally so as to place the sphere in any desired position of eccentricity.

To measure the drag on a sphere the upper end of the column was modified as follows. The sliding plate was replaced with a plate of the same thickness, through which a 1.25-in. hole was drilled. An analytical balance was mounted on a platform above the column. The distance between the tray of the balance and the upper end of the column was 18 in. A hook was attached to this tray and held a 0.01-in. wire, which was connected to the sphere and also extended to the glass section of the column so that the sphere might be observed at a point equidistant from both ends of the glass section of the column.

EXPERIMENTAL PROCEDURE

Since the data on drag are more accurate than those on pressure drop, only the former are treated in this paper. The procedure for obtaining the drag measurements follows.

A run was begun by taring the sphere and the wire on the balance with no fluid flowing through the column. The fluid was then circulated at a desired flow rate until no change in rotameter setting and fluid temperature could be observed. The sphere and wire were then reweighed with the fluid flowing through the column. The difference between this reading and the original reading was the drag due on the sphere and the wire. To measure the drag on the wire alone, the experiment was repeated under the same conditions at an additional wire length. The difference of the two readings at the two different wire lengths was due to the drag on the wire alone. This quantity was subtracted from the original reading, and thus the drag on the sphere alone was obtained.

CORRELATION AND DISCUSSION OF THE DATA*

The drag on the sphere was measured at Reynolds numbers ranging from 0.1 to 20 on the basis of the average linear velocity and sphere diameter. Spheres of diameter sizes of 1.250, 0.998, 0.750, and 0.5 in. were used. The sphere- to cylinder-diameter ratio for each of these spheres was 0.3125, 0.2495, 0.1875, and 0.1250. In addition to placing the sphere at the cylinder axis, two off-cylinder axis positions of 0.5 and 1.0 in. were studied. (Owing to the great quantity of data, only the experiments involving the 1.250-in. sphere are presented here.)

The experimental data were correlated in such a fashion as to separate the wall effect from the inertial effects. The data were fitted by the following semiempirical equation:

$$\frac{W}{6\pi\mu u_o a(1-\beta^2)} = \left[\frac{1-\frac{2}{3(1-\beta^2)}\left(\frac{a}{R}\right)^2}{1-K\,\frac{a}{R}+2.087\left(\frac{a}{R}\right)^3}+\left(\frac{C_A}{C_S}-1\right)\right] \quad (5)$$

where K is equal to 2.105 according to the theoretical developments noted previously. The term $[(C_A/C_S)-1]$ appearing in Equation (5) is due to inertial effects and is dependent on the Reynolds number only. This term is obtained by simply considering the actual drag on a sphere at an infinite distance from the cylinder wall and comparing it with the drag according to Stokes's law, which also applies to an unbounded system. C_A is the actual drag coefficient for a sphere in an unbounded system taken from experimental data (*10a*) and C_S the drag coefficient according to Stokes's law. C_A and C_S are evaluated at the Reynolds number corresponding to the approach velocity to the sphere. The term $[(C_A/C_S)-1]$ therefore represents the fractional deviation of the actual drag from the drag according to Stokes's law.

Multiplying the fluid velocity at the

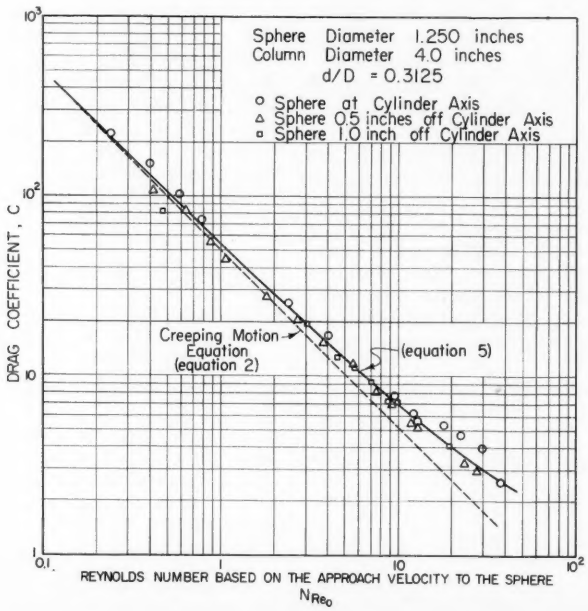

Fig. 1. Drag on a single stationary sphere at three different eccentricities.

* Part of the results are summarized in Figure 1. Complete detailed data appear in reference 3.

cylinder axis by $(1-\beta^2)$, as it appears in the denominator in the left-hand side of Equation (5), one obtains the approach velocity to the sphere.

The first term in the right-hand side of Equation (5) represents the effect of the cylindical boundary and is the same as derived from the creeping-motion equations. As calculated from this equation, the coefficient of (a/R) designated here as K is equal to 2.105. A test of the hypothesis that the wall effect and inertial effects are additive as represented by Equation (5), where the wall effect is independent of the Reynolds number, would be to determine whether or not K is constant over the whole range of Reynolds numbers investigated.

The constant K was determined from Equation (5) for each of the 118 runs performed; the average value was 1.959. A statistical analysis showed the standard deviation to be 0.383 from the average value.

The values of K were very consistent for the runs involving the spheres of 1.250- and 0.998-in. diameter. Thirty-five runs were performed with the 1.250-in. sphere in the Reynolds number range of 0.2 to 37.0, based on the approach velocity to the sphere and the diameter of the sphere. For these runs the average value of K was 2.017 and the standard deviation equal to 0.180 from the average value.

The average value of K obtained from all the experimental data, equal to 1.959, differs by 6.8% from the value of 2.105 derived from the creeping-motion equation. Owing to the high standard deviation, there is no way of telling whether the difference between these two values is significant. The value of 2.105 for K, the coefficient of a/R, was adopted in the semiempirical Equation (5).

Equation (5) reduces to Equation (2) for the drag on a sphere located at the cylinder axis at Reynolds numbers smaller than 0.3. For this case $\beta = 0$ and $[(C_A/C_S)-1] = 0$. On the other hand, when the sphere is at an infinite distance from the wall and at Reynolds numbers smaller than 0.3, $\beta = 0$, $a/R = 0$, and $[(C_A/C_S)-1] = 0$; hence Equation (5) reduces to Stokes's law. If however for the latter case the Reynolds number is higher than 0.3, Equation (5) reduces to

$$\frac{W_A}{6\pi\mu u_o a} = \frac{C_A}{C_S} \qquad (6)$$

In Figure 1 the drag coefficient calculated from the experimental data for the sphere with diameter of 1.250 in., which the authors consider the most accurate, is plotted as a function of the Reynolds number for all three sphere positions. The drag coefficient and the Reynolds number are based on the approach velocity to the sphere. The experimental data are compared with the creeping-motion equation [Equation (2)] and with the semiempirical Equation (5). At increasing Reynolds numbers, where inertial effects become appreciable, the experimental results, as had been expected, are higher than the results predicted from the creeping-motion equations. The semiempirical Equation (5) checks the experimental data reasonably well. In other words, the deviation of the experimental data from the creeping-motion equations at higher Reynolds numbers can be accounted for by simply adding to these equations the term $[(C_A/C_S - 1)]$, which accounts for the inertial effects.

The method developed here may be adapted for comparison with the data for a sedimenting sphere along the axis of a cylinder of McNown *et al.* (8). In other words, one may assume that the wall effect, as derived by the creeping-motion equations, and inertial effects are additive. Equation (5) can be slightly modified for this purpose to

$$\frac{W}{6\pi\mu u\, a} = \left[\frac{1}{1-2.105\,\frac{a}{R}+2.087\left(\frac{a}{R}\right)^3} + \left(\frac{C_A}{C_S}-1\right)\right] \qquad (7)$$

where the term $1/[1-2.105\,(a/R) + 2.087\,(a/R)^3]$ is the effect of the cylindrical boundary for a sphere sedimenting in a fluid.

In Figure 2 the drag coefficient obtained from Equation (7) is compared with the experimental results for sedimenting spheres of McNown *et al.* (8), who plotted the drag coefficient as a function of the Reynolds number at different d/D ratios. Their experimental points appearing in Figure 2 were obtained from this plot. Equation (7) is in fair agreement with McNown's data, which justifies the hypothesis that the wall effect and the inertial effects are additive whether or not the sphere is stationary in a moving fluid or sedimenting in a fluid. The drag coefficient obtained from Faxen's theory [Equation (3)] is also plotted in Figure 2. Up to Reynolds numbers of approximately 0.4 his theory is in agreement with experimental data. At higher Reynolds numbers, however, it deviates very sharply from the experimental data.

CONCLUSIONS

The study shows that over a range of Reynolds numbers of 0.1 to 40.0 based on the approach velocity to the sphere and the diameter of the sphere, the drag on a sphere surrounded by a cylindrical boundary, whether or not the sphere is stationary in a moving fluid or sedimenting in a fluid, can be expressed by a semiempirical equation composed of two additive terms. One term is due to the effect of the cylindrical boundary and the other due to inertial effects. Furthermore it can be

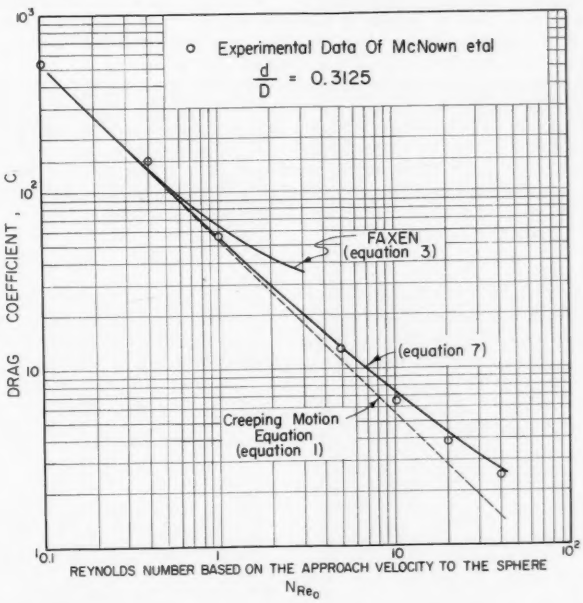

Fig 2. Drag on a single sedimenting sphere placed axially in a cylinder.

concluded that when the data are expressed as in Equation (5) or (7), the wall effect is a function of the (a/R) ratio only. Up to sphere- to-cylinder-diameter ratios of 0.3125 and eccentricities of 50% of the cylinder radius the effect of the cylindrical boundary is not affected by an increase of the Reynolds number and by various positions of eccentricity. It is the same as derived by the creeping-motion equations.

The present work does not agree with the theory of Faxen, who uses the Oseen approximation (9), where the value of $L|\delta L|$ in Equation (3) decreases with an increase of the Reynolds number.

ACKNOWLEDGMENT

The authors wish to thank the Texas Company for supporting this research through a fellowship.

NOTATION

a = radius of sphere
b = cylinder axis to center of sphere distance
C = actual drag coefficient of a sphere in a bounded medium $= W/[\rho u_o^2/2)\pi a^2]$
C_A = actual drag coefficient of a sphere in an unbounded medium
C_S = drag coefficient according to Stokes's law equal to $24/N_{Re_o}$
$[(C_A/C_S)-1]$ = dimensionless group in Equations (5) and (7), indicating fractional deviation of actual drag from drag calculated by Stokes's law
d = diameter of sphere
D = diameter of cylinder
$F(\beta)$ = function in Equations (4), (4a), and (4b) defined by $(2.105 - 0.6977\ \beta^2)$
K = constant in Equation (5)
N_{Re_o} = Reynolds number based on approach velocity to the sphere $= [(d\,u_o\,\rho/\mu)](1-\beta^2)$
R = radius of cylinder
u_o = fluid velocity at cylinder axis
u = velocity of sphere
W = drag force on the sphere in a bounded medium
W_A = drag force on a sphere in an unbounded medium
β = dimensionless number equal to b/R
μ = viscosity of fluid
ρ = density of fluid

LITERATURE CITED

1. Brenner, H., and John Happel, *J. Fluid Mechanics*, **4**, 195 (1958), and unpublished papers.
2. Craig, F. F., *Univ. Pittsburgh Bull.*, **48**, No. 10 (June 5, 1952).
3. Fayon, A. M., Sc.D. thesis, New York Univ., New York (June 1959).
4. Faxen, H., *Arkiv. Mat., Astron. Fysik*, **17** (1923).
5. Haberman, W. L., Ph.D. thesis, Univ. Maryland, College Park (1956).
6. Happel, John, and B. J. Byrne, *Ind. Eng. Chem.*, **46**, 1181 (1954).
7. Ladenburg, R., *Ann. Phys.*, **23**, 447 (1907).
8. McNown, J. S., H. M. Lee, M. B. McPherson, and S. M. Engez, *Proc. Seventh Intern. Congr. Appl. Mech.*, London (1948).
9. Oseen, C. W., "Hydrodynamik," Akademisches Verlag, Leipzig, Germany (1927).
10. Perry, J. H., "Chemical Engineers' Handbook," 3 ed., McGraw-Hill, New York (1950).

10*a* *Ibid.*, Table 4, page 1018.

11. Wakiya, S., *J. Phys. Sci. Japan*, **8**, 254 (1953).

Manuscript received January 21, 1959; revision received July 16, 1959; paper accepted July 23, 1959. Paper presented at A.I.Ch.E. Atlantic City meeting.

Centrifugal Filtration Through Beds of Small Spheres

J. B. BINGEMAN and JESSE COATES

Louisiana State University, Baton Rouge, Louisiana

In 1856 Darcy observed that water flowed through a sand bed at a rate proportional to the area of the bed and to the difference between the upstream and dowstream hydraulic heads and inversely proportional to the bed thickness. Since that time many investigators have accumulated masses of data in support of numerous theoretical and empirical relationships for correlating and predicting pressure drop, flow rate, and fluid and bed properties. Naturally certain areas of research have received less attention than others.

Among the areas receiving least attention are flow through beds composed of particles of identical shape but mixed size, flow through unconsolidated beds composed of small particles, and flow under the influence of a centrifugal driving force. Accordingly, the flow of liquids through unconsolidated beds of small spherical particles of mixed size was investigated in two laboratory centrifugal filters. Experimental conditions were such that the flow was laminar and the cakes were incompressible. While there was some difficulty in obtaining reproducibility of cakes, the data for any particular cake were correlated satisfactorily by the Darcy equation adapted for centrifugal filtration.

THEORY

A mathematical expression for laminar flow of an incompressible fluid in a centrifugal filter may be derived from the classical Darcy equation, which is written

$$\frac{\Delta P}{L} = \frac{u\mu}{\alpha g_c} \tag{1}$$

Ruth (6) used an equivalent expression:

$$\frac{\Delta P}{L} = \frac{u\mu\alpha^1\rho_c}{g_c} \tag{2}$$

It is evident from Equations (1) and (2) that

$$\alpha^1\rho_c = \frac{1}{\alpha} \tag{3}$$

The Darcy equation may be adapted to centrifugal filtration as follows:

For a centrifugal filter

$$\Delta P = \frac{a\rho_f H}{g_c} \tag{4}$$

where

$$a = \omega^2 r_{avg} = (2\pi N)^2 r_{avg} \tag{5}$$

and

$$H = \frac{\text{volume}}{\text{area}} = \frac{r_o^2 - r_f^2}{2r_{avg}} \tag{6}$$

Substitution of Equations (5) and (6) into Equation (4) yields

$$\Delta P = \frac{(2\pi N)^2 \rho_f\,(r_o^2 - r_f^2)}{2g_c} \tag{7}$$

Substituting Equation (7) into Equation (1) and noting that $u = \dfrac{Q_s}{A_c}$ leads to

$$\frac{Q_s}{A_c} = \frac{(2\pi N)^2\,\alpha\,\rho_f\,(r_o^2 - r_f^2)}{2\mu L} \tag{8}$$

Taking A_c as

$$A_c = 2\pi r_{lm} h \tag{9}$$

and substituting in Equation (8) leads finally to the expression

$$Q_s = \frac{4\pi^3 N^2 \rho_f\, h\,\alpha\,(r_o^2 - r_f^2)}{\mu \ln \dfrac{r_o}{r_c}} \tag{10}$$

Equation (10) is the theoretical expression for the rate of flow of filtrate Q_s, of density ρ_f, and of viscosity through a bed of solids of permeability α in a centrifugal filter in which the liquid level is at r_f and the cake level is at r_c. The permeability has a constant value for an incompressible cake but changes with pressure when the cake is compressible.

The resistance of the filter medium to flow of the filtrate is not included in Equation (10). It may be taken into

J. B. Bingeman is with Ethyl Corporation, Baton Rouge, Louisiana.

Fig. 1. Large basket.

account as

$$Q_T = \frac{4\pi^3 N^2 \rho_l \dot{h} (r_o^2 - r_f^2)}{\mu \left(\frac{\ln \frac{r_o}{r_c}}{\alpha} + \frac{R_m}{r_o} \right)} \quad (11)$$

Adaptations of the Darcy equation for centrifugal filtration have been proposed by Maloney (5), Smith (7), Burak and Storrow (1), Inglesent and Storrow (4), and Grace (2). The Burak-Storrow and Grace equations have been supported by experimental data and are equivalent to Equations (10) and (11) respectively. From Burak and Storrow

$$Q_s = \frac{4\pi^3 N^2 K_c h (r_o^2 - r_f^2)}{\mu g \ln \frac{r_o}{r_c}} \quad (12)$$

According to Grace

$$Q_T = \frac{4\pi^3 N^2 \rho_l h (r_o^2 - r_f^2)}{\mu \left[\rho_s \alpha' (1-\epsilon) \ln \frac{r_o}{r_c} + \frac{R_m}{r_o} \right]} \quad (13)$$

Equations (10) and (12) are seen to be equivalent, as are Equations (11) and (13), from the following relationships:

$$\alpha = \frac{K_c}{\rho_l g} = \frac{1}{\rho_s \alpha' (1-\epsilon)} \quad (14)$$

For later use it is noted here that for additive resistances

$$\frac{(\Delta P)_T}{Q_T} = \frac{(\Delta P)_m}{Q_m} + \frac{(\Delta P)_s}{Q_s} \quad (15)$$

and that

$$\frac{1}{Q_T} = \frac{1}{Q_m} + \frac{1}{Q_s} \quad (16)$$

when $(\Delta P)_T = (\Delta P)_m = (\Delta P)_s$ from separate runs.

Three types of experiments are run to check the theoretical equations: (1) centrifugal drain rates where filtrate is run through a previously deposited cake, (2) centrifugal filtration rates where a slurry is fed into the machine and a constant liquid head is maintained, and (3) modified centrifugal filtration wherein cake is deposited in successive increments and drain-rate data are taken on the beds so formed. Haruni and Storrow (3) performed several centrifugal drain-rate runs on starch, chalk, and kieselguhr cakes and

Table 1. Dimensions and Operating Ranges of Experimental Centrifugal Filters

	Small basket	Large basket
Diameter, D, in.	5	11
Radius to inside of cloth r_o, in.	2.303	5.187
Liquid levels r_f, in.		
Level 1	1.937	3.938
Level 2	2.047	4.469
Radius to cake surface r_c, in.	As required	As required
Depth of basket h, in.	1.125	2.125
Range of revolutions per minute	300-1,000	300-1,000
	1,200-4,000	1,200-4,000
Maximum gees	1,140	2,500
Maximum total hydraulic driving force for filtration (water) ΔP, lb.-force/sq. in.	13	93

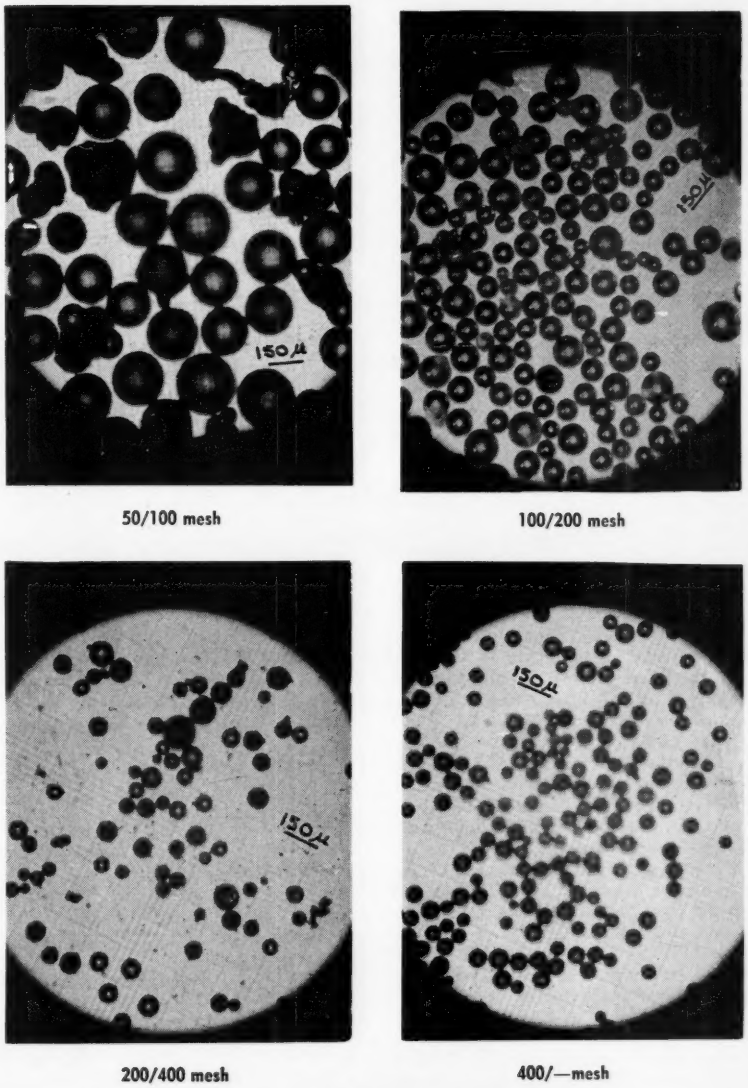

50/100 mesh

100/200 mesh

200/400 mesh

400/—mesh

Fig. 2. Photomicrographs of styrene-divinyl benzene spheres.

TABLE 2. RANGES OF VARIABLES

Revolutions per minute	Liquid depth, in.	Cake thickness, in.	Revolutions per minute squared $\times 10^{-6}$	$r_o^2 - r_f^2$, sq. in.	$(\Delta P)_T$, lb./sq. in.	Re	Particle size, mesh	Viscosity, cp.
5-in.-diameter Basket								
1,330-3,810	0.256, 0.366	0.069-0.233	1.8-14.5	1.11, 1.55	1.0-11.5	0.01-1.7	50/100, 100/200 200/400, 400/–	0.81-0.91
11-in.-diameter Basket								
1,310-2,550	0.718, 1.249	0.380-0.633	1.7-6.5	6.93, 11.4	6.1-38	0.02-0.7	50/100 200/400, 400/–	0.85, 2.2

found agreement with the revolutions per minute, liquid depth ($r_o^2 - r_f^2$), and viscosity factors of Equation (12). Earlier attempts by Burak and Storrow (*1*) and Inglesent and Storrow (*4*) had been unsuccessful. General agreement was obtained by Grace (*2*) with the revolutions per minute and cake depth $[\ln(r_o/r_c)]$ factors in drain rate and modified filtration runs on cakes of titanium dioxide, carbon, cellulose fibers, or diatomaceous earth. However values of 0.5 to 1.7 were found for the exponent of N, some of the cakes apparently being compressible. The expected value of 2 was not found, however, even with incompressible cakes. Concurrently with the work undertaken at Louisiana State University and reported in this paper, Valleroy (*8*) at the University of Kansas obtained additional support for the revolutions per minute and liquid-depth factors with drain-rate data taken on Lucite spheres.

This paper reports the data taken in twenty-five centrifugal drain-rate runs on four sizes of styrene-divinylbenzene spheres. Equation (10) is applied to the data by statistical analysis.

EQUIPMENT, METHOD OF OPERATION, MATERIALS

Equipment

Two perforated baskets for centrifugal filtration were mounted horizontally on individual drive shafts. Figure 1 shows the larger basket. By means of a variable-speed drive and two sets of pulleys, it was possible to drive either basket over the approximate ranges from 300 to 1,000 and 1,200 to 4,000 rev./min. Thus in the 5-in. –and 11-in.–diameter baskets it was possible to develop maximum centrifugal forces of approximately 1,140 and 2,500 Gees, respectively. Revolutions per minute were measured with a stroboscope.

Water or other filtrate was run into the small basket through a spray nozzle and into the large basket through a wing tip. A glycerol-water solution was supplied by means of a centrifugal pump and storage tank. Flow rates were regulated by a hand-operated needle valve.

Dimensions and operating ranges are given in Table 1 for both baskets.

From the dimensions given in Table 1 and Equation (7) the maximum driving force for the filtration of water through porous cakes is calculated to be approximately 13 lb./sq.in for the small bowl and 93 lb./sq.in. for the large one. Approximately 1,140 and 2,500 Gees, respectively, can be developed. Thus, on this laboratory installation it is possible to cover the range of Gees and pressure drop existing in normal commercial operation. For example, a 40-in.–diameter commercial machine operating at 800 rev./min. and a liquid depth of 6 in. would develop 364 Gees at the basket wall and a total hydraulic driving force of 67 lb./sq.in. when the filtrate has the density of water.

Cloth, supported by coarse wire mesh, served as the septum. Putty and caulking were forced into seals at both the back and the front of the basket to prevent leaks of filtrate around the ends of the cake. It was possible to make several runs with one cloth.

Method of Operation

Cake was deposited by spooning dry solids into a pool of liquid in the rotating basket. The mass of cake used for the small bowl was 10, 20, or 25 g., whereas 300 to 450 g. were used in the large machine. In the case of the small bowl the cake was deposited in approximately 1-g. increments, whereas the increments were 5 to 10 g. for the large bowl. This procedure forms a smooth and uniform cake and simulates the actual formation of a cake when slurry is fed and there is a liquid level above the cake. Any effect of classification is minimized by addition of the solids in many increments. A liquid level was maintained above the cake at all times during a run.

The flow rate of filtrate was measured over a range of revolutions per minute and at each of two liquid levels for each cake deposited as above. Immediately before each cake run the flow rate of filtrate through the septum only was measured over the same range of revolutions per

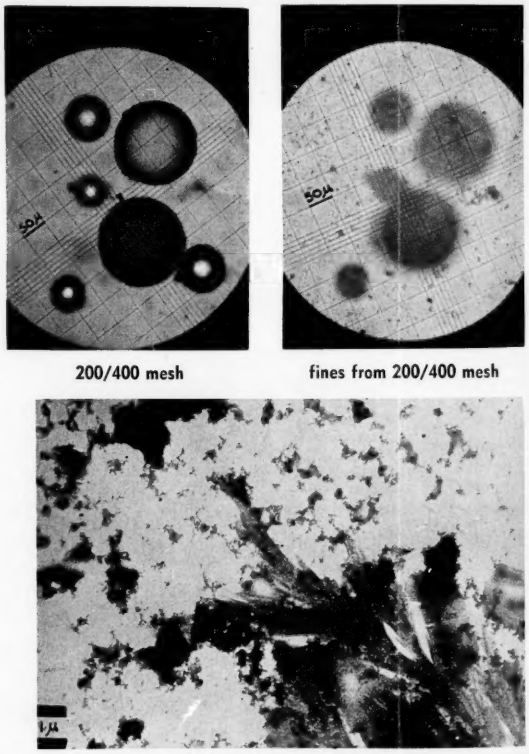

200/400 mesh | fines from 200/400 mesh

electronmicrograph, fines from 200/400 mesh

Fig. 3. Photomicrographs of styrene-divinyl benzene spheres.

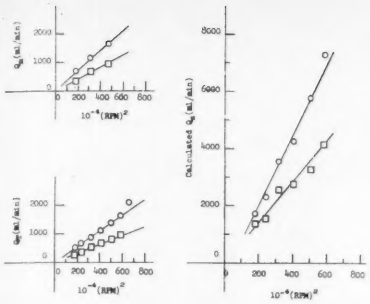

Fig. 4. Typical data (run 22), large basket, water. 400/—mesh styrene-divinyl benzene spheres.

r_t in.	Symbol
3.938	○
4.469	□

minute and at the same two liquid levels.

Materials

Styrene-divinylbenzene spheres comprised the cakes. Four mesh ranges were used as received from the manufacturer: 50/100, 100/200, 200/400, and 400/— mesh. Photomicrographs of these materials and the fines contained in them are shown in Figures 2 and 3.

DATA

The ranges of variables over which the data* were taken on the styrene-divinylbenzene spheres are shown in Table 2.

Data for a typical run (run 22) are plotted in Figure 4. As predicted by Equations (10) through (13), for an incompressible bed (constant permeability) the flow rate is proportional to revolutions per minute squared. By Equation (16) the flow rate which would exist through the solids if there were no resistance in the septum may be calculated. Plots for Q_s so calculated for run 22 are also given in Figure 4.

Q_s was calculated for individual data points for all runs. These calculated values of Q_s as well as the primary data Q_m and Q_T were used to check the theoretical correlation. To check N and the liquid-depth factor $(r_o^2-r_f^2)$, the data for each cake were fitted to the model

$$Q = A\,N^b(r_o^2-r_f^2)^c \qquad (17)$$

by the method of least squares. Table 3 summarizes the results.

Runs 11, 12, 23, and 24 were not applicable to testing Equation (17) because they contained only two data points, whereas a three-constant equation was being evaluated. The exponents calculated from Q_T and Q_s for runs 8, 13, and 16 lay outside the 1% confidence limits and therefore were excluded from the mean values. As might be expected, the precision in the values of the exponents is best where the only resistance to flow is made up by the filter medium. Greater variability of data is seen when filter medium and cake comprise the resistance to flow, and as a result of being calculated from Q_m and Q_T the values of the exponents predicted from Q_s show the greatest variability of all.

From the mean values of the exponents listed in Table 3 and their standard deviations it is concluded that the data for any particular cake may be correlated satisfactorily by the expression

$$Q_s = AN^2(r_o^2-r_f^2) \qquad (18)$$

as predicted by the theoretical Equation (10).

To check the cake-thickness factor $[\ln (r_o/r_c)]$ from run to run, it is necessary to have cakes of constant characteristics, that is the same permeability. Consequently the permeability was calculated by Equation (10) for all readings on all cakes. The averages for each cake run are listed in Table 4 except for runs 8, 13, and 16, which were eliminated above from further consideration.

If the cakes were formed reproducibly and if Equation (10) describes the flow through them, then the same permeability should be calculated for all runs in a given mesh size. However wide variation is observed in the calculated permeabilities, with the possible exception of those for 100/200 mesh particles. This general lack of reproducibility may have been caused by differing structure in the cakes (perhaps owing to the fines), by experimental difficulties such as in measuring r_c sufficiently accurately, or possibly by the inadequacy of Equation (10).

The runs on 100/200 mesh particles show the smallest variation in the calculated permeabilities, and an attempt was made to check the effect of the cake-thickness factor here. However the correlation coefficient of A [Equation (17)] plotted vs. the reciprocal of $\ln (r_o/r_c)$ is only 0.475, which constitutes relatively weak statistical support for the theoretical equation. Therefore it is concluded that other more suitable data must be taken to confirm the cake-thickness factor.

The viscosity was varied significantly for run 25, in which a glycerol-water solution served as the filtrate. But the great variation in the apparent permeabilities makes it impossible to compare run 25 with the other runs on 400/— mesh material and therefore impossible to check the effect of viscosity.

Table 3. Exponents for N and $(r_o^2-r_f^2)$

Calculated from	Number of runs	Exponent	Mean	Standard deviation, Single value	Standard deviation, Mean
Q_m	21	b	2.04	0.15	0.03
		c	1.13	0.31	0.07
Q_T	18	b	2.03	0.33	0.08
		c	1.22	0.35	0.08
Q_s	18	b	1.98	0.64	0.15
		c	1.23	0.60	0.14

Table 4. Permeabilities of Cakes of Styrene-DVB Spheres

Run	Radius to cake, in. surface	Viscosity, cp	Permeability, $\alpha\times10^{10}$, ft.[a] Mean	s of Mean
50/100 Mesh				
1	2.191	0.85	9.0	0.7
2	2.184	0.85	6.8	0.6
3	2.070	0.85	37.2	2.3
4	2.156	0.828	11.5	1.1
5	2.223	0.819	9.6	1.2
6*	4.554	0.85	20.3	0.9
100/200 Mesh				
7	2.188	0.85	5.5	0.7
8	2.188	0.838	eliminated	
9	2.164	0.819	8.9	1.0
10	2.164	0.838	6.1	0.4
11	2.196	0.814	5.8	1.2
12	2.185	0.814	6.4	1.0
23	2.195	0.907	5.1	0.5
24	2.196	0.907	3.8	0.3
200/400 Mesh				
13	2.195	0.85	eliminated	
14	2.188	0.85	12.2	1.5
15	2.230	0.85	6.0	0.6
16*	4.651	0.85	eliminated	
400/— Mesh				
17	2.195	0.828	4.6	0.4
18	2.188	0.838	11.0	0.8
19	2.230	0.866	6.4	0.4
20	2.183	0.828	13.0	1.0
21	2.234	0.828	4.5	0.3
22*	4.807	0.866	10.1	0.3
25†	2.177	2.19	27.4	2.2

* Large basket used for these runs, small basket for all others.
† Glycerol-water solution used for filtrate, all others water.

* Data and calculated results are on file at University Microfilms, 313 North First Street, Ann Arbor, Michigan, as Publication No. 21,982, Mic. 57-3157.

Appendix B
Least Squares Fit of Data to Model $Q = A N^b (r_o^2 - r_f^2)^c$

Run	Q_m $-\log A$	b	c	[Correlation coefficient]^2	Q_T $-\log A$	b	c	[Correlation coefficient]^2	Q_s $-\log A$	b	c	[Correlation coefficient]^2
50/100 Mesh												
1	4.419	2.008	1.352	0.99	4.710	2.046	1.028	0.98	4.460	2.120	0.463	0.86
2	5.416	2.310	1.227	0.99	4.889	2.063	1.606	0.99	3.519	1.743	2.090	0.98
3	3.196	1.912	0.577	0.99	5.854	2.580	0.830	0.98	6.692	2.891	0.958	0.97
4	3.468	1.765	1.294	0.99	2.873	1.504	1.498	0.96	1.593	1.222	1.716	0.86
5	4.464	1.937	1.611	0.99	5.045	2.085	1.454	0.99	6.248	2.679	0.696	0.86
6	3.630	1.894	0.850	0.99	3.415	1.756	0.876	0.99	2.327	1.538	0.912	0.99
100/200 Mesh												
7	5.265	2.250	1.258	0.99	4.656	1.985	1.885	0.86	3.568	1.710	2.425	0.66
8	4.435	2.029	1.126	0.96	4.983	2.045	2.147	0.97	4.780	2.031	2.941	0.94
9	4.218	1.868	1.587	0.99	3.279	1.551	1.370	0.99	0.235	0.826	0.859	0.82
10	4.609	2.112	1.640	0.99	5.603	2.276	1.136	0.99	5.763	2.381	1.790	0.96
11	Not enough data				Not enough data				Not enough data			
12	Not enough data				Not enough data				Not enough data			
23	Not enough data				Not enough data				Not enough data			
24	Not enough data				Not enough data				Not enough data			
200/400 Mesh												
13	4.965	2.141	1.296	0.98	9.907	3.349	2.307	0.99	10.909	3.662	2.570	0.99
14	4.033	2.032	0.728	0.99	6.652	2.703	0.888	0.99	8.371	3.290	1.004	0.99
15	4.564	2.097	0.870	0.99	5.364	2.256	0.992	0.97	5.607	2.431	1.136	0.87
16	4.251	1.985	0.842	0.99	9.751	3.358	1.553	0.99	14.455	4.683	2.249	0.99
400/— Mesh												
17	4.246	1.918	1.030	0.98	4.292	1.845	1.413	0.95	3.666	1.751	1.904	0.88
18	4.528	2.038	1.256	0.99	5.026	2.140	1.139	0.98	5.148	2.333	0.833	0.85
19	5.587	2.298	1.283	0.99	5.274	2.165	1.330	0.99	3.284	1.742	1.497	0.95
20	4.990	2.192	1.180	0.98	4.574	2.024	1.018	0.99	3.117	1.754	0.642	0.88
21	5.103	2.177	0.926	0.99	5.128	2.124	1.232	0.99	4.435	2.046	1.871	0.87
22	4.584	1.996	1.096	0.99	4.773	2.033	1.044	0.99	4.303	2.128	0.884	0.95
25	4.001	1.955	0.635	0.99	2.815	1.511	0.559	0.98	0.686	0.966	0.450	0.81

CONCLUSIONS

Centrifugal filtration data taken on four mesh sizes of styrene-divinylbenzene spheres support the theoretical form of the revolutions per minute and liquid-depth factors in the adapted Darcy equation. Indices of 2 and 1, respectively, are indicated. The data do not allow an adequate check of the cake-thickness and viscosity factors because of a general irreproducibility of cakes.

ACKNOWLEDGMENT

The authors are grateful to the Dow Chemical Company, Midland, Michigan, for the styrene-divinylbenzene resin and to B. A. Sobel, H. F. Kraemer, and C. J. Arceneaux of Ethyl Corporation, Baton Rouge, Louisiana, for their assistance in the statistical analysis, machine computations, and photomicrographs.

NOTATION

A = constant for incompressible cake
A_c = area of cake perpendicular to flow
a = acceleration in centrifugal field
b = constant
c = constant
g_c = conversion factor (32.2 lb.-mass/lb.-force-ft./sec.^{2})
h = depth of centrifugal basket parallel to the axis
H = depth of liquid in centrifugal filter
K_c = cake permeability (lb.-mass/sec.^{2})
L = depth of bed in direction of flow
L_m = thickness of filter medium
N = rate of rotation of centrifugal basket
P = pressure
$(\Delta P)_T$ = total pressure drop across cake and medium
$(\Delta P)_c$ = pressure drop across cake
$(\Delta P)_m$ = pressure drop across medium
Q_m = filtrate flow rate through medium only
Q_s = filtrate flow rate through solids only
Q_T = filtrate flow rate through medium and cake
Re = Reynolds number
R_m = filter medium resistance (ft.$^{-1}$ = L_m/α_m)
r = radius
r_{avg} = radius to average depth of liquid
r_c = radius to surface of cake
r_f = radius to surface of fluid
r_{lm} = log-mean radius
r_o = radius to inside of filter medium
u = superficial velocity of filtrate

Greek Letters

α = cake permeability, (ft.^{2}) property of the cake
α_m = permeability of filter medium
α^1 = specific resistance of cake (ft./lb.-mass)
Δ = finite change of variable
ϵ = cake porosity
μ = absolute viscosity
ρ_c = bulk density of cake
ρ_f = density of fluid
ρ_s = true density of solids comprising cake
ω = angular acceleration

LITERATURE CITED

1. Burak, N., and J. A. Storrow, *J. Soc. Chem. Ind.*, **69**, 8 (1950).
2. Grace, H. P., *Chem. Eng. Progr.*, **49**, 427 (1953).
3. Haruni, M. M., and J. A. Storrow, *Ind. Eng. Chem.*, **44**, 2751 (1952).
4. Inglesent, H., and J. A. Storrow, *Ind. Chem.*, **27**, 76 (1951).
5. Maloney, J. M., *Ind. Eng. Chem.*, **38**, 24 (1946).
6. Ruth, B. F., *ibid.*, **27**, 708, 806 (1935).
7. Smith, J. C., *ibid.*, **39**, 474 (1947).
8. Valleroy, V. V., Ph.D. dissertation, Univ. Kansas, Lawrence (August, 1956).

Manuscript received November 3, 1958; revision received June 16, 1959; paper accepted June 19, 1959. Paper presented at A.I.Ch.E. Salt Lake City meeting.

Thermal Conductivity of Packed Beds

WILLIAM SCHOTTE

E. I. du Pont de Nemours and Company, Wilmington, Delaware

A correlation has been developed to predict the thermal conductivity of packed beds for various conditions of pressure, temperature, and particle size. The correlation takes into account the reduction in thermal conductivity of the gas phase at lower pressures when the mean free path of the gas molecules is of the same order as the distance between particles which are effective in transferring heat. Radiation becomes significant for large particles and high temperatures. A new relationship for the radiation contribution to the thermal conductivity of packed beds has been developed.

Packed beds containing refractory materials are often used as insulation to minimize heat losses from furnaces and reactors. A number of correlations have been reported in the literature to predict the thermal conductivity of packed beds. Although the conduction process through such a two-phase system with undefined internal boundaries is extremely complex, simple correlations have been quite successful. Generally the thermal conductivity of the bed is expressed as a function of the thermal conductivity of the gas, the thermal conductivity of the solid, and the void fraction of the bed. The influence of particle size, pressure, and temperature has not been accounted for except insofar as they affect the primary variables mentioned above.

It has been recognized, however, that packed beds may have much lower thermal conductivities than would normally be predicted. When the effective gas spaces have dimensions which are of the same order as the mean free path of the gas molecules, the thermal conductivity of the gas phase is reduced. Since most of the conduction takes place near points of contact between particles, this reduction starts to occur when the particle diameter is about one thousand times the length of the mean free path. Deissler and Eian (3) have measured so-called "break-away pressures," below which the thermal conductivity of the packed bed will decrease with a decrease in pressure. They have also developed a correlation to predict the break-away pressure for a particular system. The break-away pressure may be quite high; for example Deissler and Eian have shown that a value of 41 lb./sq. in. abs. is obtained for 0.2 mm. magnesium oxide particles and helium at 400°F. However methods for the prediction of the thermal conductivity at pressures below the break-away value were not found in the literature. A relationship which correlates available data has been developed and is presented in this paper.

At high temperatures radiation heat transfer between particles becomes important. Damköhler (2) analyzed the contribution due to radiation but did not suggest a definite equation for its effect. Later workers have interpreted Damköhler's analysis in various ways to arrive at definite relationships. For instance McAdams (8) suggests adding the following radiation contribution to the thermal conductivity of the packed bed:

$$k_r = 0.692\,\delta\,D_p\frac{T^3}{10^8} \qquad (1)$$

Other correlations are similar but include different factors to account for the emissivity of the particles. Only recently have some data become available in the literature to evaluate the contribution due to radiation. The work of Yagi and Kunii (14) has shown that Equation (1) cannot be used. They have developed a single relationship to account for all modes of heat transfer which contribute to the conductivity of packed beds, but this correlation does not give satisfactory results when the apparent thermal conductivity of the gas phase is used for the case of small particles. A new correlation for the radiation contribution is presented in this paper.

The case of fine dusts with void fractions above 0.6, such as carbon black, has not been considered here for reasons which will be discussed later.

APPARENT THERMAL CONDUCTIVITY OF THE GAS PHASE

It has been known for a long time that the thermal conductivity of a gas is reduced when low pressures are reached. This occurs when the distance over which the conduction takes place becomes of the same order as the mean free path of the gas molecules. Since molecules can cross from one surface to another before reaching thermal equilibrium, there is an abrupt change of temperature from the surface to the gas instead of the gradual transition which occurs at higher pressures. Many authors (for example, reference 6) have related the apparent thermal conductivity of the gas, to the normal thermal conductivity with the following expression:

$$k_g = \frac{k_g^\circ}{1 + 2\dfrac{j}{b}} \qquad (2)$$

Kinetic theory (6) gives also the following equation for j:

$$j = \left(\frac{2-\alpha}{\alpha}\right)\left(\frac{2}{1+\gamma}\right)\left(\frac{k_g^\circ L}{\mu c_v}\right) \qquad (3)$$

which can be rewritten to give

$$j = \left(\frac{2-\alpha}{\alpha}\right)\left(\frac{2\gamma}{1+\gamma}\right)\left(\frac{k_B T}{\pi\sqrt{2}P\sigma^2 N_{Pr}}\right)$$

$$= 2.54\times10^{-24}\left(\frac{2-\alpha}{\alpha}\right)\left(\frac{\gamma}{1+\gamma}\right)\left(\frac{T}{P\sigma^2 N_{Pr}}\right) \qquad (4)$$

An equation for the apparent thermal conductivity of the gas phase is obtained by the substitution of Equation (4) into Equation (2):

$$k_g = \frac{k_g^\circ}{1+5.08\times10^{-24}\left(\dfrac{2-\alpha}{\alpha}\right)\left(\dfrac{\gamma}{1+\gamma}\right)\left(\dfrac{T}{Pb\sigma^2 N_{Pr}}\right)} \qquad (5)$$

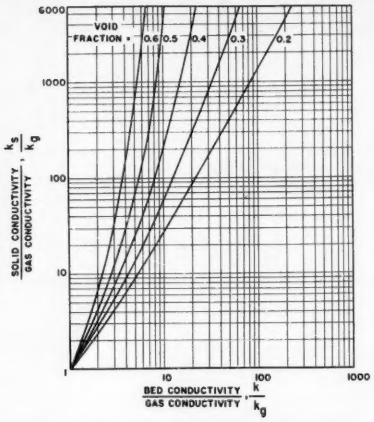

Fig. 1. Deissler-Eian correlation for the thermal conductivity of packed beds.

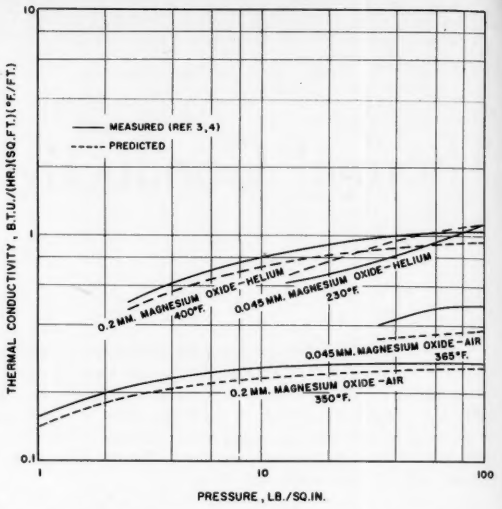

Fig. 2. Effect of pressure on the thermal conductivity of packed beds.

A useful solution of Equation (5) will require a knowledge of the accommodation coefficient and the effective distance over which the conduction takes place. Only few experimental values of the accommodation coefficient are available, and even for a given solid-gas system values differ widely depending on the condition of the surface. An exact relationship for the effective distance is also difficult to determine, since most of the conduction will take place near points of contact between the particles. However the success of Deissler and Eian in predicting break-away pressures indicates that an empirical constant may be used to include the accommodation coefficient and a proportionality factor for the evaluation of b. Actually b is equal to the heat transfer-average distance between particle surfaces. As a simplification however it will be assumed that b is proportional to the length-average distance between particle surfaces.

If one considers spherical particles in a unit cube, the number of particles within the cube will be $(1-\delta)/(\pi/6\,D_p^3)$. In a given direction these particles will present a total interfering area which is equal to the sum of their cross-sectional areas:

$$\left(\frac{\pi}{4}D_p^2\right)\left(\frac{1-\delta}{\frac{\pi}{6}D_p^3}\right) = 1.5\left(\frac{1-\delta}{D_p}\right)$$

The average interparticle distance is equal to the free volume divided by the total interfering area:

$$\frac{2}{3}\left(\frac{\delta}{1-\delta}\right)D_p$$

Then

$$b = C_1\left(\frac{\delta}{1-\delta}\right)D_p \qquad (6)$$

The final expression for the apparent thermal conductivity is obtained by the substitution of Equation (6) into (5) and by the inclusion of the term $[(2-\alpha)/\alpha]$ in C:

$$k_g = \frac{k_g^\circ}{1 + C\left(\frac{\gamma}{1+\gamma}\right)\left(\frac{1-\delta}{\delta}\right)\left(\frac{T}{PD_p\sigma^2N_{Pr}}\right)} \qquad (7)$$

A value of $C = 2.03 \times 10^{-23}$ has been determined by a comparison of the results from Equation (7) with experimental data of a number of investigators. This will be discussed below.

Table 1. Comparison of Data for Glass-Air System*

Reference	t, °C.	D_p, mm.	δ	k/k_g
(5)	10	0.32	0.35	6.62
(7)	60	4.06	0.40	12.0
(12)	80	6.77	0.40	5.35
	80	10.0	0.40	5.0
(9)	40	0.34	0.40	9.4

* All measurements made with glass spheres and at atmospheric pressure.

THERMAL CONDUCTIVITY OF A PACKED BED

A relationship is needed to predict the thermal conductivity of the packed bed. Various methods have been proposed in the literature. The most suitable one appears to be that of Deissler and Eian (3), who have presented the semiempirical relationship shown in Figure 1. The ratio of the thermal conductivity of the bed to that of the gas phase is plotted against the ratio of the thermal conductivity of the solid to that of the gas phase with the void fraction used as a parameter.

The accuracy of the correlation of Deissler and Eian, or those of other workers, is difficult to ascertain. It appears that many of the experimental data reported in the literature are somewhat inaccurate; for example, data for the system glass spheres–air at nearly the same temperature and with almost the same void fraction differ widely, as shown in Table 1. The data differ by as much as a factor of 2.4, and as a result some data which appeared to be greatly in error were not considered in this study.

Deissler and Eian's correlation (3) for the break-away pressure

$$P_b = 1.77 \times 10^{-21}\frac{T}{D_p\sigma^2}$$

can be used to determine whether pressure, temperature, or particle size will affect the gas-phase thermal conductivity. If the pressure is below the break-away pressure, the gas-phase thermal conductivity should be calculated by the use of Equation (8):

$$k_g = \frac{k_g^\circ}{1 + 2.03\times10^{-23}\left(\frac{\gamma}{1+\gamma}\right)\left(\frac{1-\delta}{\delta}\right)\left(\frac{T}{PD_p\sigma^2N_{Pr}}\right)} \qquad (8)$$

This value of k_g is used to calculate the ratio of k_s to k_g at the average bed temperature. Figure 1 then gives the ratio of k to k_g from which the bed conductivity can be determined. This procedure, but in the reverse order, was applied to calculate values of the apparent gas-phase conductivity from experimental data for the thermal conductivity of packed beds in order to arrive at values for C in Equation (7). Values of C varied by a factor of 2 possibly owing to variations in the accommodation coefficient but perhaps to an even greater extent to inaccuracies of the experimental data and to the approximations in the method of Deissler and Eian.

COMPARISON WITH EXPERIMENTAL DATA

Thermal conductivities of packed beds at different pressures have been measured by a number of investigators. For the same systems Equation (8) and Figure 1 were used to obtain predicted thermal conductivities. The results are compared in Figures 2 to 4. In addition, predicted results have been compared with data of Schumann and Voss (*11*) and have been deposited with the American Documentation Institute.*

Predicted and experimental curves compare quite well, particularly if one considers the curves on a relative rather than an absolute basis. Deviations are about as large at higher pressures, where the apparent gas-phase conductivity is nearly equal to the normal thermal conductivity of the gas, as at lower pressures. It is therefore believed that the differences are caused mainly by inaccuracies of the experimental data and by the simplified approximation of Deissler and Eian.

Theoretically there may be no lower limit for application of Equation (8). It has been reported in the literature that at very low pressures the thermal conductivity of the gas phase is proportional to the pressure. Equation (8) shows this also, since the first term, 1, in the denominator on the right-hand side of the equation becomes negligible compared with the second term at low pressures. In practice however there are limits to the use of Equation (8) and Figure 1 for the prediction of thermal conductivities of packed beds. It is therefore not advisable to extend Figure 1 beyond its limits, that is outside of $0.2 < \delta < 0.6$ or beyond $k_s/k_g = 6{,}000$. Although Deissler and Eian have included the whole range of void fractions from 0 to 1 in their correlation, the experimental values for which the correlation was tested fell in the range $0.2 < \delta < 0.6$. Fine dusts have large void fractions, up to values of 0.98, but known correlations do not apply. This is at least partly due to the formation of agglomerates. For very large values of k_s/k_g, solid conduction at contact points becomes significant. This has not been accounted for in Deissler and Eian's correlation. Wilhelm (*13*) has presented a correlation for this contact conductivity:

$$\log\ k_p = -1.76 + 0.0129\,\frac{k_s}{\delta}$$

Since this correlation does not account for the particle size, the thermal conductivity contribution due to contact conductivity is the same for larger and smaller particles; however more contact resistances must be added in series for smaller particles to obtain the conductivity over a unit distance. As a result calculations can show that predicted values may be an order of magnitude larger than experimental values for very small particles. Development of a new correlation for the contact conductivity will be difficult until more data become available.

EFFECT OF RADIATION

Radiation heat transfer between particles should be included at high temperatures, particularly when the particles are larger. For example radiation becomes important for 1 mm. particles at temperatures above 400°C. and for 0.1-mm. particles above 1,500°C. A simplified analysis can be made for spherical particles, but experimental data indicate that the final correlation will apply also to other shapes.

The derivation presented below will be limited to opaque particles which are large compared with the wave length of radiation. Transparency of the particles would increase the rate of heat transfer and therefore the thermal conductivity of the bed. When the particles are in the micron range, scattering of radiation should be considered and the absorption of radiation is more complicated.

The analysis given here is somewhat similar to that used by Argo and Smith (*1*), but a different interpretation has led to an improved correlation. When one considers the radiation from a plane located on one side of a particle to a plane located on the far side of the

* Tabular material has been deposited as document 6137 with the American Documentation Institute, Photoduplication Service, Library of Congress, Washington 25, D. C., and may be obtained for $1.25 for photoprints or 35-mm. microfilm.

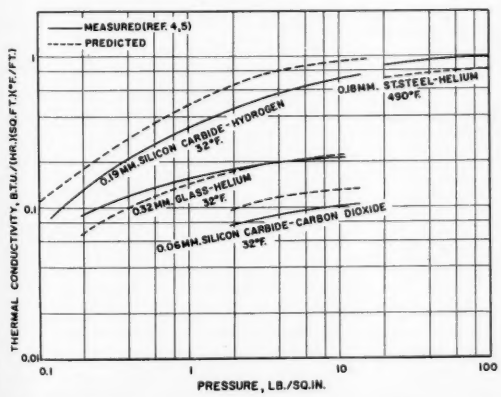

Fig. 3. Effect of pressure on the thermal conductivity of packed beds.

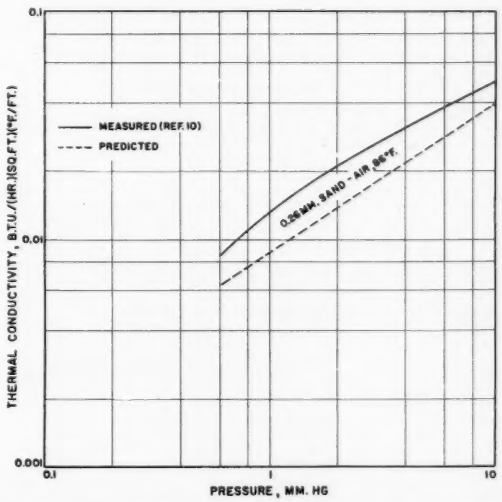

Fig. 4. Effect of pressure on the thermal conductivity of packed beds.

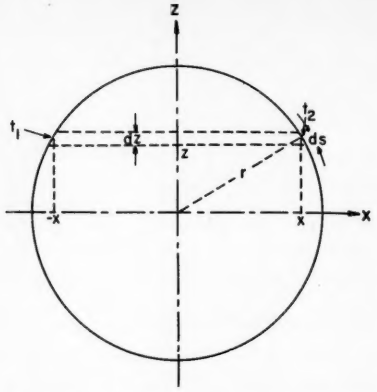

Fig. 5. Model for derivation of the radiation contribution to the thermal conductivity of a packed bed.

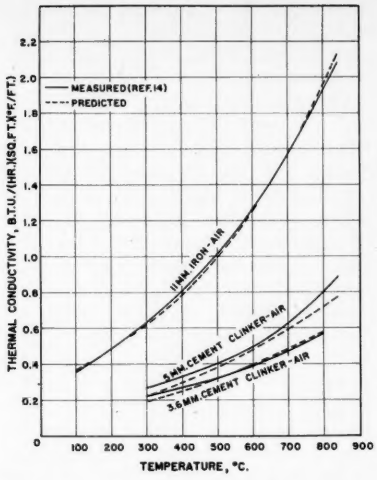

Fig. 6. Effect of radiation on the thermal conductivities of packed beds.

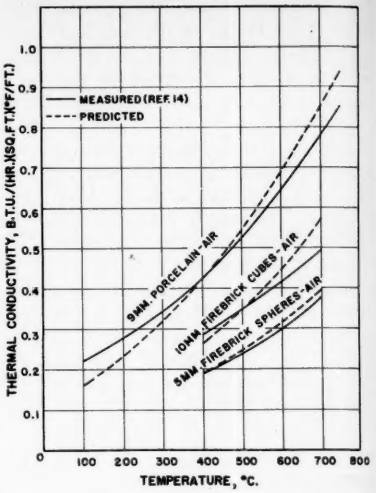

Fig. 7. Effect of radiation on the thermal conductivity of packed beds.

particle, there are two parts to be included. First, there is radiation across the void space past the particle. For a particle of cross-sectional area $\left(\frac{\pi}{4}D_p^2\right)$, the total area for heat transfer can be approximated by

$$\frac{\pi}{4}D_p^2\left(\frac{1}{1-\delta}\right) \qquad (9)$$

with a void area of

$$\frac{\pi}{4}D_p^2\frac{\delta}{1-\delta}$$

The radiation heat transfer across the void area will then be

$$q = -h_r\left(\frac{\pi}{4}D_p^2\frac{\delta}{1-\delta}\right)\left(D_p\frac{dt}{dx}\right) \qquad (10)$$

where $[D_p\,(dt/dx)]$ is the temperature difference between the planes previously mentioned.

Secondly, there is radiation from the particle in series with conduction through the particle. For an element of the particle, shown in Figure 5, the rate of heat transfer from left to right will be

$$dq = -k_s\,(2\pi z dz)\,\frac{t_2 - t_1}{2x} =$$

$$h_r\,(2\pi z ds)\,(t_2 - t_g) \qquad (11)$$

$$= h_r\,(2\pi z)\left(\frac{r dz}{x}\right)\,(t_2 - t_g)$$

Substitution of this expression for t_2 into Equation (11) gives

$$dq = k_s\left(\frac{\pi z dz}{x}\right)\left(t_1 - \frac{k_s t_1 + 2h_r r t_g}{k_s + 2h_r r}\right)$$

$$= k_s\left(\frac{\pi z dz}{x}\right)\frac{h_r D_p\,(t_1 - t_g)}{k_s + h_r D_p} \qquad (12)$$

where $2r$ has been replaced by D_p. For a simplified approximation it will be assumed that the temperature gradient, dt/dx, for the solid-gas system (packed bed) is constant for a distance of 1 particle diameter. Then

$$t_1 - t_g = -2x\left(\frac{dt}{dx}\right)$$

and Equation (12) becomes

$$dq = -k_s\,(2\pi z dz)\left(\frac{h_r D_p}{k_s + h_r D_p}\right)\left(\frac{dt}{dx}\right)$$

This expression can be integrated over the whole particle:

$$q = -k_s\,(\pi r^2)\left(\frac{h_r D_p}{k_s + h_r D_p}\right)\left(\frac{dt}{dx}\right)$$

or

$$q = -\frac{\pi}{4}D_p^2\left(\frac{k_s h_r D_p}{k_s + h_r D_p}\right)\left(\frac{dt}{dx}\right) \qquad (13)$$

Adding the two parts of radiation heat transfer, Equations (10) and (13), one gets

$$q = -\frac{\pi}{4}D_p^2\left(\frac{k_s h_r D_p}{k_s + h_r D_p}\right)\left(\frac{dt}{dx}\right) - h_r\left(\frac{\pi}{4}D_p^2\frac{\delta}{1-\delta}\right)D_p\frac{dt}{dx} \qquad (14)$$

or $k_s\,(t_1 - t_2) = 2\,h_r r\,(t_2 - t_g)$, which by elimination of t_2 gives

$$t_2 = \frac{k_s t_1 + 2\,h_r r t_g}{k_s + 2\,h_r r}$$

To determine the thermal-conductivity correction for radiation heat transfer the rate of heat transfer across the total area [see Equation (9)] can be written as

$$q = -k_r\left(\frac{\pi}{4}D_p^2\frac{1}{1-\delta}\right)\frac{dt}{dx} \qquad (15)$$

The radiation contribution is found by equating the right-hand sides of Equations (14) and (15).

$$k_r = \frac{1-\delta}{\dfrac{1}{k_s} + \dfrac{1}{k_r^\circ}} + \delta k_r^\circ \qquad (16)$$

where $k_r^\circ = h_r D_p$. The right-hand side of Equation (16) consists of two terms. The first term represents radiation heat transfer to the particle in series with conduction through the particle, while the second term accounts for radiation across the void space adjacent to the particle.

The radiation heat transfer coefficient between a particle and its neighbors can be approximated by

$$h_r = 0.692\epsilon\frac{T^3}{10^8}$$

This approximation can be made because the angle factor is unity and the emissivity factor is close to the emissivity of the particle, since the particle under consideration is surrounded by the irregular surfare of the packed bed. Then

$$k_r^\circ = 0.692\epsilon\,D_p\frac{T^3}{10^8} \qquad (17)$$

To evaluate the thermal conductivity of a packed bed it is first predicted from the correlation in Figure 1 [with Equation (8) used, if necessary], and then the radiation contribution from Equation (16) is added.

High-temperature data for which the correlation can be tested have recently become available. Yagi and Kunii (*14*) have measured thermal

conductivities of packed beds containing various types of relatively large-size particles up to 840°C. Predicted thermal conductivities have been compared with the results of their experimental study in Figures 6 and 7. Good comparisons have been obtained, particularly when it is noted that at the highest temperature the radiation contribution accounts for about 80% of the total thermal conductivity.

CONCLUSIONS

Correlations have been developed for the effect of pressure, temperature, and particle size on the thermal conductivity of packed beds. An apparent thermal conductivity of the gas phase can be calculated from Equation (8) for use in Deissler and Eian's correlation, Figure 1, to predict the thermal conductivity of the bed. The correlation has been successfully checked with the data of various investigators. However it is not applicable to fine dusts, such as carbon black, because they contain particle agglomerates and have very large void fractions. For higher temperatures and relatively large particles a radiation contribution should be added. The radiation contribution can be calculated from Equations (16) and (17). Predicted values compared well with experimental data.

NOTATION

b = distance over which conduction takes place, ft.
C, C_1 = empirical constants
c_v = specific heat at constant volume, B.t.u./(lb.)(°F.)
c_p = specific heat at constant pressure, B.t.u./(lb.)(°F.)
D_p = particle diameter, ft.
h_r = heat transfer coefficient for radiation, B.t.u./(hr.)(sq.-ft.)(°F.)
j = jump distance of temperature discontinuity, ft.
k = thermal conductivity of packed bed, B.t.u./(hr.)(sq. ft.)(°F./ft.)
k_B = Boltzmann constant, 0.565×10^{-23} (ft.)(lb.)/°R.
k_g° = thermal conductivity of gas, B.t.u./(hr.)(sq. ft.)(°F./ft.)
k_g = apparent thermal conductivity of gas phase, B.t.u./(hr.)(sq. ft.)(°F./ft.)
k_p = contact thermal conductivity between particles, B.t.u./(hr.)(sq. ft.)(°F./ft.)
k_r = radiation contribution to thermal conductivity of powder, B.t.u./(hr.)(sq. ft.)(°F./ft.)
k_r° = $h_r D_p$, B.t.u./(hr.)(sq. ft.)(°F./ft.)
k_s = thermal conductivity of solid, B.t.u./(hr.)(sq. ft.)(°F./ft.)
L = mean free path of molecules, ft.
N_{Pr} = $c_v \mu / k_g^\circ$ = Prandtl number
P = pressure, lb./sq. ft.
P_b = break-away pressure, lb./sq. ft.
q = rate of heat transfer, B.t.u./hr.
r = radius of particle, ft.
s = element of particle perimeter, ft.
t_1, t_2 = surface temperature of solid particle, °F.
t_g = gas temperature, °F.
T = absolute temperature, °R.
x = coordinate in direction of heat flow, ft.
z = coordinate perpendicular to direction of heat flow, ft.

Greek letters

α = accommodation coefficient
γ = c_p/c_v = specific heat ratio
δ = void fraction
ϵ = emissivity
μ = viscosity, lb./(ft.)(hr.)
σ = mean diameter of gas molecules, ft.

LITERATURE CITED

1. Argo, W. B., and J. M. Smith, *Chem. Eng. Progr.*, **49**, 443 (1953).
2. Damköhler, G., "Der Chemie Ingenieur," Eucken-Jakob, Vol. 3, Part I, p. 445, Leipzig, Akademische Verlagsgesellschaft M.B.H. (1937).
3. Deissler, R. G., and C. S. Eian, *Natl. Advisory Comm. Aeronaut., RM E52C05*, (1952).
4. *Ibid., RM E53G03* (1953).
5. Kannuluik, W. G., and L. H. Martin, *Proc. Roy Soc. (London)*, **A141**, 144 (1933).
6. Kennard, E. H., "Kinetic Theory of Gases," p. 311, McGraw-Hill, New York (1938).
7. Kling, G., *Forsch. Geb. Ingenieurw.*, **9A**, 82 (1938).
8. McAdams, W. H., "Heat Transmission," 3ed., McGraw-Hill, New York (1954).
9. Prins, J. A., J. Schenk, and A. J. G. L. Schram, *Physica*, **16**, 379 (1950).
10. Ribaud, G., *Chaleur & ind.*, **18**, 36 (1937).
11. Schumann, T. E. W., and V. Voss, *Fuel*, **13**, 249 (1934).
12. Sugawara, S., and S. Sato, *Trans. Soc. Mech. Engrs. (Japan)*, **13**, No. 45, 164 (1947).
13. Wilhelm, R. H., W. C. Johnson, R. Wynkoop, and D. W. Collier, *Chem. Eng. Progr.*, **44**, 105 (1948).
14. Yagi, Sakae, and Daizo Kunii, *A.I.Ch.E. Journal*, **3**, 373 (1957).

Manuscript received October 27, 1958; revision received May 15, 1959; paper accepted May 15, 1959. Paper presented at A.I.Ch.E. Atlantic City meeting.

Calculation of Equilibrium Flash Vaporization Curves by an Integration Method

C. O. BENNETT, C. J. BRASKET, and J. W. TIERNEY

Remington Rand Univac, St. Paul, Minnesota

Techniques for solving the equilibrium flash problem are reviewed and a new technique especially adapted for use on automatic digital computers is developed. Instead of a single equation with multiple roots being solved by an iterative process, as is usually done, the problem is rephrased as a differential equation, and a numerical integration is made. The isothermal and isobaric flash problems can be handled with essentially the same equations. The method is particularly advantageous when a complete flash curve is required and the equations can be used when a linear model of the equilibrium flash process is required.

If a homogenous hydrocarbon mixture is subjected to a change in pressure or temperature so that the resultant conditions are in the two-phase region, and if the two phases are in equilibrium, then the process is known as an *equilibrium flash vaporization.* This paper deals with the problem of tracing the pressure–temperature–percentage-flashed history of a mixture of known over-all composition. The inverse problem of determining the phase compositions when an equilibrium flash curve is given is more difficult. Some of the methods of solving this latter

C. O. Bennett is with the Lummus Company, New York, New York.

problem have been reviewed and tested by Filak and Sandlin (*1*).

The method presented here for computing equilibrium flash curves uses a high-speed digital computer. In the following section the necessary equations are developed to express the flash problems as a differential equation relating percentage flashed, temperature, and pressure. This equation can then be numerically integrated to give a series of values of temperature (isobaric flash) or pressure (isothermal flash) vs. percentage flashed in increments of percentage flashed. The problem has been programmed for the Remington Rand Univac Scientific Model 1103 computer with the assumption that equilibrium vaporization ratios are available in the form

$$\ln K_i p = A_i + B_i T + C_i\left(\frac{1}{T}\right) + D_i p + E_i p^2 + F_i\left(\frac{p}{T}\right) + G_i\frac{p^2}{T}$$

although other equations can be handled. The calculation of enthalpies is incorporated as an option in the program and gives an enthalpy–percentage–flashed curve (particularly useful in adiabatic flash calculations).

DERIVATIONS OF EQUATIONS

One mole of liquid feed containing n components is fed into an apparatus in which it is partially vaporized; the resulting liquid and vapor streams leave the apparatus in equilibrium at a known pressure and temperature. The following material-balance equations may be written, of which n are independent:

$$L + V = 1 \qquad (1)$$

$$Lx_i + Vy_i = z_i \quad i = 1, 2, \ldots, n \qquad (2)$$

These are rearranged and combined with the equilibrium relationship

$$y_i = K_i x_i \qquad (3)$$

to give

$$x_i = \frac{z_i}{V(K_i-1)+1} \qquad i = 1, 2, \ldots, n \qquad (4)$$

One common procedure is to use the requirement that

$$\sum_{i=1}^{n} x_i = 1.0$$

and so

$$\sum_{i=1}^{n} \frac{z_i}{V(K_i-1)+1} = 1.0 \qquad (5)$$

If the criterion $\sum_{i=1}^{n} y_i = 1.0$ is used,

$$\sum_{i=1}^{n} \frac{K_i z_i}{V(K_i-1)+1} = 1.0 \qquad (6)$$

Rachford (*10*) suggested that it is convenient to combine Equations (5) and (6) to give

$$\phi(V, T) = \sum_{i=1}^{n} \frac{(K_i-1) z_i}{V(K_i-1)+1} = 0 \qquad (7)$$

Montross (*7*) has presented a method which can be reduced to the equation

$$\sum_{i=1}^{n} \frac{Vz_i(K_i-1)}{V(K_i-1)+1} = 0 \qquad (8)$$

which is equivalent to Equation (7). Several useful rules of thumb are given by Montross to facilitate making the calculations involved by hand.

The use of any of Equations (5) to (8), given the K_i at the equilibrium conditions, involves a trial-and-error solution; values of V are assumed between 0 and 1.0 until the criterion is met, for instance $\phi = 0$ in Rachford's method [Equation (7)]. A systematic procedure for these calculations is available (*10*), and the method has further been elaborated by Organick and Meyer (*9*).

The above methods give V, x_i, and y_i for a certain feed composition, temperature, and pressure. In order to obtain a flash curve of temperature vs. fraction vaporized, it is necessary to repeat the calculations at an arbitrary number of temperatures between the bubble and dew points. The following procedure will give the entire flash curve by a single numerical integration.

If a differential amount of liquid is vaporized, Equation (3) becomes

$$d(Lx_i) + d(Vy_i) = 0 \qquad (9)$$

By using the equilibrium relations and suitable material-balance relations, one may convert Equation (9) into a form involving only p, T, V, x_i, K_i, and z_i. If the equation is solved for dx_i

$$-dx_i = \frac{z_i(K_i-1)}{[V(K_i-1)+1]^2}dV + \frac{z_i V\left(\frac{\partial K_i}{\partial T}\right)_p}{[V(K_i-1)+1]^2}dT + \frac{z_i V\left(\frac{\partial K_i}{\partial p}\right)_T}{[V(K_i-1)+1]^2}dp \qquad (10)$$

and, since $\sum_{i=1}^{n} dx_i = 0$

$$\sum_{i=1}^{n} \frac{(K_i-1)z_i\,dV}{[1+V(K_i-1)]^2} = -\sum_{i=1}^{n} \frac{Vz_i\left(\frac{\partial K_i}{\partial T}\right)_p dT}{[1+V(K_i-1)]^2} - \sum_{i=1}^{n} \frac{Vz_i\left(\frac{\partial K_i}{\partial p}\right)_T dp}{[1+V(K_i-1)]^2} \qquad (11)$$

Alternately, x_i may be eliminated and the criterion $\sum_{i=1}^{n} dy_i = 0$ employed to give

$$\sum_{i=1}^{n} \frac{K_i(K_i-1)z_i\,dV}{[1+V(K_i-1)]^2} = \sum_{i=1}^{n} \frac{(1-V)z_i\left(\frac{\partial K_i}{\partial T}\right)_p dT}{[1+V(K_i-1)]^2} + \sum_{i=1}^{n} \frac{(1-V)z_i\left(\frac{\partial K_i}{\partial p}\right)_T dp}{[1+V(K_i-1)]^2} \qquad (12)$$

Finally, subtracting Equation (11) from (12) gives

$$\sum_{i=1}^{n} \frac{(K_i-1)^2 z_i\,dV}{[1+V(K_i-1)]^2} = \sum_{i=1}^{n} \frac{z_i\left(\frac{\partial K_i}{\partial T}\right)_p dT}{[1+V(K_i-1)]^2} + \sum_{i=1}^{n} \frac{z_i\left(\frac{\partial K_i}{\partial p}\right)_T dp}{[1+V(K_i-1)]^2} \qquad (13)$$

and at constant pressure

$$\left(\frac{\partial T}{\partial V}\right)_p = \frac{\sum_{i=1}^{n} \frac{(K_i-1)^2 z_i}{[1+V(K_i-1)]^2}}{\sum_{i=1}^{n} \frac{z_i\left(\frac{\partial K_i}{\partial T}\right)_p}{[1+V(K_i-1)]^2}} = f(V, T) \qquad (14)$$

At constant pressure Equation (14) is an ordinary, linear, first-order differential equation subject to the initial conditions that $T = T_B$ when $V = 0$. The equation may be integrated to give

$$T = T_B + \int_0^V f(V, T)\,dV \qquad (15)$$

A check on the integration, which must be done numerically, is given by the requirement that at $V = 1$, $T = T_D$.

It is easy to verify that Equation (14) can also be found from Equation (7) by the relation

$$\left(\frac{\partial T}{\partial V}\right)_p = \frac{-\left(\frac{\partial \phi}{\partial V}\right)_{pT}}{\left(\frac{\partial \phi}{\partial T}\right)_{pV}} \qquad (16)$$

when one recalls that $\left(\frac{\partial T}{\partial V}\right)_p$ is evaluated along a path of $\phi = 0$.

Table 1. Constants for Calculation of Equilibrium-Vaporization Ratios

$$K_i = \frac{1}{p}\exp\left(A_i + B_iT + C_i\frac{1}{T} + D_ip + E_ip^2 + F_i\frac{p}{T} + G_i\frac{p^2}{T}\right)$$

Component	A	B	C	D	E	F	G
Multiply by	($\times 10^1$)	($\times 10^{-3}$)	($\times 10^3$)	($\times 10^{-3}$)	($\times 10^{-6}$)	($\times 10^0$)	($\times 10^{-4}$)
C_8	2.0336	−5.039	−10.055	−2.03	4.48	3.6876	−42.25
C_7	2.0047	−4.980	−9.4402	−1.596	2.659	2.9829	−21.263
C_6	1.8610	−4.287	−8.1754	−1.334	0.6002	2.0253	0.739
nC_5	1.6789	−3.448	−6.8436	−1.493	1.263	2.0316	−8.974
iC_5	1.5087	−2.341	−6.0943	−2.095	1.496	2.3574	−9.493
nC_4	1.4169	−1.879	−5.2275	−1.873	−0.02911	2.2136	−3.358
iC_4	1.2931	−1.058	−4.610	−1.428	1.80	1.6756	−9.531
C_3	1.3137	−1.43	−4.117	−1.55	2.90	1.663	−25.02
C_2	1.2535	−1.03	−3.168	4.28	−8.795	−3.607	76.51
C_1	1.0173	0.623	−1.436	1.89	−3.46	−1.880	34.23

In the preceding derivations it is assumed that K_i is a function of p and T only, that is, that the solutions are ideal. This requirement restricts the use of the method to pressures low enough so that K_i is not affected by composition, below 400 to 500 lb./sq. in. abs. for most mixtures. The K_i values used were obtained (8) and correlated by the use of

$$\ln K_ip = A_i + B_iT + C_i\left(\frac{1}{T}\right) + D_ip + E_ip^2 + F_i\left(\frac{p}{T}\right) + G_i\frac{p^2}{T} \quad (17)$$

This form is especially convenient for digital computation and represents the data well. Values for the constants are given in Table 1.

An isothermal flash curve can be obtained from Equation (13):

$$\left(\frac{\partial p}{\partial V}\right)_T = \frac{\sum_{i=1}^{n}\frac{(K_i-1)^2z_i}{[1+V(K_i-1)]^2}}{\sum_{i=1}^{n}\frac{z_i\left(\frac{\partial K_i}{\partial p}\right)_T}{[1+V(K_i-1)]^2}} = g(V,p) \quad (18)$$

and similarly the isometric equation is

$$-\left(\frac{\partial p}{\partial T}\right)_V = \frac{\sum_{i=1}^{n}\frac{z_i\left(\frac{\partial K_i}{\partial T}\right)}{[1+V(K_i-1)]^2}}{\sum_{i=1}^{n}\frac{z_i\left(\frac{\partial K_i}{\partial p}\right)_T}{[1+V(K_i-1)]^2}} \quad (19)$$

INTEGRATION PROCEDURE

Equation (15) may be written over an interval, ΔV, as

$$T(V+\Delta V) = T(V) + \int_V^{V+\Delta V} T'(V)\,dV \quad (20)$$

when

$$T'(V) = f(V,T) \quad (21)$$

It has been suggested that the integral in Equation (20) can be accurately evaluated numerically by Gaussian quadrature (2). This integration leads to

$$T(V+\Delta V) = T(V) + \frac{\Delta V}{18}\left\{5T'\left[V+\frac{\Delta V}{2}\left(1-\frac{\sqrt{15}}{5}\right)\right] + 8T'\left[V+\frac{\Delta V}{2}\right] + 5T'\left[V+\frac{\Delta V}{2}\left(1+\frac{\sqrt{15}}{5}\right)\right]\right\} \quad (22)$$

The Runge-Kutta method of fourth-order accuracy (4) can be used three times to give the values of T at $[V + \Delta V/2(1-\sqrt{15}/5)]$, $[V + \Delta V/2]$, and $[V + \Delta V/2(1 + \sqrt{15}/5)]$. $T'(V)$ is then evaluated at each of these points to obtain $T(V + \Delta V)$ from Equation (22). For certain cases tested (2), this procedure had an error about one-tenth that of the Runge-Kutta-Gill method (3). It is a self-starting method, in contrast to the various Adams procedures (5).

For the equilibrium flash problem the interval from $V = 0$ to $V = 1$ is divided into $1/\Delta V$ increments. A check is made after the first integration, and if $\sum_{i=1}^{n} x_i$ at $V = 1.0$ is not equal to $1.0 \pm \epsilon$, ΔV is halved and the process repeated until the criterion is met, on the assumption that ϵ is not chosen to be so small that round-off errors become important.

ENTHALPY BALANCE AND BUBBLE-POINT CALCULATION

The enthalpy balance for a flow process can be written as

$$h_f + Q = (1-V)h + VH \quad (23)$$

where

$$h = \sum_{i=1}^{n} x_i h_i \quad (24)$$

$$h_f = \sum_{i=1}^{n} z_i h_{fi} \quad (25)$$

$$H = \sum_{i=1}^{n} y_i H_i \quad (26)$$

Both h_i and H_i are considered here as functions of temperature only (6). For a given feed h_f is calculated by Equation (25); then for the conditions in the flash chamber h and H are calculated by Equations (24) and (26). Equation (23) is thus solved for Q, so that a curve of Q vs. V is obtained. The temperature and fraction vaporized in an adiabatic flash are obtained from the T vs. V curve and the value of V where $Q = 0$.

Since the bubble point is needed as the initial point of the integration, a word on the calculation of the bubble point is included. At this condition the following criterion must be satisfied:

$$\sum_{i=1}^{n} K_iz_i = 1.0$$

For a given pressure the bubble-point temperature can be found by the use of a Newton-Raphson iteration as follows:

$$T_{B_{j+1}} = T_{B_j} + \frac{-\left[\left(\sum_{i=1}^{n} K_iz_i\right)_j - 1\right]}{\left[\sum_{i=1}^{n} z_i\left(\frac{\partial K_i}{\partial T}\right)_p\right]} \quad (27)$$

Setting $j = 0$, one can estimate an initial value of the bubble point and calculate T_{B_1} by Equation (27). This process is then repeated, and j is advanced each time until $T_{B_{j+1}}$ is arbitrarily close to T_{B_j}.

DISCUSSION OF SAMPLE PROBLEMS

Besides those mentioned the following computations can be obtained if desired:

1. Value of Q at each integration interval.
2. The Σx_i and Σy_i at each integration interval.
3. All values of x_i and y_i at each integration interval.
4. Values of V and T and dt/dV at the three Runge-Kutta points in each interval for the isobaric flash or V, p,

Table 2. Results of Sample Isobaric and Isothermal Equilibrium Flash Calculations

Type of flash	Mixture	Number of intervals	Dew point: Actual	Dew point: By integration	Σx_i
Isobaric	A*	1	771.799 °R.	767.261 °R.	1.03918
Isobaric	A	2	771.799 °R.	770.669 °R.	1.00955
Isobaric	A	4	771.799 °R.	771.624 °R.	1.00147
Isobaric	A	8	771.799 °R.	771.788 °R.	1.00010
Isobaric	B†	1	740.359 °R.	740.909 °R.	0.99508
Isobaric	B	2	740.359 °R.	740.345 °R.	1.00013
Isothermal	B	1	492.24 lb./sq. in. abs.	474.13 °R.	0.95407
Isothermal	B	2	492.24 lb./sq. in. abs.	499.77 °R.	1.00096
Isothermal	B	4	492.24 lb./sq. in. abs.	499.36 °R.	1.00022

* Mixture A — C_1, 1%; C_2, 5%; C_3, 11%; iC_4, 6%; nC_4, 14%; iC_5, 21%; nC_5, 20%; C_6, 10%; C_7, 9%; C_8, 3%.
† Mixture B — C_2, 35%; C_3, 10%; nC_4, 10%; nC_5, 10%; C_6, 35%.

and dp/dV for the isothermal flash. This information is useful when only a few intervals are used or when interpolation between points is desired.

The flash curve is computed by the use of four intervals ($\Delta V = 1/4$). After the curve has been computed, it can be repeated with half as large an interval. This procedure can be repeated any number of times.

To illustrate the application of this method, several sample problems were solved for two different feed compositions and with different numbers of integration intervals. The results are summarized in Table 2. It was seen in the preceding sections that an integration is started at the bubble point and can be continued until the dew point is reached. The greatest error normally occurs at the dew point. The simplest test of the accuracy of the method is to compare the value calculated by the integration method with that computed directly from the K values. These values are given in the fourth and fifth columns of Table 2, and it can be seen that, with the exception of the one-interval integration with ten components, the errors are small. As might be expected, the ten-component problem was less accurate for the same number of intervals than the five-component problem. The error decreases rapidly with increase in the number of intervals. On the basis of these results four intervals were judged sufficiently accurate in all cases examined.

Another measure of errors is the Σx_i at the dew point, listed in the last column of Table 2, and the results are consistent with the conclusions based on the dew-point comparisons. The error for the one-interval case is 3.9%, decreasing to 0.009% in the eight-interval integration.

APPLICATION OF METHOD

The method described in the previous section was developed primarily to generate a complete equilibrium flash curve. Such a curve might be of interest in itself; however a more probable application would be to use the program to generate a table which would be stored in the computer. Thus a problem calling for many references to an equilibrium flash curve would obtain them by interpolation in the table. For example, the four-interval integration used in the program would give a total of fifteen temperature-volume flashed-composition points, in addition to the bubble and dew points. Also the slopes of the flash curve would be known at these points. Interpolation between these points with the slopes known would be accurate and many times faster than computing the points directly.

In addition, the equations developed in this paper can be used to reduce the highly nonlinear equilibrium flash process to a linear process in the neighborhood of some point. This linearization technique is a highly useful simplification in many problems. The analysis of control systems, for example, is limited largely to linear systems, and it is usually necessary to describe the system in terms of linear perturbations about some point. Similarly some economic analysis techniques, such as linear programming, depend on the use of linear models. Obviously the equilibrium flash process can be described in the neighborhood of a point by the equilibrium values of temperature, pressure, composition, and the appropriate slopes as obtained from Equations (10) through (19).

Although the techniques described in this paper could be used for the computation of a single point on the equilibrium flash curve, it does not seem likely that this would be desirable, since the conventional methods are faster if only one point is required.

In summary, then, these techniques seem to be best adapted to the machine computation of entire equilibrium flash curves, particularly when interpolation between points is desired. The equations are also important when a linear model of the equilibrium flash process is desired.

ACKNOWLEDGMENT

The authors wish to express their appreciation to N. R. Amundson for many valuable suggestions and to Dale F. Rudd for assistance in the calculations.

NOTATION

h_i = enthalpy of liquid component i, B.t.u./lb. mole
h_f = enthalpy of liquid mixture before flashing, B.t.u./lb. mole
H_i = enthalpy of vapor component i, B.t.u./lb. mole
K_i = y_i/x_i at equilibrium
L = moles of liquid per mole of feed
p = pressure, lb./sq. in. abs.
Q = heat added during flash, B.t.u./lb. mole of feed
T = absolute temperature, °R.
T_{B_0} = initial value of bubble point
V = moles of vapor per mole of feed
ΔV = integration interval
x_i = mole fraction component i in liquid
y_i = mole fraction component i in vapor
z_i = mole fraction component i in mixture prior to flashing

LITERATURE CITED

1. Filak, G. A., H. L. Sandlin, and C. J. Stockholm, *Petrol. Refiner*, **34**, No. 4, 153 (1955).
2. Flatt, H., and S. Conte, NN-21, The Ramo-Wooldridge Corporation (August 1956).
3. Gill, S., *Proc. Cambridge Phil. Soc.*, **47**, 96 (1951).
4. Hildebrand, F. B., "Introduction to Numerical Analysis," p. 237, McGraw-Hill, New York (1956).
5. *Ibid.*, pp. 199-202.
6. Holcomb, D. E., and G. G. Brown, *Ind. Eng. Chem.*, **34**, 590 (1942).
7. Montross, C. F., *Chem. Eng. Progr.*, **46**, 105 (1950).
8. "Natural Gasoline Supply Mens Association Data Book," 6 ed. (1951).
9. Organick, E. I., and H. I. Meyer, *J. Petrol. Technol.*, **1**, No. 5, 9 (1955).
10. Rachford, H. H., Jr., and J. D. Rice, *Trans. Am. Inst. Mech. Engrs.*, **195**, 327 (1952).

Manuscript received February 26, 1959; revision received May 14, 1959; paper accepted May 18, 1959.

Heat Transfer Characteristics of Porous Rocks

DAIZO KUNII and J. M. SMITH

Northwestern University, Evanston, Illinois

Equations are derived for predicting the effective thermal conductivity of beds of unconsolidated particles containing stagnant fluid. The effective thermal conductivity at these conditions, called the *stagnant conductivity*, is a function of the thermal conductivities of the solid and fluid phases, the void fraction, and, if radiation is important, the emissivity, mean temperature, and diameter of the solid particles. Comparison with the available experimental data indicates that the equations are satisfactory for fluids and solid particles of both high and low thermal conductivities.

To extend the theory to beds of consolidated particles, it is supposed that consolidated beds are formed by partial clogging and cementing of beds of unconsolidated particles. With this assumption the theoretical equations for packed beds are extended to include such materials as sandstone and porous metals. The resulting expressions for the stagnant conductivity involve a consolidation parameter characteristic of the solid material. This quantity accounts for the heat transfer across the contact surfaces between cemented or clogged particles. The equations correctly predict the effect of void fraction and solid and fluid thermal conductivities on the heat transfer properties of sandstones and sintered metal systems.

The heat transfer characteristics of fluid-bearing rocks are of growing importance as a result of the significance of thermal methods of petroleum production. The successful design and evaluation of these methods depends directly upon heat transfer rates in porous rocks containing stationary and flowing fluid. There have been several experimental investigations of temperature gradients in porous media filled with stationary fluid, but essentially no data have been published for the moving fluid case. Also there is a need for an adequate theory to explain heat transfer rates in consolidated media for both static and flowing fluid conditions. In contrast, the thermal characteristics of packed beds of larger sized unconsolidated particles, for example fixed-bed catalytic reactors, have been studied intensively.

This investigation is a theoretical study of effective thermal conductivities of porous media filled with stationary fluid, that is stagnant conductivities. The results are applied to beds of both unconsolidated particles and consolidated materials such as sandstone. Later studies will be concerned with heat transfer perpendicular and parallel to the direction of flowing fluid.

PREVIOUS WORK

Stagnant conductivities of porous sandstones have been measured experimentally by several observers (*2, 3, 7, 27, 50*), but few attempts have been made to explain the results in terms of physical properties such as the thermal conductivities of the solid and fluid phases and the void fraction.

In packed beds of unconsolidated particles the major experimental studies of stagnant conductivities are summarized in references *16, 19, 20, 21, 29, 40, 42, 45* and the theoretical studies in references *8, 13, 36, 38, 41, 44*. Yagi and Kunii (*45*) specifically considered the heat transfer mechanism through the fluid film near the contact surfaces, or points.

Effective thermal conductivities in packed beds with flowing fluids have been studied by a number of investigators (*1, 4, 5, 6, 9, 11, 17, 18, 21, 22, 24, 25, 26, 28, 30, 31, 35, 37, 39, 43, 46, 47, 48,* and *49*).

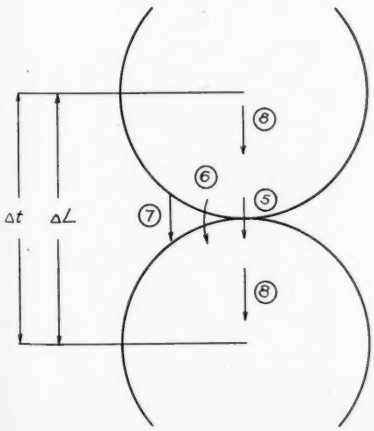

Fig. 1. Heat transfer model for packed bed of unconsolidated particles.

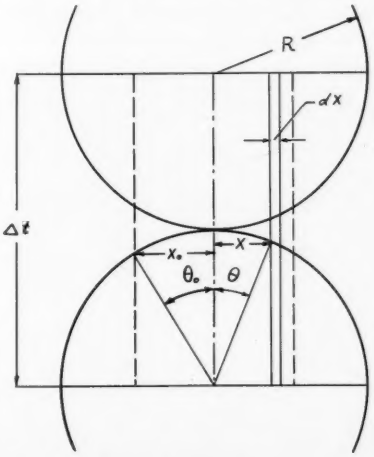

Fig. 2. Model for heat transfer near contact points of particles.

From these data approximate values of the stagnant conductivity can be obtained by extrapolation to zero flow rate.

Previous theoretical investigations of heat transfer in consolidated materials have been directed toward the refractory industry (*10, 23, 32*). Francl and Kingery (*12*) measured the effect of void fraction of a continuous solid phase with isolated small pores of air and found that the stagnant conductivity could be represented by

$$k_s^\circ/k_s = 1-\epsilon' \text{ (below 900°F.)} \qquad (1)$$

RELATIONSHIP BETWEEN PACKED BEDS AND CONSOLIDATED POROUS ROCKS

The effect of void fraction on the stagnant conductivity of consolidated porous media like sandstone is different from its effect on refractory materials. The decrease in conductivity with increasing void fraction is observed to be concave downward rather than linearly.

There are some indications that consolidated porous rocks such as sandstone are more closely related to packed beds of unconsolidated particles than to refractory materials. It is conceivable, for example, that underground sandstones were formed by consolidation of loose materials. Accordingly, it appears reasonable to analyze the heat transfer problem by first considering the behavior of beds of unconsolidated particles.

MECHANISM OF HEAT TRANSFER IN BEDS OF UNCONSOLIDATED PARTICLES

Figure 1 shows a cross section of two spherical particles in contact with each other. It is presumed that the particles are surrounded by stagnant fluid. Heat transfer is assumed to occur in the vertical direction by the following mechanisms:

1. Heat transfer through the fluid in the void space by conduction and by radiation between adjacent voids (when the voids are assumed to contain a nonabsorbing gas).
2. Heat transfer through the solid phase.
   - *a.* Heat transfer through the contact surface of the solid particles.
   - *b.* Conduction through the stagnant fluid near the contact surface.

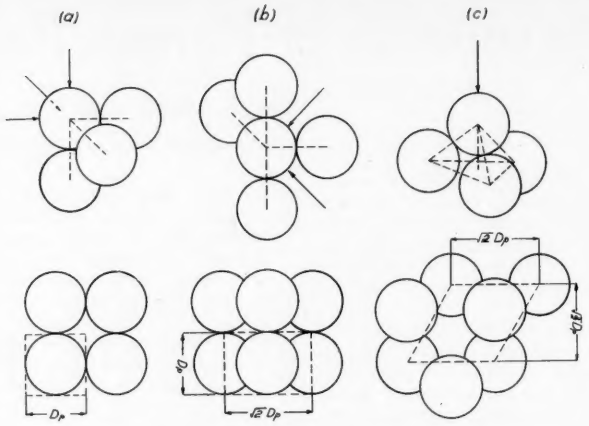

Fig. 3. Heat transfer directions for loose packing of spheres.

c. Radiation between surfaces of solid (when the voids are assumed to contain a nonabsorbing gas).

d. Conduction through the solid phase.

Over-all mechanisms 1 and 2 are in parallel with each other. Mechanism *d* is in series with the combined result of parallel mechanisms *a*, *b*, and *c*. This model is somewhat similar to that proposed by Yagi and Kunii (*45*). Mechanism *a* will be interpreted in terms of a heat transfer coefficient for convenient application to consolidated porous media such as sandstone.

According to the model in Figure 1, the effective thermal conductivity is given by $-k_e^\circ(\Delta t)/(\Delta L)$ = [heat flux in void space (mechanism 1)] + [heat flux through solid phase (mechanism 2)].

Therefore

$$-k_e^\circ\frac{\Delta t}{\Delta L} = -k_g\epsilon\frac{\Delta t}{\Delta L} + h_{rv}\epsilon(-\Delta t) + q_s \qquad (2)$$

(mechanism 1) (mechanism 2)

On the other hand the temperature drop in the particle = (temperature drop in solid phase) + (temperature drop near the contact surface), or

$$\Delta t = \Delta t_s + \Delta t_{gs} \qquad (3)$$

The individual temperature drops may be written in terms of the heat flux in the solid phase:

$$\Delta t_s = \frac{-q_s}{\left(\frac{k_s}{l_s}\right)}\frac{1}{1-\epsilon} \qquad (4)$$

$$\Delta t_{gs} = \frac{-q_s}{\frac{k_g}{l_v}+h_p+h_{rs}}\frac{1}{1-\epsilon} \qquad (5)$$

In these expresssion l_s is the thickness of a slab of solid material which would offer the same resistance to heat transfer as the spherically shaped particle; l_v is the thickness of a slab of stationary fluid which would offer the same heat transfer resistance as the filaments of fluid near the contact point between particles.

Combination of Equations (2) through (5) results in the following expression for k_e°:

$$k_e^\circ = \epsilon[k_g + h_{rv}\cdot\Delta L] + \frac{(1-\epsilon)\,\Delta L}{\frac{1}{\frac{k_g}{l_v}+h_p+h_{rs}}+\frac{l_s}{k_s}} \qquad (6)$$

which may be written

$$\frac{k_e^\circ}{k_g} = \epsilon\left[1+\beta\frac{h_{rv}\cdot D_p}{k_g}\right] + \frac{\beta(1-\epsilon)}{\frac{1}{\frac{1}{\phi}+\frac{D_p}{k_g}(h_p+h_{rs})}+\gamma\left(\frac{k_g}{k_s}\right)} \qquad (7)$$

This general equation may be simplified in many instances. For example, except at very low pressures the term for heat transfer through the contact surfaces (mechanism *a*) can be neglected. Then

$$\frac{k_e^\circ}{k_g} = \epsilon\left[1+\beta\frac{h_{rv}\cdot D_p}{k_g}\right] + \frac{\beta(1-\epsilon)}{\frac{1}{\frac{1}{\phi}+\frac{D_p\cdot h_{rs}}{k_g}}+\gamma\left(\frac{k_g}{k_s}\right)} \qquad (8)$$

When the void spaces contain liquid instead of gas, the contributions due to radiant heat transfer disappear:

$$\frac{k_e^\circ}{k_g} = \epsilon + \frac{\beta(1-\epsilon)}{\phi+\gamma\left(\frac{k_g}{k_s}\right)} \qquad (9)$$

Even for gaseous systems the radiation contributions are negligible, except for relatively large particles and high temperature (above 900°F.). The radiation coefficients, when necessary, may be estimated by the equations proposed by Yagi and Kunii (*45*).

To use Equations (7) to (9), it is necessary to know the numerical values of the three quantities β, γ, ϕ. For close packing of spheres, as shown in Figure 4, the average value of β is

$$\beta = \frac{1}{D_p}\frac{1}{3}\left[\left(\frac{2}{3}\right)^{1/2}+1+\left(\frac{3}{2}\right)^{1/2}\right]D_p = 0.895$$

For the most loose or open packing, β should be unity. Therefore its value will range from 0.9 to 1 for almost all actual packed beds. The value of γ depends upon l_s; it will be assumed to be the length of a cylinder having the same volume as the spherical particle; that is

$$l_s = \left(\frac{\pi}{6}D_p^3\right)\Big/\left(\frac{\pi}{4}D_p^2\right) = \frac{2}{3}D_p$$

$$\gamma = l_s/D_p = \frac{2}{3}$$

The most difficult quantity to evaluate is ϕ, which is a measure of the effective thickness l_v of the fluid film adjacent to the contact surface of two solid particles. It is determined theoretically in the next section.

HEAT TRANSFER THROUGH THE FLUID PHASE NEAR THE CONTACT SURFACE OF SOLID PARTICLES

Heat transfer through the fluid filaments adjacent to the solid particles may be analyzed by reference to Figure 2. Even though but one contact point is shown, each particle will have several contact points on its semispherical surface which contribute to the heat transfer in one direction. One should consider the general case and assume that the fraction $(1/n)$ of the total heat flux passes through the fluid film near one contact point. The second assumption is that the heat flow is parallel to the axis between the particles. Then the fraction of the total heat transfer associated with one contact point is

$$\frac{1}{n} = \frac{\pi x_o^2}{\pi R^2} = \sin^2\theta_o \qquad (10)$$

With these concepts the following expression can be derived for q:

$$q = \int_o^{q_o} dq = \pi R\,k_g\,\Delta t\left(-\frac{\kappa}{\kappa-1}\right)^2\left[\ln\{\kappa-(\kappa-1)\cos\theta_o\} - \frac{\kappa-1}{\kappa}(1-\cos\theta_o)\right] \qquad (11)$$

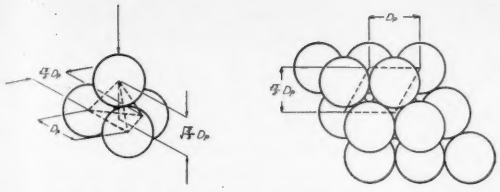

Fig. 4. Directions of heat transfer for close packing of spheres.

where κ is k_s/k_g.

Equation (11) includes the heat transfer through the solid phase in series with the filaments of fluid. Hence q can be expressed in terms of the sum of the resistances of the two steps; that is

$$q = \frac{\pi(R \sin \theta_o)^2 \Delta t}{\frac{2R\left(\frac{2}{3}\right)}{k_s} + \frac{l_v}{k_g}} \qquad (12)$$

where $2R(2/3) = \gamma D_p = l_s$ and is therefore the effective length of the spherical solid for thermal conduction.

Employing the definition of l_v in terms of ϕ and noting that $D_p = 2R$, one can combine Equations (11) and (12) to give

$$\phi = \frac{1}{2} \frac{\left(\frac{\kappa-1}{\kappa}\right)^2 \sin^2\theta_o}{l_n\{\kappa-(\kappa-1)\cos\theta_o\} - \frac{\kappa-1}{\kappa}(1-\cos\theta_o)} - \frac{2}{3}\frac{1}{\kappa} \qquad (13)$$

where $\kappa = k_s/k_g$, and $\sin^2\theta_o = 1/n$.

Equation (13) is the basic expression for ϕ for a single contact point (Figure 2). To obtain the required ϕ for use in Equations (7) to (9), the number of contact points on a surface of one half of a single particle must be determined.

To estimate n, two arrangements of particles, state 1 for the most open packing and state 2 for close packing, should be considered. For state 1, composed of spherical particles of uniform size packed with their centers at the corners of cubes, three axes of symmetry (a), (b), and (c) must be considered, with the directions of heat transfer as shown in Figure 3. Orientations (b) and (c) have two and three contact points, respectively. However these numbers must be corrected for the cross-sectional areas perpendicular to the directions of heat transfer and for the frequency of the orientations. From geometrical considerations one can show that the data for each orientation are

Orientation	(a)	(b)	(c)
Contact point	1	2	3
Area corresponding to one particle	D_p^2	$\sqrt{2}D_p^2$	$\sqrt{3}D_p^2$
Number of directions	3	2	4

The derivation of Equation (13) is based upon orientation (a), as shown in Figure 2. Hence the equivalent number of contact points for orientation (b) for use in connection with Equation (13) will be n'_1, given by the expression

$$n'_1 = (2)\frac{D_p^2}{(\sqrt{2}\,D_p^2)}\left(\frac{2}{3}\right) = 0.945$$

In this manner the average number of

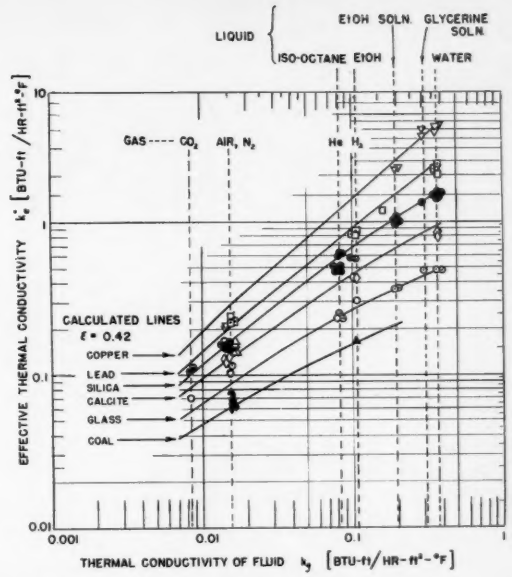

Fig. 6. Comparison of calculated and experimental data, unconsolidated particles.

TABLE 1—KEY FOR FIGURE 6

Symbol	Solid	Av. diam. (in.)	Void fraction	Observers	Ref.
▲	coal	–	0.437	Schumann and Voss	(36)
◆	coal	–	0.40	Saito and Okagaki	(33)
○	glass	0.0212	–	Weiniger and Schneider	(42)
⊙	glass	0.0132-0.089	0.408-0.431	Preston	(29)
△	calcite	0.098-0.563	0.458-0.493	Waddams	(40)
◇	calcite	0.056-0.112	0.447-0.465	Kimura	(20)
●	silica	0.00504-0.0960	0.408-0.439	Preston	(29)
⊕	alumina	0.0189-0.0429	0.432-0.461	Weiniger and Schneider	(42)
□	lead	0.103	0.40	Schumann and Voss	(36)
⊡	lead	0.0132-0.0179	0.397-0.420	Kimura	(20)
▽	copper	0.0059-0.0068	0.384-0.392	Preston	(29)

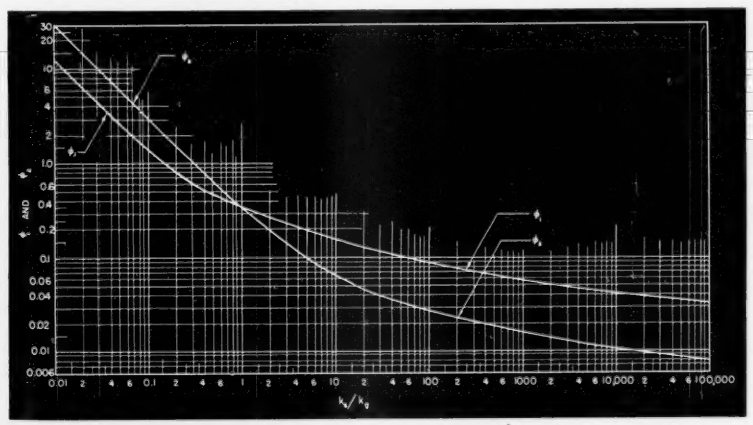

Fig. 5. ϕ vs. thermal-conductivity ratio k_s/k_g; ϕ_1-loose packing, ϕ_2-close packing.

TABLE 2—KEY FOR FIGURE 7

Symbol	Solid	Av. diam. (in.)	Void fraction	Observer	Ref.
⊙	chrome steel sphere	0.15	0.38	Kling	(21)
○	steel sphere	0.157-0.219	0.38-0.394	Waddams	(40)
●	stainless steel sphere	0.0071	0.476-0.502	Preston	(29)
△	SiC	0.00236-0.0216	0.410-0.428	Kannuluick	(19)
□	diphenyl-amine	0.00106	0.513	Kannuluick	(19)

contact points for all the three orientations will be approximately

$$n_1 = \frac{1}{3}(1 + n' + n'') =$$

$$\frac{1}{3}(1 + 0.945 + 2.31) = 1.42 \sim 1.5$$

As seen in Figure 4, one symmetrical axis is sufficient for the close packing state. The equivalent number of the contact points related to state 1, orientation (a), is

$$n_2 = (6)\frac{D_p^2}{(\sqrt{3}/2)\,D_p^2} = 4\sqrt{3}$$

When one uses these values of n to determine θ_n, Equation (13) can be used to obtain values of ϕ for each packing state. The results plotted vs. the ratio k_s/k_g are shown in Figure 5.

The void fractions for the two cases are

$$\text{State 1: } \epsilon_1 = 1 - \frac{\pi}{6} = 0.476$$

$$\text{State 2: } \epsilon_2 = 1 - \frac{\sqrt{2}\pi}{6} = 0.260$$

It is supposed that actual packed beds may be considered a composite of the two basic packing states. Since ϕ is proportional to the thermal resistance, the correct value for an actual bed should be approximately an additive function of ϕ_1 and ϕ_2. Hence for a bed with a void fraction ϵ, ϕ is given by

$$\phi = \phi_2 + (\phi_1 - \phi_2)\frac{\epsilon - \epsilon_2}{\epsilon_1 - \epsilon_2} = \phi_2 +$$

$$(\phi_1 - \phi_2)\frac{\epsilon - 0.260}{0.216} \text{ for } \epsilon_1 \geqq \epsilon \geqq \epsilon_2 \quad (14)$$

For particles of uniform size it is not possible for the void fraction to be less than ϵ_2. Therefore observed values less than ϵ_2 might be considered the result of clogging by smaller particles in the void spaces. For such cases it seems advisable to use ϵ_2 rather than the extrapolated value from Equation (14). Similarly, observed void fractions larger than ϵ_1 would be caused by the presence of exceptionally large hollow spaces compared with the average void space. This could not contribute significantly to the effective thermal conductivity. Hence for such cases it is proposed that approximately

$$\phi = \phi_1 \text{ for } \epsilon \geq \epsilon_1$$

$$\phi = \phi_2 \text{ for } \epsilon \leq \epsilon_2 \quad (15)$$

COMPARISON WITH EXPERIMENTAL DATA—UNCONSOLIDATED PARTICLES

Equations (8) and (9) were used to predict stagnant conductivities for comparison with the available experimental data. The values of k_s, k_g, D_p, ϵ, and the mean temperature, needed for the calculations, were taken from the published papers. The agreement between computed and observed stagnant conductivities is good, as illustrated graphically in Figures 6 to 8. In Figure 6 are included the systems for which the void fraction is close to 0.42 and the computed curves are based upon this value. Figure 8 includes almost all the published data that have been found for the stagnant conductivity. The ranges of experimental conditions in Figure 8 are as follow:

solids: diphenylamine, naphthalene, coal, calcite, silica, carborundum, steel, lead, copper, aluminum

average particle diameter: from 0.00106 to 0.312 in.

fluid: gas—carbon dioxide, air, nitrogen, methane, propane, helium, hydrogen
liquid—water, glycerine, *iso*-octane, ethyl alcohol, mercury

As previously mentioned, there are available a number of investigations on effective thermal conductivities in packed beds through which fluids are flowing. Although the procedure is somewhat inaccurate, k_e° can be obtained from these data by the extrapolation to zero flow rate. Figure 9 shows the comparison of k_e° values de-

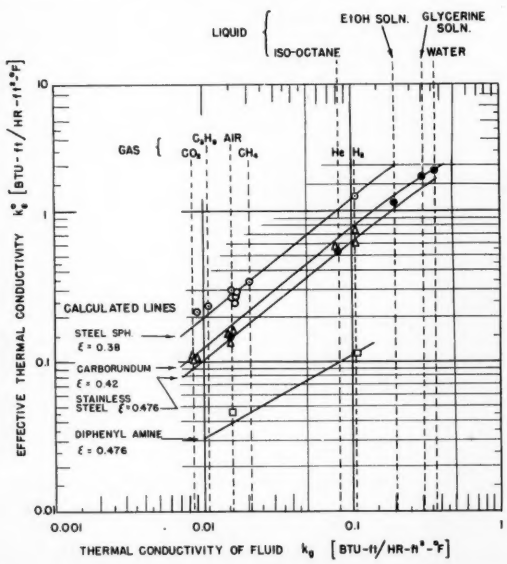

Fig. 7. Comparison of calculated and experimental data, unconsolidated particles.

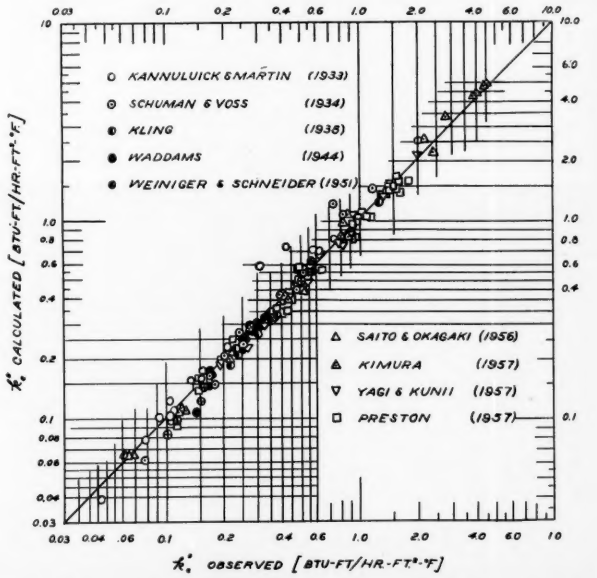

Fig. 8. Comparison of calculated and experimental data for packed beds of unconsolidated particles with motionless fluids.

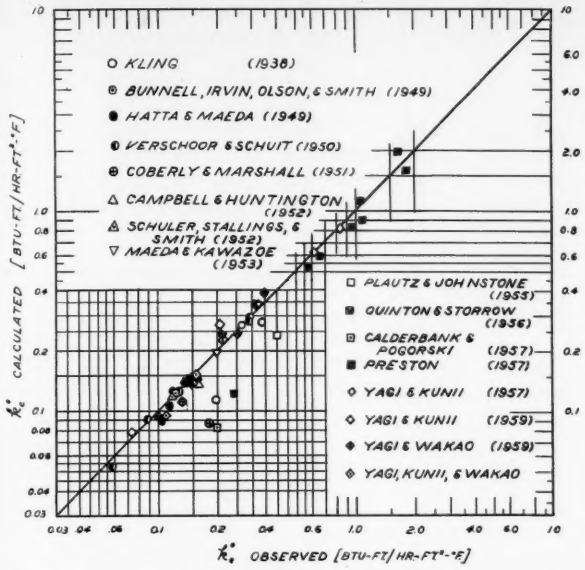

Fig. 9. Comparison of calculated and experimental data obtained by extrapolation of results for moving fluids.

termined in this manner with those computed from Equations (8) and (9). The experimental conditions for the various investigations are as follows:

solids: pumice, terrana, limestone, silica, glass, celite, insulating firebrick, alundum, steel, lead, aluminum
average diameter: from 0.0063 to 0.65 in.; spheres, cylinders, etc.
fluid: gas—air, natural gas
liquid—*iso*-octane, ethyl alcohol, water

Figures 6 to 8 show data for a large range of particle sizes and thermal conductivities of solid and fluid phases. The agreement between the predicted and observed stagnant conductivities suggests that the proposed prediction method may be used with confidence for a variety of beds of unconsolidated particles. The next step is the extension of the theory to consolidated particles.

EXTENSION OF THEORY TO CONSOLIDATED POROUS MEDIA

It has been suggested earlier that at least some kinds of consolidated porous media, for instance sandstone or sintered porous metal, originate as beds of unconsolidated particles. Then consolidation might occur by partial clogging with the cementing substance or by sintering. The original bed of unconsolidated particles is clogged with cementing substance as shown in Figure 10*a*. In this case some parts of the void space would become clogged, and the rest remain open. The result of consolidation is an increase in the average grain size. However the pore size is the same as in the original packed bed.

The mechanism of heat transfer for this model is assumed to be as shown in Figure 10*b*. Here heat is flowing in the vertical direction through the void space, ϵ' and through the solid fraction, $1-\epsilon'$. In this latter part the flow is in series through solid of thickness l', and fluid of thickness l_v. The detailed mechanisms of heat transfer are similar to those for unconsolidated particles (Figure 1), except that the shape and relative size of void and solid spaces differ.

Since the average thickness of the fluid film is assumed to be the same for both the original packed bed and the clogged porous media, the number of solid layers in the consolidated bed is proportional to its void fraction and may be written as

$$\frac{N'}{N} = \frac{\epsilon'}{\epsilon} \tag{16}$$

The average length of the unit of clogged solid is inversely proportional to the number of such solid units:

$$\frac{l_s'}{l_s} = \frac{N}{N'} \tag{17}$$

When one uses the detailed mechanisms of heat transfer similar to Figure 1, the resultant expression for k_e° is the same as Equation (6) for unconsolidated particles, except that ϵ and l_s are replaced by ϵ' and l_s'. From Figure 10 it seems reasonable to propose that

$$\Delta L = l_s' + l_v \text{ and } l_s = D_p \tag{18}$$

Combining Equations (17) and (18)

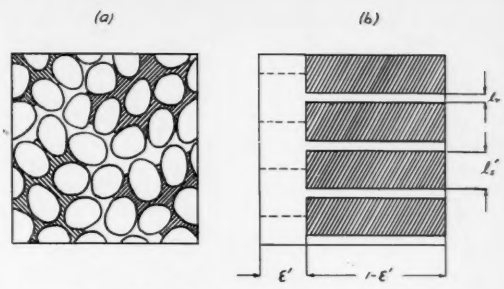

Fig. 10. Model of consolidated porous media.

yields

$$\frac{l_s'}{D_p} = \frac{N}{N'} = \frac{\epsilon}{\epsilon'} \tag{19}$$

The desired expression for k_e° can then be obtained from Equation (6) by first replacing ϵ and l_s with ϵ' and l_s' and then using Equation (18) and (19) for ΔL and l_s'. The result, converted to the form of k_e°/k_s, is

$$\frac{k_e^\circ}{k_s} = \epsilon' \frac{k_g}{k_s} + \epsilon \frac{D_p h_{rv}}{k_s}\left(1+\frac{\epsilon'}{\epsilon}\phi\right) + \frac{(1-\epsilon')\left(1+\frac{\epsilon'}{\epsilon}\phi\right)}{1+\frac{(\epsilon'/\epsilon)}{\frac{1}{\phi}\left(\frac{k_g}{k_s}\right)+\frac{D_p(h_p+h_{rs})}{k_s}}} \tag{20}$$

Equation (20) includes the term involving h_p, since this mechanism may be important in consolidated beds.

For most temperatures the radiation terms are negligible, and Equation (20) reduces to

$$\frac{k_e^\circ}{k_s} = \epsilon'\left(\frac{k_g}{k_s}\right) + \frac{(1-\epsilon')\left(1+\frac{\epsilon'}{\epsilon}\phi\right)}{1+\frac{(\epsilon'/\epsilon)}{\left(\frac{1}{\phi}\right)\frac{k_g}{k_s}+\frac{D_p h_p}{k_s}}} \tag{21}$$

The heat transfer through the contact surface between consolidated particles, represented by the dimensionless group $h_p D_p/k$, in Equation (21), cannot be easily evaluated. It is characteristic of the kind of solid material and the type of consolidation. It will be regarded as a consolidation parameter to be determined by comparing experimental data with Equation (21).

COMPARISON WITH EXPERIMENTAL DATA—CONSOLIDATED PARTICLES

To treat porous media over a relatively large range of void fraction, namely 0 to 0.40, state 1 is chosen as the basic fundamental packing arrangement for consolidated particles.

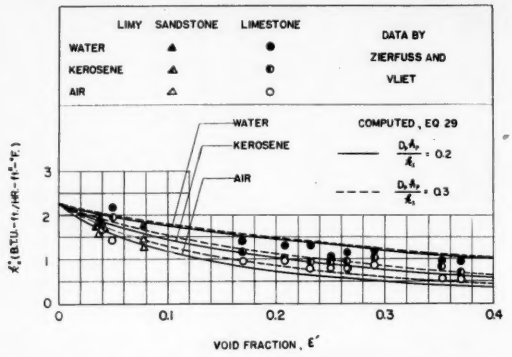

Fig. 11. Comparison of stagnant conductivities for limestone.

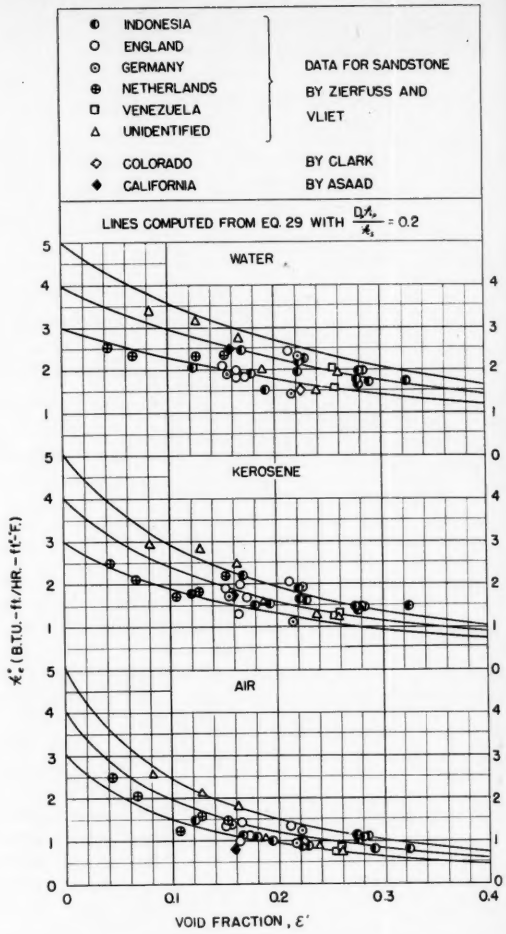

Fig. 12. Comparison of stagnant conductivities for sandstone.

Then the required ϕ value can be obtained from the line of ϕ_1, in Figure 5, and ϵ taken as 0.476, both for use in Equation (21). The consolidation parameter $D_p h_p/k_s$ is independent of the fluid in the pores of the void fraction.

Figure 11 shows the comparison of calculated lines with the experimental data for different fluids in limestone and limy sandstones originating in different places, that is the Netherlands, France, and California. When one assumes $D_p h_p/k_s$ as 0.2 and 0.3 in Equation (21), the calculated lines explain reasonably well the variation of k_e° with void fraction. These computed results are based upon a value of $k_s =$ 2.24 B.t.u./(hr.)-(ft.)(°F), as taken from the International Critical Tables.

The experimental data for sandstones by Zierfuss and Vliet (*50*), Clark (*7*), and Asaad (*2*) are compared with calculated results in Figure 12. Since the thermal conductivity of the solid phase is the mean value of the clogged group of particles, as shown in Figure 10*a*, the numerical value of k_s is not necessarily the same as that of pure quartz but rather may lie between the values of quartz and of the cementing material. In view of this, three different values of k_s, 5, 4, and 3, were used in Equation (21). Hence in Figure 12 three computed curves are shown. The consolidation parameter was taken as 0.2 for all three computed curves. It should be noted that samples from the same country originated in nearly every case from two or three different formations. Hence the consolidation parameter and thermal conductivities of the clogged material probably were different not only from country to country but for different samples from the same country. As in Figure 11, the variation of stagnant conductivity with void fraction is predicted well by Equation (21), although the absolute experimental values scatter. This suggests that the proposed theory correctly reflects the effect of void fraction. In addition, the data in Figures 11 and 12 indicate that the influence of the thermal conductivity of the fluid is adequate accounted for.

Saunders *et al.* (*15*) presented the experimental data for effective thermal conductivities of sintered porous metals within stagnant air. Since the composition of the metal, a copper-tin alloy, was not given, the arithmetic mean value of the thermal conductivity taken as $k_s = 120$ B.t.u.-ft./(hr.)(sq.ft.)-(°F.) was employed. When one assumes the dimensional group $D_p h_p/k_s$ to be 0.075, the calculated line agrees well with the experimental data, as shown in Figure 13.

CONCLUSIONS

Equations (7) to (9) appear to predict with reasonable accuracy the effective thermal conductivities for various types of beds of unconsolidated particles filled with stationary fluid. The development is based upon proposing a model for the various mechanisms of heat transfer. The data required for using Equations (7) to (9) are the thermal conductivities of the solid and fluid phases and the void fractions of the bed. If radiation contributions are significant, other information is needed.

The theory was extended to beds of consolidated particles such as sandstone and sintered-metal particles. A dimensionless consolidation parameter was introduced to account for the heat

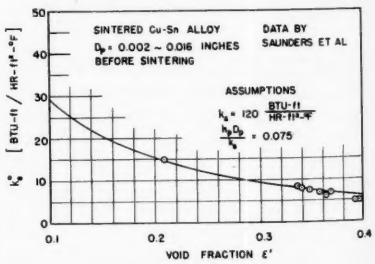
SINTERED Cu-Sn ALLOY
D_p = 0.002 ~ 0.016 INCHES BEFORE SINTERING
DATA BY SAUNDERS ET AL
ASSUMPTIONS
k_s = 120 BTU-ft / HR-ft²-°F
$\frac{h_p D_p}{k_s} = 0.075$
k_e° [BTU-ft / HR-ft²-°F]
VOID FRACTION ε'

Fig. 13. Comparison of calculated and experimental data for sintered porous copper-tin alloy.

transfer through the contact surfaces of the consolidated particles. This parameter is a specific property of the consolidation state and the solid phase. Values of 0.2 to 0.3 satisfactorily explained available data for sandstone, but smaller values were necessary for sintered metal particles, reflecting the larger thermal conductivity of the metallic solid phase. The theoretical development satisfactorily correlated data for a variety of fluid and solid materials over a range of void fraction.

In future work it is planned to extend the same method of approach to consolidated beds filled with moving fluid.

ACKNOWLEDGMENT

The authors wish to express their appreciation to The Technological Institute, Northwestern University, for its financial assistance in carrying on this study.

NOTATION

D_p = diameter of unconsolidated particles in a packed bed or diameter of original particles before clogging in consolidated porous media, ft.

h_p = heat transfer coefficient representing the heat transfer rate through the contact surface between solid particles in a bed of unconsolidated particles or between two clogged particles in a consolidated bed, B.t.u./(hr.)-(sq.ft.)(°F.)

h_{rs} = heat transfer coefficient for thermal radiation, solid surface to solid surface, B.t.u./-(hr.)(sq.ft.)(°F.)

h_{rv} = heat transfer coefficient for thermal radiation, void space to void space, B.t.u./(hr.)-(sq.ft.)(°F.)

k_e° = stagnant conductivity, that is effective thermal conductivity of porous media filled with stagnant fluid for both unconsolidated and consolidated particles, (B.t.u.)-(ft.)/(hr.)(sq.ft.)(°F.)

k_g = thermal conductivity of fluid, (B.t.u.)(ft.)/(hr.)(sq.ft.)-(°F.)

k_s = thermal conductivity of solid phase, (B.t.u.)(ft.)/(hr.)-(sq.ft.)(°F.)

ΔL = effective length between centers of two neighboring solid particles in direction of heat flow, ft.

l_s = effective length of a solid particle for heat transfer in a bed of unconsolidated particles, ft.

l_s' = effective length of a clogged particle for heat transfer in a bed of consolidated particles, ft.

l_v = effective thickness of the fluid film adjacent to the surface of two solid particles, ft.

N = number of solid particles in a unit length of packed bed, measured in the direction of heat flow

N' = number of clogged particles in a unit length of consolidated porous media, measured in the direction of heat flow

n = number of contact points on a semispherical surface of one solid particle

q = heat flow rate, B.t.u./hr.

q_s = heat flux through solid phase, B.t.u./hr.-sq.ft.

R = radius of solid particle, ft.

t = temperature, °F.

Δt = increment of temperature, °F.

x_0 = diameter of sectional area corresponding to one contact point, ft.

Greek Letters

$\beta = \Delta L/D_p$

$\gamma = l_s/D_p$

$\phi = l_v/D_p$

ϕ_1 = ϕ value corresponding to the loose or most open packing of spheres

ϕ_2 = ϕ value corresponding to the closest packing of spheres

$\kappa = k_s/k_g$

ϵ = void fraction of a packed bed of unconsolidated particles

ϵ_1 = void fraction corresponding to the most open packing arrangement

ϵ_2 = void fraction corresponding to the closest packing arrangement

ϵ' = void fraction of a bed of consolidated porous media

θ = angle, radians

θ_0 = angle corresponding to boundary of heat flow area for one contact point, radians

LITERATURE CITED

1. Argo, W. B., and J. M. Smith, *Chem. Eng. Progr.*, **49**, 1977 (1953).
2. Asaad, T., Ph. D. thesis, Univ. Calif., Berkeley (June, 1955).
3. Birch, F., and H. Clark, *Am. J. Sci.*, **238**, 529 (1940).
4. Bunnell, D. G., H. B. Irvin, R. W. Olson, and J. M. Smith, *Ind. Eng. Chem.*, **41**, 1977 (1949).
5. Calderbank, P. H., and L. A. Pogorski, *Trans. Inst. Chem. Engrs. (London)*, **35**, 195 (1957).
6. Campbell, J. M., and R. L. Huntington, *Petrol. Refiner*, **31**, 123 (1952).
7. Clark, H., *Trans. Am. Geophys. Union*, 543 (1941).
8. Clyde, O., Jr., *Ind. Eng. Chem.*, **47**, 356 (1955).
9. Coberly, C. A., and W. R. Marshall, Jr., *Chem. Eng. Progr.*, **47**, 141 (1951).
10. Eucken, A., *Forsch. Gebiete Ingenieurw.*, **133**, *Forschungsheft*, No. 353, 16 (1932).
11. Felix, J. R., and W. K. Neil, unpublished paper.
12. Francl, J., and W. D. Kingery, *J. Am. Ceram. Soc.*, **37**, 99 (1954).
13. Gemant, A., *J. Appl. Phys.*, **21**, 750 (1950).
14. Gore, D. E., and B. J. Fulker, *Status Rep. Am. Petrol. Inst.* (Aug. 1, 1957 to July 31, 1958).
15. Grootenhuis, D., R. C. A. Mackworth, and U. A. Saunder, *Inst. Mech. Engrs. (London)*, 363 (1951).
16. Harbert, W. D., D. C. Cain, and R. L. Huntington, *Ind. Eng. Chem.*, **33**, 257 (1949).
17. Hatta, S., and S. Maeda, *Chem. Eng. (Japan)*, **12**, 56 (1948); **13**, 79 (1949).
18. Hougen, J. O., and E. L. Piret, *Chem. Eng. Progr.*, **47**, 287 (1951).
19. Kannuluick, W. G., and L. H. Martin, *Proc. Roy. Soc. (London)*, **A141**, 144 (1933).
20. Kimura, M., *Chem. Eng. (Japan)*, **21**, 472 (1957).
21. Kling, G., *Forsch. Gebiete Ingenieurw.*, **9**, 28, 82 (1938).
22. Kwong, S. S., and J. M. Smith, *Ind. Eng. Chem.*, **49**, 894 (1954).
23. Loeb, A. L., *J. Am. Ceram. Soc.*, **37**, 96 (1954).
24. Maeda, S., and K. Kawazoe, *Chem. Eng. (Japan)*, **15**, 5, 9, 312 (1951); **17**, 276 (1953); **18**, 279 (1954).
25. Morales, M., C. W. Spinn, and J. M. Smith, *Ind. Eng. Chem.*, **43**, 226 (1951).
26. Molino, D. F., and J. O. Hougen, *Chem. Eng. Progr.*, **48**, 147 (1952).
27. Niven, C. D., *Can. J. Research*, **18**, 132 (1940).
28. Plautz, D. A., and H. F. Johnstone, *A.I.Ch.E. Journal*, **1**, 193 (1955).
29. Preston, F. W., Ph.D. thesis, Penn. State Univ., State College (June, 1957).
30. Quinton, J. H., and J. A. Storrow, *Chem. Eng. Sci.*, **5**, 245 (1956).
31. Ranz, W. E., *Chem. Eng. Progr.*, **48**, 247 (1952).
32. Russell, H. W., *J. Am. Ceram. Soc.*, **18**, 1 (1954).
33. Saito, T., and O. Okagaki, *Bull. Fac. Eng., Hokkaido Univ.*, No. 14, 83 (1956).
34. Schneider, W. G., *Ind. Eng. Chem.*, **46**, 828 (1954).
35. Schuler, R. W., V. P. Stallings, and J. M. Smith, *Chem. Eng. Progr. Symposium Ser. No. 4*, **48** (1952).
36. Schumann, T. E. W., and V. Voss, *Fuel*, **13**, 249 (1934).
37. Singer, E., and R. H. Wilhelm, *Chem. Eng. Progr.*, **46**, 343 (1950).
38. Stricker, H. S., *J. Chem. Phys.*, **20**, 1333 (1952).
39. Verschoor, H., and G. Schuit, *Appl. Sci. Research*, **42**, A297 (1950).
40. Waddams, A. L., *J. Soc. Chem. Ind.*,

63, 337 (1944); *Chem. & Ind. (London)*, 206 (1944).
41. Webb, J., *Nature*, **177**, 989 (1956).
42. Weiniger, J. L., and W. G. Schneider, *Ind. Eng. Chem.*, **43**, 1229 (1951).
43. Wilhelm, R. H., W. C. Wynkoop, and D. W. Collier, *Chem. Eng. Progr.*, **44**, 105 (1948).
44. Woodside, W., *Can. J. Phys.*, **36**, 815 (1958).
45. Yagi, Sakae, and Daizo Kunii, *Chem. Eng. (Japan)*, **18**, 576 (1954); *A.I.Ch.E. Journal*, **3**, 373 (1957).
46. ———, *A.I.Ch.E. Journal*, to be published.
47. ———, and Y. Shimoura, *Chem. Eng. (Japan)*, **21**, 342 (1952.
48. ———, and N. Wakao, *A.I.Ch.E. Journal*, to be published.
49. Yagi, S., and N. Wakao, *A.I.Ch.E. Journal*, **5**, 79 (1959).
50. Zierfuss, H., and G. Vliet, *Bull. Am. Assoc. Petrol. Geologists*, **40**, No. 10, 2475 (1958).

Manuscript received June 5, 1959; revision received July 17, 1959; paper accepted August 3, 1959. Paper presented at A.I.Ch.E. San Francisco meeting.

Hypothetical Standard States and the Thermodynamics of High-Pressure Phase Equilibria

J. M. PRAUSNITZ

University of California, Berkeley, California

Thermodynamic analysis of phase-equilibrium data is necessary for testing such data, for extension to new conditions, and for purposes of correlation and prediction of phase-equilibrium behavior. While such analysis is common for low-pressure systems, it is rare for high-pressure systems owing to difficulties encountered in the definition of standard states. For a gaseous solute in the liquid phase it is proposed that the standard state be taken as the hypothetical liquid at the temperature and total pressure of the solution. The properties of this standard state are specified by the temperature and total pressure and by the specific volume which the substance would have if it did not experience a phase change. This standard state is useful since it is not a function of the solution but only of the substance being considered. For a condensable component in the gas phase it is convenient for most purposes to define the standard state as the ideal gas at the temperature and total pressure of the solution, but to separate the effect of composition on the activity coefficient from that of pressure, it is proposed to define the standard state as the real hypothetical gas at the solution conditions. To illustrate these ideas, activity coefficients are computed for several high-pressure systems, and it is shown how these activity coefficients may be used in the correlation, testing, and extension of high-pressure phase-equilibrium data.

Thermodynamic analysis of phase-equilibrium data is needed for testing and correlating such data and especially for extension to new conditions and to other systems for which no data are available. It is not reasonable to expect that good data for a very large number of systems will ever be obtained over wide ranges of temperature and pressure, and it is therefore essential that available data for representative systems be carefully scrutinized and interpreted with the aid of suitable thermodynamic functions. Such thermodynamic analysis, coupled with the theory of intermolecular forces and aided by techniques like the molecular theory of corresponding states, forms the basis for a useful generalization of phase-equilibrium data. The primary justification for thermodynamic analysis is that it is the first important step toward the ultimate aim of solution theory: prediction of the properties of a mixture from those of the pure components.

In the technical literature it has been customary to subject to thermodynamic analysis equilibrium data for solutions taken at or near atmospheric pressure, but there has been a notable absence of such analyses for phase-equilibrium data obtained at higher pressures in the vicinity of 100 atm. or more. For example some of the excellent experimental studies of Sage and Lacey and W. B. Kay and their co-workers on hydrocarbon mixtures have been in the literature for many years but have received very little thermodynamic scrutiny. A major reason for the lack of thermodynamic attention to high-pressure systems is that when the customary thermodynamic functions of the high-pressure mixture are referred to those of the pure components, these components exist in physically unattainable (hypothetical) states. Thermodynamic analysis of high-pressure systems therefore requires precise definitions of hypothetical standard states as well as methods of evaluating the thermodynamic functions corresponding to those states. This paper presents techniques for the calculation of hypothetical standard-state functions and in a few examples illustrates their applicability to thermodynamic analysis of high-pressure phase equilibria.

STANDARD STATES

The activity coefficient of a compo-

nent is defined as the ratio of the activity of that component to its mole fraction; the activity in turn is defined as the ratio of the fugacity of that component in the solution to its fugacity in some standard (arbitrary) state. An activity coefficient therefore always refers to some standard state, and the numerical value of an activity coefficient is meaningless unless the standard state is also specified. While the choice of a standard state is completely arbitrary, it has been customary to use as standard states either the pure component (in the same state of aggregation as that of the solution) or the state corresponding to infinite dilution; in addition, Mauser and Kortüm (7) recently showed that for sparingly soluble solutes it is convenient to use the state corresponding to saturation. These three standard states, designated respectively by *a*, *b*, and *c*, all serve the same function of normalization whereby the activity coefficient approaches a definite limit as the standard state is approached:

$$\begin{aligned} &(a) \quad \gamma_i \to 1 \text{ as } x_i \to 1 \\ &(b) \quad \gamma_i \to 1 \text{ as } x_i \to 0 \end{aligned} \qquad (1)$$

$$(c) \quad \gamma_i \to \frac{1}{x_i} \text{ as } x_i \to x_i \quad \text{(saturated)}$$

Normalization (*a*), sometimes called the symmetric convention, is most commonly used for solutions of liquids at low pressures; normalization (*b*), sometimes called the *unsymmetric convention*, is used for solutions of electrolytes in liquids; normalization (*c*) is useful only in equilibria where one of the phases is a pure component. From the viewpoint of classical thermodynamics all three standard states are equally acceptable, but from the viewpoint of the theory of solutions standard state (*a*) is highly preferable to the other two. The activity coefficient of a component shows the effect of composition on the activity of that component relative to its activity in the standard state; since the aim of solution theory is to predict the properties of components in solution from those of the pure components, the most meaningful standard state is necessarily the pure component itself. When standard states (*b*) or (*c*) are used, the activity coefficient gives information about the activity relative to that at some other concentration; in other words in cases (*b*) and (*c*) the standard state is itself a function of the solution. While standard states (*b*) and (*c*) have certain mathematical advantages which appeal to the pure thermodynamicist, for chemical engineering purposes standard state (*a*) is by far the most useful since it is consistent with the aim of correlating and predicting the thermodynamic properties of solutions. Of the three types of standard states, method (*a*) alone permits meaningful comparisons to be made of the activity coefficient of a given solute in different solvents. Unfortunately, however, using the pure material for the standard state frequently necessitates the use of physically unattainable or hypothetical standard states.

HYPOTHETICAL STANDARD STATES

When a gaseous light component is dissolved in a heavier liquid component, and if the symmetric convention is to be used, the standard state of the gaseous solute is the pure solute as a hypothetical liquid at the temperature of the liquid solution. Similarly the standard state for a heavy component dissolved in a gaseous light component is the pure solute as a gas at the temperature of the gaseous solution; if the standard state is taken at the total pressure of the solution and if that pressure exceeds the vapor pressure of the heavy component, then that component cannot exist as a gas and hence the standard state is hypothetical. In each case, that is in gaseous and in liquid solution, it is desirable to have as the standard state the pure material in the same state of aggregation (gas or liquid) as that of the solution to which it refers. How are the properties of the hypothetical standard states to be computed? Any method is necessarily somewhat arbitrary, but some methods appear to be physically more reasonable than others. The difference between a gas and a liquid is indicated by the size of the specific volume. Hence in specifying the properties of a hypothetical liquid or a hypothetical gas it seems most reasonable to specify the volume which, together with the temperature, is sufficient to compute all other properties. Thus the fugacity of a hypothetical standard state is fixed by the temperature of the pure material (which must be the same as that of the solution) and by its specific volume, which can be determied by a reasonable extrapolation and which is subject only to the restriction that $\gamma_i \to 1$ as $x_i \to 1.0$.

CONDENSABLE COMPONENTS IN THE GAS PHASE

A gaseous solution containing one light component and one heavy component is considered. The activity coefficient of the heavy component in the gaseous solution is given by

$$\gamma_h = \overline{f}_h / y_h f_h^\circ \qquad (2)$$

The pressure to which f_h° refers is arbitrary. It has therefore been customary in many cases to use as the reference state the ideal hypothetical vapor at the total pressure, in which case f_h° is equal to the total pressure. Then the

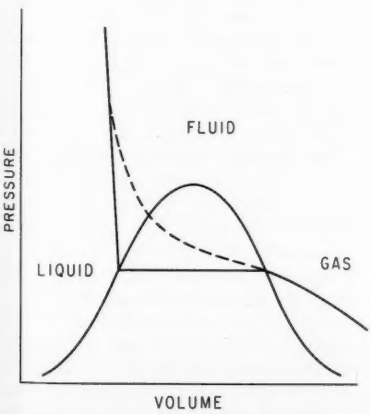

Fig. 1. Isotherm for hypothetical gas.

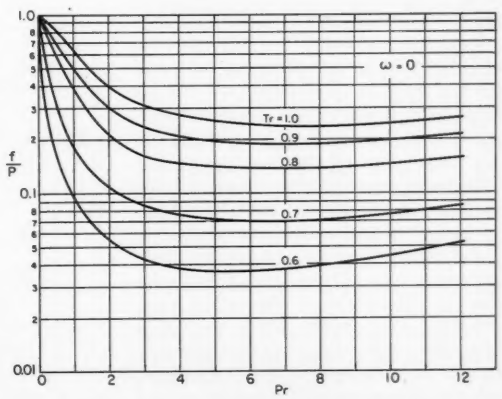

Fig. 2. Fugacity coefficients for hypothetical gases.

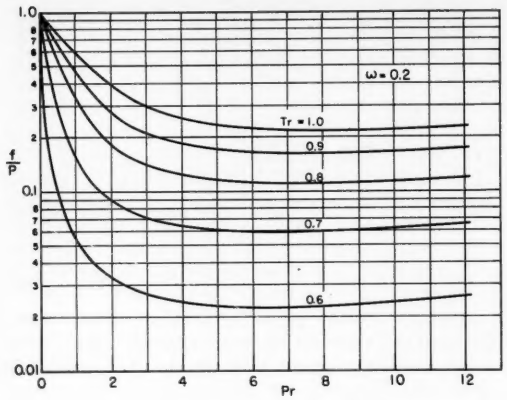

Fig. 3. Fugacity coefficients for hypothetical gases.

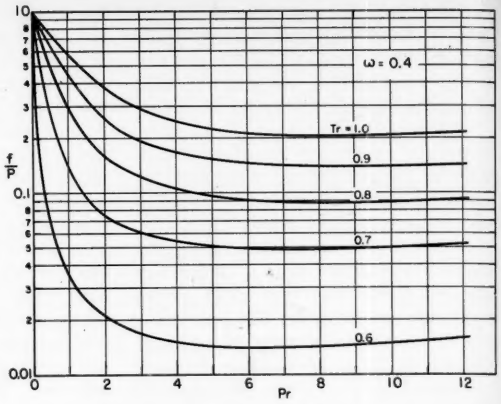

Fig. 4. Fugacity coefficients for hypothetical gases.

activity coefficient is really a fugacity coefficient defined by

$$\phi_h = \frac{\overline{f}_h}{y_h P} \qquad (3)$$

For most calculational purposes the fugacity coefficient is perfectly satisfactory. It performs the important function of relating the fugacity of a component in the gas phase to its mole fraction, and thus it takes care of half the problem in phase equilibria. (The other half, of course, is to use a similar coefficient for performing the same function for the liquid phase.) However while ϕ is very useful, its physical significance is less clear than that of γ, because the fugacity coefficient is really the product of two terms, each of which has a separate physical significance; the relationship between the activity coefficient and the fugacity coefficient is

$$\phi = v\gamma \qquad (4)$$

where $v = f/P$ for the pure component in the standard state.

As indicated by Equation (4), the fugacity coefficient ϕ is a single factor which takes into account deviations from ideality of the pure component (due to pressure) and deviations from ideal solution (due to the presence of a second component). ϕ can readily be calculated from an equation of state for the gaseous mixture (*1, 8*). To interpret its physical meaning, however, it is sometimes desirable to separate the nonideality effects due to nonideal solution from those due to nonideality of the pure vapor. In that case it is necessary to use as the standard state the pure hypothetical vapor at the temperature and total pressure of the solution. If the activity coefficient of component h is to reflect solely the effect of solution with the other component l, then it is necessary to have the limiting relation at constant temperature $\gamma_h \to 1$ as $y_h \to 1$ and to have the pressure to which f_h° refers be the total pressure of the solution. If that pressure is greater than the vapor pressure of the heavy component, then the reference state is a hypothetical one, since pure vapor h cannot exist at a pressure exceeding the vapor pressure. The calculation of hypothetical f_h° is necessarily arbitrary, but a reasonable procedure is to compute it in such a way as to reflect the properties that the heavy component would have if instead of condensing at the vapor pressure it remained a vapor. This calculation is best performed by continuing the gas-phase isotherm on a pressure vs. volume diagram through the two-phase region to the liquid portion of the isotherm in a manner shown schematically in Figure 1. At high pressures there is no distinction between gas and liquid, both states of aggregation being designated by the word *fluid*. At high pressures, therefore, the extrapolated hypothetical gas isotherm must become identical with the real liquid isotherm. While this fact does not uniquely determine the shape of the extrapolated isotherm, it gives at least some direction on how such an isotherm may be reasonably constructed. Once this hypothetical isotherm is available, the fugacity at any pressure is computed from

$$\ln f/P = \int_0^P \left(\frac{Pv}{RT} - 1 \right) \frac{dP}{P} \qquad (5)$$

Hypothetical gas-phase fugacities have been calculated in the manner described for several representative nonpolar gases having different acentric factors and the results plotted on reduced coordinates for different ω. Figures 2, 3, and 4 give the fugacities of hypothetical gases as a function of reduced temperature, reduced pressure, and acentric factor. These charts are quite different from those presented earlier by Hougen and Watson and others (*2, 13*). The earlier charts were extrapolated by use of gas-phase equilibrium data; hence they include a generalized composition effect. Such an effect cannot of course be generalized in terms of the properties of the condensable solute alone. The charts presented here do not include composition effects but are based only on pure-component extrapolations. Hence they serve merely as a basis for calculating gas-phase activity coefficients. Fugacities calculated from these charts should never be used for the prediction of phase equilibria unless it is also possible to estimate γ [see Equation (1)]. The assumption that $\gamma = 1$ (Lewis fugacity rule) can lead to very large errors. (*8*).

The fugacity as calculated from Figures 2, 3, or 4 refers to the fugacity that a substance would have if it existed in the pure state as a vapor at the prescribed conditions of temperature and pressure. As an illustration of the physical significance of this fugacity, the fugacity of hypothetical decane vapor at 75°C. and 60 atm. (the vapor pressure of decane at 75°C. is 0.0329 atm.) is considered. The fugacity coefficient of decane in various gaseous solvents has been measured experi-

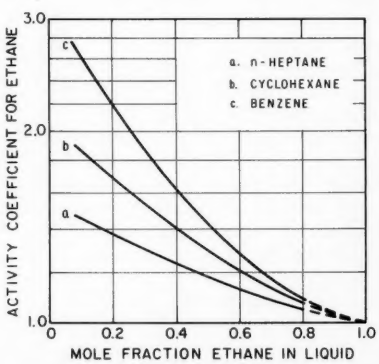

Fig. 5. Liquid-phase activity coefficient for ethane in three systems at 168°F.

mentally (9); in hydrogen it is 1.45, in nitrogen 0.620, and in carbon dioxide 0.231. These data indicate that the fugacity coefficient falls with the molecular weight of the gaseous solvent. Therefore it is to be expected that the fugacity coefficient for pure decane is much less than unity. From the generalized charts it is estimated to be 0.012.

Once f/P for the pure hypothetical vapor is known, γ_h can be calculated from Equation (4). For decane in hydrogen, nitrogen, and carbon dioxide at 75°C. and 60 atm. the activity coefficients are, respectively, 121, 51.6, and 19.3.

For most computational purposes the fugacity coefficient ϕ is satisfactory, and it is not necessary to calculate γ. It is only when one wishes to compare the effect of different gaseous solvents that it is instructive to separate ϕ into the pressure and into the composition effect. For example it is sometimes found at advanced pressure (especially in systems containing hydrogen) that ϕ is close to unity. One might therefore erroneously conclude that the gas phase is ideal. In fact, however, it is not ideal at all, but because of two compensating nonidealities ($\nu<<1$ and $\gamma>>1$) the over-all effect gives an apparent ideality.

GASEOUS SOLUTES IN THE LIQUID PHASE

The hypothetical standard-state fugacity of a gaseous solute is determined by the temperature and pressure of the solution and by the molar liquid volume of the pure solute. Several estimates of this volume may have to be made before the right one is found; the test is only that upon extrapolation $\gamma_i \to 1$ as $x_i \to 1$. Once it is found, however, it can be used for that solute in all solvents, since the standard state as used here is a function only of the pure material and not of the solution.

To fix ideas, the binary data at 75°C. for ethane in benzene, cyclohexane and *n*-heptane reported by Kay and co-workers (*5, 4, 6*) are considered. The activity coefficient of the ethane, given by γ_e, must for all three cases obey the relation $\gamma_e \to 1$ as $x_e \to 1$. The activity coefficient is given by

$$\gamma_e = \frac{\bar{f}_e}{x_e f_e^\circ} \qquad (6)$$

The pressure of the standard state is arbitrary, but it is convenient to choose the total pressure as the standard-state pressure. In that case f_e° is the fugacity of pure (hypothetical) ethane liquid at the temperature and total pressure of the solution. The system temperature, 75°C., is well above the critical

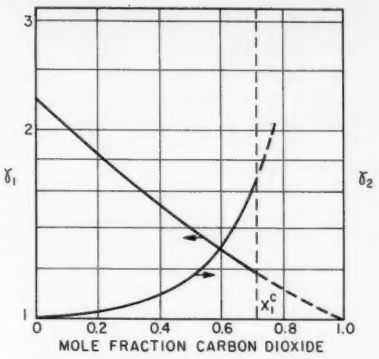

Fig. 6. Activity coefficients for carbon dioxide (1)—butane (2)—system at 160°F.

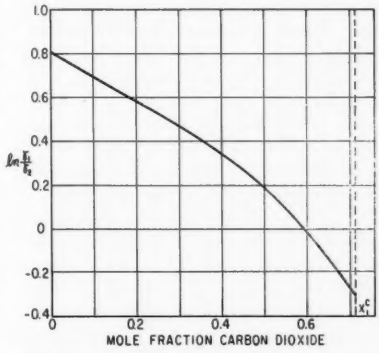

Fig. 7. Activity-coefficient ratio vs. composition for carbon dioxide-butane system at 160°F.

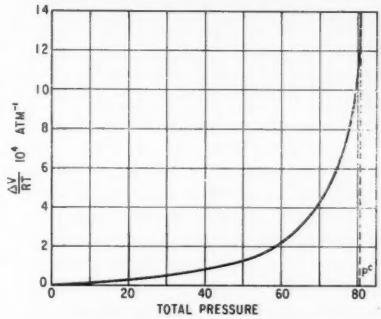

Fig. 8. Volume change vs. pressure for carbon dioxide-butane system at 160°F.

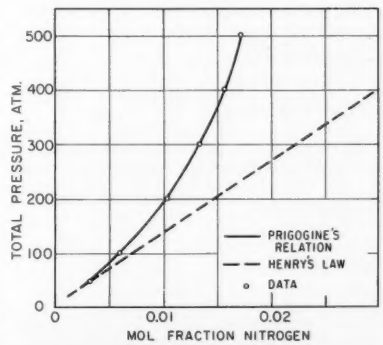

Fig. 9. Solubility of nitrogen in liquid ammonia at 0°C.

for ethane. To determine the fugacity of pure liquid ethane, therefore, it is necessary to specify the molar volume which ethane would have at 75°C. if instead of becoming a gas it had remained a liquid. This can be estimated from the volumetric data for pure ethane at lower temperature. If the volume estimated is v_e, then the standard-state fugacity is found by

$$f_e^\circ = f(v_e, T) \exp \frac{v_e(P - P_e^\circ)}{RT} \qquad (7)$$

In this case the hypothetical standard state is considered to be pure, incompressible ethane at the volume and the temperature. The properties $f(v_e, I)$ and P_e° are found from a Mollier diagram for pure ethane. The check on having chosen the right value for v_e is the condition that when $\ln \gamma_e$ is extrapolated to $x_e = 1$, the extrapolation leads to $\ln \gamma_e = 0$.

The results of such calculations for ethane in three solvents are shown in Figure 5. In these calculations $v_e = 84$ cc./g.-mole. This value was found by extrapolating with respect to temperature the molar liquid volumes of ethane in the vicinity of the normal boiling point where its molar volume is 55 cc./g.-mole. Figure 5 shows that the activity coefficient of ethane in all three solvents tends to unity as pure ethane is approached. Since the activity coefficient is a measure of the unlikeness between solute and solvent, one would expect a definite trend in the activity coefficients of ethane in the three solvents. As expected, the activity coefficient of ethane is highest in the aromatic and lowest in the paraffinic solvent, the results for the naphthenic solvent falling between these two. From these results it would not be difficult to make good predictions of the activity of ethane in other hydrocarbon solvents at 75°C.

GIBBS-DUHEM EQUATION AND THERMODYNAMIC CONSISTENCY

In a binary system at constant temperature it is not possible to vary the composition without also changing the total pressure. The Gibbs-Duhem equation for an isothermal binary system is (*3*)

$$x_1 \frac{\partial \ln \gamma_1}{\partial x_1} = x_2 \frac{\partial \ln \gamma_2}{\partial x_2} + \frac{\Delta v}{RT} \frac{\partial P}{\partial x_1} \qquad (8)$$

where the volume change is given by

$$\Delta v = v(\text{mixture}) - x_1 v_1^\circ - x_2 v_2^\circ$$

In condensed phases at low pressures the last term on the right-hand side of Equation (8) is negligible compared with the other terms. At high pressures, however, this last term is important and may not be neglected, especially when tests for thermodynamic

consistency are applied. The most useful test is that proposed by Redlich and Kister (*11*), who define a function Q

$$Q \equiv x_1 \ln \gamma_1 + x_2 \ln \gamma_2 \qquad (9)$$

In the symmetric convention $Q = 0$ at $x_1 = 0$ and $x_2 = 0$.

Differentiating Q with respect to x_1 and substituting

$$x_1 \frac{\partial \ln \gamma_1}{\partial x_1} = x_2 \frac{\partial \ln \gamma_2}{\partial x_2} \qquad (10)$$

Redlich and Kister obtain

$$\int_0^1 \ln \gamma_1/\gamma_2 \, dx_1 = 0 \qquad (11)$$

For high-pressure systems, however, Equation (8) must be used instead of Equation (10). Also it is not possible to integrate the activity coefficients from $x_1 = 0$ to $x_1 = 1$, since high-pressure systems will show a critical point $0 < x_1^c < 1$. The test for thermodynamic consistency for high-pressure systems therefore is

$$\int_0^{x_1^c} \ln \gamma_1/\gamma_2 \, dx_1 + \int_{P(x_1=0)}^{P^c} \frac{\Delta v}{RT} dP = x_1^c \ln \gamma_1^c + x_2^c \ln \gamma_2^c \qquad (12)$$

This test for thermodynamic consistency is illustrated with data for the carbon dioxide–butane system at 160°F. reported by Sage and Lacey (*12*). The critical temperature of carbon dioxide is 87.8°F.; the standard state for carbon dioxide in the liquid phase is therefore hypothetical. If the standard state for carbon dioxide is taken as the hypothetical incompressible liquid at 160°F. with a volume of 71 cc./g.-mole, the activity coefficient γ_1 of carbon dioxide obeys the relation $\gamma_1 \to 1$ as $x_1 \to 1$. Activity coefficients for this binary system are shown in Figure 6. Since Sage and Lacey also reported volumetric data for the liquid solution, it is a simple matter to calculate the volume change, which is small for low carbon dioxide concentrations but becomes large near the critical point. Figure 7 shows a plot of $\ln \gamma_1/\gamma_2$ vs. x_1 for the range $x_1 = 0$ to the critical point which occurs at $x_1^c = 0.713$. Figure 8 gives a plot of $\Delta v/RT$ vs. the pressure up to the critical point. From the areas under these plots the values of the integrals in Equation (12) are found. The left-hand side of Equation (12) gives a value of 0.2708; the right-hand side has a value of 0.2690. The thermodynamic consistency of these data is therefore very good.

EFFECT OF PRESSURE ON GAS SOLUBILITY

The effect of pressure on the solubility of a gas in a liquid is commonly expressed in the form of Henry's law, which states that the partial pressure of a gas is proportional to the mole fraction of the solute in the liquid solvent. Henry's law is essentially equivalent to assuming that the activity coefficient of the solute is a constant independent of the composition of the liquid solution. While Henry's law is frequently a very good approximation, better results can sometimes be obtained by making a more reasonable assumption about the variation of activity coefficient with solute concentration. To do this it is necessary to utilize some technique, such as that discussed above, for computing activity coefficients of gaseous solutes. To illustrate, one should consider the nitrogen-ammonia system at 0°C. The solubility of nitrogen in liquid ammonia at 0°C. and 50 atm. is $x_{s_2} = 0.0031$. It is desired to predict the solubility of nitrogen in ammonia at higher pressures up to 500 atm. First the activity coefficient of nitrogen in the liquid ammonia at 50 atm. is computed with a standard state hypothetical liquid nitrogen at a temperature of 0°C. and a volume of 79 cc./g.-mole. Second it is necessary to utilize some suitable expression for the variation of activity coefficient with mole fraction. It has been shown by Prigogine and Defay (*10*) that for dilute solutions of a nonpolar substance in an associating solvent the activity coefficient is given by

$$\gamma_1 = \frac{1}{\frac{x_2}{\Psi_2} + x_1} \qquad (13)$$

Using the previously calculated activity coefficient at 50 atm. one can evaluate Ψ_2. Equation (13), coupled with the excellent assumption that Ψ_2 does not change over the concentration interval considered here, is then used to predict the solubility at higher pressures. The results, shown in Figure 9, are compared with Henry's law and with the experimental data of Wiebe and Gaddy (*12*). In this case Henry's law leads to appreciable error in the pressure range above 200 atm.

ACKNOWLEDGMENT

The author is grateful to the donors of the Petroleum Research Fund administered by the American Chemical Society for financial support.

NOTATION

f = fugacity
f_h° = fugacity of pure heavy component as a vapor at the temperature of the solution and at a fixed pressure
f_e° = fugacity of pure (hypothetical) ethane liquid at the temperature of the solution and at a fixed pressure
P = total pressure
Q = defined by Equation (8)
R = gas constant
T = absolute temperature
v = molar volume
x_i = mole fraction of species i in the liquid phase
y_i = mole fraction of species i in the gas phase
γ_i = activity coefficient of species i

Greek Letters

ϕ = fugacity coefficient
Δv = volume change
ν = fugacity coefficient for the pure component
Ψ = average degree of association
ω = acentric factor

Superscripts

$-$ (bar) = component in solution
o = standard state
* = equilibrium
c = critical

Subscripts

h = heavy component
e = ethane
l = light component

LITERATURE CITED

1. Comings, E. W., "High Pressure Technology," Chap. 8, McGraw-Hill, New York (1956).
2. Hougen, O. A., and K. M. Watson, "Chemical Process Principles," Vol. 2, John Wiley, New York (1947).
3. Ibl, N. V., and B. F. Dodge, *Chem. Eng. Sci.*, **2**, 120 (1953).
4. Kay, W. B., and R. E. Albert, *Ind. Eng. Chem.*, **48**, 422 (1956).
5. Kay, W. B., and T. D. Nevens, *Chem. Eng. Progr. Symposium Ser. No. 3*, **48**, 108 (1952).
6. Kay, W. B., *Ind. Eng. Chem.*, **30**, 459 (1938).
7. Mauser, Heinz, and Gustav Kortüm, *Z. Naturforsch.*, **10a**, 42 (1959).
8. Prausnitz, J. M., *A.I.Ch.E. Journal*, **5**, 3 (1959).
9. ———, and P. R. Benson, *ibid.*, 161.
10. Prigogine, Ilya, and Raymond Defay, "Chemical Thermodynamics," p. 413, Longmans, Green and Company, London, England (1954).
11. Redlich, Otto, and A. T. Kister, *Ind. Eng. Chem.*, **40**, 345 (1948).
12. Sage, B. H., and W. N. Lacey, "Some Properties of the Lighter Hydrocarbons, Hydrogen Sulfide and Carbon Dioxide," American Petroleum Institute, New York (1955).
13. Smith, K. A., and K. M. Watson, *Chem. Eng. Progr.*, **45**, 494 (1949).
14. Wiebe, R., and V. L. Gaddy, *J. Am. Chem. Soc.*, **59**, 1984 (1937).

Manuscript received February 27, 1959; revision received August 12, 1959; paper accepted August 13, 1959.

The Effects of Superheat and Surface Roughness on Boiling Coefficients

H. M. KURIHARA and J. E. MYERS

Purdue University, West Lafayette, Indiana

The effects of liquid superheat and surface roughness on boiling coefficients were investigated in a series of experiments in which water, acetone, *n*-hexane, carbon tetrachloride, and carbon disulfide were boiled on a flat plate. In addition to the usual thermal measurements, the number of active boiling centers was determined, whenever possible, by visual means, and a quantitative measure of surface roughness was made. It was found that the number of active boiling centers on the plate increased with increasing surface roughness and that the calculated boiling coefficients were proportional to the one-third power of the number of bubble columns rising from the heated surface.

An equation has been derived relating boiling coefficients to fluid properties and the number of active boiling centers on a surface. A second equation, based on the theory of thermal fluctuations, has been proposed to relate the number of active boiling centers to the independent variables of surface-roughness and temperature-difference driving force. The limited data available have been found to follow this proposed relation.

The results of this work suggest a quantitative method of relating the boiling coefficient to the character of the surface which may explain the discrepancies observed in the slopes of boiling curves reported in the literature and in the actual values reported for the boiling coefficients measured on different surfaces.

When a liquid boils, vapor bubbles are formed and rise from favored spots on the heated surface. This type of boiling is called *nucleate boiling,* since it suggests the presence of some kind of nuclei at the points where the bubbles are formed. As the temperature of the surface increases, the number of active centers increases. However at high degrees of superheat the surface may produce vapor at such a rate that no active centers can be distinguished. Neither this condition, called *film boiling,* nor the transition zone between nucleate and film boiling was encountered in the present investigation.

It has been generally agreed (*13, 14, 15, 25, 27*) that the high heat transfer rates encountered in nucleate boiling are due primarily to the agitation created by the motion of the bubbles in the superheated liquid adjacent to the heater surface. Hence a knowledge of both bubble dynamics and the factors which determine the concentration of active centers would seem to be essential if the boiling process is to be understood and boiling performance predicted.

The development of a bubble has ben studied theoretically. On the basis of the work of Bashforth (*3*) and Wark (*28*), Fritz (*12*) obtained a semiempirical relationship for the diameter of a bubble breaking off the heating surface which showed good agreement with the experimental results of Jakob (*17*) and Kabanow and Frumukin (*18*). From a photographic study Jakob (*16*) discovered that the product of bubble diameter and the frequency of bubble formation seemed to be constant at small heat fluxes. More recently Perkins and Westwater (*23*) found that, at heat fluxes up to 80% of maximum, the individual terms of bubble diameter and frequency were constant themselves. From this they concluded that the increase in the boiling coefficient with increase in temperature-difference driving force was caused entirely by an increase in the number of active sites on the heating surface.

Early investigations of the effects of surface condition on boiling have been reported by Jakob and Fritz (*15*) and Sauer (*26*). A recent paper by Clark, Strenge, and Westwater (*7*) describes experiments in which pits and scratches in the metal surface were found to provide most of the nucleation sites. No nuclei appeared to be associated with grain boundaries. Nishikawa (*21*) photographed the formation of steam bubbles rising from horizontal heating surfaces fitted with concentric grooves of triangular cross section, their depths ranging from 0.1 to 0.3 mm. He observed a greater number of bubble columns on a rough surface than on a smooth one and found the boiling coefficients to be higher on the rough surface. A large effect of microroughness on the ΔT necessary to sustain nucleate boiling at a given heat flux was shown by Corty and Foust (*8*). They postulated a vapor-trapping mechanism to explain large differences in the slopes and positions of boiling-coefficient curves for surfaces of different roughness. Bankoff (*2*) has derived a theory to determine whether a surface cavity will entrap gas in contact with a liquid.

Attempts have been made by various investigators to obtain a better knowledge of the mechanism with the aid of nucleation theory. LaMer (*20*) and Bernath (*5*) reviewed the theory of Volmer (*27*) and Becker and Döring (*4*) as applied to the formation of vapor bubbles in liquids. Clark (*6*) has extended the kinetic theory of heterophase thermal fluctuations, given by Frenkel (*11*) for nucleus formation, and derived a relation between superheat required for nucleation and liquid properties.

Westwater (*29*) has summarized a number of empirical equations which have been prepared by correlating experimentally measured boiling coefficients. Recently semitheoretical equations proposed by Rohsenow (*24*) and Forster and Zuber (*9*) have met with some success in correlating results. Both equations contain modified Reynolds number groups as well as the conventional Prandtl number. The equation of Rohsenow is based on the observation of a constant product of frequency and bubble diameter as observed by Jakob (*16*). Forster and Zuber (*10*) have derived analytical expressions for bubble radii and growth, and these are employed in their proposed correlation referred to above. The main difference between the two equations is that in Rohsenow's equation the Reynolds number is based on the motion of the bubble when it is on the point of breaking off the heating surface, while in the Forster and Zuber equation the velocity in the Reynolds number term is taken as the rate of radial movement of the bubble wall.

None of the correlations referred to by Westwater contain terms which describe the nature of the heating surface, although many experimental investigations have shown that the condition of the heating surface has a major effect on boiling performance. The reason for this omission is due largely to the difficulty of describing a surface quantitatively. Until the time when the essential elements of a surface which affect boiling can be measured and are related mathematically to boiling performance, it is unlikely that any truly reliable correlation will be developed.

In the present investigation (*19*) the boiling surface was prepared before each run by polishing with emery paper to produce different degrees of roughness. The dimensions of the irregularities produced were then determined by use of a Brush surface analyzer, which recorded surface profiles. Thirty-four

H. M. Kurihara is with Shell Sekiyu Company, Ltd., Tokyo, Japan.

boiling runs were made with water, acetone, *n*-hexane, carbon tetrachloride, and carbon disulfide. The bubble columns rising from the heated surface were counted whenever possible. In addition heat flux and temperatures were measured so that boiling coefficients might be calculated. A mechanism to explain how surface roughness affects bubble formation has been postulated and a correlation found relating the number of active boiling centers to the distribution and size of the protuberances on a surface.

EXPERIMENTAL APPARATUS

The heater, shown in Figure 1, consisted of a copper cylinder 3 in. in diameter. Boiling took place on the upper surface of the cylinder, and the heat was supplied to seven copper fins (¼ in. thick and 2 in. high) which were welded to the bottom of the cylinder. The 1/5-in. spaces between the fins contained heating elements made by wrapping nichrome ribbon on a mica core. The elements were connected in series and had a total resistance of 15 ohms. A 5-in. O.D. stainless steel skirt (A.I.S.I. No. 301) was silver-soldered around the top of the copper cylinder to give a continuous nonboiling surface next to the surface on which boiling was taking place. The cylinder and skirt were then machined until the skirt was reduced to a thickness of 1/16 in. and the junction between copper and stainless steel was as free from irregularities as possible.

Figure 2 shows the location of the thermocouples. Three thermocouples were located ⅛ in. below the heating surface at various distances from the axis of the heater. Three others were placed ⅜ in. directly beneath the first three couples. Four thermocouples were fastened under the stainless steel skirt to determine its temperature gradient during operation.

Boiling took place in an 8-in.-diameter inverted glass bell jar 11 in. high. The jar was bolted to the top of the heater and sealed by a Teflon-jacketed sponge-rubber gasket as shown in Figure 3. An immersion heater consisting of a resistance wire inserted in a 6-mm. glass tube circled the periphery of the heater to help maintain a constant bulk liquid temperature over the heating surface during runs at low heat loads.

All the thermocouples employed were calibrated against a standard N.B.S. thermometer in an oil bath. Temperatures were recorded to 0.1°C. Power for the heater was obtained from a single-phase 220-v. a.c. source. Heat input was determined with two wattmeters to cover the range of 0 to 4,000 w. Voltage and current were checked with a 300-v. voltmeter and a 25-amp. ammeter.

Roughness of the heating surface was measured before and after each run by a Brush Surfindicator Model No. 110, which measures roughness by interpreting the motion of a diamond tip as it travels over a surface (*1,*). The instrument indicated a measure of the roughness in terms of the root-mean-square, but as a more accurate picture of the roughness of the surface was desired, a Brush Model BL-103 Surface Analyzer was also employed (*22*). This latter instrument consists of three parts: a motor-driven pick-up arm, a calibrating amplifier, and a direct-inking oscillograph. A spherical-tip diamond stylus with a tip radius of 0.0005 in. was attached to the crystal in the pick-up, which moved back and forth over the surface in a 10-sec. cycle. The voltage generated in the crystal by the vertical motion of the stylus was amplified, and it actuated the pen motor of the oscillograph so that a record of the surface irregularities encountered by the stylus was obtained on a moving-paper tape. The instrument was set to record in microinches and was calibrated by moving the stylus over a precision scratch on an attached glass standard.

EXPERIMENTAL PROCEDURES AND MEASUREMENTS

The heating surface was polished with six grades of emery paper (4-0, 3-0, 2-0, 0, 1, 2) and boiling measurements were taken for each surface roughness. One additional surface roughness was produced by polishing with 140-mesh carborundum. The emery paper was wrapped around a steel rod ½ in. in diameter and 3½ in. long, and the polishing was done systematically, by rubbing ten strokes in one direction and then ten strokes at an angle of 90 deg. to the initial direction. This procedure was repeated until the surface was considered thoroughly polished and reproducible.

Initially the roughness was measured before and after each run. Later it was found that the surface-roughness measurements did not change during runs with liquids other than water; measurements for these liquids were then made only before runs. Each surface-roughness determination was based on six readings, three being taken in each of the two directions in which the surface was polished.

The boiling vessel was operated with a liquid level just above the reflux return as shown in Figure 3. Because the system used a great deal of heat, it was usually necessary for vigorous boiling to be maintained for 2 hr. before the thermocouples in the system indicated that thermal equilibrium had been reached. When more than one set of measurements was taken during a single period of operation, they were always made by lowering the heat input. Condensate was returned to the system at temperatures as close to saturation as possible, and during operation at low heat loads the ring immersion heater was turned on to keep the bulk of the liquid at saturation temperature.

The measurements taken, in addition to surface-roughness readings, included the following:

1. Liquid bulk temperature was measured with a mercury thermometer placed at the center of the heater ½ in. above the heating surface.
2. Temperatures in the copper cylinder and stainless steel skirt were determined from thermocouples placed as shown in Figure 2.
3. Total heat input was determined from a wattmeter reading of the power supplied to the heater. The heat transfer rate normal to the boiling surface was determined by subtracting the rate of heat transfer through the skirt from the total heat input. The boiling-heat load was checked by condensate measurements and found to agree with a difference less than 5% for all but the lowest heat loads. Skirt losses, which were calculated from the temperatures determined by the thermocouples on the skirt, ranged from 2 to 25%.

During boiling, whenever possible, the

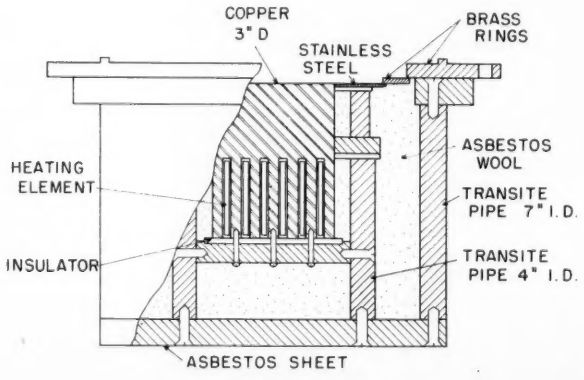

Fig. 1. Heater details.

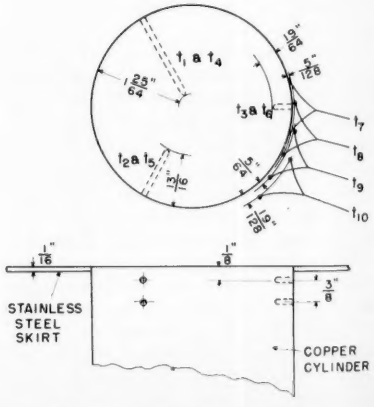

Fig. 2. Locations of thermocouples.

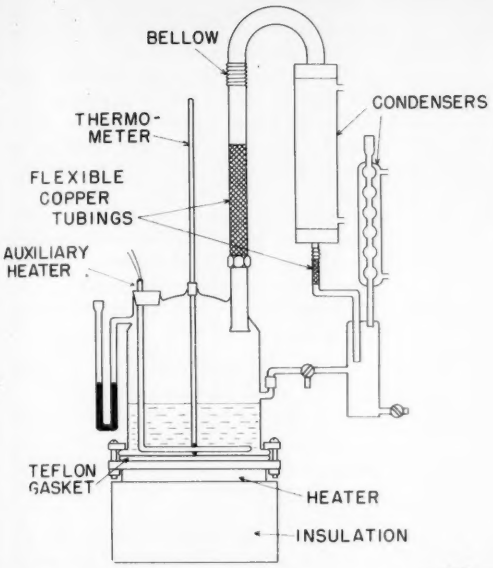

Fig. 3. Boiling apparatus for regular runs.

active boiling sites on the heater surface were counted. Although, the experimental results contain bubble populations as high as 4,000/sq. ft., it should be kept in mind that this figure corresponds to only 196 centers on the 3-in.-diameter heating surface. This was found to be the upper limit at which visual counting could be done. Most of the data however were obtained in the range of 200 to 2,000 centers/sq. ft., which meant counting only ten to one-hundred centers on the heating surface. After a few runs, counting skill was developed, and it was found that in this range the counts were reproducible within 10%.

A sample of the experimental data is shown in Table 1. The temperatures from the respective thermocouples are located as follows:

Thermocouples located in copper cylinder

	Distance from wall, in.	Distance from surface, in.
t_1	1-25/64	1/2
t_2	13/16	1/2
t_3	19/64	1/2
t_4	1-25/64	1/8
t_5	13/16	1/8
t_6	19/64	1/8

Thermocouples attached to stainless steel skirt

	Distance from copper cylinder, in.
t_7	0
t_8	5/128
t_9	5/64
t_{10}	19/128

Surface temperatures on the cylinder, obtained by a linear extrapolation of the temperatures measured in the block, were considered to be accurate within ±0.2°C., and so the error in the resulting temperature-difference driving force was usually less than 2%. The temperature gradient in the skirt adjacent to the copper wall was used to determine the rate of heat dissipation through the skirt as mentioned above.

The heat transfer rate through a differential element of area may be written as

$$dq = h\,\Delta T\,dA \qquad (1)$$

which may be integrated and solved for q if the variation of h and ΔT are known over the surface. A mean heat transfer coefficient may be defined by the equation

$$q = h_m \int_0^A \Delta t\,dA \qquad (2)$$

and a mean driving force by the equation

$$q = h_m A\,(\Delta T)_m \qquad (3)$$

Equations (2) and (3) may be combined to show that

$$\Delta T_m = \frac{\int_0^A \Delta T\,dA}{A} = \int_0^1 \Delta T\,d(r/r_o)^2 \qquad (4)$$

Values of ΔT, calculated with the aid of the data in Table 1, were plotted against $(r/r_o)^2$ as shown in Figure 4. A graphical integration of each curve shown in Figure 4 provided the value of ΔT_m for each corresponding run. This was then used to obtain the mean boiling coefficient for each run as defined in Equation (3). The value used for q in Equation (3) was the electric heat load supplied to the heater minus the calculated skirt loss in each run.

The calculated values of the mean heat transfer coefficients are shown in Figures 5 to 9. The key for identifying the runs is as follows:

1. The alphabetical designations indicate the fluid used—*A*: water, *B*: acetone, *C*: *n*-hexane, *D*: carbon tetrachloride, *E*: carbon disulfide.

2. The Roman numerals indicate the types of polishing paper used in preparing the surface before boiling.

Roman numeral	I	II	III	IV	V	VI	VII
Emery paper	4-0	3-0	2-0	0	1	2	140-mesh carborundum

3. The Arabic numerals indicate different runs with one particular fluid and a single surface condition. For example run *B*-I-2 is the second run made with acetone boiling from a surface polished with 4-0 emery paper.

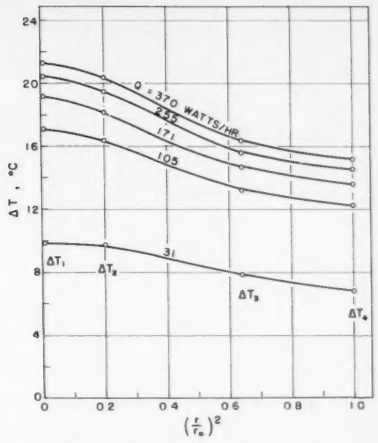

Fig. 4. Temperature difference driving force vs. $(r/r_o)^2$, run *B*-I-2.

The qualitative effects of surface roughness are indicated on Figures 5 to 9. In each case the smoothest surface (obtained with 4-0 emery paper) gave the lowest boiling coefficients. Rougher surfaces gave not only higher boiling coefficients but boiling curves of larger slope, as was also observed by Corty and Foust (8). It also appeared that the effect of roughness on h_m became less pronounced as roughness increased. This implies a roughness limit above which boiling coefficients will not be affected by surface roughness. The order of magnitude of this limit is estimated to be 30 μin. (root-mean square).

A number of runs were reproduced with considerable success, as is shown in Figures 5 and 6. The duplicate runs were made after intervals of 24 hr. to check the possibility of aging of the surface.

During some runs at high heat loads, bubble columns were observed rising from the boundary between the heating surface and the skirt. However this number was estimated to be less than 1% of the number of columns issuing from the remainder of the boiling surface, and so they were neglected. At no time was boiling observed on the stainless steel skirt.

CORRELATION OF RESULTS

Although many equations have been derived relating boiling coefficients with physical properties, they have failed to indicate the effect produced by the surface condition of the heater. Since heat transfer to a boiling liquid seems strongly affected by surface roughness, it was decided to attempt a new correlation which would include both liquid and surface properties.

Heat flux (q/A) was plotted against

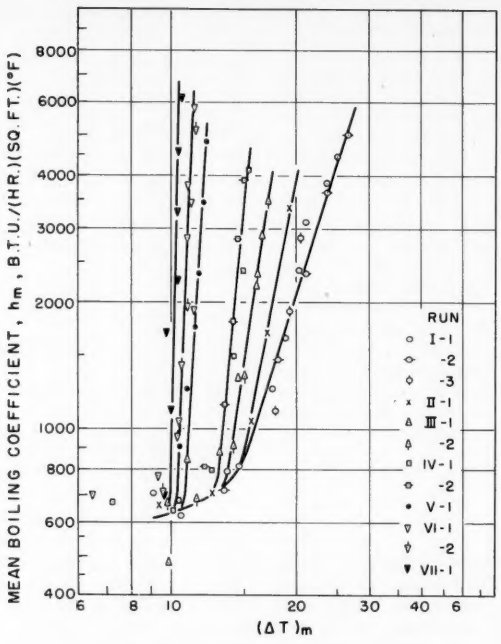

Fig. 5. Boiling curves for water.

the number of active centers, and it was seen that

1. q/A is not proportional to n as Jakob (16) observed but is rather proportional to n^m.
2. A rough surface gives a greater number of bubble columns than a smooth surface at a given heat flux.
3. The exponent m appears to be smaller for a rough surface than for a smooth surface.

As the next step, h_m was plotted against n with the result that h_m was found to be approximately proportional to $n^{1/3}$ for all liquids used and all surface conditions. The majority of the data were obtained for water and acetone; only these results are shown for the different surface conditions in Figure 10. The data at low values of h_m do not follow the above relationship, and it is felt that this may be due to the effect of the additional convection caused by the immersion heater. Although the bell jar was insulated, this heater was necessary to keep the bulk of the liquid at its saturation temperature at low heat loads. It was observed during operation that if this heater was cut off for a short period of time, a number of extra bubble columns appeared on the boiling surface to help dissipate the same heat load.

As the first step in the correlation an attempt was made to relate the boiling coefficient h_m to the number of bubble columns as well as to the physical properties of the liquid. Rohsenow (24) has defined

$$N_{Nu} = \frac{h_m D_b}{k_l}$$

$$N_{Re} = \frac{G_b D_b}{\mu_l}$$

$$N_{Pr} = \frac{C_l \mu_l}{k_l}$$

Combining these groups in the usual form of a dimensionless heat transfer equation gives

$$N_{Nu} = K' N_{Re}^{\ j} N_{Pr}^{\ w} \qquad (5)$$

When one assumes the bubbles to be spheres,

$$G_b = \frac{\pi}{6} D_b^3 \rho_o f n \qquad (6)$$

Substitution in Equation (5) gives

$$\frac{h_m D_b}{k_l} = K' \left(\frac{\pi D_b^4 \rho_o f n}{6 \mu_l} \right)^j \left(\frac{C_l \mu_l}{k_l} \right)^w \qquad (7)$$

Introducing the relation $D_b f$=constant into the above equation and grouping all the constant terms together yields

$$\frac{h_m}{k_l} = K D_b^{3j-1} \left(\frac{\rho_o n}{\mu_l} \right)^j \left(\frac{C_l \mu_l}{k_l} \right)^w \qquad (8)$$

Since h_m was shown to be approximately proportional to $n^{1/3}$, the term $j = 1/3$; thus $3j - 1$ equals zero, and the term D_b drops out of Equation (8). Although the complete omission of D_b may be only approximately correct, the effect of D_b on h_m will likely be small. Forster and Zuber (9) have shown theoretically that small bubbles grow faster than large bubbles, and so their contribution to the agitation of the fluid is approximately the same.

Substituting $j = 1/3$ in Equation (8) gives

$$\frac{h_m}{k_l} = K n^{1/3} \left(\frac{\rho_o}{\mu_l} \right)^{1/3} \left(\frac{C_l \mu_l}{k_l} \right)^w \qquad (9)$$

A cross plot of $(h_m/k_l)(\mu_l/\rho_o)^{1/3}$ vs. Pr for a constant value of $n = 4{,}000$ was made, and the slope of the straight line was found to -0.89. Figure 11 shows a plot $(h_m/k_l)(\mu_l/\rho_o)^{1/3}(Pr)^{0.89}$ vs. n for all the runs (of all the fluids) in which the number of active centers was counted. The equation of the straight line in the graph is

$$\frac{h_m}{k_l} = 820 \left(\frac{\rho_o}{\mu_l} \right)^{1/3} n^{1/3} (Pr)^{-0.69} \qquad (10)$$

EFFECTS OF SURFACE ROUGHNESS

The next phase of the problem was to find a relationship between the number of active centers and the independent variables, ΔT and surface roughness. Thorough discussions of existing notions as to the sources of nuclei, given by Westwater (29) and Clark (6), may be summarized as follows:

1. Molecular groups are formed by thermal fluctuations of molecules with energies corresponding to the new phase.
2. Bubbles of sufficient size are formed by minute explosions of highly superheated liquid.
3. Nuclei are foreign particles or pockets of dissolved gas.
4. Nuclei consist of vapor or gas trapped in small crevices in a solid from which bubbles can form during boiling. In the present investigation all liquids were boiled for several hours before each run was started, and so the effect of dissolved gas was thought to be insignificant. According to Bankoff (2) the condition that a cavity or

Table 1. Sample Experimental Data*

Run B-I-2 (second run with acetone boiling on a 4-0 surface)

t_1	t_2	t_3	t_4	t_5	t_6	t_7	t_8	t_9	t_{10}	t_l	W, watts
79.6	79.2	76.2	78.0	77.2	73.4	71.8	67.8	64.0	63.0	56.2	370
75.9	75.6	72.9	75.5	74.7	71.4	70.0	66.6	63.3	62.4	56.2	175
66.0	65.9	64.1	66.0	65.9	64.0	63.0	61.7	60.2	60.1	56.2	31

* All temperatures in °C.

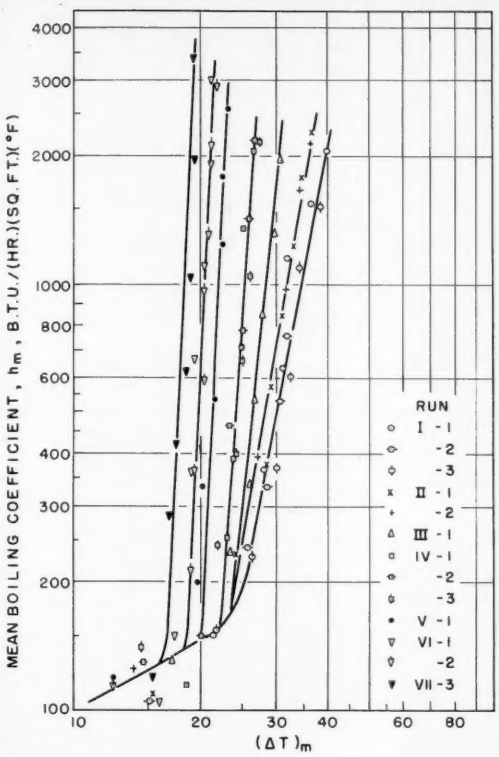

Fig. 6. Boiling curves for acetone.

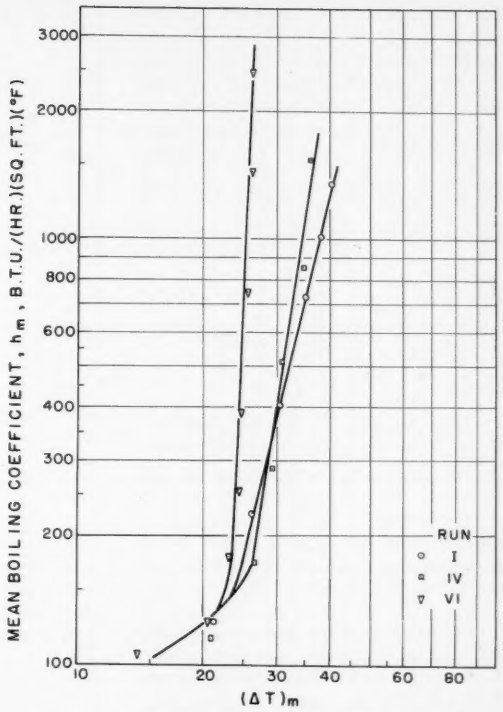

Fig. 8. Boiling curves for carbon tetrachloride.

groove entraps gas in contact with a given liquid is that $\theta > \phi$. Some of the roughness charts obtained in the present work were enlarged and analyzed for values of ϕ which were found to range from 160 to 170 deg. Since ϕ was of this magnitude, these grooves appeared to be very poor vapor traps; therefore condition 4 stated above did not appear to apply to surfaces of the type employed in the present study, although there is a definite possibility that the mechanism applies to certain

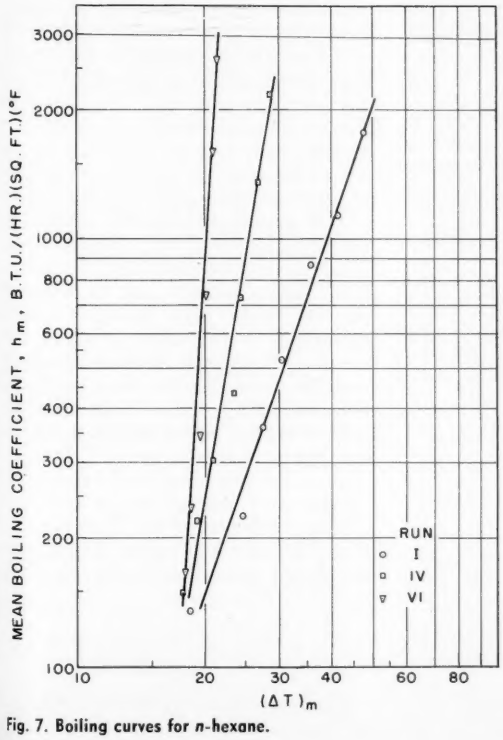

Fig. 7. Boiling curves for *n*-hexane.

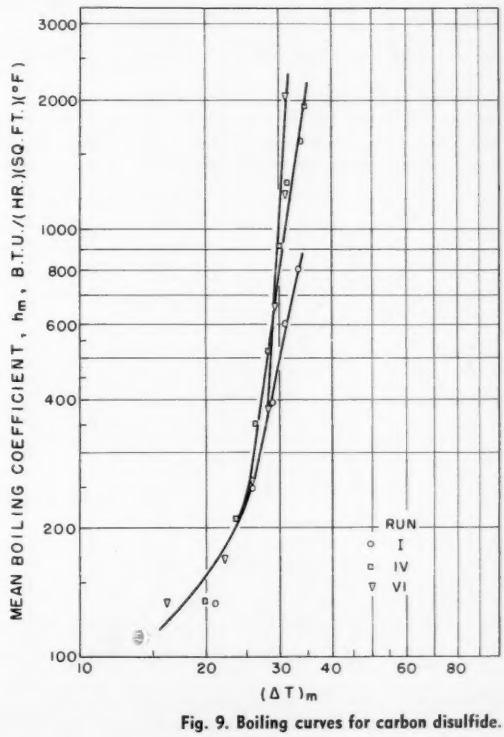

Fig. 9. Boiling curves for carbon disulfide.

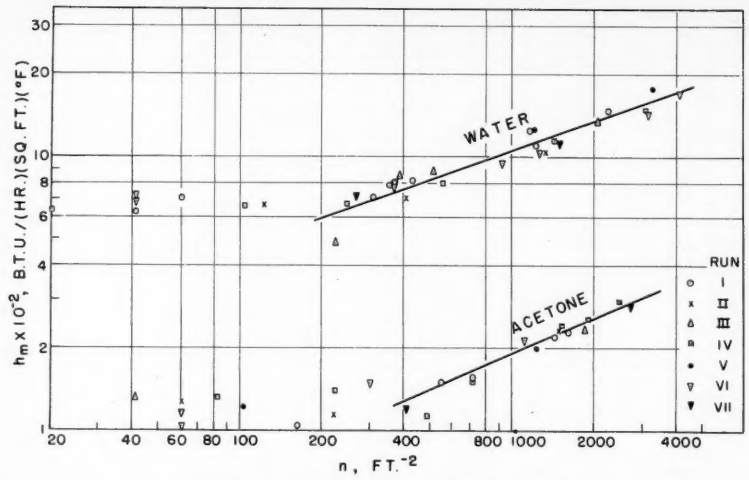

Fig. 10. Mean boiling coefficient vs. concentration of active centers for water and acetone.

surfaces. As not much seems to be known about condition 2, attention was turned to item 1.

The work required to form a nucleus having an apparent spherical radius has been given by Westwater (*30*) and Frenkel (*11*) as

$$\Delta Z = 4\pi\sigma(R^*)^2[(R/R^*)^2 - 2/3(R/R^*)^3] \quad (11)$$

where R^* is given by the equation

$$R^* = \frac{2\sigma}{p_v - p_l} \quad (12)$$

When $R = R^*$, Equation (11) becomes

$$\Delta Z^* = 4/3\,\pi\sigma(R^*)^2 \quad (13)$$

in which ΔZ^* may be considered an energy barrier which, if once surmounted, permits the autocatalytic process of vapor formation to proceed.

The problem is to find the number of nuclei of size R^* on a heating surface at a given degree of superheat. The Clausius-Clapeyron equation may be approximated in the form

$$\left(\frac{dp}{dT}\right)_s = \frac{\lambda}{v_g T} \quad (14)$$

Assuming that λ/v_g does not vary significantly, one may integrate Equation (14) to give

$$p_{s_2} - p_{s_1} = \frac{\lambda}{v_g} \ln\left(\frac{T_{s_2}}{T_{s_1}}\right) \quad (15)$$

If p_{s_1} is taken as p_l, T_{s_1} may be written as T_s. Then

$$p_{s_2} - p_l = \frac{\lambda}{v_g} \ln\left(1 + \frac{T_{s_2} - T_s}{T_s}\right) \quad (16)$$

If T_{s_2} is taken as the temperature inside the bubble at the instant of nucleation, it represents the superheat temperature. The pressure inside the bubble will be nearly equal to the vapor pressure at T_{s_2}. If $T_{s_2} - T_s$ is small compared with T_s, then equation (16) becomes

$$p_v - p_l = \frac{\lambda}{v_g}\frac{\Delta T}{T_s} \quad (17)$$

Combining Equations (12) and (17) gives

$$R^* = B/\Delta T \quad (18)$$

where

$$B = \frac{2\sigma v_g T_s}{\lambda} \quad (19)$$

Thus R^* is approximately inversely proportional to ΔT. However it should be noted that Equation (18) does not tell at what ΔT a liquid starts boiling but simply gives the size of the nucleus which is in a state of equilibrium at that degree of superheat. A nucleus smaller than this should dissipate itself, and one larger should grow.

As the experimental results of this investigation show, the shape, size, and size distribution of surface grooves have an essential influence on bubble formation during nucleate boiling. In his photographic study of boiling methanol Westwater (*23*) showed that the size of a bubble from an active center remains constant during nucleate boiling. This means that an active center, which may be a valley or groove of certain size, generates bubbles of a constant size regardless of the heat flux or ΔT when bubbles have once started to form from that spot. Thus the volume elements of superheated liquid in grooves having a radius of R^* may be the nuclei for the formation of bubbles of initial radius R^* at the corresponding ΔT. From this it follows that the number of nuclei of a certain size may be expected to be proportional to the number of grooves of corresponding size. However although there were numerous grooves of approximately the same size on a polished surface, as seen from the measured surface profiles, and all those of size R^* could have provided nuclei according to the above theory, the number of bubble columns observed was always far smaller than the number of suitable grooves. In other words, only a small fraction of the available sites were activated.

Since the process of nuclei formation requires an activation energy, one may assume, as suggested by Frenkel (*11*), that the number of nuclei of size R is distributed according to the Maxwell Boltzman expression:

$$P_R = C_1 \exp.\left(\frac{-\Delta Z}{m'R'T}\right) \quad (20)$$

This may be interpreted as follows. At a given degree of superheat, nuclei

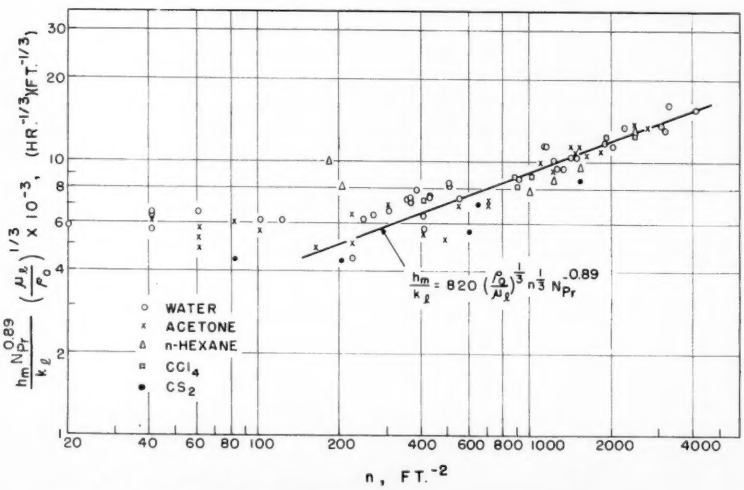

Fig. 11. Correlation of boiling coefficient with concentration of active centers.

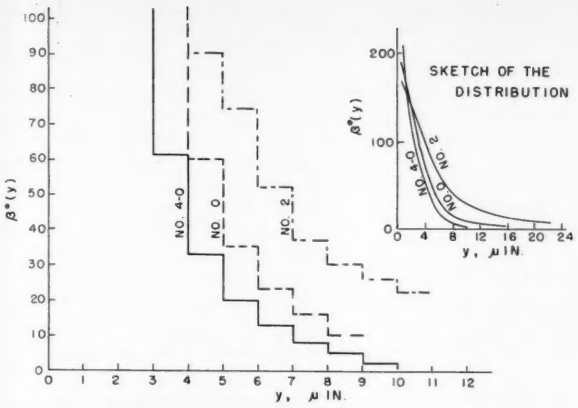

Fig. 12. Groove-size distribution on heating surfaces.

are constantly forming and dispersing owing to heterophase fluctuations, and the distribution follows the Boltzman expression. At a given ΔT all nuclei having radii smaller than R^* cannot grow, but disperse immediately.

If $\beta(R)$ represents the number of grooves of size between R and $R+1$ units over a unit area of heating surface, and β_t the total number of grooves of size between R_o and R, then the change from R to $R + dR$ will be accompanied by a change in β_t of $\beta(R)\,dR$. Therefore

$$d\beta_t = \beta(R)dR \qquad (21)$$

and the change in the number of active nuclei accompanied by a change of R may be expressed as

$$dn = P_R\,\beta(R)dR \qquad (22)$$

From Equation (18)

$$dR = \frac{-R}{\Delta T}\,d(\Delta T) = \frac{-R^2}{B}\,d(\Delta T) \qquad (23)$$

The superscript * is no longer necessary, since any R is potentially the critical radius at its corresponding ΔT.

Substituting Equation (23) in Equation (22) and integrating from ΔT_1 to ΔT_2, one gets

$$n_2 - n_1 = \frac{-1}{B}\int_{\Delta T_1}^{\Delta T_2} P_R R^2 \beta(R)\,d(\Delta T) \qquad (24)$$

Furthermore from Equations (13) and (20)

$$P_R = C_1 \exp\,(-4\pi\sigma R^2/3\,m'R'T_o) \qquad (25)$$

If one postulates the existence of a cone in a groove with depth y, one finds that

$$m' = 1/3\,(R^2\,\pi y\,\rho_l) \qquad (26)$$

Combining Equations (24), (25), and (26) and using the relation $R = y \tan(\phi/2)$, one gets

$$n_2 - n_1 = -\frac{C_1}{B}\int_{\Delta T_1}^{\Delta T_2} R^2\,\beta(R)\,\exp\left(\frac{-E}{R}\right)d(\Delta T) \qquad (27)$$

where

$$E = \frac{4\sigma\tan(\phi/2)}{\rho_l R' T_o} \qquad (28)$$

As may be seen, Equation (27) contains the constant C_1 and hence cannot be used to predict n at a given ΔT for the liquid under consideration. However the applicability of the equation may be shown by the following method.

First $\beta(R)$ must be obtained. Because of the difficulty of measuring the values of R from the strip charts, the groove depths were determined instead, and their distribution was assumed to be the same as $\beta(R)$. As described earlier, ϕ was found to be approximately constant for all grades of emery paper used, and so, although the depth of the valleys varied greatly, their shapes were similar.

Figure 12 shows $\beta^\circ(y)$ vs. y for surfaces polished with numbers 4-0, 1-0, and 2 emery paper. $\beta^\circ(y)$ is the average of the six sets of surface measurements taken on each surface at the locations indicated earlier. $\beta(y)$ was assumed to be related to $\beta^\circ(y)$ by the equation

$$\beta(y) = C_2\,\beta^\circ(y) \qquad (29)$$

where C_2 is characteristic of the roughness. Equation (27) becomes

$$n_2 - n_1 = \frac{C_3}{B}\int_{\Delta T_1}^{\Delta T_2} R^2\,\beta^\circ(y)\exp\left(\frac{-E}{R}\right)d(\Delta T) \qquad (30)$$

where $C_3 = -C_1C_2$. The values of B and E were calculated for each liquid and are shown in Table 2. The right-hand side of Equation (30) was then integrated graphically between two values of ΔT_1 and ΔT_2, so that C_3 might be determined for one liquid for each kind of surface. For the 4-0 surface C_3 was found to be 4.1 from data taken with acetone. For the 1-0 surface $C_3 = 3.5$ from acetone data and for the No. 2 surface $C_3 = 3.3$ from carbon disulfide data. With the experimental value of C_3 for each surface and one experimental set of readings of the number of nuclei at a certain degree of superheat (ΔT_1), the number of active nuclei could be calculated at other ΔT's. This was done for the three surfaces in question, and the results are shown in Figures 13, 14, and 15 compared with the experimental data. Tables 2 and 3 show the constants

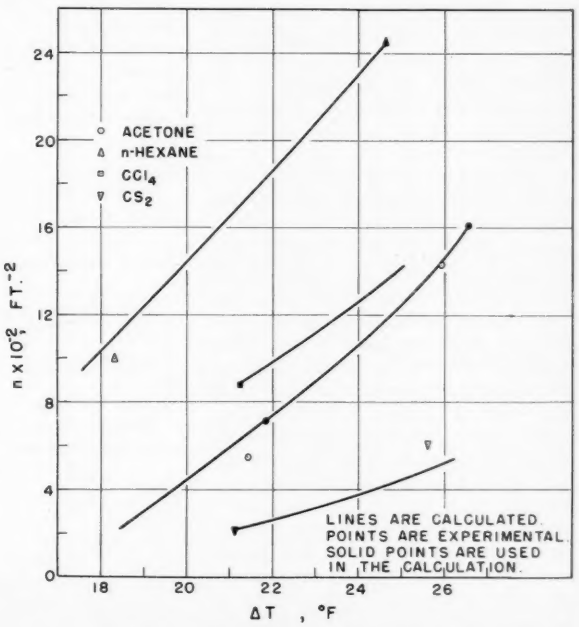

Fig. 13. Comparison of concentration of active centers calculated by Equation (30) with experimental data for number 4-0 polished surface.

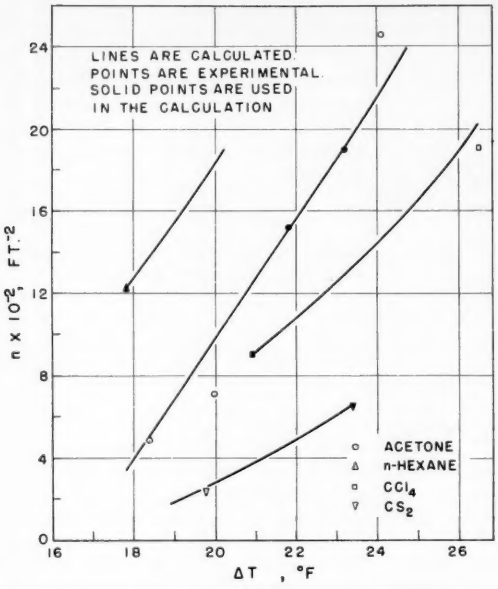

Fig. 14. Comparison of concentration of active centers calculated by Equation (30) with experimental data for number 1-0 polished surface.

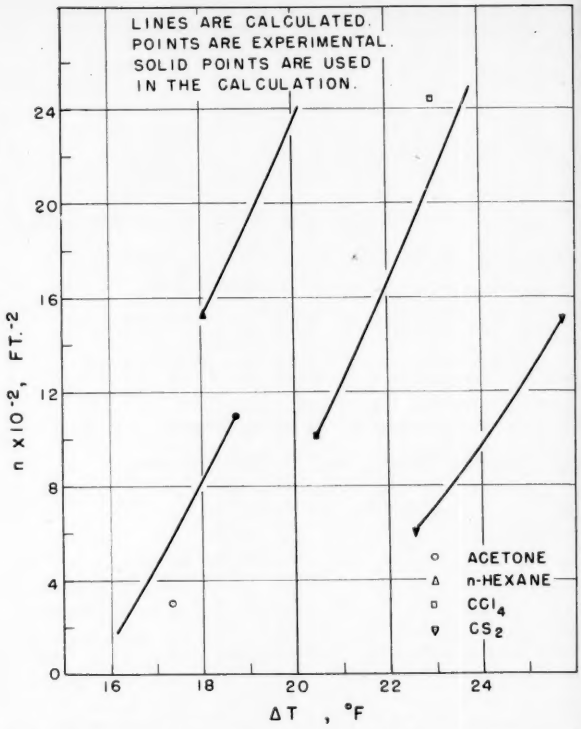

Fig. 15. Comparison of concentration of active centers calculated by Equation (30) with experimental data for number 2 polished surface.

used in the integration indicated in Equation (30) and a sample of some of the data and results.

Unfortunately not many values of n were available to test the validity of Equation (30), because the number of active centers increased so rapidly with heat flux that it was impossible to count them by eye above a certain limit. Furthermore the data at low heat fluxes could not be used because of the natural-convection effects of the immersion heater which were mentioned earlier. However the data available seem to behave as predicted by Equation (30), which shows the extremely sensitive effect of groove-size distribution on the number of active centers.

Calculations were not made for water for the following reason. The value of the term B for water is extremely large [2,300 (μin.)(°R.)] compared with that for other liquids (600 to 1,300). The radius of a nucleus computed from the value of B is about 150 μin. This corresponds to a valley depth of 20 μin. or more. Although there is almost no valley of that depth on a surface polished with 4-0 emery paper, many activated spots were observed during runs on this type of surface. This may be due to the possibility that, when the critical radius of a nucleus is very large compared with the available groove size, the nucleus could possibly be formed over several grooves. In this case $\beta(R)$ could not be predicted, since it is not indicated by a simple $\beta^\circ(y)$ for the surface. This tendency may exist for a nucleus of any size but will not be significant for small nuclei.

The proposed mechanism has several uncertain points. Contact angle was not taken into account because even if it were available for macroscopic systerms it might not be the same on a microscopic scale. Furthermore C_1 was assumed to be constant as suggested by Frenkel (*11*). However it is actually a function of temperature and thus may have varied to some extent.

Since the effect of groove-size distribution is so important, it is essential to obtain a surface profile which represents the surface exactly. The surface analyzer is an excellent instrument to measure surface roughness. Even so it is questionable whether one can extend a surface profile taken in a linear direction to represent the area under consideration. Although the valleys were assumed to be cone shaped, actually they probably had more complicated profiles.

A further difficulty arose from the use of ΔT_m for ΔT in the calculation of n in Equation (30). During boiling the temperature of the center of the heater was greater than near the wall. As a result a greater concentration of bubble columns existed near the center of the heating surface. To carry out the calculations more precisely n should have been counted over concentric segments of the heater surface, where the temperature was more nearly constant. However this was impractical with the techniques used in this investigation.

Table 2. Values of B and E in Equation (30)

	Water	Acetone	n-hexane	CCl_4	CS_2
B(μin.)(°R.)	2330	790	620	960	1280
E(μin.)°	3.8	5.7	7.3	7.8	8.1

° Average groove bottom angle taken as 164 deg.

Table 3. Data for Correlation of Number of Active Centers, Acetone, 4-0 Polished Surface

ΔT, °F.	R, μin.	y, μin.	$e^{-E/R}$	$\beta^\circ(y)$	Δn, ft.$^{-2}$	n, ft.$^{-2}$
26.5	30	4	0.83	61	470	1610
24.5	32	5	0.84	33	295	1140
22.5	35	5	0.85	33	357	845
20.5	39	6	0.86	20	270	488
18.5	—	—	—	—	—	218

CONCLUSIONS

Equation (10), relating the number of active centers to the boiling coefficient and Equation (30), relating the temperature-difference driving force to the number of active centers, offer a method of predicting the curve of h vs. ΔT for various liquids and surfaces. As

yet, some experimental information is necessary for the determination of certain constants, and in addition a graphical integration is necessary for the solution of these equations. However the equations have the present value of offering a quantitative interpretation of contradictory results in the literature, some of which are certainly due to surface effects. For example the equations make it apparent that for surfaces which have been highly polished and thus may have a very narrow spectrum of surface irregularities, the number of active boiling centers will be quite sensitive to changes in ΔT in the nucleate boiling zone. This would result in a high value for the slope of the curve of h vs. ΔT. The limiting situation would be a surface covered with cavities of identical size for which the equations would predict an infinite slope of the curve of h vs. ΔT.

ACKNOWLEDGMENT

Funds for this research were provided by the Purdue Research Foundation in the form of an X-R grant.

NOTATION

A = area of heating surface, sq. ft.

B = constant based on liquid properties, (μin.) (°R.)

C_l = specific heat of saturated liquid, B.t.u./(lb.-mass) (°F.)

C_1, C_2, C_3 = dimensionless constants

D_b = diameter of bubble when breaking off heating surface, ft.

E = characteristic term defined by Equation (28), μin.

f = frequency of bubble formation, sec.$^{-1}$

G_b = bubble flow rate, lb.-mass/(sq. ft.) (hr.)

g = acceleration of gravity, ft./hr.^{2}

g_c = conversion factor, 4.17×10^8 (lb.-mass) (ft.)/(lb.-force) (hr.^{2})

h = boiling coefficient, B.t.u./(hr.) (sq. ft.) (°F.)

h_m = mean boiling coefficient, B.t.u./(hr.) (sq. ft.) (°F.)

j = constant, dimensionless

K' = constant, dimensionless

k = thermal conductivity of saturated liquid, B.t.u./(hr.) (ft.) (°F.)

m = constant, dimensionless

m' = mass of liquid associated with one nucleus of radius R, lb.-mass

n = concentration of active centers, ft.$^{-2}$

Δn = difference between concentration of active centers at two different degrees of superheat, $n_2 - n_1$, ft.$^{-2}$

p_o = vapor pressure of saturated liquid, lb.-force/sq. ft.

p_g = pressure on vapor side of interface, lb.-force/sq. ft.

p_l = pressure on liquid side of interface, lb. force/sq. ft.

P_R = fraction of active nuclei of size R with respect to total number of nuclei, dimensionless

q = net heat input, B.t.u./hr.

R = radius of nucleus, μin.

R' = gas constant, (lb.-force) (ft.)/(°R.) (lb.-mass)

R^* = critical radius of nucleus, μin.

r = radial distance from the center of the heater, ft.

r_o = radius of copper cylinder, ft.

T_s = temperature at the surface of the heater, °C.

T_o = saturation temperature of liquid, °F.

t_l = temperature of boiling liquid, °C.

t_1, t_2, etc. = temperatures from the thermocouple readings, °C.

ΔT = temperature difference driving force, °C. or °F.

$(\Delta T)_m$ = mean temperature-difference driving force, °F.

v_g = specific volume of saturated vapor, cu.ft./lb.-mass

w = constant, dimensionless

y = depth of groove, μin.

ΔZ = free-energy change during fluctuation process, B.t.u.

ΔZ^* = nucleating free energy, B.t.u.

Greek Letters

$\beta(R)$ = number of grooves of size between R and $(R+1)$ units over unit area, ft.$^{-2}$

β_t = total number of grooves of size between R_o and R

$\beta(y)$ = number of grooves of depth between y and $(y+1)$ units over unit area, ft.$^{-2}$

$\beta^\circ(y)$ = number of grooves of depth between y and $(y+1)$ units over a distance of 1/16 in.

λ = latent heat of vaporization, B.t.u./lb.-mass

μ_l = viscosity of saturated liquid, lb.-mass/(ft.) (hr.)

ρ_l = density of saturated liquid, lb.-mass/cu. ft.

ρ_o = density of saturated vapor, lb.-mass/cu. ft.

σ = surface tension of vapor-liquid interface, dynes/cm.

ϕ = angle at the bottom of cone-shaped groove, radians

θ = bubble-contact angle, radians

Dimensionless Groups

N_{Nu} = Nusselt number

N_{Pr} = Prandtl number

N_{Re} = Reynolds number

Subscripts

o = saturation state

Superscripts

o = measurement of number of grooves; distinguishes them as being taken on a path 1/16 in. long

LITERATURE CITED

1. Albott, E. J., and S. Bousky, *Mech. Eng.*, **60**, 521 (1938).
2. Bankoff, S. G., *A.I.Ch.E. Journal*, **4**, 24 (1958).
3. Bashforth, F., "Capillary Action," Cambridge Univ. Press, London, England (1883).
4. Becker, R., and W. Döring, *Ann. Physik*, **24**, 719 (1935).
5. Bernath, L., *Ind. Eng. Chem.*, **44**, 1310 (1952).
6. Clark, J. A., *Mass. Inst. Technol. Tech. Rept. No. 7* (1956).
7. Clark, H. B., P. S. Strenge, and J. W. Westwater, *Chem. Eng. Progr. Symposium Ser. No. 29*, **55** (1959).
8. Corty, Claude, and A. S. Foust, *ibid.*, No. 17, **51** (1955).
9. Forster, H. K., and N. Zuber, *A.I.Ch.E. Journal*, **1**, No. 4, 531 (1955).
10. ———, *J. App. Physics*, **25**, 475 (1954).
11. Frenkel, J., "Kinetic Theory of Liquids," Oxford Press (1946); Dover Publications, New York (1955).
12. Fritz, W., *Phys. Z.*, **36**, 379 (1935).
13. Gunther, F. C., and F. Kreith, Heat Transfer and Fluid Mech. Inst., Berkeley, California (1949).
14. ———, *Calif. Inst. Technol. Progr. Rept.*, **44** (March, 1950).
15. Jakob, Max, and W. Fritz, *Forsch. Geb. Ing.*, **22**, 435 (1931).
16. Jakob, Max, "Temperature, Its Measurement and Control in Science and Industry," Reinhold, New York (1941).
17. ———, "Heat Transfer," p. 614, John Wiley, New York (1949).
18. Kabanow, B., and A. Frumukin, *Z. Phys. Chem.*, **165**, 433 (1933).
19. Kurihara, H. M., Ph.D. thesis, Purdue University, Lafayette, Indiana (1956).
20. La Mer, V. K., *Ind. Eng. Chem.*, **44**, 1270 (1952).
21. Nishikawa, K., *Trans. Soc. Mech. Engrs. (Japan)*, **20**, 808 (1954).
22. Operating Information of Brush Model BL-103 Surface Analyzer, Brush Electronics Co., Cleveland, Ohio.
23. Perkins, A. S., and J. W. Westwater, *A.I.Ch.E. Journal*, **2**, 471 (1956).
24. Rohsenow, W. M., *Trans. Am. Soc. Mech. Engrs.*, **74**, 969 (1952).
25. ———, and J. A. Clark, *ibid.*, **73**, 609 (1951).
26. Sauer, E. T., *et al.*, *Mech. Eng.*, **60**, 669 (1938).
27. Volmer, M., "Kinetik der Phasebildung," Edward Brothers, Ann Arbor, Michigan (1945).
28. Wark, I. W., *J. Phys. Chem.*, **37**, 623 (1933).
29. Westwater, J. W., "Advances in Chemical Engineering," Vol. I., Chap. I, Academic Press, New York (1956).

Manuscript received November 12, 1958; revision received July 7, 1959; paper accepted July 10, 1959. Paper presented at A.I.Ch.E. Atlantic City meeting.

Detonation Characteristics of Hydrogen-Oxygen Mixtures

MORTON P. MOYLE, RICHARD B. MORRISON, and STUART W. CHURCHILL

The University of Michigan, Ann Arbor, Michigan

Detonation velocities were measured in mixtures of hydrogen and oxygen containing 25 to 75 mole % hydrogen at initial temperatures from 160° to 580°K. and initial pressures from ½ to 2 atm. The measurements were made in a number of tubes of different diameter to permit extrapolation to a tube of infinite diameter. Theoretical detonation characteristics were computed for the same range of conditions. The measured and computed velocities are in good agreement except in rich mixtures and at subatmospheric pressures. Schlieren photographs reveal that the detonation wave front is very thin for a stoichiometric mixture but degenerates to a complicated zone of interacting shock waves and turbulent combustion as the percentage of hydrogen is reduced. The detonation velocity is found to depend only slightly on initial temperature and pressure. The computed pressures behind the detonation and reflected waves are roughly proportional to initial pressure and to the reciprocal of the initial temperature.

The elementary theory of detonation was initiated by Riemann (*21*) with his work on sound waves and essentially completed by Chapman (*5*) and Jouguet (*7*). This elementary theory postulates a planar discontinuity in pressure, temperature, and composition moving at sonic velocity with respect to the burned gases (the Chapman-Jouguet condition); chemical equilibrium in the burned gases; no energy, component, or momentum transfer to the surroundings; and ideal gas behavior. Subsequent refinements in the theory have been concerned primarily with the structure of the wave. The details of both the classical and the current theoretical work are presented in modern books such as Hirschfelder, Curtiss, and Bird (*10*) and Courant and Friedricks (*6*) and therefore will not be repeated herein.

Experimental work on detonation has been well reviewed by Lewis and von Elbe (*16*), and only the immediately pertinent work will be mentioned. The effect of composition on the detonation velocity of hydrogen-oxygen mixtures has been investigated extensively, but the effects of initial temperature and initial pressure have received little attention. In 1893 Dixon (*7*) measured the detonation velocity in stoichiometric mixtures at 283° and 373°K. over a range of pressures from 200 to 1,500 mm. Hg. More recently Bennett and Wedaa (*2*) reported detonation velocities over a pressure range from 10 to 400 mm. Hg and Hoelzer and Stobaugh (*11*) over a range from 1 to 10 atm.

Lewis and Friauf (*15*) in 1930 and Berets, Greene, and Kistiakowsky (*3*) in 1950 found good agreement between velocities computed from the elementary theory and experimental values in hydrogen-oxygen mixtures at atmospheric pressure and near-ambient temperatures. The objective of this investigation was to test the predictions of the elementary theory over a much wider range of initial conditions.

EXPERIMENTAL WORK

The experimental equipment for the measurement of detonation velocities consisted of six different detonation tubes, a mixing and charging system, an ignition system, and a timing system.

The characteristics of the detonation tubes are given in Table 1. The five round, straight tubes (*A, B, C, D,* and *E*) were used to determine the effect of tube diameter on detonation velocity. Tube *F* was a 10-in. coil for convenience in temperature control for the high- and low-temperature experiments. The effect of coiling was evaluated by comparison of the velocities measured in tubes *F* and *B*. Rectangular tube *G* was used only to obtain schlieren photographs. All seven tubes were closed at both ends.

The velocity of the detonation wave was measured with ionization probes. The probes were made by drilling a no. 76 drill through a Teflon insert in a stainless steel sleeve. The probes were threaded into the detonation tubes and adjusted so that the tip was flush with the wall. Each probe was connected as a shorting switch in the grid of an 884-thyratron tube. The grid bias of the thyratron tube was adjusted almost to the firing point to obtain maximum sensitivity. When the ionized gases behind the detonation front reached a probe, the resistance between the probe electrode (the drill) and ground (the tube wall) fell, and the thyratron fired. One probe and thyratron started a timer, and another probe and thyratron stopped it. The time interval was indicated to the nearest microsecond. The distances between the probes and the distance from the ignitor to the first probe are given in Table 1. The probe locations on tube *F* were on the outside of the coil and were determined before coiling. The distance between the probes was corrected for thermal expansion and contraction of the tube in computing the detonation velocity at nonambient temperatures. This correction was about 0.1% at the extreme temperatures. The starting distance for all the tubes was greater than the distance indicated by Laffitte (*14*) and Greene (*9*) as necessary to attain stable detonation in hydrogen-oxygen mixtures. The probes required replacement after 20 to 30 runs.

The high-temperature runs were made with the coiled tube in an oven, and the low-temperature runs with the coiled tube immersed in 5 gal. of normal propanol in an insulated tank. Dry ice was added to the propanol to cool to 200°K. and liquid nitrogen to reach lower temperatures. As the result of vigorous stirring, the temperature variation within the bath was held within ±2°K.

The detonation tube was evacuated and then filled with premixed oxygen and hydrogen through a manifold and switch system that kept the ignition circuit open while the filling valve was open. In the low-temperature runs the tube was evacuated at room temperature before cooling to avoid condensation. In both the high- and low-temperature runs the mixture was not ignited until the pressure indicated on a manometer had remained constant for at least 5 min. Analyses of the hydrogen and oxygen on a mass spectrograph indicated purities greater than 99.5%. The composition of the mixtures were regularly determined by the partial-pressure method but were periodically checked with a mass spectrograph.

The schlieren measurements were made by the Töpler method (*1*) in a ⅜- by ½-in. rectangular tube with a test section containing ⅜- by 14-in. windows ½-in. thick on two opposite sides. Additional details concerning the equipment and experimental procedures are given in reference *18*.

Measurements of detonation velocity were repeated five or more times at the same conditions to check reproducibility. All in all over 600 runs were carried out at over 100 conditions encompassing a range of compositions from 25 to 76 mole % hydrogen for an initial temperature of 298°K. and an initial pressure of 1 atm., a range of initial pressures from ½ to 2 atm. for an initial temperature of 298°K. and compositions from 40 to 76% hydrogen and a range of initial temperatures from 160° to 477°K. for an initial pressure of 1 atm. and compositions from 41 to 73% hydrogen. The detailed data are given in reference *18*. The averages of the repeated runs are presented herein. The maximum deviation of any individual velocity from the average was less than 1.0% except for a few runs at subatmospheric pressures.

When the velocities measured at atmospheric pressure and 298°K. in the 0.125-, 0.250-, 0.375-, 0.909-, and 3.250-in. straight tubes were plotted as a function of initial gas composition, a small but

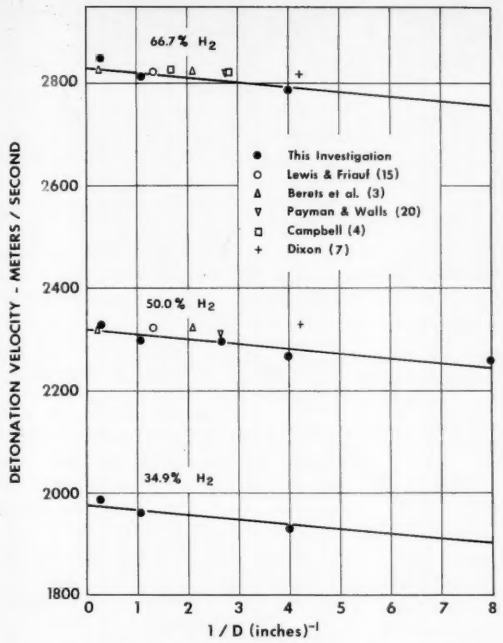

Fig. 1. Effect of tube diameter on detonation velocity.

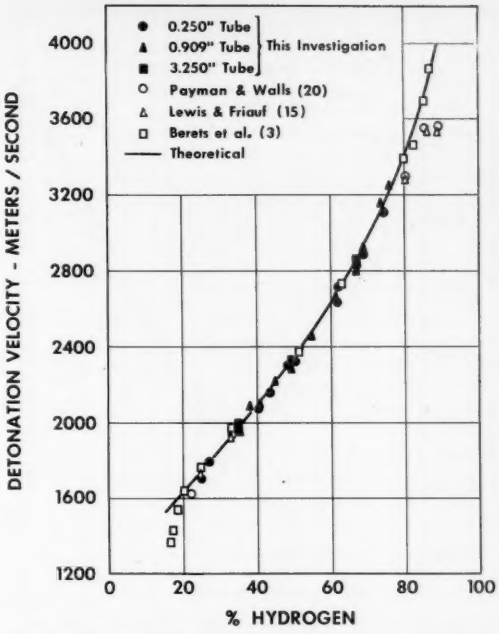

Fig. 2. Detonation velocities at atmospheric pressure and ambient temperature.

definite dependence on tube diameter was apparent. Therefore the velocities measured in mixtures containing 34.9, 50.0, and 66.7% hydrogen were plotted vs. reciprocal tube diameter in Figure 1 as suggested by Kistiakowsky and Zinman (9). The data of several previous investigators (3, 4, 7, 15, 20) for atmospheric pressure and temperatures near 298°K. are also included. The data appear to lie in parallel straight lines indicating that the wall effect is independent of composition in this range. The best set of parallel lines through the data of this investigation only was determined by least squares by the use of the method of Ergun (8). These lines are included in Figure 1. The slope of the lines was computed to be 9.04 (in.) (m.)/ sec.; therefore the velocities measured in this and previous investigations at all conditions were extrapolated to the equivalent velocity in a tube of infinite diameter by means of the equation

$$V_\infty = V + \frac{9.0}{D} \qquad (1)$$

Data at high and low temperatures were obtained only in the 0.250-in. coiled tube and only at atmospheric pressure. Comparison of data obtained in the coiled and straight 0.250-in. tubes at atmospheric pressure and 298°K. indicated that the coiled tube yielded velocities 1% lower than those measured in the straight tube. Accordingly, the velocities measured in the coiled tube at all conditions were corrected by this amount as well as by Equation (1), that is

$$V_\infty = \frac{V_e}{0.99} + \frac{9.0}{D} \qquad (2)$$

Scorah (22) maintains that the detonation velocity is unaffected by coiling or even zigzagging the tube, and the observed correction is probably due to stretching the tube in the coiling process rather than to fundamental effects.

Corrected velocities are presented in all subsequent plots.*

THEORETICAL COMPUTATIONS

The detonation characteristics of hydrogen-oxygen mixtures were computed from the elementary theory on an IBM-650 computer over essentially the same range of initial temperatures, pressures, and compositions as in the experimental work. The only species assumed to be present were water, hydrogen, oxygen, hydroxyl, atomic hydrogen and atomic oxygen. Equilibrium constants, heat capacities, and heats of formation from the National Bureau of Standards tables (23) were utilized.

The pressure, temperature, and equilibrium composition behind the detonation wave as well as the wave velocity were obtained from the computer. The further increase in pressure obtained by reflection of the detonation wave off a solid wall was also computed with no further change assumed in composition.

The experimental velocities were not measured at exactly the same temperatures, pressures, and compositions as those selected for computation. Therefore it was necessary to plot and interpolate the experimental data. Since the theoretical detonation velocity is a near linear function of initial pressure, temperature, and composition, very little uncertainty was introduced by this interpolation.

DETONATION VELOCITIES

The corrected experimental velocities of this and previous investigations for

* A tabulation of the average and corrected experimental velocities and of the computed theoretical detonation characteristics has been filed as document 6124 with the American Documentation Institute, Photoduplication Service, Library of Congress, Washington 25, D. C., and may be obtained for $1.25 photoprints or 35-mm. microfilm.

Table 1. Detonation Tubes

Tube	Material	I. D., in.	Form	Ignitor to 1st probe, ft.	Probe separation, ft.	Total length, ft.
A	Stainless steel	0.125	Straight	7.0	3.0007	11.5
B	Stainless steel	0.250	Straight	9.0	2.999	13.5
C	Stainless steel	0.375	Straight	7.5	2.0003	12.0
D	Stainless steel	0.909	Straight	7.0	3.9944	12.0
E	Carbon steel	3.250	Straight	10.0	3.000	14.0
F	Stainless steel	0.250	10-in. Coil	8.0	12.00	24.0
G	Carbon steel	(0.375 × 0.5)	Straight	6.0	—	7.5

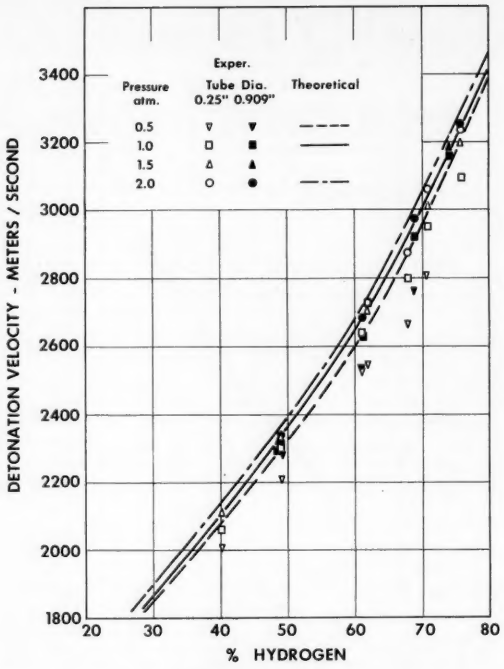

Fig. 3. Detonation velocities at several initial pressures and 298°K.

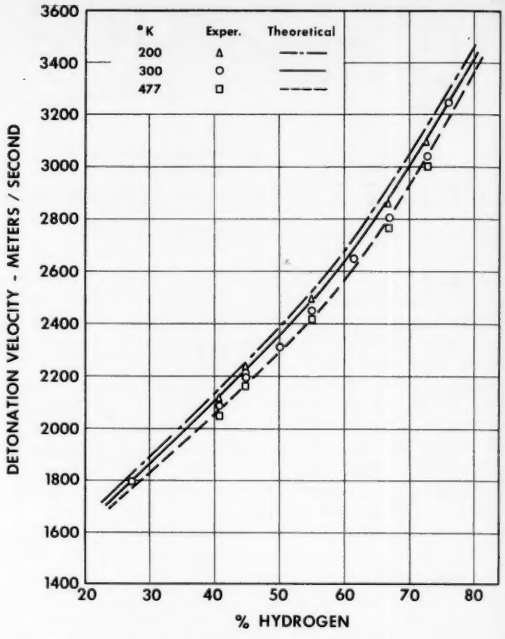

Fig. 5. Detonation velocities at several initial temperatures and 1 atm.

an initial pressure of 1 atm. and initial temperatures of approximately 298°K. are plotted as a function of initial composition in Figure 2. Excellent agreement is demonstrated with the curve representing the computed theoretical velocities over the range of composition from 20 to 80% hydrogen.

The effect of initial pressure on detonation velocity was investigated at ambient temperature only for a wide range of compositions in the straight 0.250- and 0.909-in. tubes. Difficulty was encountered in obtaining reproducible data at subatmospheric pressures in the 0.909-in. tube. Velocities

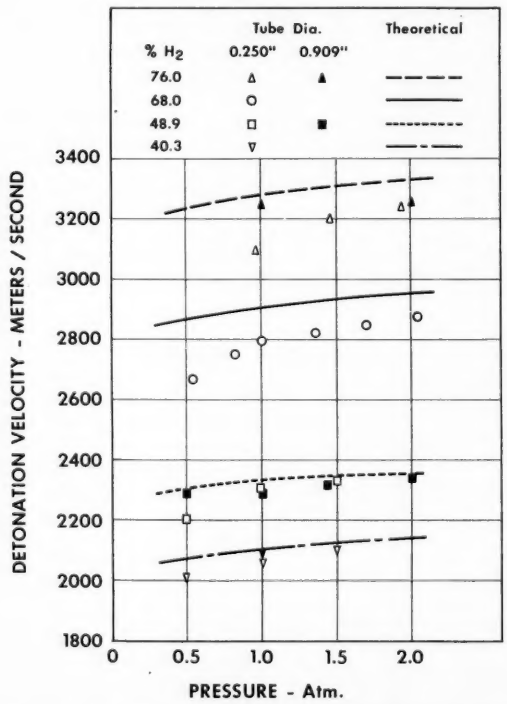

Fig. 4. The effect of initial pressure on detonation velocity at 298°K.

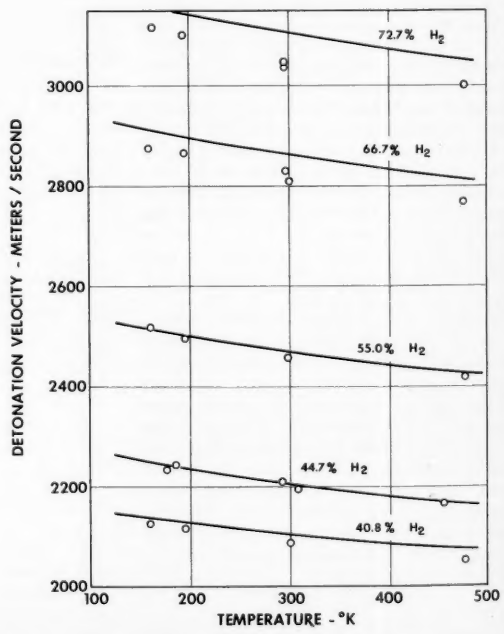

Fig. 6. The effect of temperature on detonation velocity at 1 atm.

corrected to infinite diameter by Equation (1) are plotted as a function of composition at initial pressures of 0.5, 1.0, 1.5, and 2.0 atm. in Figure 3. The data fall somewhat below but indicate the same trend with pressure as the theoretical curves. The corrected experimental velocities for several mixtures are plotted directly vs. pressure in Figure 4. This plot includes data at pressures intermediate to those in Figure 3. The limited range of the ordinate of Figure 4 exaggerates the slight effect of initial pressure on the detonation velocity and emphasizes the deviations. The experimental data are no more than 7% below the theoretical curves even at 0.5 atm. in rich mixtures.

The corrected velocities equivalent to those obtainable in an infinite straight tube are plotted as a function of gas composition in Figure 5 for temperatures of 200°, 300°, and 477°K. Although the data fall slightly below the theoretical curves, the agreement is generally good. The data for a number of mixtures are plotted directly as a function of temperature in Figure 6. Again the limited range of the ordinate exaggerates the slight variation of the velocity with initial temperatures and emphasizes the deviations from the computed velocities which are less than 2.5% even in the rich mixtures.

Schlieren photographs of detonation waves in 28.75, 39.00, and 52.50% hydrogen at ambient conditions are shown in Figure 7. The detonation wave is moving from left to right in the photographs. In Figure 7*a* (52.5% hydrogen) small-scale turbulence can be noted behind a sharp wave front. In Figure 7*b* (39.0% hydrogen) the wave front is thicker and the scale of the turbulence is greater. In Figure 7*c* (28.75% hydrogen) the wave front has degenerated into a complicated shock pattern followed by an irregular combustion zone. In view of these photographs, it is surprising that a theory which assumes chemical equilibrium in a planar wave and neglects heat, component, and momentum transfer predicts detonation velocities in reasonable agreement with the experimental values.

Table 2. Comparison of Computed and Experimental Pressure Ratios

	Computed	Experimental (*19*)
Detonation/initial pressure	17.5	20.4
Reflected/detonation pressure	2.45	3.0
Reflected/initial pressure	43.0	61.2

THEORETICAL COMPOSITIONS, TEMPERATURES, AND PRESSURES

The temperature, pressure, and equilibrium composition behind the detonation wave and the pressure behind the reflected wave are tabulated for all the computed conditions in reference *18* and also are on file with the American Documentation Institute.*

The equilibrium compostion behind the detonation wave is illustrated in Figure 8 for an initial temperature of 298°K. and an initial pressure of 1 atm. Dissociation is observed to be significant for the entire range of initial compositions.

The detonation and reflected pressure ratios are plotted as a function of initial pressure for several initial compositions in Figure 9 and as a function of initial temperature for several initial compositions in Figure 10. These pressure ratios are observed to increase steeply as the initial temperature decreases but to be relatively independent of the initial pressure. A plot (not shown) of the pressure ratios vs. reciprocal temperature demonstrates near proportionality. Thus for a given composition the developed pressures are roughly proportional to the initial density.

The temperature, pressure, and composition behind the detonation and reflected waves are extremely difficult to measure because of their brief existence, and only fragmentary experimental values are available for comparison with the computed values. The average of the detonation and reflected pressures measured by Ordin (*19*) for 55% hydrogen at 1 atm. and 298°K. are compared with the theoretical values for the same conditions in Table 2. The agreement is only fair but is probably within the range of uncertainty of these experimental values.

The absence of firm and extensive experimental confirmation of the computed temperatures, pressures, and compositions makes their validity uncertain but at the same time necessitates their use for design or other engineering purposes. The impact pressure, that is the pressure behind the reflected wave, is of particular practical interest as a possible criterion for the design of process equipment subject to detonation. Indeed, Luker and Leibson (*17*) have recently reported that the computed impact pressure for conditions under which a rupture disk just fails under detonation bears a constant ratio slightly greater than unity to the rated static bursting pressure of the disk.

CONCLUSIONS

The detonation velocity in hydrogen-oxygen mixtures depends slightly upon tube diameter. Correlation of the data for tubes of different diameter in terms of a linear relationship between velocity and the reciprocal of the tube diameter as suggested by Kistiakowsky and Zinman (9) permits correction of the velocities to their equivalent in a tube of infinite diameter.

After this correction the experimental detonation velocities agree reasonably

* See footnote, p. 93.

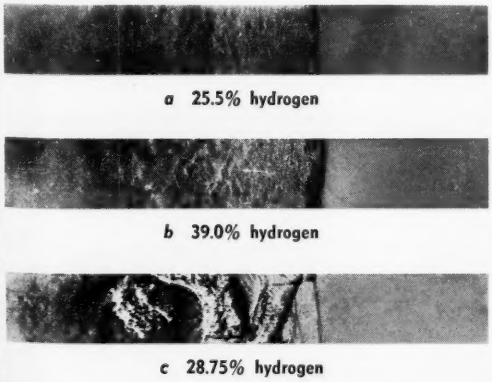

Fig. 7. Schlieren photographs of detonation waves in hydrogen-oxygen mixtures at atmospheric pressure and 298°K.

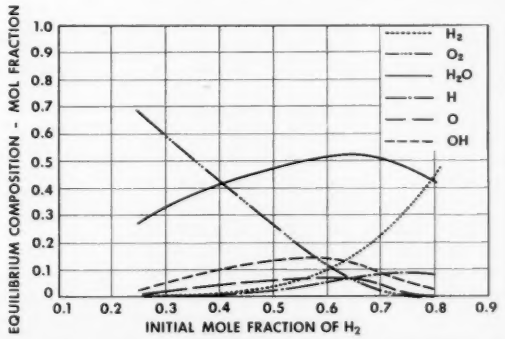

Fig. 8. Equilibrium composition behind detonation wave in hydrogen-oxygen mixtures at atmospheric pressure and 298°K.

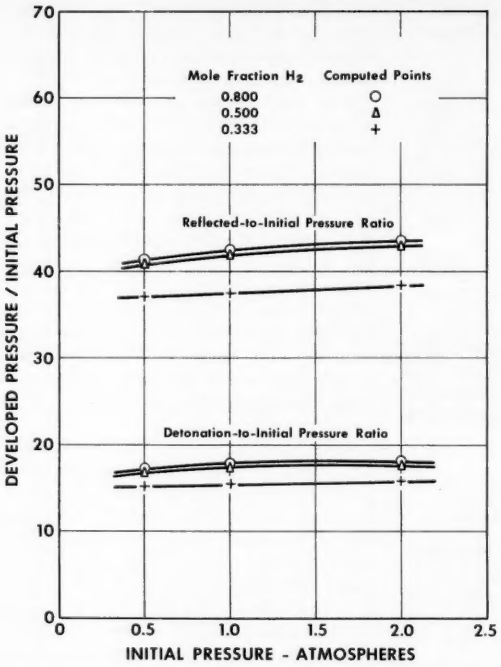

Fig. 9. Effect of initial pressure on developed pressure ratios in hydrogen-oxygen mixtures at 298°K.

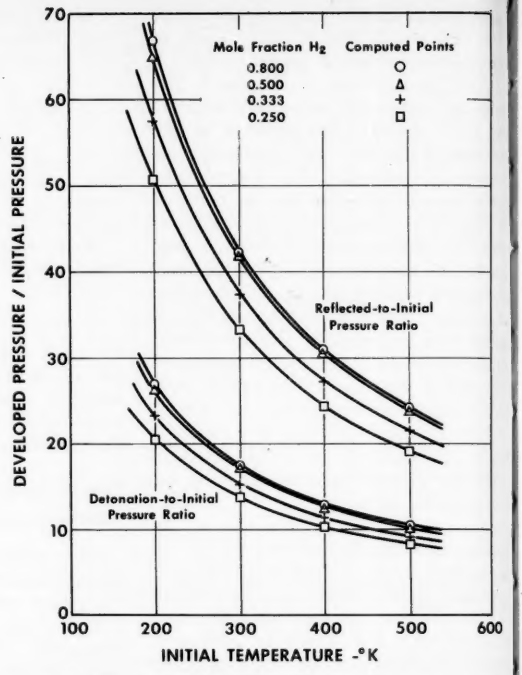

Fig. 10. Effect of initial temperature on developed pressure ratios in hydrogen-oxygen mixtures at atmospheric pressure.

well with values computed from the elementary theory of detonation over a range of compositions from 20 to 80% hydrogen, temperatures from 160° to 477°K., and pressures from ½ to 2 atm. Within this range of conditions the agreement between theory and experiment is poorest, and further investigation is warranted for rich mixtures and subatmospheric pressures. Below 20 and above 80% hydrogen the experimental velocities fall below the predicted values. The general agreement between theory and experimental velocities is surprising in view of the significant deterioration of the structure of the detonation wave front indicated by schlieren photographs for 39% and less hydrogen.

Experimental data to test the computed temperatures, pressures, and compositions are difficult to obtain and are not generally available. However recent work indicates that the computed impact pressure may be a suitable criterion for design.

The detonation velocity depends only slightly on the initial pressure and temperature but critically on the initial composition. The pressures behind the detonation and reflected waves depend only moderately on initial composition but increase linearly with initial pressure and with the reciprocal of the initial temperature.

NOTATION

D = tube diameter, in.

V = measured velocity in straight tube, m./sec.

V_c = measured velocity in coiled tube, m./sec.

V_∞ = equivalent velocity in infinite tube, m./sec.

LITERATURE CITED

1. Beams, J. W., "Physical Measurements in Gas Dynamics and Combustion," p. 26, Princeton Univ. Press, Princeton, New Jersey (1954).
2. Bennett, A. L., and H. W. Wedaa, Second "Office of Naval Research Symposium on Detonation," Washington, D.C. (February, 1955).
3. Berets, D. J., E. F. Greene, and G. B. Kistiakowsky, *J. Amer. Chem. Soc.*, **72**, 1080 (1950).
4. Campbell, C., *J. Chem. Soc.*, **121**, 2483 (1922).
5. Chapman, D. L., *Phil. Mag.*, **47**, 90 (1889).
6. Courant, R., and K. O. Friedricks, "Supersonic Flow and Shock Waves," Interscience Publishers, New York (1948).
7. Dixon, H. B., *Phil. Trans. Royal Soc.*, **A184**, 97 (1893).
8. Ergun, Sabri, *Ind. Eng. Chem.*, **48**, 2063 (1956).
9. Greene, E. F., Ph.D. thesis, Harvard Univ., Cambridge, Massachusetts (1949).
10. Hirshfelder, J. F., C. F. Curtiss, and R. B. Bird, "Molecular Theory of Gases and Liquids," John Wiley, New York (1954).
11. Hoelzer, C. A., and W. K. Stobaugh, Thesis, Air Univ. Command, USAF Inst. Technol., Wright-Patterson Air Force Base, Ohio (March, 1954).
12. Jouguet, E., "Méchanique des Explosives," O. Doin et Fils, Paris, France (1917).
13. Kistiakowsky, G. B., and W. G. Zinman, Second "Office of Naval Research Symposium on Detonation," Washington, D. C. (February 9, 1955).
14. Laffitte, P., *Ann. Phys., Ser. 10*, **4**, 587 (1925).
15. Lewis, B., and J. B. Friauf, *J. Amer. Chem. Soc.*, **52**, 3905 (1930).
16. Lewis, B., and G. von Elbe, "Combustion, Flames, and Explosions of Gases," Academic Press, New York (1951).
17. Luker, J. A., and M. J. Leibson, *J. Chem. Eng.*, **4**, 133 (1959).
18. Moyle, M. P., Ph.D. thesis, Univ. Michigan, Ann Arbor (1956).
19. Ordin, P. M., *Natl. Advisory Comm. Aeronaut. Tech. Note* 3935 (April 1957).
20. Payman, W., and J. Walls, *J. Chem. Soc.*, **123**, 420 (1923).
21. Riemann, B., "Über die Fortpflanzung ebener Luftwellen von endlicher Schwingungsweite," Abhandlungen der Gesellschaft der Wissenschaften Zu Göttingen, Mathematisch-physikalische Klasse 8, 43 (1860).
22. Scorah, R. L., *Chem. Phys.*, 3, 425 (1935).
23. U. S National Bureau of Standards, "Selected Values of Chemical Thermodynamic Properties," U S. Govt. Printing Office, Washington, D. C. (1947, 1948).

Manuscript received August 14, 1958; revision received August 7, 1959; paper accepted August 18, 1959. Paper presented at A.I.Ch.E. Chicago meeting.

Studies on Heat Transfer Near Wall Surface in Packed Beds

SAKAE YAGI and DAIZO KUNII

University of Tokyo, Tokyo, Japan

From studies of annular packed beds wherein the heat flows purely radially, the authors obtained the coefficients of heat transfer on the inner tube surface, as well as the mean effective thermal conductivities of bed. The inner and outer diameters of the annular packed bed were 22 and 70 mm. respectively, and the packings shown in Table 1 were used. The wall film coefficients obtained with air flowing axially through the bed were correlated for $N_{ReM} < 600$ by means of Equation (14).

The coefficients of heat transfer for cylindrical packed beds reported previously by other observers were correlated also by Equation (14), with 0.054 used for values of α_w in the range $N_{ReM} < 2{,}000$.

Consideration of Equation (14) in terms of a theoretical model of heat transfer showed that it was reasonable to apply it for the prediction of wall film coefficient, especially for low Reynolds numbers.

In the development of the analytical methods for the design of catalytic reactors many measurements have been made of effective thermal conductivities in cylindrical packed beds. Hatta and Maeda (*6*) analyzed their experimental data of heat transfer in packed beds with their theoretical formula, which includes the wall film coefficient of heat transfer.

The coefficient h_w, which is important for the heat transfer mechanism in packed beds, has been measured by Coberly and Marshall (*3*), Campbell and Huntington (*2*), Felix (*4*), Plautz and Johnstone (*8*), Quinton and Storrow (*9*), and Calderbank and Pogorski (*1*).

With respect to the usual packed beds of cylindrical packings Hanratty (*5*) has presented the following equation which is based on the correlation for the range $D_pG/\epsilon\mu$ of 80 to 500:

$$\frac{h_w D_p}{k_g} = 0.95 \sim 1.44\left(\frac{D_pG}{\epsilon\mu}\right)^{0.5} \qquad (1)$$

Yagi and Wakao (*13*) measured the coefficients for beds of spherical packings and correlated their data with those of Felix (*4*) and Plautz and Johnstone (*8*) by

$$\frac{h_w D_p}{k_g} = 0.18\left(\frac{D_pG}{\mu}\right)^{0.8} \qquad (2)$$

for the range $D_pG/\mu = 20 \sim 2{,}000$

Equations (1) and (2) for the wall film coefficient of heat transfer cannot be used for flow conditions of small Reynolds numbers, as they make h_wD_p/k_g become zero when $N_{ReM} = 0$.

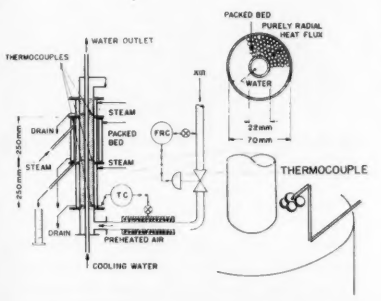

Fig. 1. Experimental annular packed bed and arrangement of copper-constantan thermocouples.

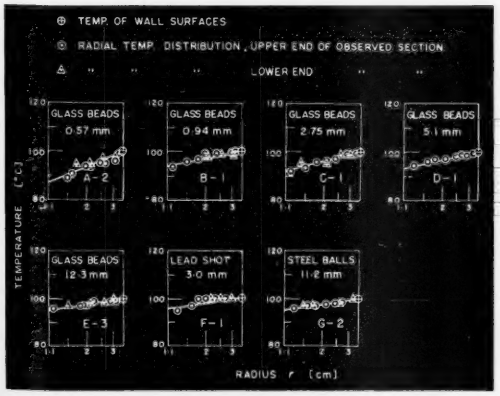

Fig. 2. Radial temperature distribution in annular packed bed, in blank tests without water flow.

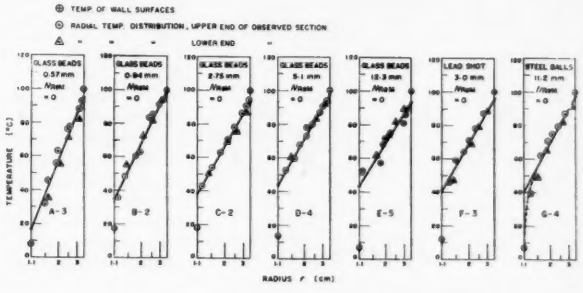

Fig. 3. Radial temperature distribution in annular packed beds without air flow; that is $N_{ReM} = 0$.

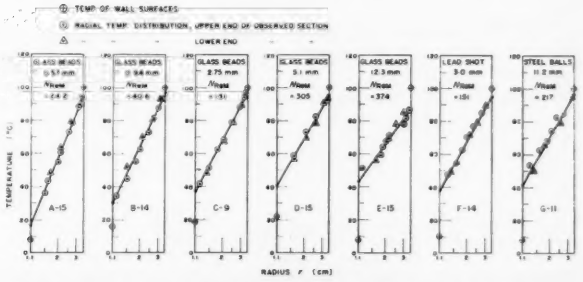

Fig. 4. Radial temperature distribution in annular packed beds with air flowing; $N_{ReM} > 0$.

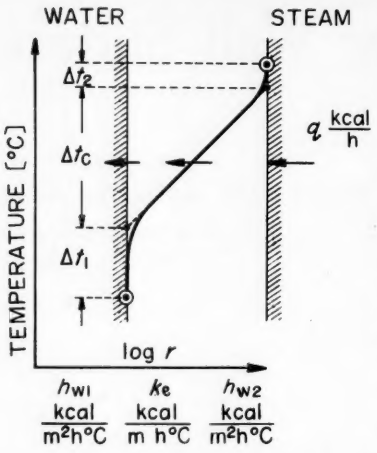

Fig. 5. Model of heat transfer system in annular packed bed.

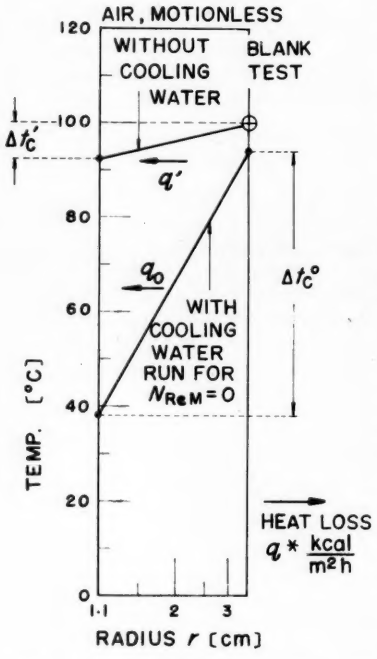

Fig. 6. Schematic illustrations of temperature distributions in annular packed bed, in both cases of blank test and of run with stationary air.

Catalytic reactors in practice have flow conditions corresponding to small Reynolds numbers, due to small catalyst diameters and low linear velocities. Therefore it is necessary for reasonable design calculations of catalytic reactors to obtain correct values of h_w for small Reynolds numbers and further to know the heat transfer mechanisms near the wall surface of packed beds.

However it is impossible to obtain the reliable data for h_w at small Reynolds numbers if the experimental method applied is similar to the previous studies. In these studies the flowing gas was heated or cooled in cylindrical packed beds, and the radial temperature distributions approached the constant wall temperature for small Reynolds numbers. This leads to inaccurate measurement. Hence the authors have made an experimental heater with an annular packed bed, wherein the heat flows purely radially, and have obtained new data for the wall film coefficient of heat transfer on the inner tube surface and mean effective thermal conductivity of the annular packed beds. The results for the wall film coefficient have provided the new correlations which have been compared with the previous experimental data from cylindrical packed beds.

EXPERIMENTAL METHODS

A diagram of the experimental packed bed is shown in Figure 1. The main part was constructed from three steam jackets and a steel pipe cooled by water, with solid particles packed in the annular space between them. The preheated air, the temperature of which is kept constant by a temperature controller, is blown upward into the bed, after being controlled at constant flow rate by a flow-recording controller. The packed bed is kept motionless by the two sheets of screen clamped on the bottom and top of the bed. The test section, the middle steam jacket, is covered by another steam jacket for the thermal insulation. Since the steam jacket of the test section was kept at atmospheric pressure by releasing the excess steam to the air, the saturated temperature of the steam was measured as 100°C. The heat transferred from the steam jacket to the cooling water was calculated from the measured rate of steam condensation, with the heat loss as obtained from preliminary blank tests taken into account. The radial temperature distributions were measured with fine and bare copper-constantan thermocouples arranged in the packed bed, (Figure 1).

To get purely radial heat flux a long calming section of the same packed bed was added below the measuring section, and the inlet air temperature was controlled to be nearly equal to the mean temperature of the outlet air. The calming section proved adequate in ensuring that radial temperature distributions were identical at inlet and outlet planes of the test section. With these conditions the experimental data could be analyzed on the basis that the air was neither heated nor cooled in flowing through any position in the test section of the bed.

Before final measurements were made, blank tests were done without cooling water to measure the heat losses in each packed bed. Figures 2, 3, and 4 show the radial temperature distributions for the blank tests without water flow, for runs without air flow (that is $N_{ReM} = 0$). Table for runs with air flow ($N_{ReM} > 0$). Table 2 includes some examples of the experimental data, from series A to G.*

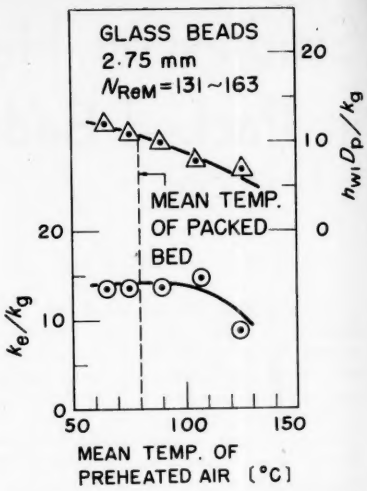

Fig. 7. Effects of preheated air temperature.

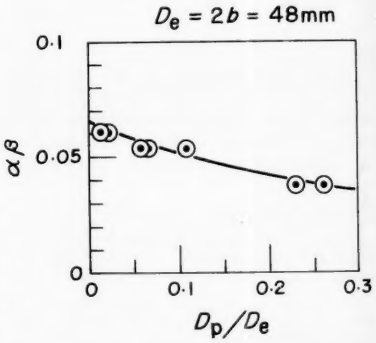

Fig. 8. Factor ($\alpha\beta$) in annular packed beds used.

EXPERIMENTAL RESULTS

In the annular packed bed with the heat flowing purely radially, theoretically the temperature distributions

Table 1. Packings Used in Experiments

	Glass beads and balls					Lead shot	Steel balls
Diameter, (mm.)	0.57	0.94	2.75	5.1	12.3	3.0	11.2
Density, (g./cc.)	2.48	2.53	2.47	2.50	2.52	10.9	7.98
Void fraction (—)	0.355	0.372	0.352	0.375	0.427	0.382	0.461

* Tabular material has been deposited as document No. 6136 with the American Documentation Institute, Photoduplication Service, Library of Congress, Washington 25, D. C., and may be obtained for $1.25 for photoprints or for 35-mm. microfilm.

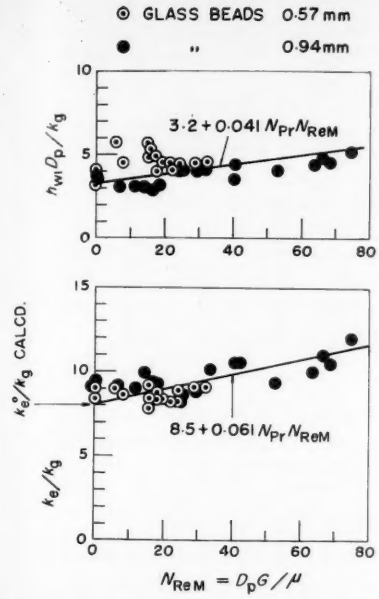

Fig. 9. Data obtained from annular packed beds, glass beads: 0.57-mm., 0.94-mm. diameter.

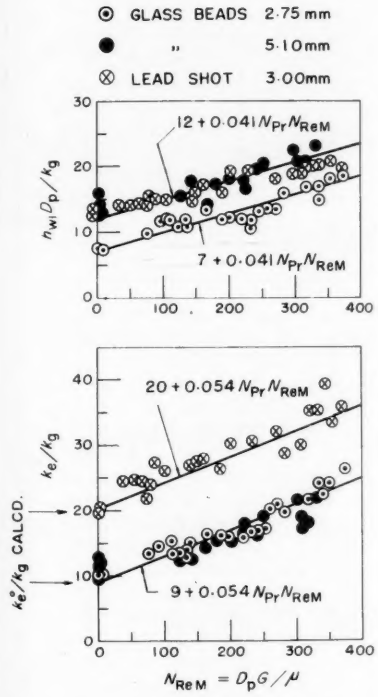

Fig. 10. Data obtained from annular packed beds, glass beads: 2.75-mm., 5.10-mm. diameter; lead shot: 3.0-mm. diameter.

should be straight on the semilogarithmic coordinates, as shown in Figure 5, if the effective thermal conductivity is assumed constant in the packed bed. From the results shown in Figures 3 and 4, it seems reasonable to think that there are thermal resistances on both the external and internal wall surfaces. The data were analyzed by applying the following equations, based on the typical model shown in Figure 5.

$$q = A_{w1} \cdot h_{w1} \cdot \Delta t_1 = A_{avg} \cdot (k_e/b)\ \Delta t_c = A_{w2} \cdot h_{w2} \cdot \Delta t_2 \qquad (3)$$

where

$$A_{avg} = (A_{w2} - A_{w1})/2.3 \log_{10}(A_{w2}/A_{w1})$$

$$A_{w1} = \pi(0.022)(0.250)\,m^2 = 0.01728\ m^2$$

$$A_{w2} = \pi(0.070)(0.250)\,m^2 = 0.05498\ m^2$$

$$A_{avg} = 0.03254\ m^2$$

$$b = (D_2 - D_1)/2 = (0.070\ m - 0.022\ m)/2 = 0.024\ m$$

When one substitutes the above values into Equation (3), the effective thermal conductivity and the wall film coefficient of heat transfer on the inner, and outer surfaces can be calculated from the following equations respectively:

$$k_e = 0.0740\ (q/\Delta t_c) \qquad (4)$$

$$h_{w1}' = 58.0\ (q/\Delta t_1) \qquad (5)$$

$$h_{w2} = 18.2\ (q/\Delta t_2) \qquad (6)$$

The values of the radial heat flow rate are evaluated from the rates of water-vapor condensation as follows:

$$q = V\gamma - q^\circ \qquad (7)$$

In the blank test for finding the heat loss from the test section the rate of water-vapor condensation would give the heat loss immediately, if the temperature at all points of the packed bed equals the wall surface temperature. Since there were small deviations of the radial temperature distribution for the blank tests as shown in Figure 2, the actual outward heat loss from the test section must be corrected. In Figure 6 the values for the blank test and for the run with stationary air are shown schematically.

In the blank test

$$q^\circ + q' = \gamma V' \qquad (8)$$

For the runs with the stationary air and with the cooling water

$$q^\circ + q_o = \gamma V_o \qquad (9)$$

The effective thermal conductivity for both cases should be the same; therefore

$$q'/q_o = \Delta t'_c/\Delta t^\circ_c \qquad (10)$$

Using Equations (8), (9) and (10), one can easily obtain the value of q° from

$$q^\circ = \gamma \frac{V' - (\Delta t'_c/\Delta t^\circ_c)V_o}{1 - (\Delta t'_c/\Delta t^\circ_c)} \qquad (11)$$

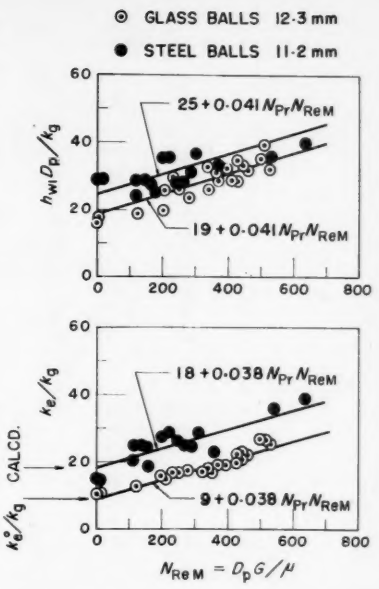

Fig. 11. Data obtained from annular packed beds, glass balls: 12.3-mm. diameter; steel balls: 11.2-mm. diameter.

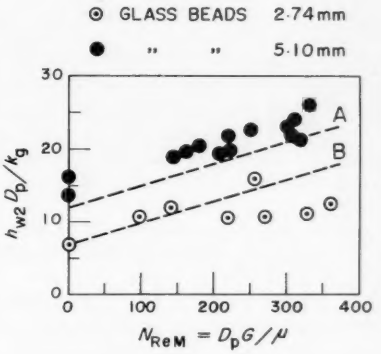

Fig. 12. Wall film coefficient on outer-tube surface in annular packed beds.

The following is a sample of the calculation for 2.75-mm. glass beads in Table 2, series C:

$$V' = 30.5\ \text{g./hr.} = (30.5)10^{-3}\ \text{kg./hr.}$$

$$V_o = 63.5\ \text{g./hr.} = (63.5)10^{-3}\ \text{kg./hr.}$$

$$\Delta t'_c = 6.5°\text{C.}$$

$$\Delta t^\circ_c = 56.0°\text{C.}$$

$$\gamma = 539.3\ \text{kg.-cal./kg.}$$

$$q' = (539.3)\frac{(30.5)10^{-3} - (6.5/56.0)(63.5)10^{-3}}{1 - (6.5/56.0)} = 14.1\ \text{kg.-cal./hr.}$$

TABLE 2. EXAMPLES OF EXPERIMENTAL DATA

Experiment No.	Packing	Diam., mm.	Inlet air Flow rate NTP, cc./sec.	Inlet air Mean temp., °C.	Bed mean temp., °C.	Vapor condensation rate, g./sec.	Cooling water flow rate, g./sec.	Cooling water mean temp., °C.	Reynolds Number	Temp. Differential Δt_c, °C.	Temp. Differential Δt_l, °C.	k_g kg.-cal. (m.)(hr.)(°C.)	h_{w1} kg.-cal. (sq. m.)(hr.)(°C.)	k_c / k_g	$h_{w1} D_p / k_g$
A-2	Glass	0.57	0	—	97	37.6	0	—	—	14	—		Blank test for heat loss		
4	beads		0	—	76	74.4	321	7	0	83	12	0.216	121	8.6	3.2
6			760	85	76	74.0	316	8	7.8	80	9	0.221	170	8.6	4.5
11			1720	85	75	74.0	316	8	17.6	81	8	0.221	185	8.6	4.9
17			3160	85	75	76.0	262	8	32.4	79	9	0.237	170	9.2	4.5
B-1	Glass	0.94	0	—	98.5	29.3	0	—	—	6	—		Blank test for heat loss		
3	beads		0	—	83	66.0	331	17	0	67	15.5	0.237	82.5	9.22	3.52
6			850	75	82.5	67.6	310	16	14.3	65	19	0.254	70.0	9.88	3.00
12			1900	79	80	69.0	310	17	32.2	65.6	14.5	0.261	95.5	10.2	4.08
19			4450	63	80	81.0	310	16	75.3	70.5	12.5	0.310	142	12.0	5.13
C-1	Glass	2.75	0	—	98	30.5	0	—	—	6.5	—		Blank test for heat loss		
3	beads		0	—	81	63.5	363	19	0	56	19.5	0.266	61.0	10.4	7.62
4			1500	80	81	75.2	297	22	74	56.5	19	0.346	82.7	13.5	10.3
9			2650	90	81	77.3	215	19	131	59.5	19	0.338	85.5	13.2	10.7
20			5400	75	78	103	286	15	266	56	21	0.548	107	21.3	13.4
26			7550	75	78	122	286	15	372	56.5	21.5	0.676	145	26.4	18.1
D-1	Glass	5.1	0	—	98.5	33.0	0	—	—	6.5	—		Blank test for heat loss		
5	beads		0	—	83	74.0	286	14	0	56	28	0.334	55.4	13.0	12.8
9			1950	79	80	84.2	271	13.5	178	57.5	24	0.395	75	15.4	17.6
13			2400	79	80	89.0	271	13.5	236	59	23	0.417	85.9	16.2	19.8
19			3650	65	80	108	245	13.5	332	57.5	26	0.560	99.5	21.8	23.0
E-1	Glass	12.3	0	—	98.5	37.2	0	—	—	4	—		Blank test for heat loss		
5	balls		0	—	81	66.4	335	7	0	48	6	0.285	28.4	11.0	15.8
6			530	85	78	70.8	366	8	116	45	36	0.343	34.0	13.3	18.9
10			1130	85	75	84.4	352	7	249	48	31	0.434	50.9	16.9	28.3
19			1930	80	77	96.3	361	7	425	49	33	0.603	61.9	23.5	34.6
24			2400	85	78	101.8	366	8	528	42	38	0.661	57.9	25.7	32.2
F-2	Lead	3.0	0	—	99.5	36.6	0	—	—	2.5	—		Blank test for heat loss		
5	shot		0	—	81.5	110.8	233	11.5	0	60.5	27	0.511	92.1	19.9	12.5
6			670	80	83.0	125	229	10.5	36.1	58	29.5	0.630	100	24.5	13.6
15			3000	80	81.5	140	311	11	161.5	59	27.5	0.720	124	28.0	16.9
21			5650	85	79.0	145.2	211	10	304	57.5	26	0.777	135	30.2	18.5
25			6550	85	78.5	160.6	273	10	352	59	26.5	0.860	151	33.5	20.6
G-1	Steel	11.2	0	—	99	33.6	0	—	—	5	—		Blank test for heat loss		
4	balls		0	—	84	80.6	393	7	0	56	29	0.371	57.0	14.8	29.1
5			520	85	85	84.8	333	8	115	54	37	0.490	56.6	25.8	28.9
11			1080	85	84	95.0	333	8	217	56	34	0.548	70.6	29.7	36.0
18			3150	80	83	125.6	290	7	634	42	44	1.015	78.3	39.5	39.9

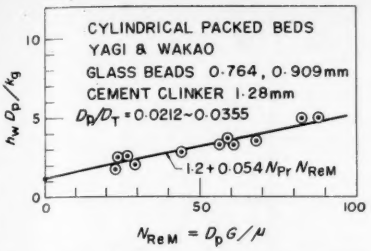

Fig. 13. Correlation of data observed by Yagi and Wakao (13) in cylindrical packed beds.

This value was used to calculate q for all of the data in series C of Table 2.

The linear velocity of the flowing water was greater than 1 m./sec., and the temperature rise of the water was less than 1°C. through the packed bed; therefore the mean temperature of water was taken as the temperature of the heat sink as shown in Figures 2, 3, and 4. The resistances for thermal conduction through the metal walls are negligible compared with those of the wall film in the packed bed. However the resistance of boundary film of the cooling water must be considered, even though the necessary corrections are a few per cent for every case. The heat transfer coefficient of the cooling water under the conditions in the experiments was estimated to be 3,670 kg.-cal./(sq.m.)(hr.)(°C.) from the Dittus-Boelter equation. A corrected value for the wall film coefficient of heat transfer on the inner tube surface was calculated from

$$\frac{1}{h_{w1}} = \frac{1}{h_{w1}'} - \frac{1}{3{,}670} \quad (12)$$

The values obtained in this way from series A to G are shown in Table 2 and correlated in Figures 9, 10, and 11, where the data for the wall film coefficient of heat transfer on the outer surface are omitted.

For the over-all heat transfer system in the annular packed bed shown in Figure 5, the temperature difference becomes too small to determine h_{w2} accurately, because both the surface area and the thermal conductivity of the air for the outer tube surface are larger than those of the inner tube surface, the ratio of their effects being $A_{w1} \cdot k_{g1}/A_{w2} \cdot k_{g2} = 0.247$.

Even though the data for Δt_2 are thus not so reliable as those for Δt_1, the examples of calculated h_{w2} are shown in Figure 12, where the two lines A and B are the correlations for $h_{w1} \cdot D_p/k_g$ on the inner tube surface for the same packings respectively.

To indicate the deviations of the observed value from the correct one when there is considerable difference between the temperatures of inlet and outlet air, the effects of the temperature of preheated air are shown in Figure 7. Since the mean temperature of the annular packed bed, which is the same as that of the outlet air, is about 80°C. for the runs in Figure 7, the correct values of k_e/k_g and $h_{w1} \cdot D_p/k_g$ should be the values corresponding to 80°C. on the abscissa. The deviations from the correct data do not exceed 10% if the inlet temperature is kept within 80° ± 15°C.

DISCUSSION

As for the values in the common cylindrical packed beds, the data of k_e/k_g obtained here are correlated by the following equation, which was described theoretically in a previous paper (12):

$$\frac{k_e}{k_g} = \frac{k_e^\circ}{k_g} + (\alpha\beta) N_{Pr} N_{ReM} \quad (13)$$

The values of $(\alpha\beta)$ are correlated with the ratio (D_p/D_e) in Figure 8. Values of k°_e/k_g calculated by Equation (15) of the authors' previous paper (12) nearly coincide with the experimental data as shown in Figures 9, 10, and 11 of this paper. The effects of the thermal conductivity of the packings seem to be considerable, especially under flow conditions of low Reynolds number.

Figure 3 shows the existence of the thermal resistances at the tube surface, or the wall film coefficients of heat transfer, when $N_{ReM} = 0$. In Figure 3 the temperature differences on both tube surfaces are too small to get the accurate data in the case of 0.57-mm. glass beads. On the other hand for large ratios of the packing diameter to the thickness of the annular space of the packed bed, 0.467 and 0.515 for the cases of 11.2-mm. steel balls and 12.3-mm. glass balls respectively, temperature measurements scatter as shown in Figures 3 and 4. For the other packings the temperature differences were determined easily, and so there are comparatively small deviations from correlations for these cases, Figures 9 and 10.

The following formula for heat transfer coefficient was obtained here. It is similar to that for effective thermal conductivity but differs very much from previously reported equations for h_w:

$$\frac{h_{w1} \cdot D_p}{k_g} = \frac{h_{w1}^\circ \cdot D_p}{k_g} + \alpha_w N_{Pr} N_{ReM} \quad (14)$$

The value of (α_w) suitable for Figures 9, 10, and 11 is 0.041 in these experiments on the annular packed beds, and the values of $h_w^\circ \cdot D_p/k_g$ are shown in Table 3.

With reference to the wall film coefficients on the outer tube surface, there are few reliable data in these experiments, as mentioned above. However comparing Figure 12 with Figure 10, one can reasonably consider that there are no fundamental differences between the two correlations for both the wall film coefficients.

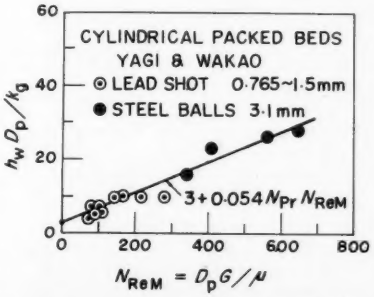

Fig. 14. Correlation of data observed by Yagi and Wakao (13) in cylindrical packed beds.

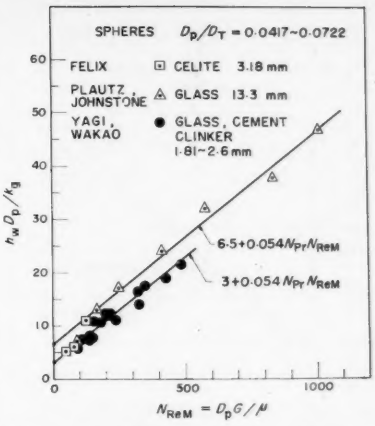
SPHERES D_p/D_T = 0·0417~0·0722
FELIX CELITE 3·18 mm
PLAUTZ, JOHNSTONE GLASS 13·3 mm
YAGI, WAKAO GLASS, CEMENT CLINKER 1·81~2·6 mm
6·5+0·054 N_{Pr} N_{ReM}
3+0·054 N_{Pr} N_{ReM}
$h_w D_p/k_g$
$N_{ReM} = D_p G/\mu$

Fig. 15. Correlation of data by Felix (4), Plautz and Johnstone (8), and Yagi and Wakao (13) in cylindrical packed beds.

APPLICATION OF NEW EQUATION TO CYLINDRICAL PACKED BEDS

If one assumes that there are no fundamental differences between the heat transfer mechanisms in cylindrical and annular packed beds, the recent and reliable data directly measured by Felix (4), Plautz and Johnstone (8), and Yagi and Wakao (13) may be correlated with the modified Reynolds number $D_p \cdot G/\mu$ as shown in Figures 13 to 16 for each value of D_p/D_T. Thus Equation (14) can be applied to the experimental values of h_w obtained previously by other observers for the common cylindrical packed beds of spherical packings. However the values of (α_w) in Equation (14) suitable for Figures 13 to 16 is 0.054, which is larger than the value 0.041 in the annular packed bed used here. Table 3 shows the values of $h_w^\circ \cdot D_p/k_g$. The difference between the two numerical values of (α_w) may be attributed to the difference in the packing states for

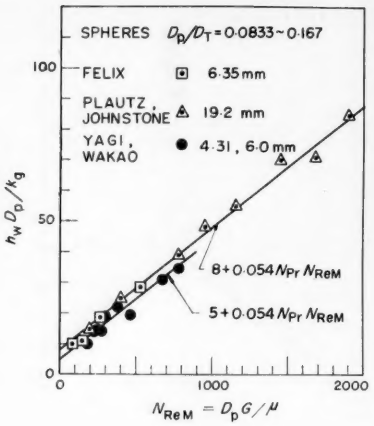
SPHERES D_p/D_T = 0.0833 ~ 0.167
FELIX ⊡ 6.35 mm
PLAUTZ, JOHNSTONE ▲ 19.2 mm
YAGI, WAKAO ● 4.31, 6.0 mm
8 + 0.054 N_{Pr} N_{ReM}
5 + 0.054 N_{Pr} N_{ReM}
$h_w D_p/k_g$
$N_{ReM} = D_p G/\mu$

Fig. 16. Correlation of data by Felix (4), Plautz and Johnstone (8), and Yagi and Wakao (13) in cylindrical packed beds.

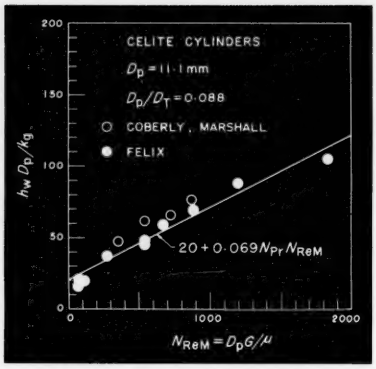

Fig. 17. Correlation of data by Coberly and Marshall (3) and Felix (4) in cylindrical beds packed with cylindrical solids.

particles in annular and cylindrical packed beds. Thus the fundamental mechanisms of heat transfer on the wall surfaces must be considered similar for both cylindrical packed beds and annular beds.

For cylindrical packings Coberly and Marshall (3) and Felix (4) have presented experimental data of h_w which are too scattered to be correlated by a simple equation. However if the data of h_w are plotted for some narrow range of D_p/D_T as shown in Figure 17, it can be assumed that the correlation similar to Equation (14) is applicable for the cylindrical packings, even though the numerical values of constants may not necessarily be the same as those for spherical packings.

THEORETICAL CONSIDERATIONS ON NEW CORRELATION

The correlation obtained here is so different from previously presented correlations, that is Equations (1) or (2), that neither the penetration theory (5) nor boundary-film theory explains the real heat transfer phenomena near the wall surface in the packed beds. Therefore another model of heat transfer must be applied.

Previously Kwong and Smith (7) reported the data for the radial distribution of the effective thermal conductivities in packed beds and showed the sharp decrease near the wall surface. These phenomena are considered most important in this paper in the analysis of the thermal resistance near the wall surface of the packed beds, especially under the flow conditions of low Reynolds numbers.

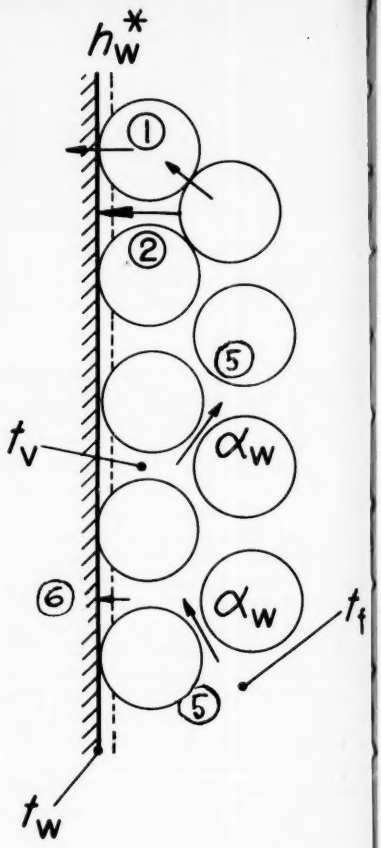

Fig. 18. Model of heat transfer near wall surface of packed bed.

Table 3. $h_{w1}{}^{\circ} D_p/k_g$ for Annular Packed Beds and for Cylindrical Packed Beds

Annular packed beds, D_e = 48 mm.

Packing	D_p/D_e	D_p, mm.	$h_{w1}{}^{\circ} D_p/k_g$
Glass beads	0.0196	0.94	3.2
Glass beads	0.0572	2.75	7
Glass beads	0.106	5.1	12
Glass beads	0.256	12.3	19
Lead shot	0.0625	3.0	12
Steel balls	0.233	11.2	25

Cylindrical packed beds

Packing	D_p/D_T	D_p, mm.	$h_w{}^{\circ} D_p/k_g$
Glass beads and cement clinkers	0.021-0.036	0.76-0.91	1.2
Celite balls and glass beads	0.0417-0.0722	1.81-3.18	3
		13.3	6.5
Celite balls, glass beads and cement clinkers	0.0833-0.167	4.31-6.35	5
		19.2	8
Lead shot	0.021-0.042	0.77-1.5	3

Schwartz and Smith (11) showed that the fraction void near the wall surface is larger than that in the core portion of the packed bed. It is reasonable to assume that the lower degree of lateral mixing is the main cause of the sharp decrease in the effective thermal conductivity near the wall surface.

In cases of analysis for wall film coefficients of heat transfer the average values of the effective thermal conductivities in packed beds are determined by all observers. Thus the sharp decrease of the effective thermal conductivities near the wall surface looks like the existence of a definite thermal resistance at that point, which may be ascribed to a fluid boundary film on the wall.

In Figure 18, which is the authors' model of heat transfer mechanisms near the wall surface in the packed bed, the following mechanisms are assumed, with the real film coefficient of heat transfer on the wall surface considered to be caused only by the true fluid boundary layer at the wall surface.

a. Heat transfer through solid phases
1. Heat transfer through the thin

TABLE 4. COMPARISON OF α_w WITH α

		Mean value in* packed bed	Near the wall surface
Cylindrical packed bed	$D_p/D_T = 0.15$	$\alpha = 0.11$†	$\alpha_w = 0.054$
Annular packed bed	$D_p/D_e = 0.15$	$\alpha = 0.078$	$\alpha_w = 0.041$

* Where β is assumed to be 0.9.
† Calculated from the correlation obtained in authors' previous paper (*12*).

gas film near contact points
2. Radiant heat transfer from solid surface to solid surface (Mechanisms 1 and 2 are parallel.)

b. Heat transfer in void spaces, independent of fluid flow
3. Molecular thermal conduction
4. Radiant heat transfer from void to void (Mechanisms 3 and 4 are parallel.)

c. Heat transfer in void spaces, dependent on fluid flow
5. Heat transfer caused by the lateral mixing of the flowing fluid
6. Heat transfer through the true boundary film (Mechanisms 5 and 6 are in series.)

As shown in Figure 18 the mechanisms *a*, *b*, and *c* can be considered in parallel. The heat flow by mechanism 5, namely by the lateral mixing of flowing fluids, is defined here as Q kg.-cal./(sq.cm.)(hr.), which can be presented with $Q = GC_p\alpha_w t_f - GC_p\alpha_w t_v = GC_p\alpha_w(t_f - t_v)$.

Therefore the heat transfer coefficient by lateral mixing can be calculated as

$$(h_w)_t = \frac{Q}{t_f - t_v} = \alpha_w G C_p \quad (15)$$

Then

$$\frac{(h_w)_t D_p}{k_g} = \alpha_w (C_p\mu/k_g)(D_pG/\mu) = \alpha_w N_{Pr} N_{ReM} \quad (16)$$

The mechanisms *a* and *b* can be assumed independent of the fluid flow, the constant term h_w° presumably originating from the above mechanisms. Therefore, considering the heat transfer mechanisms mentioned above, one can give the apparent wall film coefficient of heat transfer by

$$h_w = h_w^\circ + (h_w)_f \quad (17)$$

$$\frac{1}{(h_w)_f} = \frac{1}{h_w^*} + \frac{1}{(h_w)_t} \quad (18)$$

Therefore for all ranges of N_{ReM}

$$\frac{h_w D_p}{k_g} = \frac{h_w^\circ D_p}{k_g} + \frac{1}{\frac{1}{h_w^* D_p/k_g} + \frac{1}{\alpha_w N_{Pr} N_{ReM}}} \quad (19)$$

Since there are no reliable data which can present the correct relationship between the real wall film coefficient of heat transfer and the Reynolds number, an exact quantitative discussion is impossible here. However it seems quite probable that the numerical values of h_w° predominate under conditions of low Reynolds numbers compared with h_w^* and that in turbulent regions h_w^* is larger than $(h_w)_t$ for Reynolds numbers less than 2,000. Thus α_w in the experimental Equation (14) is approximately equal to the ratio of the lateral mixing of flowing fluid, which was defined by Ranz (*10*) as

$$\alpha_w = \frac{\text{Mass velocity of fluid flowing in the direction of heat and mass transfer (near the wall surface)}}{\text{Mass velocity of fluid based on sectional area of empty tube in the direction of fluid flowing}}$$

The numerical values of α_w are compared with those of α for the mean value of the effective thermal conductivities in Table 4. The ratios of α_w to α are almost ½ for both cases. Therefore it can be assumed that the degree of lateral mixing decreases near the wall surface to about half of that in the core.

CONCLUSIONS

The data for the wall film coefficient for the inner tube surface can be correlated with the new formula, namely Equation (14). The data previously presented for the wall film coefficient of heat transfer in the ordinary cylindrical packed beds by the other observers are replotted on Cartesian coordinates, and it is found that the above correlation, that is Equation (14), can be applied for these cases as well. The new correlation obtained by the authors is so different from the correlations previously presented that a new model of heat transfer near the wall surface in the packed beds must be applied in order to explain it.

ACKNOWLEDGMENT

The authors wish to express their appreciation to Mutsuo Takita for his assistance in performing the experimental work.

NOTATION

A_w = surface area of tube, sq. m.
b = $(D_2 - D_1)/2$ = clearance of annular space, m.
C_p = specific heat of fluid, kg.-cal./(kg.)(°C.)
D_e = $2b = D_2 - D_1$ = effective diameter of annular packed bed, m.
D_1 = diameter of inner tube, m.
D_2 = diameter of outer tube, m.
D_p = average diameter of packings, m.
D_T = diameter of cylindrical packed bed, m.
G = mass velocity of fluid, kg./(sq. m.)(hr.)
h_w = wall film coefficient of heat transfer in cylindrical packed bed, kg.-cal./(sq.m.)(hr.)(°C.)
h_w° = wall film coefficient of heat transfer in packed bed with stationary fluid, kg.-cal./(sq. m.)(hr.)(°C.)
h_{w1} = wall film coefficient of heat transfer on surface of inner tube in annular packed bed, kg. - cal./(sq.m.)(hr.)(°C.);
h_{w1}° = that with stationary gas.
h_{w1}' = uncorrected value of wall film coefficient of heat transfer on surface of inner tube in annular packed bed, kg.-cal./(sq. m.)(hr.)(°C.)
h_{w2} = wall film coefficient of heat transfer on surface of outer tube in annular packed bed, kg.-cal./(sq. m.)(hr.)(°C.)
h_w^* = wall film coefficient of heat transfer caused from boundary layer on wall surface, kg.-cal./(sq. m.)(hr.)(°C.)
$(h_w)_f$ = heat transfer coefficient concerning heat flux in void space of packed bed, kg.-cal./(sq. m.)(hr.)(°C.)
$(h_w)_t$ = heat transfer coefficient caused from lateral mixing of fluid, kg.-cal./(sq. m.)(hr.)(°C.)
k_e = mean effective thermal conductivity in packed bed, kg.-cal./(sq. m.)(hr.)(°C./m.)
k_e° = mean effective thermal conductivity in packed bed with stationary fluid, kg.-cal./(sq. m.)(hr.)(°C./m.)
k_g = thermal conductivity of fluid flowing in packed bed, kg.-cal./(sq. m.)(hr.)(°C./m.)
N_{Pr} = $C_p\mu/k_g$ = Prandtl number
N_{ReM} = D_pG/μ = Reynolds number
Q = lateral heat flux by mixing

through void space in packed bed, kg.-cal./(sq. m.)(hr.)

q = purely radial heat flow in annular packed bed, kg.-cal./(hr.)

q^* = heat loss from test section of annular packed bed, kg.-cal./(hr.)

q' = purely radial heat flow in annular packed bed for blank test, kg.-cal./(hr.)

q_o = purely radial heat flow in annular packed bed with stationary fluid, kg.-cal./(hr.)

t_f = mean temperature of fluid in void space, °C.

t_v = mean temperature of fluid in void space nearest to wall surface, °C.

Δt_c = apparent temperature difference in annular packed bed, °C.

$\Delta t_c'$ = apparent temperature difference in annular packed bed for blank test, °C.

Δt_c° = apparent temperature difference in annular packed bed with stationary fluid, °C.

Δt_1 = apparent temperature difference on inner tube surface of annular packed bed, °C.

Δt_2 = apparent temperature difference on outer tube surface of annular packed bed, °C.

V = rate of vapor condensation in annular packed bed, kg./(hr.)

V_o = rate of vapor condensation in annular packed bed with stationary flund, kg./(hr.)

V' = rate of vapor condensation in annular packed bed for blank test, kg./(hr.)

Greek letters

α = (mass velocity of fluid flowing in direction of heat or mass transfer)/(mass velocity of fluid based on sectional area of empty tube in direction of fluid flowing)

α_w = above value near wall surface in packed bed

β = (effective length between centers of two neighboring solids in direction of heat flow)/(average diameter of solid)

γ = latent heat of vapor condensation, kg.-cal./kg.

ϵ = void fraction of packed bed

μ = viscosity of fluid, kg./(m.)(hr.)

LITERATURE CITED

1. Calderbank, P. H., and L. A. Pogorski, *Trans. Inst. Chem. Engrs.* (*London*), **35**, 195 (1957).
2. Campbell, T. M., and R. L. Huntington, *Petrol. Refiner*, **31**, 123 (1952).
3. Coberly, C. A., and W. R. Marshall, Jr., *Chem. Eng. Progr.*, **47**, 141 (1951).
4. Felix, T. R., Ph.D. thesis, Univ. of Wisconsin, Madison (June, 1951).
5. Hanratty, T. J., *Chem. Eng. Sci.*, **3**, 209 (1954).
6. Hatta, S, and S. Maeda, *Chem. Eng.* (*Japan*), **12**, 56 (1948); **13**, 79 (1949).
7. Kwong, S. S., and J. M. Smith, *Ind. Eng. Chem.*, **49**, 894 (1957).
8. Plautz, D. A., and H. F. Johnstone, *A.I.Ch.E. Journal*, **1**, 193 (1955).
9. Quinton, J. H., and J. A. Storrow, *Chem. Eng. Sci.*, **5**, 245 (1956).
10. Ranz, W. E., *Chem. Eng. Progr.*, **48**, 248 (1952).
11. Schwartz, C. E., and J. M. Smith, *Ind. Eng. Chem.*, **45**, 1209 (1953).
12. Yagi, Sakae, and Daizo Kunii, *A.I.Ch.E. Journal*, **3**, 373 (1957); *Chem. Eng.* (*Japan*), **18**, 576 (1954).
13. Yagi, Sakae, and Noriaki Wakao, *A.I.Ch.E. Journal*, **5**, 79 (1959).

Manuscript received October 17, 1958; revision received May 26, 1959; paper accepted June 5, 1959.

Thermodynamic Consistency of Binary Liquid-Vapor Equilibrium Data When One Component Is Above Its Critical Temperature

S. B. ADLER, LEO FRIEND, R. L. PIGFORD, and G. M. ROSSELLI

The M. W. Kellogg Company, New York, New York

Methods are developed for testing binary system phase-equilibrium data for thermodynamic consistency when the more volatile component is above its critical temperature. The isothermal case with varying pressure and the isobaric case with varying temperature are considered individually. The rigorous form of the Duhem equation is employed rather than the simplified one, which for binary systems is inconsistent with the phase rule. Although derived for the specific case given in the title, the relationships developed are applicable to all conditions of binary systems. Sample calculations illustrating the methods are included.

As the design procedures originally applied to petroleum plant distillation problems have spread to the chemical and petrochemical fields, there has been an increasing need to use laboratory-obtained phase-equilibrium data. With this has developed the need for establishing the thermodynamic consistency of such information. Considerable attention has been given to this subject in the literature (*1*, *4* to *8*, *13*, *17*).

All methods published for making the necessary thermodynamic tests for reliability are based on some form of the Duhem equation. Some authors (*7*, *17*) have allowed for the fact that a binary system cannot change in composition when both temperature and pressure remain constant; others have not. A few have included a correction for the nonideality of the vapor phase above the solution. Most of the methods

R. L. Pigford is at the University of Delaware, Newark, Delaware.

have been developed for testing sets of isobaric data, but some pertain to isothermal data.

None of the published articles have considered the case where a stable liquid phase does not exist over the whole range of composition from one extreme of pure component A to the other of pure component B. This arises when the mixture is at a temperature above the critical temperature of the light component. Examples of data reported where one component is above its t_c are ethane-propylene (*9, 10*), hydrogen-methane (*3, 15*), methane-propane (*12*), and the many systems included in the text by Ruhemann (*14*) on the separation of gases.

The Duhem equation in the approximate form

$$x_1\, d\ln\gamma_1 + x_2\, d\ln\gamma_2 = 0 \quad \text{(constant } \pi,\ t) \tag{1}$$

is commonly associated with this problem of testing thermodynamic consistency. For the purpose of testing a set of experimental data the activity coefficients of each component are plotted vs. composition. The areas under each of the two lines are then examined. According to this test the two areas are equal if the data are consistent. A similar diagram for the case described in the preceding paragraph is given in Figure 1. In actuality, when both activity coefficients are based on the components in their pure state, as is conventionally the case in drawing these diagrams, Figure 1 cannot really be obtained. Because the lighter component is above its critical point, no vapor-pressure curve is available to calculate a γ. Unless the temperature is only slightly above t_c, any extrapolation of the vapor-pressure curve would be too inaccurate to reach a conclusion about thermodynamic consistency. Except for the work of Ibl and Dodge (*7*), all the published methods for testing the consistency of the data depend on the use of activity coefficients and vapor pressures.

It was the objective of the present work to develop methods for testing both isothermal and isobaric data for binary systems: that are not dependent on vapor pressures and activity coefficients; that are not restricted to a vapor phase that is ideal; that do not assume that the volume of the liquid is negligible; that do not necessitate drawing a tangent to temperature–composition or pressure–composition lines, with resulting compromises in accuracy; and that do not assume that the composition of the liquid for a binary system can be varied at constant temperature and pressure.

Aside from the practical difficulty of computing activity coefficients referred to the pure liquid as a standard state when the temperature is above the component's critical value, γ's have been avoided for another reason. In many cases, particularly where extrapolating data or combining various sets of data is not involved, use of activity coefficients is not only unnecessary but complicates the procedure.

It should be emphasized that although the methods of testing data developed below are for the purpose of handling problems where the more volatile component is above its critical, such methods have general application at all temperatures.

THE CONSTANT-TEMPERATURE CASE

As a starting point for the present study Equation (2), which is developed by Ibl and Dodge (*7*) as their Equation (7), is selected:

$$x_1\, d\ln f_1 + x_2\, d\ln f_2 = \frac{v^L}{RT}\, d\pi = \frac{v^L \pi}{RT}\, d\ln\pi \tag{2}$$

When one assumes that the Lewis and Randall fugacity rule applies to the vapor phase,

$$f_i = y_i f_i^{\circ} = y_i \pi \nu_{i\pi} = K_i x_i \pi \nu_{i\pi} \tag{3}$$

First one should substitute $y_i\pi_i\nu_{i\pi}$ for f_i and let

$$Z^L \equiv \frac{v^L \pi}{RT}$$

$$x_1 d\ln\,(y_1\,\pi\nu_{1\pi}) + x_2 d\ln\,(y_2\pi\nu_{2\pi}) = Z^L\, d\ln\,\pi \tag{4}$$

Alternately, in terms of K constants one should replace f_i with $K_i x_i \pi \nu_{i\pi}$ and simplify to yield

$$x_1 d\ln\,(K_1\pi\nu_{1\pi}) + x_2 d\ln\,(K_2\,\pi\nu_{2\pi}) = Z^L\, d\ln\pi \tag{5}$$

The two principal expressions obtained so far, Equations (4) and (5), make use of the fugacity coefficient to allow for the nonideality of the vapor phase. If it is more convenient to work with compressibility factors instead of $\nu_{i\pi}$, the modified Duhem equation is developed as follows:

$$f_i = \pi\, y_i\, e^{\left(\int_0^{\pi} \frac{\overline{v_i}^g}{RT}\, d\pi - \int_0^{\pi} \frac{d\pi}{\pi}\right)} \tag{6}$$

$$d\ln f_i = d\ln\,(\pi\, y_i) + \left(\frac{\pi \overline{v_i}^g}{RT} - 1\right) d\ln\,\pi \tag{7}$$

and

$$Z_i^g \equiv \frac{\pi \overline{v_i}^g}{RT}$$

Inasmuch as it is assumed that the Lewis and Randall rule applies to the vapor, one can replace $\overline{v_i}^g$ with v_i^g, the molar volume of the pure component. However for component 2, which is in a supercooled state as a gas, the value of $\overline{v_2}^g$ would have to be found by extrapolation into an unstable region. Instead $\overline{v_2}^g$ is introduced as follows.

Because $v^g = y_1\overline{v_1}^g + y_2\overline{v_2}^g$, when the partial molal values are replaced,

$$\overline{v_2}^g = \frac{v^g - y_1\overline{v_1}^g}{y_2} \cong \frac{v^g - y_1 v_1^g}{y_2}$$

If now y_i/K_i is substituted for x_i, the following expression is finally obtained from (2):

$$x_1\, d\ln K_1 + x_2\, d\ln K_2 = \left[\, Z^L + Z_1^g\, y_1 \left(\frac{1}{K_2} - \frac{1}{K_1}\right) - \frac{Z^g}{K_2}\right] d\ln\pi \tag{8}$$

All the quantities in this equation can be evaluated from the experimental equilibrium data or from data on the pure components without extrapolation into metastable regions.

When one integrates between the limits where $x_1 = 0$ and some maximum concentration $x_1 = x_b$ and between the corresponding limits for the K's,

$$\int_{K_1^{(0)}}^{K_1^{(x_b)}} x_1\, d\ln K_1 + \int_{K_2^{(1)}}^{K_2^{(1-x_b)}} x_2\, d\ln K_2 = \int_{\pi(0)}^{\pi(x_b)} \left[Z^L + Z_1^g\, y_1\left(\frac{1}{K_2} - \frac{1}{K_1}\right) - \frac{Z^g}{K_2}\right] d\ln\pi \tag{9}$$

where $K_1(x_1)$ is regarded as a function of x_1, $K_2(x_2)$ as a function of x_2, and $\pi(x_1)$ as a function of x_1.

Where experimental volumes are available, the values of Z may be found directly; otherwise they are obtained from generalized charts.

The three terms in Equation (9), or the integrated forms of Equation (4) or (5), represent areas designated from left to right as A_1, A_2, and A_3. In the commonly found simplified form of the Duhem equation, Equation (1), as noted previously $A_3 = 0$ and $A_1 = A_2$ for consistent data. Examination of Equations (4), (5), and (9) will show that with a sufficient change in pres-

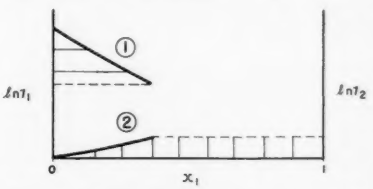

Fig. 1. Activity-coefficient—composition diagram (one component above the critical temperature).

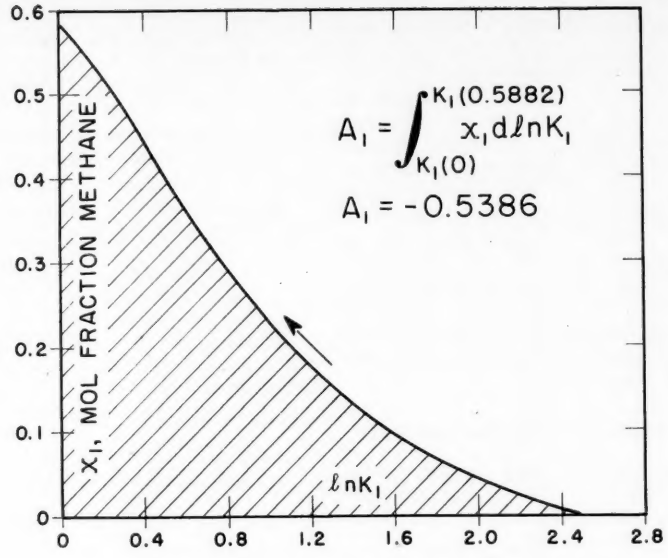

Fig. 2. Graphical integration for term 1 of Equation (9).

sure A_3 may not even be close to zero for isothermal data. In the sample calculations included with this paper, for instance, the following areas were obtained:

Equation (9)

$A_1 = -0.5386$
$A_2 = -0.3079$ } -0.8465
$A_3 = -0.8612$

Equation (4)

$A_1 = 0.3670$
$A_2 = -0.0828$ } 0.2842
$A_3 = 0.2927$

for the system methane-propane (*12, 16*). The areas are different when calculated according to Equation (9) on the one hand and Equation (4) on the other because in the former all the vapor-phase deviations from Dalton's law are included in A_3, whereas according to Equation (4) they are included in A_1 and A_2. In the latter case A_3 results only from the finite liquid volume.

In another application of Equation (9) for the ethane-propylene system, with the data of McKay (*10*) used, the A's were as follows at 10°F.:

$A_1 = 0.2204$
$A_2 = 0.2867$ } 0.5071
$A_3 = 0.5112$

The corresponding change in pressure was from 58 to 255 lb./sq. in. abs. For the same system Lu *et al.* (*9*) reported data at 14°F. which yielded the following areas:

$A_1 = 0.274$
$A_2 = 0.404$ } 0.678
$A_3 = 0.431$

In this case the pressure change was from 62 to 270 lb./sq. in. abs. (The degree of consistency of each of these sets of data for the ethane-propylene system will be discussed later in this paper.)

THE CONSTANT-PRESSURE CASE

Ibl and Dodge (7), using the same basic principles represented by Equation (2), given under the constant-temperature case, plus the fact that

$$\left(\frac{\partial \ln f_i}{\partial T}\right)_{\pi, x_i} = \frac{H_i^{vp} - \overline{H}_i^{L}}{RT^2} \qquad (10)$$

show that

$$\frac{d\ln f_1}{d\ln x_1} = \frac{d\ln f_2}{d\ln x_2} + \frac{\Delta H}{RT^2}\frac{dT}{dx_1} \qquad (11)$$

at constant pressure

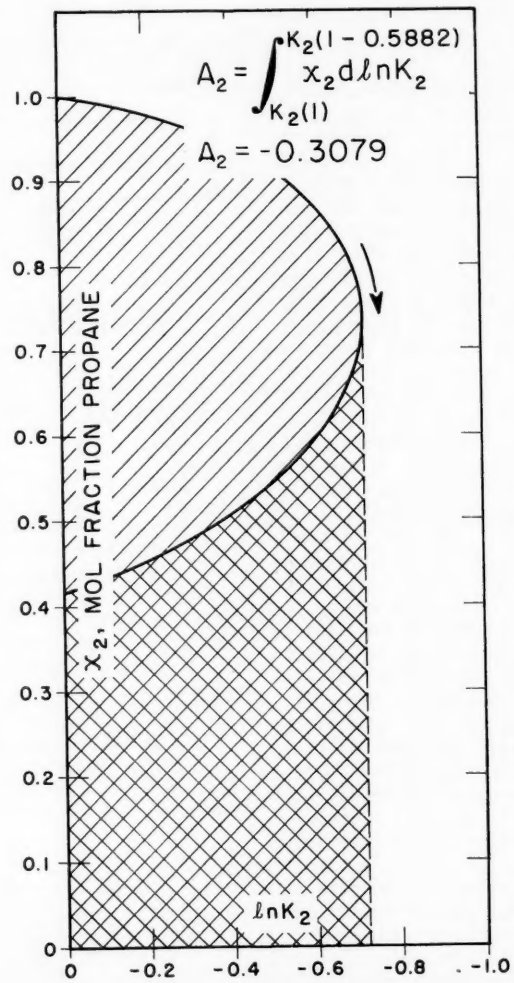

Fig. 3. Graphical integration for term 2 of Equation (9).

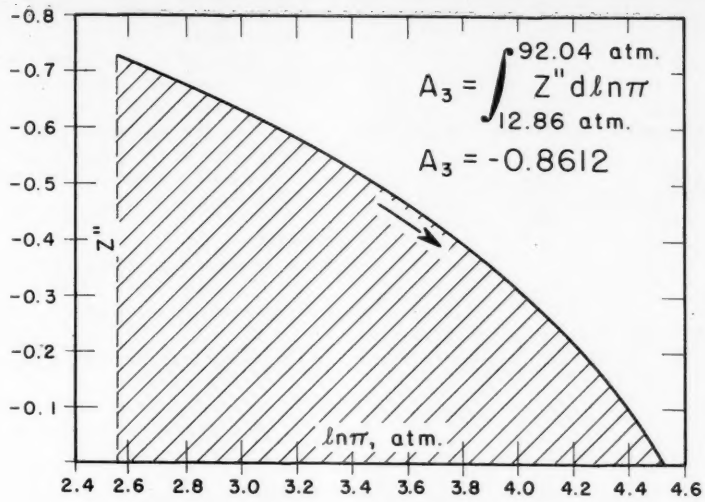

Fig. 4. Graphical integration for term 3 of Equation (9).

$$\Delta H = x_1 H_1^{\circ g} + x_2 H_2^{\circ g} - x_1 \overline{H}_1^{L} - x_2 \overline{H}_2^{L}$$

which is the molal ideal heat of vaporization for the solution. It equals the heat of mixing of the pure liquids plus the heat of vaporization of the pure liquids. Replacing $d\ln f_i$ with $d\ln (K_i x_i \pi v_{i\pi})$ as in (3), and simplifying, yields

$$x_1\, d\ln K_1 v_1 + x_2\, d\ln K_2 v_2 = \frac{\Delta H}{RT^2}\, dT \quad (12)$$

The integral form of Equation (12) again represents three areas to be designated A_1, A_2, and A_3, as before.

There are several methods of obtaining ΔH. Ibl and Dodge suggest that if the heat of mixing is not available it can be neglected and ΔH can be assumed equal to the ideal heat of vaporization. However the heat of mixing can be obtained from the heats of solution at infinite dilution when they are available (*11*); that is, $\Delta H_{mix} = x_1 x_2 (L_1^{\circ} x_2 + L_2^{\circ} x_1)$.

If more than one set of isobaric data is available, plots of the partial pressure of each component, $y\,\pi$, vs. $1/T$ at constant compositions will enable the partial molal heats of solution to be obtained. The partial heats of solution are then combined to obtain ΔH. This procedure is particularly useful if the temperature exceeds the t_c of the light component.

In order to point out the size of the terms in Equation (12) that may be expected when the temperature varies, the following areas were measured for the reported atmospheric liquid-vapor equilibria for methanol-water (*18*):

If $A_1 + A_2 = A_3$,
$A_1 = 0.614$, $A_2 = 0.726$ } 1.340
$A_3 = 1.325$

This should make it clear that one does not have to be working above the critical temperature before the third area becomes important.

SIGNIFICANCE OF THE RESULTS OF THE THERMODYNAMIC-CONSISTENCY TEST

To some degree a judgment of the thermodynamic consistency of the data tested can be made by an examination of the unbalance in the equation relating the areas; that is, $A_1 + A_2 = A_3$. Then one might ask how serious the various amounts of unbalance are. One answer may be found by the use of the K_i values or the observed y_i values in Equation (4), (5), (9), or (12) and by the calculation of the K_i's or y_i's to make the equation balance. Process requirements can then be evaluated with both sets of K's and the difference in the two designs (number of trays, reboiler duty, for example) examined.

By a comparison of the degree of unbalance obtained from testing the consistency of each of two or more sets of experimental data for the same system, one set may be accepted in preference to the others. In the section on constant temperature the results were given from testing the data of two different investigators of the ethane-propylene system. The sum of areas $A_1 + A_2$ for the data of McKay *et al.* (*10*) was 0.5071, which nearly equals an A_3 of 0.5112. On the other hand the corresponding values for the data of Lu *et al.* (9) were 0.678 and 0.431, respectively. It is obvious that the data of McKay *et al.* should be selected. This illustrates one of the most important uses of thermodynamic-consistency testing.

The unbalance in the areas may result from errors in measurement of compositions, temperatures, or pressures or from the slight inaccuracy of the Lewis fugacity rule and the corollary assumption of additivity of vapor volumes. Other methods of answering this question may lead to a sequel to this paper.

ILLUSTRATION OF THE TESTING OF ISOTHERMAL DATA

The experimental data (Table 1) of Reamer *et al.* (*12, 16*) for the methane-propane system at 100°F., where methane is above its critical temperature, are to be tested for thermodynamic consistency. The data for only the lowest, an interim, and the highest pressures are shown, inasmuch as the reference is readily available. These data, plus the corresponding calculated data in Table 2, permit the limits of the various expressions which are graphically integrated to be understood. Figures 2, 3, and 4 for the solution based on the volumes and compressibility factors [Equation (9)] present areas A_1, A_2, and A_3, respectively. A similar group of three plots for the solution based on fugacity coefficients [Equation (4)], although not included here, was also plotted to obtain these areas. These two equations, along with the numerical values of the areas, are

$$\int_{K_1(0)}^{K_1(0.5882)} x_1\, d\ln K_1 + \int_{K_2(1)}^{K_2(1-0.5882)} x_2\, d\ln K_2 = \int_{12.86\ atm.}^{92.04\ atm.} Z''\, d\ln\pi$$
$$(-0.5386) + \qquad (-0.3079) \cong \qquad (-0.8612)$$

and

$$\int_{y_1\,\pi v_{1\pi}\ at\ x_1=0}^{y_1\,\pi v_{1\pi}\ at\ x_1=0.5882} x_1\, d\ln(y_1 \pi v_{1\pi}) + \int_{y_2\,\pi v_{2\pi}\ at\ x_1=0}^{y_2\,\pi v_{2\pi}\ at\ x_1=0.5882} x_2\, d\ln(y_2 \pi v_{2\pi}) = \int_{12.86\ atm.}^{92.04\ atm.} Z^L\, d\ln\pi$$
$$(0.3670) + \qquad (-0.0828) \cong \qquad (0.2927)$$

It will be observed that on each of the figures the direction of the integration is designated. When three areas are handled simultaneously, the signs must be made consistent throughout the calculations, requiring greater care than normally. To aid in obtaining this consistency it is helpful to make the lower limits of all three integrals correspond to the lower limit in x_1, even though this may change the customary direction of integration. When integration is from a higher value of the differential variable to a lower one, the sign of the area is reversed.

LIMITATIONS OF THE METHODS PRESENTED

Equations (4), (5), and (8) for

Table 1. Methane-Propane Equilibrium Data (*12, 16*)

Temperature = 100°F.

Pressure, atm.	x_1	y_1	v^g, cu. ft./lb.-mole	v^L, cu. ft./lb.-mole	v_1^g, cu. ft./lb.-mole
12.86	0	0	24.54	1.494	31.28
47.62	0.2019	0.6073	6.30	1.448	7.96
92.04	0.5882	0.5882	2.083	2.083	3.914

Component 1 = methane.

Table 2. Methane-Propane Equilibrium Data (12)—Application of Equations

Pressure, atm.	K_1	K_2	Z^L	Z''	$\nu_{1\pi}$	$\nu_{2\pi}$	$\ln(y_1\pi\nu_{1\pi})$	$\ln(y_2\pi\nu_{2\pi})$	$\ln\pi$
12.86	—	1.0	0.0471	−0.7260	0.987	0.823	—	2.359	2.554
47.62	3.01	0.4920	0.1689	−0.3654	0.948	0.435	3.311	2.096	3.863
92.04	1.0	—	0.4698	0	0.889	0.250	3.874	2.249	4.522

testing constant-temperature data have been developed with the aid of the Lewis and Randall rule, which assumes an ideal solution for the vapor phase. When the critical pressure of the mixture is approached, such an assumption cannot be expected to hold. If no partial-volume data are available, as is usually the case, a generalized correlation for compressibility factors must be used when Equation (8) is applied. Similarly, generalized fugacity-coefficient charts are required for Equations (4) and (5).

When one tests isobaric data with the aid of Equation (12), results are not limited by the assumption of an ideal solution for the vapor phase. However the use of a generalized chart for the fugacity coefficient is again necessary.

The accuracy of the final result depends upon how the generalized fugacity correlations fit the system under study.

CONCLUSIONS

Methods have been presented for testing the thermodynamic consistency of data when the more volatile component is above its critical temperature; these methods are free of many of the restrictions and disadvantages found in procedures published earlier.

It has been demonstrated that the areas corresponding to the two terms of the Gibbs-Duhem equation in its commonly used approximate form are frequently not equal, even when the data are thermodynamically consistent. The third term, or so-called "correction term," may be larger than one of the "main" terms, and for consistent data it approximates the algebraic sum of the first two terms.

ACKNOWLEDGMENT

The authors gratefully acknowledge the contributions made by John G. Kirkwood to the work covered by this paper.

NOTATION

f = fugacity, atm.
f° = fugacity of the pure component at the same temperature and pressure as that of the solution, atm.
H = molal enthalpy, B.t.u./lb.-mole
$\overline{H}$ = partial molal enthalpy, B.t.u./lb.-mole
$H^{\circ g}$ = molar enthalpy of the ideal gas, B.t.u./lb.-mole
$H^{\circ L}$ = molar enthalpy of the pure liquid, B.t.u./lb.-mole
ΔH = ideal molal heat of vaporization of the solution, B.t.u./lb.-mole
ΔH_{miz} = molal heat of mixing, B.t.u./lb.-mole of solution
K = liquid-vapor equilibrium constant $\equiv y/x$
L_i° = heat absorbed on solution at infinite dilution of one mole of component i as a liquid $\equiv \overline{H}_i^L - H_i^{\circ L}$
R = gas constant = 0.730 atm. cu. ft./lb.-mole °R., or 1.986 B.t.u./lb.-mole °R.
T = absolute temperature, °R.
t = temperature, °F.
v = volume per mole, cu. ft./lb.-mole
$\overline{v}$ = partial molal volume, cu. ft./lb.-mole
x = mole fraction in liquid phase
y = mole fraction in vapor phase
Z = compressibility factor = $(\pi v)/(RT)$
Z'' $\equiv -Z^L + Z_1^g y_1 (1/K_2 - 1/K_1) - Z^g/K_2$
γ = liquid-phase activity coefficient
ν = fugacity coefficient (used here exclusively for the vapor phase of a pure component at the temperature and pressure of the system)
π = total pressure of the system, atm.

Subscripts

b = maximum observed concentration in the liquid of more volatile component
c = critical point
i = any component of a liquid or vapor solution
π = total pressure of the system
1, 2 = components of a binary solution

Superscripts

g = gas phase
L = liquid phase

LITERATURE CITED

1. Coulson, E. A., and E. F. G. Herrington, *Trans. Faraday* Soc., **44**, 629 (1948).
2. Dodge, B. F., "Chemical Engineering Thermodynamics," p. 98, McGraw-Hill, New York (1944).
3. Freeth, F. A., and T. T. H. Verschoyle, *Proc. Roy. Soc. (London)*, **130A**, 453 (1931).
4. Herrington, E. F. G., *Research (London)*, **3**, 41 (1950).
5. ———, *J. Inst. Petrol.*, **31**, 457 (1951).
6. ———, *J. Appl. Chem. (London)*, **2**, 11 (Jan. 1952).
7. Ibl, N. V., and B. F. Dodge, *Chem. Eng. Sci.*, **2**, 120 (1953).
8. Krishnamurty, V. V. G., and C. V. Rao, *J. Sci. Ind. Research (India)*, **14B**, 88 (1955).
9. Lu, H., D. M. Newitt, and M. Ruhemann, *Proc. Roy. Soc. (London)*, **178**, 506 (1941).
10. McKay, R. A., H. H. Reamer, B. H. Sage, and W. N. Lacey, *Ind. Eng. Chem.*, **43**, 2112 (1951).
11. Perry, J. H., "Chemical Engineers' Handbook," 3 ed., pp. 530-532, McGraw-Hill, New York (1950).
12. Reamer, H. H., B. H. Sage, and W. N. Lacey, *Ind. Eng. Chem.*, **42**, 534 (1950).
13. Redlich, O., and A. T. Kister, *ibid.*, **40**, 341 (1948).
14. Ruhemann, M., "The Separation of Gases," 2 ed., pp. 46-63, Clarendon Press, Oxford, England (1949).
15. ———, and N. Zinn, *Physik. Z. Sowjetunion*, **12**, 389 (1937).
16. Sage, B. H., W. N. Lacey, and J. G. Schaafsma, *Ind. Eng. Chem.*, **26**, 214 (1934).
17. Thijssen, H. A. C., *Chem. Eng. Sci.*, **4**, 75 (1955).
18. Uchida, S., and H. Kato, *J. Soc. Chem. Ind. (Japan)*, **37**, 525B, suppl. binding (1934).

Manuscript received March 20, 1959; revision received June 3, 1959; paper accepted June 19, 1959.

Flow Patterns in Agitated Vessels

A. B. METZNER and J. S. TAYLOR

University of Delaware, Newark, Delaware

The flow patterns obtained when viscous fluids are agitated inside baffled cylindrical tanks have been studied in both Newtonian and non-Newtonian systems. The experimental technique consisted of observing the motions of small tracer particles in highly illuminated, narrow beams of light.

The results may be broken down into two major categories. The first was a qualitative comparison between the flow patterns obtained in non-Newtonian and Newtonian fluids of the same general viscosity levels. This part of the study included observation of changes in the flow fields as one moves from laminar into turbulent conditions for both fluid systems.

The second portion of the paper deals with quantitative determinations of local flow velocities, shear rates, and power-dissipation rates in various parts of the vessel. The following conclusions may be drawn from these measurements.

1. Local fluid shear rates were found to be directly proportional to impeller speed, in both Newtonian and non-Newtonian systems. As would be expected, the shear rates decreased more rapidly with increasing distances from the impeller in pseudoplastic non-Newtonian fluids than in Newtonian systems.

2. The rates of local power dissipation decreased rapidly with distance from the impeller.

3. The fluid velocities in the horizontal plane of the impeller varied almost linearly with rotational speed in the Newtonian systems, in accordance with prior observations. On the other hand, movement in pseudoplastic systems increased exponentially with impeller speed. This effect, like the dampening of shear rates, is caused by the cumulative effects of local velocity and viscosity changes in these systems. (Increases in velocity decrease the fluid viscosity, which in turn causes further increases in velocity, etc.)

This work serves to define pertinent problems which are of importance in determining mixing rates, on a microscopic scale. Efforts may now perhaps be turned more profitably than before toward macroscopic fluid-mixing studies.

Recent investigators (5, 7) have explored the question of velocity distributions inside agitated vessels by making trace-particle photographic studies. The present study was an extension of their techniques to determine not only the velocities but also the magnitude of shear- and power-dissipation rates resulting from velocity gradients within the tank. While previous work dealt exclusively with agitation of Newtonian fluids of various viscosities, this work includes a comparison of the results from agitating both Newtonian and non-Newtonian fluids.

During agitation both mass flow around the tank and local turbulence are necessary for good mixing. First all the fluid around the tank must be moved in order that it may contact other fluids, phases, solid or gas particles, or heat transfer surfaces which may be present in the agitation vessels. Second, on a smaller scale the small local pockets of different composition, temperature, or phase must be highly sheared to ensure good blending, contact, or chemical interaction to carry out the desired process. Which part of the mixing operation is the more important from the viewpoint of over-all mixing rates depends upon the particular process in question.

While measurements of velocity distribution are most helpful in studying the rate or efficiency of the first phase of mixing, the determination of the level and distribution of shear rates may prove useful in studying some of the aspects of the second phase of the operation. A knowledge of shear rates should also prove valuable in confirming assumptions made previously in an analysis of power dissipation (2). Therefore the purposes of this work were to investigate quantitatively both factors in a common type of mixing equipment.

DESCRIPTION OF APPARATUS

The basic experimental equipment and procedure were similar to those of Sachs (5), who studied the flow patterns of water stirred with a turbine impeller. The method was essentially one of photographing illuminated trace particles in horizontal and vertical planes of light and determining the velocity distribution of the fluid for these regions from the measurement of the length of trace-particle streaks. By taking pictures of accurately known exposure times one could determine the velocity represented by the length of the streak.

A diagram of the essential parts of the apparatus is shown in Figure 1. The mixing tank was an 11.3-in. I.D. Pyrex glass cylinder cemented concentrically to the plate-glass bottom of a square, glass-enclosed outer tank. The fluid to be agitated was placed in the cylindrical tank, while water was put in between the two tanks to minimize the optical distortion caused by the curvature of the inner tank. The fluid was agitated by centrally positioned turbine impellers having six flat blades, located 4 in. from the bottom of the tank.

For most runs the tank was baffled with four 1¼-in.–wide metal strips spaced evenly at the tank wall. Flow properties were obtained with both capillary tube and rotational viscometers. Other details of the mixing and viscometric apparatus are available (2, 6).

Two different types of fluids were used in these experiments. The first was white

Karo Syrup which was determined to be a fairly viscous Newtonian fluid over the shear-rate range investigated. The other fluid was an aqueous solution of sodium carboxymethyl cellulose (CMC). The 0.7% CMC solutions had flow-behavior indexes (*1*) of 0.59 to 0.61 in the range of shear rates of interest; the flow-behavior index of the more concentrated CMC was 0.53.

The first trace particles tested were glass spheres about 0.02 in. in diameter. However since these particles have a density of about 2.3 g./cc., another lighter particle of the same size was sought and found in a Plexiglas molding powder. Most of the data were taken with the latter particles. They were nearly spherical and therefore were able to reflect light to a 90-deg. angle at all times. This last feature was considered to be absolutely necessary, for an irregularly shaped particle could be rotated in the light plane which was perpendicular to the line of sight from the camera in such a manner that the light would not be reflected from it during the full time of the exposure. It was found necessary to spray the particles with white enamel (aluminum paint is too dark) to increase their reflective properties. The Plexiglas (polymethylmethacrylate) has a density of 1.7 compared with 1.0 for the CMC solutions and 1.37 for the Karo Syrup, but because of the high viscosity of the fluids the particles continued to remain suspended for at least 5 min. in the thinnest of the solutions and for an indefinite length of time for thicker CMC solutions. It was therefore assumed that the movement of the trace particles closely represented the movement of the fluid.

Light was supplied by an arc lamp rated at 5 amp. and 115 v. However the intensity of the light was increased just before taking a photograph by increasing the no-load voltage at the source to 150 v. and drawing about 13 to 14 amp. of current briefly. Current was controlled by use of a slide-wire resistor. Originally it had been hoped that an A.C. current could have been used in the arc lamp, but the dimming of the light with the pulsation of the current was just sufficient to make the picture uncertain for analysis. Figure 1 also shows one of several slits on the sides of the tank through which the light passed and formed a nondiverging plane 3/16 in. wide.

The three views, which are pictured here, were called, respectively, *side, bottom,* and *end views* for convenience. In the side view the light enters from the side as a vertical plane which passes through the center of the tank. The impeller is then photographed at the side of the tank and perpendicular to the light plane. The side view records the image of the side of an impeller blade as shown in the sketch. The impeller for every photograph was rotating clockwise when one looked downward into the tank.

Part *b* of the same figure shows the arrangement which provided the most data. In this, the bottom view, the plane of light was horizontal. In Sachs's work it was found that the average velocity in the horizontal plane opposite the impeller blades occurred in a region just below the vertical midpoint of the impeller blade.

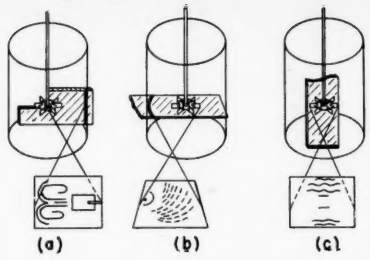

Fig. 1. Diagram of optical arrangements and mixing equipment; (*a*) side view-vertical plane, (*b*) bottom view-horizontal plane, (c) end view-vertical plane.

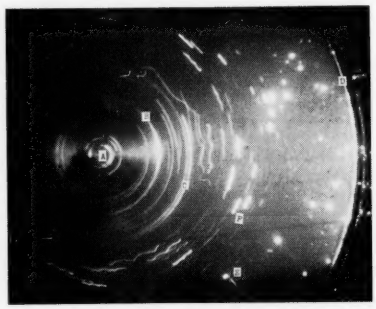

Fig. 2. Bottom-view photograph; fluid: 1.2% CMC solution, Reynolds number: 7.7, rotational speed: 60 rev./min., impeller size: 4 in. Legend: (*A*) center of impeller, (*B*) edge of stabilizing disk, (*C*) trace from tip of impeller blade, (*D*) edge of tank, (*E*) reflection from baffle, (*F*) trace-particle streak.

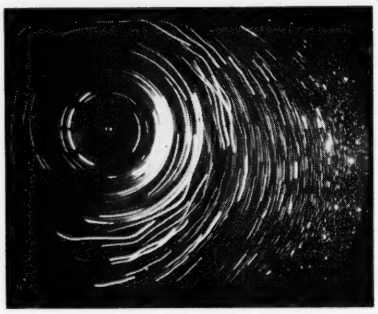

Fig. 3. Bottom-view photograph; fluid: Karo Syrup, Reynolds number: 6.2, rotational speed: 60 rev./min., impeller size: 4 in.

Therefore, to simplify the problem a thin plane in this region was the one illuminated for most of the data taken from the bottom view. In order to facilitate the focusing, a first-surface mirror was mounted just below the mixing tank, and all data were taken from photographs of the reflected image.

Part *c* of Figure 1 illustrates the end view. For this view a vertical plane of light about 3/8 in. thick was used. The light was reflected off a mirror, since convection currents from the burning arc carried both heat and ashes to the bottom of the glass tank when the lamp was placed directly beneath it. In this case the photograph was taken through the front side of the tank to record the image of the tip end of the impeller at a time when it was pointing toward the camera and in the vertical plane of light. The tip of the blade was thereby illuminated inwardly for a distance of about 3/8 in. so that trace particles in this region might be photographed. A small amount of quantitative as well as qualitative data were taken from this view.

A view camera with an f/4.7 lens was used to take the still pictures. Photographs of from one to ten exposures were taken with the position of the impeller in relation to the camera fixed for each exposure by the use of a solenoid-operated shutter. The shutter was tripped at the proper time by a cam mounted on the impeller shaft closing a microswitch and thereby activating the solenoid. The position of the image of the impeller could be set by fixing the position of the cam. Twelve volts supplied by dry cells were used, since the normal 6 v. were not quite enough to assure sufficiently rapid action of the solenoid. A toggle switch was also inserted into the circuit so that the shutter, once it had been cocked, would be closed only when desired.

Exposure times varied between 1/60 and ½ sec. All negatives were processed in a D-19 high-contrast developer for 15 min. Although additional intensification of the negative was considered several times for the CMC photographs, it was decided to be an unwise procedure since the probable result would have been an even greater increase in the background haze, which was already quite high. Were it merely a question of improper lighting, intensification might have helped, but the haziness around the image could not be overcome by this procedure.

DISCUSSION OF QUALITATIVE DATA

Figure 2 is a representative example of the bottom view in non-Newtonian fluid systems. It is apparent for this case ($N_{Re} = 7.7$, laminar region) that most of the flow is restricted to the neighborhood of the turbine blades. Perhaps the most interesting part of the photograph is the scalloped shape of the trace-particle streaks. This effect is undoubtably caused by flow over, around, and then behind the blade as it passes through the fluid. The three ridges on the trace-particle streaks are of course caused by the passage of three of the turbine blades during the ½-sec. exposure time. The disturbance is also propogated radially through the plane of liquid. However, there is no radial component of flow, the pattern having merely a net circular motion.

Figure 3 shows the flow pattern for Karo Syrup at the same rotational speed and nearly the same Reynolds number as Figure 2. It is obvious that the amount of fluid movement is greater, that the fluid velocities are larger, and that the motion in this case

extends almost to the periphery of the tank. The reasons for these differences will be discussed later is some detail.

A comparison of Figure 2 with Figure 4 shows how the radial component of velocity develops as the rotational speed of the impeller is increased. The fluid movement is now sufficient to extend to, and be influenced by, the baffles. Even at this higher impeller speed the absence of streaks near the wall shows that there is still little or no fluid movement here. The Reynolds number of 28 is just at the lower end of the transition range for these more concentrated CMC solutions (2).

Figures 5 and 6 show the early development of the usual mixing flow pattern in Karo Syrup, occurring just at the end of the laminar region. In Figure 6 the effect on the flow pattern of the baffle, which is clearly visible on the right of the photograph, is evident. In Figure 5 one sees the vortices being formed (above and below the plane of the turbine) which cause the transport of fluid and the beginning of real fluid turnover throughout the entire tank. The bottom view shows how the scalloped or saw-tooth effect from the flow over the blade has been propogated to the very edge of the tank. By contrast, Figure 4 for CMC (with nearly three times as high a Reynolds number) showed that flow was still entirely confined to the center of the tank for this pseudoplastic non-Newtonian fluid.

It is now apparent that the radial flow increases with increasing rotational speed and that as a corollary the total rate of fluid turnover within the tank increases. Likewise it was observed that the non-Newtonian CMC shows much less flow and lower velocities than does Karo Syrup under the conditions of the same rotational speed and similar Reynolds number, although small-scale mixing due to high shear rates may be greater near the impeller.

One has also observed the effect on the flow pattern upon going from the laminar into the early transition range as defined by the power number–Reynolds number correlation (2, 4). One effect of this change has been the creation of a radial component of velocity. However, Figures 7 and 8 show that a radial component of velocity can exist in both CMC and Karo Syrup even when Reynolds numbers are in the laminar region. Figure 7 shows a 2-in. turbine rotating at 200 rev./min. in 1.2% CMC. Although the actual flow is small, a definite radial component is present at the Reynolds number of 11. Figure 8 compares similar conditions in Karo Syrup, where the flow is much larger. In this picture no baffles are present, but, since the flow only extends to the position of their inner limit, this fact is not important.

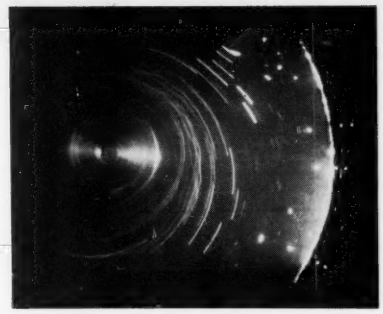

Fig. 4. Bottom-view photograph; fluid: 1.2% CMC solution, Reynolds number: 28, rotational speed: 150 rev./min., impeller size: 4 in.

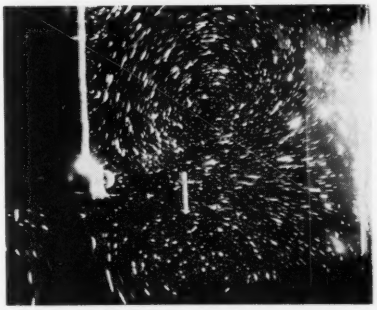

Fig. 5. Side-view photograph; fluid: Karo Syrup, Reynolds number: 10.3, rotational speed: 100 rev./min., impeller size: 4 in.

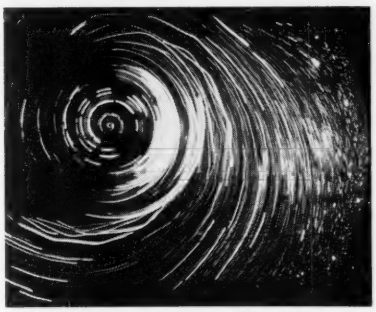

Fig. 6. Bottom-view photograph; fluid: Karo Syrup, Reynolds number: 10.3, rotational speed: 100 rev./min., impeller size: 4 in.

Although the Reynolds number has appeared to be useful in correlating the power for all fluids and impeller sizes (2, 4), it is apparent that the flow patterns for Newtonian and non-Newtonian fluids may be very different. While Figures 2 and 3 have similar laminar-region Reynolds numbers, both the velocity and the extent of the flow are much greater in Karo Syrup. Other figures (6) show that this situation continues into the transition region. Not only may a difference in the type of fluid produce a change in the flow pattern for the same Reynolds number, but Figure 7 compared with Figures 2 and 4 (which bracket it in regard to Reynolds number) shows that a change in the size of impeller may have a similar effect in non-Newtonian systems. Since each impeller was dimensionally similar, it is seen that even though one maintains the Reynolds number constant during scale up, this provision alone does not necessarily signify similar flow patterns in the model and prototype.

Figures 9 and 10 show, respectively, the bottom and end views of a 1.2% CMC solution for a rotational speed of 150 rev./min*. At the Reynolds number of 78 the flow is well into the transition region and the radial velocity component is high. The end view shows how the flow at the top (and bottom) of the blade now includes an inflowing vertical component. Figures 11 and 12 compare side-view conditions for 1.2% CMC and Karo Syrup at the highest impeller speeds recorded. Generally the two fluids are exhibiting the same general flow pattern, but there are several important differences.

While stirring low-viscosity fluids such as water, Sachs and Rushton (5) found that the vertical inflow of fluid (as shown in Figure 5) into the disklike jet issuing from the impeller contributes about 50% of the total flow of this stream. In the case of the pseudoplastic CMC solution in the above-mentioned photographs the fluid has effectively thinned out in this jet region owing to the high shear rates. Quantitative data indicate that for Figure 11 there may actually be more flow with the 1.2% CMC than with the Karo Syrup. In order for the vertical stream to feed the jet sufficiently, the vortexes above and below this stream form some distance away from the impeller.

The last series of photographs shows the beginning of well-developed turbulence, as evidenced by the fact that the path lines appear to be twisting and to cross frequently. Some of the following data indicate that the turbulence, in some cases at least, may originate above or below the moving blades rather than between them. The fluid which is being displaced by the blades in the vertical direction must be moving counter to the inflow from above and below in the region immediately ahead of the rotating blade. The flow up and over the blade then quickly changes direction as the blade passes by, flowing in behind it in a direction now parallel or coincident with the vertically inflowing stream. Figures 13 for Karo Syrup and 14 for 0.7% CMC show that this momentary outward oscillation of fluid has created a disturbance in the incoming fluid above and below the plane of the impeller. In

* Figures 9 to 13, 20, and 22 to 25 have been deposited with the American Documentation Institute, Photoduplication Service, Library of Congress, Washington 25, D. C. Copies are available as document 6051 for $2.50 for photostats and $1.75 for microfilm.

Fig. 7. Bottom-view photograph; fluid: 1.2% CMC solution, Reynolds number: 11, rotational speed: 200 rev./min., impeller size: 2 in.

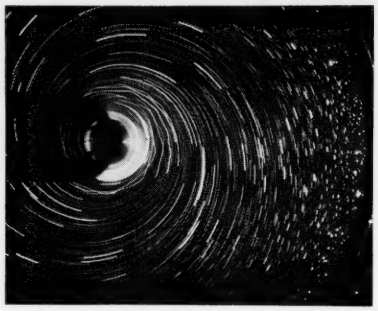

Fig. 8. Bottom-view photograph; fluid: Karo Syrup, Reynolds number: 5.15, rotational speed: 200 rev./min., impeller size: 2 in.

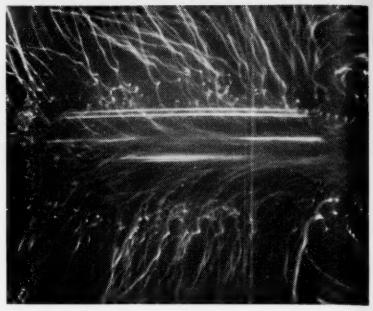

Fig. 14. End-view photograph; fluid: 0.7% CMC solution, Reynolds number: 450, rotational speed: 300 rev./min., impeller size: 6 in.

addition the high radial velocities cause the direction of the flow of the turbine discharge stream to become parallel to the impeller blades. In this case one must expect a considerable disturbance at the tip of the blade caused by the large difference in velocities between the end of tthe blade and the tangential velocity components of the neighboring stream of fluid.

Figure 15 is the bottom view which matches Figure 14. The exposure time in this case has been reduced to 1/5 sec. to minimize the haziness from the turbidity of the fluid and thereby more clearly show the turbulence which extends nearly to the wall.

It is probable that turbulence may begin in the pseudoplastic material before it does in Newtonian fluids, since shear rates are higher near the impeller (this is proven by later quantitative measurements). These higher shear rates result from the decrease in apparent viscosity of the non-Newtonian fluid and in turn lead to even greater reductions in fluid viscosity. Therefore, viscous dampening influences are greatly reduced near the impeller in pseudoplastic fluid systems. However, since the shear rate rapidly drops off and the apparent viscosity simultaneously increases as the flow progresses radially out from the impeller, this observed turbulence may be quickly dampened out. Figure 16 shows the dilute (0.7%) CMC solution being agitated at 400 rev./min. by the smaller 4-in. impeller. In this case the turbulent condition of the flow observed near the impeller changes to laminar and smooths out rapidly as the fluid proceeds further out into the tank.

It is possible, therefore, to have both laminar and turbulent regions in the mixing tank at the same time. This condition can probably occur in both Newtonian and non-Newtonian fluids, at least in the upper transition region. This fact, therefore, makes analysis of power input, flow, and mixing efficiency very difficult and would appear to indicate a considerable limitation to correlations based on over-all average conditions such as the Reynolds number.

QUANTITATIVE RESULTS

The particle streaks on photographs similar to Figures 2 to 16 were measured to obtain quantitative data on fluid velocities as a function of position within the tank. These velocities were differentiated to obtain the local shear rates, and finally the local rates of power dissipation were obtained by multiplying the observed shear rates by the corresponding shear stress, as obtained from the viscometric data. Fluctuating point velocities may not be given accurately under highly turbulent conditions by the photographic technique used, but in this work any turbulence present was sluggish and accurate results were readily obtainable.

Figures 17 to 19 show the shear-rate distribution in the horizontal plane just below the center of the impeller. It may be seen from these curves that the shear rate was highest near the impeller but that it fell off rather rapidly as one proceeded radially out into the body of the fluid. For both the Newtonian and the non-Newtonian fluid the shear rate appeared to be directly proportional to the rotational speed at all distances between the tip of the impeller and the wall of the tank. This is one of the major results sought in the present study, as it constitutes the first direct confirmation of the relationship used to correlate power consumption in non-Newtonian systems (2).

Comparison of the available data for two different impeller sizes with the same fluid show in the case of CMC that the shear rate at a given distance from the impeller is slightly greater for the larger impeller. Although the data for Karo Syrup were not as consistent, a comparison showed that the difference in shear rate is even larger in this case (6). These results indicate that the earlier (2) assumption that the average shear rates depend only on impeller speed may possibly break down under conditions of very large changes in impeller diameter. Since this effect of impeller diameter seems to be more important for Karo Syrup than CMC, other types of non-Newtonian fluids (that is dilatant fluids) may give even greater changes if this trend of increased differences with increases in the flow-behavior index continues. Should this actually turn out to be the case the earlier assumption (2) that the shear rate is a function only of impeller speed would have to be modified to include effects of diameter and flow-behavior index. However, the fact that the diameter effects appear to decrease with increasing pseudoplasticity (flow-behavior indexes approaching zero) indicates that extrapolations of the power correlation should be readily possible to larger diameters in highly pseudoplastic and Bingham plastic fluids.

Shear-rate data taken in a vertical plane, by use of end-view photographs, were similar to the results shown in Figures 17 to 19.

The second factor of interest (local rates of power dissipation) is shown in Figures 20 to 22 as a function of the actual radial distance from the tip of the impeller blade. On the same figures the horizontal dashed lines at each rotational speed give the value of the *average* rate of power dissipation. These were determined by dividing the volume of agitated fluid into the power input to the entire tank as measured with a dynamometer. At speeds up to about 150 rev./min. it is seen that the position at which the *point*, or *local*, power-dissipation rate drops to the level of the average power-consumption rate moves radially outward, especially in the case of the CMC. This is a result of the very incomplete mixing at the lowest speeds, as noted in Figures 2 and 3. Therefore, within this range, as the speed is increased the region in which the power-dissipation

rate is appreciable rapidly spreads outward from the immediate vicinity of the impeller. In other words, the mixing rates become more nearly equal in all parts of the tank as the completely unmixed region decreases in volume.

Above about 150 rev./min. (Reynolds numbers of the order of 10 to 100) one moves well into the transition region as defined by the power number-Reynolds number plots. Figures 20 to 22 show that in this region progressive increases in impeller speed tend to make the mixing process less uniform again; a large fraction of the incremental increase in power input is dissipated in the immediate vicinity of the impeller. As a result the intersection of the dashed and solid lines moves progressively closer to the impeller. In this region one has excellent fluid turnover throughout the entire tank (Figures 11, 12, 15, 16), but the level of shear rates or local power-dissipation rates is still not high except in the immediate vicinity of the impeller. In fact, the level of turbulence is so markedly low everywhere except in the region of the impeller that in more recent work (3) a model which assumes very low turbulence everywhere except in the immediate vicinity of the impeller has served to correlate mixing rates over a remarkably wide range of conditions.

This condition of nonuniformity is greater in the CMC solutions. The decrease in apparent viscosity around the impeller causes a much higher degree of shearing or turbulence in that region. Conversely, the rapid decrease in shear rates as one moves away from the impeller increases the viscosity of the fluid, which in turn dampens the velocities and their fluctuations even more. As a result, pseudoplastic non-Newtonian fluids represent an extreme case of a nearly perfect mixing zone near the impeller combined with very little mixing in other parts of the system.

Figures 23 to 25 show the velocity distributions within the vessel at the plane of the impeller. Comparison of Figures 23 and 24 shows a considerable difference between the velocity changes with increasing rotational speed for the two fluids. In the Newtonian fluid the velocity for every distance parameter appeared to vary almost linearly with rotational speed, except for the tendency toward curvature at 400 rev./min. On the other hand, the data for the pseudoplastic CMC solution showed a very large amount of curvature with increasing speed for both the 4- and 6-in. impellers. It is also apparent that at every distance shown, flow velocities were higher for the agitated Karo Syrup solutions than for 1.2% CMC solutions. Although the agitated 1.2% CMC solutions have a lower apparent viscosity near the impeller where the shear rates are high, the data and qualitative observations indicate that the great bulk of the fluid in the tank away from the impeller has shear rates less than the 4 to 6 sec.$^{-1}$ where the flow curves of the two fluids cross. As a result of this fact the pseudoplastic is effectively more viscous except near the impeller, and less circulation of fluid occurs at a given rotational speed. In the laminar region the differences in shear rate and fluid motion for CMC are very large. Therefore, the fluid near the impeller rotates much like a solid cylinder rotating in a bearing, with a lubricating layer of highly sheared, but otherwise nearly stagnant, fluid just out from the tip of the impeller. As the speed of the impeller was increased, the centrifugal forces acting on the fluid cause radial flow, and, as more of the fluid gains motion, the resulting local shear rates in CMC decrease the apparent viscosity in these regions of fluid movement. As a result of the decrease in viscosity with increasing shear rate, the amount of fluid motion (and the velocity of this motion) increases at a rate which is greater than directly proportional to the rotational speed. The convergence of the velocity data for the two fluids indicates that for higher rotational speeds (about 500 to 600 rev./min.) at least some of the local velocities for the 1.2% CMC solution will exceed those of Karo Syrup. Owing to the greater amount of fluid movement using the 6-in impeller (Figure 25) there is an even greater rate of curvature in this case.

A brief investigation was also made of the variations in velocity with respect to the angular position of the blades of the impeller (6). Except at radii close to the radius of the tips of the blades, these differences were not found to be large, however, and no further detailed study was undertaken.

CONCLUSIONS

1. In both Newtonian and non-Newtonian systems the fluid shear rates were found to be directly proportional to the rotational speed of the impeller under all conditions studied. This fact is of primary importance in supporting the basis for correlation of agitation power requirements in non-Newtonian systems.

The only indication of conditions under which the above direct proportionality might be affected by other variables was obtained by varying the impeller diameter. As a result, it appears at least possible that the earlier correlation of power requirements (2) should not be extrapolated to impellers which are greatly larger than those studied, except for very highly pseudoplastic fluids.

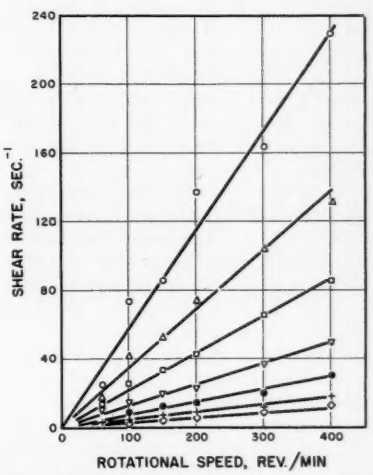

Fig. 17. Shear-rate distriubtion in Karo Syrup, horizontal plane, 4-in. impeller.

Symbol	Distance (radially) from tip of impeller
⊙	Impeller tip
△	0.10 in.
⊡	0.20 in.
▽	0.34 in.
⊗	0.50 in.
+	1.00 in.
◇	1.70 in.

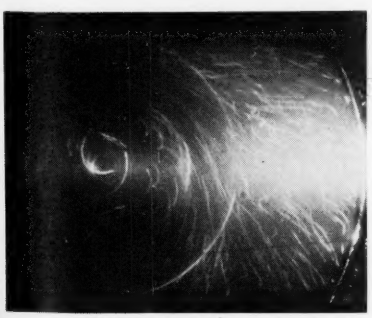

Fig. 15. Bottom-view photograph; fluid: 0.7% CMC solution, Reynolds number: 450, rotational speed: 300 rev./min., impeller size: 6 in.

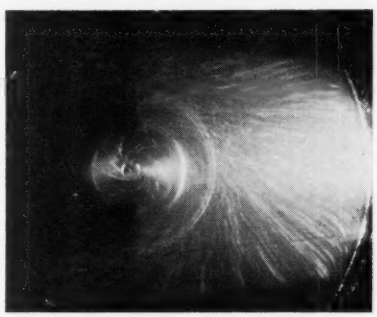

Fig. 16. Bottom-view photograph; fluid: 0.7% CMC solution, Reynolds number: 310, rotational speed: 400 rev./min., impeller size: 4 in.

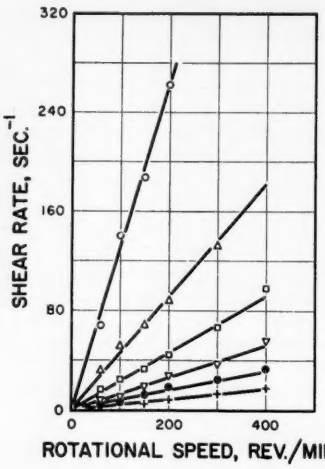

Fig. 18. Shear-rate distribution in 1.2% CMC solution, 4-in. impeller. Other conditions and symbols as in Figure 17.

2. High rates of shearing and power dissipation occur close to the impeller. Within the laminar region the large differences between the rates of power dissipation close to the impeller and elsewhere in the tank decrease with increasing impeller speed, since such speed increases serve to bring some slight mixing to other parts of the tank. At higher speeds (within the transition region) the reverse, however, appears to be true: any incremental increases in power input are to a large extent consumed in the immediate region of the impeller. Under conditions of good mixing a simplified model of the over-all process would appear to be that in which one assumes essentially all the highly turbulent mixing to be confined to the region of the impeller, with fluid motion elsewhere in the tank serving primarily to bring fresh fluid into this region.

3. Under laminar-flow conditions relatively little agitation takes place within the mixing tank. The flow is generally circular in motion and confined to the region near the impeller.

4. In the first half of the transition range the radial velocity component increases with rotational speed (and Reynolds number) quite rapidly. In this region over-all circulation of fluid and subsequent mixing begin within the tank. The mixing is carried out by the transport and blending of fluid and not as yet by any noticeable turbulence.

5. As the rotational speed approaches the middle of the transition region ($N_{Re} \approx 100$) some turbulence becomes visible on the photographs. This condition begins near or between the blades of the impeller.

Local turbulence, particularly in pseudoplastics, is rapidly dampened out in a short distance. The decrease in viscosity near the impeller where the shear rates are highest advances the formation of turbulence in this region in pseudoplastic fluids.

6. In the horizontal plane of the impeller, velocities increase only slightly more rapidly than linearly with rotational speed in the Newtonian fluids. However in the pseudoplastic fluid the velocities increase more nearly exponentially with increases in impeller speed as a result of the reduction of the apparent viscosity of the fluid with increasing shear rate. Under conditions of high shear rate and turbulence, pseudoplastics may undergo greater over-all flow with less total power imput than for Newtonian fluids having similar apparent viscosities at lower shear rates. At lower rotational speed and lower shear rates the opposite conditions may exist.

These conclusions are all based on a study under a limited range of conditions. One tank, 11.3 in. in diameter, was employed. Dimensionally similar flat-blade turbines ranging from 2 to 6 in. in diameter were used. Rotational speeds of from 60 to 600 rev./min. were studied providing a Reynolds-number variation of from 2.1 to 450, which covered the laminar region and most of the transition region. The conclusions are, therefore, most valid for this range of conditions.

ACKNOWLEDGMENT

This work was supported by the Office of Ordnance Research, U. S. Army.

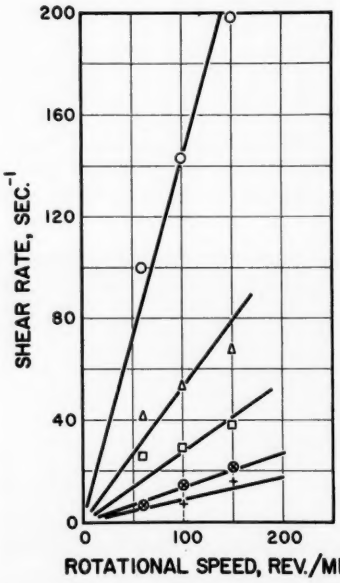

Fig. 19. Shear-rate distribution in CMC, 6-in. impeller. Other conditions and symbols as in Figure 17.

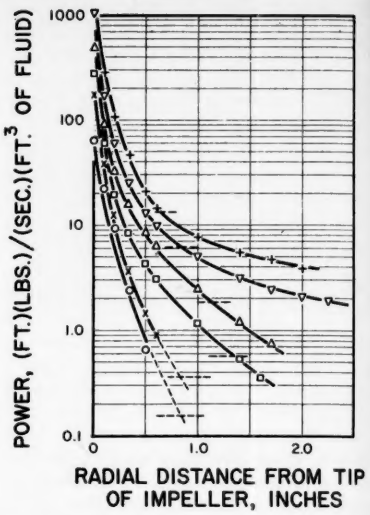

Fig. 21. Local or point power-dissipation rates. 1.2% CMC, 4-in. impeller.

Legend:
- ⊙ 60 rev./min.
- × 100 rev./min.
- ⊡ 150 rev./min.
- △ 200 rev./min.
- ▽ 300 rev./min.
- \+ 400 rev./min.

NOTATION

- du/dr = fluid shear rate, sec.$^{-1}$
- D = impeller diameter, ft.
- N = rotational speed of impeller, rev./sec.
- N_{Re} = Reynolds number, dimensionless, defined as $D^2N\rho/\mu$ for Newtonian fluids and $D^2N\rho/\mu_a$ for others; apparent viscosity μ_a is evaluated at a shear rate du/dr equal to $13N$ (2)
- μ = viscosity, lb.-mass/sec.ft.
- ρ = fluid density, lb.-mass/cu.ft.

LITERATURE CITED

1. Metzner, A. B., and J. C. Reed, *A.I.Ch.E. Journal*, **1**, 434 (1955); A. B. Metzner, in "Advances in Chemical Engineering," Vol. 1, Academic Press, New York (1956).
2. ———, and R. E. Otto, *A.I.Ch.E. Journal*, **3**, 3 (1957).
3. Norwood, K. W., Ph.D. thesis. Univ. Delaware, Newark (1959).
4 Rushton J. H., and J. Y. Oldshue, *Chem. Eng. Progr.*, **49**, 161 and 267 (1953).
5. Sachs, J. P., and J. H. Rushton, *ibid.*, **50**, 597 (1954).
6. Taylor, J. S., M.Ch.E. thesis, Univ. Delaware, Newark (1955).
7. Tennant, B. W., Thesis, Illinois Inst. Technol., Chicago (1952).

Manuscript received November 7, 1958; revision received April 30, 1959; paper accepted May 6, 1959. Paper presented at A.I.Ch.E. Cincinnati meeting.

Density Fluctuations in Fluidized Beds

P. K. BAUMGARTEN and R. L. PIGFORD

University of Delaware, Newark, Delaware

The effectiveness of fluidized beds is limited by the presence of density fluctuations such as those caused by gas bubbles. The size and frequency of such bubbles were measured in air-fluidized beds of glass beads and silica-alumina catalyst with a gamma-ray absorption technique used.

The results showed that the gas bubbles developed owing to an influx of gas from the continuous dense phase. With increasing elevation in the bed the volumetric rate of bubble flow approached as a limit the total air flow minus the flow through the dense phase corresponding to minimum fluidization. The growth rate of bubble diameter was as much as 0.17 in./in. of elevation. Fluidization was most uniform with the cracking catalyst, for which the apparent density of the dense phase decreased with increasing gas velocity.

Gas-fluidized beds of fine particles are characterized by the presence of density fluctuations. Gas bubbles or pockets appear and result in an effective bypassing of the bed. The gas bubbles form spontaneously and grow in size as they rise through the bed. This action is evident to the eye and is an important factor in the performance of the bed in terms of mass transfer, heat transfer, or chemical reaction accomplished.

For instance measuring gas composition in a commercial cracking catalyst regenerator, Askins *et al.* (*1*) noted incomplete utilization of the regenerating air because a large fraction of the gas flow took place in bubble form. Wamsley Johanson (*18*) concluded that the nonuniformity impaired gas-solid heat transfer. Excessive pressure drop and fluctuations in pressure drop have also been attributed to the density fluctuations (*16, 15*).

Direct measurement of density fluctuations have been carried out in two cases. Morse and Ballou (*12*) measured local density variations with a capacitance probe, and Grohse (*5*) measured line-average densities by X-ray absorption. In both investigations it was observed that the density fluctuations became more pronounced with increasing gas velocity and at greater heights in the bed. Data obtained by Morse and Ballou also indicated that good initial gas distribution and increased bed height improved bed uniformity at lower levels. Conclusions regarding bypassing were chiefly qualitative, as no attempt was made in either study to determine gas bubble sizes or volumetric bubble flow rates.

Because of the recognized importance of this information to any attempts to compare efficiencies of fixed and fluid bed reactions, the chief objective of the present investigation was to measure the size and frequency of the gas bubbles appearing in fluidized beds and to compute the extent of gas bypassing from the data. It was also planned to investigate the relationships between appearance of bubbles, density gradients, and pressure drop through the bed. As suggested by different authors (*9, 16*) the fluidized bed consists of two phases: the continuous or dense phase composed of a more or less uniform mixture of solid particles and interstitial gas, and the discontinuous or bubble phase consisting of gas bubbles that are essentially free of solids. One aim of the present study was to determine the density of the dense phase and to study its relationship to the uniformity of density of the whole bed.

The experimental approach to the problem consisted of measuring continuously the fluctuating absorption of a horizontal gamma-ray beam that was directed through the bed from an external source. As the extent of absorption varied with the concentration of solid material in the path of the beam in accordance with the Lambert-Beer law, a detector placed opposite the source on the other side of the bed gave a continuous record of the fluctuating density within the bed. The similar technique employed by Grohse (*5*) was published after the present investigation had begun, but the published information (*5*) did not permit a detailed interpretation to be made of the magnitude of the fluctuations themselves.

This study was concentrated on the fluidization of spherical glass beads and silica-alumina cracking catalyst with air under atmospheric pressure used. Independent variables investigated included gas superficial velocity, particle size and size distribution, and bed height. Density measurements were made at different elevations in the bed, at different displacements from the center line of the bed, and along two horizontal paths of different length.

EXPERIMENTAL

Apparatus

The fluidization and gamma-ray apparatus is shown diagrammatically in Figure 1, and the fluidization column is shown with the gamma-ray source and detector in Figure. 2. Figure 3 shows the arrangement used for calibration. Fluidization was carried out in a 3- × 6-in. rectangular column of transparent acrylic resin. Filtered and dried air entered the column through a packed section and a 3/32 in. thick sintered bronze distributor plate (pressure drop 0.8 in. of water at 2 ft./sec. superficial air velocity). Entrained solids were separated in a disengaging zone of large cross section situated above tthe column. Pressure taps equipped with filters were located just below the distributor plate and at different levels above it. Pressures were read on water *U*-tube manometers damped by constricting the base of the *U*. The gamma-ray apparatus consisted of the source and source holder, a collimator to form the gamma-ray beam, one or more attenuators to reduce beam intensity, and instruments to detect the transmitted radiation, record its mean intensity, and measure the size of its fluctuations.

Preliminary experiments with a 100-millicurie source of cerium 144-praseodymium 144 demonstrated the importance of providing a gamma-ray beam of the right intensity and penetration for a given bed of solids. Best results were obtained when the fraction of incident radiation transmitted by the bed was between 0.05 and 0.50. The final absorption measurements were carried out with a 200-mg. source of thulium 170. This source (*17*) provided a high intensity gamma-ray beam of relatively low penetrating power, required to minimize the effect of source noise resulting from the random nature of radioactive decay (*13*). Ordinarily source noise can be reduced by lengthening the period of observation, but in this case the need to observe frequent density fluctuations made this impossible. Reduction of source noise permitted detection of air bubbles having a diameter as small as 0.35 in. in the case of the glass beads or about 0.7 in. in the case of the cracking catalyst, as calculated from statically determined noise levels and absorption coefficients. The difference in the two cases was due to the larger absorption coefficient of the glass beads.

The shielded source holder could be

P. K. Baumgarten is with E. I. du Pont de Nemours and Company, Wilmington, Delaware.

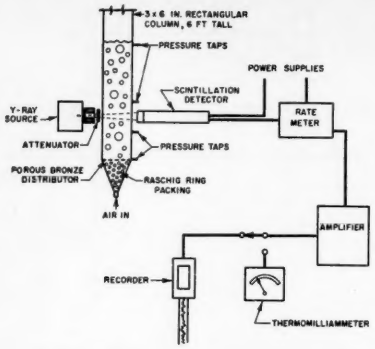

Fig. 1. Schematic diagram of apparatus.

freely positioned to irradiate different portions of the fluidized bed. By proper placement of the source the fine gamma-ray beam, a 3.2 deg. cone, was made to have the same average diameter of 0.44 in. within the fluidized bed for both the 3- and 6-in. paths.

Instruments for detecting tthe transmitted radiation and for indicating and recording the resulting signal were chosen for their rapid response to changes in the level of the transmitted radiation. This radiation, usually in the range of 10,000 to 60,000 counts/sec., was sensed by a scintillation detector and converted to electrical pulses. A pulse-rate meter employing an especially designed circuit emitted a voltage that depended on the pulse rate. The rate-meter output was passed on to a direct-writing oscillograph for continuously recording the bed's apparent density. A thermomilliammeter was also provided to measure the root-mean-square voltage of the rate-meter output. Calibration in terms of bed density permitted conversion of the thermomilliammeter reading to the standard deviation of the densiy fluctuations. To minimize detection of scattered radiation the scintillation detector intercepted the major portion of the gamma-ray beam and was positioned at a sufficient distance from the fluidization column. The rate meter gave approximately logarithmic response so that its output was an approximately linear function of fluidized-bed density.

The instruments were periodically calibrated with different thicknesses of the powdered material under study used. As shown in Figure 3 the material used for calibration was contained in *U*-shaped brass cells, the front and back of which consisted of tightly stretched paper, giving negligible absorption. Calibration compensated for a number of factors difficult to assess oherwise, such as source decay, unequal absorption of different portions of the gamma-ray spectrum, scattered radiation, and rate-meter coincidence loss.

Materials

Table 1 lists the physical properties of the materials used: commercial spent silica-alumina cracking catalyst and four grades of spherical glass beads. Three grades of the glass beads were relatively narrow size fractions. The fourth grade was a blend prepared by mixing the largest and smallest size narrow fractions in proportion, so that the mean particle diameter would be the same as for the intermediate size narrow fraction. The mean particle diameters given are the volume-surface means (7). The particle density was determined by displacement in methyl alcohol and represents the skeletal density. The settled bed density was the density of the bed that had settled from a vigorously fluidized state after the flow of air was suddenly stopped and no external means were used to compact the bed. The minimum fluidizing velocity was determined as described later. Under the microscope the glass beads appeared almost spherical, while the cracking catalyst particles were rounded and oblong in shape like pebbles.

Procedure

The column was charged with the powder, and pressure drop and the depth of the bed were observed with both increasing and decreasing gas velocity from below the minimum fluidizing velocity to about 2 ft./sec., the highest air velocity employed. The source and detector were then put in position. Instantaneous and time-average oscillographs, with integrator time constants of 0.015 and 5.25 sec. used, respectively, were obtained. The thermomilliammeter reading was obtained, usually an average of ten random readings to even out the meter fluctuations. The calibration curve for the powder and the particular attenuation was secured either before or after the fluidization runs. The absorption by the settled bed was also determined.

ANALYSIS OF GAMMA-RAY DATA

The original oscillograms and thermomilliammeter readings required suitable interpretation to obtain values for bubble size, bubble frequency, and bubble velocity. Figure 4 shows typical strip-chart oscillograms. The two instantaneous oscillograms taken at different speeds, both with an integrator time constant of 0.015 sec., indicate the time dependence of line-average density of the fluidized bed along the path of the gamma-ray beam. The trace obtained with the long-time constant of 5.25 sec. gives the time-average density. In the instantaneous oscillograms the small fluctuations near the top of the trace represent the background noise at an average level equivalent to the density of the dense phase. The large pulses extending below the dense-phase density result from the passage of bubbles through the gamma-ray beam. The distance of the peaks below the dense-phase density corresponds to the maximum thickness of the bubble as sensed by the gamma-ray detector.

Also indicated on the charts are the calibration of the oscillograms in terms of the specific gravity of the bed relative to the settled bed and the number of trace pulses counted as bubbles. The standard deviation of the instantaneous oscillogram, including the source noise, is given by the thermomilliammeter reading σ_m. Fluctuations in the oscillograms of the same order of magnitude as the source noise were omitted in the bubble count, with statistical criteria used as a guide. Specifically oscillogram fluctuations extending less than three times the standard deviation of the noise below the dense-phase density were excluded. Also, adjoining bubble traces were counted separately only if they extended more than $3\sqrt{2}\sigma_N$ beyond the trough between them.

The treatment of the experimental data consisted of calculation of a mean apparent bubble thickness from the thermomilliammeter reading and the mean bed density, conversion of this quantity to the mean bubble diameter, correction of observed bubble frequency to include bubbles outside the gamma-ray beam, and calculation of superficial and true bubble velocities. The first step could also have been accomplished by measuring individual bubble sizes on the strip charts, but this method proved

Table 1. Physical Ppoperties of Materials

Mean particle diameter, D_p, μ	Particle-size range, μ	ρ_p, g./cc.	ρ_s, g./cc.	ϵ_s	ϵ_s'	u_{omf}, ft./sec.
Glass beads, narrow fractions						
74	38-124*	2.44	1.40	0.427	0.429	0.024
119	61-175*	2.45	1.42	0.421	0.426	0.054
234	147-495*	2.60	1.56	0.400	0.404	0.17
Blend of glass beads (45.1 wt.% of $D_p = 74\mu$ and 54.9 wt.% of $D_p = 234\mu$)						
116	38-495*	2.52**	1.60	0.365	0.379	0.035
Silica-alumina cracking catalyst						
41	0-120†	2.17	0.813	0.628	0.628	0.024

* Determined by screen analysis.
** Calculated from the properties of the two components.
† Determined by Roller analysis.

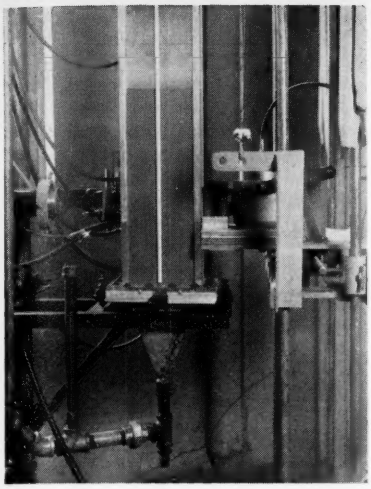

Fig. 2. Source and detector with fluidized bed.

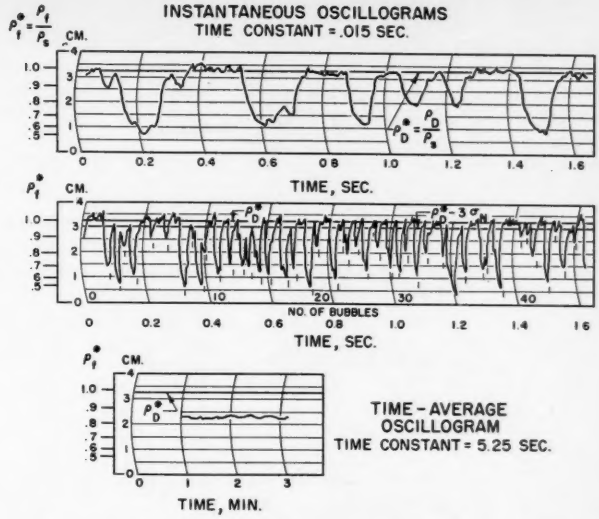

Fig. 4. Typical strip-chart oscillograms; glass beads, $D_p = 119\ \mu$; 6-in. path, $u_0 = 0.20$ ft./sec.; 15-in. settled-bed height, 8-in. level.

too time consuming for all but a few cases and the alternate statistical method described below was devised.

Mean Apparent Bubble Thickness

The calculation of the mean apparent bubble thickness will be illustrated by the idealized oscillogram depicted in Figure 5. $a(x, \theta)$ is defined as the concentration of dense phase or fraction of fluidized bed occupied by the dense phase at any point within the fluidized bed. According to its definition a can be either zero if x lies inside a bubble or one if x lies in the dense phase. Then along the beam the line-average concentration of dense phase at any time is

$$\bar{a}(\theta) = \frac{1}{X}\int_0^X a(x,\theta)\,dx \qquad (1)$$

As $\bar{a}$ is a function of time, the time-average of the line-average concentration of dense phase is given by

$$\langle\bar{a}\rangle = \operatorname*{Lim}_{T\to\infty}\frac{1}{T}\int_0^T \bar{a}(\theta)\,d\theta \qquad (2)$$

and the variance of the line-average concentration by

$$\sigma_{\bar{a}}^2 = \operatorname*{Lim}_{T\to\infty}\frac{1}{T}\int_0^T (\bar{a} - \langle\bar{a}\rangle)^2 d\theta$$

$$= \operatorname*{Lim}_{T\to\infty}\left[\frac{1}{T}\int_0^T \bar{a}^2\,d\theta\right] - \langle\bar{a}\rangle^2 \qquad (3)$$

The value of $\langle\bar{a}\rangle$ was obtained from the oscillograms by the equation

$$\langle\bar{a}\rangle = \frac{\rho_f^*}{\rho_D^*} \qquad (4)$$

The value of $\sigma_{\bar{a}}^2$ was obtained from the thermomilliammeter reading σ_m in terms of settled-bed density by allowing for the density of the dense phase, by the use of

$$\sigma_{\bar{a}}^2 = \left(\frac{1}{\rho_D^*}\right)^2 \sigma_{\rho_f^*}^2$$

$$= \frac{1}{\rho_D^*}\left[\sigma_m^2 - \sigma_N^2\right] \qquad (5)$$

Subtraction of the variance of the source noise σ_N^2 corrected for the small increase in the observed variance caused by random emission. In the few cases where σ_N^2 was a substantial fraction of σ_m^2, the mean apparent bubble thickness was determined from the strip charts.

The mean apparent bubble thickness was calculated from $\langle\bar{a}\rangle$ and $\sigma_{\bar{a}}^2$ by assuming that the passage of individual bubbles through the beam could be represented by separate rectangular deflections on the oscillogram, all of which were uniform in size. As shown by Figure 5 each bubble trace was assumed to have duration δ and height x_b/X, so that the value of $\bar{a}(\theta)$ during the passage of the bubble was $(X - x_b)/X$. In the absence of bubbles from the beam the radiation intensity reverted to that cor-

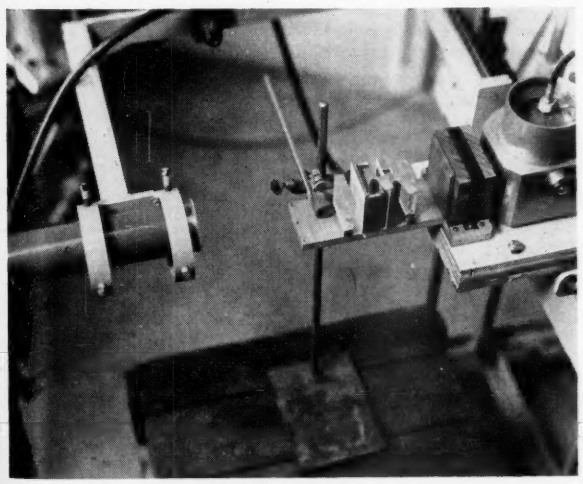

Fig. 3. Source and detector during calibration.

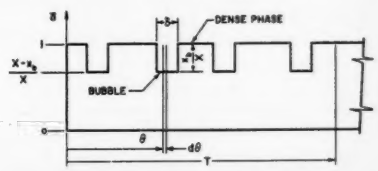

Fig. 5. Idealized strip-chart oscillogram.

responding to the dense-phase density, with $\bar{a} = 1$. Bubble traces occurred at random intervals, with a frequency f_b.

Equations (2) and (3) for $<\bar{a}>$ and $\sigma_{\bar{a}}^{-2}$ were applied to the idealized oscillograms to yield expressions in terms of f_b, δ, and x_b. The results were combined and solved for x_b and

$$<\bar{a}> = \lim_{T\to\infty} \frac{1}{T}\left\{\left[\int_0^T \bar{a}\, d\theta \text{ for the dense phase}\right] + \left[\int_0^T \bar{a}^2\, d\theta \text{ for bubbles}\right]\right\}$$

$$= \lim_{T\to\infty} \frac{1}{T}\left\{[1\cdot(T - Tf_b\,\delta)] + \left[\frac{X - x_b}{X}(Tf_b\,\delta)\right]\right\}$$

$$= 1 - f_b\,\delta(x_b/X) \qquad (6)$$

$$\sigma_{\bar{a}}^{-2} = \lim_{T\to\infty} \frac{1}{T}\left\{\left[\int_0^T \bar{a}^2 d\theta \text{ for the dense phase}\right] + \left[\int_0^T \bar{a}^2\, d\theta \text{ for bubbles}\right]\right\} - <\bar{a}>^2$$

$$= \lim_{T\to\infty} \frac{1}{T}\left\{[1\cdot(T - Tf_b\,\delta)] + \left[\left(\frac{X - x_b}{X}\right)^2 Tf_b\,\delta\right]\right\} - <\bar{a}>^2$$

$$= \left(\frac{x_b}{X}\right)^2 [f_b\,\delta - f_b^2\,\delta^2] \qquad (7)$$

Solving Equations (6) and (7) simultaneously one gets

$$x_b = X\left[1 - <\bar{a}> + \frac{\sigma_{\bar{a}}^{-2}}{1 - <\bar{a}>}\right] \qquad (8)$$

and

$$\delta = \frac{1 - <\bar{a}>}{(x_b/X)f_b}$$

Since all bubble traces were assumed to be of the same size, $\bar{x}_b = x_b$.

In spite of the drastic assumptions employed in this derivation values of $\bar{x}_b$ calculated by Equation (8) with the use of $\sigma_{\bar{a}}^{-2}$ from the thermomilliammeter were found to agree substantially with means of values obtained from the strip charts by measuring individual pen deflections beyond the background noise. The remarkable agreement is seen in Figure 6, where values of

$$X\left[1 - <\bar{a}> + \frac{\sigma_{\bar{a}}^{-2}}{1 - <\bar{a}>}\right]$$

are plotted against strip-chart values of $\bar{x}_b$ for eleven different runs. No improvement in these results was obtained by modifying Equations (6) and (7) to allow for the varying shapes of the bubble traces. $\bar{x}_b$ was therefore calculated by Equation (8) in most cases.

It might be thought that the diameter of the gamma-ray beam had an effect on the value of mean bubble thickness. It was found experimentally however that reducing the diameter of the beam by one half had no appreciable effect on the values of $\bar{x}_b$ obtained.

Bubble Diameter

When a bubble passed through the gamma-ray beam, transmission of gamma radiation was largest at the instant the bubble center was at the same horizontal level as the beam's axis. At this instant however the bubble center may have been some horizontal distance y away from the beam axis. On the assumption that the bubbles were spheres and that all values of y within the bounds set by the column walls were equally probable, the bubble's diameter was obtained from the mean apparent bubble thickness as follows:

$$\bar{x}_b = \frac{\int_0^{D_b/2} x_b\, dy}{\int_0^{D_b/2} dy} = \frac{2\int_0^{D_b/2} \sqrt{(D_b/2)^2 - y^2}\, dy}{D_b/2} = \frac{\pi}{4} D_b \qquad (10)$$

Hence

$$D_b = \frac{4}{\pi}\bar{x}_b \qquad (11)$$

This relationship was used except in the few cases where Equation (11) indicated a value of D_b larger than the width of the bed; then the bed dimension itself was used as D_b.

Bubble Frequency

To obtain the value of the bubble frequency for the entire bed cross section it was necessary in some cases to apply a correction factor to the bubble frequency read from the oscillograms. The correction factor allowed for the fact that not all bubbles passed through

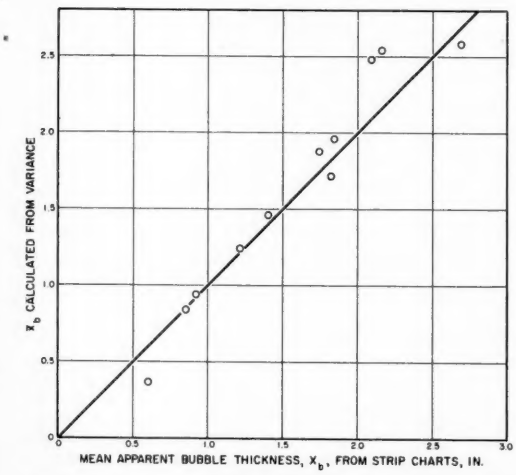

Fig. 6. Comparison of bubble thicknesses from variance and oscillogram.

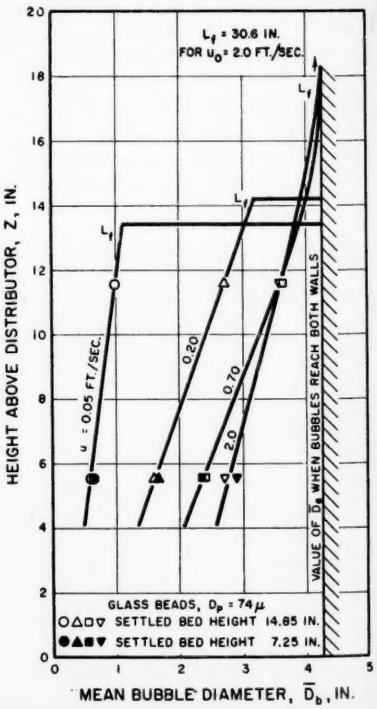

Fig. 7. Vertical bubble-size profiles.

the gamma-ray beam. It was assumed that the gamma-ray instruments probed a bed width equal to the sum of the beam diameter and twice the average bubble diameter in the direction across the gamma-ray beam. For the 6-in. path the corrected frequency was

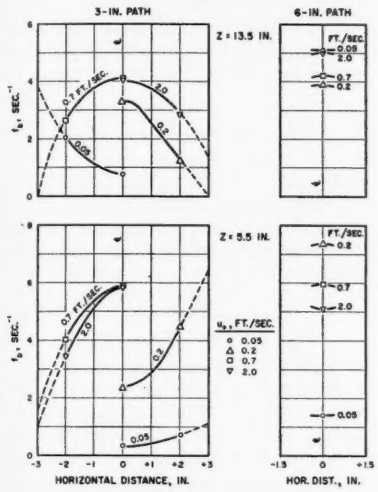

Fig. 8. Horizontal bubble-frequency profiles; glass beads, $D_p = 74\ \mu$, 15-in. bed.

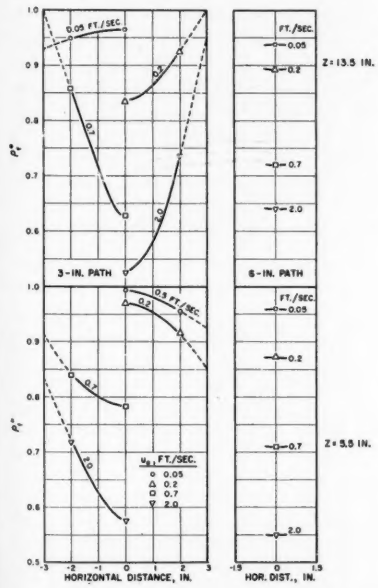

Fig. 9. Horizontal density profiles; glass beads, $D_p = 74\ \mu$, 15-in. bed.

$$f_b' = \frac{3}{2(D_b)_{3\text{-in.}} + D_\gamma} (f_b)_{6\text{-in.}} \qquad (12)$$

Here $(D_b)_{3\text{-in.}}$ is the average bubble diameter measured along the 3-in. path, and $(f_b)_{6\text{-in.}}$ is the observed bubble frequency measured along the 6-in. path and read on the strip-chart oscillogram. As a rule the bubble frequency for the 6-in. path was employed for the calculation of f_b' because the factor correcting f_b was usually smaller for the 6-in. path than for the 3-in. path and could often be omitted.

Bubble Velocity

The volumetric flow of the gas in the form of bubbles equals the product of the mean bubble volume and the frequency of bubbles at the given bed level. It was assumed that the average bubble volume was the same as that of an ellipsoid having horizontal axes equal to the experimentally observed bubble diameters along the 3- and 6-in. paths and having a vertical axis equal to the geometric mean of the two diameters. This assumption could be made for superficial gas velocities of 0.7 ft./sec. or less, since in these cases the visually observed bubbles were about the same size horizontally and vertically. The superficial bubble velocity was obtained by dividing the volumetric bubble flow by the column cross section giving

$$u_{B0} = \frac{1}{S} \cdot \frac{\pi}{6} (D_b)_{3\text{-in.}}^{1.5} (D_b)_{6\text{-in.}}^{1.5} f_b' \qquad (13)$$

Values of u_{B0} were not calculated for gas velocities greater than 0.7 ft./sec., since there was no way of estimating the vertical elongation of the bubbles. Since the source noise associated with the gamma-ray measurements set a lower limit to the size of the bubbles detected, Equation (13) and all other equations involving u_{B0} should be understood to include only bubbles larger than the minimum size detectable.

If $\langle \bar{a} \rangle$ is close to the average fraction of the bed occupied by the dense phase at any given level, the true bubble velocity is

$$u_b = \frac{u_{B0}}{1 - \langle \bar{a} \rangle} \qquad (14)$$

The superficial velocity of the gas through the dense phase was obtained by

$$u_{D0} = u_0 - u_{B0} \qquad (15)$$

Combining Equations (14) and (15) one obtains

$$u_{D0} = u_0 - u_b (1 - \langle \bar{a} \rangle) \qquad (16)$$

This equation shows that if $\langle \bar{a} \rangle$ is the same at all heights above the distributor, then the portion of gas passing through the dense phase will decrease with increasing true bubble velocity.

Reproducibility

The precision of the results was determined by making frequent duplicate determinations. The standard deviations of error for single determinations were 0.018 for ρ_f^*, 0.24 in. for $\overline{D}_b$, and 0.29 sec.$^{-1}$ for f_b. Representative standard deviations for u_{B0} and u_b were from 30 to 50%, as calculated with well-known principles of the propagation of independent errors (*14*) used. Most of the data presented herein have about half this variability because of the duplicate determinations.

The reproducibility obtained was good, considering that conditions in the fluidized bed changed constantly owing to the nature of the bed itself. Measurements over much longer time periods would have been necessary to improve reproducibility to any large extent.

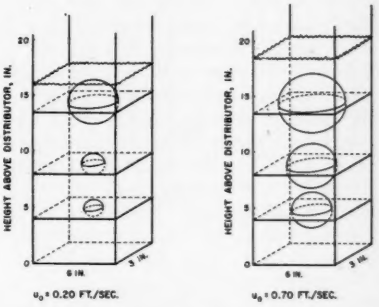

Fig. 10. Horizontal dimensions of bubbles; blend of glass beads.

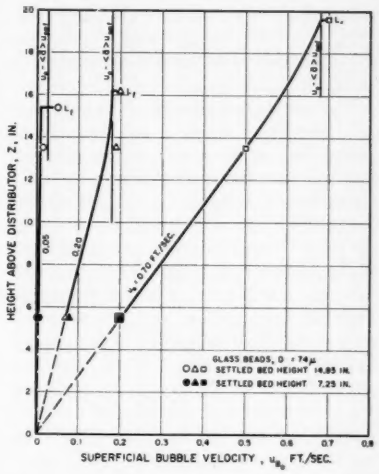
HEIGHT ABOVE DISTRIBUTOR, Z, IN.
SUPERFICIAL BUBBLE VELOCITY, u_{B_0} FT./SEC.
u_0 = 0.70 FT./SEC.
GLASS BEADS, D_p = 74 μ
SETTLED BED HEIGHT 14.85 IN.
SETTLED BED HEIGHT 7.25 IN.

Fig. 11. Bubble flow rate as function of height above distributor.

RESULTS AND DISCUSSION

Bubble Size, Frequency, and Density

Observed values of mean bubble diameter, bubble frequency, and horizontal density are shown for a 15-in. bed of 74-μ glass beads in Figures 7, 8, and 9, respectively. The estimated cross sections of an average bubble at different elevations in the bed are shown for

the blend of glass beads in Figure 10. Results are presented in detail elsewhere (3).

The fast growth of the rising bubbles from the initially small size is apparent from Figures 7 and 10. Bubbles are seen to grow until they approach or even reach the walls of the column. Then as a result of wall effects they become elongated in the direction of the longer dimension of the rectangular column. Bubble size is very evidently affected by superficial air velocity increasing with increasing u_0.

Bubble frequencies measured at different locations in the bed and along the 3- and 6-in. paths ranged from 0.3 to 7.3/sec., as shown by Figure 8. When the bubbles were large, the bubble frequency was highest at center of the column. A large bubble cross section forced the bubbles away from the walls. Small bubbles were found somewhat more frequently near the wall than along the axis, growth of large bubbles by coalescence apparently being easier away from the walls. Bubble frequencies measured along the 6-in. path were usually greater than along the 3-in. path, as would be expected if about the same number of bubbles occurred in any given path length. In cases where bubbles were large, bubble frequencies for the 3- and 6-in. paths were about the same, indicating that only a single bubble could occur in the available bed cross section in a given time interval.

The combined effects of bubble size and frequency resulted in nonuniform horizontal profiles of mean relative density, as shown by Figure 9. The mean density ranged from 55 to 99% of the settled bed density, depending on air velocity and location in the bed. As might be expected the density of the bed was found to be low where bubbles were frequent and large. Except when beds were very turbulent, the average bed density calculated from the observed height of the bed came within a few percentages of the densities determined by gamma-ray absorption. In some cases where bubbles were large, the time-average density measured along the 6-in. path was less than along the 3-in. path. In those cases it must be presumed that the greater wall interference along the 3-in. bed dimension prevented the bubbles from assuming random positions in that direction. Therefore the maximum bubble dimension, and the lowest bed density, tended to concentrate along the center 6-in. path.

Data were also obtained for a shallower bed of 74-μ glass beads, 7.5 in. tall. Results almost duplicated data for the 15-in. bed taken at the same bed level, as seen in Figure 7 for the case of average bubble diameter. Similar good agreement was also found for bubble frequency and bed density. These data indicate that the depth of the bed did not affect its uniformity at a given level. Uniformity therefore appears to be independent of the mass of fluidized material that may be present above the level in question.

Although no direct observations were made of solids circulation patterns, the results on bubble size, frequency, and bed density give indications of what these patterns may have been. When bubbles were small and well distributed over the cross section of the bed, the solid particles must have been pushed aside by the bubbles or possibly lifted a short distance until the bubble passed. When bubbles were large however and rose in the center of the fluidized bed, the solid particles would have been raised by the bubbles in the center of the bed for a considerable distance and then would have moved downward near the walls. Thus an increase in the air velocity would be expected to change the circulation pattern of the dense phase from small, localized motion to increasingly larger patterns extending throughout the beds.

Pressure Drop through the Bed and Vertical Density Profiles

In the past, variation of the pressure drop through the fluidized bed and of the rate of bed expansion with increasing gas velocity has been used to characterize fluidization quality. Gamma-ray determination of line-average densities now permits closer examination of the meaning of such information. If the friction experienced by the gas as it flows through the interstices of the bed is just sufficient to support the weight of all the particles in the bed, the vertical pressure gradient will be proportional to the density of the bed, as in the case of a liquid. The relationship between pressure gradient and bed density is then expressed by the hydrostatic equation

$$\frac{dp}{dZ} = -\frac{g_L}{g_c}\rho_f \qquad (17)$$

Integration gives

$$p_{z_1} = \frac{g_L}{g_c}\int_{z_1}^{L_f} \rho_f(Z)\,dZ \qquad (18)$$

for the pressure at a distance of Z_1 above the distributor plate. For $Z_1 = 0$, and in terms of water manometer readings, H, and bed density relative to settled bed this equation becomes

$$H = \frac{\rho_S}{\rho_W}\int_0^{L_f} \rho_f^{\circ}\,dZ \qquad (19)$$

where ρ_S/ρ_W is the specific gravity of the settled bed relative to water, the gauge fluid. When one assumes a uniform bed, the value of H also should be given by

$$H = \frac{1}{\rho_W}\frac{g_c}{g_L}\left(\frac{W}{S}\right) \qquad (20)$$

Table 2 shows a comparison of values of H obtained from manometer readings, calculated from vertical density profiles measured by gamma-ray absorption with Equation (19) used, and calculated from the weight of the powder with Equation (20) used. The value of L_f used in Equation (19) was the visually observed average height of the bed.

It will be noted that agreement between the pressure drops is good at the lowest air velocity but that it becomes increasingly poorer with increasing air velocity. Agreement among the gamma-ray data obtained along different paths also becomes poorer with increasing air velocity. It is thus seen that when the fluidized bed is not uniform, the analogy between fluidized bed behavior and hydrostatic behavior of a liquid no longer

TABLE 2. PREDICTION OF PRESSURE DROP
Total pressure drop, in. Water, 15-in. bed of 74-μ glass beads

Superficial air velocity, ft./sec.	0.05	0.2	0.7	2.0
Observed manometer reading	20.8	20.5	20.8	22.0
Calculated from gamma-Ray measurements				
from density along 3-in. path, center	21.1	20.2	17.6	17.1
from density along 3-in. path, off center	20.4	20.3	21.3	23.5
from density along 6-in. path, center	20.6	19.2	17.5	19.2
Calculated from weight of powder	20.8	20.8	20.8	20.8

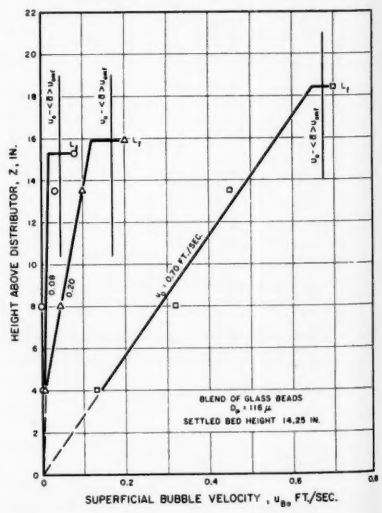

Fig. 12. Bubble flow rate as function of height above distributor.

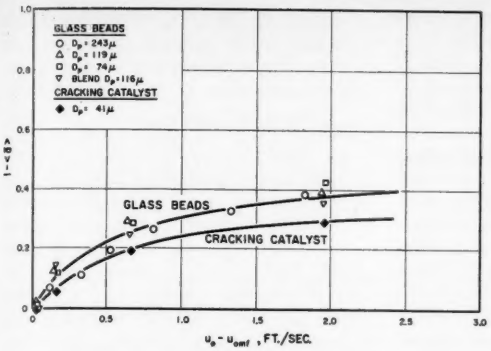

Fig. 13. Fraction of fluidized bed occupied by bubbles.

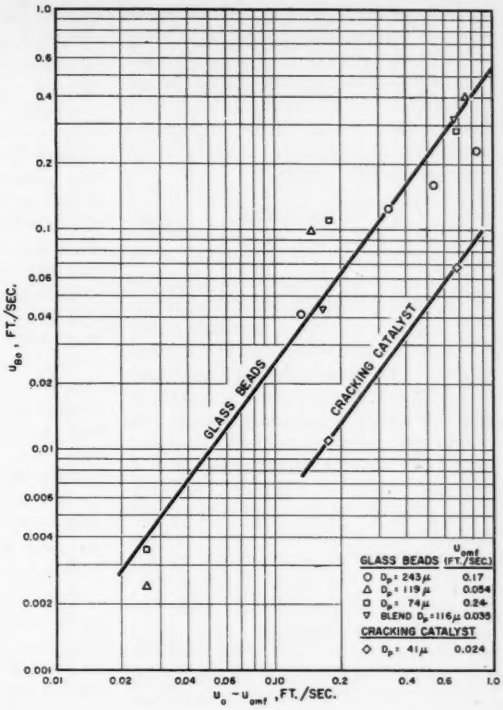

Fig. 14. Bubble flow rate—effect of air velocity.

holds. It can also be inferred that the slow increase of the manometer reading at air velocities from 0.2 to 2.0 ft./sec. results at least in part from the uneven horizontal distribution of the powder in the bed. Similar occurrence of excess pressure drop reported by some authors (*9, 16*) was probably also due in part to wall effects, that is to the accumulation of solid particles near the walls when large bubbles occupied the center of the column.

Bubble Flow Rate

The superficial bubble velocity was calculated from the gamma-ray data on bubble size and frequency with the calculation scheme as outlined earlier used. The value of u_{Bo} is in effect a measure of gas bypassing and is of real interest in the interpretation of gas-particle heat transfer and chemical reaction data obtained in fluidized beds. Figures 11 and 12 give values of u_{Bo} plotted against height above the distributor for two sizes of glass beads. Only total air velocities of 0.7 ft./sec. or less are included, because the calculation scheme does not apply if the bubbles are appreciably elongated in the vertical direction. The data show that the bubble flow rate in bubbles of detectable size increases almost linearly with increasing elevation in the bed. By detectable size is meant the bubble size that could be detected and identified by gamma-ray absorption. The minimum detectable bubble diameter was about 0.35 in. in the case of the glass beads. As indicated by the data the measured bubble flow rate has a value close to zero just above the distributor. As Z is increased, u_{Bo} approaches the quantity $u_o - \langle\bar{a}\rangle\, u_{omf}$ indicated by the vertical straight lines. This quantity is the total gas flow minus the gas flow that would occur in the dense phase at the minimum fluidizing velocity, all based on the column cross section. When $u_{Bo} = u_o - \langle\bar{a}\rangle\ u_{omf}$, the dense phase carries the quantity of gas corresponding to quiescent fluidization, as suggested by Toomey and Johnstone (*16*). It will be noted from the data however that this condition was reached only at an appreciable elevation above the distributor and did not occur in the bottom of the fluidized bed.

Although very small bubbles were not included in the measured value of u_{Bo}, the gas flow contained in them was probably quite small. Very many of these bubbles would have been necessary to carry the same quantity of gas as the large bubbles actually detected. The presence of such a large number would have had the effect of reducing the density of the dense phase. Such a reduction was not observed in the case of the glass beads. Hence the observed increase in bubble flow rate with increasing height above the distributor is believed to reflect at least qualitatively the actual situation.

As a result of this reasoning the following picture may be given of the formation of bubbles in fluidized beds. Just above the distributor the fluidized bed is a relatively uniform mixture of solid and gas. The gas velocity through the interstices of the bed is greater than the velocity needed to support the particles. Thus there is an excess of gas flowing in the dense phase. As the dense phase becomes unstable, the supporting gas flows into local regions of accidentally low density in the solid structure and forms embryo bubbles essentially free of solids. The gas encounters frictional resistance in flowing out of the dense phase. Hence there is a finite time of bubble formation. Once the bubbles are formed, they grow by coalescence with neighboring or slower rising bubbles and by sweeping up additional gas from the dense phase. Finally some distance above the distributor the gas flow through the dense phase becomes equal to u_{omf}, the quantity which is just needed to support the particles. Beyond this point bubbles grow only by coalescence.

The Minimum Fluidizing Velocity

As noted above the minimum fluidizing velocity is an important parameter needed for understanding fluidized-bed behavior. It marks the transition from a settled or quiescent bed, in which all of the gas flow takes place in the interstices between the particles, to a fully fluidized bed, in which the gas flow supports the weight of the solids and in which part of the gas flow may be in the form of bubbles. Although the transition is not necessarily sharp, the following relations may be assumed to hold for $u_o = u_{omf}$:

$$\begin{aligned} \langle\bar{a}\rangle &= 1 \\ D_b &= 0 \\ u_{Bo} &= 0 \end{aligned} \qquad (21)$$

Values of the minimum fluidizing velocity were determined by the method of Miller and Logwinuk (*11*). They are listed in Table 1. These values agreed well with the air velocity at which

bubbles were first observed to break through the surface of the bed. They also agreed with values of u_{omf} obtained from the correlations of Baerg *et al.* (2), which were developed from heat transfer data. Values of the experimental minimum fluidizing velocity were correlated within 10% by

$$u_{omf} = \frac{\epsilon_s'^3 \phi_p^2 D_p^2 (\rho_p - \rho_f) g_L}{144(1 - \epsilon_s')\mu_f} \qquad (22)$$

Here ϵ_s' is observed after decreasing the air velocity slowly from the fluidization range. The equation is a combination of the well-known equation of Carman-Kozeny (4), applicabe to randomly packed fixed beds, with the condition that the pressure difference equals bed weight per unit cross section. The constant 144 in Equation (22) is empirical and only slightly different from the value 180 commonly employed in the packed-bed correlation. The equation represented the minimum fluidizing velocity both for the spent cracking catalyst and for the glass beads. Since the catalyst had probably lost most of its porosity compared with fresh catalyst, the skeletal density (given as ρ_p in Table 1) could be employed in Equation (22) without introducing appreciable error.

Effect of Air Velocity and of Particle Parameters

The volume fraction of the fluidized bed occupied by bubbles is shown in Figure 13 as a function of the superficial air velocity minus the minimum fluidizing velocity. The upper line is a plot of the equation

$$1 - \langle \bar{a} \rangle = 0.3(u_o - u_{omf})^{0.4} \qquad (23)$$

and represents the points for the glass beads. Points for the cracking catalyst fall on a separate line. Values of $\langle \bar{a} \rangle$ are those for the centered 6-in. path at the 8-in. level, which are believed to represent closely the average values of $\langle \bar{a} \rangle$ over the whole bed. The plot indicates that the chief factor affecting the concentration of bubbles in the bed is the gas flow. Subtraction of the minimum fluidizing velocity from the superficial gas velocity recognizes that bubbles do not appear until the bed is a minimum fluidization.

The superficial bubble velocity at the 8-in. level is similarly plotted against $u_o - u_{omf}$ in Figure 14 for total superficial gas velocities up to 0.7 ft./sec. Separate lines are again obtained for the glass beads and the cracking catalyst, with the glass beads giving the greater bubble flows. Although correlation of the glass-bead data is relatively good, some scatter is evident, showing that correction of u_o by subtracting u_{omf} does not compensate completely for different particle size or particle-size range. Comparison of the points for the blend and narrow fraction of the same particle size indicates less gas bypassing for the blend at $u_o - u_{omf} \sim 0.16$ ft./sec. but little or no difference at $u_o - u_{omf} \sim 0.66$ ft./sec. Hence no clear-cut advantage is indicated for using a wide rather than a narrow size fraction to reduce gas bypassing.

As shown by Figures 11 and 12 the bubble velocity reached the value $u_o - \langle \bar{a} \rangle u_{omf}$ at a sufficient elevation in the fluidized bed. For this reason the differences in u_{Bo} shown for different powders in Figure 14 are chiefly indications of different rates of bubble growth. The rate of bubble growth is shown to be a function of particle size and other particle parameters; it is very noticeably smaller for the cracking catalyst than for the glass beads.

Density of the Dense Phase

In spite of the turbulent motions existing in a vigorously fluidized bed it was interesting to note that the density of the dense phase of the glass beads did not differ greatly from that of the settled bed. Table 3 presents the observed specific gravity of the dense phase for the different materials and different air velocities. For the glass beads the dense-phase density was always within 2% of the settled-bed density with the single exception of the blend of glass beads at $u_o = 0.08$ ft./sec., where the difference was still only 8%.

Widely different results were obtained for the silica-alumina cracking catalyst however. For this material the dense phase expanded to a density only 60% of the settled-bed density. Only part of this indicated expansion may have been a uniform expansion of the dense phase, the rest being due to the appearance of many small bubbles not detectable by gamma-ray absorption. The minimum detectable bubble size for the cracking catalyst was about twice that for the glass beads. Hence an appreciable portion of the bubble flow through this material could have been in the form of small bubbles. It is therefore possible that the actual volumetric bubble flow for the cracking catalyst was just as large as for the glass beads. The average bubble size however was much smaller for the cracking catalyst. This would be advantageous from the standpoint of achieving good gas-solids contact, since gas interchange between bubbles and dense phase would occur more readily through the greater bubble surface.

It is interesting to speculate whether a blend of glass beads could be prepared which would fluidize as uniformly as the cracking catalyst, that is whose dense phase would undergo large expansion and whose measured bubble flow rate would be as small. The data

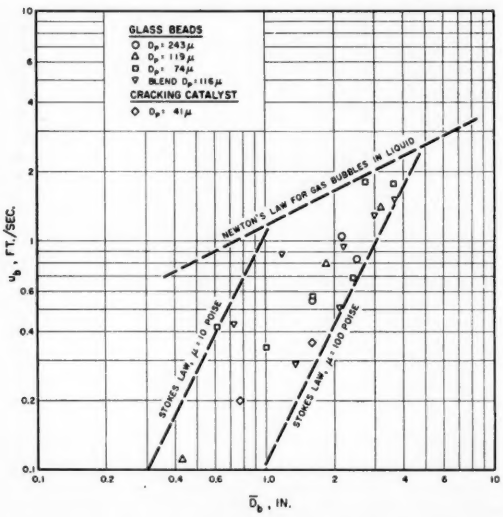

Fig. 15. Bubble velocity vs. bubble diameter.

Table 3. Dense-Phase Density Relative to Settled-Bed Density

Material	Superficial air velocity, u_o, ft./sec. 0.05	0.08	0.2	0.7	2.0
Glass beads					
$D_p = 234\mu$	—	—	—	1.00	1.00
$D_p = 119\mu$	—	0.98	0.99	1.00	1.00
$D_p = 74\mu$	0.98	—	1.00	1.00	0.99
$D_p = 116\mu$ (Blend)	—	0.92	0.98	0.98	0.98
Cracking catalyst					
$D_p = 41\mu$	0.83	—	0.84	0.77	0.60

on the blend of glass beads indicated no clear-cut improvement from using a wide particle-size range. Also the smaller glass beads gave results not appreciably different from the larger glass beads when correlated on the basis of $u_0 - u_{0mf}$. The only other important difference between the glass beads and cracking catalyst is the 45% lower bulk density of the catalyst. If bulk density is indeed a major factor in fluidized bed performance, it would not be possible to reproduce the behavior of the cracking catalyst with some size blend of the glass beads. On the other hand sufficient information is not available to state definitely that the smaller particle size and smoother particle-size distribution would not be factors. (Differences in particle shape and surface roughness are not believed to be important factors.)

Linear Bubble Velocity

In the case of gas bubbles rising through liquids the velocity of rise is a function of the bubble diameter. It is interesting to prepare a plot of this kind for the rise of bubbles in fluidized beds in order to compare the two cases. Such a plot is given in Figure 15. Lines are drawn for the terminal velocity of bubble rise through liquids according to Newton's law (motion governed by inertial forces only) and according to Stokes' law (motion governed by viscous forces only) for liquid viscosities of 10 and 100 poise (6).

Although showing appreciable scatter data points for the fluidized bed fall in a region bounded by the Newton's-Law line above and on the left and right by the two Stokes'-Law lines. If a single line were drawn to correlate the points, it would have a slope intermediate between those of the Newton's- and Stokes'-Law lines. It is interesting to note that Kramers' data on the shear stress-shear rate relation in fluidized beds (8) indicated viscosity values of the order of 40 poise. The plot therefore suggests that the rise of bubbles in fluidized beds is affected both by viscous and inertial forces and that the fluidized bed acts as if it possessed a viscosity in the range of 10 to 100 poise opposing bubble motion.

The plot also suggests the hypothesis that bubble velocity is an increasing function of bubble size. A bubble of a given size would therefore always have the same velocity regardless of its previous history, and its velocity would increase as its size grew. If this is true, it can be reasoned that bubble growth is partly due to the interception of small bubbles by larger bubbles. Small bubbles rising in the fluidized bed would be captured continually from below by larger bubbles rising faster than they do. The larger bubbles would continue to grow, so that near the top of a bed the small bubbles would have practically disappeared and only large bubbles would be left. This conclusion agrees with visual observation of large fluidized beds.

CONCLUSIONS

The gamma-ray absorption results indicate that bubbles grow chiefly from an influx of gas from the dense-phase mixture or from continuous capture of tiny bubbles too small to be detected in these experiments. The gas velocity in the dense phase ultimately drops to a value close to the minimum fluidizing velocity. Columns of limited cross section limit the horizontal growth of bubbles and may result in channeling. Good uniformity in cracking catalyst was characterized by a low rate of bubble growth and apparent expansion of the dense phase from the settled-bed density.

ACKNOWLEDGMENT

This work was carried out with the aid of a fellowship provided by the Ethyl Corporation.

NOTATION

a = concentration of dense phase, fraction by volume, 0
$\bar{a}$ = line average of a, 0
$\langle \bar{a} \rangle$ = time average of $\bar{a}$, 0
D = diameter, L
$\overline{D_b}$ = bubble diameter, mean of determinations along 3- and 6-in. path, L
f_b = bubble frequency as seen by scintillation detector, T^{-1}
f_b' = bubble frequency for the entire column cross section, T^{-1}
g_L = acceleration of gravity, LT^{-2}
g_c = conversion factor, $ML T^{-2} F^{-1}$
H = pressure head, L
I = intensity of radiation, counts per unit time
L = height of bed, L
p = pressure, FL^{-2}
S = cross section of column, L^2
T = time interval, T
u = linear velocity, LT^{-1}
W = weight of solids, F
x = horizontal dimension parallel to gamma-ray beam, L
$\overline{x}$ = mean apparent bubble thickness, L
X = length of gamma-ray path, L
y = horizontal dimension perpendicular to gamma-ray beam, L
Z = distance above distributor, L

Greek Letters

δ = duration of square bubble trace, T
ϵ = void fraction, 0
θ = time coordinate, T
μ = viscosity, $ML^{-1}T^{-1}$
ρ = density, ML^{-3}
ρ^* = density relative to settled bed, 0
σ = standard deviation
σ^2 = variance
ϕ = shape factor, 0

Subscripts

b = individual bubble
B = bubble phase
D = dense phase
f = fluidized bed
F = supporting fluid
m = measured
mf = minimum fluidization
N = noise
p = individual particle
s = settled bed
w = water
0 = superficial, taken over the entire bed cross section
γ = gamma-ray beam

Note: Dimensions of the variables are given in terms of M, mass; F, force; L, length; T, time; and 0, dimensionless.

LITERATURE CITED

1. Askins, J. W., G. P. Hinds, and F. Kunreuther, *Chem. Eng. Progr.*, **47**, 401 (1951).
2. Baerg, A., J. Klassen, and P. E. Gishler, *Can. J. Research*, **F28**, 287 (1950).
3. Baumgarten, P. K., Ph.D. dissertation, Univ. Del., Newark (1956).
4. Carman, P. C., *Trans. Inst. Chem. Eng.* (*London*), **15**, 150, Part I (1937).
5. Grohse, E. W., *A.I.Ch.E. Journal*, **1**, 358 (1955).
6. Haberman, W. L., and R. K. Morton, Report 802, NS 715-102, The David W. Taylor Model Basin, Navy Department (1953).
7. Herdan, G., and M. L. Smith, "Small Particle Statistics," Elsevier Publishing Co., New York (1953).
8. Kramers, H. A., *Chem. Eng. Sci.*, **1**, 35 (1951).
9. Lewis, W. K., E. R. Gilliland, and W. C. Bauer, *Ind. Eng. Chem.*, **41**, 1104 (1949).
10. Matheson, G. L., W. A. Herbst, and P. H. Holt, *ibid.*, 1099 (1949).
11. Miller, C. O., and A. K. Logwinuk, *ibid.*, **43**, 1220 (1951).
12. Morse, R. D., and C. O. Ballou, *Chem. Eng. Progr.*, **47**, 199 (1951).
13. Schiff, L. I., and R. D. Evans, *Rev. Sci. Instr.*, **7**, 456, 62 (1936).
14. Sherwood, T. K., and C. E. Reed, "Applied Mathematics in Chemical Engineering," Chap. 9, McGraw-Hill, New York (1939).
15. Shuster, W. W., and Peter Kisliak, *Chem. Eng. Progr.*, **9**, 455 (1952).
16. Toomey, R. D., and H. F. Johnstone, *ibid.*, **48**, 220 (1952).
17. Untermyer, S., *Nucleonics*, **12**, No. 5, 35 (1954).
18. Wamsley, W. M., and L. N. Johanson, *Chem. Eng. Progr.*, **50**, 347 (1954)

Manuscript received July 18, 1957; revision received April 13, 1959; paper accepted April 15, 1959.

Mechanics of Particle Bounce

W. E. RANZ, G. R. TALANDIS, and BERNARD GUTTERMAN

University of Minnesota, Minneapolis, Minnesota

Irregular particles bounce with randomly distributed angles of reflection. There is a certain probability that a particle striking at low angle will bounce at a high angle and be carried far out into the main fluid flow. Bounce phenomena were investigated with respect to bounce of a model particle, limitations on dust collection (back mixing), and energy loss during the flow of suspensions.

Particles with irregular shapes and mass distributions no not necessarily reflect when they strike a surface but bounce at some angle with a probability distribution about the average angle of reflection. During bounce, energy interchange can occur between particle and surface (inelastic bounce) and between the translational and rotational energies of the particle. The process is complicated further when the surface struck is itself irregular in shape and when friction occurs between particle and surface at the instant of impact.

There are practical consequences of irregular bounce. In dust collectors a particle hitting at a high angle of incidence has a certain probability of bouncing at a lower angle of reflection and at a higher lateral velocity. In this case irregular bounce limits efficiency by causing back mixing. During pneumatic conveying, irregular bounce keeps large particles suspended and moving. Here the lateral velocity of a high bounce represents kinetic energy lost because the particle must be reaccelerated axially, and the high bounce itself contributes to a general lagging of the particle behind the gas flow.

It is the purpose of this paper to discuss simply the mechanics of particle bounce and to show the importance of bounce phenomena in certain applications.

Bernard Gutterman is with the Pennsylvania Department of Health, Harrisburg, Pennsylvania.

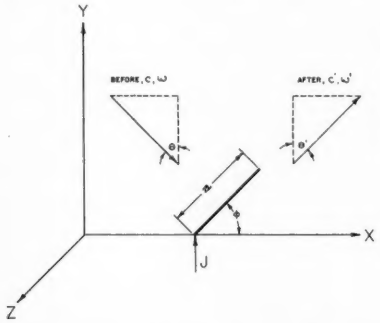

Fig. 1. Graphical representation of bouncing stick: θ = angle of incidence, θ' = angle of reflection, ϕ = angle stick makes with surface at moment of impact.

BOUNCING STICK

To establish the nature of the theory of irregular bounce and show in a simple mathematical way, the interchange of kinetic and rotational energies, and the probability of various angles of bounce, a simple theoretical model was devised. This model involves the initial bounce of a uniformly weighted line segment or stick. It is assumed that collision is between smooth, rigid surfaces and that the motion is two-dimensional with rotation in the third dimension. Figure 1 is a graphical representation of this bouncing stick. The angle made by the incident path of the center of mass with a normal to the surface is defined as the *angle of incidence*; the angle made by the reflected path of the center of mass with a normal to the surface is defined as the *angle of reflection*.

At the moment of impact the linear momentum imparted to the stick is

$$m(\mathbf{C}' - \mathbf{C}) = (\mathbf{x} + \mathbf{y})\cdot\mathbf{J} \qquad (1)$$

When there is no friction, that is, the impulsive change of momentum is upward, the linear momentum imparted in the y direction is

$$m(C'_y - C_y) = J \qquad (2)$$

and in the x direction

$$m(C'_x - C_x) = 0 \qquad (3)$$

an indication that there is no change in the velocity tangential to the surface.

For rotation about the z axis the angular momentum is $(\underline{\mathbf{I}}\cdot\omega)_z = I_{zz}\omega_z$, and at the moment of impact the angular momentum imparted to the stick is

$$I(\omega' - \omega) = J\,\mathcal{L}\cos\phi \qquad (4)$$

Since an "elastic" collision between smooth, rigid surfaces is assumed, energy is conserved, and

$$E = (1/2)m\mathbf{C}^2 + (1/2)\underline{\omega}\cdot\underline{\mathbf{I}}\cdot\underline{\omega}$$
$$= (1/2)m(C_x^2 + C_y^2) + (1/2)I\omega^2$$
$$= E' = (1/2)m(C'^2_x + C'^2_y) + (1/2)I\omega'^2 \qquad (5)$$

Solving for J from Equations (2) through (5), one gets

$$J = -2mC_y(1 + (\omega\mathcal{L}/C_y)\cos\phi)/(1 + m\mathcal{L}^2\cos^2\phi/I) \qquad (6)$$

Equations (2) and (6) give C'_y in terms of C_y and ω. Equations (4) and (6) give ω' in terms of C_y and ω.

Of particular interest are the relationships between θ and θ', between initial and final vertical velocities, and between initial and final kinetic energies. A general relationship indicating all these changes can be written as

$$\frac{\cot\theta'}{\cot\theta} = \frac{C'_y}{C_y} = 1 - \frac{2(1 + (\omega\mathcal{L}/C_y)\cos\phi)}{1 + 3\cos^2\phi} \qquad (7)$$

Figure 2 shows a plot of these ratios as a function of stick orientation at the moment of impact. Equation (7) expresses only the result of a first collision and shows the change in the trajectory angle and velocity of the center of mass. Curves in Figure 2 are drawn for $\omega\mathcal{L}/C_y = 0$, a nonrotating stick, and

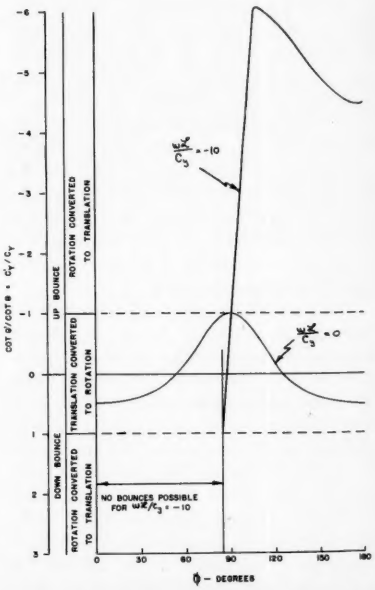

Fig. 2. Result of single collision of bouncing stick.

$\omega\mathcal{L}/C_y = -10$; the latter case is one where the velocity tangential to the surface is perhaps ten times that of the vertical velocity toward the surface, and a peripheral velocity equal to this velocity has been imparted by previous bounces.

Positive values of $\cot\theta'/\cot\theta$ indicate that the center of mass of the stick, after the initial impact, continues to move downward toward the surface. Such motion would always lead to a second impact before rebound. When $\cot\theta'/\cot\theta$ is negative, the center of mass moves upward after impact. When $\cot\theta'/\cot\theta$ is less than -1, the stick "hops" and rebounds at a higher angle and at a higher vertical velocity than the angle and velocity with which it hit. If the stick hits end down ($\phi = 90$ deg.), $\cot\theta'/\cot\theta = -1$, and the stick reflects perfectly without any change in kinetic or rotational energy. When the absolute value of $\cot\theta'/\cot\theta = C'_y/C_y$ is less than unity, and since $C'_x = C_x$, kinetic energy is interchanged for rotational energy at the moment of impact. When the absolute value is greater than unity, the energy interchange is reversed.

If the absolute value of $\omega\mathcal{L}/C_y$ is greater than one, the rotation is great enough to cause the tip of the stick to move vertically faster than the center of the mass. This will decrease the possible orientation angles (ϕ) from 180 deg. to some smaller number. Mathematically this restricts J to be negative as calculated by Equation (6). Thus the following must be true:

$$\frac{\omega\mathcal{L}}{C_y}\cos\phi_c \leq -1$$

For the example mentioned $\omega\mathcal{L}/C_y = -10$; $\phi_c = 84$ deg. 16 min. This is to say that no bounces occur with $\phi < 84$ deg. 16 min. when $\omega\mathcal{L}/C_y = -10$. Here ω is clockwise, negative; C_y is downward, positive. From Figure 2 it can be seen that 97% of the sticks will bounce upward after the first impact. It is also apparent that a significant number of these upward motions will be at lower angles of reflection than the angle of incidence and at larger upward velocities than the initial downward velocity, all brought about by the irregularity in shape.

To show this more strikingly, average values are computed. If all possible orientation angles ϕ are equally probable, the average $\cot\theta'$ and the average C'_y for $\omega\mathcal{L}/C_y = -10$ is given by

$$\frac{\overline{\cot\theta'}}{\cot\theta} = \frac{\overline{C'_y}}{C_y} = \frac{180\text{ deg.}}{\pi[180 - 84\text{ deg. }16\text{ min.}]}\int_{84\text{ deg. }16\text{ min.}}^{180\text{ deg.}} \left\{1 - \frac{2(1 - 10\cos\theta)}{1 + 3\cos^2\theta}\right\} d\theta = -4.50 \quad (8)$$

BOUNCE OF AN IRREGULAR MODEL PARTICLE

To demonstrate the bounce characteristics of irregularly shaped particles, a simple model test was devised. Ping-pong balls, distorted by boiling, were shot from a gun against a hard surface at a particular incident angle, and the distribution of ultimate angle of reflection was measured.

Incident angles were varied from 80 to 50 deg., and reflected angles were obtained by markings through carbon paper at points of contact on the bounce surface, which was horizontal, and a vertical backboard. Five representative shapes were fired about fifty times each at a constant incident angle. These shapes showed a high degree of correlation with each other, although by visual standards they were entirely different in geometry.

When the data from different incident angles were assembled, it was found that the standard deviation from the angle of reflection appeared to vary with the incident angle. As shown in Figure 3, the standard deviation from the average angle of reflection varied from approximately 9 to 10 deg. for an incident angle of 50 deg. to 5 to 6 deg. for an incident angle of 80 deg. For incident angles greater than 70 deg., the mean reflected angle was approximately equal to the incident angle, and the distribution of angular deviations was normal in shape. A sample distribution is shown in Figure 4.

Results from the bounce of a soft rubber cube on a smooth varnished wood surface and a hard Lucite cube against a smooth steel surface are also shown in Figure 3. Apparently friction plays an important role in setting the standard deviation. With rubber cubes the average angle of reflection was found to be lower than the angle of incidence for high angles of incidence and higher for low angles, the difference being more pronounced at high angles of incidence. With Lucite cubes the average angle of reflection was always more than the angle of incidence, the difference slightly increasing with decreasing angle of incidence.

BACK MIXING CAUSED BY PARTICLE BOUNCE

Large particles conveyed in horizontal gas flows remain suspended even though they are not much affected by turbulent gas motion and should, because of the gravity force, be rolling along the bottom of the duct. In dust-collection equipment back mixing against even larger separating forces limits collection efficiency. It is suggested that irregular particle bounce is a major mechanism for such back mixing.

Figure 5 shows the concentration gradient for sand particles of angular shape conveyed horizontally in a rectangular duct. The sand particles were about 90 μ in average diameter (range 74 to 105 μ) and had a terminal falling velocity of about 1.5 ft./sec. The duct was 2 in. high by 5 in. wide by 16 ft. long, and the concentration gradient was measured at 14 ft. from the inlet, where there was nearly a uniform concentration. The central air velocity was 50 ft./sec. If all the particles were traveling horizontally when they entered the duct, one would expect to find them on the bottom of the duct after 5 ft. of duct length. By

Table 1. Concentration of Bouncing Particles

Average diameter, μ	Angular tin 50		Rounded tin 50		Angular sand 93	
Sp. gr.	7.3		7.3		2.64	
$1/\delta$, deg.	3.5		1.8		3.6	
y, ft.	Observed concentration, g./sq. ft.	Calculated concentration, g./cu. ft.	Observed concentration, g./cu. ft.	Calculated concentration, g./cu. ft.	Observed concentration, g./cu. ft.	Calculated concentration, g./cu. ft.
0.0075	7.0	5.35	7.64	3.38	2.54	2.63
0.0256	4.37	4.38	2.62	2.07	1.75	1.75
0.054	3.35	3.33	1.00	0.994	1.099	1.08
0.0767	2.5	2.56	0.437	0.43	0.654	0.627
0.102	1.95	1.98	0.18	0.207	0.398	0.397
0.1275	1.42	1.515	0.093	0.0925	0.259	0.219
0.1458	—	1.255	0.067	0.051	0.204	0.167

the time the particles had traveled 14 ft. along the duct, where the concentrations of Figure 5 were measured, they must have undergone multiple bounces and were approaching some equilibrium bounce state. In accordance with the Weiss-Longwell criterion (2), turbulent diffusion could not have been the cause of back mixing.

SIMPLE THEORY FOR EQUILIBRIUM CONCENTRATION OF BOUNCING PARTICLES

A particle striking a surface at an incident angle θ with a certain velocity and initial rotation will bounce at some reflected angle $(\theta + \alpha)$ with a new velocity and rotation which is a function of the elasticity of bounce, the irregularity of the particle, and the friction encountered on impact. α consists of two parts; the first part establishes the average angle of reflection, and the second part involves a probability of dispersion about the average angle of reflection. After rebound a certain portion of the particles will have an increased lateral velocity which will carry them a large distance from the rebound surface.

To obtain the order of back mixing by bounce, a simplified system was considered. In this simplified system it is assumed that the incident angle is quite large ($\theta = 90$ deg.), that the particle bounces at the angle α to the surface, and that the particle hits at the main-stream velocity and bounces at the same velocity (no energy loss or interchange of energy). It is also assumed that the angle α is distributed normally about an average reflection angle of 90 deg., dispersion through the surface being perfectly reflected away from the surface, such that

$$(2\delta/\sqrt{\pi})\exp(-\delta^2\alpha^2)d\alpha$$

represents the fraction of the total number of bouncing particles which bounce at a positive angle between α and $d\alpha$.

The velocity away from the surface becomes

$$v_y = v_o \sin\alpha \approx v_o\alpha \qquad (9)$$

where α is nearly always less than 15 deg. It is assumed further that the stopping distance of a particle bouncing at an angle α is governed by Stokes's resistance law.

At every y distance above the surface, particles falling toward the surface are assumed to fall with their terminal velocity. This is certainly not true of particles whose bounce carries them only to this level, but the concentration at this level is made up primarily of particles raining down from much higher levels.

At equilibrium a flux balance at a certain level reads

$$CV_t = \int_a^\infty C_w V_t (2\delta/\sqrt{\pi})\exp(-\delta^2\alpha^2)d\alpha \qquad (10)$$

where the first term represents the flux toward the wall caused by the separating force, and the integral term represents the flux away from the surface of those particles which have stopping distances greater than the y level in question. $C_w V_t$ is the flux of particles into the surface; $(2\delta/\sqrt{\pi})\exp(-\delta^2\alpha^2)d\alpha$ is the fraction of particles bouncing at an angle α, reaching a stopping distance $S_t = y$. Rearrangement of the flux balance gives

$$C/C_w = 1 - \mathrm{erf}(q) = 1 - (2/\sqrt{\pi})$$
$$[q - (q^3/3.1!) + (q^5(5.2!) - \ldots] \qquad (11)$$

where $q = \alpha\,\delta$.

The effective diffusion coefficient becomes

$$\mathcal{D} = V_t C/(dC/dy) \qquad (12)$$

Since $\mathcal{D}$ cannot be obtained explicitly in terms of y, the effective diffusion coefficient must be obtained by graphical differentiation of a plot of $C = C(y)$.

It is noted finally in this theoretical development that back mixing can also occur because the particles are bouncing from randomly oriented units of bounce surface area. In this case the irregularity of the surface is of a scale which may seem small to the eye but is large with respect to the size of the particles. The mathematical treatment and theoretical results will be the same, but now α is a function of, and in special cases may be only a function of, surface characteristics.

ANGULAR DEVIATIONS OF REFLECTED ANGLES CALCULATED FROM CONCENTRATION GRADIENTS

If the simple theory for equilibrium concentration of bouncing particles is substantially correct, the angular deviation of bounce can be calculated from concentration gradients such as the one shown in Figure 5. For a point of known y distance from the wall the concentration was obtained and placed in Equa-

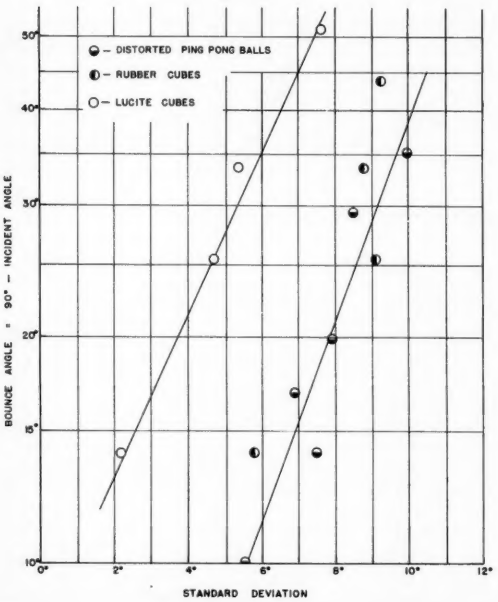

Fig. 3. Dispersion about the average bounce angle is affected by incident angle and type of contact surfaces.

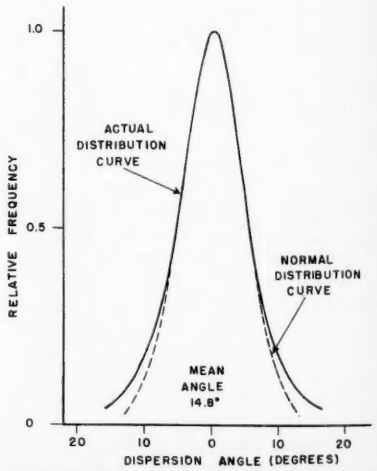

Fig. 4. Dispersion about the average angle of reflection is normal in character.

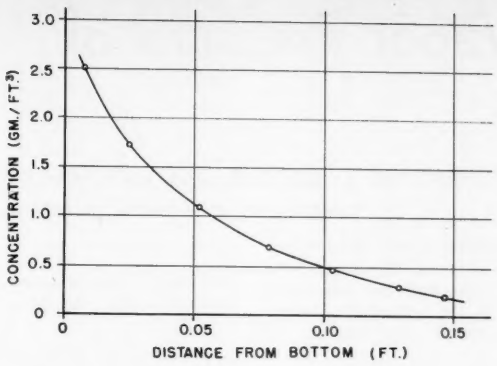

Fig. 5. Example of sand-concentration distribution maintained by bouncing particles.

tion (11). The known y represented a stopping distance related to the angle α which was required to bounce a particle to that height. A similar procedure was followed for a second point. Two equations were now available with the unknowns C_w and q, where $q_1 = \alpha_1\delta$ and $q_2 = \alpha_2\delta$. By dividing the resulting equations, an expression for δ may be obtained for each type of particulate matter in question. Once δ is established, C_w and the concentration at other levels can be calculated. It is to be noted that δ is constant for a given material, but α varies from level to level and is related to the stopping distance.

Results of such calculations for three different types of particles are shown in Table 1. It is noted that the standard-deviation angle for angular sand and tin is nearly that which would be predicted from an extrapolation of Figure 3 to the lower incident angles of these cases. As expected, the deviation angle for rounded tin particles is much less than that for angular particles.

SIMPLE THEORY FOR THE EFFECT OF IRREGULAR BOUNCE ON ENERGY LOSSES DURING PNEUMATIC CONVEYING

Using the assumptions and symbols of the section on back mixing, one can also consider the effect of irregular bounce on energy losses during the horizontal conveying of particle suspensions. It remains only to assume that kinetic energy represented by lateral velocities is lost energy and is dissipated in particle wakes in the gas volume above the bounce surface.

The energy loss rate per unit area of bounce surface is

$$\int_0^\infty (C_w V_t (v_o\alpha)^2/2g_c)\ (2\delta/\sqrt{\pi})\exp(-\delta^2\alpha^2)d\alpha = C_w V_t v_o^2/2g_c\delta^2 \quad (13)$$

If this energy is supplied by the gas moving over the surface, the gas will experience, in addition to other energy losses, an energy loss caused by the irregular bounce. In tube flow, when one assumes a floor area of DL, this energy loss per unit mass of gas flowing is given by

$$N_f = (F/L)D/(v_o^2/2g_c) = (4/\pi)(C_w/\rho)(v_o)(1/\delta^2) \quad (14)$$

For $C_w/\rho = 1$ lb.-mass solids/lb.-mass gas, $V_t/v_o = 10^{-1}$, the ratio of terminal falling velocity to flow velocity, and $1/\delta = \pi/20$ radians; $N_f = 3 \times 10^{-3}$, which is of the order of 10 to 20% of that expected for turbulent gas flow alone.

The preceding calculation is significant only so far as it suggests a method of attack on a rather complex problem. The role and significance of friction at the moment of impact and interchange of energy between translation and rotation have not been considered. C_w, the effective particle concentration in the gas near the wall, is usually unknown. The interference between particles has been neglected.

In the usual case of particle transport by bounce the average particle velocity is somewhat less than average gas velocity (3), an indication that bouncing particles are always lagging behind the gas flow. The combined particle wakes for the relative axial velocity difference also produce an energy loss in the gas. Since the measured velocity lag would result in a much more significant energy loss than that for lateral motion alone, it is presumed that the importance of irregular bounce lies primarily in its effect on the lag, or slip, velocity. However such a theoretical derivation and experimental verification is beyond the simple theory and experiment of the present paper.

ACKNOWLEDGMENT

Thanks are due to John S. Dahler for aid in defining the theoretical problem of irregular bounce.

NOTATION

- C = suspended particle concentration in gas flow
- C_w = suspended particle concentration in gas flow at bounce surface
- $\mathbf{C}$ = vector velocity of center of mass of stick
- E = total energy of stick
- F = energy loss per unit mass of gas flowing
- g_c = dimensional conversion constant = 32.2 (lb.mass/lb.-force) (ft./sec.^{2})
- $\underline{\mathbf{I}}$ = inertia tensor of bouncing stick
- $\mathbf{J}$ = impulsive change in momentum
- $2\mathcal{L}$ = length of bouncing stick
- m = mass of bouncing stick
- q = $\alpha\delta$
- S_s = stopping distance of particle if Stokes resistance law pertains
- v_o = gas-flow velocity, main stream
- V_t = terminal falling velocity of particle
- $\mathbf{x}, \mathbf{y}$ = unit vectors in x and y directions
- y = vertical distance from bounce surface

Greek Letters

- α = angular deviation of the bounce, measured from the average angle of reflection
- $1/\delta$ = standard deviation of the angular deviation of the angle of reflection
- θ = angle of incidence measured from normal to bounce surface
- θ' = angle of reflection
- ρ = gas density
- ϕ = angle between stick and surface at moment of impact
- $\underline{\omega}$ = rotation of bouncing stick

Subscripts x, y, z refer to vector components in x, y, z directions; primed quantities denote conditions after collision, unprimed quantities conditions before collision.

LITERATURE CITED

1. Gutterman, Bernard, Ph.D. thesis, The Penn. State Univ., State College (August, 1958).
2. Longwell, J. P., and M. A. Weiss, *Ind. Eng. Chem.*, **45**, 667 (1953).
3. Mehta, N. C., J. M. Smith, and E. W. Comings, *ibid.*, **49**, 986 (1957).

Manuscript received April 8, 1959; revision received July 28, 1959; paper accepted August 4, 1959. Paper presented at A.I.Ch.E. Atlantic City meeting.

Compressibility and Vapor Pressure of Methyl Borate

RICHARD G. GRISKEY, WALTER E. GORGAS, and LAWRENCE N. CANJAR

Carnegie Institute of Technology, Pittsburgh, Pennsylvania

Pressure-volume-temperature measurements have been made on methyl borate over the temperature range of 225° to 300°C. and pressures of 30 to 200 atm. in a variable volume *P-V-T* bomb. Vapor-pressure measurements from 180°C. to the critical point have also been made with the same apparatus. The vapor-pressure data are presented in the form of the Antoine equation, and the *P-V-T* data together with the vapor-pressure data have been fitted to the Benedict-Webb-Rubin equation of state.

With exception of vapor-pressure measurements made by Webster and Dennis (*7*) and the vapor-pressure and orthaboric-density measurements of Hansen and Hughes (*4*), no previous work has been done on the *P-V-T* properties of methyl borate.

The apparatus used in this investigation is a modification of the design of Keyes (*5*) and Beattie (*1*). Except for certain changes which have been described by Li and Canjar (*6*), a detailed description of the equipment was published by Cherney, Marchman, and York (*3*). The methyl-borate sample was prepared from special-grade (99.9% pure) material. After a portion of the stock had been distilled in the presence of sodium in a closed system, the middle third of the distillate was frozen, exposed to vacuum, liquefied, frozen again, exposed to vacuum, liquefied again, and sealed in a glass ampule.

It was discovered that methyl borate over mercury slowly decomposed with time, particularly at high temperatures. In order to minimize the effect of this decomposition, the data were obtained as rapidly as possible in two sets. The vapor-pressure runs were made over the temperature range of 180° to 230°C. The initial pressure measured at 180°C. was 16.722 atm. After all the vapor-pressure measurements had been made, a repeat measurement was made at 180°C., and a pressure of 16.950 atm. was obtained. Normally when these measurements are made on other compounds, the difference in the pressure of the initial measurement and the repeat measurement is negligible, indicating no chemical change. In this work the decomposition effect was appreciable.

A second set of runs was made to determine the compressibility of gaseous methyl borate in the temperature range of 225° to 300°C. One of the first measurements made at a density of 1.545 moles/liter and 300°C. gave a pressure of 49.616 atm. After all the data in this set of runs had been obtained, this same point was remeasured, and the pressure was found to be 49.749 atm., again an indication of a decomposition effect.

The uncertainty in vapor-pressure determinations is much larger. When measurements are made in the two-phase region, the pressure of a pure component remains constant when the volume is varied over an isotherm. Because of the presence of decomposition products in the methyl-borate sample, the pressure changed as vaporization took place at constant temperature. This made the exact location of the critical point impossible and added another uncertainty in the actual value of the vapor pressure. The uncertainty is a maximum at the critical point and is estimated to be 0.5 atm.

The vapor pressure data, given in Table 1, can be represented by the Antoine equation:

$$\log_{10} p_{\text{atm.}} = 4.18470 - \frac{1164.0}{T\text{-}60}$$

where T is temperature in °K

Residuals of observed pressures minus calculated pressures are given in Figure 1.

A summary of the *P-V-T* properties of gaseous methyl borate is given in Table 2. These data and the vapor-pressure data have been fitted to the Benedict-Webb-Rubin equation (*2*):

$$P = RTd + \left(BoRT - Ao - \frac{Co}{T^2}\right)d^2 + (bRT - a)d^3 + \alpha Rd^6 + \left(\frac{Cd^3}{T^2}\right)\left(1 + \gamma d^2\right)e^{-\gamma d^2}$$

where $Ao = -31.589$, $Bo = -0.4332$, $Co = 7.363 \times 10^6$, $a = 23.272$, $b = 0.3417$, $c = 2.790 \times 10^6$, $\alpha = 7.8 \times 10{-}4$, $\gamma = 0.033$, R = 0.0820567 when P is given in atm., T in °K., and d in g.-moles/liter. The average percentage deviation between observed pressures and pressures calculated from the Ben-

Table 1. Vapor Pressure of Methyl Borate

Temperatures, °C.	Vapor pressure, atm.
180.00	16.72
202.16	24.12
209.79	27.11
220.00	31.44

Table 2. Compressibility Measurements of Methyl Borate

Temperature, °C.	Density, g. moles/liter	Pressure, atm.
225	1.545	32.53
	1.943	34.26
	2.632	35.20
	3.248	35.64
	3.561	35.91
	3.805	36.08
	4.244	37.72
	4.489	39.49
	4.809	44.87
	5.244	60.66
	5.582	85.83
	6.367	211.56
—	—	—
250	1.117	34.16
	1.550	38.32
	1.790	40.79
	1.948	42.21
	2.174	43.90
	2.438	45.79
	2.848	48.00
	3.356	51.16
	4.102	59.02
	4.556	69.51
	4.943	85.34
	5.253	105.87
	5.463	131.02
	5.709	156.16
	5.862	181.68
	6.018	211.49
—	—	—
275	1.238	38.45
	1.554	44.07
	1.793	47.84
	2.585	57.99
	3.023	63.14
	3.488	69.79
	4.139	84.01
	4.658	104.79
	4.958	123.89
	5.309	156.09
	5.545	186.26
	5.701	211.41
—	—	—
300	1.236	42.63
	1.545	49.61
	1.795	54.72
	2.133	61.06
	2.745	67.19
	2.836	73.74
	3.383	85.55
	3.873	99.63
	4.321	118.73
	4.853	154.92
	5.157	186.13
	5.342	211.27
	1.545 (recheck)	49.74

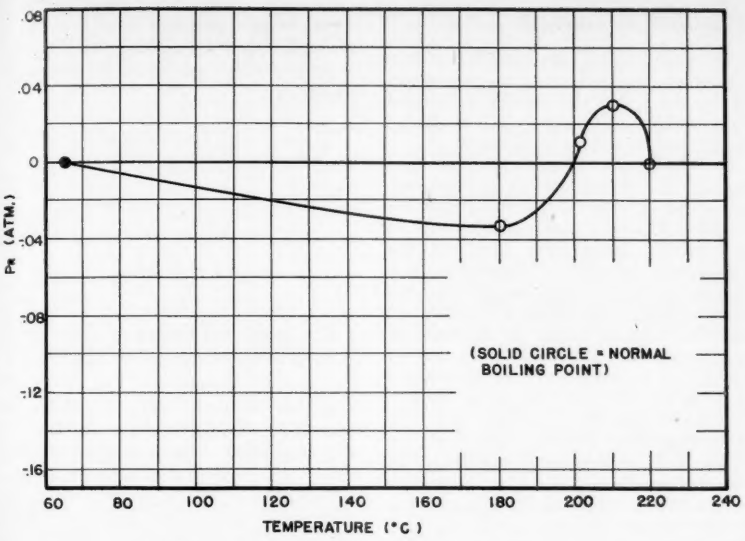

Fig. 1. Vapor pressure residual P_R vs. temperature.

edict-Webb-Ruben equation of state is 0.64%.

The critical temperature is estimated to be 228.5° ± 0.5°C. and the critical pressure 35.4 ± 0.5 atm.

ACKNOWLEDGMENT

This research was supported by the Callery Chemical Company. Grateful acknowledgment is hereby made.

LITERATURE CITED

1. Beattie, J. A., *Proc. Am. Acad. Arts Sci.*, **69**, 589 (1934).
2. Benedict, Manson, G. B. Webb, and L. C. Rubin, *J. Chem. Phys.*, **8**, 334 (1940).
3. Cherney, B. J., Henry Marchman, and Robert York, *Ind. Eng. Chem.*, **41**, 2653 (1949).
4. Hansen, C. E., and R. L. Hughes, *A.I.Ch.E. Journal*, to be published.
5. Keyes, F. G., *Proc. Am. Acad. Arts Sci.*, **68**, 505 (1933).
6. Li, Kun, and L. N. Canjar, *Chem. Eng. Progr. Symposium Series No. 7*, **49**, 147 (1953).
7. Webster, S. H., and L. M. Dennis, *J. Am. Chem. Soc.*, **55**, 3233 (1933).

Manuscript received June 25, 1959; revision received August 5, 1959; paper accepted August 10, 1959.

The Motion of Two Spheres Following Each Other in a Viscous Fluid

JOHN HAPPEL and ROBERT PFEFFER

New York University, New York, New York

The purpose of this investigation was to determine the interaction effect of one spherical particle upon another when both are falling in a viscous fluid. The velocities of two identical spheres, falling along the axis of a cylinder in a direction parallel to their line of centers, were measured experimentally as a function of the center-to-center distance between them at very low Reynolds numbers. The experimental results compared very well with theoretical studies found in the literature which predicted that two spheres will fall faster than one sphere.

At Reynolds numbers greater than 0.25 the influence of inertial effects were studied for one and two spheres. The experimental results qualitatively confirmed the Oseen equations. A definite attraction between two spheres falling one above the other was observed; the inertial forces acted to slow down the lower sphere without affecting the upper one.

The behavior of spherical particles settling in a viscous fluid is of fundamental importance in solving problems involving sedimentation, flow through packed beds, and fluidization. However both mathematical analysis and experimental observation are extremely difficult when dealing with assemblages of particles because of the many boundary conditions and interaction effects encountered. In addition to these complications, as soon as the particle Reynolds number becomes as high as 0.25, the inertial terms can no longer be neglected in the solution of the Navier-Stokes equations of motion.

For these reasons a logical start in attempting to solve problems involving many particles is to carry out a complete study of the important variables affecting the motion of one particle at very low Reynolds numbers. Then these observations can be used to study the motion of two particles and so on, until eventually enough theoretical and experimental information is available to predict the motion of the complex particle systems actually encountered in practice. The same technique can be utilized in studying the inertial effects which become important at higher Reynolds numbers.

The purpose of the investigation described in this paper was to continue to add to the information available concerning the motion of two particles settling one above the other in a viscous fluid. As an idealization of the numerous particle shapes conceivable, identical, smooth, and rigid spheres were chosen to work with.

Experimental measurements were made at low Reynolds numbers (much less than 0.25) of two spheres settling along the axis of a cylindrical tube in a direction parallel to their line of centers. This was done to determine how well the theoretical equations of motion, and the pertinent correction factors which take into account the boundary and interaction effects, could predict the actual motion. The influence of inertial effects at higher Reynolds numbers on the motion of two spheres was also determined experimentally and compared with the corresponding effects on a single sphere. A qualitative analysis of the motion of three spheres will also be discussed.

DESCRIPTION OF APPARATUS

The apparatus used for taking velocity measurements consisted of a cylindrical Pyrex glass column 32 in. long with an

I.D. of 5 11/32 in. (Figure 1). The column was equipped with a closed nipple set between two 1¼-in. gate valves which was mounted directly below the axis of the cylinder. This equipment was used to recover the spheres and also, when necessary, to empty the column. A dropping mechanism, consisting of a thin-walled brass bushing slightly larger in diameter than the spheres which were dropped, was carefully mounted on the top of the column so that the axis of the bushing coincided with the axis of the cylindrical column. This allowed the spheres to fall freely into the fluid.

Two thermometers were inserted into the glass column 8 in. from the top and bottom and ¾ in. from the glass wall so that the temperature of the fluid might be read at both of these points. Since it was impractical to surround the column by a constant-temperature bath, the experiments were performed in a relatively constant-temperature room which was maintained at a temperature between 24.5° and 26.5°C. by a Fenwall thermoswitch connected through a relay to a ¾-ton room air conditioner. The temperature of the room never varied more than ±½°C. in any 24 hr. period; temperature gradients across the room were minimized by the use of an electric fan to circulate the air.

To obtain different operating conditions two polyalkylene glycol types of fluids having different viscosities were used in the experiments. The fluids show a comparatively small change in viscosity with temperature and are also extremely stable. They have a negligible vapor pressure, low hygroscopicity, and a low specific heat; they are also water soluble which is very helpful in cleaning the apparatus. The viscosity and density of the two fluids were determined over a temperature range of 23° to 28°C. with a calibrated Ostwald type of viscometer and pycnometer.

The spheres which were used in the experiments consisted of plastic balls approximately ¼ in. in diameter. The balls, made of marbelette, Lucite, and nylon, were perfectly smooth and rigid and completely insoluble in the fluids. The density of the spheres was measured to five significant figures by the use of a constant-volume pycnometer; the diameters of the spheres were measured with a micrometer.

Some of the pertinent properties of the spheres and fluids that were used are listed below.

Spheres

Material	Color	Diameter, in.	Density, g./cc.
Nylon	White	0.250	1.1586
Lucite	Red	0.234	1.1919
Marbelette	Black	0.241	1.3249

Fluids

Ucon fluid	Viscosity at 25°C., centipoises	Density at 25°C., g./cc.
1	1,337	1.050
2	242	1.043

EXPERIMENTAL METHOD

The experimental runs consisted of taking velocity measurements of one sphere falling along the axis of the cylindrical glass column and of two spheres falling along the axis, one above the other.

For one sphere falling alone the time required for the sphere to fall between two strips of tape 12 in. apart was recorded with a stop watch which could be read to 0.1 sec. Before each run the temperature of both thermometers was read to 0.1°C. and the average value recorded. This was justified because an error as large as 0.2°C. in the average temperature would amount to an error of only 1% in the viscosity of the fluid and a completely negligible error in the density. No runs were made, however, if the temperature gradient was more than 0.4°C.

The 12-in. length of fall was located in the central section of the 32 in.-long glass column so that the possibility of errors due to unsteady motion was eliminated. This also minimized any errors due to end effects.

For two spheres falling one above the other, at very low Reynolds numbers ($N_{Re} << 0.25$), the velocities of the two spheres were found to be equal and were measured by recording the time (to 0.1 sec.) required for the bottom sphere to fall 12 in. The center-to-center distance between the spheres was taken both at the top and bottom of the 12-in. length of fall by measuring the time difference between the two spheres as they both crossed each of the tape strips; another stop watch which could be read to 0.1 sec. was used for this purpose. The observed time between the spheres at the top and bottom of the fall was converted to distance units by multiplying the time by the velocity of the spheres. The two results were averaged; if they differed by more than 1% of the total 12-in. length of fall, the run was discarded.

At higher Reynolds numbers ($N_{Re} > 0.25$) the two spheres falling one above the other were invariably observed to approach each other. Since the distance between the two spheres kept getting smaller during the run, the velocities of the spheres were neither equal nor constant. The experimental procedure in this case consisted only of measuring the velocity of each of the spheres over the 12-in. length of fall; two stop watches were used.

THE MOTION OF A SINGLE SPHERE AT $N_{Re} << 0.25$

The velocity of a single sphere falling along the axis of the cylindrical column in the high-viscosity fluid was measured at slightly different fluid temperatures (between 24° and 27°C.). The velocity measurements were taken for each of the three different density spheres and were found to be reproducible. Since the sphere-diameter–to–cylinder-diameter ratio for a ¼-in. sphere falling in a column having an inside diameter of 5 11/32 in. is less than 0.1, Stokes's Law (*10*) combined with the Faxen (*2*) correction factor, which accounts for the effect of the cylindrical boundary, can be used to predict the experimentally measured velocities:

$$U_{predicted} = \frac{(\rho_s - \rho) g d^2}{18 \mu K_I} \qquad (1)$$

$$K_I = \frac{}{1 - 2.105 \frac{d}{D}} \qquad (2)$$

The predicted values of the velocity at each temperature were calculated by the use of Equation (1); since the Reynolds numbers were all much less than 0.25, the effect of inertial forces was neglected. The average error between the calculated and measured velocities was less than 1%; these results show that inertial and end effects were indeed negligible. The single-sphere velocity measurements were plotted as a function of the temperature of the fluid.

THE MOTION OF TWO SPHERES AT $N_{Re} << 0.25$

If two spheres are falling in an infinite viscous fluid, a mutual interaction effect between them is observed. Each sphere will have a tendency to move fluid down along with it, and therefore the velocity of each sphere will be increased owing to the motion of the other. For two spheres falling one above the other in an infinite fluid at very low Reynolds numbers the drag force on each sphere can be expressed by

$$W = \lambda 3 \pi \mu \, dU \qquad (3)$$

Equation (3) is Stokes's Law modified by a correction factor to account for the interaction effect.

Smoluchowski (*8*) in a theoretical study showed that

$$\lambda = 1 - \frac{3}{4}\frac{d}{l} + \left(\frac{3}{4}\frac{d}{l}\right)^3 \qquad (4)$$

Equation (4) is an approximate expression and can only be applied to two equal-sized spheres falling with a center to center distance greater than three diameters. The mutual interaction between two spheres of different size has recently been reported in a series of studies by Andersson (*1*) based on the creeping-motion equations.

A more rigorous solution of the problem of two spheres falling with equal and constant velocities parallel to their line of centers at negligible Reynolds numbers is that given by Stimson and Jeffrey (*9*). Mathematically their expression for λ is

$$\lambda = \frac{4}{3} \sin h\alpha \sum_{n=1}^{n=\infty} \frac{n(n+1)}{(2n-1)(2n+3)} \cdot \left[\frac{1 - 4 \sin h^2 (n + \tfrac{1}{2})\alpha - (2n+1)^2 \sin h^2 \alpha}{2 \sin h (2n+1)\alpha + 2n + 1 \sin h^2 \alpha} \right] \quad (5)$$

where $\cosh \alpha = l/2a = l/d$. A numerical evaluation of this function is given below for different values of l/d

α	l/d	λ
0.5	1.128	0.663
1.0	1.543	0.702
1.5	2.352	0.768
2.0	3.762	0.836
2.5	6.132	0.892
3.0	10.068	0.931
∞	∞	1.00

Faxen (2) calculated the value of λ for the limiting case of the two spheres touching (that is, $\alpha = 0$, $l/d = 1$) and obtained $\lambda = 0.645$. This predicts that a doublet consisting of two equal spheres touching one above the other would fall 55% faster in an infinite fluid than if one sphere were falling alone.

The relationships of Ladenburg (5) and Faxen (2) which were developed for the effect of a cylindrical boundary on the motion of a single sphere can be directly applied to the study of two spheres. If two spheres A and B are falling one above the other along the axis of a cylinder, the drag on sphere A will be the result of adding four velocity fields. These include the initial undisturbed velocity field U_{A_1} and the first reflection of this field from the cylinder wall U_{A_2}; these would be the only contributions to the velocity field if sphere A were falling alone. In addition sphere B will reflect the motion of sphere A in two ways, by a direct reflection of its own velocity field U_{B_1} (interaction effect) and by the reflection of this velocity field at the cylinder wall U_{B_2}. U_{A_1} and U_{A_2} are given by Stokes's Law combined with the Faxen correction factor. Happel (4) has shown that U_{B_2} can be represented by the following series expansion is sphere B is close to sphere A and $a/R = d/D$ is less than 0.1:

$$U_{B_2} = \frac{Ua}{R}\left(2.105 - 1.139 \frac{a^3}{R^3} + 0.595 \frac{a^5}{R^4} + \ldots \right) \quad (6)$$

To convert the observed velocity for two spheres falling in a cylinder to that which would be obtained if they fell in an infinite medium, it is necessary to multiply the observed velocity by a correction factor obtained by adding unity to U_{A_2} and U_{B_2}. This factor K_{II} is found to be

$$K_{II} = 1 + 4.21 \frac{a}{R} - 1.139 \frac{a^3}{R^3} + 0.595 \frac{a^5}{R^5} + \ldots \quad (7)$$

If l/R is very small, Equation (7) reduces to

$$K_{II} = 1 + 4.21 \frac{a}{R} \quad (8)$$

and the coefficient of $a/R = d/D$ is just twice the value of the coefficient for a single sphere. If l/R is large, Equation (6) will not converge, and a numerical evaluation of U_{B_2} is required.

Equation (7) has been used to evaluate the boundary correction factor for values of $l/R < 0.3$. For the special case of $l/R = 1$, K_{II} has been evaluated numerically and was found equal to 3.45 a/R. The values of K_{II} were calculated for the three different density spheres which were used and plotted for convenience as a function of l.

If l/d is small (spheres very close together), it would be desirable to consider more than one reflection between them to completely evaluate their interaction. When the spheres are touching, for example, the constant in Equation (8) will be smaller than 4.21. This would tend to raise the values of λ determined experimentally for small values of l/d. If the drag force exerted on each sphere when two spheres fall in an infinite viscous fluid is compared with that exerted on a single sphere, it is clear that

$$\lambda = \frac{U_{I\infty}}{U_{II\infty}} \quad (9)$$

To correct the experimental velocities for the effect of the cylindrical boundary, the factors K_I and K_{II} are used. If U_{II} is the experimentally measured velocity of the two spheres at a known fluid temperature and U_I is the velocity of a single sphere at the same temperature, then

$$\lambda = \frac{K_I U_I}{K_{II} U_{II}} \quad (10)$$

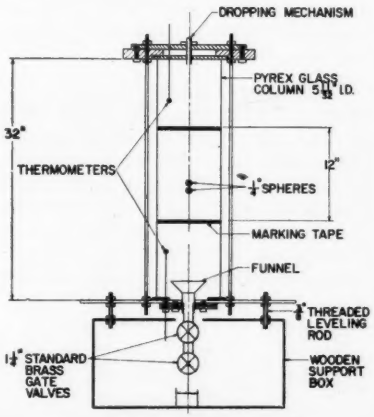

Fig. 1. Experimental apparatus.

The values of λ were calculated from Equation (10) by measuring the velocity of the two spheres. For each different run with two spheres the corresponding velocity of a single sphere at the same average temperature was obtained from the plots mentioned above, K_I was calculated by means of Equation (2), and K_{II} was obtained from the plots of K_{II} vs. l.

The experimental values of λ obtained for the three different-density ¼-in. spheres were plotted against the l/d ratio in Figure 2; the theoretical curve predicted by Stimson and Jeffrey has also been included. Figure 2 shows an excellent agreement between the observed values and the theoretical curve in the entire l/d range which was investigated. The Reynolds number range for these runs was between 0.008 and 0.03; at these low Reynolds numbers no attraction between the two spheres was observed, and inertial effects were taken to be negligible.

THE EFFECT OF INERTIAL FORCES ON THE MOTION OF ONE AND TWO SPHERES

In order to study some of the important effects on the motion of one and two spheres which are caused by inertial forces the less viscous fluid was used as the fluid medium. This resulted in the spheres falling at greater velocities and higher Reynolds numbers.

The experimentally measured velocities of the ¼-in. spheres were again compared to the predicted values given by Equation (1). The deviations were appreciably larger, varying from about 2% at a Reynolds number of 0.25 to 3% at a Reynolds number of 0.5. To obtain even higher Reynolds numbers spheres ½ in. in diameter were dropped, and velocity readings were taken. The corresponding velocities calculated from Equation (1) deviated by as much as 17% at a Reynolds number of 3.5. Fayon's (3) experiments have shown that the boundary correction factor K_I remains relatively constant up to Reynolds numbers of 20; therefore in this range Stokes's Law no longer applies for a single sphere in an infinite medium.

Oseen (6) included some of the quadratic inertial terms in his solution of the Navier-Stokes equations for a single sphere falling in an infinite fluid and derived theoretically that the drag force can be approximated at higher

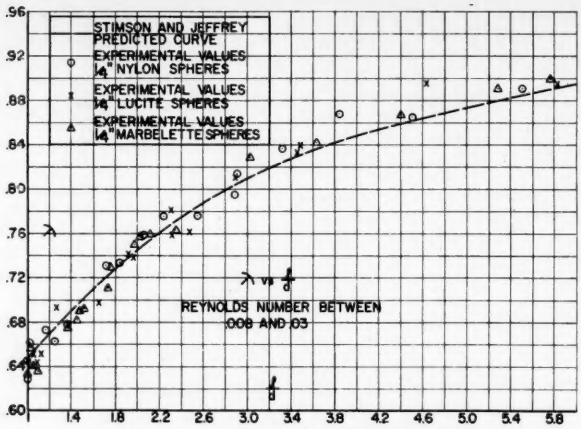

Fig. 2. Interaction effect between two spheres.

Reynolds numbers by a modification of Stokes's Law:

$$W = 3\pi\mu\, dU(1 + 3/16\, N_{Re}) \qquad (11)$$

Oseen also extended Smoluchowski's solution [Equation (4)] for the motion of two spheres so that it might be applied to higher Reynolds numbers. Oseen's equations for one sphere falling above another can be approximated when the spheres are not too far apart by

$$W_1 = 3\pi\mu\, dU \left(1 - 3/4\,\frac{d}{l} + 3/8\, N_{Re} \right) \qquad (12)$$

$$W_2 = 3\pi\mu\, dU \left(1 - 3/4\,\frac{d}{l} \right) \qquad (13)$$

These equations point out that the bottom sphere is slowed more than a single sphere owing to inertial forces [compare Equation (12) with Equation (11)] and that the slowing is a function of Reynolds number only. The top sphere, however, is not at all affected and will fall according to the Smoluchowski theory. Since the drag on two equal spheres must be equal, the velocity of the top sphere will be greater than that of the bottom sphere, and they will tend to move toward each other.

If the two spheres fall side by side with the same velocity, Oseen's equations show that the inertial force on the right sphere is

$$F = 3\pi\mu\, dU(3/32\, N_{Re}) \qquad (14)$$

and acts to the right; the corresponding force on the left sphere is equal in magnitude but opposite in direction, and the two spheres will tend to move away from each other, a phenomenon exactly opposite to that predicted for two spheres following each other.

If Oseen's equation for a single sphere is rewritten in terms of the drag coefficient and is also modified to take into account the effect of a finite cylindrical boundary around the fluid, Equation (11) becomes

$$C_D = \frac{24}{Re} K_I(1 + 3/16\, Re) \qquad (15)$$

The measured velocity data for a single sphere did not correlate with Equation (15), and in order to obtain a correlation the constant 3/16 was replaced by an empirical constant so that Equation (15) read

$$C_D = \frac{24}{N_{Re}} K_I(1 + C_I\, N_{Re}) \qquad (15a)$$

C_I was calculated from Equation (15a) in the Reynolds number range of 0.25 to 3.5 by measuring the drag coefficient and the Reynolds number; the correction factor was assumed to remain constant. At Reynolds numbers greater than 0.5 C_I was found approximately equal to 0.05; the results at the lower Reynolds numbers were not too significant, since the deviations from the Stokes-Faxen linear approximation were less than 3%.

Preliminary experiments with two spheres falling one above the other showed, as predicted by Equations (12) and (13), that they invariably will come together during the length of fall. However, it was possible to establish the effect of inertia by observing their relative velocities, thus making a wall correction factor unnecessary. From Oseen's theory the following approximation may be developed (7):

$$U_2 - U_1 \cong 3/8\,\Psi\, N_{Re} \qquad (16)$$

where

$$\Psi = \frac{(\rho_s - \rho)\, g\, d^3}{18\mu} \qquad (17)$$

and $U_2 - U_1$ is the difference in velocity between the two spheres.

The constant, 3/8, in Equation (16) was again replaced by an empirical constant so that a correlation of the experimental data could be obtained; Equation (16) was rewritten as

$$U_2 - U_1 = C_{II}\Psi\, N_{Re} \qquad (16a)$$

The average values of U_1 and U_2 were measured for the three different density 1/4-in. spheres, independent of the distance l between them, during the 12-in. length of fall. For forty-two different runs in a Reynolds number range of 0.27 to 0.73 the average value of C_{II} was 0.11. Equations (12) and (13) can thus be rewritten as

$$W_1 = 3\pi\mu\, dU \cdot \left[1 - 3/4\,\frac{d}{l} + 0.11\, N_{Re} \right] \qquad (12a)$$

$$W_2 = 3\pi\mu\, dU \left[1 - 3/4\,\frac{d}{l} \right] \qquad (13a)$$

The bracketed terms correct Stokes's Law for the interaction effect between the spheres. The interaction effect, unlike the wall correction factor, is a function of the Reynolds number.

It is interesting to point out that the average value of C_{II} (0.11) over the Reynolds number range of 0.27 to 0.73 is a little more than twice the average value of C_I (0.05) obtained over the Reynolds number range of 0.5 to 3.5. This relative effect was predicted by Oseen, his constants being 3/8 and 3/16 respectively. Obviously the representation of the effect of Reynolds number in Equations (12) and (12a) will not be applicable at large distances between the spheres.

A QUALITATIVE ANALYSIS OF THE MOTION OF TWO AND THREE SPHERES AT HIGHER REYNOLDS NUMBERS

Before prediction of the complex interactions between assemblages of particles is tried, it is interesting to observe what happens with two or three particles settling at higher Reynolds numbers.

Figure 3 shows the effect of the inertial forces on the motion of two spheres falling one above the other along the axis of a cylindrical container in the Reynolds number range of 0.3 to 0.7. At time $t = 0$, the center to center distance between the two spheres is l_0. However the inertial forces will slow down sphere B [Equation (12)] without affecting the velocity of sphere A, so that l will become smaller until at some time $t = t_2$ the spheres will touch. Since the drag force exerted on sphere A is less than that exerted on sphere B, sphere A will tend to move over sphere B sidewise until the attractive force

between the two spheres is just balanced by the repelling force given by Equation (14) ($t = t_0$ to $t = t_1$). The inertial forces will then cause the spheres to move away from the axis. This is shown at $t = t_2$ and $t = t_3$; the repelling force is about half as great as the attractive force when the spheres are falling one above the other.

It should be made clear that all the velocity measurements made to determine C_{II} were taken between $t = t_0$ and $t = t_1$ in Figure 3.

The motion of three spheres, as might be expected, is even more complex. For example (Figure 4) if spheres C, B, and A are falling in the same vertical plane so that the distance between the spheres A and B is less than the distance between spheres B and C, the two spheres A and B consitute a doublet and consequently move at a greater velocity than sphere C. At some time $t = t_1$, spheres A and B will have caught up to sphere C and so the distance between all three spheres is the same and a triplet is formed. However the triplet is not in stable equilibrium because the center sphere is influenced by interaction effects from both spheres A and C. These interaction effects cause sphere B to move closer to sphere C which produces a doublet between spheres B and C. At time $t = t_3$, the distance between sphere A and sphere B is greater than the distance between sphere B and sphere C because of the greater velocity of the doublet. These phenomena will occur even if inertial effects are negligible; the inertial forces act only to reduce the distance between the spheres in the doublet by slowing down the lower sphere during the length of fall.

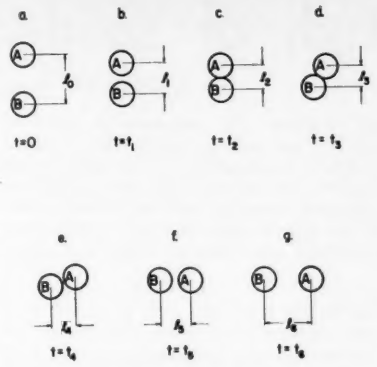

Fig. 3. Effect of inertial forces on the motion of two spheres.

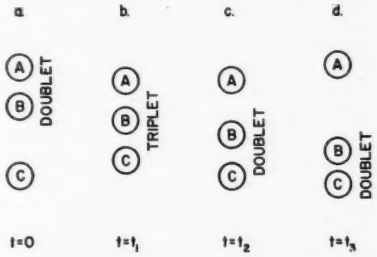

Fig. 4. The motion of three spheres.

CONCLUSIONS

The experimental values of λ obtained for the ¼-in. spheres agreed very closely with the values obtained by Stimson and Jeffrey from theoretical considerations over the l/d range of one to six diameters; no noticeable attraction between the spheres was observed. Since the Reynolds numbers were between 0.008 and 0.03, this would imply that inertial effects were negligible.

A definite attraction between two spheres falling one above the other was observed in the Reynolds number range of 0.25 to 0.7; the inertial forces acted to slow down the lower sphere without affecting the upper one.

Thus it is possible that spheres suspended in random orientation may not maintain their positions relative to each other. Perhaps the formation of doublets, and their corresponding higher velocities of fall, has been one of the causes for the wide discrepancies in the presently available fluidization data. Additional data will be required before the fundamental findings in this paper can be applied exactly to practical problems in fluidized or sedimenting systems of particles.

ACKNOWLEDGMENT

This research was supported by a grant from the Petroleum Research Fund administered by the American Chemical Society. Grateful acknowledgment is hereby made to the donors of said fund.

NOTATION

(C.G.S. Gravitational Units employed unless otherwise indicated)

a = radius of sphere, cm. or in.
C_D = drag coefficient, dimensionless
C_I = empirical constant (measures inertial effects for one sphere)
C_{II} = empirical constant (measures inertial effects for two spheres)
d = diameter of sphere, cm. or in.
D = diameter of cylindrical column, cm. or in.
g = acceleration of gravity
K_I = Faxen correction factor for a cylindrical boundary on one sphere
K_{II} = Happel correction factor for a cylindrical boundary on two spheres
l = center to center distance between spheres, cm. or in.
N_{Re} = Reynolds number = $dU\rho/\mu$, dimensionless
R = radius of cylindrical column, cm. or in.
U = terminal velocity
U_{A_1} = initial undisturbed velocity field
U_{A_2} = first reflection of initial undisturbed velocity field
U_{B_1} = first reflection of velocity field at sphere A
U_{B_2} = first reflection of velocity field at cylinder wall
$U_{I\infty}$ = terminal velocity of a single sphere in an infinite fluid
$U_{II\infty}$ = terminal velocity of two spheres in an infinite fluid
U_I = terminal velocity of a single sphere in a bounded fluid
U_{II} = terminal velocity of two spheres in a bounded fluid
W = drag force; W_1 = drag force on bottom sphere, W_2 = drag force on top sphere

Greek Letters

ρ = density of fluid
ρ_S = density of sphere
λ = correction factor for interaction effects between two spheres
Ψ = $(\rho_S - \rho)g\,d^2/18\mu$, cm./sec.
μ = viscosity of fluid
$\cosh \alpha$ = l/d, dimensionless

LITERATURE CITED

1. Andersson, O., *Svensk Papperstidn.*, **59**, 540 (1956); **60**, 153 (1957).
2. Faxen, Hilding, Dissertation, Upsala Univ., Sweden (1921); *Ann. Physik*, **68**, 89 (1922).
3. Fayon, A. M., Ph.D. thesis, New York Univ., New York (1959).
4. Happel, John, *Document 5441*, American Documentation Institute, Library of Congress, Washington, D. C. (1957).
5. Ladenburg, Rudolph, *Ann. Physik*, **22**, 287; **23**, 447 (1907).
6. Oseen, C. W., "Hydrodynamik," Akademische Verlagsgesellschaft, Leipzig, Germany (1927).
7. Pfeffer, Robert, M.S. thesis, New York Univ., New York (1958).
8. Smoluchowski, M. S., *Bull. Acad. Sci. Cracovia*, **1A**, 28 (1911); *5th Intern. Congr. Mathematicians*, **2**, 192 (1912).
9. Stimson, Margaret, and G. B. Jeffrey, *Proc. Roy. Soc. (London)*, **A111** (1926).
10. Stokes, G. G., *Trans. Cambridge Phil. Soc.*, **8** (1845); **9** (1851).

Manuscript received January 21, 1959; revision received April 17, 1959; paper accepted April 22, 1959. Paper presented at A.I.Ch.E. Atlantic City meeting.

Photographic Study of Solid-Gas Fluidization

LEOPOLDO MASSIMILLA and J. W. WESTWATER

University of Illinois, Urbana, Illinois

Motion pictures at 2,000 frames/sec. were used to measure the movements of individual solid particles and gas bubbles in a fluidized bed. Air was used to fluidize 0.028-in. glass spheres and 200-mesh alumina in a 3.75-in. glass column. Aggregates were very common, and each moved as a unit. Particles and aggregates near the wall showed pronounced alternations of fast and slow movements both upward and downward. Individual particles exhibited spin. Baffles increased the bed density and decreased the particle velocities. Small bubbles rose rapidly with little change in shape. Large cavities were slow and tended to collapse and reform elsewhere.

The advantages of a fluidized bed as compared with a fixed bed are the low pressure drop, ease of transportation of the solid from one piece of equipment to another, and good temperature control because of high internal conductivity of the solid-gas system and the high heat transfer rate at the walls. The main disadvantage is poor homogeneity of the fluid as a result of bypassing.

The homogeneity and heat fluxes are of particular importance in catalytic beds, because these factors affect the extent of the conversion and the selectivity of the reaction when competing reactions exist. Many sources report that bubbles, slugs, and channels in fluidized beds are serious handicaps, but they may sometimes be outweighed by the good thermal properties of a fluidized system, especially if a uniform temperature is required or if large quantities of heat must be added or removed.

All these properties depend on the physical distribution and velocity of the solid particles. Baffles or other mechanical devices can be used to destroy bubbles or slugs, but they limit the movement of the solid particles (*11, 12*). An important problem is how much one can afford to reduce the circulation by baffles without nullifying the desired uniformity of temperature in the bed.

Ideally one wishes to know the entire history of movements of the solids and the fluid in a bed. High-speed photography can be used to study the region near the walls. A start was made by Toomey and Johnstone (*23*), who used a metal column fitted with a window. Recently Todd *et al.* (*22*) applied the technique to a two-dimensional column, thin as compared with its width. The present research stressed the photographic technique. One object was to record the motion of individual particles with a high-speed motion picture camera. This required a size magnification at least one order of magnitude larger than that used by prior workers. A second object was to study bubbling. Both still and motion pictures were desired for this. Baffled and free beds could be studied with equal facility.

Leopold Massimilla is now at the University of Naples, Naples, Italy.

Fig. 1. Free-bed fluidization of 0.028-in. beads; run 5. Height of view = 5.5 in.

EXPERIMENTAL

Fluidization Equipment

The column was a 3.75-in.–I.D. glass cylinder, with the lower end fitted to a conic inlet section ending in a distributor consisting of a set of brass screens, the finest being 200 mesh. To minimize bubble generation at the wall, the diameter of the distributor was made ⅝ in. smaller than the column.

Two solids were fluidized in batches: glass beads of 0.028-in. diameter and fluid cracking catalyst of 120 to 200 mesh. Both solids were spheroidal. In each batch about 5% of the particles were colored to serve as tracers. A thin coat of black spray enamel was put on the glass beads, and a bismuth–manganese oxide thin coating on the alumina.

Baffles, when used, were horizontal screens of metal hardware cloth, separated 1 cm. apart by three spacers of copper tubing. Baffles *A*, *B*, and *C* in this paper refer to screens of ⅜-, ¼-, or ⅛-in. hardware cloth.

The fluid used was air from the laboratory line, which passed through a filter, a pressure regulator, and a flow meter. During run 8 part of the air (about 10%) was injected into the bed through a ¼-in. copper tube. The tube passed from the top of the column, down through the bed, made a 180-deg. turn, and emptied upward through a small piece of 200-mesh screen.

During the entire duration of runs 9 and 10 the column was inclined 10 deg. from the vertical. Although this probably modified the flow pattern somewhat, a desirable result was that some gas bubbles were near the wall and their motion could be followed for much greater distances than would have been possible otherwise.

Photographic Technique

Motion pictures were taken with 16-mm. negative film. A selection (*28*) of the results is available on request. For shots encompassing a field of view 3.5 in. high, a 35-mm. focal length lens set at *f*/4 was used, and the lens-to-object distance was about 21 in. Illumination was provided by four spotlights, each 750 w., off to one side at a 45-deg. angle. Two lights were above the camera elevation, and two were below; all were focused on the same spot. Run 10 with alumina powder was photographed in this manner at 2,000 frames/sec.

The other twelve runs listed in Tables 1 and 2 were photographed as close-ups. For these scenes a 1-in. extension tube was connected to the lens, and the lens-to-object distance was adjusted to about 3 in. The field of view was about 0.3 in. high, which is much smaller than that used by prior workers. Enlargements of single frames of movies of the glass particles taken at about 2,000 frames/sec. with an aperture of *f*/2 have been published (*27*). Figure 7 shows alumina at about the same framing speed and was taken at *f*/4.

Still pictures were taken with a 4- by 5-in. negative film. For shots having a vertical field of about 14 in. a 135-mm. focal-length

Fig. 2. Baffled-bed fluidization of 0.028-in. beads; run 3. Height of view = 5.5 in.

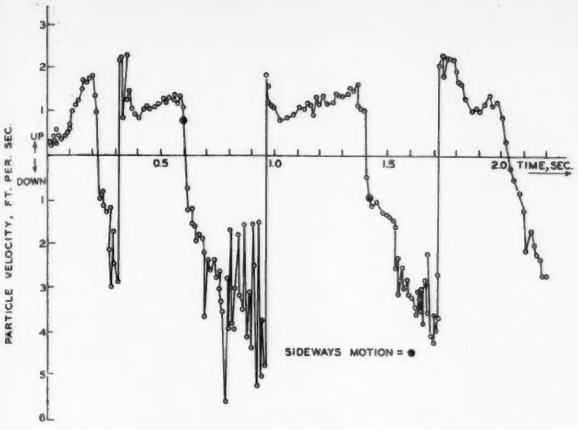

Fig. 3. Velocity of solid particles at the wall. Run 5, 0.028-in. beads, no baffles, superficial air velocity = 2.2 ft./sec.

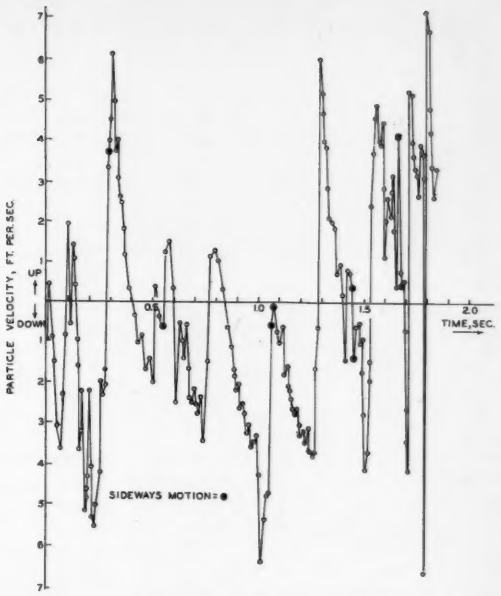

Fig. 4. Effect of gas velocity. Run 4, same as run 5 except that new air velocity = 4.2 ft./sec.

lens located about 21 in. from the column was used. The aperture was $f/4.7$ for the glass beads and $f/5.6$ for alumina, and for each an exposure of 0.001 sec. was used. The illumination was similar to the above except that the spots were spread out to cover 14 in. Figure 8 was taken this way. The column was inclined 10 deg. during the still photograph for Figure 8. The column was vertical during the motion pictures of these same runs (runs 12 and 13).

Close-up still shots were taken from a distance of about 11 in. The resulting field was 5.5 in. high and was illuminated by a flash-tube photolight. Figures 1 and 2 were obtained with an exposure of 1 μ sec. at $f/13$.

The motion pictures were analyzed frame by frame at the screen of a film-editing machine. The screen was fitted with a grid to give readings of the instantaneous space coordinates of individual particles of interest. The instantaneous framing speed of the movie camera was calculated from timing pips on the edge of the film. Thus the displacement of particles from frame to frame was converted to particle velocity in the plane of focus.

The framing rates listed in Tables 1 and 2 are the maximum values which occur at the end of the reels. The value stated in the caption for Figure 7 is the instantaneous speed for the frames selected.

SOLIDS FLOW PATTERN

The particles recorded by the photographic technique are those near the wall. At present no one as devised a successful method for photographing the interior of a fluidized bed. Nevertheless the activity at the wall is worthy of investigation. The velocity of the visible particles frequently changes abruptly in direction and intensity. These sudden changes cause difficulty in measuring and interpreting the data. The observed net flow of solid near the wall is downward, but in the unseen core of the bed the flow must be upward and is stated to be faster than it is near the wall (2). The activity of a solid particle depends on its elevation in the bed, with the velocity increasing from the bottom to the top (23).

Table 1 lists the characteristics of the systems for which the motions of individual particles were studied photographically, frame by frame. The gross particle motion is summarized in Table 1 as a root-mean-square velocity. The instantaneous velocity at various times is shown in Figures 3 to 6 for four runs. Similar graphs were constructed for the other runs. As a rule the majority of particles visible in a single frame moved in the same direction with the same velocity. Careful measurements were made for a single colored particle until it disappeared. Then a new tagged particle was selected and traced. Thus Figures 3 to 6 show symbols which indicate the successive history of one particle after another.

The most striking features of the graphs are the alternation of fast and slow action and of upward and downward motion. Periodic motion in fluidized beds has been noted previously (23).

Glass Particles

For free fluidization the effect of increasing gas velocity is shown in Figures 3 and 4. The amount of solids was not identical in the two runs; however the measurements were taken at the same distance from the top of the bed. An increase in the gas velocity caused an increase in the average velocity of the particles, an increase in the magnitude of the velocity peaks, and an increase in the occurrence of peaks. The peaks show that the particle velocity near the wall is frequently much greater than the calculated superficial gas velocity upward. Most of the peaks are downward velocities, a few are upward, none are sideways. Sideways motion does occur, but it is relatively mild.

The spin of individual particles was observed on occasion. An illustration (27) shows an elliptical particle spinning at 105 rev./sec. The spherical particles spin also, but this is more difficult to see. Spin may be important for heat and mass transport; however it has not been taken into account by any workers.

Baffles in a bed greatly reduce the bed expansion and therefore increase the particle count in a photographed area. This is obvious from a comparison of photographs taken with a bed both with and without baffles. The great difference in the homogeneity between a free bed and a baffled bed is illustrated in Figures 1 and 2. Baffles reduce the spin of the particles and also their linear velocity.

Table 1 and a comparison of Figures 3 and 5 show the enormous effect of baffles on the particle motion. The average linear velocity in a baffled bed is reduced by a factor of about 5 to 1 or 10 to 1 as compared with a free bed. The frequency of peaks is greatly reduced and shows but little change as the gas flow rate is changed. A small difference exists between the choice of baffles *A* and *B*, as seen by a comparison of runs 2 and 7 or 1 and 6. The smaller mesh resulted in the smaller average velocity. Increasing the gas velocity caused an increase in the particle average velocity as shown by a comparison of runs 1 and 2 or 6 and 7. If the gas velocity is sufficiently low, a

Table 1. Summary of Data for Study of Pattern of Flow of Solids

Run	Solids	Amount of solids, lb.	Settled bed hgt. L_o, ft.	Fluidized bed hgt., ft.	Superficial gas velocity lb./(hr.)(sq. ft.)	Superficial gas velocity ft./sec.	Baffle design	Location*, in.	Camera speed, frames/sec.	R.M.S. particle velocity, ft./sec.	Max. velocity of particles, ft./sec. Up	Max. velocity of particles, ft./sec. Down
1	Glass	5.40	0.80	0.98	635	2.2	*B*	1.97	960	0.27	0.72	0.70
2	Glass	5.91	0.88	0.98	450	1.55	*B*	1.97	1,200	0.17	0.96	0.99
3	Glass	3.66	0.54	0.98	1,225	4.2	*B*	1.97	1,920	0.22	0.81	0.72
4	Glass	3.66	0.51	Varied	1,225	4.2	None	1.97	1,820	2.44	7.15	6.39
5	Glass	5.40	0.75	Varied	635	2.2	None	1.97	1,800	1.96	2.23	5.70
6	Glass	5.40	0.80	0.98	635	2.2	*A*	1.97	1,920	0.43	0.97	1.55
7	Glass	5.91	0.88	0.98	450	1.55	*A*	1.97	1,080	0.22	0.97	0.99
11	Alumina	5.04	1.08	Varied	82	0.29	None	1.58	2,040	0.38	0.22	1.24
12	Alumina	5.04	1.08	Varied	114	0.39	None	1.58	1,920	0.75	0.75	2.30
13	Alumina	5.04	1.08	—	114	0.39	*C*	1.58	2,160	0.30	0.49	1.01

* Distance between the photographed field and the top of the fluidized bed.

portion of a fluidized bed can become stagnant temporarily. This is particularly likely in a baffled bed. During run 2 the photographed section of the bed showed no motion for about 30% of the time. Runs 1, 5, and 6 showed that baffles *A* produced more peak velocities upward than were observed with baffles *B* or with a free bed.

Alumina Particles

Table 1 shows data for three runs with alumina. One set is shown in Figure 6. Velocity peaks and flow reversals are similar to the effects noted for the larger glass particles. The effect of increasing gas flow is similar.

Although the values of G/G_o were higher for the alumina, the velocities of the alumina particles were less than those for the glass beads. The probable reason is the greater severity of slugging with the glass beads. Thus alumina particles moved at roughly one-fifth the velocity of the glass particles, for free-fluidized beds of equal bed expansions. The superficial gas velocity for the runs with alumina was 0.29 and 0.39 ft./sec. compared with 2.2 and 4.2 ft./sec. for the glass beads.

One difference between the alumina and the glass particles was that baffles reduced the average velocity of the alumina particles by about 3 to 1, a much smaller change than was noted with the glass beads.

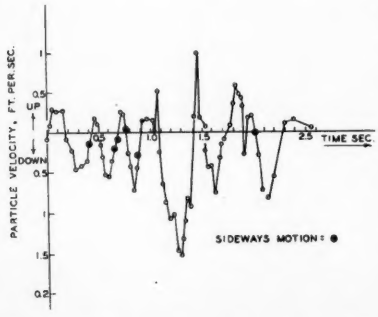

Fig. 5. Effect of baffles. Run 6, same as run 5 except that baffles *A* were installed.

Remarks on Temperature Profile

The solids flow pattern explain certain heat transfer observations. A prior study (*13*) made with a bed having the same diameter, height, baffle design, solids, gas, and gas velocities shows temperature measurements along the geometric axis. Air entered at about 90°C.; the walls were cooled with water at about 30°C. For free fluidization a near-constant temperature profile resulted for a gas flow which was 1.2 times the flow for incipient fluidization. For a baffled bed the profile was not this flat until the gas velocity was increased beyond the incipient value by over 100%. Thus although baffles prevent channeling and slugging, they cause some impoverishment in the heat exchange between one region in the bed and another. The reason of course is that baffles decrease the average velocity of the particles.

Particle Diffusivity

Runs 6 and 7 were duplicates of prior runs (*12*) carried out to determine diffusivities of the solid particles. In the early work trace particles were dropped on the top of a fluidized bed, and samples were removed at a point 4.7 in. below. Concentration vs. time data were used to calculate diffusivities for the particles. These prior tests were designed to test the equation of Trawinsky (*25*) which extended the kinetic molecular theory of Shafer:

$$D = (K/1 - \epsilon_o)\, G\, d\, (\Delta L/L_o) \quad (1)$$

The equation could not be checked for a free-fluidized bed, presumably because of nonuniformities in the gas-solid system, but the results were promising for baffled beds. A linear relationship was obtained for the prior data:

$$D = 0.050\ (G)\ (\Delta L/L_o) \quad (2)$$

The present photographs permit an independent check of the equation. A convenient comparison can be made in terms of the average velocity of the particles. For run 7 the relative expansion of the bed was 0.11, and the particle diffusivity was 2.5 sq. ft./hr. Einstein's expression $V = 2D/\Delta X$ and the expression $\Delta X = (\pi\sqrt{2}\, n\, d^2)^{-1}$ combine to give a corresponding velocity of about 3 ft./sec. for the particles. The motion picture evidence showed that the particle root-mean-square velocity at the walls was 0.22 ft./sec. A similar discrepancy exists for run 6; the diffusivity value from Equation (2) coupled with the bed expansion of 0.22 leads to a predicted velocity of about 6 ft./sec., whereas the photographs show an actual R.M.S. velocity of 0.43 ft./sec. The discrepancy of about 15 to 1 between the predicted velocities and the observed velocities can be explained. The equations assume that the kinetic molecular theory applies to individual solid particles and that each particle moves as an individual. The motion pictures show that aggregates of particles move as a unit, even in baffled beds. The particles in an aggregate have approximately the same velocity in the same direction. Perhaps one should use the average diameter of an aggregate and the number of aggregates per unit volume in the above equations instead of the particle diameter and concentration. At present these

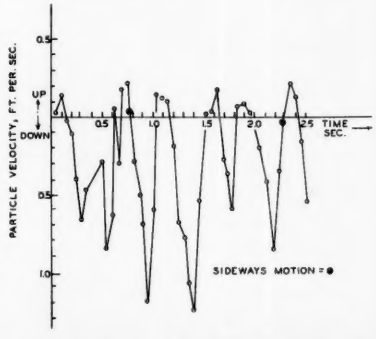

Fig. 6. Velocity of 200-mesh alumina powder at the wall. Run 11, no baffles, superficial air velocity = 0.29 ft./sec.

suggested measurements are not available.

It is significant that the diffusivity of the particles in the baffled bed is of rather small magnitude. This means that a well-baffled bed is more like a fixed bed than a free-fluidized bed, at least from the standpoint of the circulation of the solids.

GAS FLOW PATTERN

Previous investigators have been greatly concerned with the gas flow pattern in fluidized beds. The performance of fluidized reactors and the variables affecting the gas flow pattern have been referred to by numerous workers (*4 to 10, 17, 18, 24, 25, 29, 30*). The process of bubbling has received special attention. Baumgarten and Pigford (*3*) consider it from the standpoints of the extent of bubbling and the conditions under which it occurs. Rice and Wilhelm (*19*) consider the dynamics of the boundary between the dense suspension and the gas bypassing as bubbles. Other problems involve the amount of bypassing gas and the stability of the above-named boundary. The phase boundary may sometimes seem to be lacking or nonexistent in short columns; however it has been shown that a uniform distribution of solid particles is unstable, and if a column is of sufficient height, growing bubbles of gas must always appear (*1*).

It is important whether bubbles do or do not occur because bubbles affect the gas-solid mixing. Two counteracting effects take place when the gas velocity is increased. One has been pointed out by Toomey and Johnstone (*24*) and Trawinski (*25*), who show that the number of bubbles increases. Because bubbles represent bypassing gas, this effect should cause a reduction in the rates of heat and mass transfer. The second effect of velocity increase is an increase in the agitation of the particles in the phase boundaries. Of course this tends to cause improvement in the heat and mass transfer. Which effect predominates depends on the operating conditions, but the second effect seems to be more significant in most experiments. Shen and Johnstone (*20*) found that increases in the gas velocity caused increases in the heat and mass transfer between the solids and the gas. Massimilla and Johnstone (*14*) obtained similar results. Shuster and Kisliak (*21*) found that the bed uniformity increased up to a certain gas velocity. On the other hand Mathis and Watson (*16*) found that for the dealkylation of cumene the conversion depended on the flow rate in a complex fashion, with increases and decreases both being possible as the velocity increases.

Bubbling is analogous to the rise of gas bubbles in a liquid. Toomey and Johnstone (*24*) have suggested that a simple model for a fluidized bed is obtained by imagining bubbles of pure gas to rise through a second dense phase, a uniform suspension. Trawinski (*25*) stated that bubbles form at the bottom of a bed and begin to rise only when they are sufficiently large to overcome downward forces. The use of Stokes's law was suggested because the Reynolds numbers were small.

Runs 8, 9, and 10 were conducted to study bubbling in the absence of baffles. The conditions are summarized in Table 2. The remainder of this paper consists of observations based on the motion pictures for those runs.

For run 9 two patterns of gas flow occurred at 0.6 in. from the bottom. Type 1 consisted of cavities that passed through the field of view with no substantial modifications beyond certain deformations somewhat similar to those which occur also for gas bubbles in liquids. These bubbles can be classified according to size. The bigger bubbles of, say, 0.5-in. diameter moved rapidly upward (at about 1 ft./sec.). Very few solids were suspended in these bubbles. The boundary surfaces were not spherical but were well defined. Surrounding particles in the dense phase showed a pronounced motion downward as these bubbles rose. Very small cavities occur also. Figure 7 illustrates a bubble of about 0.06-in. diameter. Both the bubble and the surrounding phase moved upward with their absolute velocities being 0.70 and 0.57 ft./sec.

Table 2. Summary of Data for Study of Pattern of Gas Flow
Solids: 120- to 200-Mesh Alumina

Run	Settled bed height L_o, ft.	Superficial gas velocity, lb./(hr.)(sq. ft.) Main feed	Superficial gas velocity, lb./(hr.)(sq. ft.) Injected	Location*, in.	Height of field of view, in.	Camera speed, frames/sec.	Notes
8	0.89	28.5	3.1	2.4	0.33	1,920	Injection nozzle of ¼-in. tubing.
9	0.89	31.6	0	0.6	0.33	2,160	Column inclined 10 deg.
10	1.08	31.6	0	6.9	3.5	2,160	Inclined 10 deg.

* Distance between the photographed field and the bottom of the fluidized bed.

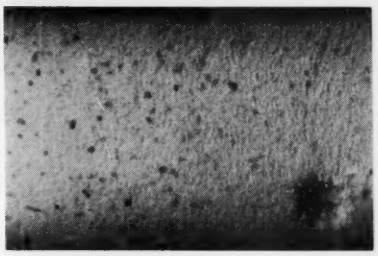

a

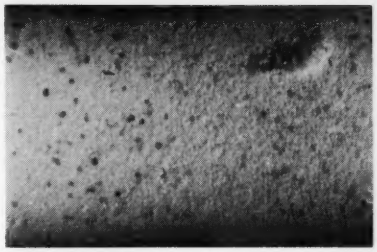

b

Fig. 7. Small bubble rising in alumina. Bubble width = about 0.06 in. Height of view = 0.33 in. Run 9 at 1,200 frames/sec., (*a*) frame 0, (*b*) frame 28.

The equations of Baron and Mugele (*1*) can be used to estimate the largest bubble which could be empty of solids for an appreciable time. The viscosity of the dense phase can be guessed as roughly 250 centipoise by comparing the solid to some described in the literature (*15*). This leads to a value of 0.94 in. for the maximum diameter of stable empty bubbles. The bubbles described above were smaller than this.

Some cavities originated, grew, decreased, and vanished in the small field of view (0.47 × 0.33 in.) during run 9; these are type 2, also called gas pockets herein. Typically the birth of such a cavity starts as a small hole which moves upward splitting the dense phase like a wedge. The cavity then expands, with a typical increase in width occurring at a rate of about 0.43 ft./sec. Eventually the growth ceases, and collapse sets in. Collapse frequently takes place by a break in the roof of the cavity which allows simultaneous leakage of solids inward and gas outward and a rise of solids from below. Occasionally the roof of a cavity breaks at one point only. Then the gas leaks out quickly, possibly to form a new cavity at a higher elevation.

Type 2 cavities should not be likened to bubbles in a liquid. Rather these cavities appear to be regions of high gas pressure. As the gas enters a zone having a minor resistance to gas flow, it blasts open a cavity. The cavity grows until a rupture occurs which provides a leak into a new zone or zones of minor resistance. Collapse occurs as the pressure falls. This gas motion is quite

Fig. 8. Collapsing gas pockets. 3.75-in. column, inclined 10 deg., run 13, 200-mesh alumina.

unlike that of gas bubbles in a liquid. The motion of type 2 cavities or pockets is slow compared with that of type 1 bubbles. The gas inside type 2 cavities does not possess enough energy to split the bed all the way up. Instead the gas inside is destined usually to leak into new zones to form new pockets. However two interesting possibilities exist and seem to occur; the gas can be partly captured by fast bubbles passing by or can simply leak in all directions and become distributed throughout the dense phase.

Photographs midway up the bed for run 10 showed gas flow patterns similar to those near the bottom. One exception was that formation of cavities by the coalescence of two or more bubbles was frequent in the midsection. Such cavities moved faster than cavities near the bottom. Figure 8 illustrates a typical large pocket near the midsection of the bed. A rain of particles down from the roof of the cavity occurs in the picture. The prominent cavities in these photographs are larger than the theoretical critical size of 0.94 in.

Run 8 included the injection of about 10% of the gas at a fixed point in the bed. Motion pictures showed discrete small bubbles at this point indicating that the gas injection was discontinuous. The same thing occurs of course when gas is injected into a liquid from an orifice. The motion of the surroundings, first outward, then down and in to pinch off the bubble, is quite evident when solids are present. The last part of this solids movement is much faster than the earlier part.

The gas flow patterns can be used to postulate why the difference between the conversion in a fluidized and in a fixed bed can first decrease and then increase as the flow rate is progressively increased. At low flow rates small bubbles and quasistable pockets predominate. These move rapidly through the bed with the gas inside excluded from good contact with the catalyst powder. At higher flow rates unstable pockets predominate. The rain of solids through these slow-moving pockets provides contact for catalysis, and the efficiency of the reactor is thus improved. Eventually a flow rate could be reached which would be so great that severe channeling would result and finally the bed would become inoperable. This extreme case was not studied in the present investigation. It was reached in tests on a catalytic reactor described by Mathis and Watson (*16*).

ACKNOWLEDGMENT

The authors express appreciation to the Italian Rotary Clubs for a fellowship for part of the work. Helpful advice in analyzing motion pictures was given by V. E. Putnam. The preparation of the manuscript was aided by Virgilio Causa.

NOTATION

d = average diameter of particles, ft.
D = diffusivity of solid particles, sq. ft./hr.
G = superficial gas flow rate, lb./(hr.)(sq. ft.)
G_o = superficial gas flow rate for incipient fluidization, lb./(hr.)(sq. ft.)
K = dimensional constant cu. ft./lb.
L_o = settled height of bed, ft.
ΔL = bed expansion, ft.
n = number of particles per unit volume, ft.$^{-3}$
V = particle velocity, ft./hr.
ΔX = particle displacement, ft.
ϵ_o = fractional voids in settled bed, dimensionless

LITERATURE CITED

1. Baron, Thomas, and R. A. Mugele, *A.I.Ch.E. Journal*, to be published.
2. Bart, Roger, D. Sc. thesis, Mass. Inst. Technol., Cambridge (1950).
3. Baumgarten, P. K., and R. L. Pigford, *A.I.Ch.E. Journal*, **6**, 1 (1960).
4. Brötz, Walter, *Chem.-Ing.-Tech.*, **24**, 60 (1952).
5. Gilliland, E. R., and E. A. Mason, *Ind. Eng. Chem.*, **41**, 1191 (1949).
6. *Ibid.*, **44**, 218 (1952).
7. ———, and R. C. Oliver, *ibid.*, **45**, 1177 (1953).
8. Leva, Max, Murray Weintraub, and Milton Grummer, *Chem. Eng. Progr.*, **45**, 563 (1949).
9. ———, and Milton Grummer, *ibid.*, **48**, 307 (1952).
10. Lewis, W. K., E. R. Gilliland, and W. C. Bauer, *Ind. Eng. Chem.*, **41**, 1104 (1949).
11. Massimilla, Leopoldo, and Sergio Bracale, *Ricerca Sci.*, **26**, 487 (1956).
12. *Ibid.*, **27**, 1509 (1957).
13. ———, and Antonio Cabella, *ibid*, **27**, 1853 (1957).
14. Massimilla, Leopoldo, and H. F. Johnstone, in preparation.
15. Matheson, G. L., W. A. Herbst, and P. H. Holt, *Ind. Eng. Chem.*, **41**, 1099 (1949)
16. Mathis, J. F., and E. C. Watson, *A.I.Ch.E. Journal*, **2**, 518 (1956).
17. Morse, R. D., *Ind. Eng. Chem.*, **42**, 117 (1949).
18. ———, and C. O. Ballou, *Chem. Eng. Progr.*, **47**, 199 (1951).
19. Rice, W. J., and R. H. Wilhelm, *A.I.Ch.E. Journal*, **4**, 4 (1958).
20. Shen, C. Y., and H. F. Johnstone, *ibid.*, **1**, 349 (1955).
21. Shuster, W. W., and Peter Kisliak, *Chem. Eng. Progr.*, **48**, 455 (1952).
22. Todd, D. B., R. H. Overcashier, and D. B. Olney, Motion Picture, "Fluidization Characteristics in a Two-Dimensional Fluid Bed," Shell Development Company, Emeryville, California (1957)
23. Toomey, R. D., and H. F. Johnstone, *Chem. Eng. Progr. Symposium Ser. No. 5*, **49**, 51 (1953). (1953).
24. ———, *Chem. Eng. Progr.*, **48**, 220 (1952).
25. Trawinski, H., *Chem.-Ing.-Tech.*, **25**, 229 (1953).
26. Wamsley, W. W., and L. N. Johanson, *Chem. Eng. Progr.*, **50**, 347 (1954).
27. Westwater, J. W., *ibid.*, **55**, No. 6, 49 (1959).
28. ———, and Leopoldo Massimilla, Motion Picture "Photographic Study of Solid-Gas Fluidization," Univ. Ill., Urbana (1958).
29. Wicke, E., and H. Trawinski, *Chem.-Ing.-Tech.*, **25**, 114 (1953).
30. Wilhelm, R. H., and Mooson Kwauk, *Chem. Eng. Progr.*, **44**, 201 (1948).

Manuscript received November 17, 1958; revision received August 3, 1959; paper accepted August 10, 1959. Paper presented at A.I.Ch.E. Cincinnati meeting.

Mass Transfer in Liquid-Lithium Systems

WILLIAM N. GILL, RICHARD P. VANEK, ROBERT V. JELINEK, and C. S. GROVE, JR.

Syracuse University, Syracuse, New York

The behavior of type-304 stainless steel in a forced-convection closed-loop lithium system was investigated over a wide range of temperatures and velocities. Fundamental information concerning the mechanism for mass transport has been obtained by examining solution and deposition effects along flat plates. The rate-determining process for solution is transport from the solid to the interface, whereas deposition rates are liquid-phase controlled.

Liquid-phase mass transfer coefficients were correlated with a maximum deviation of approximately 15% by the use of von Kàrmàn's analysis of the turbulent boundary layer along a flat plate, combined with the Chilton-Colburn empirical modification of the Schmidt group. In contrast no adequate model is available for the prediction of solution rate constants which must be determined experimentally. Mean values of the solution rate constants ranged from 0.154 to 0.750 x 10^{-5} cm./sec. at temperatures from 510° to 612°C. These values are on the order of 10^3 smaller than corresponding liquid-phase mass transfer coefficients.

Significant theoretical developments and quantitative data relating to liquid-metal heat transfer are available. Comparable contributions for mass transport phenomena, except for mercury systems, have not been forthcoming. Several studies have provided qualitative data about the corrosive effect of liquid alkali metals and their compounds on various materials of construction. Descriptive information is available concerning thermal-gradient mass transfer in lithium systems for both natural and forced convection (*1, 2, 3*). These studies suggested general solution as the principal over-all mechanism for mass transfer to the fluid phase. Other types of corrosion have been observed (*4*) which contribute to some extent to the total transport of material.

Epstein (5) investigated the mass transfer problem in dynamic-sodium and mercury-loop systems by employing quantitative techniques. Two mechanisms for corrosion were considered. The rate-determining step for solution-limited corrosion is the transfer of material from the metal surface to the adjacent liquid boundary layer. For the diffusion-limited mechanism the rate of transfer of material through the liquid boundary layer controls the process. The principal difference between these mechanisms is that the interfacial liquid concentration is in equilibrium with the solid phase in the diffusion-limited case, whereas it is not saturated and is approximately equal to the average bulk-stream concentration in solution-limited corrosion. The mercury-iron and sodium-iron systems are described respectively as diffusion limited and solution limited.

Dunn *et al.* (*6*) studied mass transfer rates for metals quite soluble in mercury at room temperature. The data were correlated by use of the various dimensionless correlations applicable to the systems studied. Linton and Sherwood (7) investigated the solution of tubes and plates for both laminar and turbulent flow. This investigation represented a considerable extension of mass transfer data to higher values of $(\mu/\rho D_L)$, and the data were correlated by use of conventional dimensionless equations.

A recent study by Bennett and Lewis (*8*) discusses the applicability of boundary-layer analysis and the more recently developed surface-renewal theory (*9, 10*). It has been shown (*11*) that the laminar-sublayer and surface-renewal models yield similar equations, and thus mass transport may be expressed in traditional form independent of the frame of reference used. To test these theories, two designs of apparatus were used in the experiments by Bennett and Lewis, and two equations were employed to correlate the data, depending on the method used. Although an exponent of 0.5 for the Schmidt group (as predicted by the surface-renewal theory) was applicable to one system, this was not considered sufficient evidence to confirm or reject the surface-renewal theory.

EXPERIMENTAL PROCEDURE

The apparatus employed is shown schematically in Figure 1. Lithium was charged to the hold tank through a sintered stainless steel filter with 5-μ pore size. The entire system was pretreated with low-temperature lithium to reduce surface films. Type-304 stainless steel plates (1 by ⅝ by 1/16 in.) which had previously been electropolished to eliminate surface films were arranged to form a continuous flat plate parallel to the direction of flow. This was accomplished with ⅝-in. tubes 27-in. long which were machined to hold ten to twenty-five plates rigidly to form one continuous plate. The ⅝-in. tube together with the inserted plates was placed inside a ¾-in. tube and the assembly locked together to hold the two tubes concentrically.

Lithium flowed parallel to both sides of the plate causing material to be transferred identically on both sides. This arrangement enabled the measurement of mass flux to and from plates 1 to 25 in. long under invariant conditions for a given run. The temperature and flow conditions were altered as desired for different runs. Plate assemblies were varied in length from 10 to 25 in. Two test sections were incorporated in the system; one was placed in the hottest and the other in the coldest part of the system. During all runs the low-temperature test section was maintained at a constant temperature, whereas both isothermal and nonisothermal conditions were established in the hot section. As expected, material was transferred from the plates to the liquid stream in the hot zone and from the liquid stream to the plates in the low-temperature section.

The lithium used was high-purity vacuum-distilled material reported to have the following analysis:

Lithium analysis

Na	K	Ca	N	Fe	Li
0.005%	0.01%	0.02%	0.06%	0.001%	99+%

During each run lithium was filtered continuously to reduce contamination and to justify the assumption of a steady state concentration distribution; the outlet stream from the filter was assumed to be saturated at the filter temperature. The filter also served to remove particulate matter resulting from crystal growth in the liquid stream. In addition the lithium was filtered continuously at approximately 0.5 to 1°C. above its melting point at the termination of each run to maintain contamination at a low level. The absolute magnitude and consistency of results indicate that this is an effective procedure and that catalytic effects due to oxides and nitrides were minimized. It is concluded that continuous filtration is probably the single most fruitful method to obtain consistent and reliable experimental results.

The entire system was made of type-304 stainless steel with the exception of the fittings which were of type-316 stainless steel. A single material was used to eliminate dissimilar metal transfer which would undoubtedly bias the results. A preliminary study on static isothermal assemblies indicated that austenitic stainless steels were superior to other stainless steels. Also a statistical analysis of the results showed no significant differences between type-304 and the other series-300 steels up to 500°C. Refractory metals, which are more inert, present considerable experimental difficulty because of oxidation problems unless the entire system is operated in an inert atmosphere. Therefore type-304 stainless steel was chosen for this investigation, despite its complexity, because of its practical importance in handling lithium. Small fluxes could be anticipated with this material, which satisfied most assumptions made in theoretical investigations. The principal limitation in using a complex alloy is that several components, rather than one, are

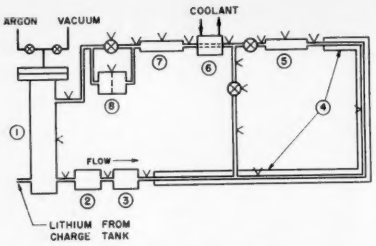

Fig. 1. Closed-loop mass transfer system: 1—surge tank, 2—electromagnetic pump, 3—electromagnetic flowmeter, 4—heating section, 5—hot sample section, 6—cooler, 7—cold sample section, 8—filter, ∨—thermocouple, ⊗—valve.

transferred simultaneously. Consequently mean diffusivities must be used in the calculations, but this is not a severe limitation because the diffusivities of iron, nickel, and chromium in liquid lithium are about equal, as indicated by the Stokes-Einstein equation.

Thermocouples positioned at various points in the system measured the temperature distribution. The temperature in each sample section and throughout the system was measured periodically by use of a *K*-2 potentiometer and also monitored continuously on a multipoint recorder.

An electromagnetic pump circulated the lithium, and a calibrated electromagnetic flowmeter measured the fluid velocity. This type of pump is particularly convenient for experimental work with liquid metals, since it provides excellent velocity control and reliable operation.

After a specified time, from 67 to 100 hr., the plates were removed, and the mass flux was measured by weight difference. Photomicrographic, X-ray, and chemical analyses were employed to determine structural changes occurring in the solid phase and to identify the components transferred. Crystals were also cold trapped upstream of the filter and analyzed for this purpose.

MASS FLUX AND THE TRANSPORT MECHANISM

Theory

In most liquid lithium mass transfer investigations the material transported is the containing system. Therefore the solubility levels of interest are on the order of parts per million. Changes in the bulk-stream concentration around the system can be less than 1 part/million as in this investigation. This precludes direct measurement of concentration differences by chemical means and requires the use of a different method. It is desirable to formulate equations describing the process in terms of mass flux at the phase boundary which can be measured directly. With known fluxes concentration distributions can be deduced from the continuity equations.

Bird (*12*) discusses various frames of reference for defining fluxes and clearly presents the relationships between them. The nature of turbulence and its role in thermal and material transport are described by Opfell and Sage (*13*). On the basis of the general equations described in these monographs it is easily shown that

$$V_z \frac{\partial C_L}{\partial z} = \overline{\Sigma}_{d,K} \frac{1}{r} \frac{\partial}{\partial r}\left(r \frac{\partial C_L}{\partial r} \right) \quad (1)$$

for steady flow of an incompressible fluid in a constant cross-sectional area, circular conduit. Solutions to the heat transfer analogue of Equation (1) have been obtained for plug, laminar, and turbulent flow in tubes by Lévèque, Graetz, and Latzko (*14*) assuming constant physical properties. These solutions have been compared with experimental data with considerable success (*14, 15*).

Practical problems are usually complicated by large thermal gradients and the nature of the solid phase, when this offers appreciable resistance to transfer. This has made it necessary to state the continuity equation in the simplest possible form so that it can be integrated over the system considered. It is desirable to examine this approach for circular tubes, since the procedure was used in this study. The macroscopic steady state continuity equation for each component in the liquid stream is

$$\frac{dC_L}{dz} = \left[\frac{A_p}{V_{av} A_c} \right] N_r \quad (2)$$

In addition local mass transfer coefficients, for steady state conditions, are defined for each component by

$$N_r = k_s (C_s - C_s^\circ) \quad (3a)$$

$$= k_c (\gamma^\circ C_L^\circ - \gamma C_L^\circ) \quad (3b)$$

$$= k_L (C_L^\circ - C_L) \quad (3c)$$

Equations (3*a*), (3*b*), and (3*c*) describe solid-phase diffusion, interfacial chemical rates, and liquid-phase diffusion, respectively. It should be noted that γ° and C_L° in Equation (3*b*) refer to quantities in thermodynamic equilibrium with the solid phase immediately adjacent to the liquid; this may not be identical with the bulk solid.

Solution Phenomena Epstein (*5*) suggested two distinct mechanisms for

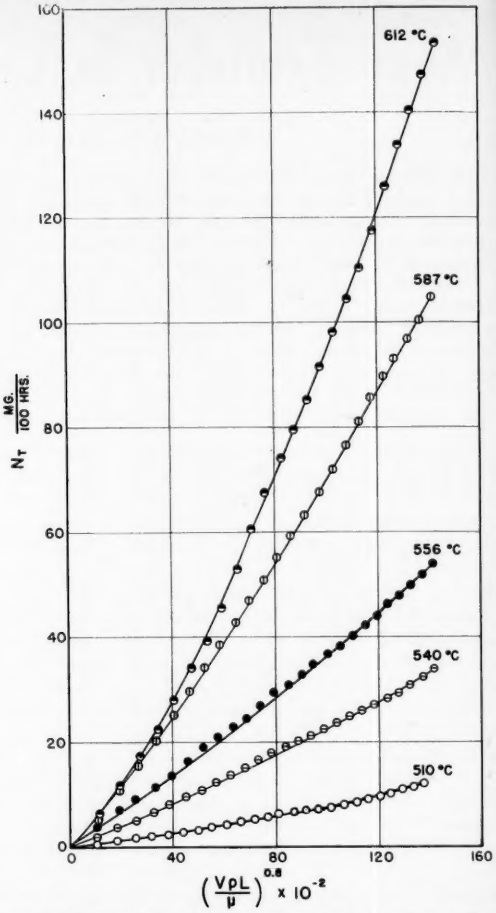

Fig. 2. Solution of flat plates in lithium (variation of mass flux with Reynolds number).

- ⊖ 612°C.
- ⊕ 587°C.
- ● 556°C.
- ⊖ 540°C.
- ○ 510°C.

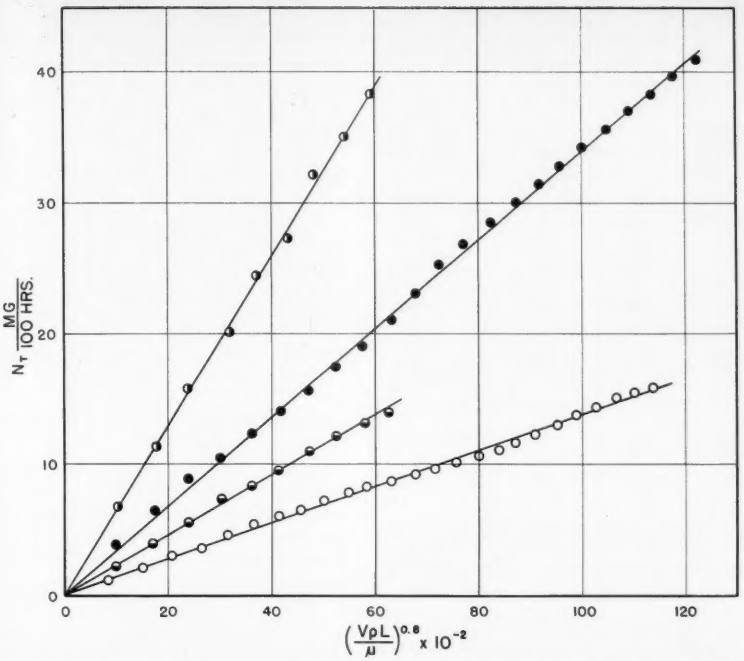

Fig. 3. Deposition on flat plates from lithium (variation of mass flux with Reynolds number).

- ◒ 490°C.
- ● 450°C.
- ◒ 445°C.
- ○ 328°C.

solution phenomena in liquid-metal systems as previously described. The diffusion-limited mechanism controls for single-component solids, where k_c is large and C_L^* is approximately equal to C_L°. It is readily seen that these conditions give directly

$$N_r = k_L (C_L^\circ - C_L) = k_L (C_L^* - C_L) \qquad (3c)$$

Hydrodynamic effects are most pronounced for systems that can be so described. This behavior has been observed in mercury systems with iron, tin, lead, and cadmium solutes (*6, 8*). When the interfacial liquid boundary-layer cannot be considered saturated, several possibilities arise and have been observed experimentally. For pure solids the chemical-rate factor may enter into the solution process as observed with zinc in several solvents (*8*). Also the solution rate may be affected by the existence of a solid boundary layer of reaction products resulting from a chemical reaction between the solid and an impurity of the liquid or the liquid itself. The iron-sodium system exhibits this behavior (*5*). Solution of multicomponent solid alloys is further complicated by solid-phase diffusion. All these effects are included in an over-all mass transfer coefficient frequently designated a "solution-rate constant," and the mass flux is written

$$N_r = \alpha (C_L^\circ - C_L) \qquad (4)$$

If the origin of the coordinate system is chosen at a point in the system where the liquid stream is saturated, that is the outlet from the filter, the flux distribution around the system can be obtained directly. Differentiating Equation (4), combining this with Equation (2), and integrating with the condition $N_r=0$ at $z=0$ (at the filter outlet this condition is satisfied since the bulk stream is saturated), one obtains

$$N_r = \alpha_m e^{-\lambda_m z} \int_0^z \left(\frac{dc_L^\circ}{dT} \frac{dT}{dz} \right) e^{\lambda_m z} dz \qquad (5)$$

where

$$\lambda_m = \frac{A_p\ \alpha_m}{V_{av} A_c}$$

If analytical expressions are available for the temperature coefficient of solubility and the temperature distribution in the system, the integral is easily evaluated; α_m and λ_m are best determined by

$$\lambda_m = \frac{1}{z} \int_0^z \lambda(z)\, dz \qquad (6)$$

Epstein (*5*) simplified Equation (5) by assuming that $(dC_L^\circ)/(dT)$ was essentially constant over small temperature intervals and that the temperature distribution can be approximated by a simple cosine function. Employing these assumptions, one obtained order-of-magnitude agreement.

Deposition Phenomena For deposition processes only k_c and k_L need be examined. If k_c is large, as it is shown to be for the system investigated, the interfacial liquid is assumed to be in thermodynamic equilibrium with the solid. Consequently the mass flux can be written as

$$N_r = k_L(C_L - C_L^\circ) = k_L(C_L - C_L^*) \qquad (7)$$

Since the transfer mechanism cannot be observed directly, it must be determined by inference. Transport in turbulent flow parallel to a flat plate is ideal for this purpose. This system has been the subject of considerable theoretical investigation, particularly as it relates to heat and momentum transfer. Von Kàrmàn (*16*) studied the heat transfer problem. From a heat balance over the boundary layer, based on the 1/7 power velocity distribution law, he derived the following relationships for local and total fluxes respectively:

$$q_r = 0.0285\ \rho C_p V_\infty \theta \left(\frac{\mu}{\rho V_\infty x} \right)^{0.2} \qquad (8)$$

$$q_T = 0.0356\, \mu\, C_p\, \theta_\infty \left(\frac{\rho V_\infty L}{\mu} \right)^{0.8} \qquad (9)$$

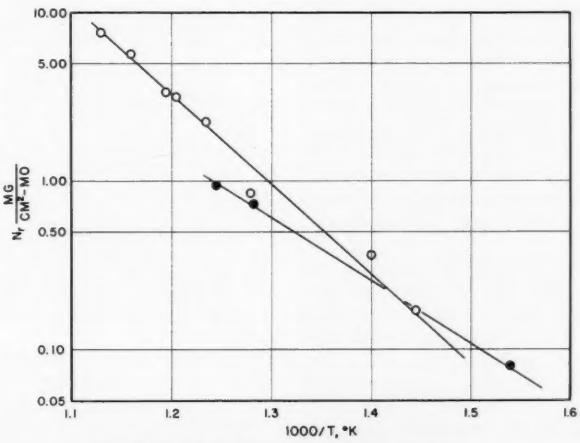

Fig. 4. Variation of mass flux with temperature.

- ○ present data on lithium
- ● data of Epstein (5) on sodium

Table 1. Conditions For Solution-Rate Data In Figure 4

Lithium

N_T (mg./sq. cm.-mo)	$T_{soln.}$, °C.	T_{filter}, °C.	ΔT, °C.	Time, hr.	V, cm./sec.	Type of specimen dissolving
7.6	612	490*	122	100	15.5	plate
5.7	587	450*	137	100	15.5	plate
4.7	583	548*	35	100	40.0	plate
3.4	563***	543	20	100	60.0	tube
3.15	556	445*	111	67	15.5	plate
2.21	541	328*	212	100	15.5	plate
0.85	510	374	136	100	15.5	plate
0.36	440**	430	10	100	85.0	plate
0.17	421**	374	45	100	85.0	plate
		Sodium				
0.94	535	425	110	—	30	
0.71	500	460	40	—	60	
0.08	375	225	150	—	45	

* Deposition rates were measured at these conditions and are shown in Figures 3 and 5.
** Preliminary measurements were made to determine the temperature level necessary to obtain reliably reassurable rates.
*** Fifteen measurements on tubes were made under these conditions to test the assumption that the solution rate is independent of geometry.

Von Kàrmàn's analysis assumes a stream of infinite extent, where the main stream above the boundary layer is undisturbed. This is approximated by flat plates in tubes along a relatively short length before the tube-and-plate boundary layers interact. By analogy it would be expected, for a given ΔC_o, that the total mass flux over the length is proportional to $[(V_oL)/\nu]^{0.8}$ for an isothermal system if the fluid resistance predominates. Conversely, if the transfer process is controlled by crystal orientation or solid-phase diffusion effects, the growth of the boundary layer should affect mass transfer to a lesser extent and the rate is essentially independent of the fluid velocity and directly proportional to the length of the plate.

Experimental Results

Mass-Flux Data Figures 2, 3, and 4 are representative mass-flux data obtained in this study. The behavior of each individual curve in Figures 2 and 3 is independent of the driving force, since this is constant for a given curve. Figure 2 shows fluxes from the plates to the lithium stream. All runs indicate some degree of positive curvature, and this curvature increases with increased flux as expected for solution-limited transfer.

In contrast Figure 3 for fluxes to the plates corroborates von Kàrmàn's predicted effect of the Reynolds number. It is seen that the total flux in this case is linear in $[(V_oL)/\nu]^{0.8}$ within experimental error. This suggests a solid-phase controlled-solution process and a fluid mechanically controlled precipitation process. Subsequent examination of mass transfer coefficients and solution-rate constants corroborates this. In large measure this explains the plugging phenomena observed in nonisothermal closed-loop systems. Since the precipitation process is rapid relative to the solution process, the deposition of material in the system is limited only by the concentration or activity potential available.

Each point in Figure 4 is based on twenty-five observations of solution rates under a given set of conditions. It is seen that the mass flux is substantially linear in $1/T$, despite the variation in temperature differences and velocities shown in Table 1. This experimental result strongly suggests that the observed solution rate, under the range of conditions investigated, is an exponential function of the solution temperature. This is quite reasonable considering that a large number of diffusion processes, reaction-velocity constants, and solubility concentrations can be expressed by an Arrhenius type of equation over limited temperature ranges. An identical result was obtained for the mercury-iron system (5), and the reasons for this were discussed rather extensively.

Figure 4, together with the temperature distribution, can be employed to determine the concentration distribution around the system with the continuity equation used in the form

$$C_L = C^\circ_{filter} + \frac{A_p \int_o^L N_r dz}{V_{avg} A_c} \quad (10)$$

The stream leaving the filter is assumed to be saturated.

Mass Transfer Coefficients. A search of the diffusion literature (17) on liquid metals led to the conclusion that measured diffusivities were one to two times those calculated with the Stokes-Einstein equation:

$$\frac{D_L \mu}{T} = \frac{K}{6R_A \pi} \quad (11)$$

This then provides a reasonable approximation for use in dimensionless correlations to predict mass transfer coefficients.

The atomic radii of iron, nickel, and chromium are 1.26, 1.24, and 1.25 Å. respectively, and therefore diffusivities of these elements in dilute solutions should, on the basis of the Stokes-Einstein equation, be essentially the same. A value of 1.25 Å. was used to calculate the mean diffusivity.

Von Kàrmàn's analysis modified for mass transfer as a Chilton-Colburn j-factor correlation leads to

$$j_d = 0.0356\ (N_{Re_L})^{-0.2} \quad (12)$$

or, with a slightly modified friction

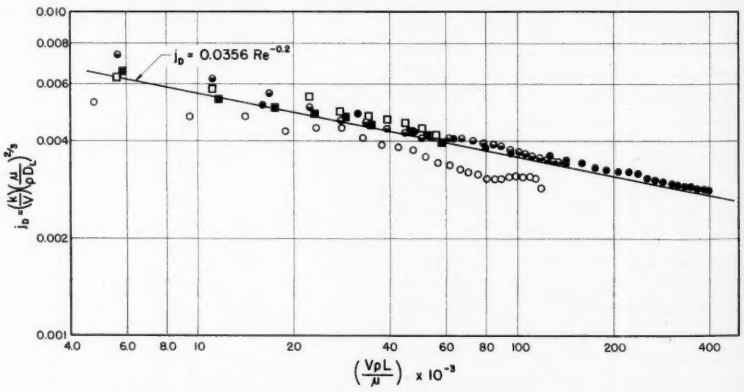

Fig. 5. Correlation of liquid-phase mass transfer coefficients for flat plates.

	Temp., °C.	Velocity, cm./sec.	Plate length, cm.	ΔC x 10^1 mg./cc.
□	445	15.5	2.54-25.4	1.30
■	490	15.5	2.54-25.4	3.63
○	328	15.5	2.54-63.5	1.17
◎	450	15.5	2.54-63.5	2.00
●	548	40.0	2.54-63.5	1.38

factor for smooth flat plates as suggested by Schlichting (*18*), to

$$j_d = 0.0370\ (N_{Re_L})^{-0.2} \qquad (13)$$

The coefficients in these relations are mean values over the plate length.

Since the filter and cold-section plates were maintained at the same temperature, the equilibrium solubility was the same in both. In addition if the deposition process is fluid mechanically controlled, as suggested by the previous discussion of von Kàrmàn's analysis, the interfacial concentration at the plate is an equilibrium value identical with the outlet concentration of the filter. Consequently the driving force for deposition is equal to the increase in concentration experienced by the lithium in travelling from the filter outlet to the plate entrance. These values are given in Figure 5. Therefore mass transfer coefficients were calculated by the use of

$$k_L = \frac{N_r}{A\Delta C_o} \qquad (14)$$

where ΔC_o is determined with Equation (10) and measured solution rates used.

The data falling below the solid line in Figure 5 were all obtained at 328°C., whereas the data on or above the line represent temperature between 445° and 548°C. No consistent bias is observable in the higher-temperature data, and the experimental error is apparently small. The larger deviations from predicted values for the 328°C. data are probably due to error in ΔC_o. The temperature gradient throughout the heat exchanger was particularly high for the 328°C. data (8.5°C./in.) and may have caused a significant decrease in the concentration of the stream approaching the plates via deposition in the exchanger. This may account for the low experimental values of k_L.

Table 2. Solution-Rate Constants

$\alpha_m \times 10^5$, (cm./sec.)*	$\alpha \times 10^5$, (range)*	ΔC, mg./cc.	t, °C.	Δt system, °C.	$N_{Re} \times 10^3$
0.154	0.204-0.142	0.129	510	136°C	6-150
0.299	0.398-0.259	0.206	541	212°C	6-154
0.504	0.775-0.428	0.204	556	111°C	6-155
0.670	0.764-0.616	0.289	587	137°C	6-160
0.750	0.792-0.694	0.331	612	122°C	6-163

* The mean values and ranges for solution-rate constants were based on twenty-five measurements in all cases.

These data contrast with those obtained by Linton and Sherwood (*7*). For plates their results in all cases were 1.5 to twofold above the solid line in Figure (5). These authors logically suggest that this is attributable to the induced roughness of the plates caused by solution effects. This is a reasonable conclusion as discussed extensively by Schlichting (*18*).

Solution-Rate Constants. Unlike the mass transfer coefficients discussed previously for fluxes to the solid phase, the mechanism for solution is not readily discernible because of its inherent complexity and the lack of sufficient solubility data. Solubility data were obtained for nickel from the the work of Bagley and Montgomery (*19*) and for iron from Sand *et al.* (*20*). No chromium solubility data were available. Therefore the solution-rate constants shown in Table 1 were calculated on the basis of these data. It is readily seen that the absolute magnitude of the solution rate constants is smaller, by a factor of 10^5, than expected for diffusion-limited processes. A simple calculation with the approximate relationship

$$\frac{1}{\alpha} = \frac{1}{k_L} + \frac{1}{\gamma^\circ k_c} + \frac{1}{Kk_s} \qquad (15)$$

shows that

$$\frac{1}{\alpha} \approx \frac{1}{\gamma^\circ k_c} + \frac{1}{Kk_s} \qquad (16)$$

within less than 1%. Therefore the solution-rate constant is dependent on the solid phase and interfacial resistances only.

The proper driving force to use for solution-rate constant calculations is the difference between the equilibrium concentration and the bulk-stream concentration. This is exactly equivalent to the difference in solubility between the solution temperature and the filter temperature plus the bulk-stream concentration increase caused by solution between these points. These values are given in Table 2. According to Figure 4 log N_r is essentially linear in $1/T$. Therefore the solution-rate constants should be linear in this variable. This condition is only approximately satisfied. Deviations from linearity are probably attributable to the lack of complete solubility data.

It is clear from the behavior of the individual solution-rate constants* that the solution process is controlled primarily by the solid phase, in contrast to the precipitation process. Although there is a slight tendency for these constants to decrease with increasing Reynold's number, this is not nearly so pronounced as that observed in fluid mechanically controlled systems.

Solid-Phase Analysis. The photomicrographs in Figure 6 provide a means of estimating quite accurately the depth of deposition product layers due to mass transfer in the low-temperature section of the system. The band above the stainless steel substrate represents the deposition layer. It can be seen that this layer is well delineated, and no diffusion into the substrate is evident. Fluxes observed by weight differences for Figure 6*a* and *b* were in the ratio of 1/2.83, which corresponds to the respective band widths shown. The exact structure of the de-

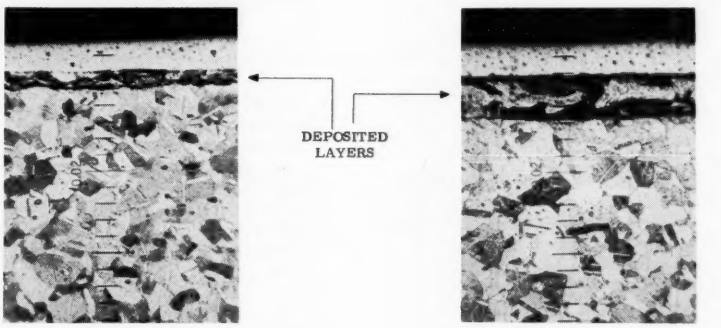

a

MAX. SYSTEM TEMPERATURE (556°C)
DEPOSITION TEMPERATURE (445°C)
3 divisions = 0.002 in.
x 300

b

MAX. SYSTEM TEMPERATURE (612°C)
DEPOSITION TEMPERATURE (490°C)
3 divisions = 0.002 in.
x 300

Fig. 6. Photomicrographs showing deposition layer.

* Tabular material has been deposited as document No. 6125 with the American Documentation Institute, Photoduplication Service, Library of Congress, Washington 25, D.C., and may be obtained for $1.25 for photoprints or for 35-mm. microfilm.

position products is difficult to determine, but spectrographic analysis of crystals trapped upstream of the filter showed that nickel was the principal component transferred and that chromium, manganese, silicon, and carbon were present in detectable amounts.

X-ray diffraction and photomicrographic analysis of the plates in the high-temperature section of the system where solution occurs showed transformation of the austenitic structure to a ferritic structure. Corresponding to mass-flux rates, the degree of conversion to ferrite increased rapidly with temperature. In an inert atmosphere the austenitic structure of type 304 stainless steel is quite stable at 600°C.; therefore transformation to ferrite can be attributed to the preferential loss of nickel, which is the major stabilizing component for austenite in type-304 stainless steel. Precipitation of chromium carbide at grain boundaries, thereby depleting the matrix of carbon, also enhances ferrite formation.

CONCLUSIONS

1. Mass transfer coefficients in alkali metal systems for fluxes to the solid phase are predicted within experimental error by von Kàrmàn's theoretical analysis of the turbulent boundary layer for flow parallel to a flat plate, combined with the Chilton-Colburn empirical modification of the Schmidt group.

2. The fundamental transfer mechanism is unaltered by the system geometry. Therefore j-factor correlations would be expected to predict mass transfer coefficients in circular tubes.

3. Mass transfer from the solid to the liquid stream is controlled by solid-phase diffusion and cannot be predicted from correlations based on liquid-phase diffusion.

4. No interfacial chemical resistance was evident for mass transfer to the solid phase. It was not possible to determine the effect of interfacial resistance in the solution process because of its complexity.

5. Closed-loop forced-convection systems are very satisfactory for mass transfer investigations of sparingly soluble materials. The idealized steady state condition can be closely approached and transient behavior studied if desired. Isothermal and nonisothermal conditions are easily established simultaneously in separate sections of a single system. The opportunity to study solution and deposition rates simultaneously is particularly important for investigating the transport mechanism. A wide continuous range of fluid velocities is easily obtained, and the velocity can be controlled extremely well.

6. Type-304 stainless steel is a suitable material for handling liquid lithium up to 1,100°F. because solution mass transfer rates are low. This condition minimizes the tendency for equipment failure by either corrosion or plugging.

ACKNOWLEDGMENT

The authors wish to thank the National Science Foundation for making this study possible.

Material supplied by M. S. A. Research Corporation, Crawford Fitting Company, and Olin Mathieson Chemical Corporation is gratefully acknowledged.

The assistance given by Volker Weiss concerning the metallurgical aspects of the study was very valuable.

NOTATION

A = area, sq. cm.
C = concentration of solute, g./cc.
C_P = heat capacity, cal./(g. °K.)
D_L = molecular diffusivity, sq.cm./sec.
j_d = $(k_L/V)[(\mu)/(\rho D_L)]^{2/3}$
k_c = reaction velocity constant, cm./sec.
k_L = liquid-phase mass tranfer coefficient, cm./sec.
k_s = solid-phase mass transfer coefficient, cm./sec.
K = distribution constant
L = plate length, cm.
N = local mass flux, g./(sq.cm.)(sec.)
N_T = total mass flux, g./sec.
q = heat flux, cal./(sq. cm.)(sec.)
r = radius, cm.
R = gas constant
T = temperature, °K.
t = time, sec.

Greek Letters

α = solution rate constant, cm./sec., over-all mass transfer coefficient
γ = activity coefficient
Δ = difference
θ = temperature difference, (To-Tw) °K.
κ = Boltzman constant (1.38×10^{-6} erg./°K.)
μ = viscosity, g./(cm.)(sec.)
ν = kinematic viscosity, sq.cm./sec.
ρ = density of liquid mixture, g./cc.

Dimensionless Groups

N_{Re} = Reynolds number for flat plate, $(V\rho L/\mu)$
N_{Sc} = Schmidt number $(\mu/\rho D_L)$

Subscripts

c = cross sectional
d = mass transfer
f = final value
K = K^{th} component
L = liquid phase
m = mean value
o = origin of coordinate system
p = peripheral
r = radial direction
s = solid phase
T = total
z = direction

Superscripts

o = equilibrium value
$*$ = interfacial value

LITERATURE CITED

1. Dana, A. W., O. H. Baker, and M. Ferguson, Technical Report III, ES 783, The Babcock and Wilcox Company (April 21, 1952).
2. Dana, A. W., *et al.*, Reports DC-52-27-45 (BW 5230) (May 1942) and DC-52-5-19 (August 20, 1952), The Babcock and Wilcox Company.
3. General Electric Co., Aircraft Nuclear Propulsion Project, Reports DC-51-9-36 (Sept. 1951) and DC-51-12-52 (Dec. 1951).
4. Hoffman, E. E., and W. D. Manly, "Corrosion Resistance of Metals and Alloys to Sodium and Lithium, Handling and Uses of the Alkali Metals," American Chemical Society (1957).
5. Epstein, L. F., *Proc. Intern. Congr. Peaceful Uses of Atomic Energy, Geneva, Aug. 1955*, **9**, 311 (1956).
6. Dunn, W. E., C. F. Bonilla, C. Ferstenberg, and B. Gross, *A.I.Ch.E. Journal*, **2**, 184 (1956).
7. Linton, W. H., and T. K. Sherwood, *Chem. Eng. Progr.*, **46**, 258 (1950).
8. Bennett, J. A. R., and J. B. Lewis, *A.I.Ch.E. Journal*, **4**, 418 (1958).
9. Higbie, Ralph, *Trans. Am. Inst. Chem. Engrs.*, **31**, 365 (1935).
10. Danckwerts, P. V., *Ind. Eng. Chem.*, **43**, 1460 (1951).
11. ———and Kennedy, *Trans. Inst. Chem. Engrs. (London)*, **32**, S49 (1954).
12. Bird, R. B., in "Advances in Chemical, Engineering," Vol. I, Academic Press, New York (1955).
13. Opfell, J. F., and B. H. Sage, *ibid.*
14. Jakob, Max, "Heat Transfer," Vol. I, John Wiley, New York (1949).
15. Sherwood, T. K., and R. L. Pigford, "Absorption and Extraction," McGraw-Hill, New York (1952).
16. Kàrmàn, Th. von, *Z. angew. Math. u. Mech.*, **1**, 233 (1921).
17. Bonilla, C. F., R. N. Roy-Choudhury, *et al.*, "Mass Transfer in Liquid Metal and Fused Salt Systems" NYO-3088, 3090, U.S.A.F.C. (1952).
18. Schlichting, Hermann, "The Boundary Layer Theory," Pergamon Press, New York (1955).
19. Bagley, K. Q., and K. R. Montgomery, United Kingdom Atomic Energy Authority, Report No. IGR-TN/C 250.
20. Sand, J., W. N. Gill, R. V. Jelinek, and C. S. Grove, "Solubility of Iron in Lithium," Syracuse University Research Institute Report (1958).

Manuscript received May 11, 1959; revision received June 26, 1959; paper accepted July 2, 1959. Paper presented at A.I.Ch.E. Kansas City meeting.

Mass Transfer Inside Drops

A. I. JOHNSON and A. E. HAMIELEC

University of Toronto, Toronto, Canada

The transfer rates of *n*-butanol, cyclohexanol, and ethyl acetate into water drops have been measured for circulating and oscillating drops.

Methods of allowing for the end-effect transfer have been extended and measured values compared with predictions of a model.

Various mechanisms for transfer inside drops have been examined in terms of a correlation factor.

Many recent studies on heat and mass transfer rates to and from bubbles and drops as they pass through continuous media have been aimed at elucidating the transfer mechanisms during formation, rise or fall, and coalescence or bursting of the drops or bubbles. In particular, the transfer mechanisms during the steady rise or fall period have been analyzed for a variety of situations. It is apparent that if proposed mechanisms are to be checked experimentally, corrections for transfer during formation and coalescence must be made, or there must be some device for contacting two phases without these end effects.

This paper discusses methods of correcting for transfer in end effects. The experimental work reported is concerned with mass transfer inside liquid drops, and for convenience in discussing the development of the equations used drops heavier than the continuous phase will be discussed. The methods may be extended to other situations.

Possible mechanisms describing the steady-fall period will also be examined.

PREVIOUS WORK

In a recent paper (*15*) the authors discussed end-effect measurements and techniques previously reported in the literature. Attempts to measure end effects in an extraction column were made by Johnson and Bliss (*14*); Sherwood, Evans, and Longcor (*20*); Treybal (*21*) and West *et al.* (*23*). Among workers on single drops Licht and Conway (*17*) and Licht and Pansing (*18*) attempted to determine end effects separately from the steady fall transfer. Coulson and Skinner (*3*) injected and rapidly withdrew drops to study the mass transferred during formation.

$$E_m = \frac{C_2 - C_3}{C_2 - C^*} = 1 - 6\sum_{n=1}^{\infty} B_n \exp\left[-\lambda_n^2 \frac{Dt}{a^2}\right] \qquad (1)$$

Other end-effect measurements, by Geankoplis and Hixson (*5*); Geankoplis, Wells, and Hawk (*6*); and Gier and Hougen (*7*), were made by probing the continuous phase to determine abnormal transfer in the end zones.

The present authors have employed a simple mathematical analysis of end effects, introducing efficiencies for these periods, and have developed techniques to be used for plotting data both to check the mechanism and to obtain numerical values of a combined end effect. These methods will be expanded in the theoretical section of this paper.

For heat and mass transfer rates inside drops recent studies (*2, 4, 11*) have centered on the application of theory for a stagnant (noncirculating) sphere or for a drop whose circulation pattern was assumed to be that developed by Hadamard (*9*). The latter situation was analyzed by Kronig and Brink (*16*). Although the Kronig and Brink theory should apply only to slowly moving drops (Reynolds number below unity), it has been used at higher Reynolds numbers. Recently Handlos and Baron (*10*) have modified the Kronig and Brink theory, allowing for turbulent motion inside the drops.

Mass transfer studies involving two component systems have been used in this study. To the authors' knowledge, only Heertjes *et al.* (*11*), working on a spray column, have examined mechanisms for mass transfer inside drops using such systems.

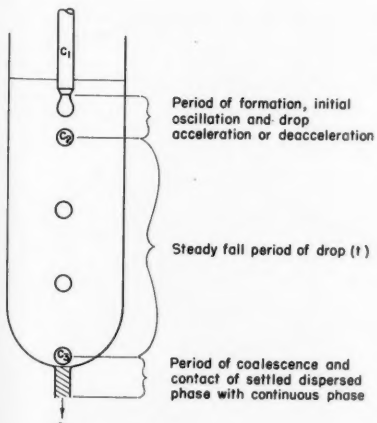
C_1
C_2
C_3
C_4
Period of formation, initial oscillation and drop acceleration or deacceleration
Steady fall period of drop (t)
Period of coalescence and contact of settled dispersed phase with continuous phase

Fig. 1. Definitions of the concentrations and the periods of drop life used in this research.

THEORETICAL DISCUSSION

Transfer mechanisms

This first section will summarize the equations describing the transient mass transfer process inside a drop. For all mechanisms spherical drops, constant molecular diffusivity, uniform initial concentration, and absence of any interface resistance are assumed.

Diffusion into a stagnant drop. The fraction approach to equilibrium or the efficiency for the steady-fall period for a stagnant drop with continuous-phase resistance has been derived by Grober (*8*):

Here C_2 and C_3 are the uniformly mixed drop concentrations for the ends of the steady-fall period as indicated in Figure 1. The quantities B_n and λ_n have been tabulated for various Nusselt numbers by Grober (*8*).

For the particular case of no resistance to transfer in the continuous phase this equation reduces to the equation ascribed to Newman (*19*):

$$E_m = 1 - \frac{6}{\pi^2}\sum_{n=1}^{\infty}\frac{1}{n^2}\exp\left[\frac{-n^2 D\pi^2 t}{a^2}\right] \qquad (2)$$

Diffusion into a circulating drop. For negligible interfacial tension and for a drop Reynolds number less than unity Kronig and Brink (*16*) derived the following equation for diffusion into a circulating drop with no continuous-phase resistance:

$$E_m = 1 - 3/8\sum_{n=1}^{\infty} B_n^2 \exp\left[-\lambda_n \frac{16Dt}{a^2}\right] \qquad (3)$$

Elzinga and Banchero (*4*) obtained the same equation for the case of a finite continuous-phase resistance and calculated values of the quantities B_n and λ_n for various Nusselt numbers. Table 1 summarizes values of B_n and λ_n for the case of no continuous-phase resistance (as encountered in this study).

Transfer into a drop at high Reynolds numbers. Handlos and Baron (*10*) proposed a circulation model which included radial motion. For their mechanism

$$E_m = 1 - 2\sum_{n=1}^{\infty} B_n \exp\left[-\frac{\lambda_n 16Dt\, N_{Re_1}}{2048d^2}\right] \qquad (4)$$

Table 1. Summary of Values of B_n and λ_n for Equation (3) with Zero Continuous-Phase Resistance

n	B_n	λ_n	Source
1	1.29	1.656	
2	0.596	9.08	(4)
3	0.386	22.2	
4	0.35	38.5	
5	0.28	63.0	
6	0.22	89.8	(11)
7	0.16	123.8	

They claim that only one term of this series with $\lambda_1 = 2.88$ need be used. They derived an effective diffusivity as a function of radius as

$$E_{(r)} = \frac{D\,N_{Pe_4}}{2{,}048}\,(6r^2 - 8r + 3) \qquad (5)$$

where

$$N_{Pe_4} = \frac{N_{Pe_4}}{(1 + \mu_i/\mu_o)} \qquad (6)$$

A correlation factor for diffusion inside drops. The factor R proposed by Korchinski (2) and used by him with the Vermeulen equation (22) is used in this study as a multiplier of the molecular diffusivity to compare transfer rates with rates encountered in a stagnant drop. The following modification of Equation (1) may be considered to define R:

$$E_m = 1 - 6\sum_{n=1}^{\infty} B_n \exp\left[\frac{-\lambda_n^2\,RDt}{a^2}\right] \qquad (7)$$

The Vermeulen equation is an empirical fit of Equation (1), and hence the R value used by Korchinski is essentially the same as the one defined by Equation (7).

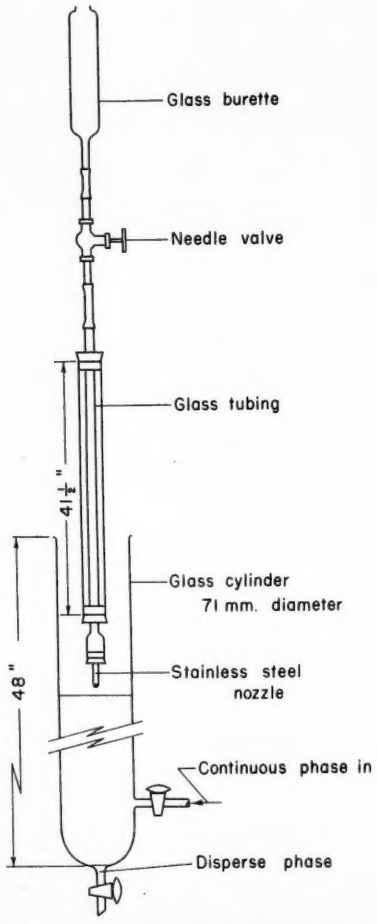

Fig. 2. Apparatus for studying mass transfer into circulating and oscillating drops.

Definition of end effects

With reference to Figure 1, the fractional approach to equilibrium in the formation, steady-fall, and coalescence periods may be defined by

$$E_{f_1} = \frac{C_1 - C_2}{C_1 - C^*},\quad E_m = \frac{C_2 - C_3}{C_2 - C^*},\quad \text{and}$$

$$E_{f_2} = \frac{C_3 - C_4}{C_3 - C^*} \qquad (8a,b,c)$$

Here C_1, C_2, C_3, and C_4 are the uniformly mixed concentrations illustrated by Figure 1.

In practice only C_1 and C_4 are directly measurable, and the only accurately measured efficiency is the over-all or total efficiency:

$$E_T = \frac{C_1 - C_4}{C_1 - C^*} \qquad (9)$$

By simple algebraic manipulation of (8) and (9) the following equation results:

$$E_m = \frac{E_T - E_{f_1} - E_{f_2} + E_{f_1} \times E_{f_2}}{1 - E_{f_1} - E_{f_2} + E_{f_1} \times E_{f_2}} = \frac{E_T - E_F}{1 - E_F} \qquad (10)$$

where E_F is a combined end effect, $E_{f_1} + E_{f_2} - E_{f_1} \times E_{f_2}$.

At constant drop-formation time, drop size, coalesced dispersed-phase holdup, and continuous-phase flow rate, E_{f_1} and E_{f_2} may be considered constant. This will be considered more fully below.

Determination of E_F and R

Low efficiency studies. For low E_m values ($E_m < 0.5$) the following empirical equation has been found to fit Equation (7):

$$E_m = 0.905\sqrt{\frac{RD\pi^2 t}{a^2}} + 0.0189 \qquad (11)$$

This is an improvement over the Vermeulen equation as used by the authors in a previous study (15).

Combining (10) and (11) results in

$$E_T = 0.905\,(1 - E_F)\sqrt{\frac{RD\pi^2 t}{a^2}} + (0.0189 + 0.981\,E_F) \qquad (12)$$

At low efficiencies and for a constant R a plot of E_T against the square root of contact time should yield a straight line the intercept of which may be used to yield E_F. Knowing E_F, one can use the slope of the line to obtain the correlation factor R.

High efficiency studies. At higher E_m values all but the first term of the series on the right side of Equation (7) are negligible. Equation (7) reduces to

$$\ln(1 - E_m) = -\lambda_1^2\frac{RDt}{a^2} + \ln 6B_1 \qquad (13)$$

Combining (13) and (10) results in

$$\ln(1 - E_T) = -\lambda_1^2\frac{RDt}{a^2} + \ln 6B_1\,(1 - E_F) \qquad (14)$$

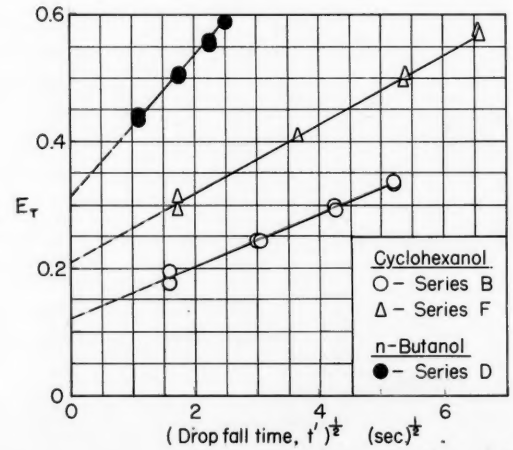

Fig. 3. Typical plot of data in accordance with Equation (12).

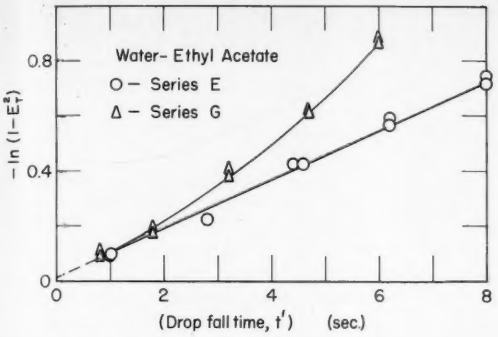

Fig. 4. Plot of data for ethylacetate diffusing into water, in accordance with modified Vermeulen equation.

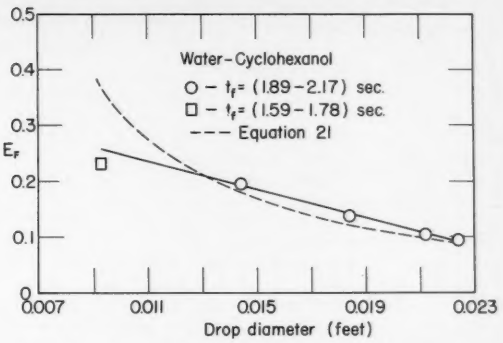

Fig. 5. Experimental E_F for water-cyclohexanol compared with a theoretical equation.

For high-efficiency data for a constant R, Equation (14) dictates that one should plot ln $(1-E_T)$ against time of contact to obtain E_F from the intercept and R from the slope. A knowledge of B_1 and λ_1 is necessary.

Prediction of R for various mechanisms

It is apparent from the above discussion that for data for noncirculation drops application of either Equation (12) or (14) should yield $R = 1$. For a circulating drop under the conditions of the Kronig and Brink model R should be about 3.

For drops with turbulent circulation R should be larger. When one uses the Handlos and Baron model for comparison purposes,

$$R = \frac{N_{Pe_1}}{2{,}048}\int_0^1 (6r^3 - 8r + 3)\,dr = \frac{N_{Pe_1}}{2{,}048} \qquad (15)$$

Hence this model predicts that R is directly proportional to the modified Peclet number.

For any mechanism it is apparent from Equation (10) that

$$\ln(1-E_m) = \ln(1-E_T) - \ln(1-E_F) \qquad (16)$$

whence

$$\frac{d\ln(1-E_m)}{dt} = \frac{d\ln(1-E_T)}{dt} \qquad (17)$$

for E_F constant

It follows from equation (17) that on a plot of ln $(1-E)$ against contact time the slope of the experimental curve is independent of the magnitude of the combined end effect. This is a necessary condition that a transfer mechanism for the steady-fall period holds.

Transfer mechanisms during formation and coalescence

In order that the method discussed above for the calculation of the combined end effect be applicable it is necessary that E_{f1} and particularly E_{f2} be independent of concentration.

By assuming Higbie's equation (*13*) for transient diffusion into the surface of a drop as it is formed, Heertjes *et al.* (*11*) developed the following equation for the formation efficiency:

$$E_{f1} = \frac{20.6}{d}\sqrt{\frac{D\theta}{\pi}} \qquad (18)$$

For the coalescence end it was assumed that as each drop settled it spread as a layer of initial uniform concentration C_s across the previously settled phase and that transient mass transfer occurred until the next drop arrived to cover the surface.

If the interface area is A_i and the instantaneous rate is again given by Higbie's equation, the amount transferred is that which occurs in time θ and is equal to the mass gained by the drop in the coalescence zone:

$$\int_0^\theta A_i(C^\circ - C_s)\sqrt{\frac{D}{\pi t}}\,dt = 2A_i(C^\circ - C_s)\sqrt{\frac{D}{\pi}}\,\theta^{1/2} = v(C_s - C_s) \qquad (19)$$

whence

$$E_{f2} = \frac{2A_i}{v}\sqrt{\frac{D\theta}{\pi}} \qquad (20)$$

By these mechanisms it is apparent that E_{f1} and E_{f2} should be functions of the drop size and time of formation. These variables and, no doubt, the continuous-phase velocity must be kept constant during a given series of runs in which the contact time is varied. It is particularly important to argue that E_{f2} is independent of the concentration C_s, since the latter varies with the column height during a particular study for a given drop size and drop rate.

Combining Equations (18) and (20) yields the following estimate of the combined end effect:

$$E_F = E_{f1} + E_{f2} - E_{f1} \times E_{f2} = \left(\frac{20.6}{d} + \frac{2A_i}{v}\right)\sqrt{\frac{D\theta}{\pi}} - \left(\frac{41.2A_iD\theta}{dv\pi}\right) \qquad (21)$$

Experimental details

The data reported and discussed in this paper are for the transfer of cyclohexanol, *n*-butanol, and ethyl acetate into water drops falling through these phases previously saturated with water. The relevant physical properties for these compounds are listed in Table 2.

Figure 2 shows the simple apparatus used in this study. The continuous phase was contained in a column 71 mm. I.D. This column was equipped with a drain cock for continuous removal of the settled dispersed phase and also with a side arm near the bottom for adjustment of the level of the continuous phase in the column.

Table 2. Relevant Physical Properties for the Systems Used in This Study at 24.5° ± 0.5°C.

	Cyclohexanol	*n*-Butanol	Ethyl acetate
ρ_c (lb./cu. ft.)	59.5	52.4	55.8
μ_c [(lb./(ft.)(sec.)]	0.0120	0.00191	0.000336
σ [lb./(sec.)^2]†	0.00716	0.00330	0.0113
C° (wt. %)	3.90	7.35	8.73
D (sq. ft./sec.)‡ 10^5	0.910	0.957	0.998

† ρ_D was determined with water as solvent by the use of the Wilke correlation (*24*).
‡ σ was determined by the pendant drop method (*1*).

Table 3. Nozzles Used in This Study

Series	Nozzle type	Size, in. I.D.	O.D.
C	45 deg., beveled end	9/30	1/2
B	45 deg., beveled end	7/30	1/2
A	45 deg., beveled end	1/6	1/4
D	45 deg., beveled end	3/20	1/4
E	45 deg., beveled end	1/10	1/4
F	45 deg., beveled end	1/12	1/4
G	plane-end, thin-wall tube	3/60	
H	45 deg., beveled-end glass tube	1/30	1/4
J	plane-end, hypodermic needle	B-D 20	
K	plane-end, hypodermic needle	VIM 23	

The holdup of coalesced dispersed phase and the diameter of the interface at coalescence were kept constant for all runs at approximately 0.75 cc. and 3/8 in. respectively.

The water was admitted from a burette through a long jacketed nozzle with interchangeable tips of various diameters. For the most part, sharp-edged nozzles of the type used by Hayworth and Treybal (*12*) were used; details are listed in Table 3. All drops except for the series *A*, *B*, *C*, and *D* for the water-butanol system were formed in the continuous phase. For the series noted, the drops were formed about one drop diameter above the continuous phase to prevent the continuous phase from running up the nozzle.

The drop rate and the drop volume were determined by counting the drops formed from a given volume of water over a time period. The drop contact time was obtained by timing the fall of drops by a stop watch, the watch being started as a drop detached itself from the nozzle and stopped when the drop struck the coalesced dispersed phase.

Drops of each size and for the various drop-formation times indicated in Table 4 were allowed to fall through various depths of the continuous phase. The first settled dispersed phase was discarded; then the settled aqueous phase leaving the column was sampled until a steady final concentration (C_4) was obtained.

All experimental work was carried out in a constant-temperature room at 24.5° ± 0.5°C. The dispersed phase leaving the apparatus was analyzed with a Bausch and Lomb dipping refractometer which had been previously calibrated with known solutions.

For series *A* and *B* (where $E_F = 0.100$) for the water–*n*-butanol system a layer of linseed oil was used to separate the continuous phase from the coalesced dispersed phase in an effort to lower E_{f2}. However for series *B* without linseed oil as a separating layer E_F was found to be less than it was when the separating layer was used. This indicated that the linseed oil separating layer served no useful purpose and was abandoned in later work.

DISCUSSION OF DATA OBTAINED

Use of the proposed plotting techniques

Figure 3 shows typical data plotted in the manner indicated by Equation (12), that is as E_T directly against $t^{1/2}$. Intercept values on such graphs yielded E_F values, and the slopes of the lines combined with these E_F numbers gave numerical values of the correlation factor. This method was found suitable for *n*-butanol and for cyclohexanol diffusing into water.

Figure 4 indicates the method of plotting efficiency data over a large range indicated by the Vermeulen equation (*22*). These data were for ethyl acetate diffusing into water, and these drops in all cases were oscillating. It appears that the high transfer rates encountered in the fall period of these drops obscure the end-effect transfer efficiency. The slight curvature of the upper line on Figure 4 is not explained. Values of R were obtained for this system with no end effect assumed and the straight-line portion of the curves at low contact times used.

Combined end effects

A comparison of the experimental combined end effect with that predicted by Equation (21) for cyclohexanol diffusing into water is shown as Figure 5. It is seen that the trend of E_F with diameter is as predicted.

Studies of the correlation factor R

Figure 6 indicates plots of the correlation factor of this study plotted against the modified Peclet number by Handlos and Baron. This was chosen as a correlation group to permit comparison of data with their model and also because this group includes the product of the drop velocity and diameter, both of which are significant variables in discussing the flow characteristics of a drop.

This figure shows the data for cyclohexanol and for *n*-butanol diffusing into

Table 4. Summary of Experimental Data for Water Drops in Organic Liquid Saturated with Water at 24.5° ± 0.5°C.

Series	Drop diameter *d*, ft.	Drop formation time, sec.	Drop velocity *V*, ft./sec.	Drop Reynolds number N_{Re}	Modified Peclet number $(N_{Pe}'_4)\ 10^{-5}$	Combined end effect E_F	Experimental R	R_{KB}	R_{HB}	
C	0.0224	1.89-2.17	0.142	15.7	3.32	0.0947	3.8	3.7	160	
B	0.0212	1.89-2.17	0.139	14.6	3.07	0.103	3.2	3.7	150	
A	0.0184	1.89-2.17	0.121	11.0	2.32	0.137	2.3	3.7	110	Cyclohexanol
F	0.0142	1.89-2.17	0.0863	6.06	1.28	0.194	3.2	3.4	63	
J	0.00924	1.59-1.78	0.0482	2.20	0.464	0.232	2.2	3.0	23	
A	0.0114	3.03-3.45	0.258	80.8	2.33	0.224	15	3.2	110	
D	0.00982	1.10-1.21	0.260	70.3	2.02	0.290	7.8	3.2	99	
E	0.00804	1.00-1.11	0.232	51.2	1.48	0.311	3.8	3.2	72	
F	0.00722	1.00-1.11	0.212	42.0	1.21	0.303	2.7	3.2	59	*n*-Butanol
B	0.0121	1.20-1.49	0.240	79.8	2.30	0.040	35	2.8	110	
B	0.0124	1.49-1.69	0.240	81.8	2.36	0.100	34	2.8	110	
C	0.0133	3.00-4.00	0.238	87.0	2.51	0.070	33	2.8	120	
E	0.0149	1.30-1.40	0.283	699	1.51		52	2.8	74	
F	0.0131	1.20-1.39	0.289	628	1.36		39	2.8	66	
G	0.0116	1.20-1.39	0.303	583	1.26		42	2.8	61	Ethyl acetate
J	0.00992	1.00-1.21	0.319	526	1.14		32	2.8	56	
K	0.00845	1.00-1.21	0.305	429	0.926		29	2.8	45	

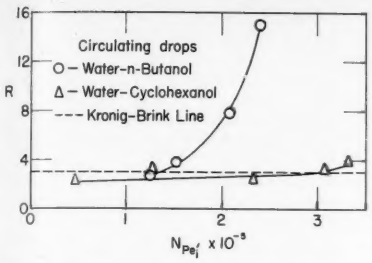

Fig. 6. Experimental R compared with a theoretical model.

water. All drops in this study were observed to be circulating, with Hadamard type of streamlines, when aluminum powder was suspended in the water.

It would appear that the R values of the Kronig and Brink equation are approached at low drop Reynolds numbers but that R increases with the product of drop diameter and velocity to values several times the value of the Kronig-Brink correlation.

Figure 7 shows similar R values of ethyl acetate diffusing into water drops. Here all drops were oscillating, and aluminum powder inside the drops showed no regular circulation pattern. Values of R in the range 29 to 52 have been observed. The trend is similar to that predicted by the Handlos and Baron correlation, but the observed values are somewhat lower.

Time of contact

It may be noted in the nomenclature that the contact time in the steady-fall–period equations may be slightly less (by Δt) than the observed time t^1. In practice in this paper Δt was assumed to be negligible.

CONCLUDING REMARKS

This paper has reported data on mass transfer rates inside circulating and oscillating drops. By use of two component systems with the continuous phase saturated with the dispersed phase, the transfer rates inside the drops could be studied without the necessity for correcting for an outside resistance.

The choice of the system and the use of end-effect efficiencies have permitted the comparison of the magnitude both of the combined end effect and of the correlation factor with values predicted by various mechanisms in the literature.

The Kronig and Brink mechanism applies well for low drop Reynolds numbers, but it has been shown that the correlation factor may rise above that predicted by Kronig and Brink even though a drop is apparently circulating.

For oscillating drops the Handlos and Baron model shows considerable promise.

A model for transfer at the settling end has been proposed. Combined with the Heertjes model for drop formation, it predicted the combined end effect fairly well. However this may have been accidental.

NOTATION

A_i = interfacial area at coalescence
a = drop radius
B = coefficient
C = concentration of dispersed phase (uniformly mixed)
d = drop diameter
D = molecular diffusivity
E = effective diffusivity
E = dimensionless number given by $(E_m \leqq E \leqq E_T)$
E = transfer efficiency
N_{Re} = Reynolds number, $(dV\rho_o)/(\mu_o)$
N_{Pe_i} = modified inside Peclet number, $(dV)/[D(1 + \mu_i/\mu_o)]$
R = dimensionless correlation factor
r = $\rho/(d/4)$
Δt = time from the point of drop release from the nozzle to the point when transfer mechanism of the steady-fall period holds
t^1 = time taken by drop to strike the coalesced dispersed phase from the point of drop release from the nozzle
t = $(t^1 - \Delta t)$
v = drop volume
V = drop velocity

Greek letters

λ = eigenvalue
σ = interfacial tension
ρ = density, radius of circulation patterns
θ = drop formation time
μ = viscosity

Subscripts

1 = in the nozzle
2 = beginning of transfer mechanism of the steady-fall period
3 = point at which drop strikes the coalesced dispersed phase
4 = at column outlet
T = over-all, based on points 1, 4
o = continuous phase
i = drop or dispersed phase
m = steady-fall period
n = term number in series sum
f_1 = end effect at entry end for dispersed phase
f_2 = end effect at exit end for dispersed phase
KB = predicted by Kronig and Brink [Equation (3)]
HB = predicted by Handlos and Baron [Equation (4)]
* = at equilibrium with respect to transfer of solute to or from dispersed phase

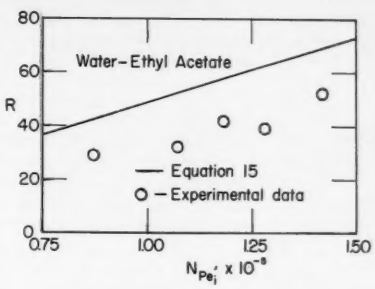

Fig. 7. Experimental R for oscillating drops compared with a theoretical model.

LITERATURE CITED

1. Andreas, J. M., E. A. Hauser, and W. B. Tucker, *J. Phys. Chem.*, **42**, 1001 (1938).
2. Calderbank, P. H., and I. J. O. Korchinski, *Chem. Eng. Sci.*, **6**, 65, 78 (1956).
3. Coulson, J. M., and S. J. Skinner, *ibid.*, **1**, No. 5, 197 (1952).
4. Elzinga, E. R., and J. T. Banchero, *A.I.Ch.E. Journal*, to be published.
5. Geankoplis, C. J., and N. A. Hixson, *Ind. Eng. Chem.*, **42**, 1141 (1950).
6. Geankoplis, C. J., R. L. Wells, and E. Hawk, *ibid.*, **43**, 1848 (1951).
7. Gier, T. E., and J. D. Hougen, *ibid.*, **45**, 1362 (1953).
8. Grober, H., *Z. Ver. deut. Ing.*, **69**, 705 (1925).
9. Hadamard, J., *Compt. Rend.*, **152**, 1735 (1911).
10. Handlos, A. E., and T. Baron, *A.I.Ch.E. Journal*, **3**, 127 (1957).
11. Heertjes, P. M., W. A. Holve, and H. Talsma, *Chem. Eng. Sci.*, **3**, 122 (1954).
12. Heyworth, C. B., and R. E. Treybal, *Ind. Eng. Chem.*, **42**, 1174 (1950).
13. Higbie, Ralph, *Trans. Am. Inst. Chem. Engrs.*, **31**, 365 (1935).
14. Johnson, H. F., Harding Bliss, *ibid.*, **42**, 331 (1946).
15. Johnson, A. I., A. E. Hamielec, D. Ward, and A. Golding, *Canadian J. Chem. Eng.*, **36**, 221 (1958).
16. Kronig, R., and J. C. Brink, *Appl. Sci. Res.*, **A-2**, 142 (1950).
17. Licht, William, and C. J. Conway, *Ind. Eng. Chem.*, **42**, 1151 (1950).
18. Licht, William, and W. F. Pansing, *ibid.*, **45**, 1885 (1953).
19. Newman, A. B., *Trans. Am. Inst. Chem. Engrs.*, **27**, 203 (1931).
20. Sherwood, T. K., J. E. Evans, and J. V. A. Longcor, *Ind. Eng. Chem.*, **31**, 1144 (1939).
21. Treybal, R. E., "Liquid Extraction," p. 381 McGraw-Hill, New York (1951).
22. Vermeulen, Theodore, *Ind. Eng. Chem.*, **45**, 1664 (1953).
23. West, F. B., P. A. Robinson, A. C. Morgenthaler, T. R. Beck, and D. K. McGregor, *ibid.*, **43**, 234 (1951).
24. Wilke, C. R., *Chem. Eng. Progr.*, **45**, 218 (1949).

Manuscript received April 3, 1959; revision received July 29, 1959; paper accepted August 5, 1959. Paper presented at A.I.Ch.E. Atlantic City meeting.

Compressions of Liquids

This three-part paper reports on the first step of a study of the liquid state initiated in 1954 by Union Carbide Chemicals Company. The ultimate objectives of this program are to elucidate the mechanism of the flow process and to write an equation of state that is valid continuously from the melting point through the ideal-gas region.

Only the compressions of the *n*-alkanes (ratios of the volumes under the pressures of measurement to the volume under the initial pressure at the same temperature) are here considered. An accuracy of four significant figures in the measurement was sought to enable the subsequent calculation of the thermodynamic properties of these liquids to be made with equivalent accuracy.

I. Apparatus and Method of Measurement

ARTHUR K. DOOLITTLE

Union Carbide Chemicals Company, South Charleston, West Virginia

IVAN SIMON and RAYMOND M. CORNISH

Arthur D. Little, Inc., Cambridge, Massachusetts

A novel type of piezometer used to measure the compressions of liquids from 20° to 300°C. and from 1 to 4,000 kg./sq. cm. is described. The accuracy anticipated is 4 parts in 10,000.

The four essential operations involved in the determination of the compressions of liquids are measurements of volume, pressure, temperature, and mass of the sample. Of these the determination of volume with an accuracy better than one part in 10,000 under pressures up to 4,000 kg./sq. cm. and temperatures up to 300°C. was the most difficult problem experimentally. Several known methods of measurement were considered and rejected. For example the method of Beattie (*1*), which depends upon the accuracy of the calibrated mercury injector and the sample bulb, was not applicable beyond the pressure range of 0 to 500 kg./sq. cm. The piston-displacement method of Bridgman (*2*) has limited accuracy in the lower pressure range because of friction and is not easily adapted for temperatures higher than 100°C. The accuracy of the method of metallic bellows (*3*) suffers from the inelastic hysteresis of the bellows. The glass piezometer of Adams and Gibson (*4*) allows determination of only one volume at one filling and therefore is too slow. The glass piezometer with sealed-in contacts used extensively by Michels (*5*) and his co-workers has high accuracy but is not operable above 200°C. because the mercury dissolves the platinum contacts at the higher temperatures. Since none of these and other known methods were entirely satisfactory for the purpose of this investigation, a novel type of piezometer was developed.

Although the piezometer is the most critical part of the apparatus, the other components such as the pressure plant, the pressure gauge, and the temperature control will also be described because they are all functionally interconnected.

APPARATUS

The piezometers to be described were based on the idea that the displacement of a small iron core could be measured from the outside of a pressure container made of an austenitic, nonmagnetic steel by means of a linear differential transformer (*6*). The iron core floated on the surface of mercury enclosing the liquid under test.

The piezometers were made of lengths (about 19 in.) of precision-drawn, thin-walled stainless steel (type 321) tubing (0.097-in. O.D., 0.005-in. wall) terminated by screw closures at the top and mercury valves at the bottom. During measurements the piezometer was positioned in a pressure container consisting of thick-walled, high-pressure stainless steel (type 316) tubing (0.375-in. O.D., 0.125-in. I.D.) which was filled with light mineral oil as a pressure-transmitting medium. The pressure was transmitted to the sample via a column of mercury which communicated with the oil medium in the mercury cup at the bottom of the apparatus (Figure 1).

The construction of the piezometer is shown in detail in Figure 2. The top, which was silver-soldered to the stainless steel piezometer tube, was provided with a closure consisting of a steel socket set screw (No. 2-56, ½ in. long) fitting into a cone seat with a 60 deg. angle. The sample, introduced into the piezometer through the top with a long hypodermic syringe, filled it to the cone seat. Then the socket screw was put in and tightened with a miniature wrench. Repeated tests with a helium-leak detector proved that this seal remained completely tight over the whole temperature range.

The small lateral dimensions of the piezometer resulted in a considerable saving on the volume of sample and in a great reduction of the thermal capacity of the entire apparatus. The length of the sample column was sufficient to allow accurate determination of the compression; in a typical arrangement the sample column was approximately 100 mm. long, its length being determined by readings on the external micrometer directly to 0.01 mm. (Five microns can be estimated on the dial.)

Volume Measurement

The volume of the sample in the piezometer was essentially the volume between the electromagnetic centers of the plug at the top and the float that rode on the mercury column.

These electromagnetic centers were located from without the apparatus by means of two small linear differential transformers, which slid with small clearance over the surface of the pressure vessel. These two coils were mounted securely on a stainless steel rod so that their distance apart was fixed (*a* in Figure 1). An Invar wire passing over a pulley connected the coil suspension with a precision micrometer slide. It was necessary to use two coils because the micrometer slide commercially available did not have a span large enough to cover the whole length of the sample column directly.

The transformers were connected to an A.C. 1,000 cycles/sec. bridge with a vacuum-tube voltmeter as a null indicator (*7*). Either coil might be switched into this circuit at will. To balance the bridge, one of the coils was moved until either the plug or the float, depending on which coil was moved, lay in the exact electromagnetic center of that coil. This position, indicated by a very sharp minimum deflection of the voltmeter, could be located easily to within 5 μ on the dial scale of the micrometer. Manipulation of the dial thus permitted one to center the top coil on the plug and the bottom coil on the float.

The difference between these two readings x established the distance X

between the float and the plug. Thus if a was the difference between two coils and x the difference between the two readings of the micrometer, the length of sample in the piezometer would be $X = x + a$. The volume of sample contained in the instrument at the temperature and pressure of measurement could then be determined from the length X, the cross-sectional area A of the piezometer, and the initial volume.

Measurement of Mass

The mass of the sample contained in the piezometer was measured by direct weighing of the piezometer before and after filling it with the sample.

A simple plug valve at the bottom of the piezometer made it possible to introduce the predetermined amount of mercury; then the piezometer was weighed before being filled with sample, as described above. After the two weights had been obtained, this valve was opened by rotating it with a key until a small inner hole lined up with a similar hole in the wall of the piezometer. This was done with the piezometer dipping into the mercury reservoir at the base of the apparatus (Figure 1).

The weight of the sample was also checked by weighing the filling pipette (hypodermic syringe) before and after the sample was transferred to the piezometer. By either method the mass could be weighed to 0.2 or 0.3 mg, but on a sample weight of 0.3 g. this represented accuracy of only one part in 1,000, which is at least an order of magnitude less than the accuracy attainable in the measurements of pressure, volume, and temperature. For this and other reasons the mass of sample was determined by indirect methods, as described in a companion paper (*8*).

Temperature Control and Measurement

Because the steel piezometer with its surrounding pressure vessel represented a relatively small mass of low heat capacity, the temperature control was simplified with respect to both changing from one temperature to another and maintaining a fixed temperature accurately during a set of volume measurements at various pressures.

The pressure vessel containing the piezometer and surrounded by the two differential transformer coils was immersed in an oil bath 3 in. in diameter and extending approximately 8 in. above and 5 in. below the sample. The bath was insulated with magnesia-pipe insulation and asbestos soaked with water glass. Two heaters were employed; one, an electric heating tape, was wound spirally around the outside of the oil bath container, and the other was an immersion heater inside the oil bath. Dow-Corning No. 710 fluid was used as the heat transfer medium, and a small electric stirrer provided adequate circulation. The external heater was controlled manually by a variac; the immersion heater was connected to a thyratron controller, but it was found that even better temperature control could be maintained during the period of a run by manual operation of the variac. The vertical temperature gradients were checked by means of three thermocouples attached to the steel tube containing the piezometer, and the variations never exceeded a few hundredths of a degree. The temperature was maintained uniform to within $\pm 0.1°C.$, but the actual temperature was measured to five significant figures at the moment of each measurement of volume. Temperatures were measured with a platinum resistance thermometer and Mueller resistance bridge.

Pressure Measurement

The dead-weight or free-piston gauge was chosen for the measurement of high pressures because of its accuracy and its ability to maintain the pressure constant during operation. In such a gauge the internal pressure in a system is balanced by the force of a known weight acting upon a piston of known area. Two conditions must be satisfied for the practical application of this principle: first, there must be negligible friction between the piston and the cylinder walls, and, second, there must be little leak of the pressure-transmitting oil. These conditions are resolved by the rotation of the piston above the critical velocity so that a continuous film of oil is maintained.

The Michels dead-weight gauge, or pressure balance, which became available shortly after this project was started, consists essentially of a differential piston moving in a cylinder that contains two coaxial bores. The cylinder is mounted in a frame, and the piston is connected to a weight-carrying shaft at the bottom and a pointer arm at the top. The assembled pressure balance, as made by the 'T Hart Company, is shown in Figure 3.

The piston is a tight fit in the cylinder until pressure is applied, the hydraulic pressure causing a slight expansion in the

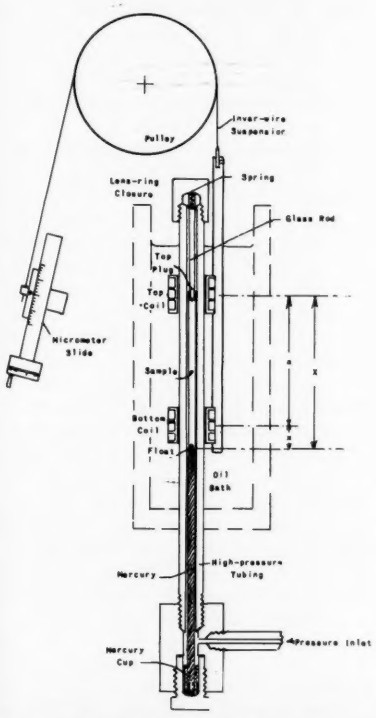

Fig. 1. Schematic diagram of steel piezometer and measuring assembly (not a scale drawing; mechanical details omitted).

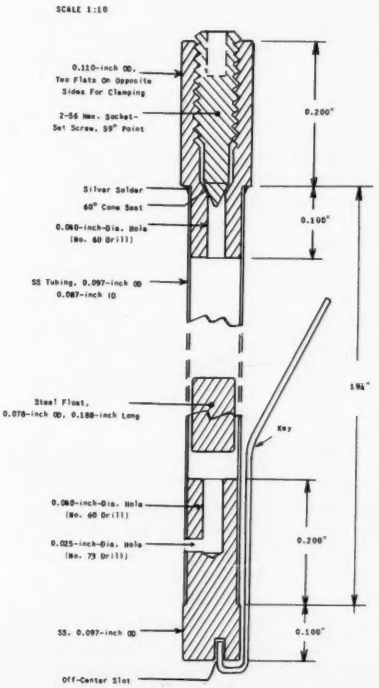

Fig. 2. Steel piezometer.

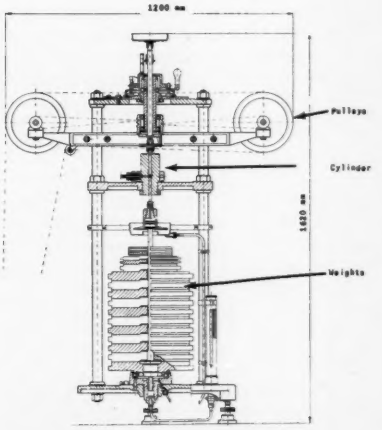

Fig. 3. Michels pressure balance.

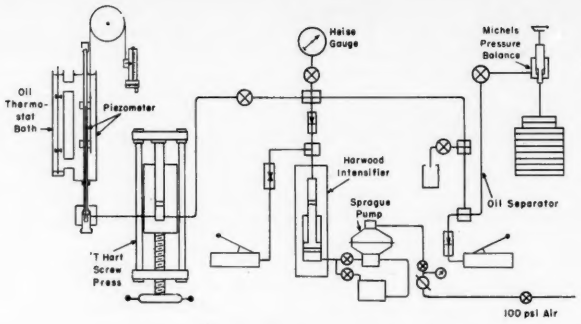

Fig. 4. Pressure plant.

cylinder walls and also a slight decrease in the area of the piston. Under these conditions the piston can rotate freely, and there is sufficient leakage to ensure continuous oil-film lubrication. A motor-driven pulley system rotates the piston and the column of weights above the critical velocity of about 50 to 60 rev./min. At the time of measurement a clutch is disengaged, and the piston and weights can therefore rotate freely by their own momentum. A mixture of 75% Shell Talpa 30 and 25% Shell Diala AX (by volume), having a viscosity of approximately 80 centipoises at 25°C., was found to be satisfactory. Under pressure the piston and weights can fall through 2 cm. of free travel. With an oil of proper viscosity a good cylinder with piston and weights rotating freely takes 5 to 10 min. to fall this 2 cm.

The Michels pressure balance has a series of six measuring cylinders that cover a range from 118 to 4,000 kg./sq. cm. There are twelve 50-kg., one 10-kg., two 5-kg., and five 1-kg. weights, all calibrated to 0.1 g.

For low pressures a Bourdon-tube gauge was employed which, over the range of 0 to 250 kg./sq. cm., had an accuracy of better than 1 part in 1,000, as demonstrated repeatedly by checks against the Michels pressure balance.

Pressure Plant

The diagram of the pressure plant is shown in Figure 4. Pressures up to 8,000 kg./sq. cm. can be generated by means of a Harwood intensifier operated by a 1,500-kg./sq. cm. Sprague air/oil booster pump or by a Blackhawk hand pump. A screw press allows fine adjustments of volume and pressure directly on the high-pressure side (up to 4,000 kg./sq. cm.).

The high-pressure vessel consists of a vertical section of ⅜-in. O.D. by ⅛-in. I.D. cold-drawn stainless steel tubing, approximately 40 in. long, connected to the various components of the system through 5/16-in. O.D. by 1/16-in. I.D. cold-drawn stainless steel (type 316) tubing which was proof tested by the supplier at 130,000 lb./sq. in. The rupture pressure is 20,000 to 40,000 lb./sq. in. above the proof test. Harwood series 5 M fittings, designed for service to 100,000 lb./sq. in., are used for connecting the various components.

The pressure-transmitting fluid is Shell Diala AX, which has a viscosity of approximately 30 centipoises at 25°C. and can withstand the maximum operating temperature (300°C.) without excessive decomposition. Its viscosity rises rather rapidly with pressure. Thus in the upper limit of the working range (4,000 kg./sq. cm.) the time necessary to reach equilibrium between the pressure gauge and the pressure vessel may be a minute or more, which makes it difficult to obtain pressure equalization throughout the system in the time allowed for the piston to sink freely on the leaking oil film.

Since the pressure balance requires a different type of oil for satisfactory operation, a fluid separator, consisting of a 4-ft. vertical section of the same ⅜-in. O.D. by ⅛-in. I.D. high-pressure tubing, was inserted. A second Blackhawk pump supplied fresh balance oil from a reservoir through a high-pressure check valve.

CALIBRATION

Volume-Measuring Instrument

The cross-sectional areas of the piezometers were determined at atmospheric pressure by weighing small increments of mercury released from the instrument and observing the corresponding drop in the level of the steel float by means of the sensing coil. From the density of mercury the volume of mercury released is computed. This volume divided by the corresponding difference in level is equal to the area of cross section. The precision-drawn polished stainless steel tubing was found to be uniform to better than ± 0.05% in cross section over the length used.

The setting constant a, which represents essentially the distance between the electromagnetic centers of the two sensing coils, can be determined by filling the sample space with a known volume of liquid. The difference between the top and bottom coil readings added to the length of the column of liquid is equal to the setting constant. As long as the distance between the coils is mechanically fixed, and if the float and the plug are not changed, the value of the setting constant is fixed except for the change resulting from the thermal expansion of the apparatus. The accuracy of the measurements, reduced as explained in the succeeding papers, does not depend on the accuracy of the setting constant, since the extrapolated zero-pressure volumes are shown to be far more accurate than the initial volumes computed from low-pressure measurements by use of the setting constant.

The change in the cross-sectional area of the piezometer as a result of the thermal expansion of the metal must be taken into account, but any change in the length of the piezometer or in the column of mercury inside it is immaterial, since the length of the column of sample is measured independently of its surroundings.

The temperature dependence of the setting constant results from the linear expansion of the section of the stainless steel suspension rod between the sensing coils; the value of $1.62 \cdot 10^{-5}$ deg.$^{-1}$ was used for the thermal expansion coefficient of the steel used (type 321). Similarly the thermal expansion causes an increase of the cross-sectional area of the piezometer at a rate of $3.24 \cdot 10^{-5}$ deg.$^{-1}$

Hydrostatic pressure decreases the cross-sectional area of the piezometer tubing by a factor of approximately $(1 - 3.9 \cdot 10^{-7}\, p)$, where p is in kg./sq. cm. A series of test runs with pure water up to pressures of 3,000 kg./sq. cm. indicated that the compression is actually smaller than the value estimated from the formula above and below the limits of observational accuracy.

The combined experimental errors involved allowed the measurements of volume to be made with an accuracy of one part in 10,000 at all temperatures and at all pressures except those in the neighborhood of 1 atm. The loss of accuracy at very low pressures is presumably occasioned by a change in the shape of the meniscus at the mercury-sample interface.

Temperature-Measuring Instrument

The platinum resistance thermometer was calibrated by the manufacturer by comparison with a platinum resistance thermometer certified by the National Bureau of Standards. One check of the resistance at the ice point agreed exactly with the manufacturer's calibration; which assures an accuracy in the measurement of temperature of at least one part in 10,000.

Pressure-Measuring Instrument

The calibration of the dead-weight gauge was supplied by the manufacturer. Certificates of calibration by The Netherlands Bureau of Standards

accompanied the weights and cylinders, guaranteeing an accuracy of one part in 10,000 in the measurement of pressure.

Over-All Accuracy

When one combines the errors in the measurement of temperature and volume, a conservative estimate of the probable over-all accuracy of measurement may be placed at 4 parts in 10,000, which assures four significant figures in specific volume. [Statistical analyses of the data on two compounds, *n*-heptane and *n*-eicosane, described in a companion paper (8), indicate that the over-all accuracy for the entire range of temperatures and pressures is more likely to be of the order of 3 parts in 10,000.]

Over 4,000 measurements of volume under pressure were made in the course of this program. The presentation and complete evaluation of these and other liquid *n*-alkane data is the subject of the companion papers (8, 9).

ACKNOWLEDGMENT

J. A. Beattie of the Massachusetts Institute of Technology and A. Michels of the University of Amsterdam served as consultants on the experimental phases of this project and contributed to its successful outcome in many ways. R. W. Zwanzig of Johns Hopkins University and J. C. Poirier of Duke University were retained as consultants on other phases of the project. The experimental work was carried out at Ohio State Research Foundation, Columbus, Ohio (preparation of *n*-triacontane and *n*-tetracontane) and at Arthur D. Little, Inc., Acorn Park, Cambridge, Massachusetts (measurements of volume under pressure), under contracts with Union Carbide Chemicals Company.

II. Critical Evaluation of New *n*-Alkane Data: *n*-Heptane to *n*-Tetracontane

ARTHUR K. DOOLITTLE and DORTHA B. DOOLITTLE

Union Carbide Chemicals Company, South Charleston, West Virginia

New measurements of the volumes of liquid *n*-alkanes of 7, 9, 11, 13, 17, 20, 30, and 40 carbon atoms over a range of temperatures from 20° to 300°C. and pressures from 0 to 4,000 kg./sq. cm. have been made. These volume measurements are here reduced to compressions $(vol^p_T)/(vol^o_T)$, and the accuracy of the measurements has been determined. Analysis of the data for *n*-heptane and *n*-eicosane shows that the order of accuracy of the compressions of each of these compounds appears to be approximately 3 parts in 10,000. Evaluation of random multiple measurements on the remaining six compounds indicates that their over-all accuracy is likewise of this same order.

The volumes of small samples of eight *n*-alkanes, from 7 to 40 carbons, were measured by Simon and Cornish at a number of temperatures from 20° to 300°C. and over a range of pressures from 0 to 4,000 kg./sq. cm., with the apparatus and method described in the prior paper (10). This method has the advantage of very high accuracy in the measurement of volumes under pressure, but it does not afford equivalent accuracy in the direct measurement of the weight of the material whose volume is being measured. It is therefore necessary to resort to indirect means of determining the sample weight.

Also this procedure measures volumes very accurately under high pressure, but somewhat less accurately at low pressures. Therefore, to realize the full advantage of the method it is necessary to establish the values of the zero-pressure volumes with more certainty than is possible by extrapolating the lower pressure values alone.

A procedure was devised for making an indirect extrapolation to zero pressure of the volumes measured at higher pressures which gives values fully as accurate as the measurements. When applied to the Simon and Cornish data, this procedure permits the results to be reported as compressions or ratios of the volume at the pressure of measurement to the zero-pressure volume $(vol^p_T)/(vol^o_T)$.

Dortha B. Doolittle is at the West Virginia Institute of Technology, Montgomery, West Virginia.

PURITY OF SAMPLES

The preparation and characterization of the samples of *n*-heptane, *n*-nonane, *n*-undecane, *n*-tridecane, and *n*-heptadecane used in this study have been described elsewhere (11). The remaining pure compound *n*-eicosane, was synthesized as follows. Decanol-1, was purified and brominated with anhydrous hydrogen bromide at 100°C. The purified 1-bromodecane was converted to *n*-eicosane by a Wurtz reaction with sodium. The crude distilled product was hydrogenated and fractionated, the fractions of common density being combined. The composite had a freezing point of 36.51°C.; the freezing point of pure *n*-eicosane is reported (12) to be 36.8°C.

The other two samples were characterized as follows: *n*-tricontane freezing point 65.512°C., purity (13) 99.48%; *n*-tetracontane freezing point 81.030°C., purity 98.6%.

DETERMINATION OF ZERO-PRESSURE VOLUME

Linear extrapolation of the volumes of sample under pressure is satisfactory at temperatures well below the normal boiling point of the substance being measured, but this method fails in the neighborhood of the normal boiling point and is obviously inapplicable above this temperature. An indirect extrapolation procedure was therefore devised which makes use of a pressure-volume relationship that has so far received very little attention in this country. This relationship used by Bett, Weale, and Newitt (14) for evaluating data on the compression of liquids, was originally proposed by Hudleston (15):

$$\ln \frac{P(vol^p_T)^{2/3}}{(vol^o_T)^{1/3}-(vol^p_T)^{1/3}} = C_1 + C_2[(vol^o_T)^{1/3}-(vol^p_T)^{1/3}]$$

One of the features of the Hudleston equation is that at low pressures the left-hand member of the equation is very sensitive to small changes in the zero-pressure volume. As the pressure is reduced in the low-pressure region, $(vol^p_T)^{1/3}$ approaches $(vol^o_T)^{1/3}$ and the denominator becomes vanishingly small. A slight error in $(vol^o_T)^{1/3}$ therefore makes a large difference in the quotient at the limit. Since the fit of data to the Hudleston equation is determined principally by the higher pressure points, deviations of the lower pressure points generally suggest an error in the value assigned to $(vol^o_T)^{1/3}$. This feature of the Hudleston equation makes it ideal for the indirect extrapolation of the volumes to the zero-pressure value, as it involves simply trying different values of $(vol^o_T)^{1/3}$ until a value is found that provides the best fit of the lower pressure points to the line determined by the higher pressure points. In this way the best fitting values of (vol^o_T) were determined for each compound at all temperatures of measurements, thereby enabling the compressions to be calcu-

Table 2. Precision of Measurements, *n*-Heptane Deviations in Specific Volume from the Mean of Duplicate Measurements

Temperature, °C.	Pressure range, bars	No. of duplicate measurements	SPE, %
30	116.1 to 3011	18	0.006
50	98.1 to 3011	20	0.006
100	116.1 to 3011	19	0.013
150	39.2 to 1866	17	0.053
200	116.1 to 1577	18	0.012
250	312.3 to 1015	11	0.046
300	508.5 to 1015	6	0.068
		109	

lated with an accuracy as good as the volume measurements themselves.

TYPICAL DATA

As it will be shown in the succeeding paper (9) that the compressions can be reproduced from equations with an accuracy equal in most cases to that of the measurements, only a few typical results for each compound will be given. These data have been chosen to cover the pressure range of the measurements, the points being selected at identical pressures wherever possible.*

PRECISION AND ACCURACY OF MEASUREMENTS

General Considerations

It was first necessary to establish the validity of the extrapolation to the zero-pressure volume by means of the Hudleston equation. The approximately 700 measurements made on *n*-heptane and *n*-eicosane were selected for this purpose for several reasons. *n*-Heptane is the lowest molecular weight compound measured by Simon and Cornish, whereas *n*-eicosane is the lowest molecular weight compound of the group measured which had a normal boiling point substantially above the highest temperature of measurement. Thus the maximum molecular weight and temperature ranges that it is practical to deal with are encompassed by these two compounds. Two independent runs were made with *n*-heptane, in each of which the initial sample filling was used at all temperatures of measurement. This coincidence enabled calculation of the specific volumes of *n*-heptane under pressure at all temperatures, which was desirable because, *n*-heptane having been extensively studied by others, comparisons were possible. With *n*-eicosane specific volumes under pressure could be calculated at all temperatures, since atmospheric-pressure densities were available over the entire range of temperatures.

* Data have been deposited as Table 1, document 6127, with the American Documentation Institute, Photoduplication Service, Library of Congress, Washington 25, D. C., and may be obtained for $1.25 for photoprints or 35-mm. microfilm.

PRECISION OF THE MEASUREMENTS ON N-HEPTANE

The zero-pressure volume is actually the volume of a hypothetical liquid of zero vapor pressure. At temperatures well below the normal boiling point the density of such a liquid should not differ appreciably from the atmospheric-pressure density of a real liquid. Validation of the Hudleston equation for *n*-heptane was therefore carried out in two parallel runs. In each case the weight of the sample in the piezometer was measured (independently of any Hudleston equation calculation) at each of two temperatures. The results were as follows:

Temperature, °C.	Measured weight, run A, g.	Avg., g.	Measured weight, run B, g.	Avg., g.
30	0.30934	0.30948	0.29943	0.29924
50	0.30961		0.29905	

The volumes in the piezometer were measured over a considerable range of pressures at each of these two temperatures and were converted to specific volumes by dividing each by the average measured weight for each of the two runs. A statistical analysis of the differences between the two runs at identical pressures and temperatures showed the root-mean-square deviation from the mean (standard percentage error, or SPE) for both 18 points at 30°C. and 20 points at 50°C. to be 0.006%.

Since the specific volumes from both runs were practically identical, all the values at each temperature were thrown together and fitted to a single Hudleston plot. The value of v°_T giving the best fit to the Hudleston line was then determined at each temperature. The results were as follow:

Temperature, °C.	Calculated v°_T	$1/\rho^\circ_T$ from reference 12
30	1.4807	1.4808
50	1.5191	1.5191

The agreement is one part in 14,808 for 30° and exact for 50°, which establishes the fact that the extrapolation of higher pressure volumes to atmospheric pressure by the Hudleston equation is valid for *n*-heptane.

The measured volumes for each run were converted to specific volumes by dividing them by the corresponding average of the sample weights computed at 30° and 50°C. The fractional deviation from the mean was calculated for each pair of points, and the SPE was determined with the results shown in Table 2. The over-all SPE in specific volume for 109 duplicate points was 0.031%.

Table 3. Precision of Measurements, *n*-Heptane, 0 to 3,000 Bars. Deviations of Calculated from Observed Values of Specific Volume, (IBM Run 5)

Temperature, °C.	No. of points	SPE, %
30	9	0.015
50	9	0.004
100	9	0.011
150	9	0.018
200	9	0.046
250	6*	0.052
300	4*	0.053
	55	

* At temperatures in the neighborhood of and above the critical temperature the lower pressure points lie above the line determined by the higher pressure points, because the zero-pressure volume may equal or exceed the volume at the critical temperature and pressure. Thus at 250°C. it was necessary to reject values through 214.2 bars and at 300°C. values through 508.5 bars.

CALCULATION OF SPECIFIC VOLUME BY HUDLESTON EQUATION

For a single substance the values of C_1 and C_2 of the Hudleston equation are somewhat dependent on the quantity of sample taken, since if $C_1 = A$ and $C_2 = B$ when the sample is 1 g., for any other weight of sample w, $C_1 = A + \ln w^{1/3}$ and $C_2 = B/w^{1/3}$. Therefore when comparing Hudleston parameters one must deal with the same quantity of sample.

The zero-pressure specific volumes for *n*-heptane at the various temperatures of measurement were calculated by dividing the extrapolated zero-pressure volumes by the average of the 30° and 50°C. sample weights. The values of A and B were calculated from the data by the method of least squares.

The extreme accuracy with which the Hudleston equation, with the parameters referred to, reproduces the

Table 4. Hudleston Parameters for *n*-Heptane, Melting Point —90.61°; Boiling Point 98.43°C.

Ref.	t, °C.	A (From velocity of sound)	A (From compressions)	B	$(v^0_T)^{1/3}$
19	0	10.254	10.25	13.2	1.1259
20	0	10.254	10.25	12.9	1.1259
21	4.44	10.221	10.22	13.2	1.1280
22	25	10.005	10.12	12.3	1.1375
20	25	10.065	10.06	12.9	1.1375
24	30	10.026	10.023	13.18	1.1398
23	30	10.026			
21	37.78	9.964	9.95	13.2	1.1435
20	40	9.945	9.94	12.8	1.1447
24	50	9.862	9.854	13.16	1.1495
19	50	9.862	9.80	13.3	1.1492
20	60	9.776	9.77	12.8	1.1548
21	71.11	9.675	9.67	13.2	1.1608
19	95	9.441	9.43	13.2	1.1745
24	100	9.388	9.365	13.18	1.1776
23	100	9.388			
21	104.44	9.341	9.32	13.2	1.1810
21	137.78		8.86	12.7	1.2055
24	150		8.694	13.27	1.2149
23	150		8.72	13.5	1.2133
21	171.11		8.40	13.0	1.2327
24	200		7.566	13.65	1.2756
23	200		7.64	13.9	1.2713
21	204.44		7.44	13.9	1.2800
21	237.78		5.86	14.5	1.3625
24	250		4.752	14.25	1.4300
23	250		4.90	13.5	1.4300
24	300		—17.79	15.60	2.7531

Values of A in column 4 that are carried to three decimal places were calculated from data of Simon and Cornish by the method of least squares. All others were obtained graphically. Data of reference 23 do not extend to high enough pressures to determine the Hudleston line accurately at 30° and 100°C. Column 3 gives the values of A calculated from velocity-of-sound data as explained in the text.

observed specific volumes for *n*-heptane was shown by a machine calculation made on the IBM-650 computer. Temperatures and pressures were chosen for the calculations that exactly duplicated certain Simon and Cornish measurements, and so deviations of the calculated from the measured values could be observed directly. Calculations at each of the following pressures: 116.1, 214.2, 312.3, 508.5, 1,051, 1,577, 2,089, and 3,011 bars were made at each of the following temperatures: 30°, 50°, 100°, 150°, 200°, 250°, and 300°C. (IBM run 5).

The SPE of the deviations calculated from the measured specific volumes are given in Table 3. It will be noted that at 30°, 50°, and 100°C. (up to approximately the normal boiling point) the Hudleston equation duplicates the specific volumes fully as accurately as the values themselves were measured at these three temperatures, whereas above 100° the agreement, while good, diminishes as the temperature of the measurement increases. The SPE for the entire spread of temperatures and pressures for 55 points (weighted in accordance with the number of measurements at each temperature) is 0.025%.

INDEPENDENT CHECK OF HUDLESTON INTERCEPTS

Bett, Weale, and Newitt (*14*) point out that the intercepts of the Hudleston lines can be checked independently of compression measurements if data on the velocity of sound, specific heat, coefficient of expansion at 1 atm., and liquid density are available at the temperatures of interest. Such data were available on *n*-heptane (*16*) up to 50°C. and were extrapolated up to 100°C. (*17, 18*). The results of these calculations are shown in column 3 of Table 4. The agreement of the Hudleston A's calculated from velocity of sound data with those calculated from the authors' compression data is excellent.

COMPARISON WITH DATA OF OTHERS

For a further check on the Simon and Cornish data, calculations of the best values of the Hudleston parameters were made on published *n*-heptane data of other investigators. These results are shown in columns 4 and 5 of Table 4. The values of A from these and other sources are shown on Figure 5. It will be observed that the Hudleston A's calculated from the authors' compressions (open circles) fall on the smooth curve running through most of the A's calculated from the data of other investigators.

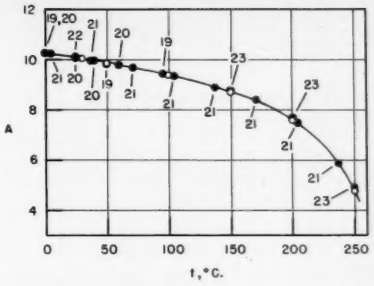

Fig. 5. *n*-Heptane. [Numbers refer to literature. Open circles are data of Simon and Cornish (*24*)].

ESTIMATE OF THE ACCURACY OF THE *N*-HEPTANE DATA

The following factors have been weighed in arriving at an estimate of the accuracy of the *n*-heptane data.

1. The root-mean-square percentage deviation from the mean of duplicate measurements of specific volume at 109 different temperatures and/or pressures was 0.031%.

2. Values of specific volume calculated from the Hudleston equation differed from the observed average specific volumes at 55 points with an SPE of 0.025%.

3. Since the sample weight is the product of the atmospheric-pressure density and the extrapolated zero-pressure volume at temperatures well below the normal boiling point, the Pv isotherms must extrapolate to $1/\rho$, at these temperatures.

4. The Hudleston A's calculated from the Simon and Cornish data agree well with the corresponding parameters calculated from the data of most other investigators whose results have been examined and with values of A calculated from velocity-of-sound data.

The agreement of two independent runs at 109 identical temperatures and pressures establishes the precision of the measurements. This coincidence taken in conjunction with the agreement of the extrapolated specific volumes with $1/\rho$ and of the Hudleston A's with those based on the work of other investigators may be taken as evidence of accuracy as well as precision. It is very unlikely that any systematic error could be common to both independent runs and still achieve the conformity indicated by the other criteria. It is therefore concluded that the over-all accuracy is of the same order as the over-all precision or ap-

proximately three parts in 10,000 for the entire spread of the measurements on *n*-heptane.

PRECISION OF THE *N*-EICOSANE MEASUREMENTS

Duplicate runs at identical temperatures and pressures were not made with *n*-eicosane, so the method of analysis that was used with *n*-heptane was not applicable. However with *n*-eicosane the normal boiling point (342.7°C.) is well above the highest temperature of measurement; therefore the published densities could be used to convert the measured compressions to specific volumes at all temperatures.

The measured compressions were obtained as follows. The volumes of sample in the piezometer over a range of pressures at constant temperature were fitted to the Hudleston equation, and the zero-pressure volume giving the best fit of the points to the line was calculated. Since the volumes were of the order of 0.5 ml., the zero-pressure volume was not a specific volume. However these measurements were converted to compressions by dividing each measured volume by the extrapolated zero-pressure volume. The multiplication of each value of compression by $1/\rho$ converts these numbers into specific volumes, and of course the zero pressure number is $1/\rho$ itself.

The establishment of the validity of the Hudleston extrapolation was done in the next step. (It is to be clearly understood that all that had been done so far was to multiply each measured volume by a constant.)

The specific volumes were next fitted to the Hudleston equation, and the value of the zero-pressure specific volume that gave the best fit of the points to the line was calculated for each temperature.

The results were as follow:

Temperature, °C.	Calculated v°_T	$1/\rho^\circ_T$ from reference 12
50	1.3007	1.3007
100	1.3598	1.3598
150	1.4267	1.4267
200	1.5013	1.5013
250	1.5876	1.5876
300	1.6926	1.6926

Since the agreement was perfect at all temperatures, it is established that the extrapolation of higher pressure volumes to atmospheric pressure by the Hudleston equation is likewise valid for *n*-eicosane.

For the purpose of making a statistical analysis of the precision of the measurements, a large number of points (163) were taken. Table 5 gives the Hudleston parameters resulting from these calculations.

Over a relatively limited range of temperature Bett, Weale, and Newitt (*14*) concluded that the slope of *B* of the Hudleston lines was a constant for a given liquid. The Simon and Cornish data, over a considerably greater range, confirm this observation except at temperatures somewhat above the normal boiling point where the *B*'s are observed to increase. Since the Hudleston equation fails at the critical point, where v^p_T may exceed v°_T, there is some uncertainty about the highest temperature at which the equation can be used with confidence. Therefore the observed increase in *B* as the critical temperature is approached may not be significant.

In the case of *n*-eicosane all temperatures of measurement were substantially below the normal boiling point, and so the *B*'s may be presumed to be constant. The actual values obtained were therefore averaged and the *A*'s adjusted accordingly. The parameters used in the Hudleston equation calculations are given in Table 6.

The differences between the calculated and the observed specific volumes gave a standard percentage error for the 163 points of 0.033%.

ESTIMATE OF THE ACCURACY OF THE *N*-EICOSANE DATA

The above calculation establishes the degree of precision attained in these measurements. However the Hudleston equation has been found to represent correctly the dependence of the volume of liquids on pressure at constant temperature by others (*14*) as well as the authors, and so the curvature of the *Pv* isotherms is presumed to be correct. Therefore since the extrapolated zero-pressure volumes correspond in all cases to $1/\rho$, it follows that the accuracy must again be substantially equivalent to the precision or an over-all SPE for the 163 points of the order of 0.03%.

ACCURACY OF OTHER SIMON AND CORNISH *N*-ALKANE MEASUREMENTS

Since the order of accuracy of the Simon and Cornish measurements was sufficiently well established by the analyses of the *n*-heptane and *n*-eicosane data, it was not considered necessary to go into such detail with the remaining six compounds (*n*-alkanes of 9, 11, 13, 17, 30, and 40 carbons). However an indication that these measurements are of the same order of accuracy may be taken from the observation that the root-mean-square percentage deviation from the mean volume for each of 190 random multiple points (458 measurements at identical temperatures and pressures) was 0.035%. These random points represent all the instances in which multiple measurements were made at identical temperatures and pressures on these six compounds. Although the agreement of multiple measurements at identical temperatures and pressures is a measure only of precision, other criteria lead the authors to believe that the accuracies are again of the same order as the precisions, except for *n*-tetracontane, which contained 1.4% impurity.

SUMMARY

The compressions of eight pure liquid *n*-alkanes have been calculated from new measurements of volumes under pressure at a series of temperatures. The zero-pressure volumes used for the calculation of the compressions were obtained by extrapolation of the measurements of the volumes under pressure.

Analyses of the data for *n*-heptane and *n*-eicosane indicate that the over-all accuracy of the compressions for each of these compounds appears to be of the order of 3 parts in 10,000. Less comprehensive analysis of the data for the other six compounds indicates an accuracy of approximately the same order.

TABLE 5. HUDLESTON PARAMETERS, *n*-EICOSANE

Temperature, °C.	Pressure range, bars	No. of measurements	*A*	*B*
50	165.2 to 557.6	9	10.483	14.186
100	165.2 to 3292	25	10.185	14.754
150	116.1 to 2534	32	9.865	14.216
200	116.1 to 3932	37	9.522	13.876
250	116.1 to 4007	30	9.124	13.872
300	116.1 to 3456	30	8.581	14.094

TABLE 6. HUDLESTON PARAMETERS, *n*-EICOSANE, CONSTANT *B*

Temperature, °C.	*A*	*B*	$(v^0_T)^{1/80}$
50	10.482	14.118	1.0916
100	10.206	14.118	1.1079
150	9.869	14.118	1.1258
200	9.509	14.118	1.1450
250	9.109	14.118	1.1666
300	8.579	14.118	1.1917

° From reference *12*.

III. Temperature and Molecular Weight Dependence of the Hudleston Parameters for the *n*-Alkanes

ARTHUR K. DOOLITTLE and DORTHA B. DOOLITTLE

Union Carbide Chemicals Company, South Charleston, West Virginia

General equations for the temperature dependence of the parameters of the Hudleston equation are given which were deduced from a study of *n*-alkane compression data. Empirical expressions for the molecular-weight dependence of the constants of these equations are likewise given which are applicable only to *n*-alkanes. By use of these relations in the Hudleston equation the compressions of the family of liquid *n*-alkanes over ranges of *T*, *P*, and *m* were calculated on an IBM-650 computer. The over-all standard percentage error (SPE) of the computer calculations for *n*-alkanes of 7 to 20 carbons up to temperatures not exceeding their normal boiling points was 0.10%. The over-all SPE for *n*-alkanes of 7 to 40 carbons up to temperatures substantially above their normal boiling points (but not exceeding 300°C.) was 0.21%.

Since the Hudleston (*15*) equation has been shown (*8*, *14*) to represent pressure-volume data on liquids at constant temperature with high accuracy, it seemed desirable to investigate the temperature-dependent parameters of this equation so that it could be used as an equation of state for the purpose of making certain liquid-state thermodynamic calculations.

To permit the calculation of compressions for all members of the *n*-alkane family, empirical equations for the molecular-weight dependence of all parameters involved were determined. These are applicable to the *n*-alkanes only. With all variables defined as functions of temperature and molecular weight, a trial-and-error solution of the Hudleston equation was programed for the IBM-650 computer, and a set of tables was listed giving the specific volumes of all the *n*-alkanes studied at their temperatures of measurement but at even pressures.

The purpose of carrying out this empirical study was twofold: to determine the nature of the variation, particularly that of the temperature dependence, as a step toward a better understanding of the liquid state and to provide a body of compression data at even pressures for use in subsequent calculations involving the behavior of liquids.

The apparatus and method used by Simon and Cornish to measure the volumes of liquids under pressure have been described (*10*), and their data on eight *n*-alkanes of 7 to 40 carbons has been evaluated (*8*). It has been shown that the data for *n*-heptane and *n*-eicosane are very well represented by the Hudleston (*15*) equation. This paper considers all the Simon and Cornish data and the *n*-alkane data of other investigators for the purpose of establishing the temperature and molecular-weight dependence of the parameters of the Hudleston equation.

Dortha B. Doolittle is at the West Virginia Institute of Technology, Montgomery, West Virginia.

The Hudleston equation for a sample weight of 1 g. may be written as

$$\ln \frac{P(v^p_T)^{2/3}}{(v^\circ_T)^{1/3} - (v^p_T)^{1/3}} = A_T + B[(v^\circ_T)^{1/3} - (v^p_T)^{1/3}] \quad (1)$$

The constant B is substantially independent of temperature except in the neighborhood of the critical point, but A_T and v°_T are temperature dependent. In addition, v°_T, A_T, and B depend on the nature of the substance; thus when only the *n*-alkanes are considered, they depend on the molecular weight.

TEMPERATURE DEPENDENCE

The Parameter v°_T

To explore $v^\circ = f(T)$ a study of *n*-alkane liquid-density data (*12*) was made which yielded the following relationship:

$$\left.\begin{aligned} \ln \frac{(v^\circ_T)}{(v^\circ_\circ)} &= e^z - 1 \\ z &= e^y - 1 \\ y &= k\,(T + \Delta) \end{aligned}\right\} \quad (2)$$

The values of ln $(v^\circ_\circ)$ and k were determined for each of the twenty *n*-alkanes (methane to *n*-eicosane) in the following manner. Specific volumes from A.P.I.-44 density data (*12*) were assumed to be identical with v°_T at temperatures from the melting point to within 30 to 50 centigrade degrees of the normal boiling point. Trial values of $v^\circ_\circ$ were calculated from ln $(v^\circ_\circ) = 10/m$ (25). The quantity y in Equation (2) may be expressed as

$$y = \ln \left\{ \ln \left[\ln \frac{(v^\circ_T)}{(v^\circ_\circ)} + 1 \right] + 1 \right\} \quad (2a)$$

At temperatures well below the normal boiling point no correction Δ is necessary. Hence over the range specified, a series of values of y from Equation (2*a*) was calculated for each compound at intervals of 20 centigrade degrees. Values thus calculated plotted as straight lines, and their slopes and intercepts were determined by least-squares calculations. In accordance with Equation (2), the intercepts of these lines should be zero in all cases. Since calculation from ln $(v^\circ_\circ) = 10/m$ did not provide zero intercepts (or more exactly intercepts $< \pm 0.0001$), trial calculations were continued until a value of ln $(v^\circ_\circ)$ was found for which the intercept was $< \pm 0.0001$. This gave twenty pairs of parameters ln $(v^\circ_\circ)$ and k. It is interesting to note that in an earlier publication (*6*), it was stated that ln $(v^\circ_\circ)$ could have been read as $(10/m) - 0.005$, but the value $10/m$ was used for simplicity. The method here employed in Equation (2) gives values of ln $(v^\circ_\circ)$ almost exactly $= (10/m) - 0.005$, and these values are used here since more precise quantities are dealt with in this paper.

Calculations were made (IBM run 4) of the specific volumes of the *n*-alkanes with the twenty pairs of parameters, ln $(v^\circ_\circ)$ and k. For sixteen *n*-alkanes, *n*-pentane to *n*-eicosane, over a temperature range from the melting to within 30 to 50 centigrade degrees of the normal boiling temperature (309 points), the SPE of the calculated specific volumes was 0.05%. At temperatures in the neighborhood of the normal boiling point (and at higher temperatures) data on liquid density obtained at atmospheric pressure cannot be used to check values calculated from Equation (2). Another method was therefore used. It has been mentioned (*8*) that the Hudleston equation is an excellent device for extrapolating accurate measurements of volume under pressure to the zero-pressure volume. With *n*-heptane, accurate measurements of the specific volumes under pressure over a wide range of temperatures have been made by a number of investigators, including Simon and Cornish (*8*). Application of the Hudleston equation to these data therefore enabled the zero-pressure specific volumes of *n*-heptane to be calculated at temperatures beyond the

range of the atmospheric-pressure densities.

When the values of y for n-heptane were calculated from these data according to Equation (2), the linear relationship was observed to hold up to approximately 0.6 T_c or 324°K. Above this temperature the observed values of y were greater than kT. The nature of the deviation was exponential and took the following form:

$$\Delta = \frac{y - kT}{k}$$

$$= [\exp c_1 (T - c_2 T_c)] - 1 \quad (3)$$

It was anticipated that $c_2 = 0.6$ would apply to all members of the n-alkane series, but a trial calculation with n-eicosane showed that the correction was applied at too low a temperature with the higher molecular-weight compound. This parameter was therefore made molecular-weight dependent.

The Parameter A

With the dependence of v°_T on T established, attention was directed to the other temperature-dependent parameter of the Hudleston equation. Bett, Weale, and Newitt (*14*), from a study of data extending over a rather limited range of temperatures, suggested that perhaps the Hudleston A was linear with temperature. Figure 1 of a prior paper (*8*) indicates however, that this linearity does not extend to the higher temperatures.

To explore $A_T = f(T)$, n-alkane compression data of a number of investigators were analyzed according to the Hudleston equation, and thus values of A were provided at a variety of molecular weights and temperatures. The published data have frequently been reported as specific volumes or have been given in a form that can be converted to specific volumes. Such data were extrapolated to zero pressure by use of the trial-and-error procedure described in the prior paper (*8*). In the few instances where the available data (well below the normal boiling point) did not extrapolate to $1/\rho$ [ρ = A.P.I.-44 liquid density (*12*)], such data were not included in this study.

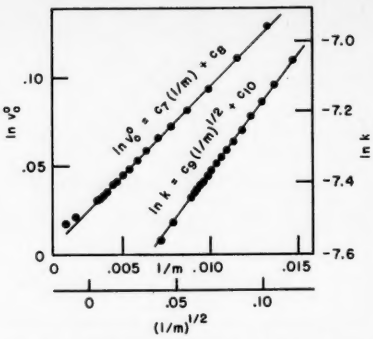

Fig. 6. n-Alkanes. Parameters of the relationship defining the dependence of specific volume on temperature.

The Simon and Cornish data and those of some other investigators are reported as compressions. These were converted to specific volumes by multiplying by v°_T calculated from Equation (2). With the authors' data the intercepts A and slopes B of the Hudleston lines were generally calculated by the method of least squares. Graphical determinations of the A's and B's were made in all other instances except n-octane, where several values calculated from velocity of sound data seemed more reliable. Table 7 presents the results of these calculations and lists the values of A, B, and $(v^\circ_T)^{1/3}$ for all compounds and temperatures involved.

Study of $A = f(T)$ with these extensive data led to the following relationship for the temperature dependence of the Hudleston A's:

$$e^{A/2} = c_3 \left(1 - \frac{T}{c_4}\right)$$

or

$$A = 2 \ln \left[c_3 \left(1 - \frac{T}{c_4}\right) \right] \quad (4)$$

The degree of fit of the observed values to the lines determined by Equation (4) is discussed in a later section.

MOLECULAR-WEIGHT DEPENDENCE

The Parameter B

Definition of B as a function of molecular weight was complicated by the fact that the values of B for n-triacontane and n-tetracontane appear to be less than for n-eicosane. Since confidence in the results for the highest molecular weight n-alkanes is less than for the lower members of the series, a compromise was made by choosing a function, Equation (5), that well represents the B's for the lower molecular weight n-alkanes but continues to increase slowly as the molecular weight increases. This function

$$\ln B = c_5 \left(\frac{1}{m}\right) + c_6 \quad (5)$$

TABLE 7. HUDLESTON PARAMETERS

Ref.	t, °C	A	B	$(v^\circ_T)^{1/3}$ from IBM 7 *
C_5, mp -129.72°C; bp 36.074°C.				
3	0	9.834	12.8	1.1576
26	37.78	9.610	12.8	1.1805
3	50	9.340	12.8	1.1886
26	71.11	9.126	12.8	1.2038
3	95	8.746	12.8	1.2239
26	104.44	8.606	12.8	1.2330
26	137.78	7.798	12.8	1.2748
26	171.11	6.19	12.8	1.3493
26	204.44	0.64	12.8	1.5325
C_6, mp -95.35°C; bp 68.74°C.				
3	0	10.13	13.2	1.1390
20	0	10.13	13.0	1.1390
20	25	9.93	13.0	1.1516
27	37.78	9.81	10.8	1.1584
20	40	9.82	12.8	1.1597
3	50	9.70	13.2	1.1653
20	60	9.63	12.7	1.1711
27	71.11	9.40	12.8	1.1779
3	95	9.18	13.3	1.1937
28	100	9.10	13.0	1.1973
27	104.44	9.00	12.8	1.2006
27	137.78	8.47	13.2	1.2292
28	150	8.25	13.2	1.2424
27	171.11	7.80	13.0	1.2713
28	200	6.60	13.0	1.3351
27	204.44	6.52	13.2	1.3493
27	237.78	4.21	13.6	1.5507
C_7, mp -90.61°C; bp 98.43°C.				
3	0	10.25	13.2	1.1259
20	0	10.25	12.9	1.1259
29	4.44	10.22	13.2	1.1279
22	25	10.12	12.3	1.1375
20	25	10.06	12.9	1.1375
24	30	10.023	13.18	1.1399
23	30	-----	-----	1.1399
29	37.78	9.95	13.2	1.1436
20	40	9.94	12.8	1.1447
24	50	9.854	13.16	1.1497
3	50	9.80	13.3	1.1497
20	60	9.77	12.8	1.1548
29	71.11	9.67	13.2	1.1608
3	95	9.43	13.2	1.1743
24	100	9.365	13.18	1.1774
23	100	-----	-----	1.1774
29	104.44	9.32	13.2	1.1801
29	137.78	8.86	12.7	1.2029
24	150	8.694	13.27	1.2126
23	150	8.72	13.5	1.2126
29	171.11	8.40	13.0	1.2325
24	200	7.566	13.65	1.2705
23	200	7.64	13.9	1.2705
29	204.44	7.44	13.9	1.2781
29	237.78	5.86	14.5	1.3684
24	250	4.752	14.25	1.4289
23	250	4.90	13.5	1.4289
24	300	-17.79	15.60	2.7478

represents the values of B over the entire range with an SPE of 2.5%. Practically all this error occurs in the B's for the two highest molecular-weight compounds.

Parameters of Equations (2) and (3)

The parameters of Equations (2) and (3) that are molecular-weight dependent are v°_o, k, and c_2. The following equations express these relationships:

Table 8.

$c_1 = 0.02536$	$c_9 = 6.65397$
$c_3 = 335$	$c_{10} = -7.838779$
$c_5 = -9.3000$	$c_{11} = 0.000835$
$c_6 = 2.6720$	$c_{12} = 0.52$
$c_7 = 9.911902$	$c_{13} = 22.040$
$c_8 = -0.0057157$	$c_{14} = -71.428$

$$\ln (v^\circ_o) = c_7\left(\frac{1}{m}\right) + c_8 \qquad (6)$$

$$\ln k = c_9\left(\frac{1}{m}\right)^{1/2} + c_{10} \qquad (7)$$

$$c_2 = c_{11} \cdot m + c_{12} \qquad (8)$$

The conformity of the data to lines representing Equations (6) and (7) is shown on Figure 6. It will be observed that the values of ln (v°_o) for molecular weights below n-octane and above n-nonadecane are not well represented by Equation (6). Since time was not

Table 7. *(continued)*

Ref.	t, °C	A	B	$(v^o_T)^{1/3}$ from IBM 7
C_8, mp -56.80°C; bp 125.66°C.				
3	0	10.35	13.3	1.1162
20	0	10.40	12.9	1.1162
22	25	10.24	12.6	1.1269
20	25	10.23	12.8	1.1269
20	40	10.12	12.8	1.1336
3	50	10.01	13.1	1.1382
20	60	9.97	12.9	1.1429
3	95	9.58	13.6	1.1602
30	100	----	----	1.1629
30	150	9.00	11.6	1.1925
30	200	8.37	11.1	1.2332
30	250	6.84	18.4	1.3126
Values Calculated from Velocity of Sound				
	0	10.33	----	------
	25	10.16	----	------
33,17,18	40	10.05	----	------
	50	9.98	----	------
	60	9.90	----	------
C_9, mp -53.52°C; bp 150.80°C.				
24	30	10.238	13.24	1.1210
31	37.78	------	-----	1.1243
24	50	10.073	13.36	1.1295
24	100	9.677	13.26	1.1524
31	104.44	9.63	13.0	1.1546
24	150	9.152	13.50	1.1790
31	171.11	8.92	13.0	1.1919
24	200	8.486	13.64	1.2125
31	237.78	7.66	13.9	1.2497
24	250	7.32	14.0	1.2666
24	300	2.64	15.7	1.4098
C_{10}, mp -29.66°C; bp 174.12°C.				
22	25	10.38	12.50	1.1125
32	37.78	-----	-----	1.1176
32	104.44	-----	-----	1.1463
32	171.11	-----	-----	1.1803
C_{11}, mp -25.59°C; bp 195.89°C.				
24	50	10.160	14.2	1.1169
24	100	9.828	14.0	1.1376
24	150	9.408	13.9	1.1606
24	200	8.918	13.6	1.1874
24	250	8.062	14.2	1.2220
24	300	6.03	15.7	1.2811
C_{13}, mp -5.39°C; bp 235.44°C.				
24	30	10.405	14.97	1.1009
24	50	10.254	14.97	1.1081
24	100	9.947	14.14	1.1274
24	150	9.593	13.74	1.1485
24	200	9.13	13.7	1.1720
24	250	8.49	14.1	1.1999
24	300	7.29	14.9	1.2375

Table 7. *(continued)*

Ref.	t, °C	A	B	$(v^o_T)^{1/3}$ from IBM 7
C_{17}, mp 21.98°C; bp 301.82°C.				
24	50	10.42	14.2	1.0966
24	100	10.13	13.8	1.1140
24	150	9.77	14.0	1.1330
24	200	9.40	13.9	1.1537
24	250	8.94	13.9	1.1763
24	300	8.35	13.9	1.2022
C_{20}, mp 36.8°C; bp 342.7°C				*
24	50	10.482	14.12	1.0914
24	100	10.206	14.12	1.1079
24	150	9.869	14.12	1.1258
24	200	9.509	14.12	1.1452
24	250	9.109	14.12	1.1665
24	300	8.579	14.12	1.1896
C_{30}, mp 65.8°C; bp 446.4°C.				*
24	100	10.34	15.8	1.0959
24	150	10.05	13.2	1.1117
24	200	9.75	13.3	1.1288
24	250	9.41	13.2	1.1474
24	300	9.01	13.2	1.1674
C_{40}, mp 81.5°C; bp 520°C.				*
24	150	10.12	13.9	1.1044
24	200	9.86	13.5	1.1202
24	250	9.57	13.3	1.1374
24	300	9.19	13.4	1.1559

* IBM Run 7 $(v^o_T)^{1/3}$ values corrected by using observed ln (v^o_o) values instead of those calculated from Equation (6).

TABLE 9. MACHINE CALCULATION OF COMPRESSIONS, IBM RUN 9

t, °C	30	50	100	150	200	250	300
C_7, mp -90.61°C; bp 98.43°C; T_c 540.2°K.							
P, bars							
0	1.0000	1.0000	1.0000	1.0000	1.0000		
50	.9927	.9914	.9859	.9738	.9402		
100	.9860	.9836	.9739	.9540	.9059		
200	.9740	.9698	.9540	.9244	.8623		
300	.9635	.9579	.9378	.9023	.8333		
500	.9455	.9381	.9122	.8698	.7940		
1000	.9119	.9018	.8688	.8189	.7374		
1500	.8874	.8759	.8393	.7863	.7033		
2000	.8679	.8555	.8170	.7624	.6788		
3000	.8380	.8246	.7839	.7278	.6444		
5000	.7969	.7827	.7403	.6834	.6013		
SPE, %	0.019	0.008	0.035	0.193	0.457		
Range, bars	0-3000	0-3000	0-3000	0-3000	0-3000		
C_9, mp -53.52°C; bp 150.80°C; T_c 595°K.							
P, bars							
0	1.0000	1.0000	1.0000	1.0000	1.0000		
50	.9940	.9931	.9897	.9832	.9690		
100	.9884	.9867	.9805	.9693	.9465		
200	.9783	.9753	.9647	.9468	.9141		
300	.9692	.9651	.9514	.9290	.8905		
500	.9534	.9479	.9296	.9016	.8566		
1000	.9230	.9153	.8909	.8561	.8044		
1500	.9003	.8913	.8637	.8259	.7716		
2000	.8820	.8723	.8428	.8032	.7475		
3000	.8536	.8429	.8112	.7698	.7131		
5000	.8140	.8025	.7689	.7268	.6690		
SPE,%	0.113	0.031	0.036	0.065	0.262		
Range, bars	0-3000	0-3000	0-3000	0-3000	0-3000		

TABLE 9. *(continued)*

t, °C	50	100	150	200	250	300
C_{11}, mp -25.59°C; bp 195.89°C; T_c 640°K.						
P, bars						
0	1.0000	1.0000	1.0000	1.0000		
50	.9940	.9914	.9869	.9781		
100	.9883	.9836	.9756	.9609		
200	.9781	.9699	.9568	.9345		
300	.9690	.9581	.9414	.9142		
500	.9532	.9385	.9169	.8840		
1000	.9228	.9026	.8749	.8356		
1500	.9001	.8770	.8463	.8042		
2000	.8818	.8570	.8246	.7809		
3000	.8535	.8265	.7922	.7471		
5000	.8141	.7852	.7494	.7034		
SPE, %	0.065	0.020	0.063	0.367		
Range, bars	0-3000	0-3000	0-3000	0-3000		
C_{13}, mp -5.39°C; bp 235.44°C; T_c 677°K.						
P, Bars						
0	1.0000	1.0000	1.0000	1.0000	1.0000	
50	.9951	.9924	.9889	.9825	.9694	
100	.9893	.9854	.9791	.9681	.9473	
200	.9799	.9730	.9624	.9452	.9153	
300	.9714	.9622	.9485	.9271	.8921	
500	.9565	.9439	.9260	.8994	.8585	
1000	.9276	.9101	.8864	.8538	.8069	
1500	.9058	.8855	.8590	.8237	.7743	
2000	.8881	.8661	.8380	.8011	.7505	
3000	----	.8364	.8064	.7679	.7163	
5000	----	.7958	.7642	.7246	.6727	
SPE, %	0.057	0.045	0.090	0.108	0.391	
Range, bars	0-2000	0-3000	0-3000	0-3000	0-3000	

available to make further refinements, a run was made on the IBM computer (run 7) in which Equation (6) was used only for *n*-alkanes *n*-heptane to *n*-eicosane. Observed values of v° were used for *n*-alkanes below and above these limits. Equation (7) was satisfactory for defining k over the entire range. IBM run 7 duplicated the specific volumes of the *n*-alkanes *n*-pentane to *n*-tetracontane over the range from the melting point to within a few degrees of the normal boiling point with an SPE of 0.05%. Values of $(v^\circ_T)^{1/3}$ from IBM run 7 are listed in Table 7 for the various temperatures of interest.

Parameters of Equation (4)

The only molecular-weight–dependent parameter of Equation (4) is c_4, which is a number nearly but not exactly equal to the critical temperature. Its dependence on molecular weight is given by

$$c_4 = 10^2 \, (c_{13} \ln m + c_{14})^{1/2} \qquad (9)$$

Equations (4) and (9) represent the observed A's with an SPE of 0.16%. The constants involved in all the equations discussed above are given in Table 8.

OVER-ALL EVALUATION

The Hudleston equation, Equation

TABLE 9. *(continued)*

t, °C	50	100	150	200	250	300
C_{17}, mp 21.98°C; bp 301.82°C; T_c 735°K.						
P, bars						
0	1.0000	1.0000	1.0000	1.0000	1.0000	1.0000
50	.9951	.9935	.9910	.9867	.9790	.9649
100	.9905	.9875	.9828	.9754	.9624	.9373
200	.9820	.9766	.9686	.9564	.9367	.9009
300	.9743	.9670	.9565	.9410	.9170	.8767
500	.9606	.9504	.9364	.9165	.8874	.8436
1000	.9336	.9191	.9001	.8747	.8398	.7940
1500	----	.8959	.8742	.8462	.8089	.7627
2000	----	.8774	.8542	.8246	.7859	.7372
3000	----	.8488	.8237	.7925	.7525	.6992
5000	----	.8093	.7825	.7500	.7091	.6567
SPE, %	0.096	0.047	0.038	0.046	0.313	0.675
Range, bars	0-1000	0-3000	0-3000	0-3000	0-3000	0-3000
C_{20}, mp 36.8°C; bp 342.7°C; T_c 775°K.						
P, bars						
0	1.0000	1.0000	1.0000	1.0000	1.0000	1.0000
50	.9954	.9940	.9918	.9884	.9824	.9709
100	.9911	.9884	.9844	.9782	.9680	.9496
200	.9830	.9782	.9713	.9611	.9450	.9186
300	.9756	.9691	.9600	.9468	.9270	.8959
500	.9626	.9534	.9411	.9239	.8993	.8630
1000	----	.9233	.9063	.8840	.8540	.8121
1500	----	.9008	.8813	.8565	.8240	.7800
2000	----	.8828	.8618	.8354	.8015	.7564
3000	----	.8548	.8319	.8038	.7686	.7225
5000	----	.8158	.7913	.7618	.7256	.6791
SPE, %	0.060	0.156	0.053	0.091	0.198	0.483
Range, bars	0-500	0-3000	0-2000	0-3000	0-3000	0-3000

TABLE 9. *(continued)*

t, °C	100	150	200	250	300
C_{30}, mp 65.8°C; bp 446.4°C					
P, bars					
0	1.0000	1.0000	1.0000	1.0000	1.0000
50	.9949	.9933	.9910	.9874	.9813
100	.9900	.9872	.9830	.9765	.9661
200	.9811	.9761	.9689	.9583	.9422
300	.9731	.9663	.9568	.9434	.9237
500	.9590	.9495	.9369	.9196	.8954
1000	----	.9179	.9008	.8787	.8495
1500	----	----	.8752	.8508	.8193
2000	----	----	.8553	.8295	.7968
3000	----	----	.8251	.7978	.7638
5000	----	----	.7843	.7558	.7210
SPE, %	0.039	0.205	0.311	0.321	0.256
Range, bars	0-500	0-1000	0-1000	0-1000	0-1000
C_{40}, mp 815°C; bp 520°C					
P, bars					
0		1.0000	1.0000	1.0000	1.0000
50		.9940	.9922	.9894	.9850
100		.9885	.9851	.9801	.9724
200		.9783	.9725	.9641	.9519
300		.9693	.9615	.9507	.9355
500		.9537	.9431	.9290	.9098
1000		.9238	.9092	.8906	.8667
1500		.9015	.8847	.8639	.8378
2000		.8836	.8655	.8434	.8160
3000		.8558	.8361	.8125	.7838
5000		.8171	.7959	.7711	.7414
SPE, %		0.479	0.605	0.664	0.869
Range, bars		0-3000*	0-3000	0-3000	0-3000

*NOTE: Sample did not freeze under 3000 bars. Presumably because of impurity of 1.4%.

(1) with auxiliary Equations (2) to (4), defines completely the PvT relations of liquids over its range of validity. By further relating all parameters to the molecular weight of the *n*-alkanes in Equations (5) to (9), one can make a general calculation giving the compressions of any of the *n*-alkanes at any temperature and pressure, in which the only independent variable is molecular weight. Such a calculation, which evaluates the combined accuracy of all the empirical equations, was made (IBM run 9). The compressions were computed for all compounds studied at all temperatures of interest and at the following even pressures: 0, 50, 100, 200, 300, 500, 1,000, 1,500 2,000, 3,000, and 5,000 bars. At the same time the compressions were likewise listed at 0, 116.1, 214.2, 312.3, 508.5, 1,015, 1,577, 2,089, and 3,011 bars so that the experimental values might be compared with the machine calculations. The even-pressure values for *n*-alkanes 7 to 40 carbons are presented in Table 9, and the fit of the Simon and Cornish data to the equation over the indicated pressure ranges is shown for each compound.

This comparison indicates that over a pressure range of 0 to 3,000 bars the over-all SPE of the computed values

for n-alkanes of 7 to 20 carbons at all temperatures from 30°C. to somewhat below the normal boiling temperature is 0.10%. The over-all SPE for the entire range of molecular weights and pressures and over a range of temperatures extending considerably above the normal boiling point (but not exceeding 300°C.) is 0.21%.

At temperatures considerably above the normal boiling temperatures for all compounds, and for n-triacontane and n-tetracontane at all temperatures, the agreement of the calculated with the observed values is not so good as elsewhere. The discrepancies at these extremes of temperature and molecular weight are due principally to slight disagreement between the calculated and observed values of the Hudleston paameters A and B at the upper limits of these ranges.

The relatively poor agreement of n-tetracontane may be due in part to the lower purity of this sample compared with the other compounds (8). The observed Hudleston A's for n-tetracontane (Table 6) are somewhat less than those calculated from Equation (4), whereas those for n-triacontane are well represented by the calculation. With both these compounds the observed Hudleston B's are less than those for the preceding members of the series and are therefore not properly represented by Equation (5).

SUMMARY

1. Equation (1) with one physical constant v°_T and two arbitrary constants A and B defines completely the Pv relations of a single liquid at a single temperature (substantially below the critical temperature).

2. Equations (1), (2), and (4) with one extrapolated physical constant v°_o and four arbitrary constants k, B, c_3, c_4 define completely the PvT relations of a single liquid n-alkane at all temperatures substantially below the normal boiling temperature.

3. Equations (1), (2), (3), and (4) with two physical constants v°_o and T_c and six arbitrary constants k, B, c_1, c_2, c_3, c_4 define completely the PvT relations of a single liquid n-alkane up to temperatures substantially above the normal boiling temperature.

4. The PvT relations of the family of liquid n-alkanes from 7 to 40 carbons may be completely defined by nine equations involving one physical constant T_c and twelve arbitrary constants up to temperatures substantially above the normal boiling temperature.

ACKNOWLEDGMENT

William H. Cargile and Genevieve Banton assisted with the calculations. Mr. Cargile contributed materially to the progress of the work by programing the calculations that were run on the IBM computers. The financial support of this entire project by Union Carbide Chemicals Company over a period of four years is gratefully acknowledged. This support included contracts with Ohio State Research Foundation for synthesizing n-alkanes triacontane and tetracontane and with Arthur D. Little, Inc., for measuring volume under pressure, and the maintenance of a computing team at the Research Laboratory of Union Carbide Chemicals to process the data.

NOTATION

A = Hudleston intercept for sample weight of 1 g.

a = setting constant

B = Hudleston slope for sample weight of 1 g.

C_1 = Hudleston intercept for any sample weight

C_2 = Hudleston slope for any sample weight

c_1 = numerical constant

c_2 = molecular - weight – dependent constant in Equation (3)
$= c_{11}\ m + c_{12}$

c_3 = numerical constant

c_4 = molecular - weight – dependent constant in Equation (4), nearly but not exactly equal to the critical temperature
$= 10^2\ (c_{13} \ln m + c_{14})^{1/3}$

c_5 to c_{14} = numerical constants

k = molecular - weight – dependent constant in Equation (2)
$= \exp\left[c_9 \left(\frac{1}{m}\right)^{1/2} + c_{10}\right]$

P = external pressure, bars

T = absolute temperature, °K.

T_c = absolute critical temperature, °K.

vol^p_T = volume of sample at temperature T and pressure P

vol^o_T = zero-pressure volume of sample at temperature T

v^p_T = specific volume of sample at temperature T and pressure P

v°_T = zero-pressure specific volume of sample at temperature T

v°_o = limiting specific volume at zero pressure and zero temperature (See reference 34.)

y = variable in Equation (2)
$= k\ (T + \Delta)$

z = variable in Equation (2)
$= (\exp\ y) - 1$

Δ = variable in Equation (2)
$= [\exp\ c_1\ (T - c_2 T_c)\ ] - 1$

ρ = liquid density

LITERATURE CITED

1. Beattie, J. A., *Proc. Am. Acad. Arts Sci.*, **69**, 389 (1934).
2. Bridgman, P. W., *ibid.*, **77**, 129 (1949).
3. ———, "The Physics of High Pressure." 2 ed., p. 126, G. Bell, London, England (1949).
4. Adams, L. H., and R. E. Gibson, *J. Am. Chem. Soc.*, **53**, 3769 (1931).
5. Michels, A., *Proc. Roy. Soc. (London)*, **A160**, 358 (1937).
6. Reitzel, J., I. Simon, and J. A. Walker, *Rev. Sci. Instr.*, **28**, 828 (1957).
7. Bridgman, P. W., *Proc. Am. Acad. Arts Sci.*, **77**, 214 (1949).
8. Doolittle, A. K., and D. B. Doolittle, Paper II of this series.
9. ———, Paper III of this series.
10. Doolittle, A. K., Ivan Simon, and R. K. Cornish, Paper I of this series.
11. Doolittle, A. K., and R. H. Peterson, *J. Am. Chem. Soc.*, **73**, 2145 (1951).
12. Rossini, F. D., *et al.*, "Selected Values of Physical and Thermodynamic Properties of Hydrocarbons and Related Compounds," API Research Project 44, Carnegie Press, Pittsburgh (1953).
13. Glasgow, A. R., Jr., A. J. Strieff, and F. D. Rossini, *J. Research Natl. Bur. Standards*, **35**, 355 (1945).
14. Bett, K. E., K. E. Weale, and D. M. Newitt, *Brit. J. Appl. Phys.*, **5**, 243 (1954).
15. Hudleston, L. J., *Trans. Faraday Soc.*, **33**, 97 (1937).
16. Freyer, E. B., J. C. Hubbard, and D. H. Andrews, *J. Am. Chem. Soc.*, **51**, 759 (1929).
17. Rao, M. R., *J. Chem. Phys.*, **9**, 682 (1941).
18. Osborne, N. S., and D. C. Ginnings, *J. Research Natl. Bur. Standards*, **39**, 453 (1947).
19. Reference 3, p. 129.
20. Eduljee, H. E., D M. Newitt, and K. E. Weale, *J. Chem. Soc. (London)*, 3086 (1951).
21. Nichols, W. B., H. H. Reamer, and B. H. Sage, *Ind. Eng. Chem.*, **47**, 2219 (1955).
22. Bridgman, P. W., *Proc. Am. Acad. Arts Sci.*, **77**, 117 (1949).
23. Smith, L. B., J. A. Beattie, and W. C. Kay, *J. Am. Chem. Soc.*, **59**, 1587 (1937).
24. Calculated from data of Simon and Cornish in reference 8.
25. Doolittle, A. K., *J. Appl. Phys.*, **22**, 1471 (1951).
26. Sage, B. H., and W. N. Lacey, *Ind. Eng. Chem.*, **34**, 730 (1942).
27. Stewart, D. E., B. H. Sage, and W. N. Lacey, *ibid.*, **46**, 2529 (1954).
28. Kelso, E. A., and W. A. Felsing, *J. Am. Chem. Soc.*, **62**, 3132 (1940).
29. Nichols, W. B., H. H. Reamer, and B. H. Sage, *Ind. Eng. Chem.*, **47**, 2219 (1955).
30. Felsing, W. A., and G. M. Watson, *J. Am. Chem. Soc.*, **64**, 1822 (1942).
31. Carmichael, L. T., B. H. Sage, and W. N. Lacey, *Ind. Eng. Chem.*, **45**, 2697 (1953).
32. Sage, B. H., and W. N. Lacey, "Thermodynamic Properties of Hydrocarbons," p. 83, API (1950).
33. Freyer, E. B., J. C. Hubbard, and D. H. Andrews, *J. Am. Chem. Soc.*, **51**, 759 (1929).
34. Doolittle, A. K., and D. B. Doolittle, *J. Appl. Phys.*, **28**, 901 (1957).

Manuscript received December 30, 1958; revision received July 22, 1959; paper accepted August 4, 1959.

Temperature Measurements in a Spherical Field: Transfer Coefficients and Corrections for Thermocouples in Boundary Flows

W. W. SHORT and B. H. SAGE

California Institute of Technology, Pasadena, California

A study was made of the deviation between the temperature of thermocouple junctions and the temperature of the fluid surrounding them which arises as a result of conduction along the thermocouple leads. Measurements around a ½-in. heated sphere in the plane of the equator normal to an air stream having a velocity of 16 ft./sec. were made with a 0.001-in.-diam. thermocouple of platinum and platinum rhodium. Air temperatures in the boundary flows of the sphere were predicted from the indications of the thermocouple. The method of prediction employed also determined the heat transfer coefficients for the thermocouple wire in the boundary layer. These local heat transfer coefficients are lower than those observed in a uniform stream having a velocity equal to the estimated local velocity in the boundary layer.

Measurement of the local temperature of a fluid in the presence of large temperature gradients is a major experimental problem encountered in many heat transfer studies. The differential equations used to describe the temperature in and around temperature-sensing devices are usually simple, but the analytical solution to these equations is often impossible because of unusual geometry or irregular boundary conditions. Carslaw (*4*) and Ingersoll (*13*) presented equations and a few solutions applicable to heat-conduction problems encountered when thermocouples are used.

Several investigators have studied the problem of conduction in thermocouples. Johnson (*15*) determined analytically the thermocouple temperature for each of five air-temperature distributions along the thermocouple leads. Boelter (3) corrected the readings of thermocouples mounted on flat plates in heaters. Hsu (*10*) presented an analogue method for correcting thermocouple readings taken in the boundary layer surrounding a heated sphere. Extensive studies of corrections for hot-wire anemometers were made by King (*17*), whose results in many cases can be applied to thermocouples because of similar geometry and boundary conditions. The application of all these results presumes a knowledge of the heat transfer coefficient for the wire. The present paper describes a method which does not require an independent knowledge of the heat transfer coefficient for predicting point air temperatures from the indications of small thermocouples.

METHODS

A study of the effect of free-stream turbulence on the local thermal and material transfer from spheres has been under way for a number of years. To determine the local thermal flux from the surface of a silver sphere, temperatures were measured as a function of position in the fluid adjacent to the surface. Temperature traverses were obtained by moving a thermocouple junction through the thermal-boundary layer to the surface of the sphere. Traverse data of this type were presented by Hsu (*10, 12*) and Short (*21*). Junction temperatures from a typical experimental traverse are shown in Figure 1. The term *junction temperature* refers to the measured temperature as distinguished from the true *air temperature* at the same point in space. The term *wire temperature* denotes temperatures in the thermocouple wire at points other than the junction. The *thermocouple correction* is the difference between the air temperature and the junction temperature. The term *surface temperature* represents the temperature determined with thermocouples mounted within the surface of the sphere.

The difference between the junction temperature and the surface temperature, as shown in Figure 1, indicates that the junction temperatures are considerably lower than the corresponding air temperatures. Earlier investigators believed that thermal conduction along the thermocouple wires caused these deviations.

EQUIPMENT

The probe thermocouple used for this investigation was made of 0.001-in.-diameter wires of platinum and of platinum–10% rhodium. The thermocouple was soldered to the tips of two needles on a probe, as shown in Figure 2. Wires of this size were chosen because they were the smallest that could be butt-welded in an oxy-natural gas flame to form a smooth cylindrical junction. No irregularities at the junction were observed under a 36-power binocular microscope. Thermocouples which were made from wires 0.0003 in. in diameter showed nonuniform junctions.

The probe thermocouple could be moved about the sphere parallel to each of the three coordinate axes shown in Figure 3. Dial indicators reading to 0.001 in. measured the displacement of the probe in the two directions normal to flow. The thermocouple wires were always parallel to the y axis, which is normal to the air stream.

The 0.5-in. sphere used in this investigation was employed by Baer (*1*), Hsu (*12*), and Sato (*18*) in earlier studies of heat transfer from spheres. The surface of the sphere was formed by two hemispheres of polished silver 0.016 in. thick fitted over a copper core on which an electrical

W. W. Short is with Convair, San Diego, California.

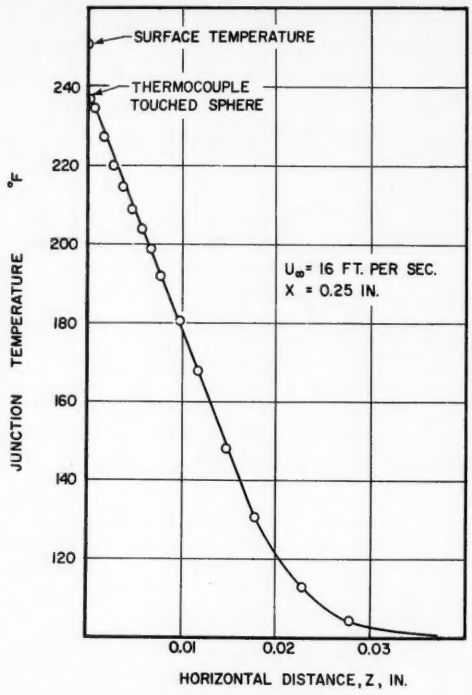

Fig. 1. Typical junction-temperature traverse.

heater was wound. Four copper constantan thermocouples were embedded in the inner surface of the silver shell to measure surface temperatures. The sphere was mounted on stainless steel tubes 0.096 in. in diameter provided with compensating heaters. When the heaters were properly adjusted, no measurable amount of energy was conducted to or from the sphere along the supporting tubes.

The air stream in which the sphere was suspended was supplied by equipment described by Corcoran (*6*) and Hsu (*11*). The air stream was maintained at a velocity of 16 ft./sec., a temperature of 100°F., and an apparent level of turbulence of 0.013. The level of turbulence is defined as the ratio of the root-mean-square of the lateral fluctuating velocity component to the average longitudinal velocity. The turbulence value was established by Sato (*18*) using the data of Schubauer (*19*) in conjunction with measurements of the divergence of the temperature profile in the wake of a heated wire.

The copper-constantan and platinum–platinum-rhodium probe thermocouples were calibrated in the laboratory against a standard resistance thermometer. These calibrations, which indicated a maximum deviation of 0.8°F. from reference values (*20*), were used in obtaining all temperatures. The reference junction for all thermocouples was at the ice point.

ANALYSIS

The analysis of thermocouple corrections which follows is presented in three parts. First, the assumptions pertinent to the analysis are discussed; then a differential equation to describe temperature in the vicinity of the thermocouple, with only conductive and convective thermal transport taken into account, is developed and discussed; and finally a method of solving the differential equation to obtain air temperatures from junction temperatures is presented.

Assumptions

Thermal transport by radiation from both the sphere and the thermocouple is small compared with the transport by convection. At 212°F. the total emissivity of polished silver is 0.02 and that of unoxidized platinum is 0.047 (*9*). Since the wire surface near the junction became oxidized during welding, it is believed that the emissivity was higher than 0.047. Radiation transfer from an unoxidized platinum wire at 238.8°F., the maximum junction temperature observed experimentally, to surroundings at 80°F. is 0.0035 B.t.u./(sq. ft.)(sec.). The minimum heat transfer coefficient

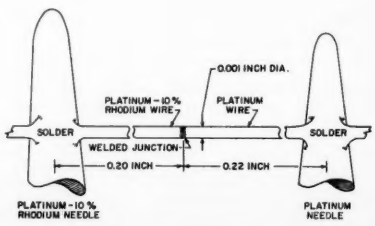

Fig. 2. Outline drawing of probe thermocouple.

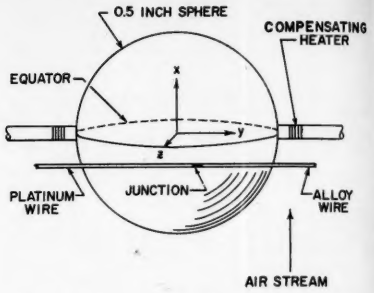

Fig. 3. Orientation of probe thermocouple and sphere.

encountered in this investigation was 0.04 B.t.u./(°F.)(sq. ft.)(sec.). To transfer energy at a rate of 0.0035 B.t.u./(sq. ft.)(sec.) from a body having this heat transfer coefficient, a temperature difference of 0.09°F. is required. Under any of the experimental conditions encountered, the thermocouple correction due to radiation effects is of this magnitude.

Additional errors are expected to arise from temperature jump (*7, 16, 22*) and stagnation effects. The maximum temperature jump for a surface gradient of 6,000°F./in. was calculated from the empirical equation of Kennard (*16*) to be 0.041°F. A maximum stagnation temperature rise at a gross velocity of 16 ft./sec. was predicted from potential flow theory to be 0.048°F.

The difference in temperature between the inner and outer surfaces of the silver shell of the sphere was computed to be 0.008°F. at the maximum thermal flux. The internal thermocouples were embedded in a nearly isothermal surface; therefore errors due to conduction along these thermocouples are negligible.

Since the position of the thermocouple junction is known to within ±0.0005 in. in the z direction, an uncertainty of 0.3°F. in the junction temperature exists at the maximum gradient observed. It is thus seen that the effects discussed above are of the same order of magnitude as this uncertainty and may be neglected. Hence the difference between the surface temperature and the temperature of the junction when nearly in contact with the surface, which was found to be 12.28°F., is considered equal to the thermocouple correction at the surface.

Differential Equation

To determine the thermocouple correction at a point in the air stream, a differential equation describing the temperature in the vicinity of the wire was developed. The convective thermal transfer rate per unit area results from the difference between the local air

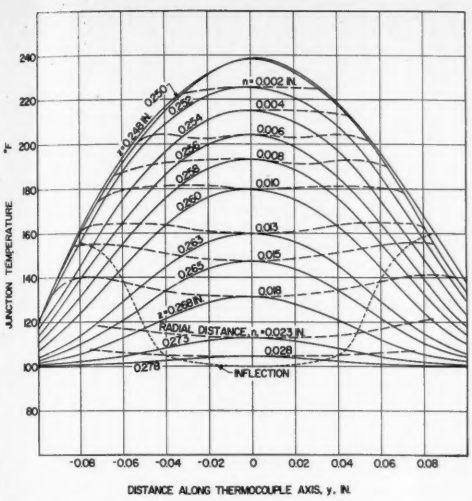

Fig. 4. Experimental junction temperatures in plane of equator.

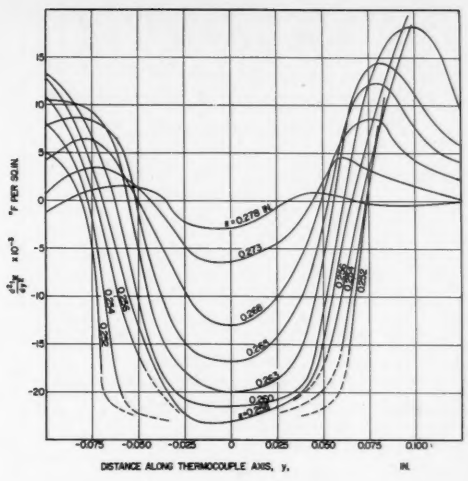

Fig. 5. Second derivative of experimental junction temperatures.

temperature and the wire temperature as indicated by Equation (1):

$$\mathring{Q} = h(t_a - t_w) \qquad (1)$$

The heat transfer coefficient of Equation (1) is based on the difference between air temperature and wire temperature rather than on the difference between free-stream temperature and wire temperature, as is usually the case. This distinction is of consequence when high-temperature gradients surround the wire.

The convective thermal transfer rate per unit length of wire is

$$\mathring{Q} = \pi h D(t_a - t_w) \qquad (2)$$

For steady state to exist, this must be equal to the rate of energy loss per unit length of wire by conduction along the wire, which is given by

$$\mathring{Q} = -\frac{\pi D^2}{4}\frac{d}{dy}\left(k\frac{dt_w}{dy}\right) \qquad (3)$$

Hence combining Equations (2) and (3) and simplifying results in the following equation

$$t_a - t_w = -\frac{D}{4h}\frac{d}{dy}\left(k\frac{dt_w}{dy}\right) \qquad (4)$$

The thermal conductivity of platinum is more than twice that of the platinum-rhodium alloy (*14*). The evaluation of the temperature gradient, dt_w/dy, near the junction, and of the thermal flux through the junction, $k(dt_w/dy)$, offers some difficulty, as these factors require a knowledge of the wire temperature in the neighborhood of the junction. The thermocouple junction was moved a short distance along the axis of the wire on either side of the point to which Equation (4) was being applied to establish a temperature distribution. Movement of the junction changes one boundary condition defining the solution to Equation (4). This boundary condition is the thermal conductivity of the wire as a function of y. Each junction temperature measured in this manner is one temperature from a different solution to the differential equation. The thermal flux $k(dt_w/dy)$ established from these temperatures may be in error.

From the foregoing discussion it is apparent that the direct solution of Equation (4) without further simplifying assumptions would require a numerical method involving detailed information concerning the temperature gradients near the junction. Some further simplifications appear desirable if the method is to be useful.

Solution to the Differential Equation

To gain insight into this problem, it is assumed that the thermal conductivities of the metals in the thermocouple are constant and equal. Under these circumstances it is possible to employ an apparent, consistent thermal conductivity which will satisfy the equation at several points in the temperature field and thus afford a good approximation to the actual behavior involving two different and variable thermal conductivities. Equation (4) then becomes

$$t_a - t_w = -\frac{Dk^*}{4h}\left(\frac{d^2t_w}{dy^2}\right) \qquad (5)$$

It should be recognized that the apparent thermal conductivity which is determined from experimental measurements with thermocouples at several points in the temperature field is not any particular kind of average of the thermal conductivities of the two metals. In the case of Equation (5) the location of the junction is not one of the boundary conditions. The second derivative of wire temperature and of the thermal flux in the wire in this instance can be approximated from a knowledge of junction temperatures as a function of position. The assumption of constant thermal conductivity throughout the wire permits the evaluation of all factors on the right side of Equation (5) except the heat transfer coefficient.

The data of Cole (*5*) for values of the heat transfer coefficient as a function of velocity can be used in conjunction with the velocity-distribution equation developed by Frössling (*8*) to obtain heat transfer coefficients as a function of position. However the presence of the wire in the boundary layer introduces uncertainties in the application of the heat transfer coefficients obtained in this way. To circumvent this problem it was assumed that the velocity and temperature fields are symmetrical about the x axis. By appropriate assumptions of symmetry with respect to temperature, velocity, and hence heat transfer coefficient, it is possible to establish the temperature correction from data at the two points of symmetry. The two points through which the thermocouple may pass are designated 1 and 2. These points are such than $n_1 \neq n_2 > r$.

The resulting equation is

$$t_{a1} = \frac{t_{w1} - t_{w2}\left[\left(\frac{d^2t_w}{dy^2}\right)_1 \Big/ \left(\frac{d^2t_w}{dy^2}\right)_2\right]}{1 - \left[\left(\frac{d^2t_w}{dy^2}\right)_1 \Big/ \left(\frac{d^2t_w}{dy^2}\right)_2\right]} \qquad (6)$$

Although Equation (6) does not contain the apparent thermal conductivity, it is implicit in its derivation that a single value of the apparent thermal conductivity may be applied. Air temperatures can be computed from junction temperatures by means of Equation

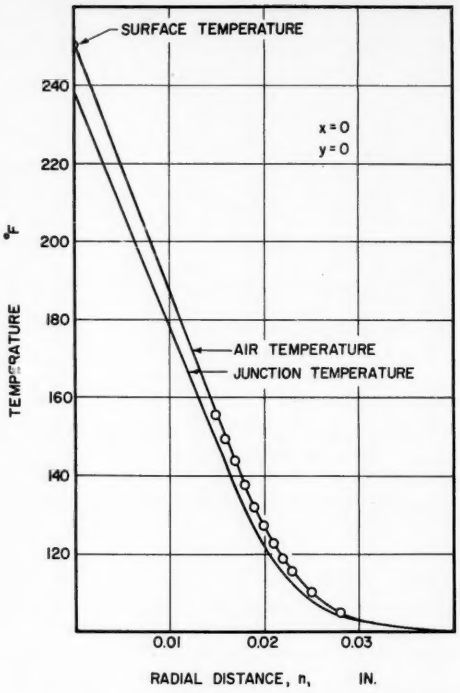

Fig. 6. Radial temperature distribution at equator.

(6), which is subject to the following restrictions:

$$h = \phi(n) \qquad t_{w1} \neq t_{w2}$$

$$k = \text{constant} \left(\frac{d^2 t_w}{dy^2} \right)_1 \neq \left(\frac{d^2 t_w}{dy^2} \right)_2$$

As a result of the existence of a number of assumptions, it appears advantageous to utilize Equation (6) in regions where the corrections are small. In the present instance Equation (5) was employed to delineate the locus of states where the correction was equal to zero, which corresponded to $d^2t_w/dy^2 = 0$.

EXPERIMENTAL RESULTS

Figure 4 illustrates the data obtained from experimental traverses. The temperatures, which were nearly linear with respect to z over a large portion of the field, were smoothed graphically. This operation yielded a standard deviation of approximately 0.15°F. The second derivatives of junction temperature with respect to y were computed from the smoothed data by the use of a three-point approximation (23). The curves for the second derivative in this region are shown in Figure 5. A five-point approximation (23) was tried, but it was found that use of fewer points gave more consistent results, because of the limited number of total points available. Undoubtedly the five-point approximation gave more accurate results near the center of the curve but apparently gave biased values at each end.

Since $d^2t_w/dy^2 = 0$ at an inflection point, it follows from Equation (5) that the thermocouple correction should be zero at such a point. By a numerical solution of Equation (5) it was established that the difference between the air temperature and junction temperature at an inflection point was less than 0.1% of the difference between the free stream and the surface temperatures if a shift in position of 0.0013 in the y direction was made. By the use of this corrected coordinate system, the junction temperature was assumed equal to the air temperature where $d^2t_w/dy^2 = 0$.

The line of inflection shown in Figure 4 was obtained from Figure 5. The intersection of each constant-radius curve with the inflection curve corres-

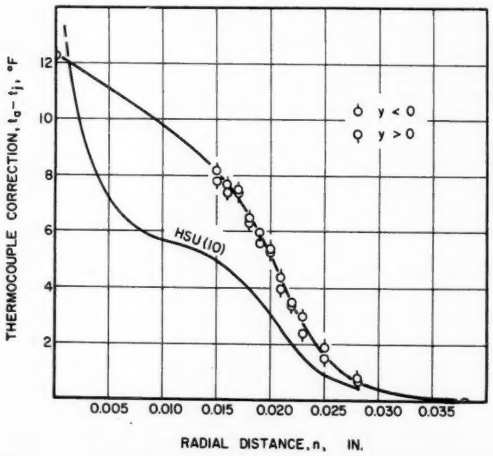

Fig. 7. Thermocouple corrections for a 0.001-in.-diameter thermocouple.

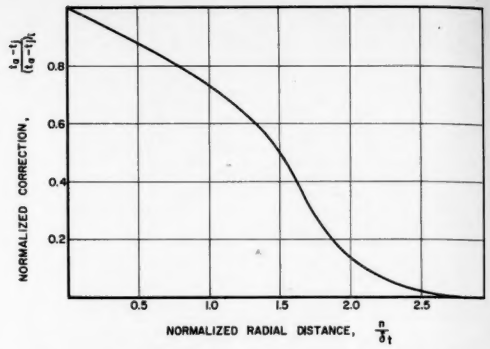

Fig. 8. Dimensionless thermocouple corrections for a 0.001-in.-diameter wire.

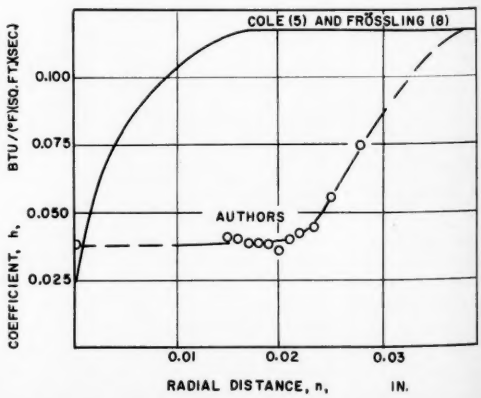

Fig. 9. Experimental convective heat transfer coefficients for a 0.001-in.-diameter wire near a 0.5-in. sphere.

ponds to the air temperature at that radius. The arithmetic average of the two air temperatures is shown in Figure 6. In Figure 7 the thermocouple corrections are compared with the thermocouple corrections computed by the method of Hsu (*10*) for the same conditions of flow. As the inflection curve of Figure 4 did not approach the sphere closer than 0.014 in. the air temperature, and consequently the thermocouple correction, could not be established in the region closer to the sphere than 0.014 in. The corrections calculated in the manner described are in good agreement with the value determined from the junction temperature near the interface and the surface temperature.

The measured junction-temperature gradient normal to the sphere at the equator is 5,730°F./in. This value is the slope of the junction-temperature curve in Figure 5 in the range $0 < n < 0.012$. The air-temperature gradient over the same range is 6,010°F./in. The local thermal flux established from the junction-temperature gradient is 4.9% low in this instance. The error in the local thermal flux determined in this manner varies with position around the sphere because, as observed in other heat transfer studies (*12*), the thermocouple correction at the surface decreases with increasing polar angle measured from the stagnation point.

Figure 8 shows values of thermocouple corrections which were obtained by normalizing the thermocouple corrections in Figure 6 with respect to the correction at the surface. The radial distances were normalized with respect to the thermal boundary-layer thickness, defined as

$$\delta_t = \int_0^x \frac{t_a - t_x}{t_i - t_s} dn \qquad (7)$$

For a fluid with constant physical properties the normalized correction may be a function of one or more of the following parameters: free-stream velocity, free-stream turbulence, diameter of sphere, and polar angle. Hsu (*12*) related temperatures in the boundary layer of a sphere to the Blasius function (*2*).

To calculate heat transfer coefficients it was necessary to obtain a suitable value of the thermal conductivity of the thermocouple. An apparent conductivity of 6.478×10^{-5} B.t.u./(sec.)(sq.ft.)(°F./ft.) was found by using a numerical solution of Equation (4) in conjunction with experimental data and assumed heat transfer coefficients of appropriate orders of magnitude.

Heat transfer coefficients for the thermocouple wire, computed by the use of the apparent thermal conductivity of platinum and platinum rhodium, are presented in Figure 9. Also shown, for comparison, are the heat transfer coefficients obtained with the equations of Frössling (*8*) and data of Cole (*5*). The large difference between the two sets of heat transfer coefficients is not surprising. As remarked earlier, the heat transfer coefficients used in this paper are based on air temperatures rather than free-stream temperatures. Close to the sphere the difference between the temperature potentials may well explain at least 75% of the discrepancy between the two sets of data. Furthermore the velocity gradient produces pressure gradients in the boundary layer of the wire, and flow parallel to the wire axis develops. Since temperature and velocity gradients at the equator are in opposite directions, this leads to a heat transfer coefficient lower than that determined in a free stream. This phenomenon may also explain the flat appearance of the curves of Figure 5 in the region near the surface of the sphere.

It is expected that the heat transfer coefficients obtained are applicable only in the vicinity of the equator, since gradient effects in other regions of the sphere are different.

ACKNOWLEDGMENT

The assistance of R. A. S. Brown, a Peter E. Fluor fellow, in connection with the experimental work reported here is acknowledged. Emilio Venezian contributed to the technical appraisal of the results and made several useful suggestions, and Ann Hansen contributed to preparation of the manuscript.

NOTATIONS

d	= differential operator
D	= diameter of thermocouple wire, in.
h	= thermal transfer coefficient, B.t.u./(°F.)(sq.ft.)(sec.)
k	= thermal conductivity, B.t.u./(°F./ft.)(sq.ft.)(sec.)
k^*	= apparent thermal conductivity B.t.u./(°F./ft.)(sq.ft.)(sec.)
n	= radial distance from surface of sphere, in.
$\dot{Q}$	= thermal flux, B.t.u./(sec.)(sq.ft.)
$\underline{\dot{Q}}$	= thermal transfer rate per unit length, B.t.u./(sec.)(sq.ft.)
r	= radius of sphere, 0.250 in.
t_a	= air temperature, °F.
t_i	= surface temperature, °F.
t_j	= junction temperature, °F.
t_w	= wire temperature, °F.
t_∞	= free-stream temperature, °F.
U_∞	= free-stream velocity, ft./sec.
x,y,z	= coordinate axes, in.
δ_t	= thermal boundary-layer thickness, in.
$\phi(\ )$	= function of

Subscripts

i	= surface of sphere
1,2	= points in the air stream

LITERATURE CITED

1. Baer, D. H., W. G. Schlinger, V. J. Berry, and B. H Sage, *J Appl. Mechanics*, **20**, 407 (1953).
2. Blasius, Heinrich, *Z. angew. Math. u. Phys.*, **56**, 1 (1908).
3. Boelter, L. M. K., and R. W. Lockhart, *Natl. Advisory Comm. Aeronaut. Tech. Note 2427* (1951).
4. Carslaw, H. S., and J. C. Jaeger, "Conduction of Heat in Solids," Clarendon Press, Oxford, England (1947).
5. Cole, Julian, and Anatol Roshko, in "1954 Heat Transfer and Fluid Mechanics Institute," pp. 12-23, California Book Company, Ltd., Berkeley, California (1954).
6. Corcoran, W. H., Franklin Page, Jr., W. G. Schlinger, and B. H. Sage, *Ind. Eng. Chem.*, **44**, 410 (1952).
7. Dickins, B. G., *Proc. Roy. Soc.* (*London*), **A143**, 517 (1934).
8. Frössling, Nils, *Natl. Advisory Comm. Aeronaut. Tech. Memo. 1432* (1958).
9. "Handbook of Chemistry and Physics," p. 2751, Chemical Rubber Publishing Company, Cleveland, Ohio (1957).
10. Hsu, N. T., Ph.D. thesis, California Inst. Technol., Pasadena (1956).
11. ———, H. H. Reamer, and B. H. Sage, Document 4219, Am. Doc. Inst., Washington 25, D. C. (1954).
12. ———, and B. H. Sage, *A.I.Ch.E. Journal*, **3**, 405 (1957).
13. Ingersoll, L. R., O. J. Zobel, and A. C. Ingersoll, "Heat Conduction with Engineering and Geological Applications," McGraw-Hill, New York (1948).
14. "International Critical Tables," Vol. V, p. 226, McGraw-Hill, New York (1929).
15. Johnson, N. R., A. S. Weinstein, and Fletcher Osterle, *Paper 57-HT-18*, Am. Soc. Mech. Engrs.—A.I.Ch.E. Heat Transfer Conference, University Park, Pennsylvania (August 1957).
16. Kennard, E. H., "Kinetic Theory of Gases," pp. 149, 311, McGraw-Hill, New York (1938).
17. King, L. V., *Trans. Roy. Soc.* (*London*), **A214**, 373 (1914).
18. Sato, Kazuhiko, and B. H. Sage, *Trans. Am. Soc. Mech. Engrs.*, **80**, 1380 (1958).
19. Schubauer, G. B., *Natl. Advisory Comm. Aeronaut. Tech. Rept. 524* (1935).
20. Shenker, Henry, J. I. Lauritzen, Jr., R. J. Corruccini, and S. T. Lonberger, *Reference Tables for Thermocouples*, National Bureau of Standards Circular 561 (1955).
21. Short, W. W., and B. H. Sage, *J. Appl. Mechanics*, to be published.
22. Smoluchowski, M., *Ann. Physik*, *64*, 101 (1898).
23. Southwell, R. V., "Relaxation Methods in Theoretical Physics," p. 17, Clarendon Press, Oxford, England (1946).

Manuscript received March 24, 1959; revision received July 24, 1959; paper accepted August 4, 1959.

On the Separation of Gas Mixtures in a Jet

EARL E. GOSE

University of California, Berkeley, California

In 1954 Becker found that the components of a gas mixture could be separated by allowing a jet of the gas mixture to expand in a low-pressure chamber. The heavier molecules would concentrate near the center of the jet and the lighter ones near the edge. Thus the jet could be split into two streams, one containing more of the heavy component and one containing more of the light component. In this paper it will be shown that this effect can be predicted from the kinetic theory of gases and that the predicted magnitude of the effect agrees favorably with the experimental data of Becker.

A diagram of the jet-separation apparatus employing an axially symmetric jet is shown in Figure 1. The axis of symmetry has been designated as the X axis. The gas mixture to be separated flows through the feed tube and expands into the low-pressure chamber. Here the jet is separated into two streams by the conically shaped divider D. The center stream will contain more of the heavy component, and the side stream will contain more of the light component. These streams may then be recompressed and sent to other jet-separation units. A typical separation process would employ many such units, arranged in a cascade.

An alternative to the circular orifice indicated in Figure 1 would be one in the form of a long slit. Although the calculated separations are somewhat lower for this geometry, it would allow a much greater throughput per unit and could effect a substantial saving in equipment cost.

THEORY

The basic assumptions in this development are

1. The gas in the feed tube has a Maxwell-Boltzmann distribution of velocities superimposed on the mean bulk-gas velocity.
2. The jet is axially symmetric.
3. Collisions between molecules in the low-pressure region (collector) may be neglected.

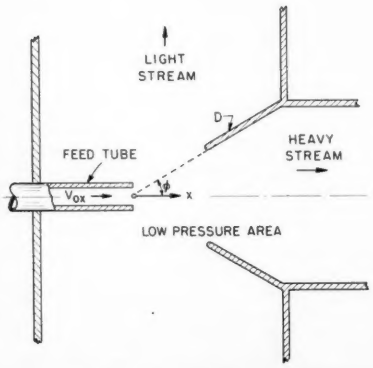

Fig. 1. Diagram of jet separation apparatus.

Allowing no collisions between molecules in the collector describes the limiting case of zero pressure in the collector. Actual pressures used by Becker were on the order of 0.01 mm. Hg. At this pressure and room temperature the mean free path of N_2 is 6 mm. As the dimensions of the apparatus were about 1 mm., it is seen that neglecting collisions is not unreasonable so long as the dimensions of the apparatus are kept small.

The Maxwell-Boltzmann velocity-distribution function for a pure gas in three dimensions may be written as

$$dn = n_o \left(\frac{m}{2\pi kT}\right)^{3/2} e^{-\frac{m}{2kT}[(V_x - V_{ox})^2 + V_y^2 + V_z^2]}\, dV_x\, dV_y\, dV_z \qquad (1)$$

Figure 2 shows that

$$V_y^2 + V_z^2 = V_*^2 = V_x^2 \tan^2\theta \qquad (2)$$

In the V_*, θ α coordinate system Equation (1) becomes

$$dn = n_o \left(\frac{m}{2\pi kT}\right)^{3/2} e^{-\frac{m}{2kT}V_{ox}^2 \sin^2\theta}\, e^{-\frac{m}{2kT}\left[\frac{V_*}{\sin\theta} - V_{ox}\cos\theta\right]^2} \frac{V_*^2}{\sin^2\theta}\, dV_*\, d\theta\, d\alpha \qquad (3)$$

To obtain the angular distribution of molecules, Equation (3) is integrated over the range $0 \leq \alpha \leq 2\pi$ and $0 \leq V_* \leq \infty$. This gives the angular distribution of molecules:

$$dn = n_e e^{-\beta^2}\left[e^{\beta^2\cos^2\theta}\left(\frac{1}{2} + \beta^2\cos^2\theta\right)\operatorname{erfc}(-\beta\cos\theta) + \frac{\beta}{\sqrt{\pi}}\cos\theta\right]\sin\theta\, d\theta \qquad (4)$$

where the dimensionless parameter is defined as

$$\beta = V_{ox}\sqrt{\frac{m}{2kT}} \qquad (5)$$

and the complementary error function is

$$\operatorname{erfc}(t) = \frac{2}{\sqrt{\pi}}\int_t^\infty e^{-t_1^2}\, dt_1 \qquad (6)$$

The jet is now broken into two streams. All molecules moving at an angle greater than some particular value of θ, say ϕ, go into the side stream; the remainder go into the center stream. The number in the side stream is found by integrating (4) from $\theta = 180$ deg. to $\theta = \phi$. This yields

$$f = \frac{1}{2}\cos\phi\, e^{-\beta^2\sin^2\phi}\operatorname{erfc}(-\beta\cos\phi) + \frac{1}{2}\operatorname{erfc}(\beta) \qquad (7)$$

where $f = n/n_o$.

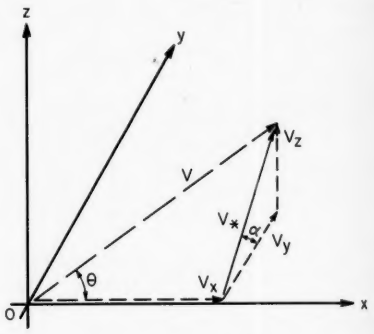

Fig. 2. Vector diagram.

According to kinetic theory, the velocity distribution of one component of a gas mixture is unaffected by the presence of the other components. Thus for a multicomponent mixture Equation (7) will be valid for each component separately, with the appropriate value of β inserted for each component. This equation may be used to predict separations of multicomponent mixtures. For a two-component mixture the separation coefficient is defined by the ratio of light to heavy molecules in the light stream divided by the same ratio for the heavy stream:

$$A = \frac{\left[\frac{\%\text{ light}}{\%\text{ heavy}}\right]_{\text{light stream}}}{\left[\frac{\%\text{ light}}{\%\text{ heavy}}\right]_{\text{heavy stream}}} \qquad (8)$$

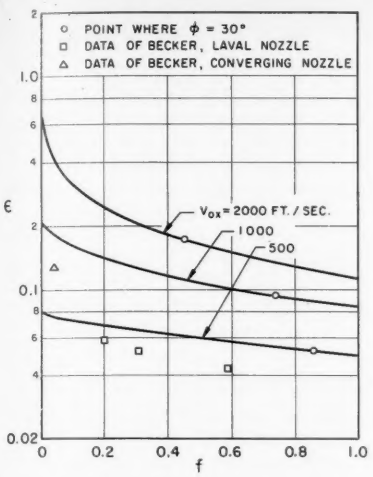

Fig. 3. Separation factors for mixtures of argon-36 and argon-40 at 300°K. For the converging nozzle, the calculated velocity and temperature was 600 ft./sec. at 226°K. This gives the same value of β as 693 ft./sec. at 300°K. For the De Laval nozzle the calculated velocity and temperature was 1,010 ft./sec. at 39°K. This gives the same value of β as 2,790 ft./sec. at 300 °K.

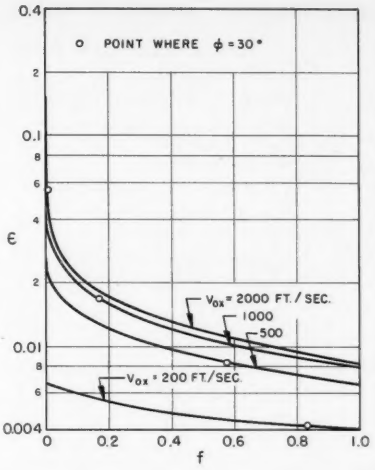

Fig. 4. Separation factors for mixtures of $U^{235}F_6$ and $U^{238}F_6$ at 300°K.

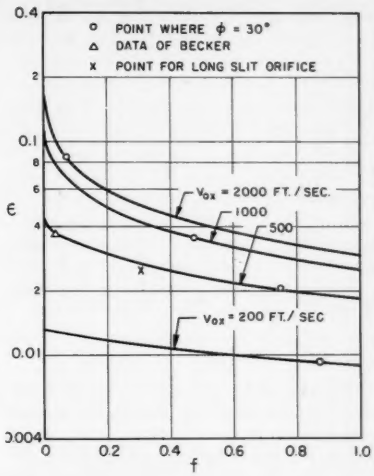

Fig. 5. Separation factors for mixtures of xenon-130 and xenon-134 at 300°K. The data of Becker were taken at a calculated velocity of 600 ft./sec. and a calculated temperature of 226°K. The point for the long slit was calculated for a velocity of 1,000 ft./sec., a temperature of 300°K., and an angle of 30 deg.

The enrichment factor is defined as $A-1=\epsilon$; thus $\epsilon \geq 0$. When ϵ is small, it is essentially independent of the feed composition. Substituting Equation (7) into this definition, one gets

$$\epsilon = \frac{\left[\cos\phi\, e^{-\beta_L{}^2 \sin^2\phi}\ \mathrm{erfc}\ (-\beta_L\cos\phi) + \mathrm{erfc}\ (\beta_L)\right] - \left[\cos\phi\, e^{-\beta_H{}^2 \sin^2\phi}\ \mathrm{erfc}\ (-\beta_H\cos\phi) + \mathrm{erfc}\ (\beta_H)\right]}{\left[\cos\phi\, e^{-\beta_H{}^2 \sin^2\phi}\ \mathrm{erfc}\ (-\beta_H\cos\phi) + \mathrm{erfc}\ (\beta_H)\right]\left[1-\frac{1}{2}\cos\phi\, e^{-\beta_L{}^2 \sin^2\phi}\ \mathrm{erfc}\ (-\beta_L\cos\phi) - \frac{1}{2}\mathrm{erfc}\ (\beta_L)\right]} \tag{9}$$

For separations where the difference in β values is small, as in isotopic separations, Equation (9) involves a small difference between large numbers. When one uses digital computers capable of a large number of significant figures, this is no hindrance. However for hand calculation a more convenient form may be obtained by expanding f in a Taylor series and retaining only the first term. The result of this is

$$\epsilon = \frac{\left(\frac{\partial f}{\partial \beta}\right)_\phi (\beta_L - \beta_H)}{f(1-f)} \tag{10}$$

Here f is found from Equation (7), and $(\partial f/\partial\beta)_\phi$ is

$$\left(\frac{\partial f}{\partial \beta}\right)_\phi = \frac{e^{-\beta^2}}{\sqrt{\pi}}\left[\cos^2\phi - 1 - \sqrt{\pi}\,\beta e^{\beta^2 \cos^2\phi}\ \mathrm{erfc}\ (-\beta\cos\phi)\sin^2\phi\cos\phi\right] \tag{11}$$

Equation (10) applies only if the relative difference between the values of β, and hence of f, for the two components is small.

TWO-DIMENSIONAL JET

For a two-dimensional jet, that is one where the orifice is a long narrow slit, expressions for f and ϵ may be derived in a manner similar to the above for the axially symmetric jet. In this case one of the integrals cannot be expressed in closed form. The result for f is

$$f = e^{-\beta^2}\left[1 - \frac{\phi}{\pi} + \int_\phi^\pi \frac{\beta}{\sqrt{\pi}}\cos\theta\, e^{\beta^2 \cos^2\theta}\ \mathrm{erfc}\ (-\beta\cos\theta)\, d\theta\right] \tag{12}$$

NUMERICAL RESULTS

Predicted enrichments have been calculated for some typical separations with the aid of an IBM-650 computer and are presented in Figures 3, 4, and 5. It was assumed here that the inlet temperature was 300°K.; inlet velocities were 200, 500 1,000 and 2,000 ft./sec. When the velocities are supersonic, the curves indicated will apply only if no shock waves are formed in the separation zone. Approximate sonic velocities at 300°K. for argon, xenon, and uranium hexafluoride are 900, 500 and 300 ft./sec. respectively. Becker's data (*1, 2*) on the separation of Ar^{36}–Ar^{40} mixtures are plotted in Figure 3 for comparison. In Becker's experiment the pressure in the inlet tube was 30 mm. Hg, and the pressure in the collector was 0.01 mm. Hg. The orifice dimensions and the approximate throughputs were given by Becker, and from these, inlet velocities and temperatures have been calculated as indicated on the figures. The DeLaval (converging-diverging) nozzle gave smaller enrichment factors than the converging nozzle, even though the calculated velocity is greater and the calculated temperature is less. This may be due to mixing caused by shock waves formed in the low-pressure region by the DeLaval nozzle. On each theoretical curve the point at which the collection angle ϕ is 30 deg. has been indicated by a circle; this gives an indication of the variation of geometry which the other parameters involved.

For the separation of the isotopes of uranium hexafluoride (Figure 4) it is seen that the predicted enrichment factor for jet separation is larger than 0.003, the value for the commonly used process of barrier effusion. This indicates that jet separation should be given serious consideration for separations of this type. One great advantage of jet separation as contrasted with the competing process of barrier effusion is the extreme simplicity of the apparatus used. This would allow construction and maintenance costs to be kept very low.

From Figure 5 it may be seen that

the values of ϵ for the long slit are lower than the values for the circular orifice. However the long slit may be more practical because of the reduced equipment cost; for example a circular orifice 1 mm. in diameter will pass only 700 g. uranium hexafluoride/hr. at a pressure of 30 mm. Hg and a velocity of 1,000 ft./sec., while a slit 1 mm. by 1 m. will pass 900 kg. under the same conditions. Thus the smaller enrichment may be justified by the greatly increased throughput made possible by the long slit.

ACKNOWLEDGMENT

The author would like to thank Lawrence M. Grossman for his suggestions and criticism concerning this work, and Andreas Acrivos and E. E. Petersen for their valuable interest. This research was supported in part by a grant from the National Science Foundation.

NOTATION

A = separation coefficient for a two-component mixture
f = fraction of feed entering the side stream
k = gas law constant
m = mass of molecule
n_c = total number of molecules
T = absolute temperature
V = molecular velocity
V_{ox} = bulk-gas velocity at orifice
V_x = molecular velocity component in the x direction
V_y = molecular velocity component in the y direction
V_z = molecular velocity component in the z direction
V_* = sum of x and y velocity components

Greek Letters

α = angle between V_* and V_y
β = dimensionless parameter, $\beta = V_{ox}\sqrt{\frac{m}{2kT}}$
β_H = value of β for the member of a two-component mixture having the higher molecular weight
β_L = value of β for the member of a two-component mixture having the lower molecular weight
ϵ = enrichment factor for a two-component mixture
θ = angle between V and the x axis
ϕ = angle at which jet is broken into two streams by the divider

LITERATURE CITED

1. Becker, Bier, and Buyhoff, Z. *Naturforsch.*, **10a**, 565 (1955).
2. Becker, *ibid.*, **12a**, 609 (1957).

Manuscript received September 23, 1958; revision received May 4, 1959; paper accepted May 7, 1959.

COMMUNICATIONS TO THE EDITOR

Dear Editor:

The policy of publishing translations of the better papers which appear in Japanese Journals is a good one. Since we have been studying heat transfer to Bingham plastics, the paper by Hirai which appeared recently in the *Journal* (*1*) was not unknown to us; however having the English translation was quite helpful. The problem of heat transfer to a Bingham plastic in laminar flow is important because of the extreme velocities required to attain turbulent flow, and consequently in many industrial applications the flow will be laminar. The same problem considered by Hirai has been solved independently by the writers (*2*) using an entirely different approach. Owing to differences in the mean temperature reported by Hirai in Figure 4 of the original paper and the mean temperatures that we calculated, we have studied the paper rather carefully. The following errors or omissions were noted.

Equations (1.18), (1.19), and (1.20) are improper because the functions $P_m(\xi)$ are not orthogonal on the interval $(a, 1)$. This can be seen by observing that $P_m(\xi)$ satisfies

$$\frac{d^2P_m}{d\xi^2} + \frac{1}{\xi}\frac{dP_m}{d\xi} + \beta^2{}_m\left[1 - \left(\frac{\xi-a}{1-a}\right)^2\right]P_m = 0 \quad (1.10)$$

$$P_m(1) = 0$$

$$\frac{dP_m(0)}{dr} = 0 \text{ (not specified by Hirai)}$$

Equations (1.18), (1.19), and (1.20) are valid only if

$$\int_a^1 P_m(\xi)P_n(\xi)\xi\left[1 - \left(\frac{\xi-a}{1-a}\right)^2\right]d\xi$$

$$= 0 \text{ if } m = n$$

$$= \text{constant if } m = n$$

From Equation (1.10)

$$\int_a^1 P_m(\xi)P_n(\xi)\xi\left[1 - \left(\frac{\xi-a}{1-a}\right)^2\right]d\xi$$

$$= \left(\frac{a}{\beta_m{}^2 - \beta_n{}^2}\right)\left[\frac{dP_m(a)}{d\xi}P_n(a) - \frac{dP_n(a)}{d\xi}P_m(a)\right]$$

The right-hand side can be zero only if

$$P_m(a) = 0$$

or if

$$\frac{1}{P_m(a)}\frac{dP_m(a)}{d\xi} = \frac{1}{P_n(a)}\frac{dP_n(a)}{d\xi}$$

Referring to Figure 3 of Hirai's original paper, we see that neither of these conditions is satisfied by P_0, P_1, and P_2. Consequently the functions $P_m(\xi)$ are not orthogonal, and even if a set of A_m's existed as defined in Equation (1.18), they could not be determined by the use of Equations (1.19) and (1.20).

We wonder why Hirai has not mentioned the second solution of Equation (1.10). This solution cannot be thrown out because of its singularity at $\xi = 0$, since the solution is used only in the region from $\xi = a$ to $\xi = 1$. As a result of this omission Hirai has apparently satisfied only the condition

$$\theta(r_p) = \theta_p(r_p)$$

and assumed that the condition

$$\frac{\partial\theta(r_p)}{\partial r} = \frac{\partial\theta_p(r_p)}{\partial r}$$

is satisfied.

1. Hirai, E., *A.I.Ch.E. Journal*, **5**, 13 (1959).
2. Wissler, E. H., and R. S. Schechter, *Chem. Engr. Progr. Symposium Ser. No. 29*, **55**, 203 (1959).

Yours very truly,
ROBERT S. SCHECHTER AND EUGENE H. WISSLER
The University of Texas, Austin, Texas

Pseudocritical Constants for Gas Mixtures

L. C. CASE and H. C. WEBER

Massachusetts Institute of Technology, Cambridge, Massachusetts

Among a number of methods for predicting the *PVT* behavior of gas mixtures, one of the simplest is the use of the compressibility-factor chart and Kay's rule for pseudocritical constants. The Beattie-Bridgman equation gives good results but is tedious. Recently methods based upon a statistico-mechanical treatment of suitable molecular models have appeared. The method of the present note is intended to give a quick estimate from limited empirical data. Although its precision and generality are less than those of the more basic approaches, it is considerably superior to Kay's rule, which is still widely used.

Using Kay's rule one assumes that the pseudocritical temperatures and pressure of gaseous mixtures are linear combinations of those of the components. However the deviations from actual data are considerable. In this work the pseudocritical values for a number of gas mixtures were determined and compared with Kay's rule. It was hoped that systematic deviations would be found and that a general treatment of the deviations would be possible.

PROCEDURE

The data of Su as reported by Seferian (*6*) were used in constructing the compressibility-factor chart, which was used as the generalized compressibility-factor plot. For each isotherm of the μ chart the minimum value of the compressibility factor was plotted vs. reduced pressure (Figure 1). The corresponding values of reduced temperature are noted on the curve. Note that the minimum compressibility factor for a chosen isotherm corresponds to a particular value of reduced temperature and pressure.

For example, suppose that for a certain gas mixture the isotherm minimum in compressibility factor occurs at 585°R. and 127 atm. and that the compressibility factor at that point is 0.80. From Figure 1 the reduced temperature and pressure for that point are 1.50 and 3.44, respectively. The pseudocritical temperature, which will be called the *experimental pseudocritical*, is then 585/1.50 = 390°R., and the experimental pseudocritical pressure is 127/3.44 = 36.9 atm.

In some cases adjusted pseudocriticals are also reported. These give a better fit to the entire isotherm than those values determined by the simple procedure.

Table 1. Pseudocriticals for Carbon Dioxide

Temperature, °F.	Pseudocriticals: Temperature, °R.	Pseudocriticals: Pressure, atm.
100	550	85.0
160	547	75.5
220	545	63.3
280	536	75.1
340	531	72.7
400	521	71.3
460	504	69.4
Average	535	73.2
True critical	547.7	73.0

RESULTS

As a first example of the use of the method, pseudocritical values for carbon dioxide were calculated from the data of Reamer, Olds, Sage, and Lacey (*2*). The values for isotherms from 100° to 460°F., obtained by the use of the minima chart, are given in Table 1.

The pseudocritical values for methane-propane mixtures are given in Table 2. Both the approximate values calculated from the minima chart and adjusted values for good fit along the

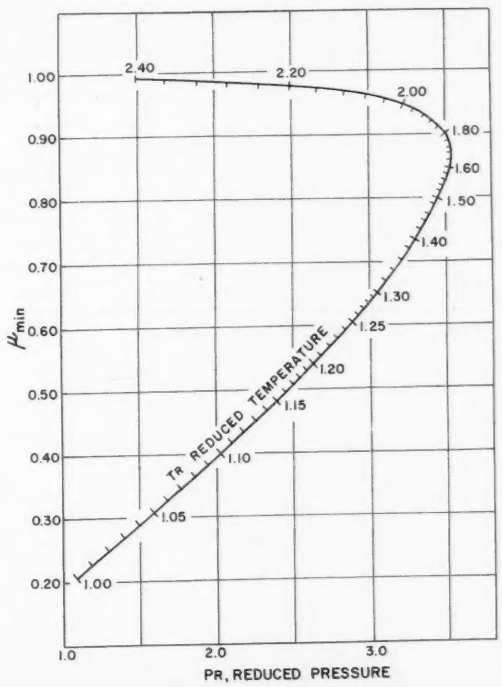

Fig. 1. Plot of μ-chart minima.

L. C. Case is with Purdue University, Lafayette, Indiana.

isotherm are given in some cases. If only one value is given, it is the approximate value.

In Table 3 a typical comparison for calculated and observed compressibilities is given. The comparison is made for a mixture of 60% methane and 40% propane at 55°C. In Figure 2 are shown the deviations of the experimental pseudocritical values from those predicted by Kay's rule for this mixture.

DISCUSSION

It is seen that the method used here allows a facile determination of approximate pseudocriticals for a gas or a gas mixture, provided that an isotherm has been determined in the region of $1 \leqq T_r \leqq 2$. Once the approximate values are known, it is a relatively simple matter to adjust the values empirically to provide a good fit to the entire isotherm. The method gives a very good value for the pseudocritical temperature, and little adjustment is needed. However because of the low curvature of the isotherm near the minimum, it is frequently found that the pseudocritical pressure requires substantial adjustment.

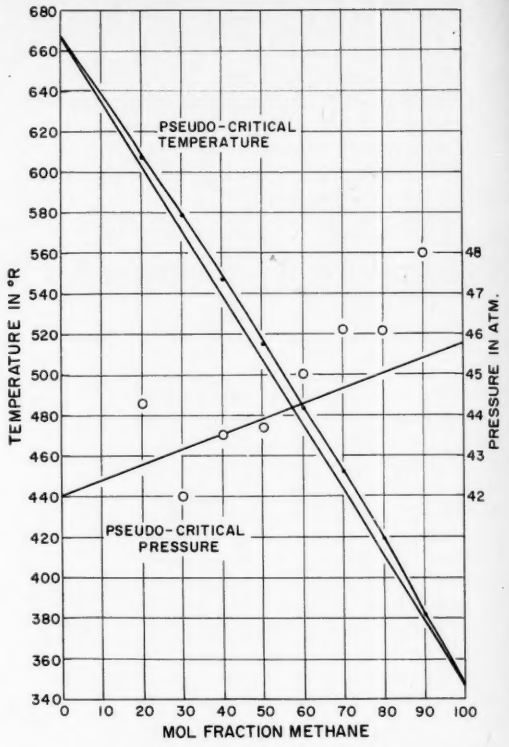

Fig. 2. Pseudocriticals, methane-propane.

Table 2. Pseudocriticals, Methane-Propane
(First value is approximate, second is adjusted)
Mole fraction methane

Temperature, °C.	0.2	0.3	0.4	0.5	0.6	0.7	0.8	0.9
				Pseudocritical temperature, °R.				
20							417, 417	381, 377
40					484, 484	452, 452	418, 417	384
55				514	482, 484	448, 451	415, 417	378
70			549	515	485	453, 451	418, 418	382
90	607	579	547	517	482	454, 454	415, 424	389
				Pseudocritical pressure, atm.				
20							46.6, 46.6	50.5, 47.0
40					43.3, 44.5	46.8, 45.5	43.9, 45.5	48.8
55				42.8	38.2, 44.5	48.0, 45.5	45.5, 46.6	48.7
70			43.7	45.0	47.0	51.4, 48.0	49.8, 48.0	48.7
90	44.3	42.0	43.3	43.2	44.0	46.4, 45.5	42.2, 44.0	45.9

Table 3. Compressibility Factor, Methane-Propane
0.60 mole fraction methane, 55°C.

Pressure, atm.	Experimental compressibility	Calculated compressibility Adjusted-fit values $T_c = 484$°R., $P_c = 44.5$ atm.	Calculated compressibility Kay's rule $T_c = 472.8$°R., $P_c = 44.3$ atm.
20	0.920	0.913	0.920
40	0.847	0.825	0.841
60	0.739	0.737	0.754
80	0.655	0.650	0.687
100	0.602	0.590	0.635
120	0.575	0.569	0.609
140	0.583	0.579	0.610
160	0.604	0.604	0.627
180	0.631	0.637	0.655
200	0.664	0.665	0.687

The deviations of the pseudocriticals from Kay's rule are seen to be substantial. The deviations are positive for both pressure and temperature for the system methane-propane but are symmetrical for temperature only. The deviations for methane-ethane (5) and methane–*n*-butane (4) are similar but not identical. The deviations of the hydrocarbons and carbon dioxide, including those for methane–carbon dioxide (2), ethane–carbon dioxide (3), and *n*-butane–carbon dioxide (1), are substantially negative. Thus it seems unlikely that an over-all generalization can be made regarding the deviations. However because of the similarity of the deviations in similar systems limited generalizations are possible, and these generalizations give considerably better estimates of the compressibility factor than does Kay's rule.

LITERATURE CITED

1. Olds, R. H., H. H. Reamer, B. H. Sage, and W. N Lacey, *Ind. Eng. Chem.*, **41**, 475 (1949).
2. *Ibid.*, **36**, 88 (1944).
3. *Ibid.*, **37**, 688 (1945).
4. Sage, B. H., R. A. Budenholzer, and W. N. Lacey, *ibid.*, **32**, 1262 (1940).
5. Sage, B. H., and W. N. Lacey, *ibid.*, **31**, 1497 (1939).
6. Seferian, Ralph, thesis, Mass. Inst. Technol., Cambridge (1950).

A Distribution Function for Oil Mixtures and Polymers

OTTO REDLICH

Shell Development Company, Emeryville, California

The representation of the composition of various oil mixtures by continuous functions was discussed by Lederer (*1*) long ago. He also pointed out that algebraic distribution functions were desirable. Nowadays the need for algebraic functions is more pressing, since they are by far the best means of feeding extensive data into an automatic computer. The obvious independent variable for oil mixtures is the vapor pressure, and so the value of the distribution function $X(p)$ gives the mole fraction of the material that has a vapor pressure higher than p. Continuous distribution functions have been introduced also by Bowman and Edmister (*2*), although they did not use algebraic functions.

In a search for a useful distribution function the first choice will be, of course, the normal function dependent on an appropriate argument. Since the vapor pressure is essentially a partition coefficient, its value is just as significant as the value of its reciprocal. Whenever a quantity and its reciprocal are *a priori* equally significant, the best choice of a variable is usually the logarithm since a transformation from p to $1/p$ changes only the sign of $\log p$. Indeed the logarithmic-normal distribution furnishes a fairly good representation of quite a few oil mixtures. Still there are, in general, systematic deviations exceeding the limits of experimental error.

A much better representation is achieved by generalizing the log-normal function in the same way that the normal distribution function was generalized by Charlier (*3*). The Gram-Charlier series generalizes the Gaussian function by adding its derivatives, multiplied by empirical coefficients. The term of order zero is the Gaussian. The two coefficients of the Gaussian (mean and standard deviation) are always so chosen that the coefficients of the first and second order terms of the Gram-Charlier series are zero. Following Charlier, we restrict the expansion of the series to the terms of third and fourth order, thus obtaining a function containing four experimental parameters. It will be called the *nearly log-normal* function. Most of the properties of the nearly normal function are discussed in textbooks (*3*) and need not be repeated here. The values and significance of various means of the vapor pressure are of interest.

THE NEARLY LOG-NORMAL FUNCTION

We start from the Gaussian

$$G = (2\pi)^{-0.5} \exp(-0.5t^2) \qquad (1)$$

expressed in the reduced variable

$$t = (1/r) \log (p_m/p) \qquad (2)$$

We prefer to take $\log (1/p)$ as the independent variable rather than $\log p$, so that we may count the cumulative mole fraction, as usually, beginning with the light material and ending with the heavy material. The function G/r is then the log-normal frequency function of $1/p$; that is the mole fraction of substances with vapor pressures between p and $p + \Delta p$ is given by

$$(G/r)\Delta\log(1/p) = (2\pi)^{-0.5} \exp(-0.5t^2)\Delta t. \qquad (3)$$

For the nearly log-normal distribution we introduce, in addition to p_m and r, two more individual parameters h_3 and h_4. The frequency function is now given by

$$f\Delta\log(1/p) = G[1 - h_3(t^3 - 3t) + h_4(t^4 - 6t^2 + 3)]\Delta t \qquad (4)$$

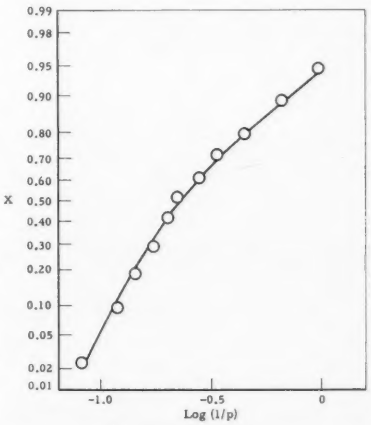

Fig. 1. Vapor-pressure distribution of a gas oil at 370°C. Curve: log p_m = 0.585; r = 0.288; h_3 = −0.176; h_4 = −0.013, pressure in atmospheres.

Integration furnishes the distribution function

$$X = \int_{-\infty}^{t} G(z)dz + G(t)[h_3(t^2 - 1) - h_4(t^3 - 3t)] \qquad (5)$$

which gives the cumulative mole fraction of the substances with vapor pressures above p.

For the determination of the coefficients we assume that average vapor pressures p_i have been found for a number of cuts containing mole fractions x_i of the oil mixture. The coefficients are then given by

$$\log p_m = \Sigma x_i \log p_i;$$

$$r^2 = \Sigma x_i [\log(p_m/p_i)]^2 \qquad (6)$$

$$h_3 = -\Sigma x_i [\log(p_m/p_i)]^3/6r^3 \qquad (7)$$

$$h_4 = \Sigma x_i [\log(p_m/p_i)]^4/24r^4 - 0.125 \qquad (8)$$

The vapor-pressure distribution of a gas oil at 370°C., as calculated from determinations of true boiling points, is shown in Figure 1. The ordinate is the cumulative mole fraction on a so-called "probability scale"; that is any distribution normal in the abscissa values (log normal in $1/p$ or p) appears as a straight line. The observations shown in Figure 1 can be crudely approximated by a straight line, but the deviations are systematic and by no means negligible; however, the curve, calculated according to (*5*), represents the measurements within the experimental errors. Other oil mixtures (kerosene, various refinery streams) have been found to show similar distributions.

POLYMERS

The nearly log-normal function is equally useful for polymers. Wesslau (*4*) and recently Chiang (*5*) discussed the use of the log-normal distribution function for polymers. Actually the situation is precisely the same as in the case of oil mixtures. As soon as reasonably accurate data are available, systematic deviations are found, which however are small enough to

allow a representation by Equations (4) and (5).

For polymers we replace $1/p$ by the molal weight, and so instead of (2) we have

$$t = (1/r)\log(M/M_m) \qquad (9)$$

Similar substitutions are made in (6), (7), and (8). In addition, we prefer to use weight fractions rather than mole fractions so that X in Equation (5) is replaced by the cumulative weight fraction W and x_i in (6) to (8) by the weight fraction w_i. It makes little difference which kind of variable we choose; indeed, it can be shown that a log-normal distribution for weight fractions implies a log-normal distribution for mole fractions with the same standard deviation (6).

Various average molal weights are of interest for polymers. In order to obtain a general result, we define the average molal weight of order g by

$$(M_g)^g = \int_{-\infty}^{\infty} M^g f d\log M \qquad (10)$$

We introduce the nearly normal frequency function (4) (after replacing $1/p$ by M) into (10) and obtain after a slightly involved calculation* for the average molal weight of order g:

$$\log M_g = \log M_m + 1.152\, gr^2 + g^{-1}\log[1 - h_3(2.3\, gr)^3 + h_4(2.3\, gr)^4] \qquad (11)$$

Thus we have quite convenient expressions for the number average molal weight $M_n(g = -1)$:

$$\log M_n = \log M_m - 1.152\, r^2 - \log[1 + h_3(2.3r)^3 + h_4(2.3r)^4], \qquad (12)$$

for the viscosity molal weight by writing the exponent a of the relation of Mark and Houwink for g in (11), and for the weight average molal weight $M_w(g = 1)$

$$\log M_w = \log M_m + 1.152\, r^2 + \log[1 - h_3(2.3r)^3 + h_4(2.3r)^4] \qquad (13)$$

The relations given by Chiang (5) for the log-normal distribution follow from (11) with $h_3 = h_4 = 0$.

In general one will interpret the terms containing h_3 and h_4 in all these relations as correction terms, representing small deviations from the log-normal distribution. In other words, h_3 and h_4 should be small compared with unity. Practically the permissible limits of h_3 and h_4 will depend on the magnitude of r and also on the specific application.

AVERAGE VAPOR PRESSURES

Returning to oil mixtures, we define the average ideal vapor pressure and the average reciprocal ideal vapor pressure by

$$p_a = \sum_i x_i p_i; \quad 1/p_r = \sum_i x_i/p_i \qquad (14)$$

The reciprocal vapor pressure determines the dew point of the mixture. Replacing M by $1/p$, we obtain from (13) and (12)

$$\log p_a = \log p_m + 1.151 r^2 + \log[1 + h_3(2.3r)^3 + h_4(2.3r)^4] \qquad (15)$$

$$\log p_r = \log p_m - 1.151 r^2 - \log[1 - h_3(2.3r)^3 + h_4(2.3r)^4] \qquad (16)$$

NOTATION

G	= Gaussian [Equation (1)]
M	= molal weight
M_g	= average molal weight of order g
M_m	= geometric average molal weight
M_n	= number average molal weight
M_w	= weight average molal weight
W	= cumulative weight fraction
X	= cumulative mole fraction
f	= frequency function [Equation (4)]
h_3, h_4	= coefficients of the Hermitian terms
p	= vapor pressure
p_i	= vapor pressure of species i
p_m	= geometric mean vapor pressure
p_a	= average vapor pressure
p_r	= average reciprocal vapor pressure
r	= standard deviation
t	= reduced distribution variable [Equations (2), (9)]
w_i	= weight fraction of species i
x_i	= mole fraction of species i

ACKNOWLEDGMENT

We are obliged to R. M. Smith and W. H. McFadden for help and discussions.

LITERATURE CITED

1. Lederer, E. L., *Petroleum*, **31**, No. 6, 1 (1935).
2. Bowman, J. R., *Ind. Eng. Chem.*, **41**, 2007 (1949); **43**, 2622 (1951). ———, and W. C. Edmister, *Chem. Eng. Progr. Symposium Ser. No. 2*, **48**, 112 (1952); **48**, No. 3, 76 (1952). Edmister, W. C., and D. H. Buchanan, *ibid.*, **49**, No. 6, 69 (1953). *Ind. Eng. Chem.*, **47**, 1685 (1955).
3. Charlier, C. V. L., "Vorlesungen über die Grundzüge der mathematischen Statistik," Lund, Sweden (1931). See also H. Cramér, "Mathematical Methods of Statistics," Princeton Univ. Press, Princeton, (1951).
4. Wesslau, H., *Makromol. Chem.*, **20**, 111 (1956).
5. Chiang, R., *J. Polymer Sci.*, **36**, 91 (1959).
6. Mussa, C., *J. Appl. Polymer Sci.*, **1**, 300 (1959).

* We substitute t for M with the aid of (9), transform to a new variable $y = t - 2.303\, gr$, and order the polynomial into Hermitian polynomials. Then the integration is easy because of the relation between Hermitian polynomials and the derivatives of G.

Liquid-side Mass Transfer Coefficients in Packed Towers

H. L. SHULMAN, STANLEY PRESS, and W. G. WHITEHOUSE

Clarkson College of Technology, Potsdam, New York

In the June, 1959, issue of the *A.I.Ch.E. Journal*, Onda, Sada, and Murase (4) presented a correlation for liquid-phase mass transfer coefficients based on values of k_L for Raschig rings obtained by dividing the volumetric coefficient, by the wetted area of Fujita (2). Since the authors showed that their correlation does not provide insight into the mechanism of absorption, because the same correlation is obtained with either the two-film theory

or the penetration theory assumed, the only justification for the correlation is that it is more convenient or can be used where other design methods fail.

For design purposes the correlation must be used with the wetted-area data of Fujita (2) which limits its application to Raschig rings and water systems. In a recent communication Professor Onda (5) mentions having obtained an equation for the wetted area of Berl saddles which was used to check his correlation for Raschig rings. He found that he could use the same type of correlation, but the constant for Berl saddles was 0.018 instead of the 0.013 recommended for Raschig rings. It is obvious then that the correlation is not of a general enough nature to be useful for extension to other packing systems. For design purposes the equations of Sherwood and Holloway (6) are more convenient and thoroughly tested.

The authors claim that their correlation supports the assumption that the effective interfacial area is directly proportional to the wetted areas which they employed. If this were true, it should be possible to use a_w to extract k_G from k_Ga and obtain a correlation in terms of the gas-phase Reynolds and Schmidt numbers and/or other dimensionless groups. To test this possibility the Raschig-ring data of Fellinger (1) (corrected for liquid-phase resistance) and Houston and Walker (3) were divided by the appropriate Fujita value of a_w to extract k_G, which is plotted in Figure 1 for nine systems. An examination of the figure indicates that any correlation of the k_G values will show k_G as a function of liquid rate. If a_w was directly proportional to the true a, the resulting values of k_G would be almost independent of the liquid rate. In addition the curvature of the lines implies that no simple function of the gas rate would be suitable for a correlation. On the basis of these two observations it is possible to conclude that wetted areas are not equal to, or directly proportional to, the true effective areas in packed absorption towers.

A basic weakness in the authors' approach to the problem is the assumption that the effective interfacial area is independent of gas rate. This assumption is based on extensive k_La data taken at very low gas rates with the exception of a few points by Sherwood and Holloway (6) for 1.5-in. rings. Shulman and co-workers (7) pointed out how an erroneous conclusion can be reached because the few points taken at high gas rates happen to be in a region where a is just about independent of gas rate. Moreover their data for a (7) indicate a strong dependence on gas rate for the smaller packings, such as the rings used in the paper under discussion.

Correlations for k_L and k_G based on the same effective interfacial areas were published by Shulman and coworkers (7) some time ago. Recently Yoshida and Koyanagi (8) determined effective interfacial areas, by means of an entirely different method, which were in agreement. In both cases a seemed to be unrelated to a_w. Literature surveys (8) show greater disagreement in the extensive data for a_w than in the data for a.

Enough basic work on mass transfer rates has been done to predict that major advances in the understanding of packed columns must come from studies of effective interfacial areas, rather than from the reworking of data obtained from columns which are not representative of those in use.

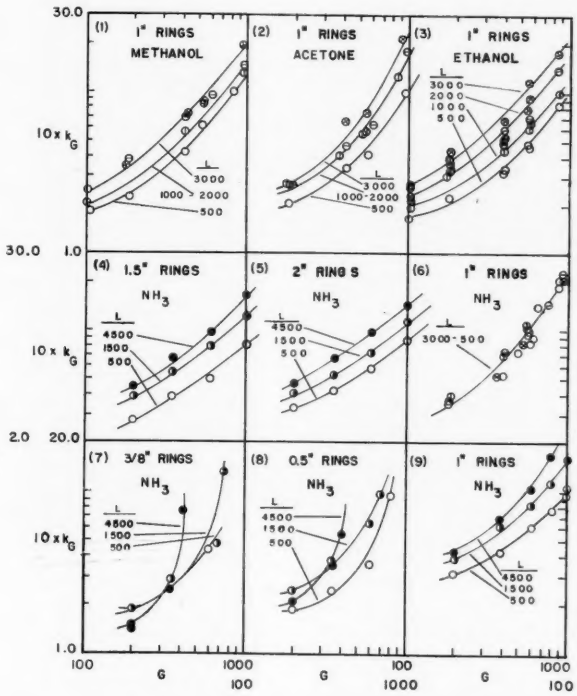

Fig. 1. k_G obtained from k_Ga for Raschig ring, air-water-solute systems: 1, 2, 3, and 6 from Houston and Walker (3), and 4, 5, 7, 8, and 9 from Fellinger (1).

NOTATION

a = effective interfacial area, sq.-ft./cu.ft.
a_w = wetted area, sq.ft./cu.ft.
G = superficial gas rate, lb./(hr.)(sq.ft.)
k_G = gas-phase mass transfer coefficient, lb. moles/(hr.)(sq. ft.)(atm.)
k_L = liquid-phase mass transfer coefficient, lb. moles/(hr.)-(sq.ft.)(lb.moles/cu.ft.)
L = superficial liquid rate, lb./(hr.)(sq.ft.)

LITERATURE CITED

1. Fellinger, L., Sc.D. thesis, Mass. Inst. Technol., Cambridge (1941).
2. Fujita, S., and S. Sakuma, *Chem. Eng. (Japan)*, **18**, 64 (1954).
3. Houston, R. W., and C. A. Walker, *Ind. Eng. Chem.*, **42**, 1105 (1950).
4. Onda, Kakusaburo, Eizo Sada, and Yasuhiro Murase, *A.I.Ch.E. Journal*, **5**, 235 (1959).
5. Onda, Kakusaburo, Private Communication.
6. Sherwood, T. K., and F. A. L. Holloway, *Trans. Am. Inst. Chem. Engrs.*, **36**, 39 (1940).
7. Shulman, H. L., C. F. Ullrich, A. Z. Proulx, and J. O. Zimmerman, *A.I.Ch.E. Journal*, **1**, 253 (1955).
8. Yoshida, F., and T. Koyanagi, *Ind. Eng. Chem.*, **50**, 365 (1958).

CHEMICAL ENGINEERING PROGRESS SYMPOSIUM SERIES ABSTRACTS

The Chemical Engineering Progress Symposium Series is composed of papers on specific subjects conveniently bound in individual books, which are published at intervals. The books are 8½ by 11 inches, paper covered, and cost as follows: "Adsorption, Dialysis, and Ion Exchange," $3.50 to members, $4.50 to nonmembers; "Nuclear Engineering Part VI," $3.50 to members, $4.50 to nonmembers. They may be ordered from the Secretary's Office, the American Institute of Chemical Engineers, 25 West 45 Street, New York 36, New York.

The *A. I. Ch. E. Journal* will publish, from time to time, abstracts of the articles appearing in the Symposium Series volumes.

ADSORPTION, DIALYSIS, AND ION EXCHANGE, Vol. 55, No. 24, 1959

Basic Principles Involved in the Macroseparation of Adjacent Rare Earths from Each Other by Means of Ion Exchange, J. E. Powell and F. H. Spedding. The separation of rare-earth mixtures by ion exchange with ammonium ethylenediaminetetraacetate and ammonium *N*-hydroxyethylethylenediaminetriacetate as eluting agents has been discussed in detail. It has been shown how simple countercurrent separation theory can be applied to more complex systems, and experimental data have been presented for some of the groups of rare-earth species that are separated with difficulty. **Gaseous Diffusion Through Microporous and Adsorbent Membranes,** Karl Kammermeyer. General knowledge about gaseous diffusion plants is limited. No commercial installations have as yet materialized which utilize barrier separation. This paper discusses the definition of barrier, permeability as a mass transfer coefficient, effect of variables on permeability, the correlation between adsorption isotherm and surface flow, and the applications of barrier separation. **Dialysis,** J. A. Lane and J. W. Riggle. Methods and equations are presented for estimating the over-all dialysis coefficients for the dialysis of a single electrolyte or a single electrolyte and many nonelectrolytes from the physical properties of the dialysis membrane and the diffusion coefficient of the dialyzing material. A differential equation is presented. The conditions under which each integrated form may be used for the design of commercial equipment are illustrated. The possibility of making a separation by means of dialysis between two different-sized solute molecules also is explored. **Molecular Separations by Solution Ultrafiltration,** W. E. Henderson and C. M. Sliepcevich. The purpose of this investigation was to determine the factors which control the retention of nonelectrolytes by ultrafiltration membranes having heterogeneous pore structures. This investigation was also extended to a ternary solution. Proposed mechanisms for the observed effects were tested by correlating the experimental data. **Applications of Ion Exchange Membranes in Electrodialysis,** E. A. Mason and Walter Juda. Various typical examples of membrane-cell configurations used for electrodialysis are presented to show the versatility of application of these new materials. Included are the dilution or concentration of electrolytes, the separation of electrolytes and nonelectrolytes, metathesis reactions, oxidation-reduction reactions, acid-base reactions, and the separation of ions of like charge. **Gas and Vapor Flow in Microporous Barriers,** Karl Kammermeyer and Lenard O. Rutz. Gaseous flow through any microporous membrane or barrier will not take place unless accompanied by some flow in a condensed phase. If a membrane possesses a fine enough microporous structure to act as a barrier in gaseous flow, it represents a capillary system with a sufficiently high adsorptive capacity to give rise to adsorbed or surface flow. The term *condensed flow* is used to describe this phenomenon in a generic manner. **Filtration of Strong Electrolytes,** Ernest J. Breton, Jr., and C. E. Reid. Physical separations of some sort are important steps in many chemical processes, ranging from the removal of suspended materials from liquids by sedimentation, filtration, or centrifuging to the removal of dissolved molecules by crystallization or distillation. In this work electrical resistance measurements were made of specific ions across cellulose acetate membranes. **Design of Electrodialysis Equipment,** E. A. Mason and T. A. Kirkham. The principles of operation, design, and cost evaluation of equipment using ion exchange membranes for electrodialysis applications are discussed. Design equations for prediction of electrical resistance, transfer-area requirements, and energy consumption are presented.

Metathesis Reactions by Means of Ionic Membranes, G. P. Monet. Metathesis reactions can be carried out by electrodialysis used with ionic membranes. Experimental techniques are described for measuring the potential drop across a unit cell and for measuring the selectivity and resistance of a single ionic membrane. At present metathesis applications appear limited because of the poor selectivity of ionic membranes in acidic and basic solutions. **Ultrafiltration of Salt Solutions Through Ion Exchange Membranes,** J. G. McKelvey, Jr., K. S. Spiegler, and M. R. J. Wyllie. Ion exchange resin membranes were used in the ultrafiltration of sodium chloride solutions of various concentrations. The experiments were conducted in a special ultrafilter which was electrically insulated and contained silver-silver chloride electrodes for streaming potential measurements, and a thermal-convection type of arrangement for continuous mixing of the solution. **Selective Adsorption of Toluene From *n*-Heptane by Silica Gel,** E. R. Schmelzer, M. C. Molstad, and P. F. Hagerty. The transfer of a component to a fixed bed of adsorbent is widely prevalent in chemical operations. The method is employed for purposes of purification, recovery, separation, or analysis. Examples of such usage include the dehumidification of gases, the clarification of oils and syrups, the elimination of noxious gases from the respiratory atmosphere, the fractionation of hydrocarbons, and the chromatographic analysis of multicomponent and complex mixtures.

NUCLEAR ENGINEERING—PART VI, Vol. 55, No. 23, 1959

Recovery of Radioactive Cesium at Hanford, B. F. Judson, R. L. Moore, H. H. Van Tuyl, and R. W. Wirta. Methods are being developed for recovering radioactive cesium present in high-level waste streams from Hanford's plutonium separations plants. Precipitates would be converted to a stable, radiochemically pure cesium salt, packaged for shipment as a radiation source. A survey of the potential market for radiation sources has been initiated to determine whether enough demand can be forseen for Hanford's operation of a cesium recovery plant. **Control-Rod Drive Mechanism for the Argonne Low Power Reactor,** W. J. Kahn. The control-rod drive mechanism for the Argonne Low Power Reactor (ALPR) is a rack-and-pinion type that operates in contact with the primary reactor fluid. The mechanism is located above the reactor, with the pinion drive shaft extending through a pressure-breakdown, collected-leakage seal. This paper will describe the characteristics of the drive mechanism and its design, development, and testing. **Radiolytic and Pyrolytic Decomposition of Organic Reactor Coolants,** D. R. de Halas. A rate law has been derived for the combination of radiolytic and pyrolytic damage to organic coolants in a dynamic system. Based on obser-

(*Continued on page 4M*)

COMPUTER PROGRAM abstracts

Readers of the *A.I.Ch.E. Journal* who are interested in programming for machine computation of chemical engineering problems will find in each issue of *Chemical Engineering Progress* abstracts of programs submitted by companies in the chemical process industries. Collected by the Machine Computation Committee of the A.I.Ch.E., these programs will be published as manuals where sufficient interest is indicated. The following abstracts have appeared:

CEP (May, 1959), p. 94

Line Sizing*
Shell and Tube Heat Exchanger Rating
Orifice Design
Flange Design

* Manual available.

CEP (June, 1959), p. 134

Tarner Method
Bubble Cap Tray Design (Two Programs)
Regression Analysis
Piping Flexibility

CEP (July, 1959), p. 90

Non-linear Estimation (016)
Humble Plate-to-Plate Distillation Procedure for Conventional and Complex Columns (017)
Liquid-Liquid Heat Exchanger Design (018)
Multicomponent Distillation (020)

CEP (August, 1959), p. 78

Specific Impulse Calculations (019)
Generalized Flash Sub-Program (021)
Curve Fitting (022)
Mass Spectrometer Calculations (023)

CEP (September, 1959), p. 86

Circuit Shaft Speeds (005)
Box Cooler (007)
Curve Plotting Routine (013)
Response Surface Evaluation (025)

CEP (October, 1959), p. 90

Resistance Temperature Tables (024)
Solution of the Brunauer, Emmett and Teller Multimolecular Adsorption Equation (027)
TRAP – Tape Regression Analysis Program (IBM 650–Tape); RAPA– Regression Analysis Program (Augmented IBM 650); RAP–Regression Analysis Program (Basic IBM 650) (028)

CEP (November, 1959), p. 92

Self Supporting Steel Stack (009)
Growth Curves (029)
Calculation of Tension in Span Adjacent to Broken Conductor (026)

CEP (December, 1959), p. 88

Flange Rating (031)
Pressure Drop in Piping Networks (030)
Minimum Reflux for Distillation by the Bachelor Method (032)

A. I. Ch. E. TECHNICAL MANUALS

PUMP Manual

An indispensable guide for the engineer!

Contained in the manual are descriptions and illustrations of the most generally used types of pumps, with a guide to the best type for a given service; a glossary of terms; standard data sheets for inquiry and record; a brief guide to the solution of pump corrosion problems.

The manual is an 8½- by 11-inch looseleaf binder convenient for the addition of further material. The price is $10 to members of A.I.Ch.E., $20 to nonmembers.

American Institute of Chemical Engineers, 25 West 45 Street, New York 36, N. Y.

Send me ——— copies of the Pump Manual. ☐ Check for $——— enclosed, (Please add 3% sales tax for delivery in New York City.)

☐ Bill me.

NAME

ADDRESS

Member ☐ Nonmember ☐

J-3-60

TWO ROUTES TO THE TOP

for Engineers and Scientists

...new, long range commercial development programs have created two distinctive career routes for engineers and scientists:

PROJECT ENGINEERS

To coordinate the efforts of an engineering team in the R & D of new concepts in fields of Gas Cromatography or IR or UV Spectroscopy. These positions require a strong academic background in physical science or engineering plus ability to assume major responsibility for complete development programs.

SENIOR SCIENTISTS

To investigate basic theoretical concepts for new analytical instruments and to serve as consultant to project groups in fields of Gas Chromatography or IR or UV Spectroscopy. Qualified candidates will probably have an advanced degree and recent academic or industrial experience related to instrument development.

In addition to professional growth and recognition, these positions offer top salaries, benefits and services, plus an opportunity to enjoy Southern California living at its best.

For further details, airmail a brief sketch of your background to T. O. Williams.

Beckman® *Instruments, Inc.*
2500 Fullerton Road, Fullerton, California

Reprints Available:

DIMENSIONLESS NUMBERS

Pages 55-64, September CEP

Members and Nonmembers

1-9	copies	$.50 each
10-99	copies	.40 "
100-999	copies	.25 "
1000	copies	.15 "

Student Chapters and Colleges

1-9	copies	$.25 each
10-99	copies	.20 "
100-999	copies	.15 "
1000	copies	.13 "

Add 3% Sales Tax for delivery in New York City.

Order from Publications Dept.

American Institute of Chemical Engineers
25 West 45 Street
New York 36, N. Y.

(*Continued from page 176*)

vations of the radiolytic damage in the test loop and of the behavior of the radiolytic tars toward heat, this law provides a simple method of determining the maximum utilizable temperature for an organic coolant. **Some Aspects of the Use of an Organic Coolant in a Heavy-Water-Moderated Power Reactor,** Malcolm J. McNelly. Organic materials have been assessed as a possible alternative to the heavy water coolant in a natural-uranium-fueled heavy-water-moderated power reactor. These materials provide scope for appreciable cost reduction in this reactor system. **Studies on Characteristics of Savannah River Wastes,** Bernard Manowitz, C. W. Pierce, and Samuel Zwickler. Laboratory and pilot plant studies were carried out at Brookhaven National Laboratory in support of the Savannah River program on the storage and concentration of liquid wastes. Vertical temperature distribution, over-all heat transfer coefficients, and foaming characteristics were observed during storage. The foaming and scaling characteristics of low-level wastes were followed for evaluation of waste-concentration criteria. **Blending VS. Reenrichment for Slightly Enriched Uranium,** Donald Kallman and John E. Brennan. Although the A.E.C. has contemplated tthe reenrichment of irradiated but decontaminated uranium, there may be economic advantage to the power plant operator to blend irradiated fuels with highly enriched uranium instead. **Nuclear Safety Considerations in the Storage and Handling of Fuel Elements,** Norman Ketzlach. Calculation methods to determine design criteria for nuclear safety specifications in the storage and handling of slightly enriched fuels are presented. The importance of understanding the reactor theory involved in interpreting results of calculation so that they may safely be applied to plant process conditions cannot be over-emphasized. The importance of standardization of transportation specifications for shipping large quantities of these fuels is also been indicated. **Heat Transfer Characteristics of Polyphenyl Coolants,** M. Silberberg and D. A. Huber. In support of the Organic Moderated Reactor Experiment, heat transfer characteristics of several polyphenyls were investigated in a laboratory heat transfer loop. The operation conditions were as follows: fluid temperatures, 480° to 770°F.; heater surface temperatures, 565° to 875°F.; fluid velocities, 5 to 25 ft./sec.; heat fluxes, 40,000 to 290,000 B.t.u./(hr.)(sq.ft.); and Reynolds number, 20,000 to 300,000. Heat transfer correlations obtained by a digital-computer technique are discussed. **Corrosion-Screening of Component Materials for Potassium Soda Heat-Exchange Systems,** Samuel J. Basham, John H. Stang, and Eugene M. Simons. Sixty-one materials, including high-temperature alloys, pure metals, cermets, and ceramics, which might be useful for special components are discussed. In high-temperature sodium-potassium flow systems were screened in tilting-furnace corrosion experiments. Post-test corrosion evaluations were based on metallographic examinations of the specimens, specimen weight-change measurements, container compatibility examinations, and specimen surface-roughness changes. The materials were divided into three classes according to corrosion resistance. **Boiling Pressure Drop in Thin Rectangular Channels,** N. C. Sher and S. J. Green. Methods for predicting boiling and nonboiling pressure drop in thin rectangular channels, independently of the void data, have been developed for 2,000 lb./sq. in. abs. Void data, obtained at Battelle by the use of rectangular channel at 2,000 lb./sq. in. abs., have been reviewed. These data generally show that the homogeneous model is adequate for boiling at 2,000 lb./sq. in. abs. at qualities above 10%. Techniques for utilizing experimental void data in pressure drop data analyses have been developed. Two-

Phase Steam-Water Pressure Drops, H. S. Isbin, R. H. Moen, R. O. Wickey, D. R. Mosher, and H. C. Larson. Frictional pressure drops for steam-water mixtures have been determined for the following ranges of conditions: pressure, 25 to 1,415 lb./sq. in. abs.; total flow rate, 454 to 4,350 lb./hr.; and quality from about 0.008 to 0.98. The steam-water mixtures were synthesized by mixing steam and water, and pressure drops were measured for adiabatic flow in horizontal pipes 0.484- and 1.062-in. I.D. The data are compared to standard correlations, and a new restricted correlation is suggested which takes into account the pressure and flow rate dependencies. **Free-Convection Heat Transfer to Water and Mercury in an Enclosed Cylindrical Tube,** J. P. Hartnett, W. E. Welsh, Jr., and F. W. Larsen. Local free-convection heat transfer results are reported for water and mercury with uniform heat flux. The system was found to be inherently quasisteady with the temperature oscillations more pronounced with mercury as the working fluid. Experimental data were also obtained with the tube inclined 30 deg. from the vertical, and the resulting heat transfer performance was found to be significantly increased. **Auxiliary Equipment for Radiochemical Processing,** W. E. Unger. Most radiochemical processing equipment are basically similar to their industrial counterparts. The principal distinguishing differences are details of design, the quality standards to which radiochemical equipment is fabricated, and the massive shielding peculiar to the latter. Examples of both specially designed items, and the adaptation of commercial equipment, including valves, filters, centrifuges, samplers, and carrier-chargers, are described. **Flow Generation, Measurement, and Control,** J. Dunn and H. M. Jones. The design criteria for equipment in a remotely operated aqueous separations plant are presented. Improved materials of construction, seal design, and methods of remote replacement have made it possible to adapt submerged regenerative and deep-well turbine pumps, driven by motors located above and sealed from the tanks, to chemical-separations service. Description of a typical flow-system installation is presented, together with a detailed description of the rotameter-transmitter, amplifier-converter, recorder-controller, and control valve. **Treatment of Radioactive Wastes with Ion Transfer Membranes: Removal of Bulk Electrolytes,** E. A. Mason, E. J. Parsi, and A. J. Giuffrida. Use of anion transfer membranes in electrolytic cells was investigated as a means of removing and separating bulk electrolytes from cationic fission products. Nitric acid and aluminum nitrate were used as typical electrolytes, and sodium was used as a tracer representing cationic species. Deacidification of nitric acid and precipitation of hydrous aluminum oxide in granular form were accomplished. The mechanism of deacidification, effect of operating variables, and stability of membranes to chemical and radiation attack are discussed. A brief cost estimate is included.

ERRATUM

The term k_e in Equations (13) and (15) and in Figure 3 of "Estimation of Stage Efficiency of Simple Agitated Vessels Used in Mixer-Settler Extractors" by Robert E. Treybal appearing on page 202 of the June, 1958, issue should be replaced by (mk_e), where $m = dc_e/dc_D$, the notation being the same as in the paper.

This change results in a slight improvement in the over-all agreement of observed and calculated efficiencies. The correction has been incorporated in the paper "The Economic Design of Mixer-Settler Extractors," page 474 of the December, 1959, issue.

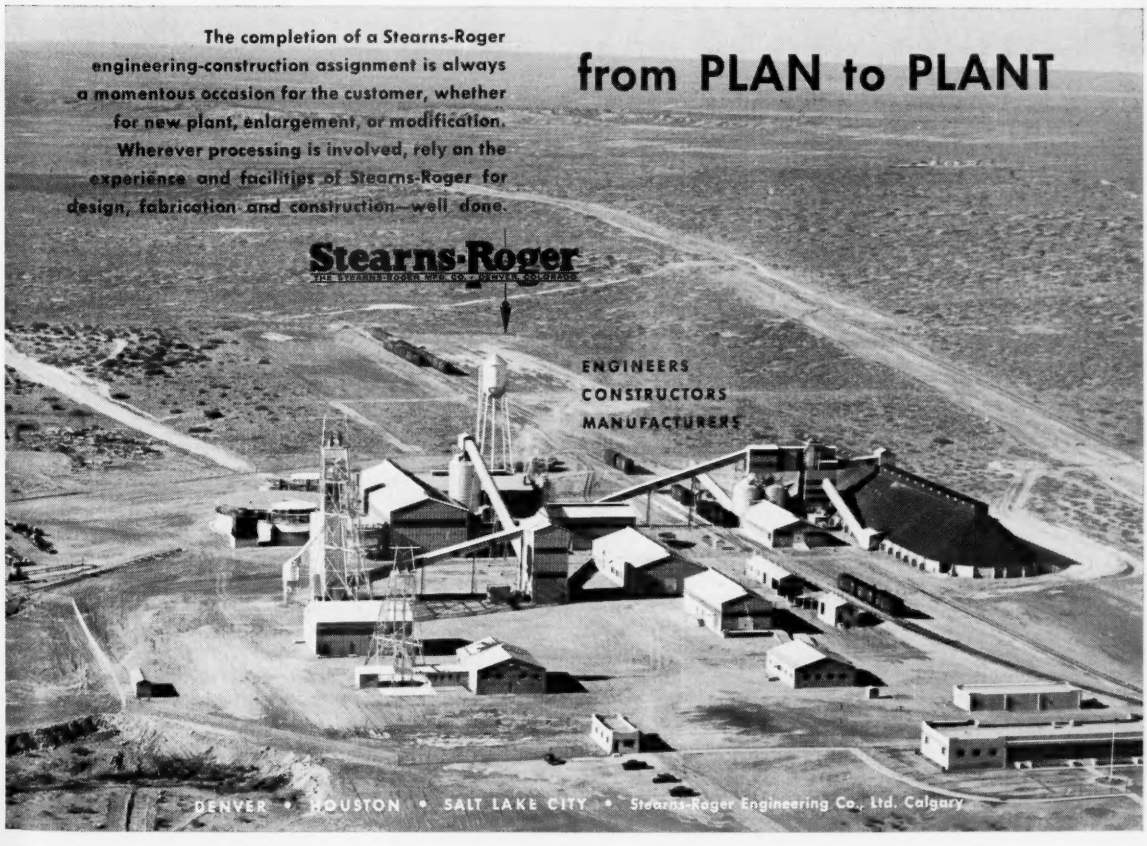
The completion of a Stearns-Roger engineering-construction assignment is always a momentous occasion for the customer, whether for new plant, enlargement, or modification. Wherever processing is involved, rely on the experience and facilities of Stearns-Roger for design, fabrication and construction—well done.
from PLAN to PLANT
Stearns-Roger
ENGINEERS
CONSTRUCTORS
MANUFACTURERS
DENVER • HOUSTON • SALT LAKE CITY • Stearns-Roger Engineering Co., Ltd. Calgary

STAND and be counted

for the SYMPOSIUM SERIES

A STANDING ORDER

ensures your not missing a needed book and saves you 10% on each book

Each book in the Series is a collection of papers in a specific field of chemical engineering. Some papers have been presented at A.I.Ch.E. symposia during national meetings; some have been submitted directly for publication. All are reviewed by experts in the particular fields and revised before publication.

During 1959 eight books were published—on heat transfer; nuclear engineering; computer techniques, chemical engineering education; reaction kinetics; adsorption, dialysis, and ion exchange.

At least six more are planned for 1960—on rockets and missiles, computer techniques, nuclear engineering, and heat transfer.

This Series is produced in an attractive but economical format—8½ x 11 inch volumes, paper covered, averaging 150 to 200 pages. It is priced as close to cost as possible for Members and about one-third higher for others.

MONOGRAPH & SYMPOSIUM SERIES

29-S. Heat Transfer—Chicago: The A.I.Ch.E.-sponsored papers presented at the Joint Heat Transfer Conference in 1958. $4.00 to members, $5.00 to nonmembers.

28-S. Nuclear Engineering, Part VIII: The A.I.Ch.E.-sponsored papers presented at the 1958 Nuclear Congress, together with additional papers from A.I.Ch.E. Symposia. $3.50 to members, $4.50 to nonmembers.

26-S. Chemical Engineering Education—Academic and Industrial: The new philosophies behind both graduate and undergraduate curricula, together with descriptions of successful programs held in industry. $3.00 to members, $4.00 to nonmembers.

25-S. Reaction Kinetics and Unit Operations: 23 surveys of the basic fields in chemical engineering, covering the most recent developments and future trends. $3.50 to members, $4.50 to nonmembers.

24-S. Adsorption, Dialysis, and Ion Exchange: Detailed discussion of the use of these operations in fractionation and other operations, with emphasis on the chemical viewpoint. $3.50 to members, $4.50 to nonmembers.

18-S. Heat Transfer—Louisville: Studies of vertical tubes, forced-circulation boiling, cross-flow cooling tower, burnout, boiling liquids, metal vapors, condensation, large temperature differences, single-baffle exchangers. Vol. 52; paper bound; about 125 pp.; $3.00 to members, $4.00 to nonmembers.

17-S. Heat Transfer—St. Louis: Data on surface boiling, liquid metals, gas-solid contact, convection; solids melting, immiscible liquids, nonisothermal flow, and jacketed agitated kettles. Vol. 51; paper bound; 125 pp.; $3.00 to members, $4.00 to nonmembers.

9-S. Heat Transfer—Research Studies: Data on fluidized systems, free convection between horizontal surfaces, temperature-level and radiation effects, liquid-solid suspensions, two-phase, two-component flow, pyrolisis-coil designs, and metal wetting and gas entrainment. Vol. 50; paper bound; 67 pp.; $1.50 to members, $2.25 to nonmembers.

5-S. Heat Transfer—Atlantic City: Studies of heated tubes, liquid metals, fluidized beds, three-fluid exchangers, etc. Vol. 49; paper bound; 162 pp.; $3.00 to members, $4.00 to nonmembers.

22-S, 23-S, and 27-S Nuclear Engineering—Parts V, VI, and VII: In all, 63 papers on the chemical engineering aspects of the nuclear field. Most of the A.I.Ch.E.-sponsored papers presented at the 1958 Nuclear Congress are included in Part VI. $3.50 each to members, $4.50 each to nonmembers.

19-S. Nuclear Engineering, Part IV: Containing papers sponsored by the A.I.Ch.E. at the second nuclear engineering and science congress, in Cleveland, this volume of 206 pages contains more on reactors, solvent extraction systems, economic design of power packages, neutron flux in critical assemblies, engineering design, reactor site selection, metallurgy, etc. Vol. 52; paper bound; $3.00 to members, $4.00 to nonmembers.

13-S. Nuclear Engineering, Part III: The third volume from the Ann Arbor meeting covers pulsed-column techniques; the breeder reactor; recovery of uranium from pitchblende; radiochemical processes; a series of articles on the impact of the atomic field on health, safety of individuals, education, etc.; materials testing reactor, radioisotope utilization. Vol. 50, 274 pp., paper bound; $3.00 to members, $4.00 to nonmembers.

12-S. Nuclear Engineering, Part II: The second volume from the first nuclear engineering congress, held at Ann Arbor, continues the technology of the first volume—reactors, analog computing techniques for reactor analysis, evaluation of reactor coolants, metallurgy, waste disposal, radiation damages and effects on structural materials. Vol. 50, 259 pp., paper bound; $3.00 to members, $4.00 to nonmembers.

11-S. Nuclear Engineering, Part I: The first volume from the first nuclear engineering congress, held at Ann Arbor, contains articles on the metallurgy of zirconium, beryllium, thorium, uranium, heat transfer studies in the nuclear field; and articles on reactors including the Swedish reactor; chlorination of aromatics under gamma radiation; gamma-ray polymerization of styrene and methyl methacrylate. Vol. 50, 280 pp., paper bound; $3.00 to members, $4.00 to nonmembers.

AMERICAN INSTITUTE OF CHEMICAL ENGINEERS
25 West 45 Street, New York 36, New York

Enroll us in your Symposium Series STANDING ORDER GROUP to receive all future publications as soon as published, and bill them at 10% discount. Ship books to attention of the following person who will be acquainted with this operation:

PRINT NAME _____

ORGANIZATION _____

STREET _____

CITY _____ ZONE _____ STATE _____

Member ( ) Nonmember ( )

If you would like to start with some of the earlier publications you may have missed, enter the numbers here:

_____

16-S. Mass Transfer—Transport Properties: Studies of gas bubbles, gas-film transfer, nonisothermal systems, liquid drops, thermal diffusion, gas viscosity, rotating cylinders, intermolecular forces. Vol. 51; paper bound; 125 pp.; $3.00 to members, $4.00 to nonmembers.

15-S. Mineral Engineering Techniques: Studies of the separation techniques of flotation, fine sizing, and sink and float and various related concentrating devices, together with cost and design considerations, assembled with a view toward acquainting the chemical engineer with the possibility of applying these techniques in his own field. Vol. 50; paper bound; 85 pp.; $2.50 to members, $3.75 nonmembers.

14-S. Ion Exchange: Data on mixed-bed deionization rare-earth separation, adsorption and stripping, economic evaluation, hydroxide-cycle operations, asymptotic solution of mechanisms, use of gross components. Vol. 50; paper bound; 134 pp.; $3.00 to members, $4.00 to nonmembers.

20-S. Liquid Metals Technology, Part I: A volume on liquid metals problems of special interest to the chemical engineer, it contains ten articles (84 pages) on the manufacture and availability of alkali metals, sodium heat transfer, sampling analysis for impurities, description of high-temperature loops, material transport, corrosion and mass transfer, thermal conductivity, etc. Vol. 53; paper bound; $3.00 to members, $4.00 to nonmembers.

7-S. Applied Thermodynamics: Experimental data, largely on hydrocarbons, and the results of various calculation programs covering enthalpies of mixtures, vapor liquid equilibria, and the thermodynamic properties of single components. Vo. 49; paper bound; 165 pages; $3.00 to members, $4.00 to nonmembers.

6-S. Phase-Equilibria—Collected Research Papers: Papers on the methane-nitrogen ethane-ethylene, and ethyl alcohol-water systems; reduced crudes at subatmospheric pressures; hydrocarbon mixtures; integral calculation, and graphical methods for distillation. Vol. 49; paper bound; 113 pp.; $3.00 to members, $4.00 to nonmembers.

3-S. Phase-Equilibria—Minneapolis and Columbus: Studies of pressure-vapor temperature relations, solubility, graphical techniques, solvent extractions, etc. Vol. 48; paper bound; 122 pp.; $3.00 to members, $4.00 to nonmembers.

2-S. Phase-Equilibria—Pittsburgh and Houston: Studies of vapor-liquid equilibria under such topics as flash vaporization, nomographs, extraction, thermodynamics, isothermal and isobaric equations. Vol. 48; paper bound; 138 pp.; $3.00 to members, $4.00 to nonmembers.

4-S. Reaction Kinetics and Transfer Processes: Data on transfer phenomena in heterogeneous systems, including studies of fixed and fluidized beds, catalytic dehydration, alcoholysis, and diffusion. Vol. 48; paper bound; 125 pp.; $3.00 to members, $4.00 to nonmembers.

1-S. Ultrasonics—Two Symposia: Papers examining possibilities and limitations of applied acoustics in chemical processes and unit operations. Vol. 47; paper bound; 87 pp.; $2.00 to members, $2.75 to nonmembers.

8-S. Communications: Papers stressing accuracy and clarity in written and spoken communication and treating corollary problems such as sound psychological approaches, proper routing of correspondence and information, better accounting and statistical reports, and scientific organization of paper work. Vol. 49; paper bound; 57 pages; $1.00 to members, $1.50 to nonmembers.

21-S. Computer Techniques in Chemical Engineering: 12 papers, primarily on digital-computer techniques in use the the chemical industry. $3.00 to members, $4.00 to nonmembers.

10-S. Collected Research Papers: Developments of air and water-clay suspensions, mass transfer, diffusion, gas-film absorption coefficient, evaporation, vapor-liquid phase equilibria, and vaporization of methanol-benzene mixtures. Vol. 50; paper bound; 142 pp.; $3.00 to members, $4.00 to nonmembers.

1-M Reaction Kinetics in Chemical Engineering by Olaf A. Hougen: A survey of the historical development of chemical kinetics as applied to process design, of the present state of this technology, and of the most promising fields therein for immediate investigation. Vol. 47; paper bound; 78 pp.; $2.25 to members, $3.00 to nonmembers.

2-M. Atomization and Spray Drying by W. R. Marshall, Jr.: Covering the theory of spray drying and its industrial applications. Vol. 50; paper bound; 122 pp.; $3.00 to members, $4.00 to nonmembers.

To be certain receiving all the Symposium Series volumes from now on, return the STANDING ORDER coupon now.

5 DAYS FREE EXAMINATION

Tray Efficiencies in Distillation Columns—Final Report from University of Delaware and North Carolina State College. Research carried out under grants awarded by the Research Committee of the A.I.Ch.E. with funds from forty-one chemical and petroleum companies:

Delaware Report, 120 pp., paper bound. Members $5.00, nonmembers $10.00.

North Carolina Report, 28 pp., paper bound. Members $2.00, nonmembers $4.00.

A.I.Ch.E. MANUALS

Bubble-Tray Design Manual—a concise, practical manual that enables the engineer to predict efficiencies for commercial bubble trays used in multi-component fractionation. It includes sample calculations made on plant-scale columns and contains calculation form sheets for the use of the reader. This manual was produced by the Distillation Subcommittee of the A.I.Ch.E. Research Committee as a culmination of five years of research sponsored by the Institute and the chemical industry. 6 by 9 in., hard cover, $5.00 to A.I.Ch.E. members, $10.00 to nonmembers.

Pump Manual—a comprehensive presentation of available data on chemical pumps, including classification of pumps, relationships among categories and types, nomenclature, installation check lists, inquiry and record forms, guides to materials of construction, ASA mechanical standards, and the A.I.Ch.E. Performance Testing Procedure. 8½ by 11 in., loose-leaf format, $10.00 to A.I.Ch.E. members, $20.00 to nonmembers. Published February, 1960.

A.I.Ch.E. STANDARD TESTING PROCEDURES

Directions for directing and interpreting tests of equipment for comparison with the manufacturer's predicted performance.

1. **Heat Exchangers—Sensible Shell and Tube, members** ..... **$ .25, nonmembers** ..... **$ .50**
2. **Heat Exchangers—Condensers,** **$1.00**
3. **Absorbers,** **$1.00**
4. **Impeller-Type Mixing Equipment,** **$1.50**
5. **Centrifugal Pumps Newtonian Liquids,** **$2.00**

AMERICAN INSTITUTE OF CHEMICAL ENGINEERS
25 West 45 Street
New York 36, New York

Please send these publications:

	Memb.	Nonmember
TRAY EFFICIENCIES IN DISTILLATION COLUMNS		
☐ University of Delaware Report	$ 5.00	$10.00
☐ N. C. State College Report	2.00	4.00
A.I.Ch.E. MANUALS		
☐ Bubble-Tray Design Manual	$ 5.00	$10.00
☐ Calculation Form Sheets	.25	.25
☐ Pump Manual	10.00	20.00
A.I.Ch.E. STANDARD TESTING PROCEDURES		
☐ Heat Exchangers—Sensible Shell and Tube	$ .25	$ .50
☐ Heat Exchangers—Condensers	1.00	1.00
☐ Standard Testing Procedure for Absorbers	1.00	1.00
☐ Impeller-Type Mixing Equipment	1.50	1.50
☐ Centrifugal Pumps (Newtonian Liquids)	2.00	2.00

PRINT Name _____

Company _____

Street _____

City _____

☐ Member ☐ Nonmember

☐ Check enclosed (add 3% sales tax for delivery in New York City)

☐ Bill me J-3-60

INDEX OF ADVERTISERS

Beckman Instruments Inc. 4M
Computer Systems, Inc. 2
Stearns Roger Mfg. Co. 5M
Vulcan-Cincinnati, Inc. ..... Inside Front Cover

Advertising Officers

New York 36—Paul A. Jolcuvar, Adv. Sales Mgr., Carl G. Lassen, Asst. Adv. Sales Mgr., Donald J. Stroop, Dist. Mgr., Robert S. Bugbee, Dist. Mgr.; 25 W. 45th St., COlumbus 5-7330.

Philadelphia—Lee W. Swift, Jr., Dist. Mgr.; 1207 Broad-Locust Bldg., PEnnypacker 5-5560.

Chicago 4—Martin J. Crowley, Jr., Dist. Mgr.; Robert Kliesch, Dist. Mgr.; 53 West Jackson Blvd., Room 504, HArrison 7-3760.

Cleveland 15—Harry L. Gebauer, Dist. Mgr., 1501 Euclid Ave., SUperior 1-3315.

Pasadena 1, Calif.—Richard P. McKey, Dist. Mgr., 465 East Union St., MUrray 1-0685.

Dallas 18—Richard E. Hoierman, Dist. Mgr., 9006 Capri Drive, DIamond 8-1229.

Birmingham 9, Ala.—Fred W. Smith, Dist. Mgr., 1201 Forest View Lane, Vesthaven, TRemont 1-5762.

IMPORTANT NOTICE

If your address has changed, please fill out this form and mail to A.I.Ch.E. JOURNAL, 25 West 45th Street, New York 36, New York.

EFFECTIVE DATE OF NEW ADDRESS _____ DATE OF THIS NOTICE _____

PREVIOUS ADDRESS

STREET NUMBER, STREET NAME, POST OFFICE BOX NUMBER _____

NAME OF CITY OR TOWN _____ ZONE NO. _____ NAME OF STATE _____

NEW ADDRESS

STREET NUMBER, STREET NAME, POST OFFICE BOX NUMBER _____

NAME OF CITY OR TOWN _____ ZONE NO. _____ NAME OF STATE _____

PRINT NAME & MEM. REF. NO. _____ SIGN NAME HERE _____